Seismic Performance of Steel Plate Shear Walls Considering Various Design Approaches
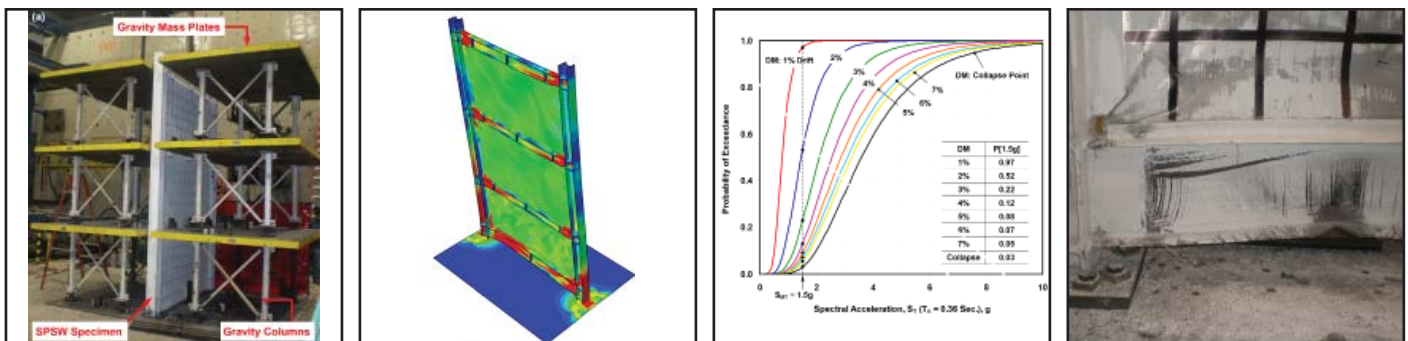
by

Ronny Purba and Michel Bruneau

NOTICE

Seismic Performance of Steel Plate Shear Walls Considering Various Design Approaches

by

Ronny Purba[1] and Michel Bruneau[2]

Publication Date: October 31, 2014
Submittal Date: May 7, 2014

Technical Report MCEER-14-0005

1   Assistant Professor, Department of Civil Engineering, University of Minnesota Duluth and Former Ph.D. Candidate, Department of Civil, Structural and Environmental Engineering, University at Buffalo, State University of New York
2   Professor, Department of Civil, Structural, and Environmental Engineering, University at Buffalo, State University of New York

PREFACE

MCEER is a national center of excellence dedicated to the discovery and development of new knowledge, tools and technologies that equip communities to become more disaster resilient in the face of earthquakes and other extreme events. MCEER accomplishes this through a system of multidisciplinary, multi-hazard research, education and outreach initiatives.

Headquartered at the University at Buffalo, State University of New York, MCEER was originally established by the National Science Foundation (NSF) in 1986, as the first National Center for Earthquake Engineering Research (NCEER). In 1998, it became known as the Multidisciplinary Center for Earthquake Engineering Research (MCEER), from which the current name, MCEER, evolved.

Comprising a consortium of researchers and industry partners from numerous disciplines and institutions throughout the United States, MCEER's mission has expanded from its original focus on earthquake engineering to one which addresses the technical and socioeconomic impacts of a variety of hazards, both natural and man-made, on critical infrastructure, facilities, and society.

MCEER investigators derive support from the State of New York, National Science Foundation, Federal Highway Administration, National Institute of Standards and Technology, Department of Homeland Security/Federal Emergency Management Agency, other state governments, academic institutions, foreign governments and private industry.

This report presents the results of experimental and analytical studies to investigate the seismic performance of steel plate shear walls (SPSWs) considering different design philosophies of horizontal boundary elements (HBEs) and infill plates. The experimental study on a three-story SPSW specimen showed the development of HBE in-span hinges which resulted in an accumulation of plastic incremental deformations. A finite element investigation on the tested SPSW specimen demonstrated similar behavior. Furthermore, collapse assessment of SPSWs with various structural configurations (e.g., panel aspect ratio, seismic weight intensity, and number of stories) was conducted to investigate impact of sharing of story shear forces between the boundary frames and infill plates on the performance of SPSWs. SPSWs designed with the current seismic performance factors specified in the ASCE 7-10 and neglecting the contribution of their boundary moment resisting frames to resist story shear forces met the FEMA P695 performance criterion, while that was not the case for SPSWs designed considering the sharing of story shear forces between the boundary frame and infill plates. Adjusted seismic performance factors were required for the latter SPSWs to rigorously meet the FEMA P695 performance criteria. Most importantly, the latter SPSWs were found to have a higher probability to suffer significantly larger interstory drift than the former. This research extends work reported in "Impact of Horizontal Boundary Elements Design on Seismic Behavior of Steel Plate Shear Walls" by R. Purba and M. Bruneau, MCEER-10-0007. The finite element analysis was performed using the software ABAQUS/Standard while the collapse assessment was performed using the software OpenSees.

ABSTRACT

Research was conducted to investigate the seismic performance of steel plate shear walls (SPSWs) considering different design philosophies of horizontal boundary elements (HBEs) and infill plates. First, an experimental study on a three-story SPSW specimen was performed to investigate the impact of HBE in-span hinges on the seismic behavior of SPSW. A finite element investigation on the tested SPSW specimen demonstrated the development of in-span plastification and accumulation of plastic incremental deformations.

Second, collapse assessment of SPSWs with various structural configurations (e.g., panel aspect ratio, seismic weight intensity, and number of stories) was conducted to investigate impact of sharing of story shear forces between the boundary frames and infill plates on the performance of SPSWs. The FEMA P695 methodology was used for this purpose. SPSWs designed with the current seismic performance factors specified in the ASCE 7-10 (i.e., R, Ω_o, and C_d factors are 7, 2, and 6, respectively) and neglecting the contribution of their boundary moment resisting frames to resist story shear forces met the FEMA P695 performance criterion, while that was not the case for SPSWs designed considering the sharing of story shear forces between the boundary frame and infill plates. Adjusted seismic performance factors (i.e., R, Ω_o, and C_d factors are 5, 1, and 5, respectively) were required for the latter SPSWs to rigorously meet the FEMA P695 performance criteria. Most importantly, the latter SPSWs were found to have a higher probability to suffer significantly larger interstory drift than the former.

ACKNOWLEDGEMENTS

TABLE OF CONTENTS

TABLE OF CONTENTS (CONT'D)

TABLE OF CONTENTS (CONT'D)

LIST OF FIGURES

LIST OF FIGURES (CONT'D)

LIST OF FIGURES (CONT'D)

LIST OF FIGURES (CONT'D)

LIST OF FIGURES (CONT'D)

LIST OF FIGURES (CONT'D)

LIST OF FIGURES (CONT'D)

LIST OF FIGURES (CONT'D)

FIGURE   TITLE   PAGE

LIST OF TABLES

LIST OF TABLES (CONT'D)

NOTATIONS

A_b	gross cross-sectional areas of the story HBE
A_c	gross cross-sectional areas of the story VBE
$ACMR_{10\%}$	acceptable ACMR corresponding to a 10% collapse probability
$ACMR_{20\%}$	acceptable ACMR corresponding to a 20% collapse probability
A_w	web area of boundary elements
B_I	constant specified in Table 18.6-1 of ASCE 7-05 for a given β_I
b	flange width of boundary element section
C_d	deflection amplification factor
d	total depth of boundary element section
E	Young's modulus
F_D	design story shear force
F_p	panel plastic strength
F_y	yield stress of steel
F_{yb}	HBE yield stress
F_{yp}	infill plate yield stress
h	frame story height; web length or the distance between top and bottom flanges
h_i	height from the base to the i-th story
H_s	story height
I_c	moment inertia of VBE.
L	frame bay width
L_b	HBE span
L_p	clear length of the infill plate; plastic hinge length
M_p	theoretical flexural plastic moment capacity
M_w	moment magnitude of seismic source
R	site-to-source distance
$R_y; R_{yp}$	ratio of the expected to the specified steel (plate) yield stress
$\hat{S}_{CT}$	median collapse capacity
S_{DI}	one-second spectral ordinates
S_{DS}	design short spectral ordinates

S_{MT}	response spectrum of MCE ground motions
T	fundamental period of a structure
t_i; t_{pi}	infill thickness provided at the i-th story
t_w; t_{wi}	required infill plate thickness to resist story shear forces at the i-th story
V	total base shear, design base shear strength
V_b	shear force on HBE
V_{ei}	expected shear strength at the i-th story
V_{max}	maximum base shear strength for a given archetype model
V_i	story shear force or applied lateral load at the i-th story
V_{ui}	lateral seismic force at the i-th story
W_i	i-th story weight
W_m	total tributary weight for specimen
W_p	prototype tributary weight
W_t	total weight of the structure
y^*	distance from the neutral axis to the location where strain reaches yield point
Z	plastic modulus

α	tension field inclination angle
β_{DR}	uncertainty related to the completeness and robustness of design requirements
β_I	inherent effective damping
β_{MDL}	uncertainty related to modeling nonlinear collapse behavior
β_{RTR}	ground motion record-to-record uncertainty
β_{TD}	uncertainty related to the completeness and robustness of test data
β_{TOT}	total system collapse uncertainty
δ	HBE vertical deformations
δ_u	ultimate roof displacement of the archetype model
$\delta_{y,eff}$	effective yield roof displacement of the archetype model
Δ	top story lateral displacement
$\Delta_{failure}$	specimen cyclic capacity at failure point
Δ_{max}	specimen cyclic capacity at capping point

δ_y	strip yield displacement
ε_{nom}	nominal strain obtained from coupon tests
$\varepsilon_{\ln}^{pl}$	logarithmic plastic strain
ε_y	yield strain of steel
ϕ	strength resistance factor for SPSW web; cross-section curvature; mode shape
κ	percentage of total design story shear forces assigned to the infill plate
$\kappa_{balanced}$	percentage of total design story shear forces assigned to the infill plate at balanced condition ($\Omega_\kappa = 1.0$)
λ_E	scale factors for material properties
λ_F	scale factors for forces
λ_L	scale factors for length (geometry)
μ_T	period base ductility in FEMA P695
θ	angle between the deformed structure and the vertical in kinematic method; angle of flexural rotation
$\theta_{0.03}$	required plastic rotation capacity of a SMRF (0.03 radians)
σ_y	yield stress of steel
σ_{nom}	nominal stress obtained from coupon tests
σ_{true}	"true" stress (Cauchy stress)
Ω_κ	system overstrength factor at a specific κ factor
Ω_o	system overstrength factor in FEMA P695
ω_i	scale factor in imperfection analysis

ABBREVIATIONS

ACMR	Adjusted Collapse Margin Ratios
AISC	American Institute of Steel Construction
ASCE	American Society of Civil Engineers
ASTM	American Society for Testing and Materials Standard
ATC	Applied Technology Council
BCH	Beam with Concentrated Hinge element
CDF	Cumulative Distribution Function
CFRP	Carbon Fiber Reinforced Polymer
CJP	Complete Joint Penetration
CMR	Collapse Margin Ratios
CSA	Canadian Standards Association
DAQ	Data Acquisition
DBE	Design Basis Earthquake
EBC	Elastic Beam-Column element
EDC	Energy Dissipated per Cycle
EMR	Exceedance Margin Ratio
FBE	Failure of Boundary Elements
FEA	Finite Element Analysis
FEM	Finite Element Method
FEMA	Federal Emergency Management Agency
HBE	Horizontal Boundary Elements
HAZ	Heat Affected Zone
ICD	Indirect Capacity Design
IBE	Instability of Boundary Elements
IDA	Incremental Dynamic Analysis
LED	Light-Emitting Diode
LTB	Lateral Torsional Buckling
LVDT	Linear Variable Differential Transformers
MCE	Maximum Considered Earthquake

NDT	Non-Destructive Testing
NEES	Network for Earthquake Engineering Simulation
NGA	Next Generation Attenuation
NLB	Nonlinear Beam-Column element
PEC	Partially Encased Column
PEER	Pacific Earthquake Engineering Research Center
PGA	Peak Ground Accelerations
PTFE	Poly-Tetra-Fluoro-Ethylene
RBS	Reduced Beam Section
SAP2000	Structural Analysis Program 2000
SEESL	Structural Engineering and Earthquake Simulation Laboratory
SDC	Seismic Design Category
SMRF	Special Moment Resisting Frame
SPF	Seismic Performance Factors
SPSW	Steel Plate Shear Wall
SSF	Spectral Shape Factor
TFA	Tension Field Action
VBE	Vertical Boundary Elements
WT	Web Tearing
WUF-W	Welded Unreinforced Flange-Welded Web
ZLS	Zero-Length Section element

SECTION 1

INTRODUCTION

1.1 Motivation and Background

There have been numerous experimental and analytical studies investigating the behavior of unstiffened steel plate shear walls (SPSWs) in the past thirty years. An AISC Design Guide (Sabelli and Bruneau 2007) summarizes that research which has addressed the design and modeling of SPSW web plates, general SPSW analysis methods, validation of satisfactory cyclic inelastic and seismic performances, and analytical procedures to calculate demands in the horizontal and vertical boundary elements (HBEs and VBEs) of SPSWs (e.g., Thorburn *et al.* 1983; Timler and Kulak 1983; Caccese *et al.* 1993; Driver *et al.* 1997, Berman and Bruneau 2003, 2008; Qu *et al.* 2008). This information, together with a detailed presentation of the latest knowledge on the behavior and design of SPSWs, is also available in Bruneau *et al.* (2011). As a result of this research, provisions for SPSW design have been adopted (e.g. the 2005 and 2010 AISC Seismic Provisions for Structural Steel Buildings) and they have been increasingly implemented in seismic regions.

However, even though SPSWs are commonly designed nowadays, two important ambiguities remain regarding how they should be designed; how engineers address each of these ambiguities can have significant cost implications. Available design examples in the literature have added to the confusion by arbitrarily dealing with the ambiguities, in absence of data providing substantive guidance on how to make those design decisions. These two design ambiguities are described in the following two sub-sections. Section 1.2 summarizes the work conducted here to generate the knowledge needed to resolve the ambiguities and to ensure the satisfactory seismic performance of SPSWs.

1.1.1 Impact of In-span Plastic Hinges

In seismic design applications, the primary energy dissipating elements of SPSWs resisting lateral loads are their unstiffened infill plates (webs), which buckle in shear and form a series of

diagonal tension field action (TFA). In a capacity design perspective, the tension force from the infill plates must be resisted by the surrounding HBEs and VBEs. The seismic provisions (i.e., AISC 2005, 2010) requires that HBEs and VBEs be designed to remain essentially elastic under the maximum tension forces from the yielded infill plates, with the exception of plastic hinging at the ends of HBEs. Implicitly, this indicates that in-span plastic hinges should be avoided.

However, the provisions do not specify an analysis procedure to guarantee that this intent is met (although the commentary provides some guidance that could be used for this purpose). As a result, structural engineers might not anticipate that their designs may lead to in-span HBE plastic hinges (unless these analyses are complemented by the use of nonlinear analysis programs to predict the plastic mechanism of structures). In parallel, some structural engineers fully recognize the potential for in-span hinging to develop, but question the merit of limiting the location of plastic hinges to only occur at the ends of HBEs because, in general, this design requirement results in relatively larger boundary elements. Thus, to achieve more economical designs, these structural engineers may try to minimize overstrength by allowing plastic hinges to occur along HBE span, as this leads to relatively smaller boundary elements. Whether or not in-span hinging is acceptable has been a contentious issue, particularly in the absence of factual data to support either position.

1.1.2 Story Shear Distribution between Infill Plate and Boundary Frame

In most applications of SPSWs, rigid connections are specified between HBEs and VBEs, as well as between VBEs and the ground. This implies that a boundary moment resisting frame action exists within SPSWs. While such boundary frames do contribute to the lateral load resistance of SPSWs, it is unclear whether that boundary frame should be accounted to resist the code-specified story shear forces.

The current Canadian Standard (i.e., CSA 2009) for the design of steel structures specifies that infill plates of SPSWs must be designed to resist the entire lateral loads, without considering the possible contribution from the surrounding boundary moment resisting frame. Such a statement is not explicitly included in the American Seismic Provisions (i.e., AISC 2010b), but one possible interpretation of the AISC design specifications could lead to the same design approach. In this

approach, HBEs and VBEs are designed to resist the tension field forces generated by the fully yielded infill plates, and the resulting boundary frame moment resisting action contributes to the global plastic lateral strength of the SPSW by adding overstrength (i.e., lateral load resistance above the specified story-shear force).

In another approach, resistance of the specified story-shear forces is divided between the infill plate and the boundary frame, in arbitrary proportions. This results in more economical SPSWs (due to less tonnage of steel) and a reduction of wall overstrength. As reported in past experiments, this overstrength in conventional SPSWs can be quite significant. For example, Driver *et al*. (1997) reported that boundary frame moment resisting action contributed about 25% to the global plastic strength of their four-story SPSW specimen. The same observation was also made by Berman and Bruneau (2005), who indicated that the boundary frame of their single story SPSW specimen contributed 38% to the total strength of the wall. Qu and Bruneau (2009) demonstrated that boundary frame moment resisting action can contribute up to 50% of the total strength of a SPSW with aspect ratio of 2.0 when its boundary elements are designed per capacity design principles. In other words, in such a case, the total lateral strength of the SPSW is twice that needed to resist the total specified lateral loads. Such reports provide a significant incentive to reduce overstrength by explicitly considering the boundary frame moment resisting action of SPSW to resist a share of the specified story shear forces. However, the consequences of reducing this overstrength are unknown, and opinions vary as to whether this should be permitted.

1.2   Scope and Objectives

The research presented here investigates the seismic performance of SPSWs considering various design approaches to address the above two design issues related to the in-span HBE plastic hinging and to the sharing of lateral loads between the boundary frame and infill plates.

To investigate the first design issue, one must first determine whether in-span HBE plastic hinging, when it happens, can impact in any way the seismic performance of SPSWs – irrespectively of whether it develops in a SPSW intentionally or as a result of unintended design consequences. Specifically, this is done by investigating the seismic behavior of two SPSWs

3

having HBEs designed to have different plastic mechanisms. The first design approach does not guarantee that formation of in-span plastic hinges on HBEs will be prevented, whereas the second approach guarantees that plastic hinges can only occur at the ends of HBEs. Monotonic and cyclic pushover analyses as well as nonlinear time-history analyses are conducted to assess the relative performance of the two SPSWs. Findings of this analytical investigation on in-span HBE plastic hinge have been presented in Purba and Bruneau (2010). The current report complements this previous analytical study by presenting an experimental investigation conducted to observe whether in-span HBE plastic hinging can actually occur in SPSWs. A three-story SPSW specimen tested under cyclic pushover loading is selected for this purpose. Subsequently, a finite element investigation of the tested specimen is conducted.

To address the second design issue, this research investigates the seismic performance of SPSWs having infill plates designed per two different philosophies, to resist different percentages of the specified story shear forces. Using the FEMA P695 methodology (FEMA 2009b), which defines the performance in terms of collapse potential under maximum considered earthquake (MCE) ground motions, the assessment is first conducted on SPSWs designed neglecting the contribution of their boundary moment resisting frames to resist story shear forces. In other words, infill plates are designed to resist the entire story shear forces. Then, this assessment of collapse potential is repeated for SPSWs designed considering the sharing of story shear forces between the boundary frames and infill plates.

For this second design issue, note that the validity of the results obtained using the FEMA P695 methodology critically depends on the accuracy of the structural numerical models used to simulate the component strength deterioration that will eventually lead to global collapse of the system, as these will affect the results of the incremental dynamic analyses used to assess the seismic performance. Therefore, work is conducted to develop component strength deterioration models for infill plates and boundary elements to be used in the collapse assessment of SPSWs.

1.3 Outline of Report

Section 2 presents brief reviews of past research on the use of unstiffened SPSWs as a lateral force resisting system, degradation modeling of structural components to provide a basis in constructing degradation models for SPSW components (i.e., infill plates and boundary elements), and the FEMA P695 collapse assessment methodology used to investigate the seismic performance of SPSWs designed per different philosophies.

Section 3 describes the design of a three-story 1/3 scale SPSW specimen to be tested under cyclic pushover loading. Specifically, this section describes design considerations to reflect a case when in-span plastic hinging is predicted to develop, fabrication process, experimental setting, and development of loading protocol of three dynamic actuators.

Experimental observations and results for the cyclic pushover testing of the three-story SPSW specimen are presented in Section 4. To investigate whether the experimental objectives are achieved, several key experimental results are examined such as hysteretic behavior of story shear versus specimen lateral displacement, plastic hinge and infill plate yielding distributions, HBE vertical deformations, and moment-rotation hysteresis.

Section 5 describes model development and analytical results of a finite element investigation of the tested SPSW specimen. Eigenvalue buckling analysis, monotonic pushover analysis, and cyclic pushover analysis are conducted to investigate behavior. The effectiveness of the finite element model developed simulating the experimental results is discussed.

Section 6 describes the development of SPSW component strength deterioration models to be used in collapse assessment of SPSWs, focusing on developing stress-strain or force-deformation relationships for infill plates and boundary elements. Based on 36 tested specimens, deterioration and failure modes are identified; and initial deterioration models for SPSWs components are developed. The chosen deteriorated material models for infill plates and boundary elements are then calibrated to four selected SPSW specimen varying from one- to four-story.

Section 7 describes the development of archetypes and non-linear models for collapse assessment of SPSWs. SPSW archetypes are designed considering the two different philosophies of infill plates mentioned in the previous section. The concept of "balanced" sharing between infill plate and boundary frame proposed by Qu and Bruneau (2009) is revisited.

Using the strength degradation material model and nonlinear structural model developed in the two previous sections, Section 8 investigates the collapse assessment results. Seismic performance factors (i.e., response modification coefficient or R-factor, system overstrength Ω_0 factor, and deflection amplification C_d factor) for both types of SPSWs are identified and compared. Adjustments to improve collapse performance and factors that affect collapse potential are presented, along with collapse fragility curves for archetypes having various structural configurations (i.e., panel aspect ratio, intensity level of seismic weight, and number of story). Finally, summary, conclusions, and recommendations for future research are presented in Section 9.

SECTION 2

LITERATURE REVIEW

2.1 General

This section consists of three parts. First is a brief review of past research relevant to this study on unstiffened steel plate shear walls (SPSWs) as a lateral force resisting system, focusing on the aspects of system behavior and design principles, modeling and analysis, and experimental research. Second is a summary of previous studies on modeling the degradation of structural components, for the purpose of identifying the aspects of degradation models needed to construct them for SPSW components (i.e., infill plates and boundary elements). Finally, a review is provided of the collapse assessment methodology outlined in FEMA P695, as this methodology is used in Sections 6 to 7 to investigate the seismic performance of SPSWs designed per different philosophies. A comprehensive presentation of the entire body of knowledge on SPSWs is not provided here, since many other recent publications provide such extensive reviews.

2.2 Steel Plate Shear Walls as a Lateral Force Resisting System

Steel plate shear walls (SPSWs) have been used as a lateral force resisting system since first developed in early 1970s. The system typically used in North American construction projects consists of unstiffened steel infill plates connected to the surrounding beams and columns (a.k.a. horizontal boundary elements (HBEs) and vertical boundary elements (VBEs), respectively) and generally installed along the full height of a structure to form a cantilever wall, as schematically shown in Figure 2-1. The main advantage of SPSW systems that contributes to their progressively more widespread acceptance is the significant stiffness and strength they can provide to buildings compared to other lateral force resisting systems. SPSWs are also lighter than reinforced concrete shear walls, applicable for new design or retrofit projects, and relatively easy to construct (Astaneh-Asl 2001; Sabelli and Bruneau 2007). In addition, SPSWs can be economically attractive compared to reinforced concrete shear walls (Timler *et al*. 1998).
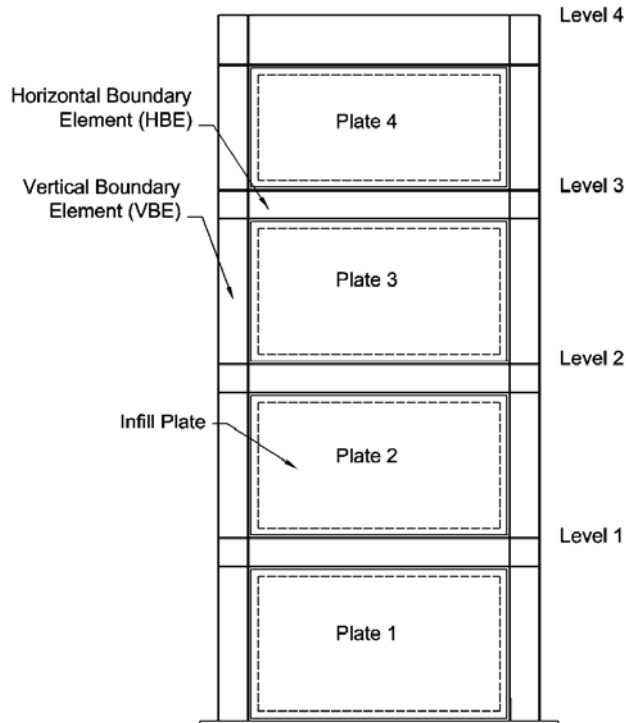
Figure 2-1 Schematic of Steel Plate Shear Walls (AISC 2010b)

Many publications have provided an extensive review on the historical development of steel plate shear walls (e.g., Astaneh-Asl 2001; Purba and Bruneau 2007; Sabelli and Bruneau 2007; Bruneau *et al.* 2011). Those publications reviewed the design philosophy of SPSWs (which evolved from a system designed with highly stiffened infill plates to that with unstiffened infill plates used nowadays in several countries, such as the United States, Canada, and Mexico), the analytical and experimental studies conducted by many researchers over several decades, the design and modeling of SPSWs, and the codification of SPSWs. The review presented in this section is not intended to reiterate the same information reported in those publications but rather to highlight the key aspects of unstiffened SPSWs behavior and modeling that would provide sufficient background to this research.

2.2.1 System Behavior and Design Principles of Steel Plate Shear Walls

In seismic design applications, the primary energy dissipating elements of SPSWs resisting lateral loads are their unstiffened infill plates (webs), which buckle in shear and form a series of diagonal tension field action (TFA). In a capacity design perspective, the tension force from the infill plates must be resisted by the surrounding boundary elements (i.e., HBEs and VBEs). Figure 2-2 shows

8

free-body diagrams of internal forces developed in a typical SPSW. Note that, for simplicity, no end moments are shown in those diagrams and the tension force from the infill plates is uniform along the length of boundary elements. This uniform tension force will develop if the boundary elements are infinitely rigid (Thorburn *et al*. 1983, Purba and Bruneau 2007), or at drifts sufficiently large to fully yield the infill for the case of flexible HBEs, which typically is the case at approximately 1% drift (Qu and Bruneau 2010). The tension force distribution from the infill plates attached to regular size boundary elements is discussed in Purba and Bruneau (2010).

When rigid connections are specified between HBEs and VBEs, as well as between VBEs and the ground (as specified in many applications of SPSWs), SPSWs also benefit from the boundary frame's moment resisting action to resist the applied lateral loads. Recognizing the contribution of the boundary frame to the overall strength of the system, Qu and Bruneau (2009) reported that the attraction may exist to account for it as a means to optimize SPSW designs, rather than relying on the presence of the system overstrength it may provide to resist the specified lateral loads. A more detailed review of this topic will be presented in Section 7 when investigating the behavior of SPSW considering boundary frame moment resisting action.

Several researchers (e.g., Roberts and Sabouri-Ghomi 1991; Sabouri-Ghomi *et al*. 2005; Alinia and Dastfan 2006) used the well-known elastic buckling load of flat unstiffened plates (such as the one presented in Timoshenko and Gere 1961) to investigate the behavior of thin and slender infill plates in SPSWs, and found it to predict strength largely below the ultimate strength that SPSWs can develop. This is because the infill plates, which have relatively large resistance in tension but practically no compression resistance, behave analogously to tension-only bracing, with the exception that the tension forces from the infill plates act along the entire length of the boundary elements rather than at only one point (e.g., at the intersections of beams and columns in the case of a concentric braced frame). In some ways, because of this diagonal tension field action, the behavior of SPSW has sometimes been compared to that of a vertical plate girder. However, while this analogy provides a conceptual understanding of SPSW behavior, it cannot be used for design as many significant differences related to the behavior and strength of the two systems exist; detailed explanations and comparisons between the two systems can be found in Berman and Bruneau (2004).
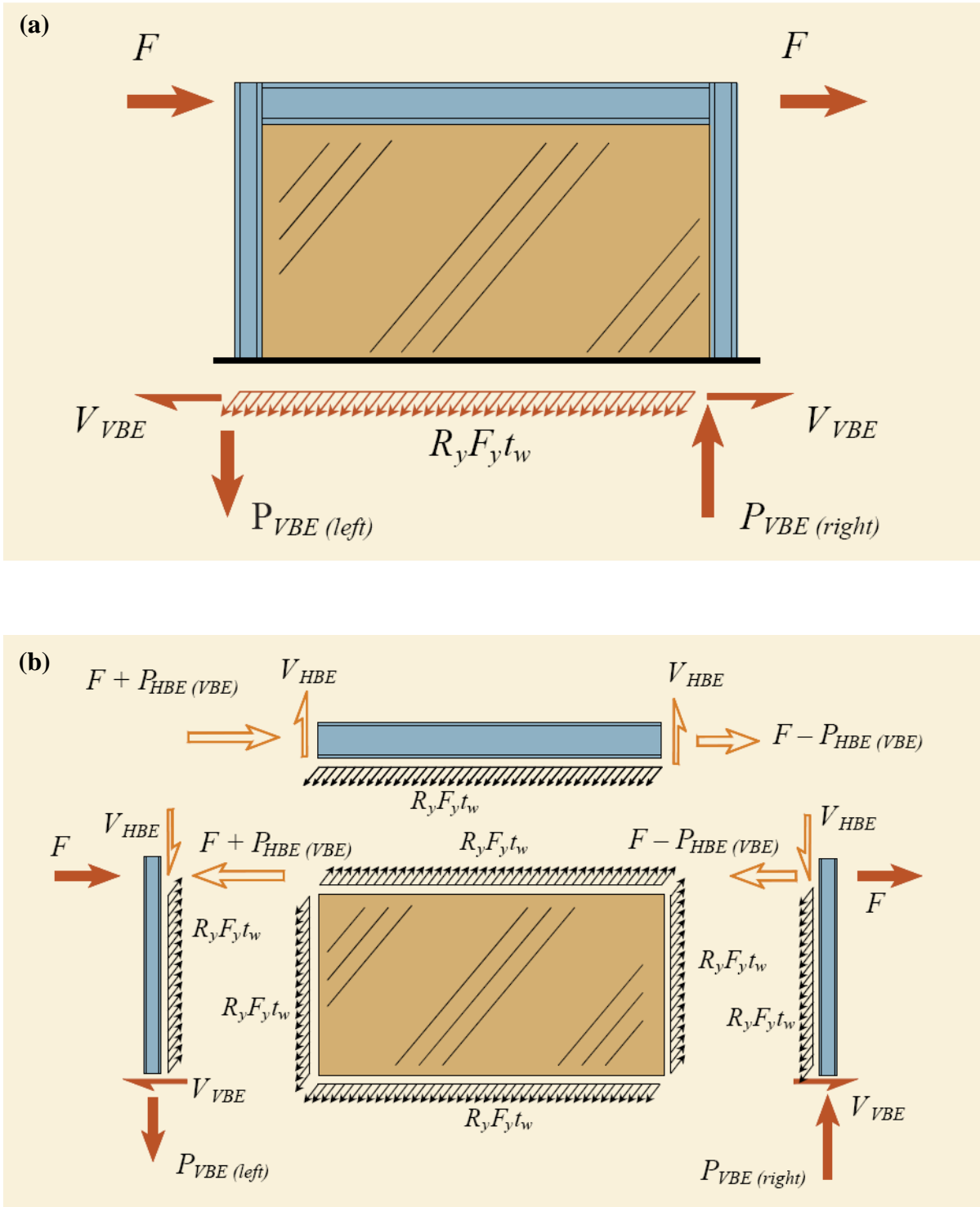
Figure 2-2 Free-body Diagrams of Steel Plate Shear Walls (Ericksen and Sabelli 2008): (a) Applied Force and Base Reactions; (b) Forces on Infill Plate and Boundary Elements

(c)

Figure 2-2 Free-body Diagrams of Steel Plate Shear Walls – Cont'd: (c) Forces on Intermediate HBE and VBEs

Using capacity design principles, one can design SPSWs to behave in a ductile manner when subjected to earthquake loading. Assuming that tension field action can be developed across the entire panel (which is possible when providing adequately stiff boundary elements), the surrounding boundary elements must be designed to be able to sustain the maximum forces developed by the fully yielded infill plates (AISC 2010b, CSA 2009). When resisting the maximum expected forces from the yielded infill plates, the surrounding HBEs and VBEs are to remain elastic, with the exception of plastic hinging at HBE ends and at the base of the first story VBEs, which are needed to allow development of the uniform plastic collapse sway mechanism of the system (further shown in Figure 2-6b). As a result of the SPSW response to the overall overturning and story shear force, as well as due to the tension force from yielded infill plates, axial and shear member forces can be significant in the boundary elements and can cause substantial reduction on their plastic moment capacity. Hence, it is important to consider the combination of axial forces, shears, and moments (i.e., P-V-M interaction) when sizing the boundary elements (Berman and Bruneau 2008; Qu and Bruneau 2008; Qu and Bruneau 2010).

11

The commentary to the 2010 AISC Seismic Provisions for Structural Steel Buildings (AISC 2010b) provides some guidance regarding the analytical methods that could be used to perform the capacity design for SPSWs, namely: nonlinear pushover analysis, indirect capacity design (ICD) approach, and combined plastic and linear analysis. The first method requires analysis using a strip model (see the following sub-section) to verify that the desirable uniform plastic collapse mechanism is achieved, and to obtain axial forces, shears and moments in the boundary elements as a result of these fully yielded infill plates and specified external loads. Like in the first method, a strip model is also required for the ICD approach. This method however, only relies on elastic analysis of the strip model. The resulting internal forces in the boundary elements from this elastic analysis due to the design seismic loads are then multiplied by an amplification factor, with an expectation it would produce similar internal forces as that from a nonlinear pushover analysis (AISC 2010b). By contrast, the last approach does not require analysis of a strip model to estimate the internal forces in the boundary elements; rather, they are estimated from the free-body diagrams obtained from an assumed uniform plastic collapse mechanism. It was reported that this procedure provided comparable results to those from a nonlinear pushover analysis (Berman and Bruneau 2008).

2.2.2 Modeling and Analysis of Steel Plate Shear Walls

A number of techniques for the modeling and analysis of steel plate shear walls has been reported in the literature. The three most common techniques are highlighted and briefly explained here, namely: strip model, plastic analysis, and finite element analysis.

Strip Model

The strip model is the most widely used model to analyze steel plate shear walls. Originally proposed by Thorburn *et al.* (1983), the strip model consists of series of tension strips (typically of equal area), pin-connected to the surrounding boundary frame and inclined in the direction of the tension field (Figure 2-3a). A schematic of strip model for multi-story SPSW is shown in Figure 2-3b. A minimum of 10 strips per panel is required to represent the infill plate behavior. Timler and Kulak (1983) developed the following equation to estimate the inclination angle of the tension field (α), which considers geometric properties of the infill plates and boundary elements at the story level of interest:

$$\tan^4 \alpha = \left[\dfrac{1 + \dfrac{t_w L}{2 A_c}}{1 + t_w h \cdot \left(\dfrac{1}{A_b} + \dfrac{h^3}{360 I_c L} \right)} \right] \qquad (2\text{-}1)$$

where L is the frame bay width, h is the frame story height, t_w is the panel thickness, A_b and A_c are gross cross-sectional areas of the story HBE and VBE, respectively, and I_c is the moment inertia of VBE. This equation was adopted by the Canadian and American codes for design of SPSWs (i.e., CSA 2009 and AISC 2010b). The strength of well-designed SPSW is not sensitive to the tension field angle (Rezai 1999; Dastfan and Driver 2008) and therefore selecting a constant value of 40° is permitted by these codes as it will typically lead to reliable results. For modeling simplicity, however, it is deemed appropriate to assume the angle of the tension strip as 45° from the vertical, especially for a dual strip model (further shown in Figure 2-4).
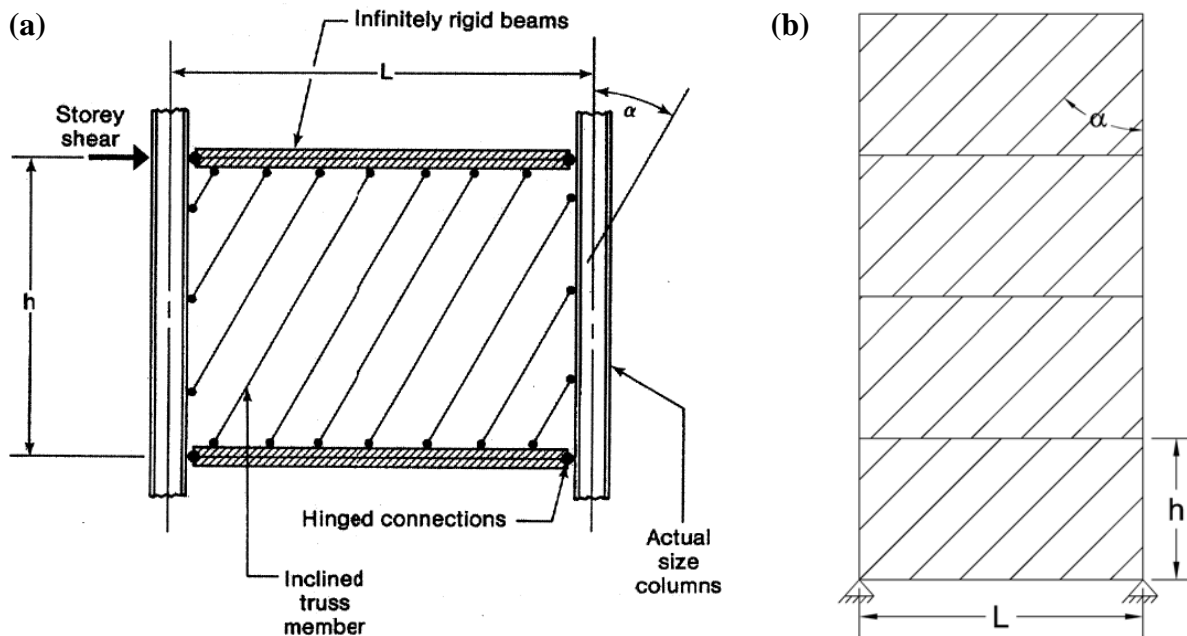
Figure 2-3 Schematic of SPSW Strip Model: (a) Single Story (Thorburn et al. 1983); (b) Multi Story (AISC 2010b)

In addition to the ability of the strip model to closely approximate the behavior of unstiffened infill plates observed in experimental studies, the strip model is relatively simple to apply using structural analysis softwares (e.g., SAP2000, OpenSees, etc.). Researchers have reported that this

model can be reliably used for single-story as well as multistory SPSWs with unstiffened infill plates (e.g., Timler and Kulak 1983; Tromposch and Kulak 1987; Driver *et al.*, 1998; Elgaaly 1998; Berman and Bruneau 2003, 2005; Qu and Bruneau 2008). For cyclic loading, a dual strip model is required to account for reorientation of the tension field direction as the loading direction changes (Figure 2-4). This model is similar to the standard strip model, except that strips are added in the opposite direction at the same inclination angle. Elgaaly *et al.* (1993) reported that the dual strip model shown in Figure 2-4a adequately replicated the global behavior of their 3-story SPSW specimens subjected to cyclic pushover loading. The same was also reported by Qu and Bruneau (2008) for their 2-story SPSW specimen (Figure 2-4b) subjected to pseudo-dynamic loading.
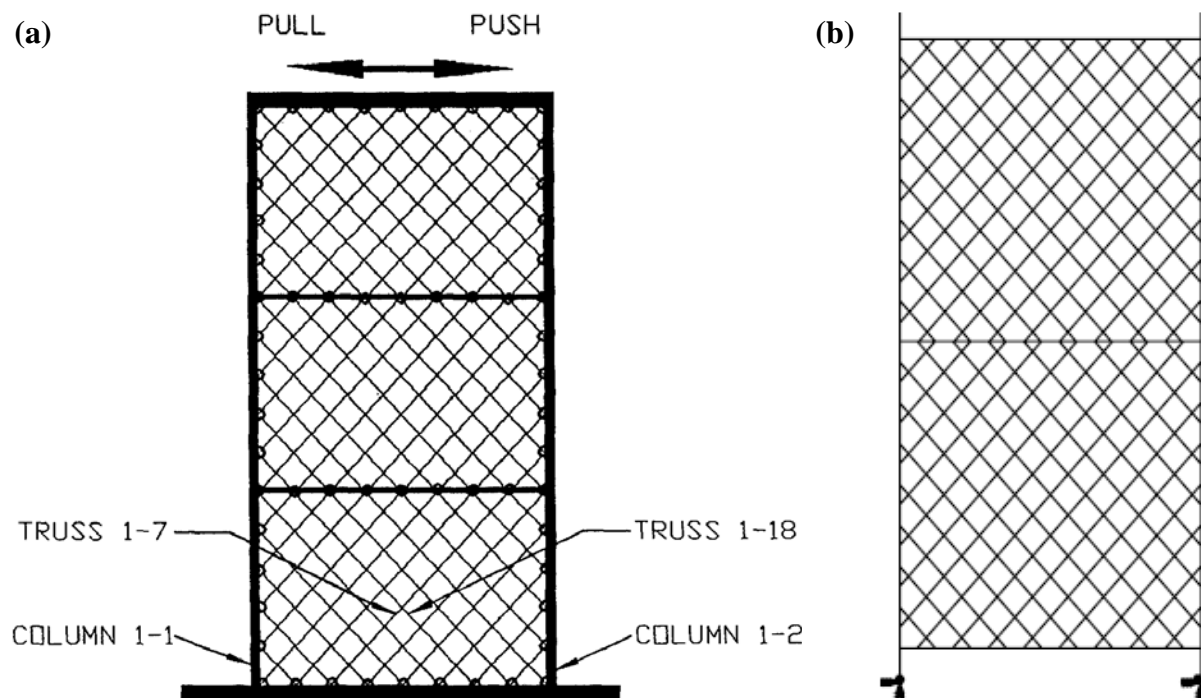
Figure 2-4 Dual Strip Model for Cyclic Simulation: (a) Application for 3-Story SPSW (Elgaaly *et al*. 1993); Application for 2-Story SPSW (Qu and Bruneau 2008)

Rezai (1999) and Shishkin *et al*. (2009) used alternative strip models in their research. The former proposed a multi-angle strip model to capture the variation of the tension field action across the panel. One strip was placed diagonally between opposite panel corners and another four strips were placed from the corners to the mid-span of boundary elements (Figure 2-5a). The latter proposed a modification to the standard strip model by adding a compression strip (strut)

14

placed on the opposite direction to the tension strips (Figure 2-5b) as a means to account for the compression resistance of the infill plates, which may be significant in the corner regions. Both researchers reported a good correlation between their analytical results using these modified strip models and selected experimental results.
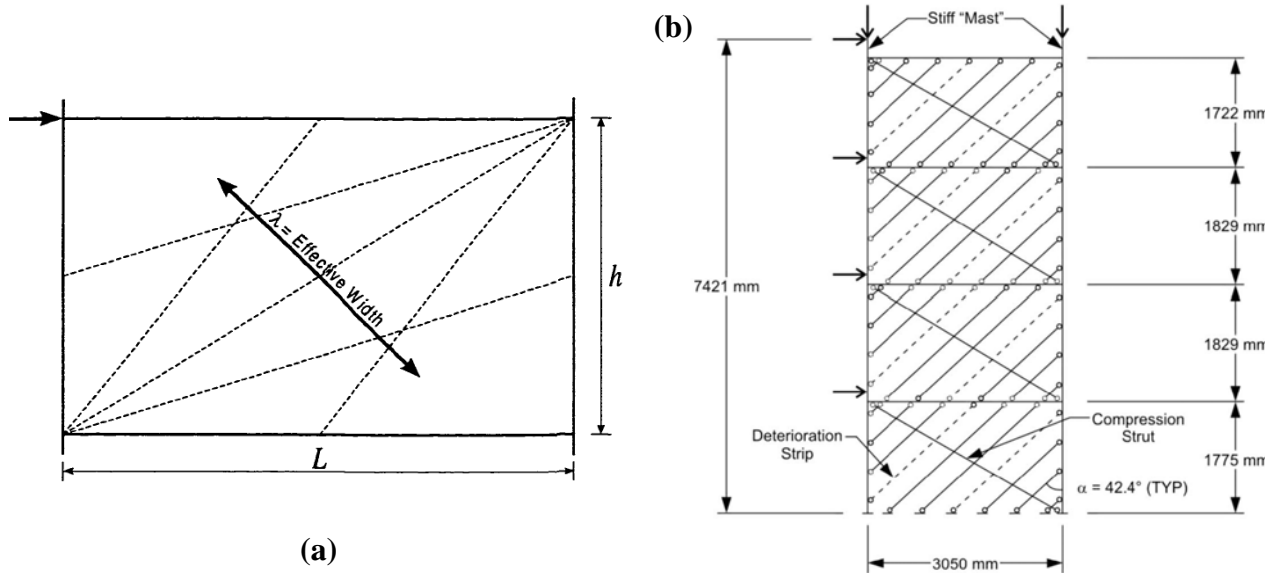
Figure 2-5 Modified Strip Model: (a) Multi-angle Strip Model Proposed by Rezai (1999); (b) Strip Model with Compression Strut Proposed by Shishkin *et al*. (2009)

Plastic Analysis

Berman and Bruneau (2003) performed plastic analysis of steel plate shear walls using the standard strip model as a basis to obtain the ultimate strength of single and multistory SPSWs with either simple or rigid connections. Two types of plastic collapse mechanisms were considered, namely: a uniform collapse mechanism and a soft-story collapse mechanism (Figure 2-6). The resulting general equation for the ultimate strength of SPSWs (for the desirable uniform collapse mechanism case) is expressed as follows:

$$\sum_{i=1}^{n_s} V_i \, h_i = 2 M_{pc1} + 2 M_{pcn} + \sum_{i=1}^{n_s - 1} M_{pbi} + \sum_{i=1}^{n_s} \frac{1}{2} F_y \, L h_i (t_i - t_{i+1}) \sin(2\alpha) \qquad (2\text{-}2)$$

where V_i is the story shear force at the i-th story; h_i is the story elevation from the base; M_{pc1} and M_{pcn} are the first and top story column (VBE) plastic moment, respectively; F_y is the infill plate yield stress; L is the bay width; h_i is the story height; t_i is the plate thickness at the i-th story; α is

15

the tension field action angle from the vertical; and n_s is total number of story. The equation provides simple checks of results from more advanced computer models used to analyze SPSWs.
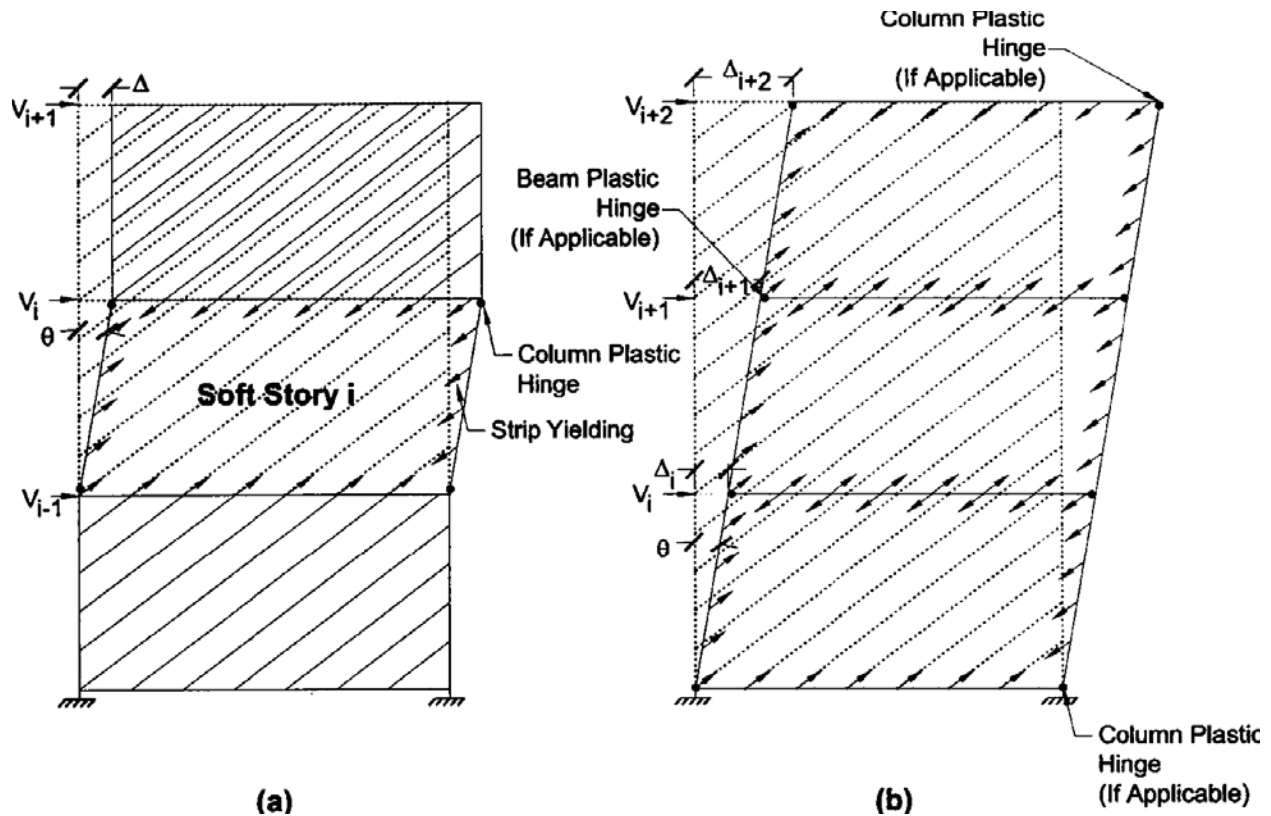
Figure 2-6 Examples of Plastic Collapse Mechanisms for Multistory Steel Plate Shear Walls (Berman and Bruneau 2003)

While (2-2) was derived for the uniform collapse mechanism of multistory SPSW with rigid connection (Figure 2-6b), the equation can easily be adapted to other cases considered. For example, to estimate the ultimate strength of SPSW having the soft-story mechanism shown in Figure 2-6a, one can exclude the third component on the right side of the equation and remove the summation from the remaining equation. To calculate the ultimate strength of multistory SPSWs with simple connections, the first three parts on the right side of the equation should be canceled out (i.e., considering only the contribution from the infill plates). The ultimate strengths predicted by the above equation were validated by the experimental data from past research and a reasonably good match was reported.

16

Finite Element Analysis

Finite element analysis (FEA) is another useful method to investigate behavior of steel plate shear walls. As summarized in Table 2-1, finite element analysis conducted in past research generally was intended to investigate behavior of SPSW specimens (typically in conjunction with experimental research). Many researchers reported satisfactory FEA results in comparison to their experimental results. In addition, several researchers used FEA to perform parametric studies investigating specific aspects of SPSW behavior (e.g., Behbahanifard *et al*. 2003; Kharrazi *et al*. 2008; Purba and Bruneau 2009).

Shell element has been typically used to model infill plates. For boundary elements (BE), either beam or shell elements were selected; the former reduced computational costs but the latter provided more accurate results. Nie *et al*. (2013) used a solid (brick) element to model the composite VBEs used in their specimen. In such finite element models, it is important to include initial imperfections of the infill plates to help initiate panel buckling and development of TFA. Excluding the initial imperfections would result in a stiffer finite element (FE) model compared to the actual "imperfect" structure (as reported by Elgaaly *et al*. 1993). ABAQUS offers three ways to define an imperfection: as a linear superposition of buckling eigenmodes, from the displacements of a static analysis, or by specifying the node number and imperfection values directly (Dassault Systèmes 2009b). Many researchers have selected the first option to apply the initial imperfections in their FE models. Other significant factors that influence the accuracy of FEA results are geometric and material nonlinearities. Researchers who considered these factors in their FE models reported a reasonably good match between analytical and experimental results.

2.2.3 Previous Experimental Research on Steel Plate Shear Walls

At the time of this writing, previous experimental investigations have resulted in a relatively broad understanding of the fundamental behavior of SPSWs. Focus of the experimental studies on SPSWs in the last thirty years can be categorized as follows:

1. **Overall Behavior of the System**. In the early development of SPSWs, experimental studies were intended to understand the overall behavior of the system subjected to cyclic loading. As fundamental understanding of the system developed, researchers then expanded their investigation to other topics. Within this category, the focus of

Table 2-1 Database of Finite Element Investigation on Steel Plate Shear Walls

Researcher	Type of Element		Summary of Objectives and Notable Findings
	Infill	BE	
Elgaaly *et al*. (1993)	Shell	Beam	Investigated two 3-story specimens. Finite element (FE) model was stiffer than the actual specimens as a result of neglecting plate initial imperfections and beam element only able to deform in-plane direction.
Driver *et al*. (1998)	Shell	Beam	Investigated a 4-story specimen. Pinching on the experimental hysteretic curve was not duplicated due to neglecting the second order effects.
Rezai (1999)	Shell	Shell	Investigated a single-story specimen of Lubell *et al*. (2000).
Behbahanifard *et al*. (2003)	Shell	Shell	Investigated a 3-story specimen, validated the results of Driver et al. (1997), and conducted a parametric study to assess factors that affect SPSW behavior. Utilized ABAQUS/Explicit for quasi-static problems and obtained easier and quicker convergence of results.
Vian and Bruneau (2005)	Shell	Shell	Investigated three single-story specimens: solid and perforated SPSWs.
Qu *et al*. (2008)	Shell	Shell	Investigated a 2-story specimen with composite floor system.
Rezai and Ventura (2008)	Shell	Shell	Investigated the use of orthotropic material for shell element on the infill plates. The orthotropic FE model predicted the overall response of a 4-story SPSW.
Kharrazi *et al*. (2008)	Shell	Shell	Conducted a parametric study on 3-, 9-, and 27-story SPSW to validate the proposed Plate-Frame Interaction (PFI) design methodology.
Purba and Bruneau (2009)	Shell	Shell	Validated the results of Vian and Bruneau (2005), validated individual strip model, and conducted a parametric study to assess impact of perforations on SPSW strength.
Tsai *et al*. (2010)	Shell	Shell	Compared the behavior of a single story specimen with or without out-of-plate restrainers.
Choi and Park (2010)	Shell	Rigid	Investigated infill plate buckling behavior and developed hysteresis model for infill plates.
Bhowmick *et al*. (2010)	Shell	Shell	Validated the results of selected SPSW specimens, compared behavior of ductile and limited-ductile 4- and 8-story SPSWs. Strain-rate effect was considered.
Nie *et al*. (2013)	Shell	Brick	Investigated a 2-bay, 5-story specimen with composite column and various configurations of infill plates: stiffened vs. unstiffened and bolted vs. welded connection.

experimental studies have been on: (a) behavior of single-bay, stand-alone single- or multi-story SPSWs; (b) behavior of coupled walls or two-bay SPSWs; (c) impact of strong, weak, or non-compact vertical boundary elements to the overall performance of the system; (d) impact of connecting the infill plate only to HBEs; (e) replaceability of infill steel plates following an earthquake; (f) impact of floor system; and (g) performance of modular SPSWs (Timler and Kulak 1983; Tromposch and Kulak 1987; Caccese *et al*. 1993; Driver *et al*. 1997; Lubell *et al*. 2000; Behbahanifard *et al*. 2003; Park *et al*. 2007; Qu et al. 2008; Choi and Park 2008, 2009; Neagu *et al*. 2011; Dastfan 2011; Jahanpour *et al*. 2012; Kurata *et al*. 2012; Nie *et al*. 2013).

2. **Connection of Infill Plates to the Surrounding Boundary Frame**. Other researchers investigated effective ways to connect infill plates to the surrounding boundary frame that would result in considerably ductile performance and delay development of fractures on the infill plates, considering: (a) bolted connection; (b) welded connection; (c) industrial grade epoxy connection; and (d) specific connection details at the panel corners (Elgaaly and Liu 1997; Schumacher *et al*. 1997; Berman and Bruneau 2005; Choi and Park 2009; Nie *et al*. 2013).

3. **Behavior of Infill Plates and Infill Plate Out-of-Plane Buckling**. As the main source of SPSW lateral resistance relies on buckling of the infill, the behavior of infill plates received attention and design alternatives to reduce or prevent infill plate out-of-plane buckling have been proposed and investigated. Within this category, the focus of experimental studies have been on: (a) behavior of unstiffened infill plates; (b) behavior of infill plates with limited stiffeners; (c) composite infill plates created by adding concrete or carbon fiber reinforced polymer (CFRP); and (d) impact of restrainers on reducing infill plate out-of-plane buckling (Roberts and Sabouri-Ghomi 1991; Lin and Tsai 2004; Zhao and Astaneh-Asl 2004; Jalali and Sazgari 2006; Li *et al*. 2010; Sabouri-Ghomi and Sajjadi 2012; Nie *et al*. 2013).

4. **Modification on Infill Plate Properties**. In several applications, the strength required by design could be significantly less than that provided when using the thinnest hot-rolled plate available; as a result, if the engineer wishes to use a hot rolled plate in such cases, demand on the boundary frame would significantly increase, because of capacity design principles. To alleviate this concern, researcher investigated several possible alternatives,

namely: (a) perforated infill plates; (b) infill plates with slits; (c) corrugated plates; (d) light gauge plates; and (e) infill plates made of low yield steel (Roberts and Sabouri-Ghomi 1992; Caccese *et al*. 1993; Hitaka and Matsui 2003; Berman and Bruneau 2005; Vian and Bruneau 2005; Chen and Jhang 2006; Valizadeh *et al*. 2012).

5. **Connection between Boundary Elements**. Researchers also investigated the use of several connections typically used in other structural systems and applied them to steel plate shear walls, namely: (a) pinned connection; (b) rigid connection; (c) column splice; (d) reduced beam section (RBS) connection; and (e) self-centering connection as a means to reduce permanent deformation after earthquakes (Timler and Kulak 1983; Caccese *et al*. 1993; Astaneh-Asl and Zhao 2002; Vian and Bruneau 2005; Qu *et al*. 2008; Sabouri-Ghomi and Gholhaki 2008; Clayton *et al*. 2012; Dowden and Bruneau 2014).

6. **Variations of Vertical Boundary Elements**. Several variations of VBEs other than standard W-shape steel sections have been investigated, namely: (a) concrete-filled steel tube column; (b) partially-encased column (PEC); and (c) concrete VBEs (Astaneh-Asl and Zhao 2002; Choi and Park 2011; Dastfan 2011; Deng 2012; Nie *et al*. 2013). The first two were intended to increase the strength and rigidity of VBEs when resisting significant forces from yielded infill plates and HBEs.

7. **Loading Protocols**. In addition to investigating SPSW performance subjected to cyclic pushover loading, several researchers investigated behavior under other type of loadings, namely: (a) pseudo-dynamic loading; (b) dynamic loading using a shake table; and (c) blast loading (Rezai 1999; Qu *et al*. 2008; Warn and Bruneau 2009).

Table 2-2 presents a database of previous experimental studies on SPSWs which summarizes the contributions of various studies to one or more of the above categories. Further review of previous SPSW experimental research will be presented in Section 7 when addressing the development of deterioration models for collapse assessment of SPSW based on the results of selected experimental research.

2.2.4 Issues with Design Approaches for Steel Plate Shear Walls

While the system behavior and design principles of steel plate shear walls have been established and validation of satisfactory cyclic performance has been reported, further research is still

Table 2-2 Database of Experimental Studies on Steel Plate Shear Walls

Researcher	Focus of Experimental Study[†]						
	1	**2**	**3**	**4**	**5**	**6**	**7**
Timler and Kulak (1983)	a				a, b		
Tromposch and Kulak (1987)	a						
Roberts and Sabouri-Ghomi (1991, 1992)			a	a			
Caccese *et al*. (1993)	c			d	a, b		
Driver *et al*. (1997)	a						
Elgaaly and Liu (1997)		a, b					
Schumacher *et al*. (1997)		d					
Rezai (1999)							b
Lubell *et al*. (2000)	a						
Astaneh-Asl and Zhao (2002)					c	a	
Behbahanifard *et al*. (2003)	a						
Hitaka and Matsui (2003)				b			
Lin and Tsai (2004)			c, d				
Zhao and Astaneh-Asl (2004)			c				
Berman and Bruneau (2005)		b, c		c, d			
Vian and Bruneau (2005)				a, e	d		
Chen and Jhang (2006)				e			
Jalali and Sazgari (2006)			a				
Park *et al*. (2007)	c						
Choi and Park (2008, 2009, 2011)	a, b, c, d	a, b				c	
Qu et al. (2008)	e, f				d		a
Sabouri-Ghomi and Gholhaki (2008)					a, b		
Warn and Bruneau (2009)							c
Li *et al*. (2010)			d				
Neagu *et al*. (2011)	b						
Clayton *et al*. (2012)					e		
Dastfan (2011)	g					b	
Deng (2012)						b	
Hatami *et al*. (2012)			c				
Jahanpour *et al*. (2012)	d						
Kurata *et al*. (2012)	d						
Sabouri-Ghomi and Sajjadi (2012)			a, b				
Valizadeh *et al*. (2012)				a			
Dowden and Bruneau (2014)					e		
Nie *et al*. (2013)	b	a, b	a, b			a	

Note:
[†] See Section 2.2.3 for detail descriptions.

needed to advance the current understanding of the system in ways that might improve the available design procedures. For example, the AISC 2010 requires that HBEs and VBEs be designed to remain essentially elastic under the maximum tension forces from the yielded infill plates, except for plastic hinging at the ends of HBEs which are permitted. Implicitly, this indicates that in-span plastic hinges should be avoided. Whether or not in-span hinging is acceptable has been a contentious issue, particularly in the absence of factual data to support either position. Recently, Purba and Bruneau (2010) conducted an analytical investigation on the impact of in-span HBE plastic hinge on seismic performance of SPSWs. While the report established various potential consequences of in-span hinging, an experimental verification would be desirable to observe whether in-span HBE plastic hinging can actually occur in SPSWs.

Moreover, the seismic behavior of SPSWs has traditionally benefited from the overstrength introduced in the HBEs and VBEs of the boundary frame by capacity design principle requirements (see Section 2.2.1). However, as practicing engineers are becoming more familiar with this structural system, they are finding ways to optimize the system and eliminate much of that overstrength, to achieve smaller boundary element member sizes. One way to achieve that is by having the boundary frame and the infill plates each resist a portion of the lateral loads (Qu and Bruneau 2009). There is a particularly significant incentive to optimize the load distribution in SPSW implementations, particularly in high-rise buildings. Qu and Bruneau (2009) investigated this concept of sharing lateral loads between the boundary frame and infill plates, and reported that SPSWs designed per this approach would result in reduction of steel quantities needed. However, the researchers left it to future research to verify whether such SPSWs should be designed for the same response modification coefficient (i.e., R-factor) of 7. In other words, future research is still needed to investigate whether R-factor for this type of SPSWs should be the same as for those currently used for the standard SPSWs, prior to definitively being able to conclude whether the proposed procedure could provide a substantial reduction on the amount of steels required for SPSWs.

The research presented in the sections that follow is intended to address the above two concerns. An experimental investigation is used to address the first issue, and the FEMA P695 procedure (reviewed in Section 2.4) is utilized to address the other one. Note that one of the key aspects of

the FEMA P695 procedure is that results depend on the accuracy of the structural numerical models used to simulate component strength deterioration, as this degradation is what leads to global collapse of the system. For this reason, it is useful to review previous research on modeling the degradation of structural components, for the purpose of identifying key aspects of degradation models and providing guidance on how to select degradation models for SPSW components (i.e., infill plates and boundary elements). The following section presents a limited review of such studies.

2.3   Degradation Models of Structural Components

2.3.1   Previous Studies on Modeling Degradation of Structural Components

The FEMA 356 document (FEMA 2000b), which was adapted to become the ASCE 41 document (ASCE 2013), provides provisions for evaluation and rehabilitation of buildings to improve their seismic performance. In this document, structural components with reliable ductility (prior to exhibiting strength deterioration) are modeled as shown in Figure 2-7a. This conceptual force-displacement relationship, commonly known as the "backbone" curve, consists of four stages, namely: (1) an elastic stage, between unloaded point A and effective yield point B; (2) a strain hardening stage with a slope equal to a small percentage of the elastic slope (e.g., 0-10%) until reaching the ultimate strength at point C (i.e., the capping point); (3) a degradation stage where the ultimate strength (point C) rapidly deteriorates to a substantially reduced strength at point D; and (4) a residual strength stage, where the residual strength is sustained until deformation reaches a specified value at point E and the strength drops to zero beyond this point.

Many other models developed in past research on modeling the deterioration of structural components share similarities with the FEMA 356 backbone model. Two examples are shown in Figures 2-7b and 2-7c. The first example was developed by Song and Pincheira (2000) to analyze the cyclic response of non-ductile reinforced concrete columns, while the second one was developed by Ibarra and Krawinkler (2005) and had been implemented to investigate the cyclic response of concrete and steel structures (Haselton and Deierlein 2007; Liel and Deierlein 2008; Lignos and Krawinkler 2009).
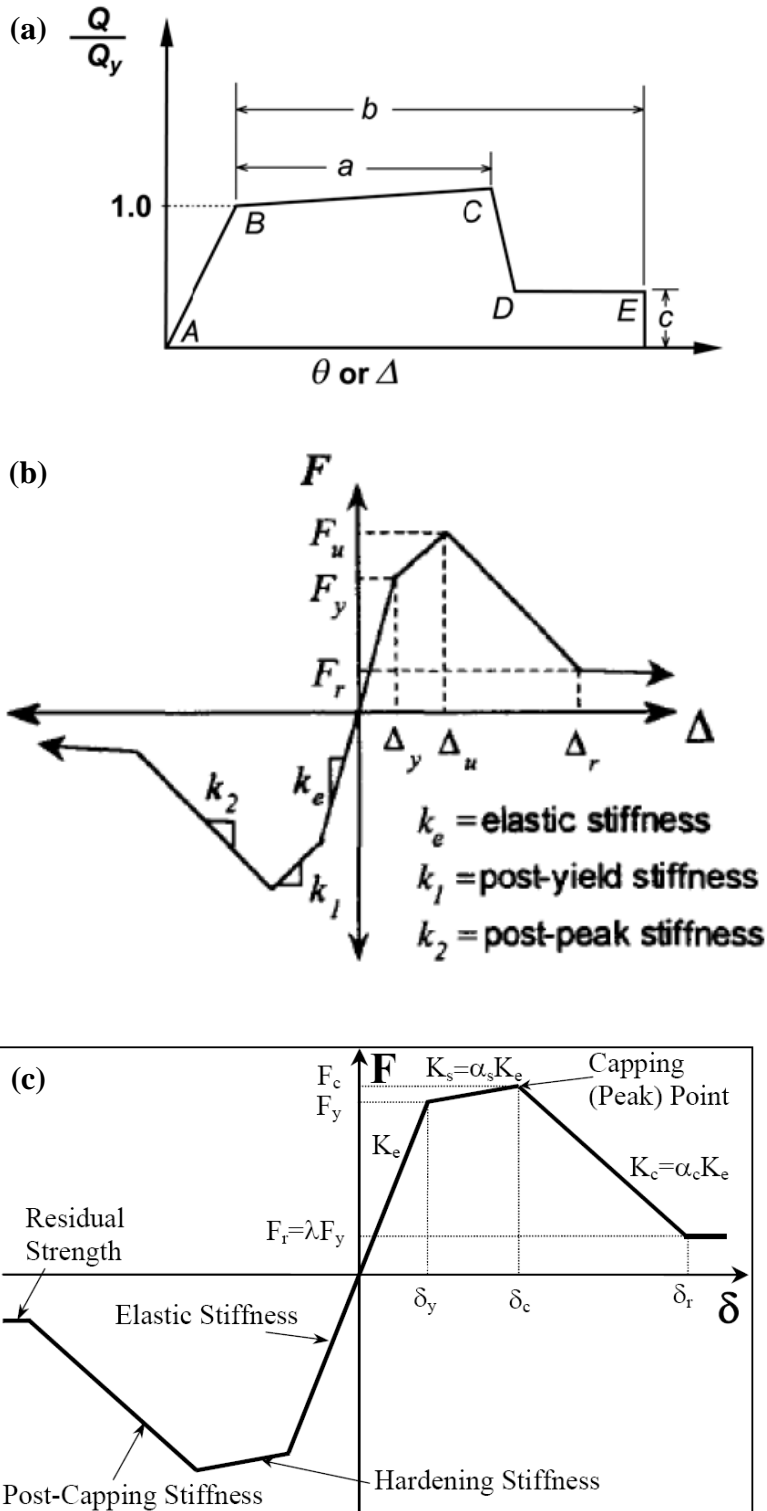
Figure 2-7 Examples of Force-Deformation Relations for Structural Components that Incorporate Deterioration: (a) FEMA 356; (b) Song and Pincheira (2000); (c) Ibarra and Krawinkler (2005)

One of the key differences between the last two models and the FEMA 356 model is that they have less sudden degradation slope (i.e., post-peak or post-capping stiffness), which alleviates computational difficulties and inability to converge in non-linear dynamic analysis. In addition, the last two models have additional hysteretic rules to account for cyclic deterioration modes while that is not the case for the FEMA 356 model. In other words, structural components modeled according to the FEMA 356 model would only experience strength degradation when cycled beyond point C, while the component stiffness from one cycle to another cycle of loading would remain unchanged. By contrast, structural components modeled according to the last two models could experience stiffness degradation (even before reaching the ultimate point) in addition to strength degradation beyond the capping point. In fact, the last model has more versatile features that could control four cyclic deterioration modes as shown in Figure 2-8. Basically, one can control these hysteretic rules to simulate strength deterioration in structural components due to increasing inelastic displacement and due to repeated cycles of the same displacement, unloading and reloading stiffness degradations, and pinching cyclic strength degradation. The post-capping strength deterioration (Figure 2-8b) can simulate structural components that have more severe strength degradation under cyclic loading than under monotonic loading (i.e., cyclic envelope is smaller than force-displacement backbone boundary).

It should be emphasized that there are many other hysteretic models which are able to incorporate stiffness degradation (e.g., Clough and Johnson 1966; Takeda *et al.* 1970; to name a few), strength degradation (e.g., Park and Ang 1985, Park *et al.* 1987, Sivaselvan and Reinhorn 2000, to name a few), or combination of both deteriorations (e.g., Rahnama and Krawinkler 1993; Sucuoglu and Erberik 2004, to name a few). An extensive review of these hysteric models can be found elsewhere (i.e., FEMA P440A document 2009).

2.3.2 Selecting Degradation Models for SPSW Components

While many SPSW specimens have been tested beyond the ultimate point and strength degradations were recorded and reported in some of this research, and while fragility curves have been developed to relate SPSW damage states to drift values (Baldvins *et al.* 2012), no attempt to simulate the strength degradation through numerical investigation was found in the existing literature. Using numerical simulations, it is possible to investigate several contributing

(a) Basic Strength Deterioration　　(b) Post-Capping Strength Deterioration

(c) Unloading Stiffness Deterioration　　(d) Accelerated Reloading Stiffness Det.
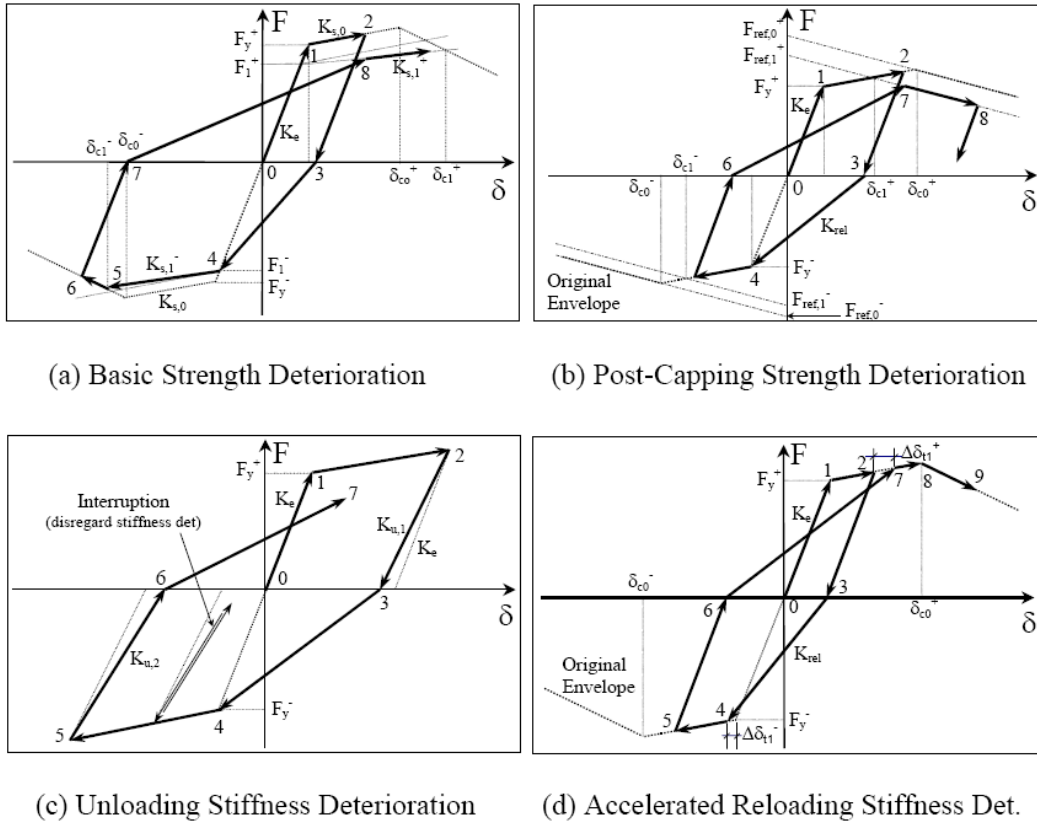
Figure 2-8 Hysteretic Rules for Cyclic Deterioration in Ibarra and Krawinkler (2005) Model

parameters that affect performance of SPSWs when strength degradation occurred, which might be economically impractical to investigate only through experiments. One of the objectives of the research presented in this report is to develop degradation models for SPSW components (i.e., boundary elements and infill plates) and to calibrate them to the available experimental data. However, since experimental data for SPSWs are only available at the global structural level, moment-rotation and axial force-deformation degradation models for boundary elements and infill plates, respectively, will be defined in terms of observations made at that global structural level. Here, it is assumed that the degradation pattern at the global structural level is an expression of behavior at the component level.

Figure 2-9 presents several examples of force-displacement hysteretic curves for SPSW specimens, representing one- to four-story specimens. In relating those to the hysteretic rules for cyclic deterioration plotted in Figure 2-8, several observations can be made, as follows:
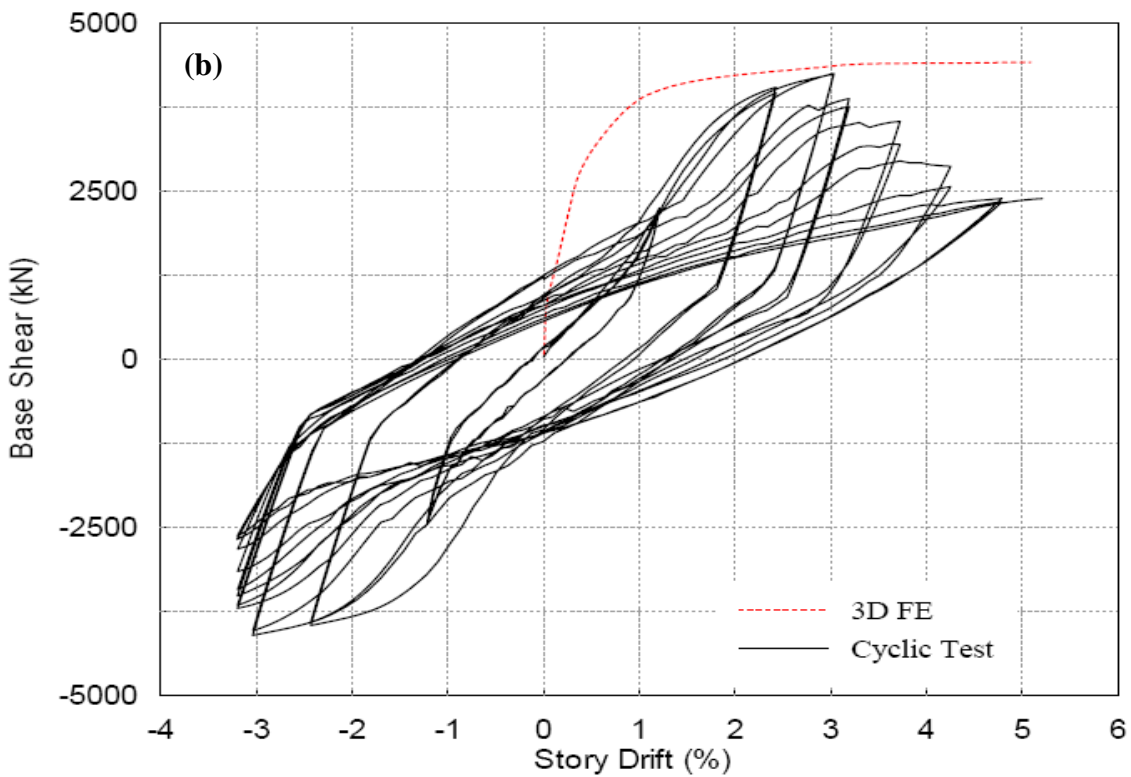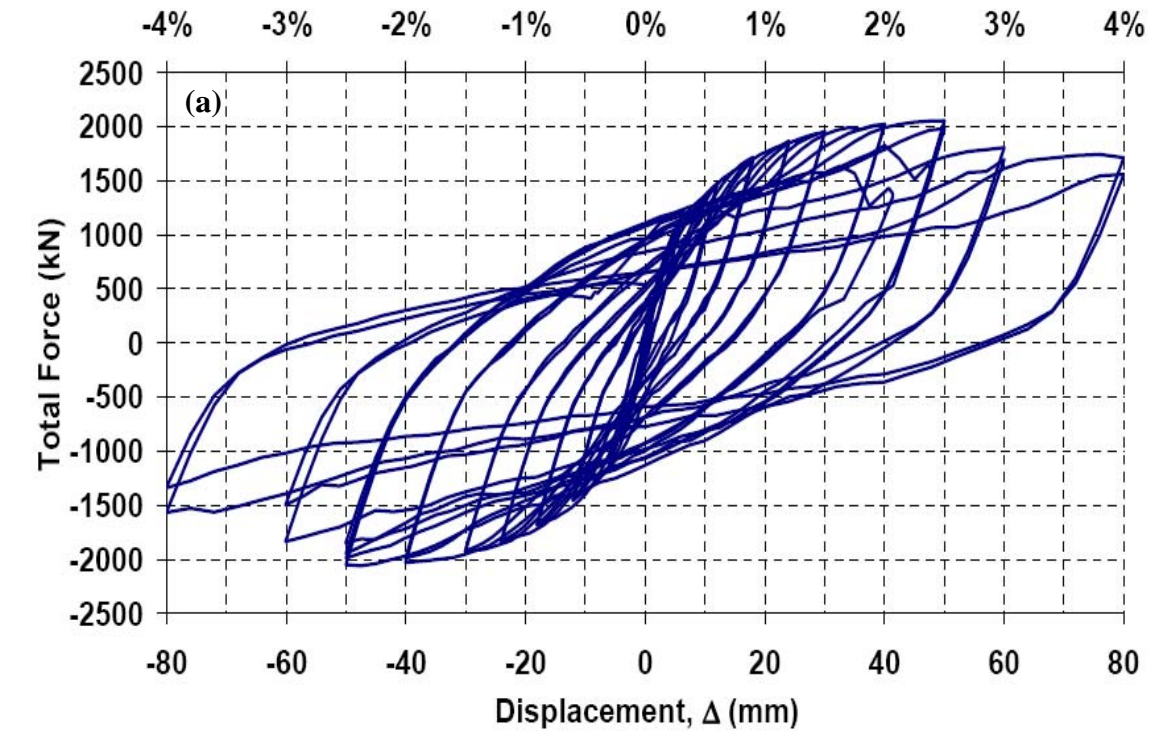
Figure 2-9 Force-Displacement Hysteretic Curves for SPSW Specimens: (a) One-story Specimen (Vian and Bruneau 2005); (b) Two-Story Specimen (Qu and Bruneau 2008)
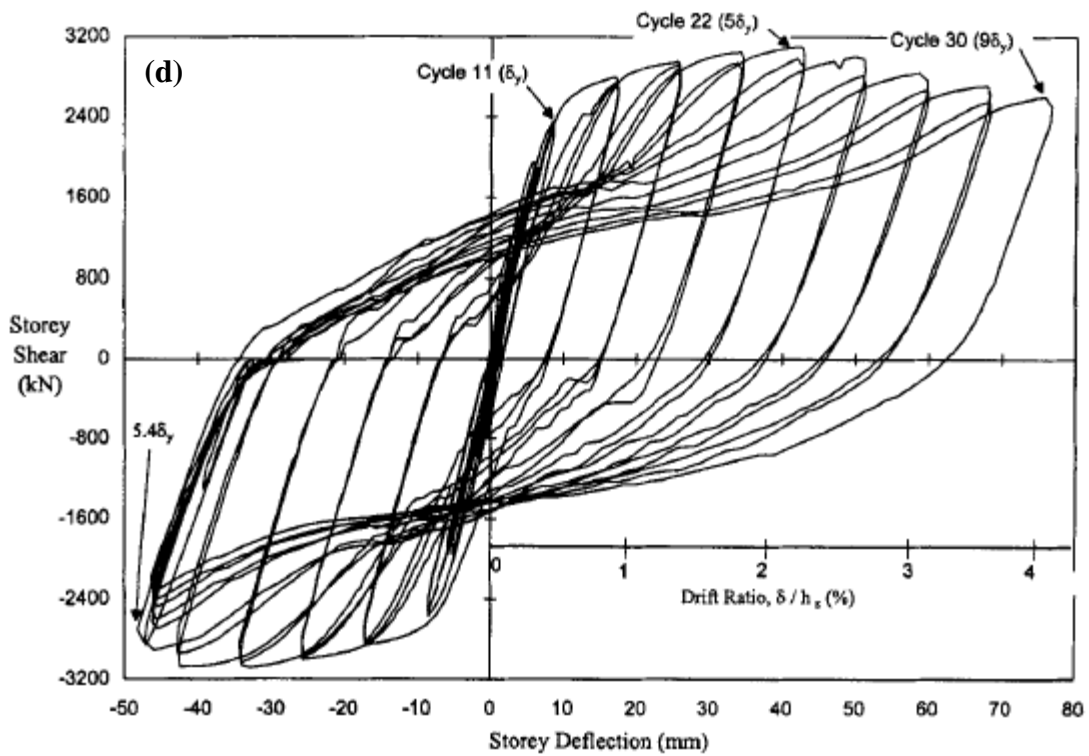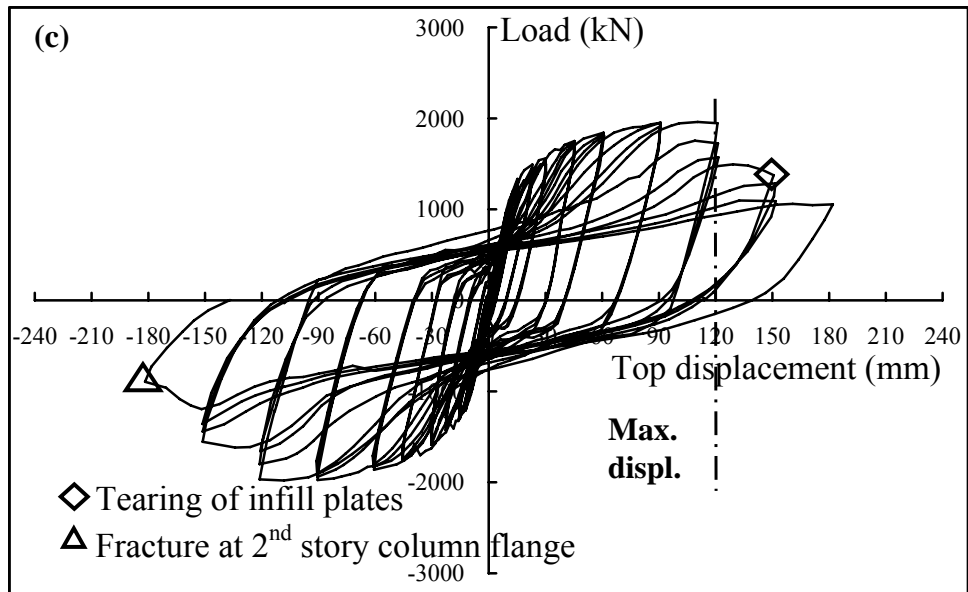
Figure 2-9 Force-Displacement Hysteretic Curves for SPSW Specimens – Cont'd: (c) Three-story Specimen (Choi and Park 2009); (d) Four-Story Specimen (Driver *et al*. 1997)

28

1. Up to the capping point, hysteretic slopes both during loading and unloading are somewhat the same between one and another hysteretic loop. Moderate change of hysteretic slope is only observed after strength degradation occurred. This behavior indicates that incorporating stiffness degradation in the deterioration models for SPSW components does not seem crucial, especially for the collapse analysis of SPSWs intended in this research.

2. Strength degradation due to repeated cycles at the same displacement is relatively small; as such, basic strength deterioration (Figure 2-8c) can be neglected in the deterioration models of SPSW components.

3. Strength degradation mainly occurs when the increasing inelastic displacements pass the ultimate point in the backbone curve. Here, the cyclic envelope is assumed similar to the force-displacement backbone boundary.

4. As for the significant pinching behavior exhibited in the hysteretic curve of those SPSWs, it is a consequence of the fact that the infill plates behave analogously to slender tension-only bracing. Roberts and Sabouri-Ghomi (1991) tested SPSWs with pin-connected boundary elements and reported a significant pinching behavior exhibited by the unstiffened plates (Figure 2-10). Moreover, Berman and Bruneau (2005) subtracted the semi-rigid boundary frame contribution from the total hysteretic response of their single-story SPSW specimen and obtained the same results for infill-only hysteresis, as shown in Figure 2-11.
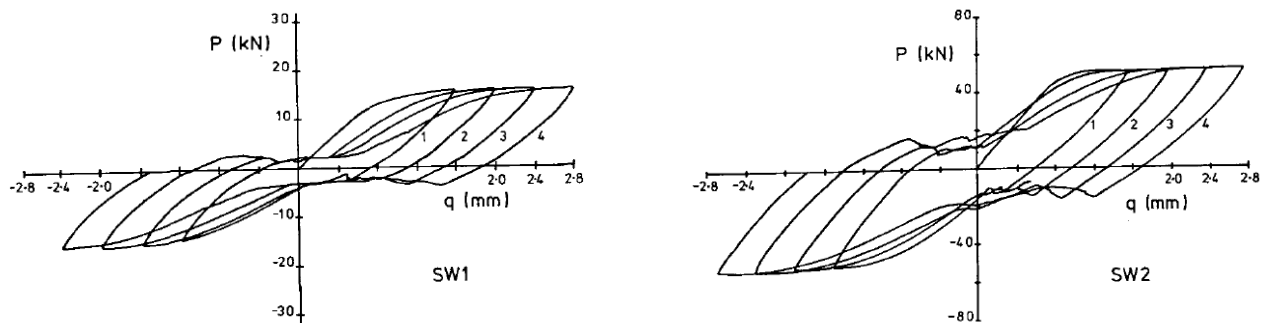
Figure 2-10 Typical Hysteretic Curves for Unstiffened Steel Plates (Roberts and Sabouri-Ghomi 1991)

29
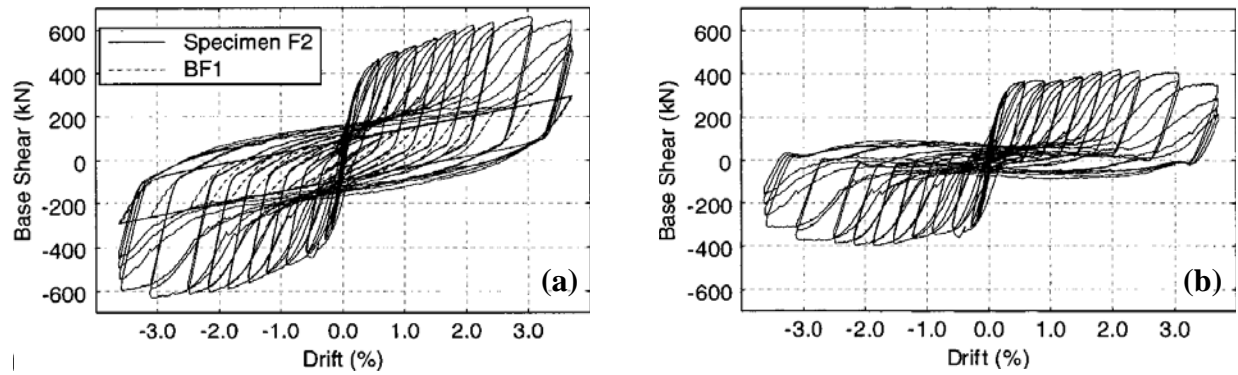
Figure 2-11 Hysteretic Curves for Berman and Bruneau (2005) Single Story Specimen: (a) Specimen and Modeled Boundary Frame Hystereses; (b) Infill-only Hysteresis

Recognizing the above behavior of infill plates (observation #4), several researchers proposed non-deteriorating models for infill plates as shown in Figure 2-12. Two of the models consider the small compression strength of the infill plates and pinching behavior during reloading (Figures 2-12a and 2-12c) while another one excludes these two components (Figure 2-12b). While the former would provide good correlation with the actual infill plate hysteretic behavior, the latter is preferred for its simplicity and is deemed sufficient to model the infill plates for the purpose intended in this research. Using the knowledge from previous studies on modeling degradation of structural components in other systems (reviewed in the previous section), this non-deteriorating model for infill plates will be adjusted in Section 7 to consider strength degradation.

Ibarra and Krawinkler (2005) reported that degradation parameters, such as plastic deformation when reaching the point of maximum strength before strength degradation starts to occur (i.e., the capping point) and post-capping stiffness can be estimated in a probabilistic framework, as illustrated in Figure 2-13. These degradation parameters for both infill plates and boundary elements and whether or not residual strength would be considered will be addressed in Section 7. These parameters would be statistically determined based on the results of previous SPSW experiments, using an approach similar to the one shown in Figure 2-13. This approach will also assume that the simple backbone curve without cyclic degradation rules (plotted in Figure 2-7c) is sufficient to represent degradation models for boundary elements and infill plates, as the literature reviewed suggests that the approach is appropriate for SPSWs. Note that the infill plates would have an un-symmetric degradation model without compression capacity.

30
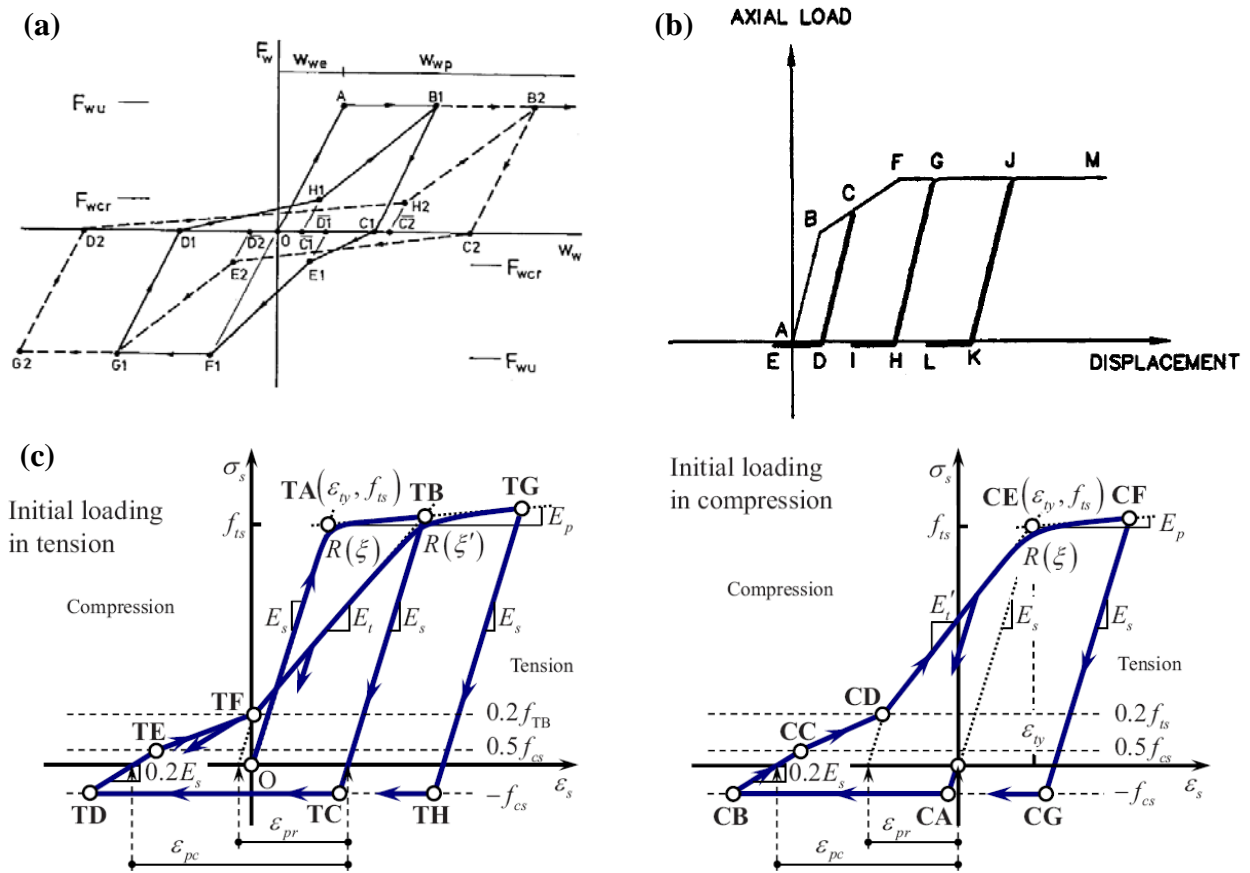
Figure 2-12 Non-Deteriorating Model for Infill Plates: (a) Proposed by Roberts and Sabouri-Ghomi (1991); (b) Proposed by Elgaaly and Liu (1997); (c) Proposed by Choi and Park (2010)
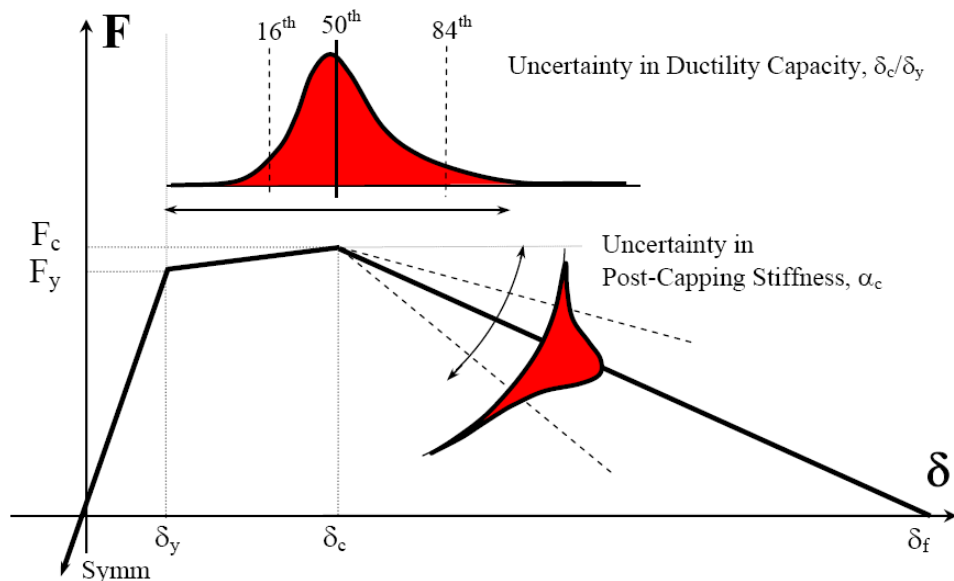
Figure 2-13 Uncertainty in Degradation Model Parameters (Ibarra and Krawinkler 2005)

2.4 Collapse Assessment Methodology: Overview of FEMA P695 Procedure

The FEMA P695 document, developed by the Applied Technology Council (ATC) under the ATC-63 project name, presents a methodology to quantify global seismic performance factors (SPF) for seismic-force-resisting systems. It is used in Sections 6 to 8 to investigate the seismic performance of SPSWs designed per different philosophies, and is therefore briefly reviewed here.

This FEMA P695 procedure requires simulating nonlinear response of structural system archetypes under Maximum Considered Earthquake (MCE) ground motions and probabilistically assessing their collapse risk. Specifically, the methodology provides a rational basis to quantify response modification coefficient (R factor), system overstrength factor (Ω_0 factor), and deflection amplification factor (C_d factor). Key steps of the methodology for establishing these factors include development of structural system archetypes, formulation of nonlinear analytical model development that accounts for strength degradation, performance of nonlinear static and dynamic analyses (i.e., pushover and incremental dynamic analyses), and evaluation of system performance in terms of probabilistic collapse assessment under MCE ground motions. A brief overview of each of these key steps is summarized in the subsequent sub-sections.

2.4.1 Development of Structural System Archetypes

The FEMA P695 methodology defines an archetype as "a prototypical representation of a seismic-force-resisting system configuration that embodies key features and behaviors related to collapse performance when the system is subjected to earthquake ground motions." Rigorous application of the methodology requires the consideration of a series of archetypes that reflect a reasonably broad range of design parameters for which investigation of key seismic behaviors of the proposed seismic-force resisting system is possible. Design parameters that are typically considered in developing structural system archetypes include occupancy and building usage, range of elevation and plan configuration (e.g., frame span length, story height, number of stories, geometric variation of seismic-force resisting system), structural component type (e.g., different type of moment-resisting connections, type of bracing members), range of seismic design category, and variations in gravity loads.

Archetypes with similar design criteria are assembled into a performance group. Typically, archetypes in one performance group have similar basic structural configuration, gravity load level, seismic design category, period domain, and other design features that result in similar seismic behavior. On the basis of statistical assessment for each performance group (i.e., minimum and average collapse margin ratios), seismic performance factors for the system are determined. As a minimum, three archetypes are needed for each performance group. Accounting for two assumed basic structural configurations, high and low tributary seismic masses, two seismic design categories (i.e., max and min SDC), and two period domains (short and long periods), 48 archetypes in 16 performance groups would need to be designed to apply the FEMA P695 to a given structural system. However, the methodology provides flexibility by allowing the design of a smaller number of archetypes if it can be supported by proper justifications that doing so would not detrimentally impact the investigation of key behaviors for the proposed seismic-force resisting system under consideration. Using this FEMA P695 procedure, development of archetypes for collapse assessment of steel plate shear walls is presented in Section 7.

2.4.2 Nonlinear Analytical Model Development

The nonlinear analytical models used in the FEMA P695 procedure must be capable of simulating all important deterioration and failure modes that contribute to global structural collapse of the seismic-force resisting system being investigated. This can be accomplished by first reviewing previous experimental data or observations from past earthquakes to identify all reported component and global failure modes of the system. Afterward, likelihood of each failure mode can be assessed based on the system design requirements and engineering judgment. Failure modes that can be prevented by enforcing principles outlined in the system design requirements need not be accounted for by the nonlinear model.

At the component level, deterioration behavior typically can be represented by the nonlinear model shown in Figure 2-14a. The nonlinear model should explicitly simulate yielding condition, maximum strength (i.e., the capping point), post capping tangent stiffness (i.e., rate of degradation), and residual strength. In addition, cyclic deterioration that reduces stiffness and

lowers energy dissipated per cycle should be considered, as shown in Figure 2-14b. Proposed nonlinear models should be calibrated to available experimental data to verify their ability to
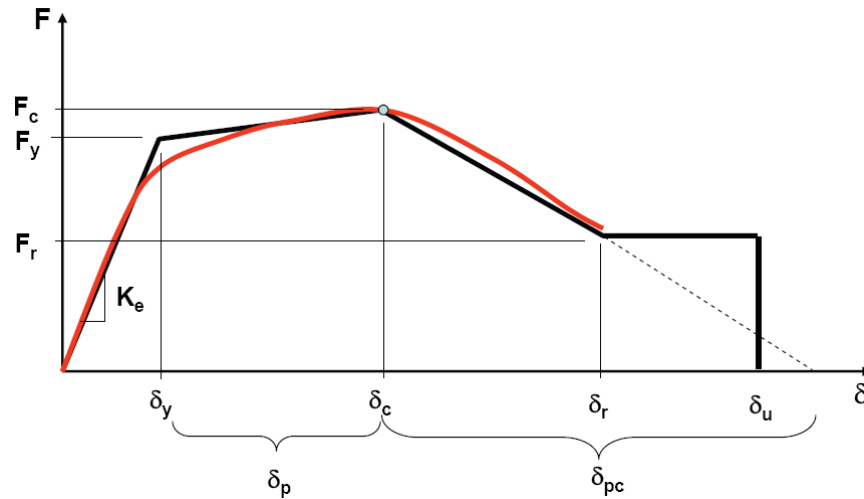
Effective yield strength and deformation (F_y and δ_y)
Effective elastic stiffness, $K_e = F_y/\delta_y$
Strength cap and associated deformation for monotonic loading (F_c and δ_c)
Pre-capping plastic deformation for monotonic loading, δ_p
Effective post-yield tangent stiffness, $K_p = (F_c - F_y)/\delta_p$
Post-capping deformation range, δ_{pc}
Effective post-capping tangent stiffness, $K_{pc} = F_c/\delta_{pc}$
Residual strength, F_r
Ultimate deformation, δ_u

(a)
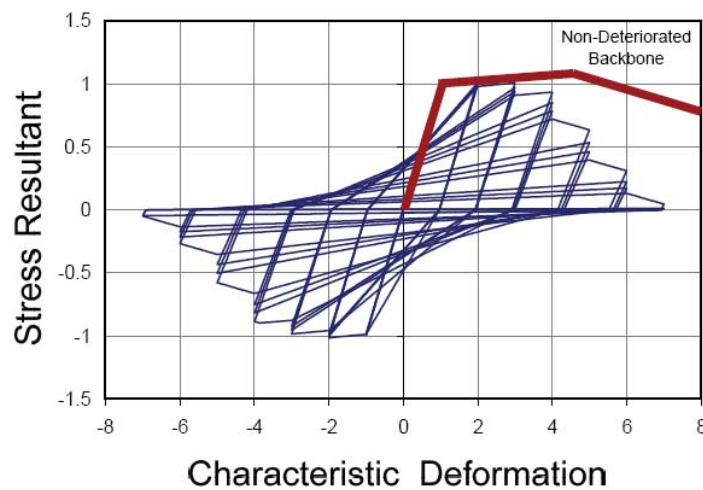
(b)

Figure 2-14 Nonlinear Model: (a) Typical Monotonic Backbone Curve; (b) Cyclic Behavior of Structural Components with Strength and Stiffness Degradation (FEMA P965)

replicate the results. At the global level, destabilizing P-Δ effects associated with gravity load effects at large lateral deformations must be taken into account. Development of deteriorating material models for collapse assessment of steel plate shear walls is presented in Section 6.

2.4.3 Nonlinear Static and Dynamic Analyses

Nonlinear static (pushover) and nonlinear dynamic (response history) analyses are performed on all archetype numerical models developed in the previous step. Pushover analyses are used to verify that the numerical models behave as expected, and to obtain statistical information on system overstrength, Ω_o, and period base ductility, μ_T. As further explained in Section 2.4.4, the period base ductility is one of the factors used to estimate collapse capacity of a proposed seismic-force-resisting system. The system overstrength factor and period base ductility are defined as follows:

$$\Omega_o = \frac{V_{max}}{V} \tag{2-3}$$

$$\mu_T = \frac{\delta_u}{\delta_{y,eff}} \tag{2-4}$$

where V_{max} and V are the maximum and design base shear strength for a given archetype model; δ_u and $\delta_{y,eff}$ are the ultimate and effective yield roof displacement of the archetype model. Figure 2-15 illustrates those parameters in a typical pushover curve. As shown in the figure, the ultimate roof displacement is measured as the roof displacement when the structure loses 20% of its base shear capacity while the effective yield displacement is measured as the roof displacement corresponding to an intersection point of the elastic stiffness and maximum base shear tangents. As a reference, an alternative theoretical equation to calculate effective yield roof displacement was provided in the FEMA P695 document.

Nonlinear dynamic analyses are performed to obtain median collapse capacity, $\hat{S}_{CT}$, and collapse margin ratios, *CMR*. Ground motion records used in the nonlinear dynamic analyses for collapse assessment consist of 22 ground motion record pairs (44 individual components) of large magnitude (M > 6.5) from sites located at distances greater than or equal to 10 km from fault rupture (i.e., "Far-Field" record set), made available in the Pacific Earthquake Engineering Research Center (PEER) Next Generation Attenuation (NGA) database (PEER 2005). A
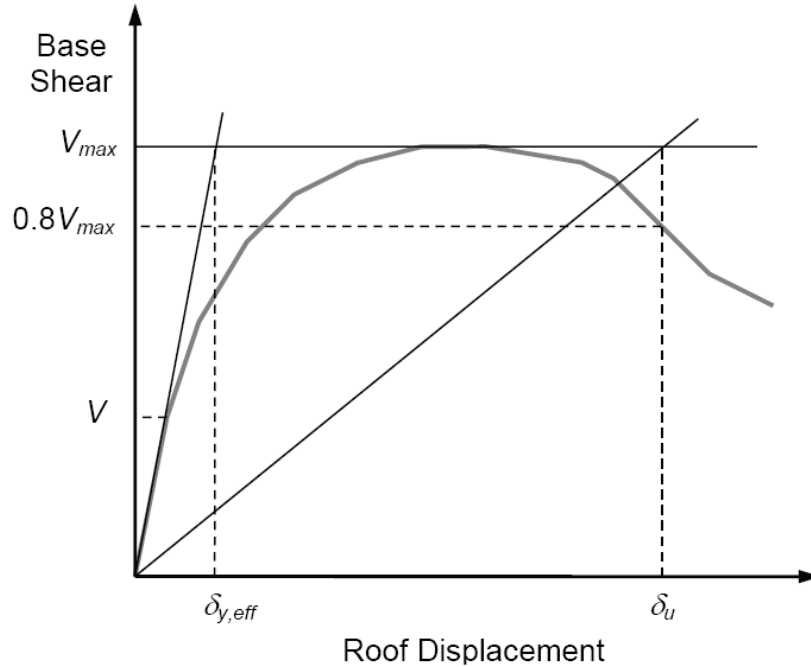
Figure 2-15 Typical Nonlinear Pushover Curve (FEMA P695)

summary of the far-field record sets specified in the FEMA P695 procedure is presented in Appendix C. The median collapse capacity is defined as the spectral intensity when half of the specified ground motions cause an archetype to collapse; and the collapse margin ratio is defined as follows:

$$CMR = \frac{\hat{S}_{CT}}{S_{MT}} \qquad (2\text{-}5)$$

where S_{MT} is the response spectrum of MCE ground motions at the fundamental period of a given archetype. Figure 2-16 illustrates how to determine the value of these two parameters for one particular archetype using the incremental dynamic analysis (IDA) concept (Vamvatsikos and Cornell 2002). Part (a) of the figure presents nonlinear dynamic analysis results in terms of spectral acceleration for all considered ground motions versus maximum story drift obtained in each analysis. Each point represents the maximum story drift obtained from one nonlinear dynamic analysis for an archetype model subjected to one particular scaled ground motion. Consequently, each curve represents results for one ground motion scaled to increasing intensity levels, until collapse of the archetype model occurs. The collapse point is indicated by the nearly flat part of an IDA curve as evidence of the archetype's excessive lateral displacement for a

36
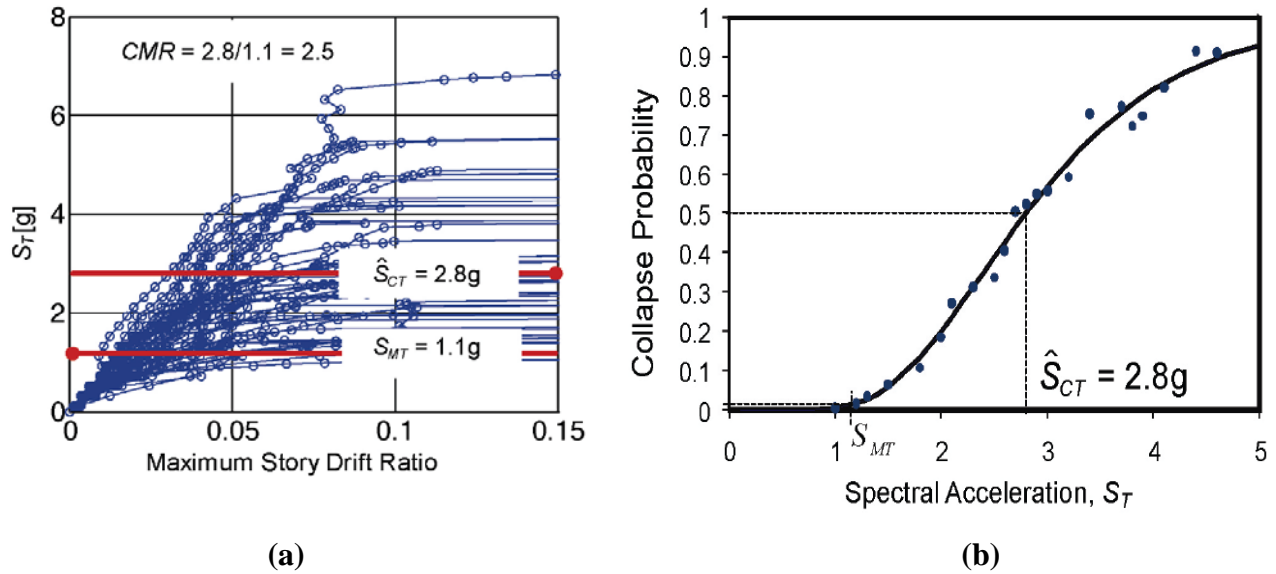
Figure 2-16 Typical Incremental Dynamic Analysis: (a) Spectral Acceleration versus maximum story drift; (b) Collapse Fragility Curve (FEMA P695)

relatively small increment of ground motion intensity. In this example, the lowest spectral intensity at which 22 ground motions cause the archetype to collapse is 2.8g. In other words, the median collapse capacity, $\hat{S}_{CT}$, equals 2.8g. A convenient way to determine $\hat{S}_{CT}$ is to construct a collapse fragility curve, as shown in part (b) of Figure 2-16. This figure is a lognormal cumulative distribution function (CDF) of the collapse data points obtained in part (a) of Figure 2-16 for each earthquake excitation. It informs the probability of archetype collapse for a given spectral acceleration. The median collapse capacity corresponds to a 50% probability of collapse, which in this example, occurs when $\hat{S}_{CT}$ equals 2.8g. Based on (2-3), the CMR equals 2.5 in this example for a MCE intensity, S_{MT}, of 1.1g. Monotonic pushover and incremental dynamic analyses conducted on a series of SPSW archetypes for the purpose of quantifying the seismic performance factors are presented in Section 8.

2.4.4 Performance Evaluation

Performance evaluation of a proposed seismic-force-resisting system, designed with a trial R factor, is conducted by assessing whether the collapse margin ratios obtained from nonlinear time history analyses are greater than a pre-established acceptable threshold value. For CMR values obtained for all considered archetypes, this evaluation procedure proceeds as follows.

Step 1: Adjust Collapse Margin Ratio

To account for the effects of spectral shape (i.e., frequency content of the specified ground motions), the CMR obtained from nonlinear time history analyses (Section 2.4.3) is first modified to obtain an adjusted collapse margin ratio (ACMR). This can be done by multiplying the CMR for each archetype by the spectral shape factor (SSF):

$$ACMR = SSF\,(T, \mu_T) \times CMR \tag{2-6}$$

where SSF value is a function of the fundamental period T of a given archetype and period-based ductility μ_T obtained from pushover analysis (2-3). Archetypes with larger ductility and longer fundamental periods are given larger SSF values. SSF values for archetypes designed with different seismic design category (SDC) were presented in the FEMA P695 document. Adapted from the FEMA 695 Document, the SSF values for archetypes design using SDC D_{max} (corresponding to short and one-second spectral ordinates at the MCE level, S_{MS} and S_{M1}, of 1.5g and 0.9g, respectively) that will be used in this research are presented in Table 2-3. Further description on the background and development of SSF can be found in Appendix B of the FEMA P695 document.

Table 2-3 Spectral Shape Factor (SSF) for Archetypes Designed
using SDC D_{max} (FEMA P695)

T (sec.)	Period-Based Ductility, μ_T							
	1.0	1.1	1.5	2	3	4	6	≥ 8
≤ 0.5	1.00	1.05	1.1	1.13	1.18	1.22	1.28	1.33
0.6	1.00	1.05	1.11	1.14	1.2	1.24	1.3	1.36
0.7	1.00	1.06	1.11	1.15	1.21	1.25	1.32	1.38
0.8	1.00	1.06	1.12	1.16	1.22	1.27	1.35	1.41
0.9	1.00	1.06	1.13	1.17	1.24	1.29	1.37	1.44
1.0	1.00	1.07	1.13	1.18	1.25	1.31	1.39	1.46
1.1	1.00	1.07	1.14	1.19	1.27	1.32	1.41	1.49
1.2	1.00	1.07	1.15	1.2	1.28	1.34	1.44	1.52
1.3	1.00	1.08	1.16	1.21	1.29	1.36	1.46	1.55
1.4	1.00	1.08	1.16	1.22	1.31	1.38	1.49	1.58
≥ 1.5	1.00	1.08	1.17	1.23	1.32	1.4	1.51	1.61

Step 2: Estimate Total System Collapse Uncertainty

Acceptable values of the ACMR (determined in Step 3) are based on total system collapse uncertainty and specified acceptable collapse probabilities. The total system collapse uncertainty (β_{TOT}) is estimated by combining the effect of four sources of uncertainties, namely: (1) ground motion record-to-record uncertainty (β_{RTR}); (2) uncertainty related to the completeness and robustness of design requirements (β_{DR}); (3) uncertainty related to the completeness and robustness of test data (β_{TD}); and (4) uncertainty related to modeling (β_{MDL}) in terms of how well nonlinear models could capture the actual structural collapse behavior.

$$\beta_{TOT} = \sqrt{\beta_{RTR}^2 + \beta_{DR}^2 + \beta_{TD}^2 + \beta_{MDL}^2} \tag{2-7}$$

Based on the far-field ground motions selected, FEMA P695 methodology assigns a fixed value of β_{RTR} equal to 0.4 for archetypes with $\mu_T \geq 3$. Values of the other uncertainties factor are presented in Tables 2-4 to 2-6 for β_{DR}, β_{TD}, and β_{MDL}, respectively. As shown in these tables, seismic-force-resisting systems that have well defined design requirements, more comprehensive experimental data, and more accurate nonlinear models capturing the actual collapse behavior are given smaller uncertainty factors, which imply that such systems have less uncertainty in their expected seismic performance.

Table 2-4 Quality Rating of Design Requirements (FEMA P695)

Completeness and Robustness	Confidence in Basis of Design Requirements		
	High	Medium	Low
High. Extensive safeguards against unanticipated failure modes. All important design and quality assurance issues are addressed.	(A) Superior $\beta_{DR} = 0.10$	(B) Good $\beta_{DR} = 0.20$	(C) Fair $\beta_{DR} = 0.35$
Medium. Reasonable safeguards against unanticipated failure modes. Most of the important design and quality assurance issues are addressed.	(B) Good $\beta_{DR} = 0.20$	(C) Fair $\beta_{DR} = 0.35$	(D) Poor $\beta_{DR} = 0.50$
Low. Questionable safeguards against unanticipated failure modes. Many important design and quality assurance issues are not addressed.	(C) Fair $\beta_{DR} = 0.35$	(D) Poor $\beta_{DR} = 0.50$	--

Table 2-5 Quality Rating of Test Data from an Experimental Investigation (FEMA P695)

Completeness and Robustness	Confidence in Test Results		
	High	Medium	Low
High. Material, component, connection, assembly, and system behavior well understood and accounted for. All, or nearly all, important testing issues addressed.	(A) Superior $\beta_{TD} = 0.10$	(B) Good $\beta_{TD} = 0.20$	(C) Fair $\beta_{TD} = 0.35$
Medium. Material, component, connection, assembly, and system behavior generally understood and accounted for. Most important testing issues addressed.	(B) Good $\beta_{TD} = 0.20$	(C) Fair $\beta_{TD} = 0.35$	(D) Poor $\beta_{TD} = 0.50$
Low. Material, component, connection, assembly, and system behavior fairly understood and accounted for. Several important testing issues not addressed.	(C) Fair $\beta_{TD} = 0.35$	(D) Poor $\beta_{TD} = 0.50$	--

Table 2-6 Quality Rating of Index Archetype Models (FEMA P695)

Representation of Collapse Characteristics	Accuracy and Robustness of Models		
	High	Medium	Low
High. Index models capture the full range of the archetype design space and structural behavioral effects that contribute to collapse.	(A) Superior $\beta_{MDL} = 0.10$	(B) Good $\beta_{MDL} = 0.20$	(C) Fair $\beta_{MDL} = 0.35$
Medium. Index models are generally comprehensive and representative of the design space and behavioral effects that contribute to collapse.	(B) Good $\beta_{MDL} = 0.20$	(C) Fair $\beta_{MDL} = 0.35$	(D) Poor $\beta_{MDL} = 0.50$
Low. Significant aspects of the design space and/or collapse behavior are not captured in the index models.	(C) Fair $\beta_{MDL} = 0.35$	(D) Poor $\beta_{MDL} = 0.50$	--

Step 3: Determine Acceptable Value of Adjusted Collapse Margin Ratio

Once β_{TOT} is estimated and an acceptable collapse probability is specified, acceptable value of ACMR can be determined from Table 2-7, adapted from the FEMA P695 document. To achieve an equivalent level of safety, a higher acceptable value of ACMR must be satisfied by a seismic-force resisting system with higher total system collapse uncertainty (i.e., a less established system) compared to that with lower uncertainty (i.e., a well-established system).

Table 2-7 Acceptable Values of Adjusted Collapse Margin Ratio (FEMA P695)

Total System Collapse Uncertainty	Collapse Probability				
	5%	10% (ACMR$_{10\%}$)	15%	20% (ACMR$_{20\%}$)	25%
0.275	1.57	1.42	1.33	1.26	1.20
0.300	1.64	1.47	1.36	1.29	1.22
0.325	1.71	1.52	1.40	1.31	1.25
0.350	1.78	1.57	1.44	1.34	1.27
0.375	1.85	1.62	1.48	1.37	1.29
0.400	1.93	1.67	1.51	1.40	1.31
0.425	2.01	1.72	1.55	1.43	1.33
0.450	2.10	1.78	1.59	1.46	1.35
0.475	2.18	1.84	1.64	1.49	1.38
0.500	2.28	1.90	1.68	1.52	1.40
0.525	2.37	1.96	1.72	1.56	1.42
0.550	2.47	2.02	1.77	1.59	1.45
0.575	2.57	2.09	1.81	1.62	1.47
0.600	2.68	2.16	1.86	1.66	1.50
0.625	2.80	2.23	1.91	1.69	1.52
0.650	2.91	2.30	1.96	1.73	1.55
0.675	3.04	2.38	2.01	1.76	1.58
0.700	3.16	2.45	2.07	1.80	1.60
0.725	3.30	2.53	2.12	1.84	1.63
0.750	3.43	2.61	2.18	1.88	1.66
0.775	3.58	2.70	2.23	1.92	1.69
0.800	3.73	2.79	2.29	1.96	1.72
0.825	3.88	2.88	2.35	2.00	1.74
0.850	4.05	2.97	2.41	2.04	1.77
0.875	4.22	3.07	2.48	2.09	1.80
0.900	4.39	3.17	2.54	2.13	1.83
0.925	4.58	3.27	2.61	2.18	1.87
0.950	4.77	3.38	2.68	2.22	1.90

Step 4: Evaluation of Response Modification Coefficient (*R* Factor)

To assess whether the initial *R* factor used to design archetypes satisfies the performance criteria, the calculated ACMR (Step 1) is compared with the acceptable ACMR (Step 3). The FEMA P695 methodology specifies two acceptable performance criteria for individual archetype and performance groups as follows:

1. The probability of collapse under MCE ground motions applied to an individual archetype is limited to 20%. In other words, the calculated ACMR for individual archetype should exceed an acceptable ACMR corresponding to a 20% collapse probability (ACMR$_{20\%}$):

$$ACMR \geq ACMR_{20\%} \tag{2-8}$$

2. The probability of collapse under MCE ground motions applied to a population of archetypes in one performance group is limited to 10%. In other words, the average of the calculated ACMR within a performance group should exceed an acceptable ACMR corresponding to a 10% collapse probability ($ACMR_{10\%}$):

$$\overline{ACMR} \geq ACMR_{10\%} \tag{2-9}$$

If these two performance criteria are satisfied, then the adjusted collapse margin ratio is large enough to provide an acceptably small probability of collapse at the MCE level, and the initial value of R considered is deemed acceptable. Otherwise, further iteration of the evaluation process is required to determine acceptable seismic performance factors. This can be done by improving design requirements and nonlinear archetype models to eliminate total collapse uncertainty or redesigning archetypes with lower R factor.

Step 5: Evaluation of System Overstrength (Ω_o) and Deflection Amplification (C_d) Factors

Once an acceptable R factor is determined, system overstrength (Ω_o) and deflection amplification (C_d) factors can be evaluated. The system overstrength, Ω_o, should be taken as the largest average value of the calculated archetype overstrength (Section 2.4.3) across all considered performance groups. However, Ω_o should not exceed 1.5 times the acceptable R factor and be limited to 3.0 to be consistent with the largest value specified in Table 12.2-1 of ASCE 7-05 for lateral-force resisting system overstrength. The deflection amplification factor, C_d, is determined as follows:

$$C_d = \frac{R}{B_I} \tag{2-10}$$

where R is the acceptable value of the response modification factor (Step 4) and B_I is the constant specified in Table 18.6-1 of ASCE 7-05 for a given inherent effective damping β_I of the structure and the fundamental period, T. For an assumed inherent damping of 5% of critical damping, B_I equals 1.0. Thus, C_d factor will be equal to R factor. Performance evaluation to quantify seismic performance factors for steel plate shear walls is presented in Section 9.

SECTION 3

DESIGN OF SPECIMEN AND EXPERIMENTAL PROGRAM:
CYCLIC PUSHOVER TESTING OF THREE-STORY SPSW

3.1 General

Purba and Bruneau (2010) conducted a comprehensive analytical investigation on the impact of plastic hinges that develop along the span of horizontal boundary elements (HBE) (a.k.a. in-span hinges) on the seismic behavior of steel plate shear walls (SPSW). Results of monotonic and cyclic pushover analyses as well as those from nonlinear time history analyses showed that the development of in-span hinges has significant consequences on the behavior of SPSW, namely: lower lateral strength due to partial yielding of the infill plates and significant plastic incremental deformations on the HBEs that can reach total HBE rotations greatly exceeding 0.03 radians (reaching nearly 0.06 radians) when the structure is pushed cyclically up to a maximum lateral drift of 3%. While that research has established these potential consequences of developing in-span hinges, an experimental program was deemed desirable to investigate whether these undesirable behaviors could also be observed in an actual SPSW.

Cyclic pushover testing of a three-story SPSW specimen was selected for this purpose. Specifically, given that this experimental program was intended to observe whether in-span HBE plastic hinging will actually occur in actual SPSW (and not just an artifact of unavoidable simplifications in numerical models), the specimen was chosen to reflect a case when such behavior was predicted to develop, and instrumented such as to attempt quantifying possible accumulation of plastic incremental deformations on the HBEs and partial yielding of the infill plates. In particular, because the hysteresis curves showing large cross-section rotations at HBE ends reported in Purba and Bruneau (2010) were not symmetric but looping with a bias toward one direction due to tension forces from infill plates that are always pulling the HBE in the direction of the tension forces, this experimental program also aimed to assess the performance of special-moment resisting connections that could resist this kind of behavior. In this case, rotation capacities of these connections at fracture (if it developed) could be compared to the well

documented rotation capacity of connections in conventional special moment-resisting frames which typically exhibit symmetric hysteresis curve.

This section describes the design of the specimen for the experimental program developed to meet the above stated objectives; experimental results and observations will be presented in the subsequent section. Design of the specimen, taken as a 1/3 scale version of a selected prototype structure, is presented first. After briefly discussing issues related to specimen design and special design considerations needed to achieve the experimental objectives, the specimen fabrication process is described. Discussion regarding experimental setting (i.e., how the specimen, gravity column and lateral support systems, actuators, and instrumentation are assembled together) and development of loading protocol (i.e., how force distribution among three dynamic actuators is defined and cyclic displacement loading history is formulated) are presented toward the end of this section. The section ends with a presentation of predicted response obtained from preliminary nonlinear static analysis of the specimen numerical model with actual material properties.

3.2   Prototype Description

The three-story SAC[1] model building (FEMA 355-C) was selected as a prototype for the experimental program described in this section. As shown in Figure 3-1, the building consists of a three-story steel building with a plan dimension of 120 feet by 180 feet and a typical story height of 13 feet. It has seven frames in the North-South (NS) direction and five frames in the East-West (EW) direction. The structure is located on Class B soil in downtown Los Angeles, California, and designed as an office building. The total weight of the structure is 6504 kips, distributed as 2109 kips per story on each of the first two stories and 2285 kips on the roof.

In this study, steel plate shear walls that act as the primary lateral load resisting system in the direction of interest (i.e., in the NS direction) were assumed to carry seismic loads corresponding

---

[1] SAC was a joint venture between the Structural Engineers Association of California (**S**EAOC), the Applied Technology Council (**A**TC), and the California Universities for Research in Earthquake Engineering (**C**UREe). It was established after the 1994 Northridge earthquake to provide recommendations for the design and construction of new steel moment-resisting frame buildings to resist the effects of earthquakes.

44
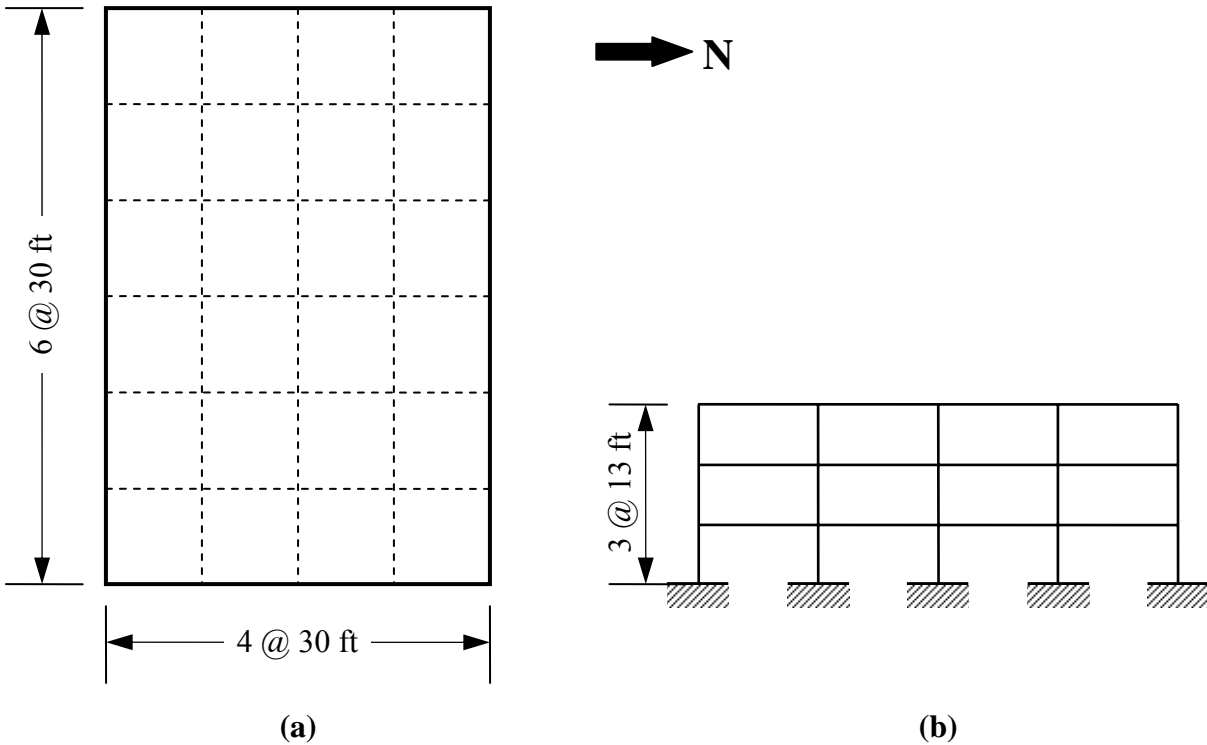
Figure 3-1 Prototype Structure: (a) Plan View; (b) N-S Elevation View (FEMA 355-C)

to half of the total weight of the structure. In other words, there were two single-bay SPSWs in the NS direction, each one of them assumed to carry a tributary weight, W_p , of 3252 kips, distributed as 1055 kips at each of the first two stories and 1142 kips at the roof.

However, for the cyclic pushover test planned in this study, full compliance with geometric and dynamic similitude laws between the properties of prototype and that of model/specimen was not necessary. For simplicity, design of the three-story single-bay SPSW specimen was not conducted at the prototype level; rather, directly at the specimen level, as described in the following section.

3.3 Design of Specimen

Geometric properties of the specimen used in this experimental program were determined by applying a scale factor λ_L of 1/3 to the prototype, which resulted in a three-story SPSW specimen with a typical story height of 52 inches and a bay width of 120 inches. However, due to

dimensional restrictions of the gravity column system used to apply loads and provide lateral supports to the specimen (see Section 3.7.2) available in the Structural Engineering and Earthquake Simulation Laboratory (SEESL) of the University at Buffalo, as well as to minimize design differences with another research project conducted in parallel to this study (i.e., the SMART Walls research project described in Dowden and Bruneau 2014), the final specimen dimensions were slightly modified. The bay width was changed to 90 inches and the average story height was 51 inches.

The total tributary weight for the specimen W_m was determined as follows:

$$W_m = \lambda_F W_p = \left(\lambda_E \lambda_L^2\right) W_p \tag{3-1}$$

where λ_F, λ_E, and λ_L are scale factors for forces, material properties, and length (geometry), respectively; and W_p is the prototype tributary weight. Since the same material is generally used for the prototype and the model, λ_E equals 1. Hence, the total tributary weight for the specimen was equal to 361 kips, distributed to the floors with the same proportion as that in the prototype. Note that when calculating the tributary weight for the specimen, a scale factor of 1/3 was used for λ_L even though the actual geometric properties of the specimen have been slightly different from this scale factor.

The design procedure for SPSW-ID presented in Purba and Bruneau (2010) was closely followed when designing the specimen. On the basis of the spectral acceleration maps in the FEMA 450 provisions (FEMA 2003), the design short and one-second spectral ordinates, S_{DS} and S_{D1}, for the site where the prototype located were 1.3g and 0.58g, respectively. The fundamental period of the specimen T was estimated using the FEMA 450 procedures as 0.13 sec; and using a response modification factor R of 7 and an importance factor I of 1, the total design base shear V resisted by the specimen was 65 kips. The equivalent lateral loads along the height of the specimen were 32, 22, and 11 kips from the third to the first floor. These story forces were resisted entirely by infill plates without considering the possible contribution to lateral strength provided by the surrounding boundary frames. The Indirect Capacity Design (ICD) approach, described in the commentary to the AISC seismic provisions (AISC 2005b, 2010b), was applied to design the boundary frames. The design results of the specimen are explained briefly in the following sub-sections while their detail design checks and calculations are presented in Appendix A.

3.3.1 Specimen Elevation

The overall specimen frame and section details are shown in Figures 3-2 and 3-3, respectively. The height of the specimen from its base (installed on an existing steel floor plate connected to the laboratory's strong floor) to the tip of column pedestal was 160 in. and the width of the specimen measured between the outer flanges of the East and West columns was 96.75 in. As mentioned previously, story height was partly dictated by the dimension of the existing gravity column systems. Here, the first story height was 51.50 in. (measured to the top of first story beam) while the other two stories have a slightly different height of 50.75 in. Note that in SPSWs, beams and columns are also knows as horizontal and vertical boundary elements (HBEs and VBEs), respectively. In this section, these terms are used interchangeably.

The columns were welded to base plates, themselves anchored to an existing larger steel floor plate using a group of high strength slip-critical bolts capable of transferring the plastic moment capacity of the columns. The existing steel floor plate was anchored to the strong floor using high strength tension rods to prevent uplift of the specimen during testing. The first story infill plate was connected to an anchor beam rather than directly connected to the existing floor plate. The columns were continuous over full height of the specimen and 2 in. diameter holes at the column pedestals were provided for erection purpose.

3.3.2 Infill Plates

Light gauge steel with nominal yield strength of 30 ksi was used for the infill plates. Calculated by (F5-1) of the 2010 AISC Seismic Provisions, the minimum required infill plate thicknesses to resist the aforementioned story forces were 0.071, 0.060, and 0.037 in. for the first, second, and third floor, respectively. The closest commercially available gauge steel plates that satisfy these required thicknesses for the same respective floors were 14-gauge (0.0747 in.), 15-gauge (0.0673 in.), and 19-gauge (0.0418 in.) plates.

However, for reasons further explained in Section 4.4, the first story plate was changed to be 13-gauge (0.0897 in.). In addition, the 15-gauge plate for the second story infill was not available from local suppliers, and therefore was changed to be 14-gauge plate. The impact of changing this gauge plate on the behavior of SPSW specimen is also addressed in Section 3.4.
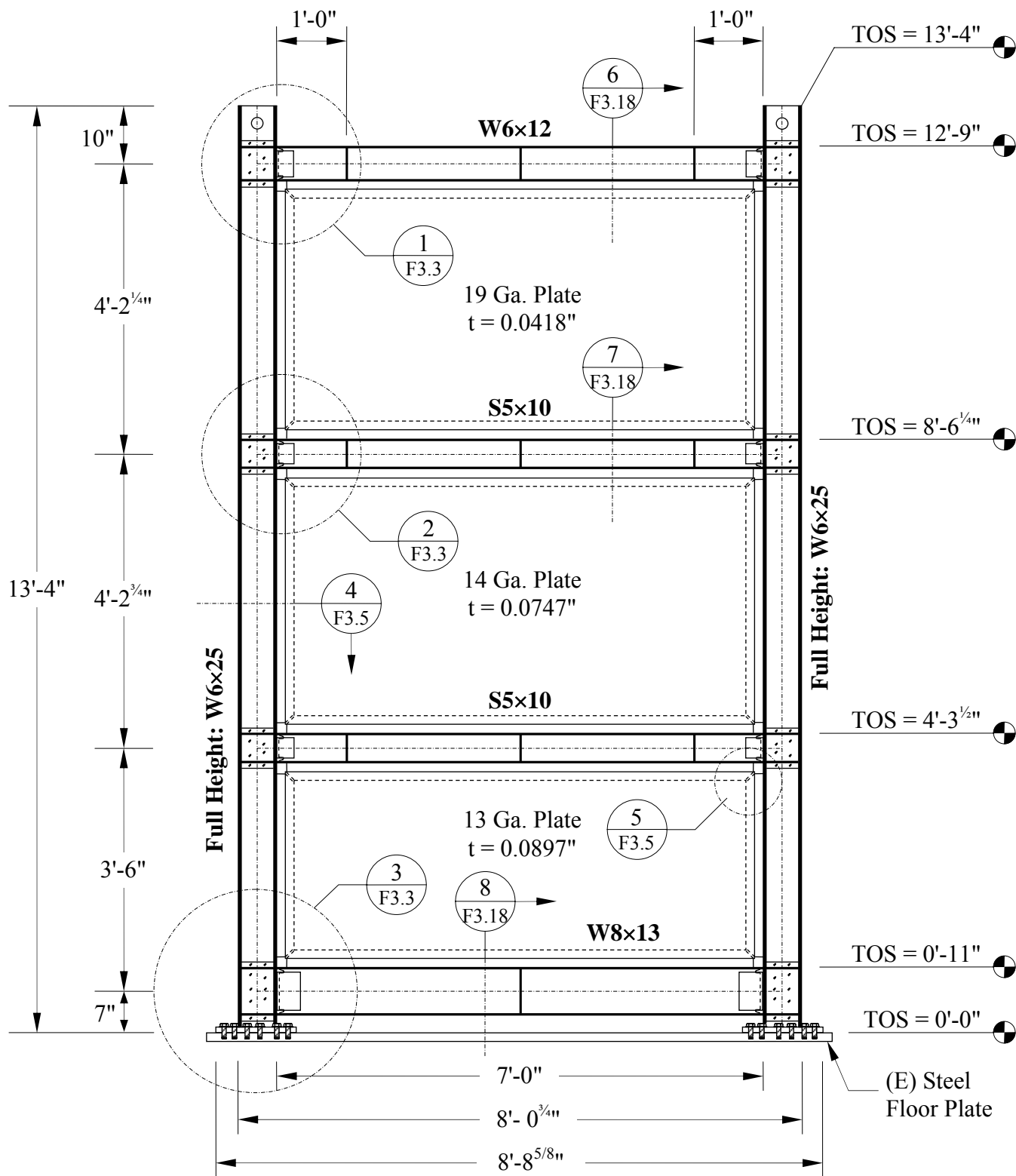
Figure 3-2 Elevation View of Three-Story SPSW Specimen

(a)

Centerline of
W6×25

2" Dia. Hole for Frame Erection/Lifting
Provide at Each End of W6×25 Columns

Stiffener for Lateral Support
(See Section 6/F4.20)

3"

7"

$^3/_8$" Continuity
Plate (A572)

Shear Tab (A572)
PL $^3/_8$ × 3 × 0'-4$^{1/2}$"

1" (Typ.)

¼" Web Doubler
Plate (A572)

W6x12

$^3/_8$" Continuity
Plate (A572)

Light Gauge
Plate G19
(0.0418")

W6×25

12"
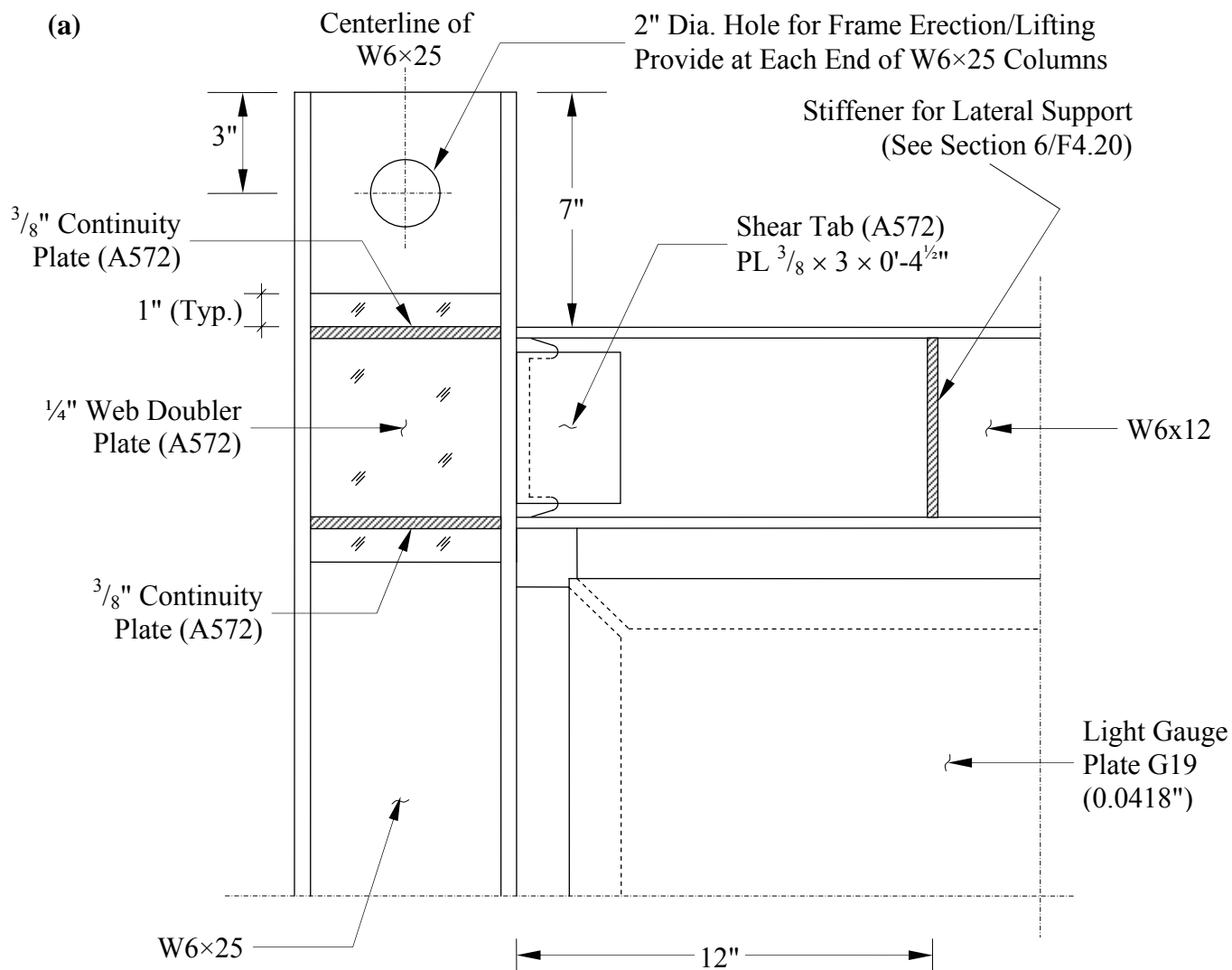
Figure 3-3 Specimen Section Details:
(a) Detail 1: Top Story VBE-to-HBE Joint

3.3.3 Boundary Frames

ASTM A572 Gr. 50 (F_y = 50 ksi) steel was selected for the boundary frames. Based on the Indirect Capacity Design procedure, W8×13 and W6×12 were selected for the bottom and top anchor beams (i.e., HBE0 and HBE3) while S5×10 was selected for the intermediate beams (i.e., HBE1 and HBE2). In addition, W6×25 was selected for the columns (i.e., VBE1 to VBE3).

In the preliminary design process, the adequacy of several possible sections for HBEs and VBEs were investigated. Final section selection, however, was partly dictated by the available steels donated by the American Institute of Steel Construction (AISC) for this study. The above

sections were the most optimum design choices from those available shapes to achieve the objectives of this experimental program (previously described in Section 3.1). This preliminary investigation considered the possible effects (on expected behavior) of strain hardening and probable increases on yielding strength of the infill plates and boundary frames, as further explained in Section 3.4.

(b)
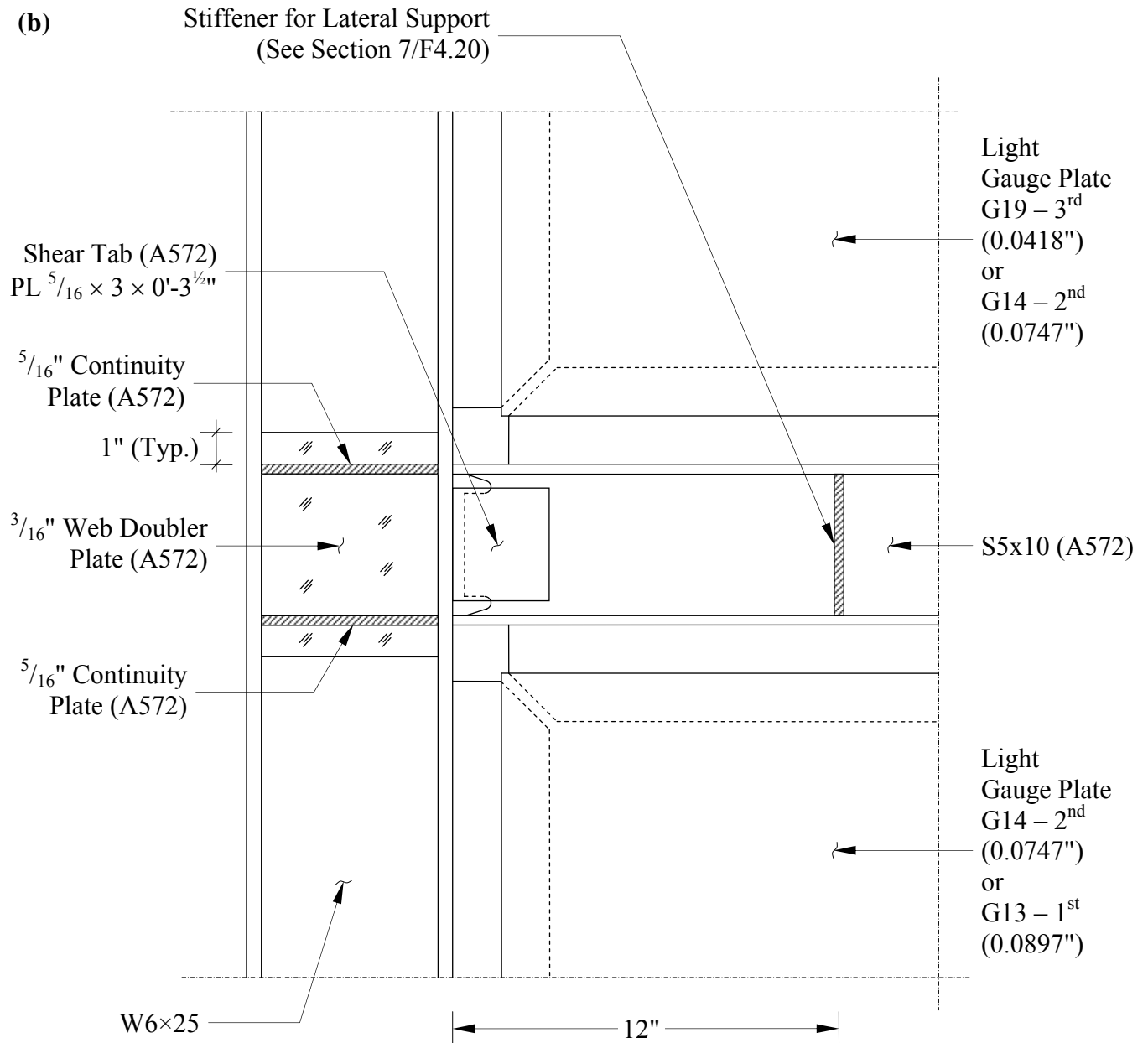
Figure 3-3 Specimen Section Details – Cont'd:
(b) Detail 2: Intermediate Story VBE-to-HBE Joint

50

W6×25

½" Continuity
Plate (A572)

1" (Typ.)

¼" Web Doubler
Plate (A572)

½" Continuity
Plate (A572)

1" Min. Embedment

(E) 1.5" Steel
Floor Plate

Light Gauge
Plate G13
(0.0897")

Shear Tab (A572)
PL ½ × 4 × 0'-6½"

W8x13

1" Base Plate
(A572)

3"

10 Holes Follow the
Hole Pattern on
(E) Steel Floor Plate

4 (N) Holes with
New Pattern

¾" Dia. A490-SC Bolts in
Oversized Holes + ASTM
F436 1¾"×1¾"×⁵/₁₆" Std.
Plate Washers

12"

14¼"

(c)
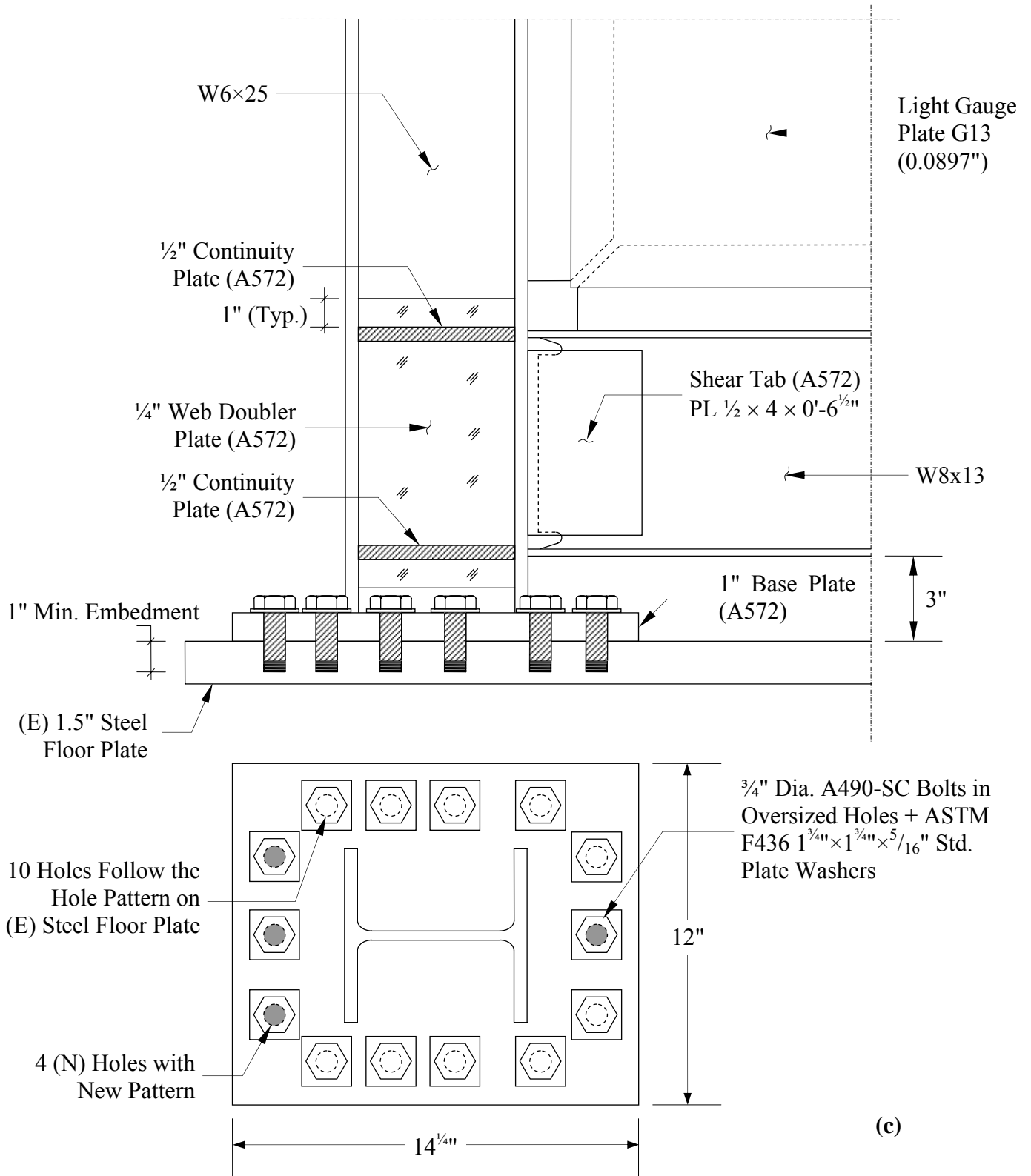
Figure 3-3 Specimen Section Details – Cont'd:
(c) Detail 3: Bottom Story VBE-to-HBE Joint and Base Plate

51

All selected HBEs and VBEs complied with the compactness criteria specified in the AISC Specification for Structural Steel Buildings (AISC 2005a, 2010a). They also complied with the compactness criteria specified in the AISC Seismic Provisions for Structural Steel Buildings (AISC 2005b, 2010b), except for W8×13 used for HBE0, which slightly exceeded the flange compactness criteria. More specifically, the W8×13 flange compactness ratio of 7.8 was 8% greater than the permitted value of 7.2. The impact of this slight insufficiency can be observed in the experimentation program results further presented in Section 4.

3.3.4 Design of Connections

Special moment resisting connections were designed for all HBE-to-VBE connections, and details of the connections are shown in Figure 3-4. The connections were designed to be similar to a Welded Unreinforced Flange-Welded Web (WUF-W) connection specified in the FEMA 350 and AISC 358-10 documents. In this type of connection, complete joint penetration (CJP) groove welds were used to connect HBE flanges directly to VBE flanges; weld access holes (Figure 3-4b) were provided for quality and constructability purposes (i.e., to ensure the continuity of the CJP groove welds throughout the HBE flanges); fillet and CJP groove welds were used to connect shear tabs to HBE webs and to VBE flanges, respectively; and continuity plates were provided. In addition, doubler plates were used in all HBE-to-VBE connections and designed according to the procedure described in Chapter K of the AISC Specification for Structural Steel Buildings (AISC 2005a). Each doubler plate was designed to extend 1 in. beyond the top and bottom continuity plates (Figure 3-3) and provided on one side of the panel zone. The doubler plate was welded to the VBE webs and flanges using fillet and CJP groove welds, respectively.

It is important to note that not all prescribed limits and details for prequalified WUF-W connection were respected in designing the connections of this 1/3 scaled specimen. For example, a W6 column was used, which is shallower than the pre-qualified W12 or W14 column. The shear tab was not beveled at its corner adjacent to the weld access holes; rather, a rectangular shear tab was used. The geometry of the weld access hole was smaller than the minimum specified dimensions in the FEMA 350 (e.g., the specimen's weld access hole radius of 3/16 in. and the distance from the center of the weld access holes to the inside of the adjacent flanges of 3/8 in. were smaller than the corresponding specified values of 3/8 and 3/4, respectively). Note
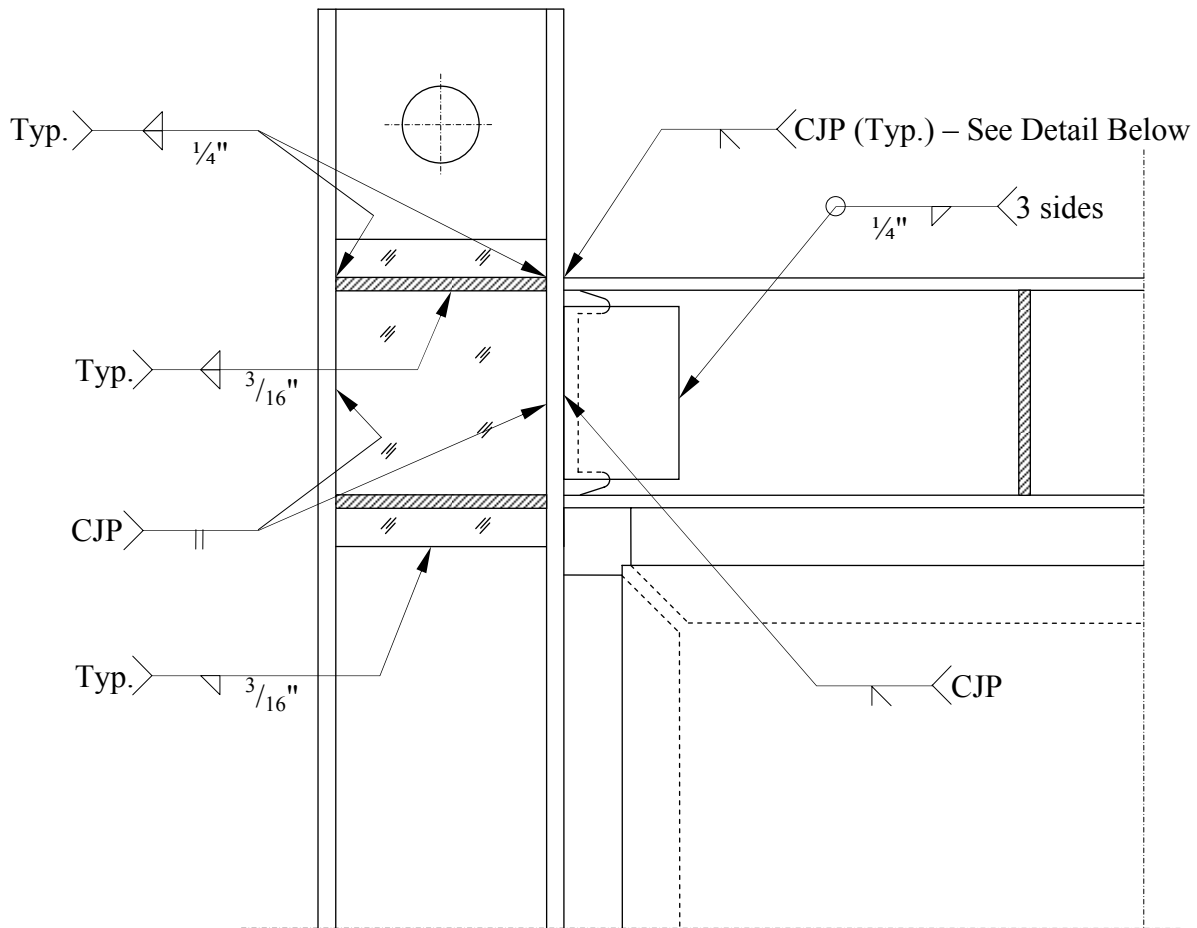
(a)
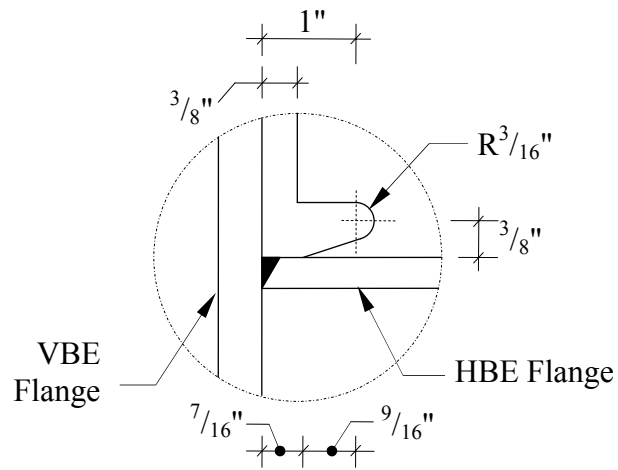
(b)

Figure 3-4 Welded Connection Details: (a) Weld Detail 1: Top Story VBE-to-HBE Joint; (b) Typical Weld Access Hole
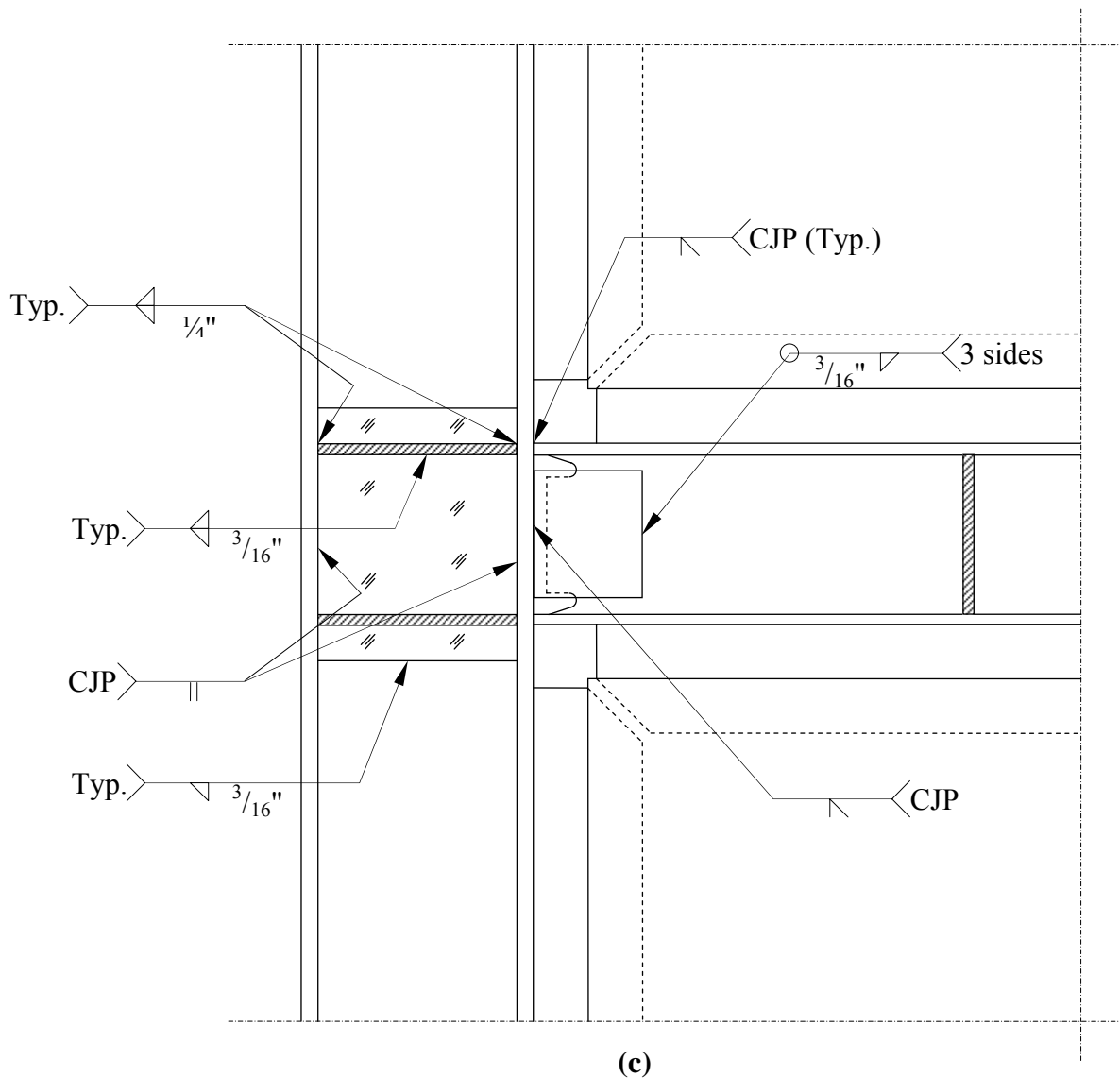
Figure 3-4 Welded Connection Details – Cont'd:
(c) Weld Detail 2: Intermediate Story VBE-to-HBE Joint

that while results from this study would provide useful information, full-scale testing may be desirable to validate findings and recommendations obtained from the behaviors of the 1/3 scale connections used in this study.

Each column was connected to a 1 in. thick base plate using CJP groove and fillet welds for the flanges and the webs, respectively. As shown in Figure 3-3c, the footprint of one base plate was 14 in. by 12 in. Fourteen ¾ in. diameter A490 high-strength slip-critical bolts were required on each base plate to resist the combination of axial forces, base shears, and base moments that were
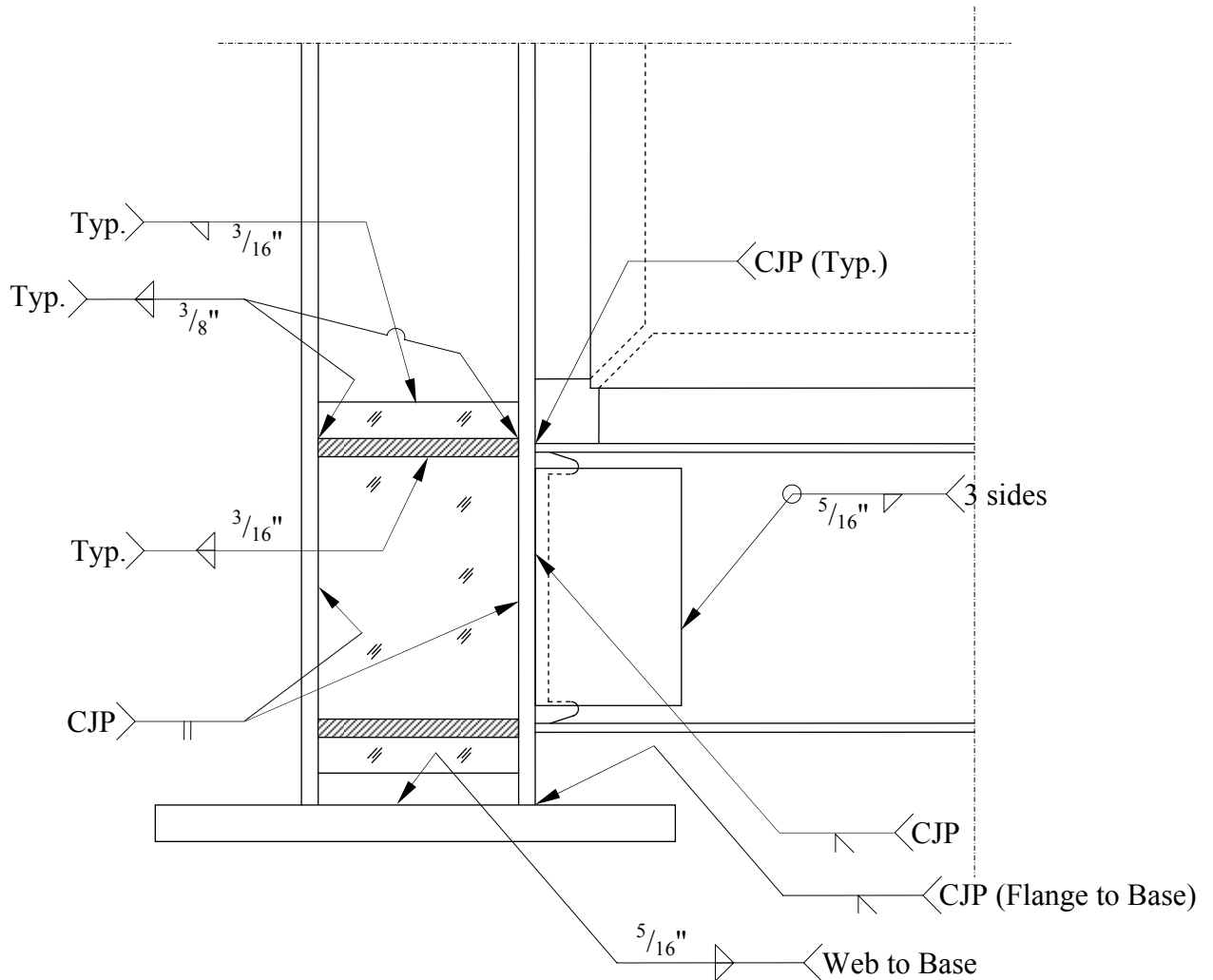
(d)

Figure 3-4 Welded Connection Details – Cont'd:
(d) Weld Detail 3: Bottom Story VBE-to-HBE Joint and Base Plate

expected to develop at a 4% top story drift. Since 10 out of 14 holes had to be positioned to match pre-existing holes located on the 9 ft. by 12 ft. floor plate used to transfer loads to the strong floor, oversized holes of 3/16 in. larger than ¾ in. diameter bolts were specified for constructability. As a result, bolts were arranged slightly un-symmetrically around the column axis, and each base plate had slightly different bolt arrangement (Appendix A). Design of base plates followed the procedures described in the AISC Design Guide No. 1 (entitled Base Plate and Anchor Rod Design) and No. 4 (entitled Extended End-Plate Moment Connections). Electrodes E70XX (F_y = 70 ksi) was selected for all fillet and CJP groove welds and ASTM A572 Gr. 50

(F_y = 50 ksi) steel was selected for continuity, doubler, and base plates. Detail design checks and calculations including reaction forces for each base plate are presented in Appendix A.

The infill plates were connected to the surrounding vertical and horizontal boundary elements using ¼ in. thick and 3 in. wide fish plates of A36 steel (F_y = 36 ksi). Fillet welds were used on both sides of the fish plate to connect it to the HBE and VBE flanges, as shown in Figure 3-5a, while the light gauge plate was welded to the fish plate on one side only. At each HBE to VBE intersection, the fish plate was beveled at a 45° angle and cut to create a corner cut-out of 1.75 in. by 1.75 in. This type of corner detail, shown in Figure 3-5b, was similar to the "Modified Detail B" recommended by Schumacher *et al.* (1997) and has been used previously in several SPSW tests (e.g., Vian and Bruneau 2005, Qu *et al.* 2008, Li *et al.* 2010).

3.4 Design Considerations to Achieve Experimental Objectives

As in any general design process, design of the specimen for this experimental program underwent various trials and modifications to ensure that the experimental objectives presented in this section were met. Key aspects of these modifications are briefly discussed in this section. The commercially available software SAP2000 v. 11.0.8 (CSI 2007) was used throughout the design trials and nonlinear static analysis (monotonic pushover analysis) was conducted for each design trial to investigate whether the intended behaviors were obtained. A strip model that featured the use of fiber-hinges and axial-hinges was used to model inelastic behaviors of each design outcome.

The original intent was to design a three-story SPSW specimen with an aspect ratio of 2.0 similar to that of the SPSW-ID presented in the preceding section. Development of in-span plastic hinges is equally likely to occur in similarly designed SPSWs having different aspect ratios, but choosing a comparable aspect ratio with that of SPSW-ID was a reasonable starting point. Incidentally, note that the selected prototype structure (i.e., the three story SAC model building mentioned earlier in Section 3.2) has a 2.3 aspect ratio, and it was desirable for the 1/3 scaled specimen to have an aspect ratio somewhat close to that of this prototype.
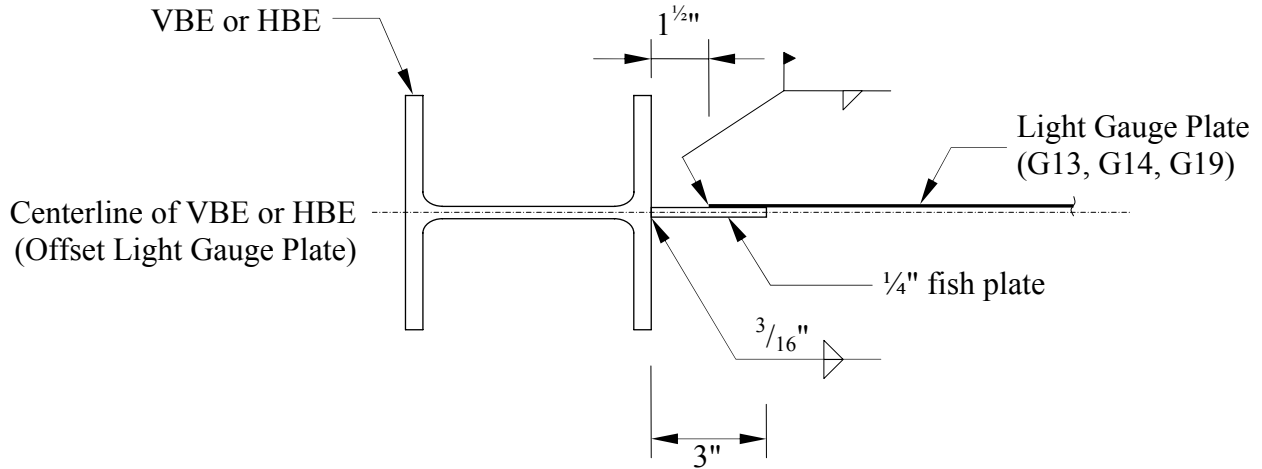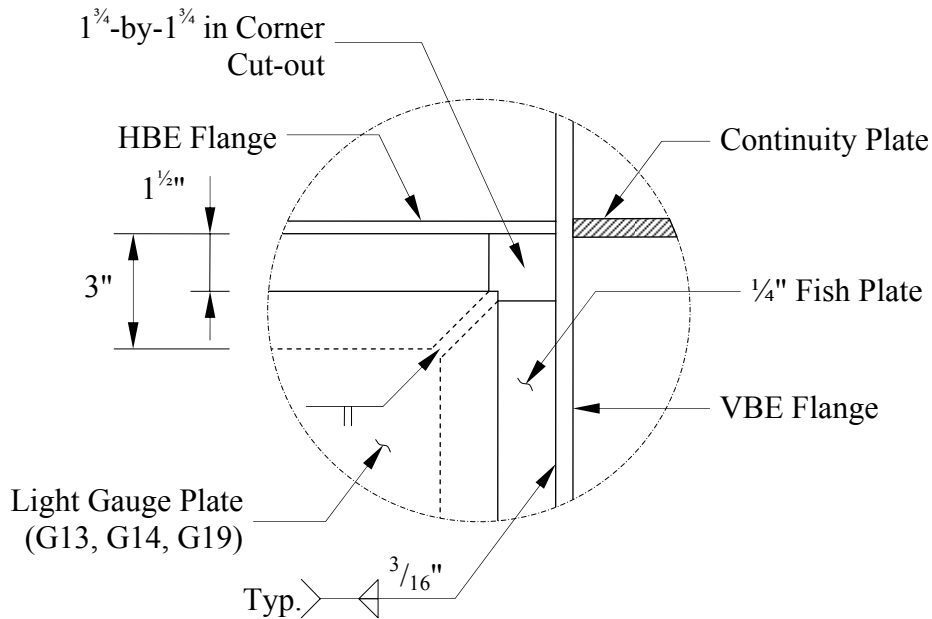
Figure 3-5 Infill Plate Connections: (a) Section 4: Fishplate and Panel Section Detail; (b) Detail 5: Typical Fishplate Corner Detail

Taking the above into consideration, together with constraints due to dimensions of an existing floor plate and gravity column system available in the SEESL facilities, the final aspect ratio was chosen to be 1.8. This smaller than desired aspect ratio corresponded to a 30 in. decrease in beam length (from the intended 120 in. long beam), while the story height remained somewhat the same. If the infill plate thickness selected in the aforementioned first design had been used, this

decrease in beam length would have resulted in a 25% reduction in tension forces acting on HBEs, and this would have lowered the likelihood of developing in-span HBE plastic hinges. Two options were available to compensate for the effects of this constraint: either design for a thicker infill plate or choose a smaller HBE. In a second design trial, combinations of both options were examined. Note that section selection for boundary elements was limited by the available steels donated by the AISC for this study. One design approach was to utilize as many of these available sections as possible to minimize the cost of this experimentation program. It turned out that the thickness of infill plates needed to cause in-span plastic hinging in even the smallest of HBE chosen from those donated W-shapes (i.e., W6×12) would have also yielded the biggest available donated W-shape for VBEs (i.e., W6×25). Hence to ensure that the intended behaviors could be observed, the resulting second trial design was done based on a decision to purchase the necessary smaller W-shapes for intermediate HBEs, and using thicker infill plates compared to that in the first trial design. The resulting design outcomes for this second trial are presented in Table 3-1 denoted as "Case 01".

Up to this point, the design process was based on an assumption that the specified nominal yield strength of 30 ksi for the infill plates and 50 ksi for boundary elements could be achieved. In addition, no strain hardening was specified for the material properties in the aforementioned numerical model. To account for possible strain hardening and greater than specified yield strength for the actual material properties, a series of third design trials considering a "bracket" of steel properties was examined. The resulting design trial denoted as "Case 02" in Table 3-1 was obtained as a result of analyses that considered a bilinear material, with the second slope defined by 30% strain hardening developing in the material properties when reaching an ultimate strain of 20%. Note that an alternative tri-linear material was also considered, in which strain hardening was defined by a second slope (tangent modulus at the onset of strain hardening) set to be 1/15 of the elastic modulus of elasticity up to the point when a 30% increase of yield strength was reached, and a zero-slope plateau of no strain hardening beyond that point. In spite of the faster strain hardening rate in that second model, no significant differences were observed between the designs obtained from these two models with two different strain hardening definitions, and therefore, only the result obtained considering the first of these two strain hardening material models are presented here.

Table 3-1 Monotonic Pushover Results at 4% Top Story Drift of Several Specimen Designs
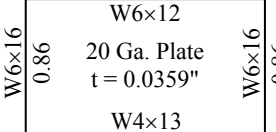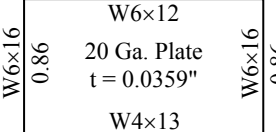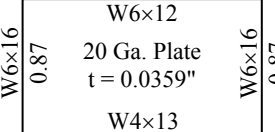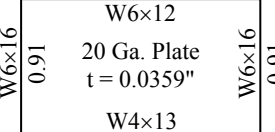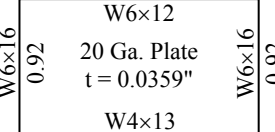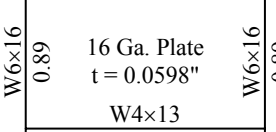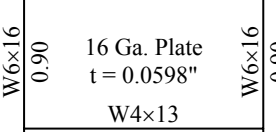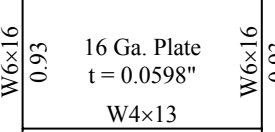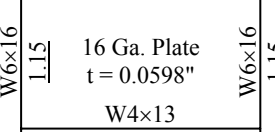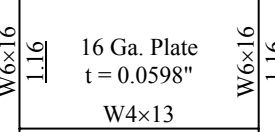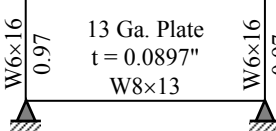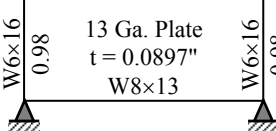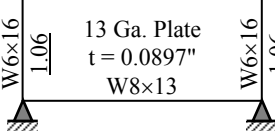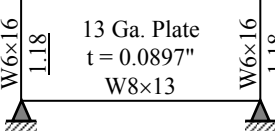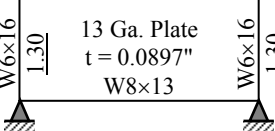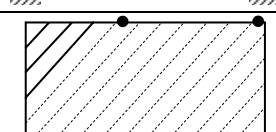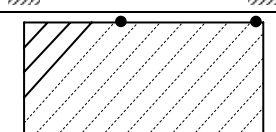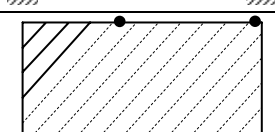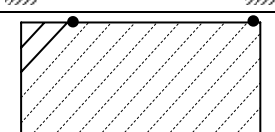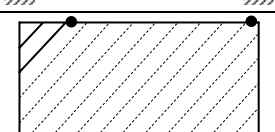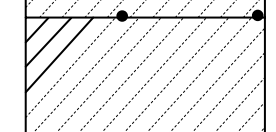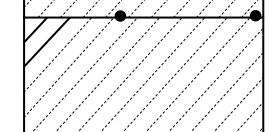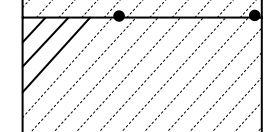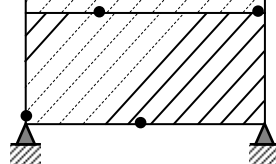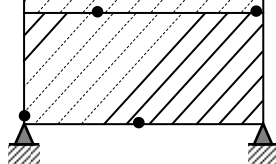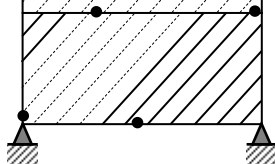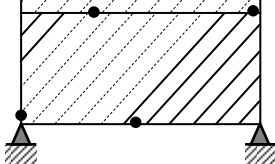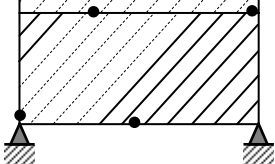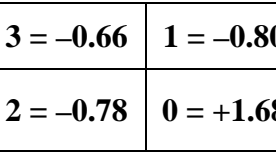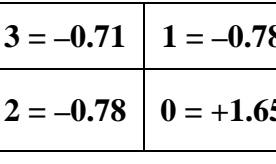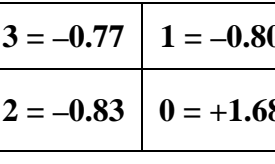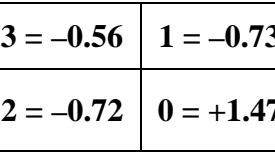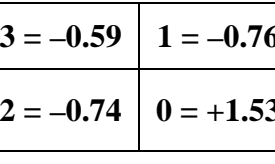
Items	Case 01	Case 02	Case 03	Case 04	Case 05
Design Summary and P-M Ratio (strips are not shown for clarity)	W6×16 / 0.86; W6×12; 20 Ga. Plate t = 0.0359"; W4×13; W6×16 / 0.86 — W6×16 / 0.89; 16 Ga. Plate t = 0.0598"; W4×13; W6×16 / 0.89 — W6×16 / 0.97; 13 Ga. Plate t = 0.0897"; W8×13; W6×16 / 0.97	W6×16 / 0.86; W6×12; 20 Ga. Plate t = 0.0359"; W4×13; W6×16 / 0.86 — W6×16 / 0.90; 16 Ga. Plate t = 0.0598"; W4×13; W6×16 / 0.90 — W6×16 / 0.98; 13 Ga. Plate t = 0.0897"; W8×13; W6×16 / 0.98	W6×16 / 0.87; W6×12; 20 Ga. Plate t = 0.0359"; W4×13; W6×16 / 0.87 — W6×16 / 0.93; 16 Ga. Plate t = 0.0598"; W4×13; W6×16 / 0.93 — W6×16 / 1.06; 13 Ga. Plate t = 0.0897"; W8×13; W6×16 / 1.06	W6×16 / 0.91; W6×12; 20 Ga. Plate t = 0.0359"; W4×13; W6×16 / 0.91 — W6×16 / 1.15; 16 Ga. Plate t = 0.0598"; W4×13; W6×16 / 1.15 — W6×16 / 1.18; 13 Ga. Plate t = 0.0897"; W8×13; W6×16 / 1.18	W6×16 / 0.92; W6×12; 20 Ga. Plate t = 0.0359"; W4×13; W6×16 / 0.92 — W6×16 / 1.16; 16 Ga. Plate t = 0.0598"; W4×13; W6×16 / 1.16 — W6×16 / 1.30; 13 Ga. Plate t = 0.0897"; W8×13; W6×16 / 1.30
Strip Yielding & Plastic Hinge Distribution	(diagram)	(diagram)	(diagram)	(diagram)	(diagram)
HBE… Vertical Deformation (in.)	3 = −0.66 / 1 = −0.80 / 2 = −0.78 / 0 = +1.68	3 = −0.71 / 1 = −0.78 / 2 = −0.78 / 0 = +1.65	3 = −0.77 / 1 = −0.80 / 2 = −0.83 / 0 = +1.68	3 = −0.56 / 1 = −0.73 / 2 = −0.72 / 0 = +1.47	3 = −0.59 / 1 = −0.76 / 2 = −0.74 / 0 = +1.53
V_u (kips)	105.2	108.4	113.9	120.8	126.8

Table 3-1 Monotonic Pushover Results at 4% Top Story Drift of Several Specimen Designs – Cont'd

Items	Case 06		Case 07		Case 08		Case 09		Case 10	
Design Summary and P-M Ratio (strips are not shown for clarity)	W6×25 0.44 · W6×12 (0.91) 19 Ga. Plate t = 0.0418" S5×10 0.73 · W6×25 0.44 / W6×25 0.72 · 15 Ga. Plate t = 0.0673" S5×10 0.68 · W6×25 0.72 / W6×25 0.85 · 13 Ga. Plate t = 0.0897" W8×13 0.89 · W6×25 0.85		W6×25 · W6×12 19 Ga. Plate t = 0.0418" S5×10 · W6×25 / W6×25 · 14 Ga. Plate t = 0.0747" S5×10 · W6×25 / W6×25 · 13 Ga. Plate t = 0.0897" W8×13 · W6×25		W6×25 · W6×12 19 Ga. Plate t = 0.0418" S5×10 · W6×25 / W6×25 · 14 Ga. Plate t = 0.0747" S5×10 · W6×25 / W6×25 · 13 Ga. Plate t = 0.0897" W8×13 · W6×25		W6×25 · W6×12 19 Ga. Plate t = 0.0418" S5×10 · W6×25 / W6×25 · 14 Ga. Plate t = 0.0747" S5×10 · W6×25 / W6×25 · 13 Ga. Plate t = 0.0897" W8×13 · W6×25		W6×25 · W6×12 19 Ga. Plate t = 0.0418" S5×10 · W6×25 / W6×25 · 14 Ga. Plate t = 0.0747" S5×10 · W6×25 / W6×25 · 13 Ga. Plate t = 0.0897" W8×13 · W6×25	
Strip Yielding & Plastic Hinge Distribution										
HBE… Vertical Deformation (in.)	3 = –0.98	1 = –0.34	3 = –0.99	1 = –0.24	3 = –0.76	1 = –0.17	3 = –0.94	1 = –0.22	3 = –0.81	1 = –0.44
	2 = –0.73	0 = +1.40	2 = –0.89	0 = +1.40	2 = –0.50	0 = +1.41	2 = –0.75	0 = +1.41	2 = –0.99	0 = +1.33
V_u (kips)	149.9		153.4		178.7		160.6		128.0	

In the design trials denoted as "Case 03" and "Case 04", the yield strengths of the infill plates and boundary elements, respectively, were factored by a R_y value of 1.1, which is the ratio of the expected yield stress to the specified minimum yield stress (AISC 2010b). In "Case 05", both the infill plate and boundary element yield strengths were factored by a R_y value of 1.1. For those three cases, strain hardening was also modeled in both the infill plates and boundary elements. Conservatively, except at the base, VBEs were assumed to remain elastic for all cases considered (i.e., neither strain hardening nor greater than specified yield strength were considered).

The information in Table 3-1 is provided to document the progression in the design process. Several important insights are outlined as follows:

- Results of monotonic pushover analyses up to a 4% top story drift suggest that strain hardenings in the infill plate as well as in the boundary elements are expected to have minor impacts on the behavior of the specimen. Specifically, strip yielding and plastic hinge distribution for Case 01 and Case 02 are practically the same. Demand-to-capacity ratios for their boundary elements are somewhat the same and all of them are less than 1.0.

- Vertical deformations on the two upper HBEs in Case 02 were slightly greater than those in Case 01, but for the other two HBEs, they were actually slightly less. For example, HBE3 vertical deformation was 0.66 and 0.71 in. for Case 01 and Case 02, respectively. When the specimen is pushed up to 4% top story drift, total base shear of 108.4 kips was obtained in Case 02, which is a 3% increase of total base shear as a result of strain hardening.

- A more pronounced impact on specimen behavior is due to greater than specified yield strength combined with the presence of strain hardening. If the greater yield strength predominantly occurred in the infill plate while HBEs remain at the specified minimum yield strength (i.e., Case 03), higher tension forces generated by the infill plates cause HBE of the same strength as that in the previous case to deflect more, and consequently more of the infill plates remain elastic. In this case, an 8% increase of total base shear was obtained. By contrast, when the greater yield strength predominantly occurred in HBEs (i.e., Case 04), the effects are reversed because the HBEs have additional strength to resist the same amount of tension forces from the infill plates. As a result, HBE deformations

decrease, more infill plates elongate beyond the yield limit, and higher total base shear develops at the same 4% top story drift (a 15% greater total base shear is reached).

- These two cases (i.e., Case 03 and 04) bound the range of possible outcomes (i.e., strip yielding, plastic hinge distribution, and HBE vertical deformation) of this experimental program, and the magnitude of these outcomes for Case 05 fall within these two extremes. Case 05 represents the realistic condition for which strain hardening and greater than specified yield strengths for both infill plates and HBEs occur.

- Regardless the source of greater yield strength, a bigger VBE section is required to sustain pulling forces from the infill plates and internal forces from the HBEs. As a result, W6×16 selected in Case 01 had to be replaced by larger W6×25 to provide a satisfactory design (i.e., Case 06).

After obtaining the Case 06 design, two design checks were conducted and their results are summarized in Table 3-1. The first check investigated the consequence of non-availability of the desirable light-gauge plates in the market. This is because the 15-gauge plate of 0.0673 in. thickness used for the second story infill plate was not available at local suppliers and had to be replaced by either a thinner or thicker gauge. If a thinner gauge (i.e., 16-gauge plate of 0.0598 in. thick) had been used, HBE1 and HBE2 would have undergone larger and smaller deformations, respectively, compared to those in the Case 06 design because the thickness difference between the first and second story infill plates attached to HBE1 would have increased while that between the second and third story infill plates attached to HBE2 would have decreased. Consequently, this would have allowed the entire second story infill plate to elongate beyond the yield point. In terms of the overall behavior of the specimen, the development of in-span plastic hinges would not have changed even though the extent of their plastification would have been reduced, again, compared to that in the Case 06 design. By comparison, if a thicker gauge (i.e., 14-gauge plate of 0.0747 in. thick) was to be used, the above effects would be reversed. Here, HBE1 and HBE2 would have undergone smaller and larger deformations, respectively, along with partial yielding of the second story infill plate, and significant development of in-span plastic hinge development. Hence, the latter option was chosen for the second story infill plate, for which the resulting design and response quantities are shown in Table 3-1, denoted as "Case 07".

One might question whether it would have been more effective to instead maintain the same proportion among the infill plates, which could have been achieved by replacing the entire set of infill plates (dropping one gauge-notch below or above those considered in Case 06) instead of only replacing the second story infill plate. This option was unfortunately not possible because the boundary frame had been ordered for fabrication and the first story infill plate was already in-hand prior to ordering of the other infill plates (see information in Section 3.5).

As latter discussed in Section 3.6, another check on the specimen design was conducted to investigate whether the fish plates could potentially increase the HBE cross section properties. Results of a modified analytical model that included the corresponding greater HBE cross section properties due to the attached 3 in. wide fish plates (denoted as "Case 08" in Table 3-1) suggested that the possibility to observe partial yielding of the infill plates, in-span plastic hinge, and accumulation of plastic incremental deformations on the HBEs would be greatly diminished if a 3 in. fish plate was to be used. Therefore, smaller 1 in. wide fish plates (denoted as "Case 09" in Table 3-1) were used to make the specimen behave as intended.

Finally, for completeness, specimen response modeled using actual material properties obtained from tensile coupon tests (as later presented in the following section) is shown in Table 3-1 as "Case 10", which exhibits somewhat similar behavior to that observed in Case 09.

3.5 Material Properties

A total of 27 tensile coupons from 7 different sources were prepared. A group of four coupons was cut from each of the 13-, 14-, and 19-gauge steel plates as well as from the W6×25, W6×12, and W8×13 sections used for VBEs, HBE0, and HBE3, respectively. For these W-sections, two coupons each were taken from their web and flange (either top flange or bottom flange) while for the intermediate HBE1 and HBE2 however, due to the sloping inside face of S5×10 flanges, a group of three coupons were cut from its web. To ensure that the light-gauge steel supplied by the Ryerson Coil Processing company exhibited ductile behavior, coupons from the 13-gauge steel plate were tested first before ordering the other two gauge sizes. One coupon was taken from each plate direction (i.e., parallel to and perpendicular to the rolling direction) while the other two

coupons were cut at an angle of 45° to the rolling direction, considering that tension fields typically develop along the diagonal direction of infill plates. As further presented in this section, all four coupons displayed ductile behavior and have somewhat similar yield and ultimate strengths. Based on this result, for simplicity, all coupons for the 14- and 19-gauge steel plates were taken parallel to the rolling direction.

Tensile coupon testing followed the requirements of ASTM E8 Standard for "Sheet-Type" specimens. Overall length of the specimen was 8 in. with 2 in. gauge length within where strains were recorded. Figure 3-6 presents examples of coupons taken from infill plates and boundary elements, together with a schematic drawing of the Sheet-Type specimen. A typical tensile test setup is shown in Figure 3-7, which consists of an MTS universal testing machine of 20 kip capacity, an MTS electro-mechanical extensometer attached to the coupon, and Data Acquisition (DAQ) system to record forces and displacements data, which then can be viewed in a real time display. The coupon was pulled using displacement control with a rate of 1/16 in. per minute.

Prior to obtaining the mechanical properties of the coupons, a post-process of the raw data from the DAQ system was generally required. The process included removing several records at the beginning of the test to eliminate jaggedness, offsetting the data such that it started from the point of origin (0,0), removing data after fracture as this phenomenon has no physical meaning, and reducing noise through smoothing data processing. For the latter data processing, 3-, 5-, and 7-point Moving Average with Uniform and Gaussian Weight was investigated. No significant differences were observed among these smoothing data processing schemes. Results presented in this report were based on the 5-point Moving Average with Uniform Weight.

Examples of processed stress-strain curves for light-gauge and ASTM A572 steels are shown in Figure 3-8. The first set of curves presents the results from the 13-gauge steel. GA13-1 and GA13-2 are coupons taken from parallel to and perpendicular to the rolling direction, respectively, while both GA13-3 and GA13-4 are coupons taken at an angle of 45° to the rolling direction. As stated previously, all four coupons have somewhat similar mechanical properties and displayed ductile behavior. On the second set of curves, results from ASTM A572 steels are shown, for the W6×25, W6×12, W8×13, and S5×10 sections. While all coupons made of light-
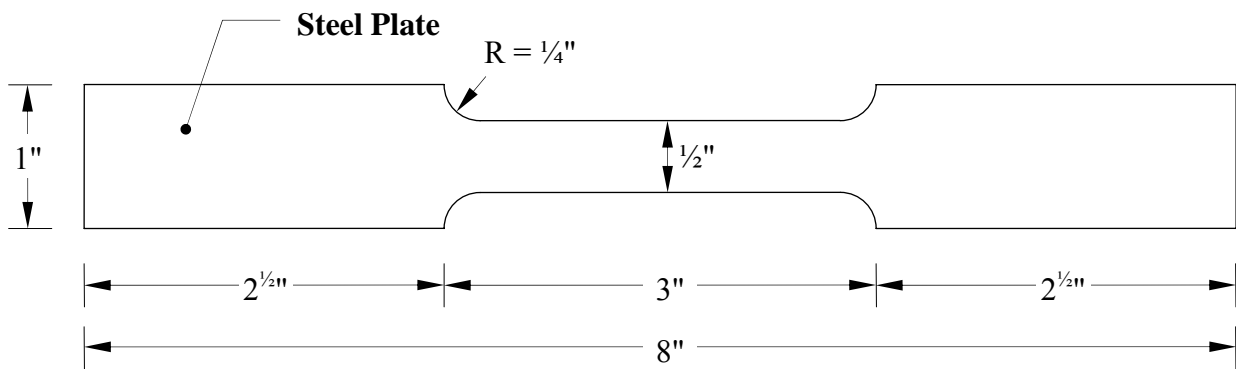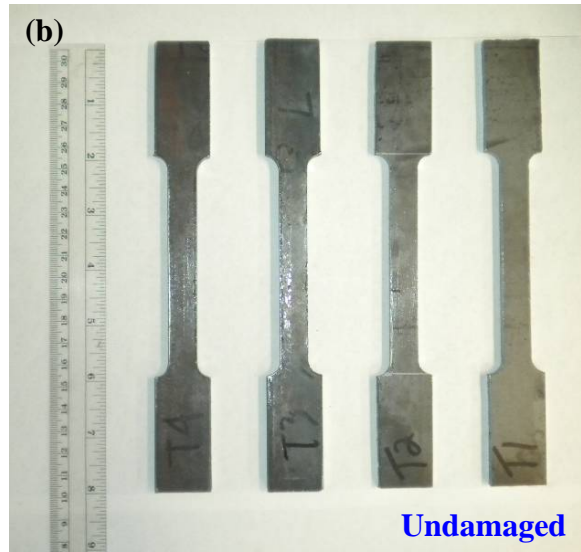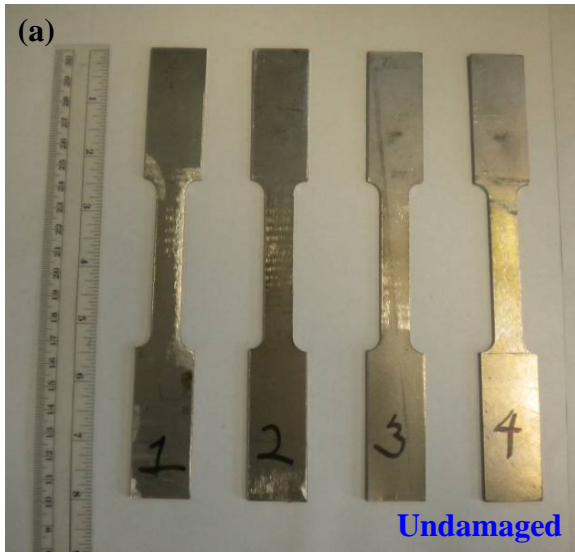
Figure 3-6 Tensile Coupon Specimens: (a) Samples Taken from Infill Plates (13-Gauge); (b) Samples Taken from Boundary Elements (HBE3: W6×12); (c) ASTM E8 Standard "Sheet-Type" Coupon Dimension
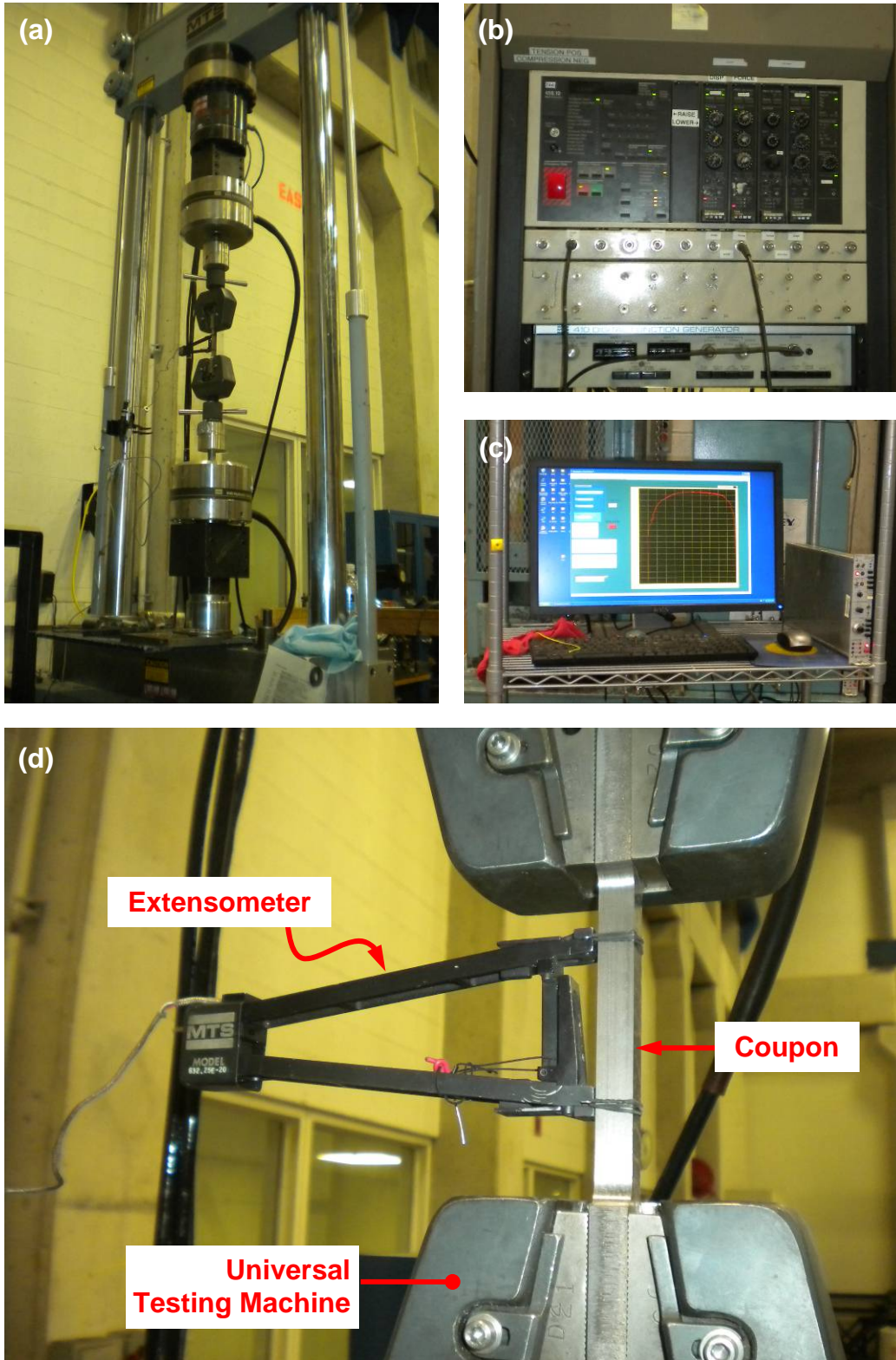
Figure 3-7 Tensile Coupon Test Setup: (a) MTS Universal Testing Machine; (b) DAQ System; (c) Real Time Display; (d) Detail Setup
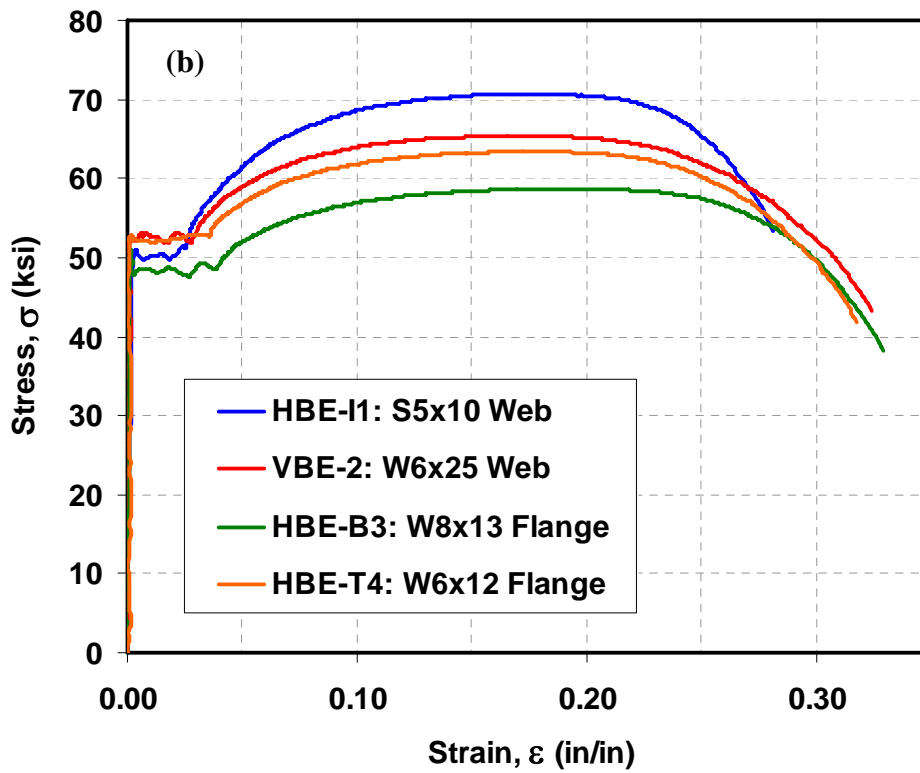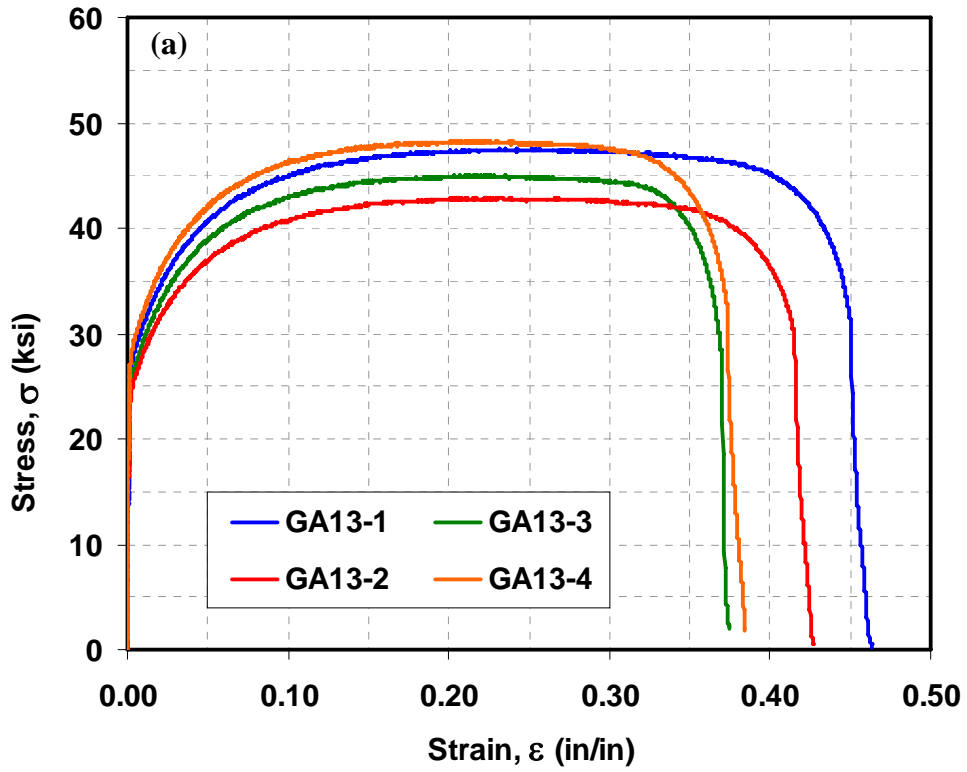
Figure 3-8 Engineering Stress-Strain Curve: (a) Infill Plates (Light-Gauge Steel); (b) Boundary Elements (ASTM A572 Gr. 50 Steel)

gauge and ASTM A572 steels display ductile behavior, several key differences are observed when comparing these two sets of curves. Light-gauge steel has stiffer strain hardening compared to that of ASTM A572 steel, especially at a strain level smaller than 0.05. The latter steel, however, has a well-defined yield point, which is not the case for the plate steels. In addition, rupture points on these two sets of curves indicate that fracture of ASTM A572 coupons exhibited large ductility during necking and fractured at a large stress, compared to that of light-gauge coupons, which also exhibited large ductility but lost more strength during necking prior to fracture. Consequently to this phenomenon, the ASTM A572 steel fractured with a loud noise, compared to the relatively subtle sounds heard at the end of testing for the light-gauge steel. Figure 3-6 shows the final condition of some of the coupons for both types of steel. Compared to their initial conditions, all coupons underwent more than 28% elongation before fracture.

Table 3-2 summarizes the average material properties of each component. For light-gauge steels, modulus of elasticity was obtained from a linear regression slope of processed data up to 2/3 of the theoretical yield strength (i.e., up to 20 ksi), yield strength was defined per the *0.2% offset method*, and rupture strain was based on the strain reading when stresses dropped to about 80% of the ultimate strength. The modulus elasticity of ASTM A572 steels was also estimated from a linear regression slope, but taken up to the observed yield points, because the yield point (and rupture strain for that matter) was well identified in this steel. Interestingly, the actual yield strengths of light-gauge steels were slightly below the expected 30 ksi yield strength, while that of ASTM A572 steels were slightly above the expected 50 ksi yield strength. The impact of these actual material properties on the specimen behavior is further discussed in Section 3.9. Detailed results presenting variability of mechanical properties between one coupon and another and additional supporting data recorded during the tensile coupon test are presented in Appendix A.

3.6   Specimen Preparation and Modifications

The boundary frame was manufactured first at a local steel fabricator (i.e., K & E Fabricating Co., Inc.). Several snapshots of the fabrication process are shown in Figure 3-9. All stiffener, continuity, and doubler plates were welded to HBE and VBE components (Figures 3-9a and 3-9b) first, before they were assembled to a complete frame. Shear tabs, fish plates, and base plates were added at the last stage (Figures 3-9c to 3-9e).

Table 3-2 Summary of Material Properties from Tensile Coupon Test

Component	Nominal Thickness (in)	Actual Thickness (in)	Modulus of Elasticity (ksi)	Yield Strength (ksi)	Ultimate Strength (ksi)	Rupture Strain (%)
Plate GA13	0.0897	0.0886	28420	26.668	45.933	39.31
Plate GA14	0.0747	0.0713	27736	23.598	42.292	46.29
Plate GA19	0.0418	0.0402	26772	20.034	39.270	42.58
W6x25 Web	0.320	0.3458	33522	52.875	65.664	33.97
W6x25 Flange	0.455	0.4322	32136	52.475	66.768	34.27
W6x12 Web	0.230	0.2268	34473	52.775	64.460	36.65
W6x12 Flange	0.280	0.2799	29441	52.350	63.776	33.64
S5x10 Web	0.214	0.2028	30323	49.975	70.521	27.85
W8x13 Web	0.230	0.2360	24080	54.200	66.175	32.98
W8x13 Flange	0.255	0.2405	30126	50.805	62.222	31.22

W6x25 = VBE   W6x12 = HBE-T   S5x10 = HBE-I   W8x13 = HBE-B

One of the experimental objectives is to investigate the performance of special moment resisting connections in steel plate shear walls. As such, the quality of welding at CJP groove welded connections between HBE and VBE flanges was controlled by means of nondestructive testing (NDT) and visual inspection performed by a certified welding inspector. This was done to eliminate possible doubts on quality of welds should fractures develop at those connections during the experiment. However, it is important to acknowledge that the flange thicknesses of the HBEs used in the specimen were either equal or smaller than the threshold thickness of 5/16 in., below which ultrasonic testing (UT) may not work properly due to interference from adjacent back-side metal on ultrasonic waves when detecting weld defects (personal communication with Jimmy Hayes of Niagara Testing). Note that the AISC seismic provision (AISC 2010b) actually does not require UT inspection for CJP groove welds with materials less than that minimum thickness. Annex S of AWS D1.1 (AWS 2008) provides alternative techniques for UT examination in material thinner than 5/16 in., but for practical reasons and because these alternative techniques were deemed too complex for the task at hand, such alternative procedures
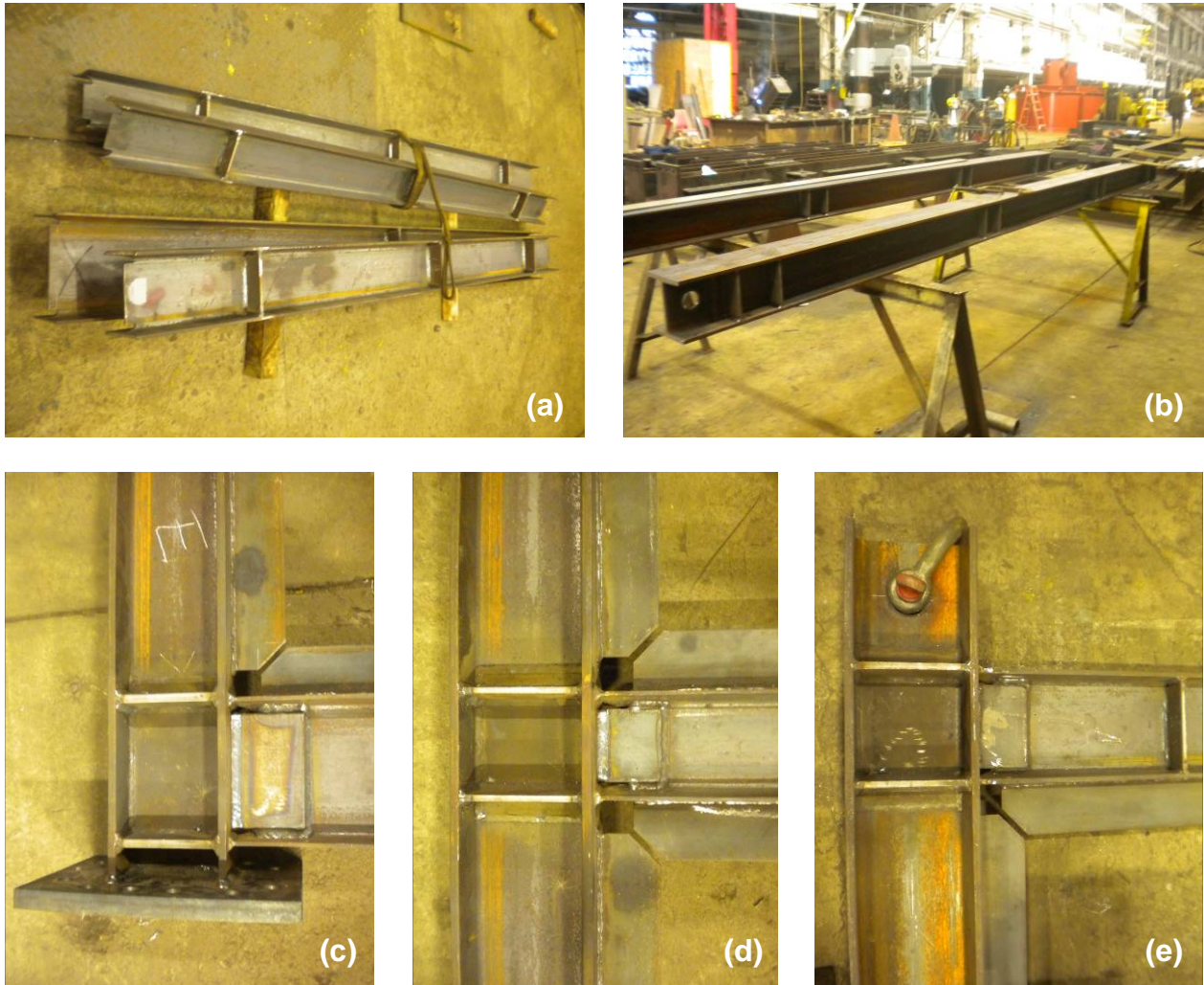
Figure 3-9 Fabrication Process of Boundary Frame: (a) HBE components; (b) VBE components; (c) Bottom Joint Assembly; (d) Intermediate Joint Assembly; (e) Top Joint Assembly

was not applied in this study. Personal communications with experts in the field of NDT (e.g., Professor Salvatore Salamone of the University at Buffalo, Charles Hayes of Lincoln Electric, and Jimmy Hayes of Niagara Testing) provided the same insights on the limitation of UT inspection within thin materials and on the impracticality of applying the Annex S procedure.

In spite of the above limitations, Niagara Testing performed inspection on several CJP Groove welds on the specimen. Ultrasonic testing (UT) was conducted on the West joints of HBE1 and HBE2 as well as the East joint of HBE3. In addition, Phase array (PA) testing was conducted on both East and West joints of HBE2 as well as the West joint of HBE1. The UT and PA

examinations during the fabrication of the boundary frame are displayed in Figure 3-10. To the best ability of the technician interpreting the real time display of UT and PA data, no major weld defects were reported.

Figure 3-10 Nondestructive Testing: (a) Phase Array (PA) Testing; (b) Real Time Display for PA; (c) Ultrasound Testing (UT); (d) Real Time Display for UT

By the time the boundary frame shipped to the SEESL facilities, the parallel SMART Walls research project (Dowden and Bruneau 2014) had completed a series of testing on SPSW with a similar size to the specimen in this study, but with rocking connections. In that project, the strains recorded by uniaxial strain gauges attached to HBE flanges were smaller than expected. The large fish plates used (relative to the HBE size in that 1/3 scale specimen) were suspected to contribute to this phenomenon, possibly behaving as a part of HBE cross section and creating a build-up member with having higher inertia and cross section depth. Due to the fact that the specimens of

interest here had been built with the same size fish plates (¼ in. thick by 3 in. wide) and comparable HBEs, a limited investigation was conducted to check whether the same phenomenon might occur in this experimental program and whether this could impact the predicted behavior of the specimen. It was found that if the fish plate was assumed to be part of HBE cross section, the moment of inertia increased by a factor 1.6 and 1.7 for HBE3 and HBE0, respectively, while it increased three times for HBE1 and HBE2. In addition, the plastic section modulus increased by a factor of 1.3 for HBE3 and HBE0 and 2 times for HBE1 and HBE2. As a result of these HBEs having unexpected overstrength to resist tension forces developed by yielded infill plate, the possibility to observe partial yielding of the infill plates, in-span plastic hinging, and accumulation of plastic incremental deformations on the HBEs would be diminished. Note that in the analytical models used during the design process (Section 3.4), the fish plates were not considered and the infill plates were modeled as a series of strips attached directly to the surrounding boundary elements. Results of a modified analytical model that included the increased HBE cross section properties (due to presence of the fish plates) confirmed these concerns (Section 3.4).

To alleviate that possible problem, the fish plates attached to the HBEs were flame cut from their original 3 in. width to be only 1 in. wide, leaving only enough space for the technicians to weld the infill plates to the fish plates. Another modified analytical model with this new size fish plate showed behavior somewhat similar to that of presented in Section 3.4. Prior to attaching the infill plates, edges of the fish plate were de-burred with a power grinder to remove small notches left from the flame cutting process. Note that although the fish plates similarly provided overstrength to the VBEs, this did not negatively impact the intended experimental objectives. Consequently for practical reason, the fish plates attached to VBEs were left unmodified (i.e. 3 in. wide, as originally designed and fabricated).

Following the above modification, uniaxial and Rosette strain gauges were installed on HBEs and VBEs on both sides of the specimen. A complete layout of strain gauges installed in the specimen is presented in Section 3.7.4. The strain gauges located on HBE flanges where the fish plates attached, however, were installed after the infill plates were welded to the boundary frame. This was to avoid strain gauge damage from overheating during the welding of the infill plates to the narrow 1 in. wide fish plate.

To control the quality of welds during welding of the infill plates, the boundary frame was laid down on stable "horse" platforms and the infill panels were welded to the fish plates along the boundary frame, proceeding with the first, third, and second story infill plates. A temporary wooden platform laid down between the columns was installed to make it possible for the technicians to access and weld the second story infill plate. The finished SPSW specimen is shown in Figure 3-11.

Figure 3-11 Three-Story SPSW Specimen

In the last stage of the specimen preparation, the remaining strain gauges were installed, and then grids were made on each side of the infill plates. For a better visualization of infill plate deformations, gridlines ¾ in. thick were drawn with a permanent black marker, spaced at 7 in. in both the horizontal and vertical directions. After covering the grids with painters tape and cleaning up the specimen of its dust and loose particles, the whole specimen was whitewashed. Removing of the tape was done a day prior to the test. Several snapshots of the specimen's final preparation are shown in Figure 3-12.
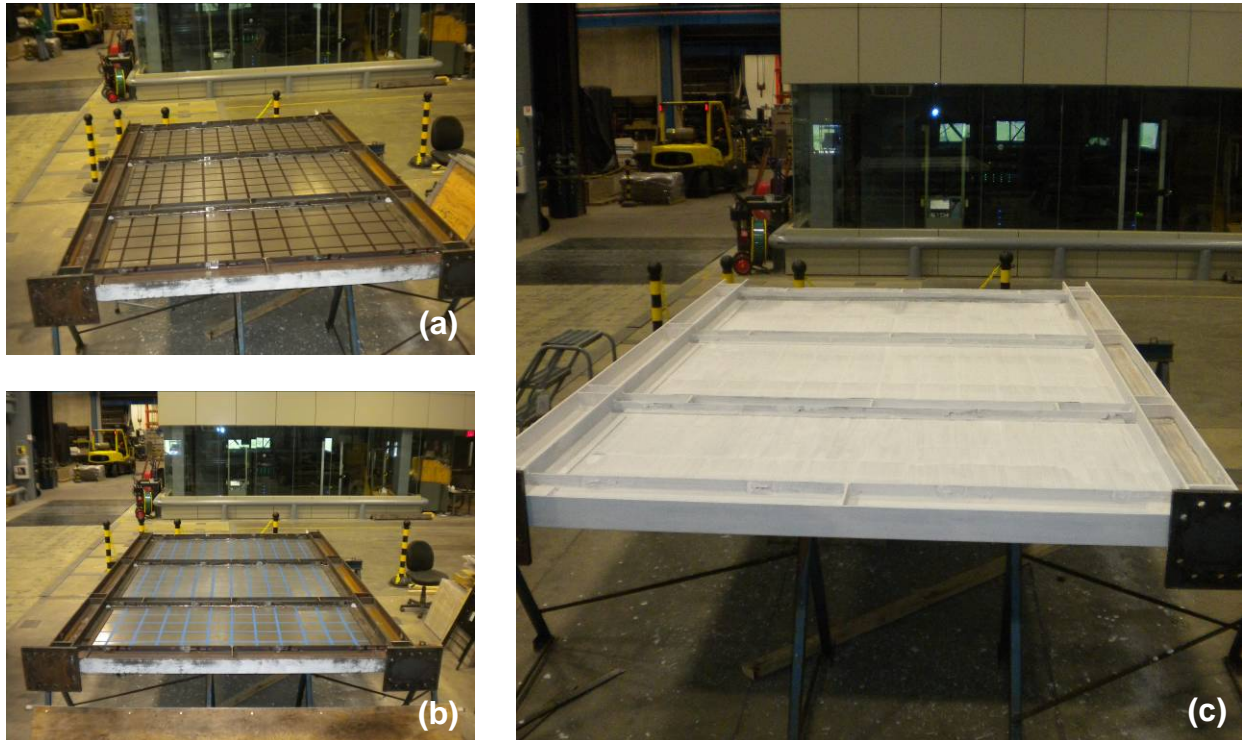
Figure 3-12 Specimen Final Preparation: (a) Making Gridlines; (b) Covering Gridlines with Painters Tape; (c) Whitewashing Specimen

Figure 3-13 shows the specimen attached to the existing floor plate. During this installation, it was discovered that one of bolts on each column base plate could not be installed due to limited access. Located exactly beneath the HBE0, these bolts could not be tightened using the available torque wrench in the SEESL facilities. After reviewing outputs of the analytical model with actual material properties of infill plates and boundary elements (Section 4.4), it was deemed safe to proceed with the remaining thirteen ¾ in. diameter A490 high-strength slip-critical bolts on each column base plate. Each bolt was tightened up to 450 pound-ft torques to achieve clamping forces of 35 kips. After all the bolts were tightened, level measurement showed that the specimen was practically plumb (Figure 3-13d).

3.7   Experimental Setting

The experimental program was conducted at the SEESL facilities of the University at Buffalo. Detail information about this state of the art earthquake engineering laboratory can be found at http://nees.buffalo.edu/. The experimental setting planned in this study for the cyclic pushover
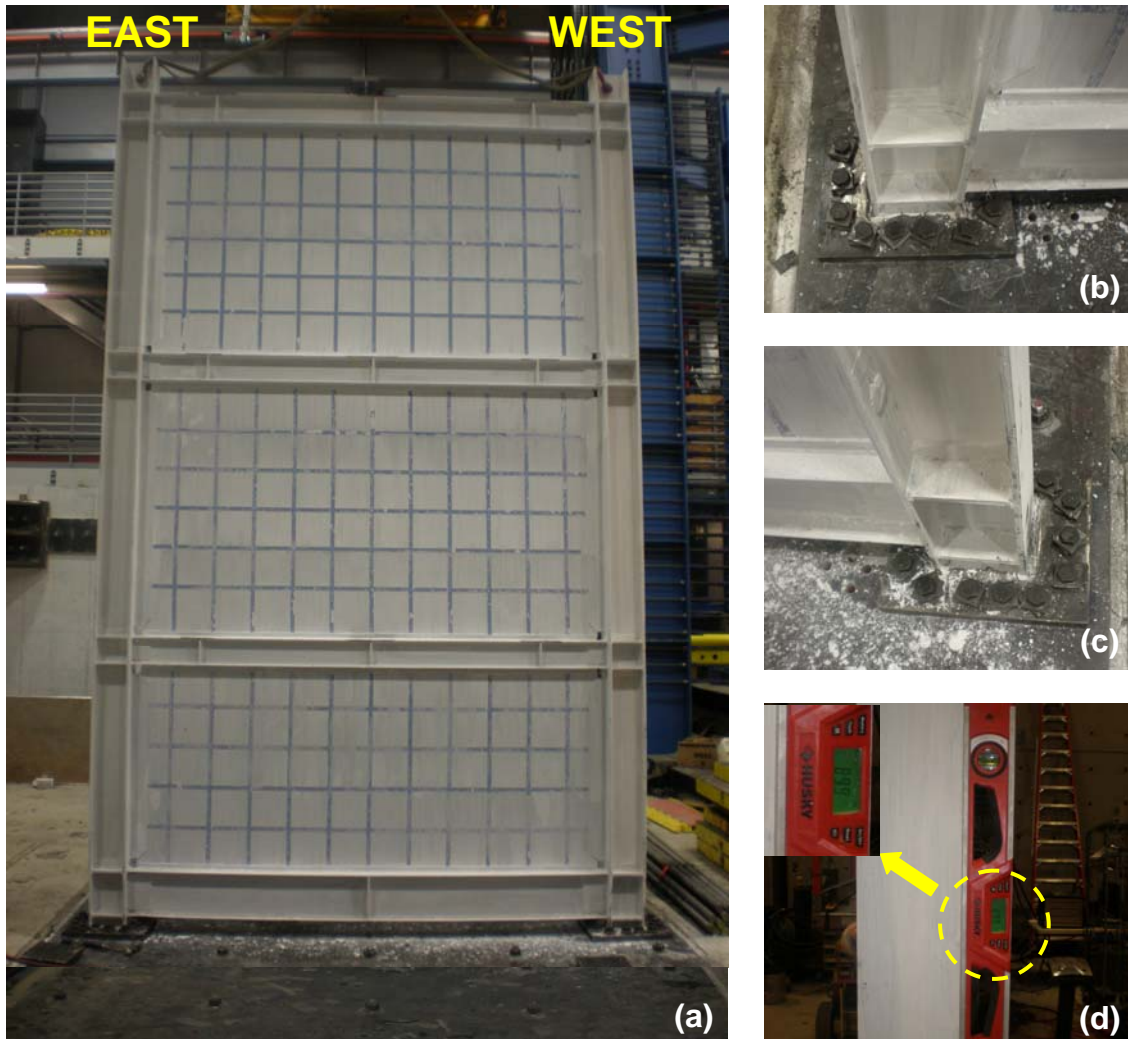
Figure 3-13 Specimen Mounting on Floor Plate: (a) Overall View; (b) East Column Base Plate; (c) West Column Base Plate; (d) Vertical Level Measurement

testing of a 1/3 scaled three-story SPSW is explained in this section, focusing on how the specimen, gravity column and lateral support systems, actuators, and instrumentation were assembled together for the purpose of achieving the aforementioned research objectives. The experimental setting has several similarities with that of the SMART Walls research project by Dowden and Bruneau (2014).

3.7.1 Specimen Mounting

As shown in Figure 3.13, the specimen was positioned in the East to West direction and anchored to an existing 9 ft. by 12 ft., 1.5 in. thick floor plate using high-strength bolts on each column base plate. The existing floor plate was anchored to the 24 in. thick concrete strong floor using 22

high strength tension rods of $1\frac{1}{8}$ in. diameter. The tension rods were uniformly distributed throughout the floor plate footprint of 9 ft. by 12 ft., with a corresponding tributary area of 24 in. by 24 in. per rod, supplemented by one tension rod at each corner of the plate (Figure 3-14a). The specimen was exactly located at the centerline of the floor plate.

3.7.2 Gravity Column System and Lateral Supports

The gravity column system is a set of removable frames and reactive masses that has been used for many different purposes. Originally developed by Kusumastuti *et al*. (2005), the system was designed as an independent vertical load support system separated from a lateral load resisting system. Since then, the system has been used in various earthquake simulation research projects at the University at Buffalo. During experimentations, structural damage concentrates in the lateral load resisting system designed for this purpose, which in this study is steel plate shear walls, while the gravity column system remains intact. At the same time, the gravity column system can provide out-of-plane resistance to the tested specimen. Figure 3-14 shows the setup used in this study: the gravity column system sandwiches the steel plate shear wall specimen and is fitted with supports to prevent lateral torsional buckling of the beams. A complete view of the experimental setting with the gravity column system is shown in Figure 3-15. Connected by several angles to the specimen, the essentially rigid mass plates can also transfer the actuator loads to the tested specimen. More information regarding load transfer mechanism is presented in Section 3.7.3. Key features of this system consist of: (1) columns that have negligible resistance in the plane of the specimen (i.e., in the longitudinal direction) but diagonally braced in the transverse direction; (2) spherically shaped rockers at the top and bottom of each column at each story to facilitate the in-plane movement of the columns (Figure 3-15b), and; (3) gravity mass plates made of 3.5 in. thick, 79 in. wide, and 118 in. long steel plates which weight about 8.5 kips each.

The construction process of the gravity column system for this experimental program is presented in Figure 3-16. It started with positioning of the South and North gravity columns, followed by erection of the South mass plate (Figure 3-16a and b). After the mass plate was positioned at the correct location (while remaining suspended at four points to a crane), a technician welded a set of angles connecting the gravity mass to the specimen (detail further shown in Figure 3-17).
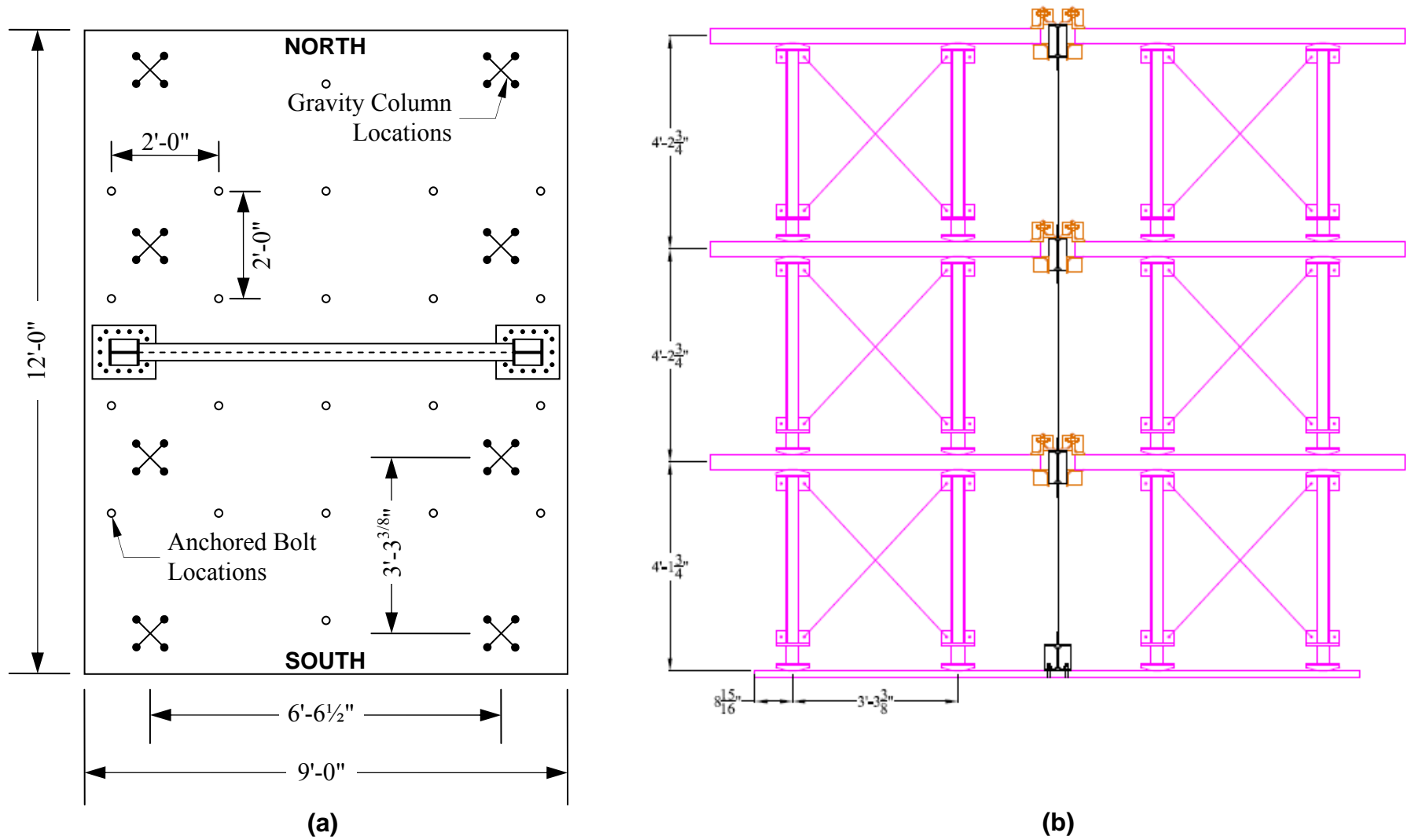
Figure 3-14 Schematic of Gravity Column System and Lateral Supports: (a) Floor Plate Plan; (b) North-South Elevation (Courtesy of Daniel Dowden)
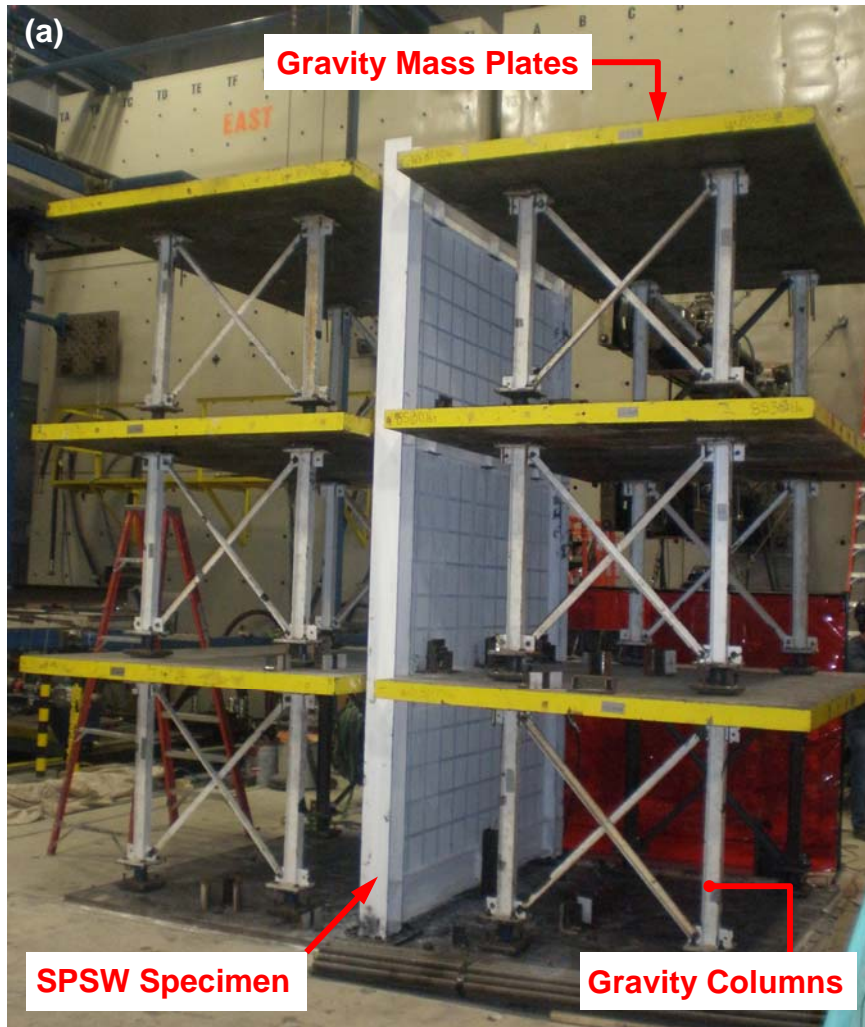
Figure 3-15 Specimen Setup with Gravity Column System: (a) Overview; (b) Detail of Spherically Shape Rocker Support

78

Using the South mass plate as a benchmark, the North mass plate was then erected (Figure 3-16c), following the same welding process. Prior to welding the connecting angles to the North mass plate, the technician first installed an angle-shaped component (called "actuator shoes") that linked both mass plates (further shown in Figure 3-20c) and made sure that the outside faces of the two mass plates were in line with the vertical side of the angle. (Incidentally, the order in which the gravity columns and mass plates were erected was a consequence of how the components were stored after a previous test and, thus, the order in which they could be retrieved.) The same process was repeated for the second and third floors (Figure 3-16d and h). Another technician operating a cherry-picker (Figure 3-16f) was needed when placing the mass plates on the third floor.

The angles connecting the gravity mass to the specimen (Figure 3-17) served both to provide out-of-plane lateral support and as a load transfer mechanism. Three sets of angles were provided on each side of the beam at each story (Figures 3-17a and 3-17b). Typical for each story, two of them were located 12 in. apart from the inner flange faces of the East and West columns, while the third one was located at the mid-span of the beam. The schematic of these angles are shown respectively in Figures 3-18a and 3-18b for the top story and middle stories. In the process of erecting the gravity column system, only angles on top of the gravity mass plate were installed. After their completion, the bottom angles were added (Figure 3-17c) to laterally brace the beam bottom flanges, followed by adding lateral supports at the column locations both on the top and bottom sides of the gravity mass (Figure 3-17d). A schematic of the lateral supports at a typical column is shown in Figure 3-18d.

Furthermore, lateral supports for the bottom anchor beam (HBE0) were welded to the floor plate as shown in Figure 3-18c. Two WT3×4.5 sandwiched the beam at its mid-point. To reduce friction between the specimen and its lateral supports, 1/8 in. thick polytetrafluoroethylene (PTFE) sheets were used on each angle-to-angle and angle-to-specimen surfaces. The function of the angles as load transfer mechanism is explained in the following section.

3.7.3 Loading Transfer Mechanism and Actuator Mounting

Lateral loads generated by actuators were directly applied to each floor's rigid mass plates, which afterward transferred loading to the specimen via twelve ¾ in. diameter A325 high-strength bolts
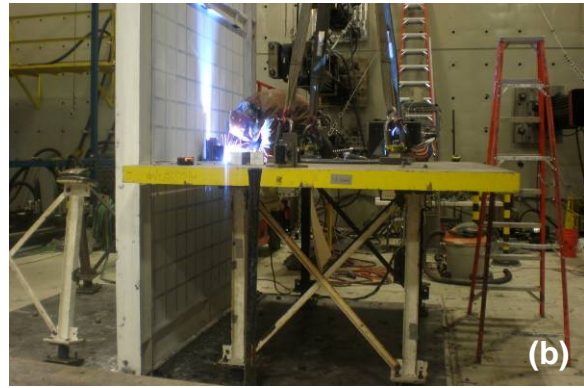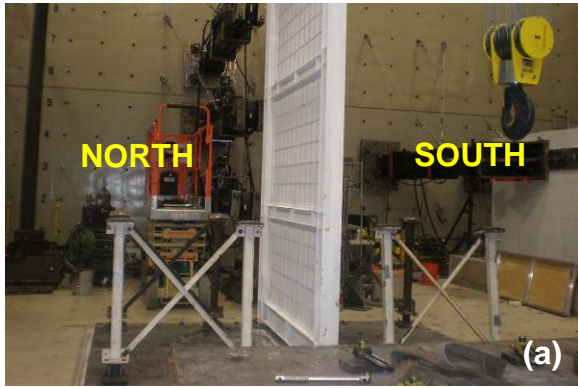
Figure 3-16 Construction Process of Gravity Column System
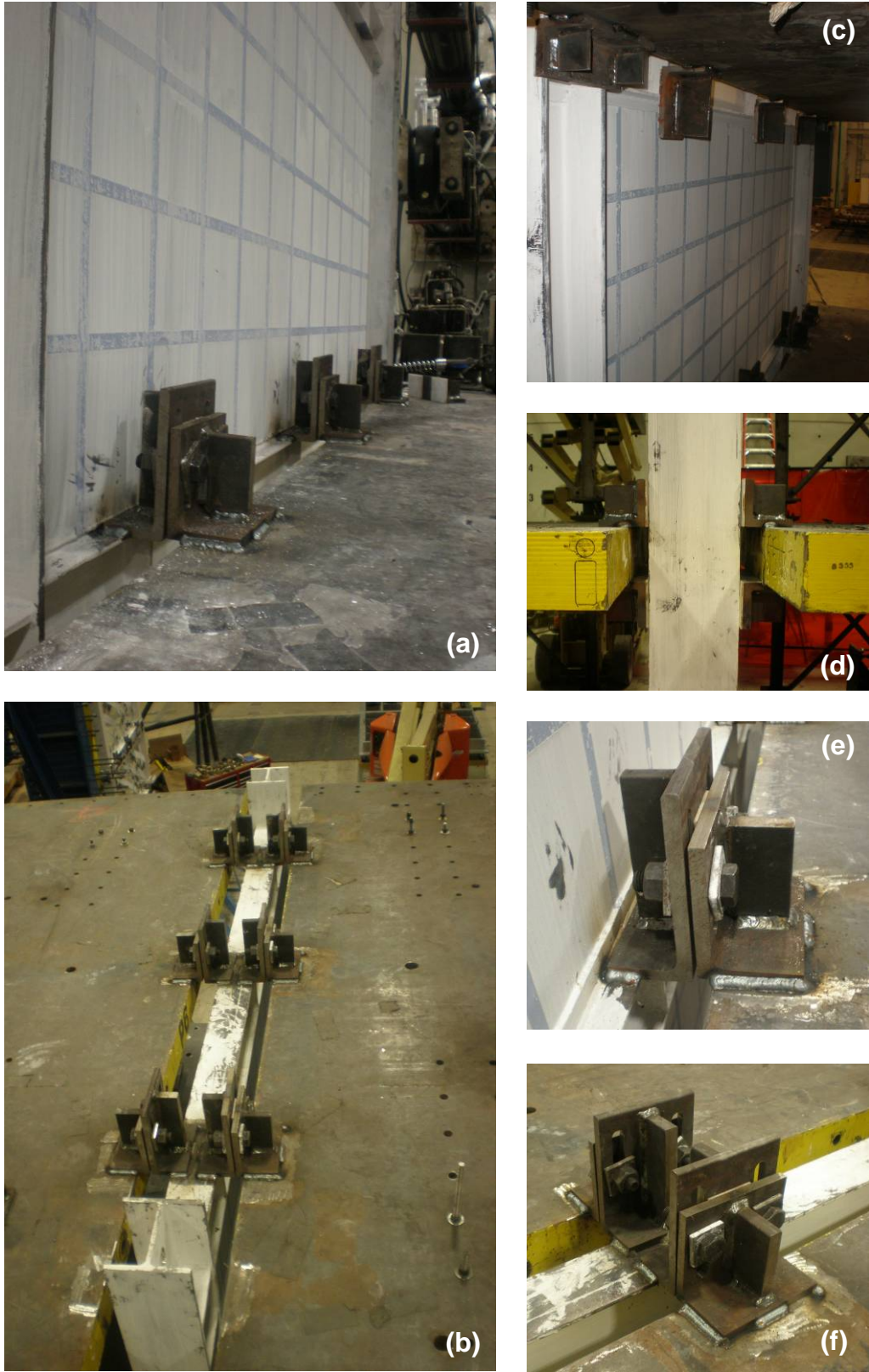
Figure 3-17 Angles for Load Transfer Mechanism and Lateral Supports: (a) at Intermediate Story; (b) on the Top Floor; (c) at HBE Bottom Flange; (d) Both Sides of VBE on the Top and Bottom of Mass Plates; (e) Detail of Angle in Part (a); (f) Detail of Angle in Part (b)

L7×4×½×0'-6" L.L.V
with 1" cut on horizontal leg
(Hole Dimension:
    Horiz. = Bolt Dia + $^1/_{32}$" Tol.
    Vert. = 3" slotted holes)

L5×3½×½×0'-6" L.L.V
with $^1/_8$" thick PTFE Sliding
Surface on vertical leg between
the bolts (Typ.)
(Hole Dimension:
    Horiz. = Bolt Dia + $^1/_{32}$" Tol.
    Vert. = 3" slotted holes)

$1^1/_8$"(Typ.)

3"

● Centerline Stiffener Plate

3"

Cut 1" from
horizontal leg

¾" Stiffener Plate
(A572 Gr. 50) at Double
Angles (Typ.)

1"

$^7/_{16}$"

Typ.

PLAN DETAIL

Snug Tight ¾" Dia. A325-X Bolts
with ASTM F436 $1^{¾}$"×$1^{¾}$"×$^5/_{16}$"
Std. Plate Washers (Typ.)

$1^½$" (Typ.)

See Plan Detail above

1" from Edge to Slotted Holes (Typ.)

3" Vertical Slotted Holes (Typ.)

Typ.

¼"

½"

(E) $3^½$" Steel Plate
Diaphragm

$^5/_{16}$" Stiffener Plate each
side align with stiffener
plates L-section above

Light Gauge
Plate G19 (0.0418")
attached to Fish Plate
PL ¼"×3"

W6×12

L6×4×½×0'-4" with ¼"
Stiffener Plate at mid-length
and $^1/_8$" thick PTFE Sliding
Surface on vertical leg (Typ.)

Figure 3-18 Schematic of Load Transfer Mechanism and Lateral Supports:
(a) Detail 6: on the Top Floor (HBE3)

8"

Gap between
Steel Plate Diaphragm

Light Gauge Plate
G19 (0.0418") or G14 (0.0747")
attached to Fish Plate PL ¼"×3"

For Plan Detail see
Detail 6/S6

1½" (Typ.)

1" from Edge to Slotted Holes (Typ.)

3" Vertical Slotted Holes

Typ.

¼"

(E) 3½" Steel Plate
Diaphragm

½"

⁵/₁₆" Stiffener Plate each
side align with stiffener
plates L-section above

L6×4×½×0'-4" with ¼"
Stiffener Plate at mid-length
and ¹/₈" thick PTFE Sliding
Surface on vertical leg (Typ.)

Light Gauge Plate
G14 (0.0747") or G13 (0.0897")
attached to Fish Plate PL ¼"×3"

S5×10

Figure 3-18 Schematic of Load Transfer Mechanism and Lateral Supports – Cont'd:
(b) Detail 7: at the Intermediate Story (HBE2 & HBE1)

at the three connected locations from both sides of the specimen, as schematically shown in Figure 3-19. As previously shown in Figure 3-18, each bolt was snug-tightened and positioned at the bottom edge of a 3 in. long vertically slotted hole of an angle welded to the specimen, which was collocated with the top edge of another slotted hole of the same length in an angle welded to the gravity mass plate. This design of overlapping vertically slotted holes theoretically allowed downward movements of the beams for a maximum displacement of 5.25 in. while the frame was cycled laterally in the East and West directions.

PLAN DETAIL

1" (Typ.)

¼"

1" on each side of web (Typ.)

¼"

WT3×4.5

W8×13 (outside flange shown)

Light Gauge Plate G13 (0.0897") attached to Fish Plate PL ¼"×3"

See Plan Detail above

⁵/₁₆" Stiffener Plate on both sides

12"

WT3×4$^{1/2}$×1'-3" with $^{1}/_{8}$" thick PTFE Sliding Surface on the flange L = 13" (Typ.)

3"

W8×13

(E) 1$^{1/2}$" Steel Floor Plate
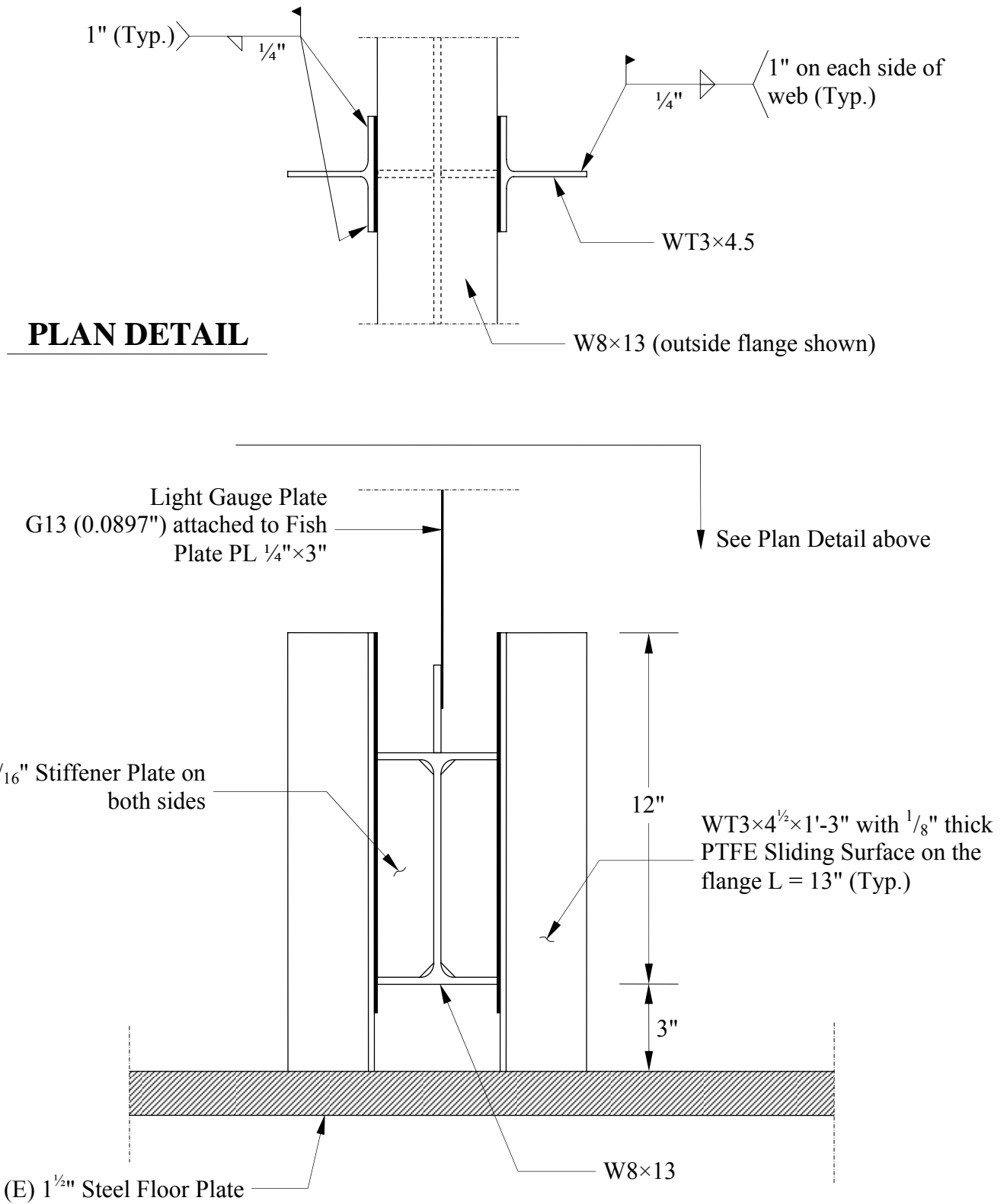
Figure 3-18 Schematic of Load Transfer Mechanism and Lateral Supports – Cont'd: (c) Detail 8: at the Base (HBE0)

84

Panel Zone
Stiffener Plate

¼" Stiffener Plate
(A572 Gr. 50) at both
Angles (Typ.)

8"

PLAN DETAIL

See Plan Detail Above

¼"   1" Return (Typ.)

¼"   3" concentrically
located along Horiz.
Leg only (Typ.)

(E) 3½" Steel Plate
Diaphragm

L3×3×½×0'-8" with ¼" Stiffener
Plate align with column flange
(see Plan Detail below) and
$^1/_8$" thick PTFE Sliding Surface
on vertical leg (Typ.)

W6×25
(outside flange shown)
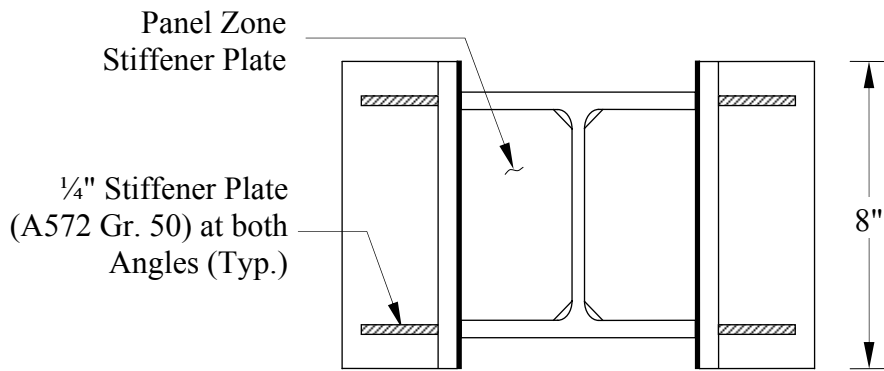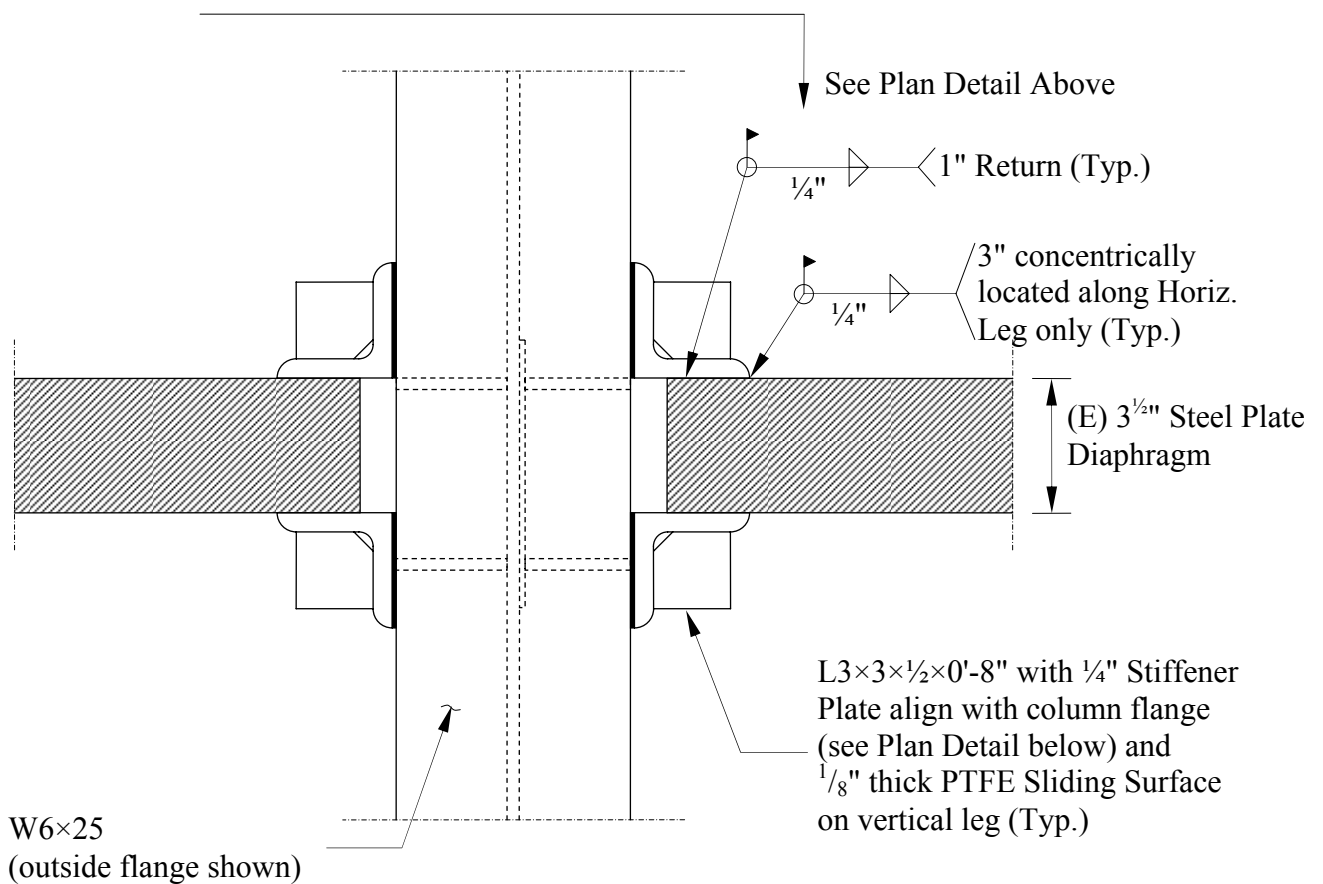
Figure 3-18 Schematic of Load Transfer Mechanism and Lateral Supports – Cont'd:
(d) at the VBE Location

One MTS dynamic actuator at each floor, capable of delivering 100 ton payloads and 40 in. strokes (i.e., +/− 20 in. travels), was used in this experiment. Schematically shown in Figure 3-20a, swivel heads of the actuators were connected to the gravity mass plate through custom-made actuator shoes (Dowden and Bruneau 2014). At the other side, swivel bases of the actuators were
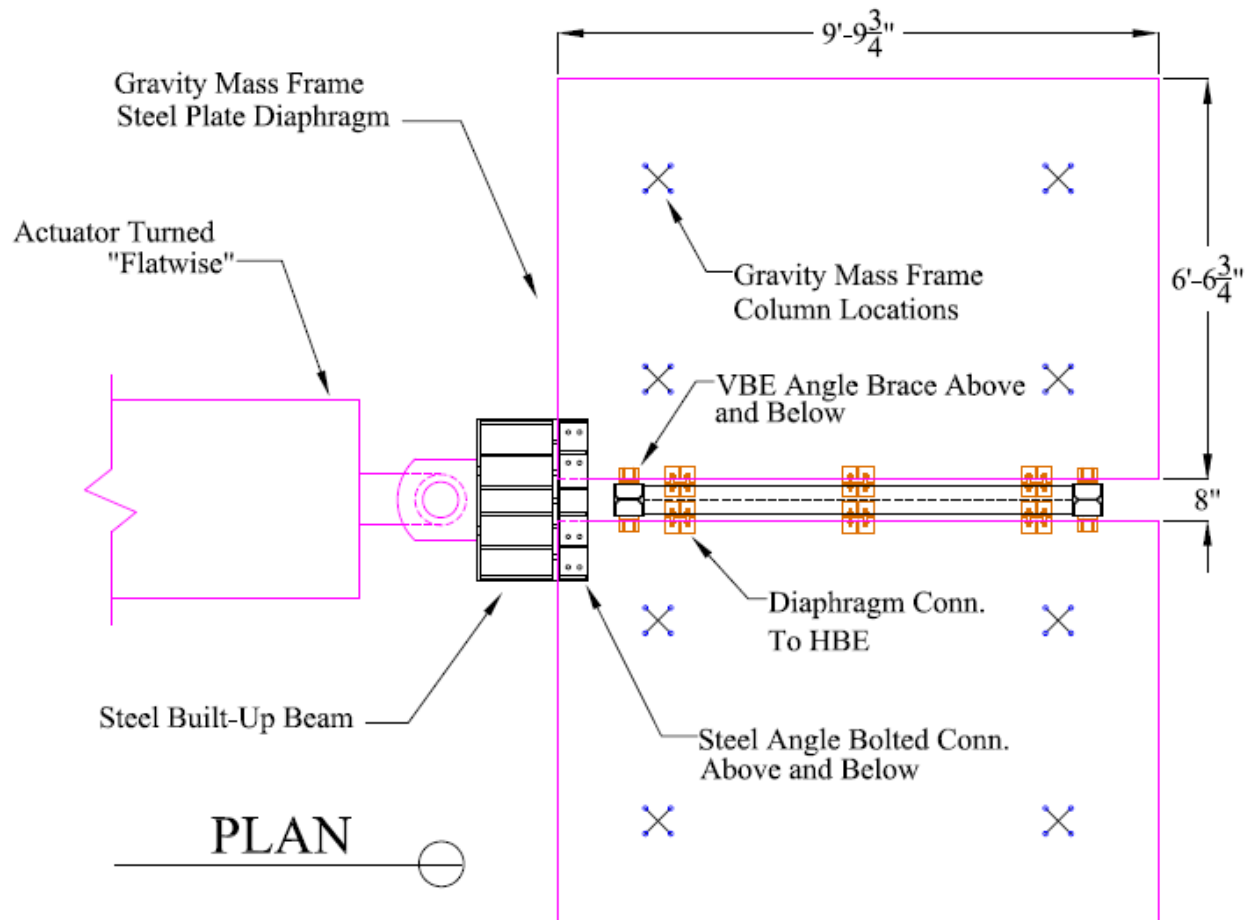
Figure 3-19 Schematic of Lateral Load Transfer Mechanism (Courtesy of Daniel Dowden)

connected to mounting plates which themselves were anchored to the SEESL 24 in. strong reaction wall by high strength tension rods. The three dynamic actuators and the actuator shoes are shown in Figures 3-20b and 3-20c, respectively.

3.7.4 Instrumentation and Data Acquisition System

Instrumentation for this experimental program was designed to measure global response of the SPSW specimen and local behaviors of its components. Global response of the specimen includes recording story displacements in the direction of loading and shear forces at each story level. Component local behaviors of interest include beam vertical deformations, internal moments and axial forces in the beams, cross-section rotations at each end of the beams, and yielding distributions in the infill plates.
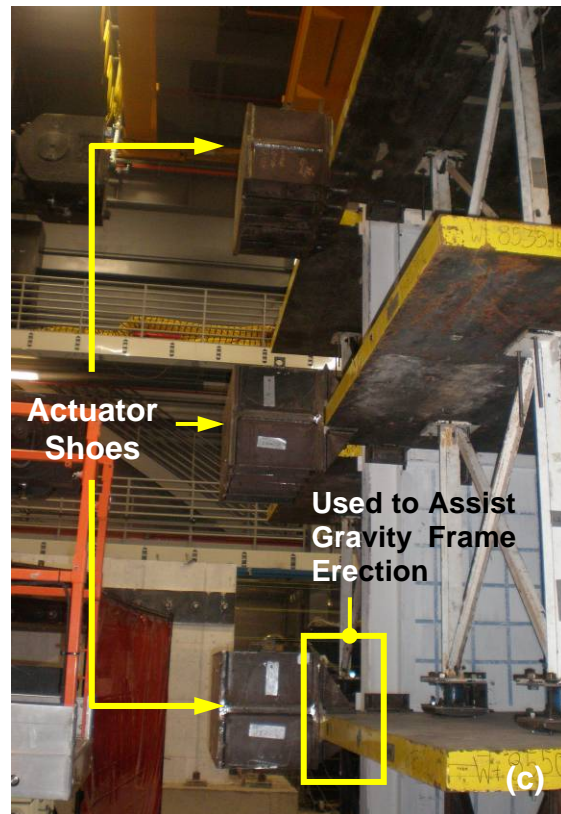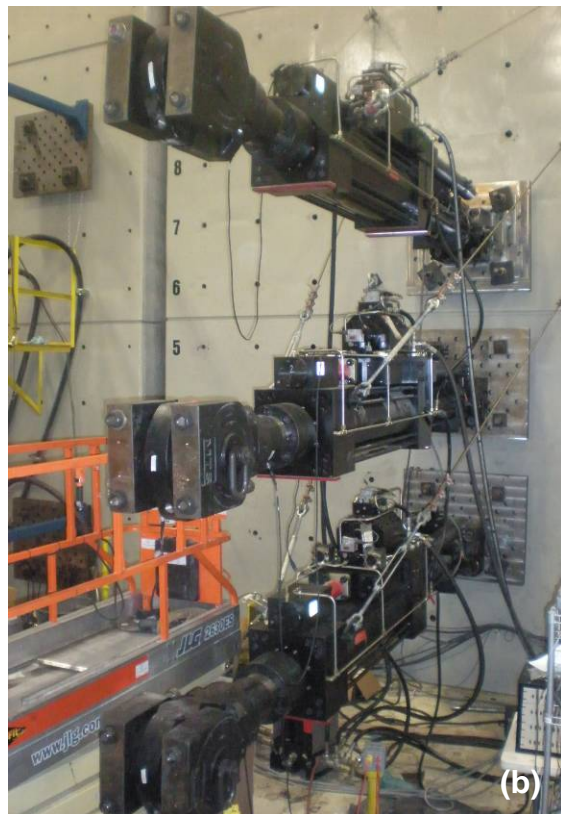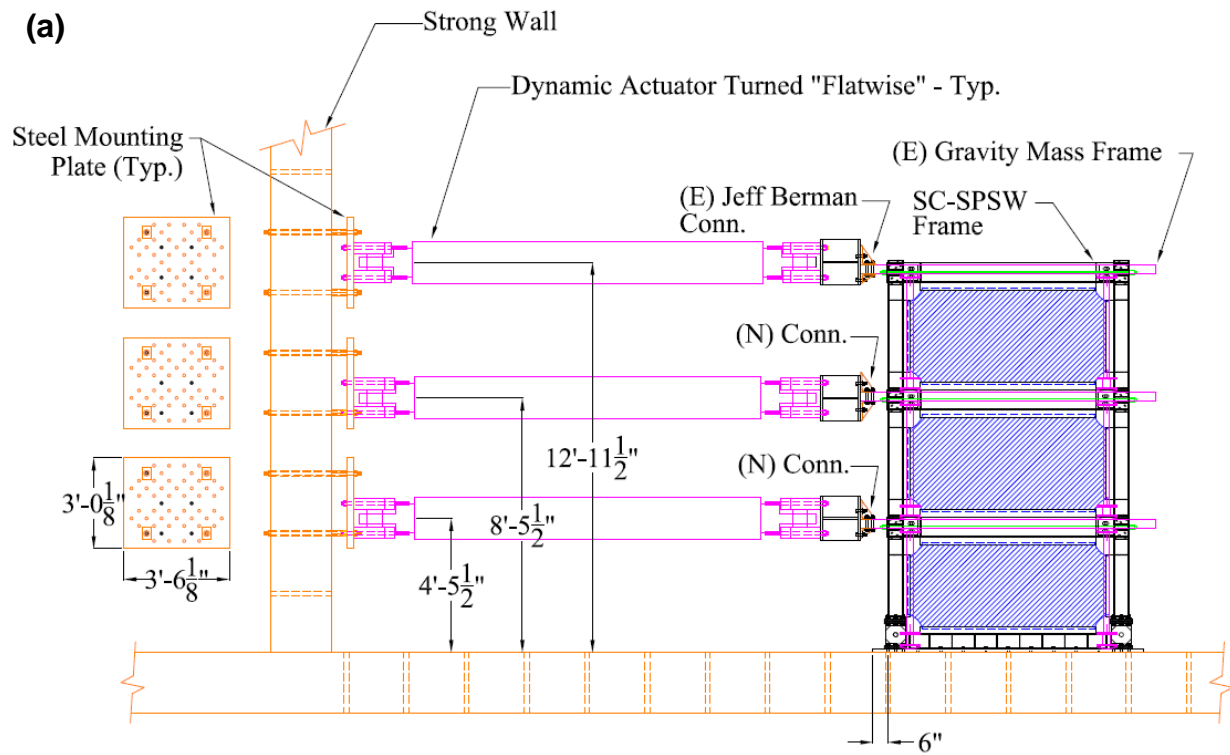
Figure 3-20 Actuator Mounting: (a) Overview of Test Setup (Courtesy of Daniel Dowden); (b) MTS Dynamic Actuators; (c) Actuator shoes

Story displacements were recorded by string pots attached to the outer flange of the West column, as shown in Figure 3-21a. In addition to installing one string pot at each floor, two string pots were added at the base of the East and West columns to monitor slippage between the specimen and the steel floor plate. Story shear forces were obtained directly from the load cells in the actuators. In addition, displacement transducers internal to the actuators provided displacement histories of each actuator, for comparison with the displacements recorded by the string pots at the same levels. The naming convention established identified the type of instrumentation, the type of structural members to which the instrument was attached, and its locations on the specimen (Figure 3-21e). Specific identification is explained accordingly throughout this section when presenting the respective instruments.

Moreover, string pots were used to measure vertical deformations of the second and third story beams labeled as B2 and B3 in Figure 3-21a, respectively. Three string pots were installed at the quarter-, mid-, and third-quarter-span of each beam. Note that these instruments measured the relative movement of beams with respect to the gravity mass plates. Though the mass plates are essentially rigid and insignificant vertical movements were expected, three additional string pots were added to monitor their rigid body movements to capture possible uplifts while sliding around the rocker curvature, especially at large specimen lateral displacements. In this case, SPG3, SPG2, and SPG1 were arranged in series (Detail 1 in Figure 3-21e) to monitor rigid body movements of the third, second, and first gravity mass plates, respectively, with respect to each other and to the ground. Unlike the two upper beams, vertical deformation histories of the bottom anchor beam and the first story beam were recorded using Krypton sensors, which are described in a later paragraph.

Uniaxial strain gauges manufactured by Micro-Measurements were installed primarily on the beam flanges clustered at four critical sections along the span of each beam. Positioned longitudinally, four strain gauges per section were used to measure strains in the direction of each beam's longitudinal axis. Strains recorded by these gauges were intended to allow calculation of axial forces and moments at the respective sections. Procedures for data post-processing are presented in Section 4 when explaining experimental results and observations. Other uniaxial strain gauges were added to record strains adjacent to the base of the East and West columns.
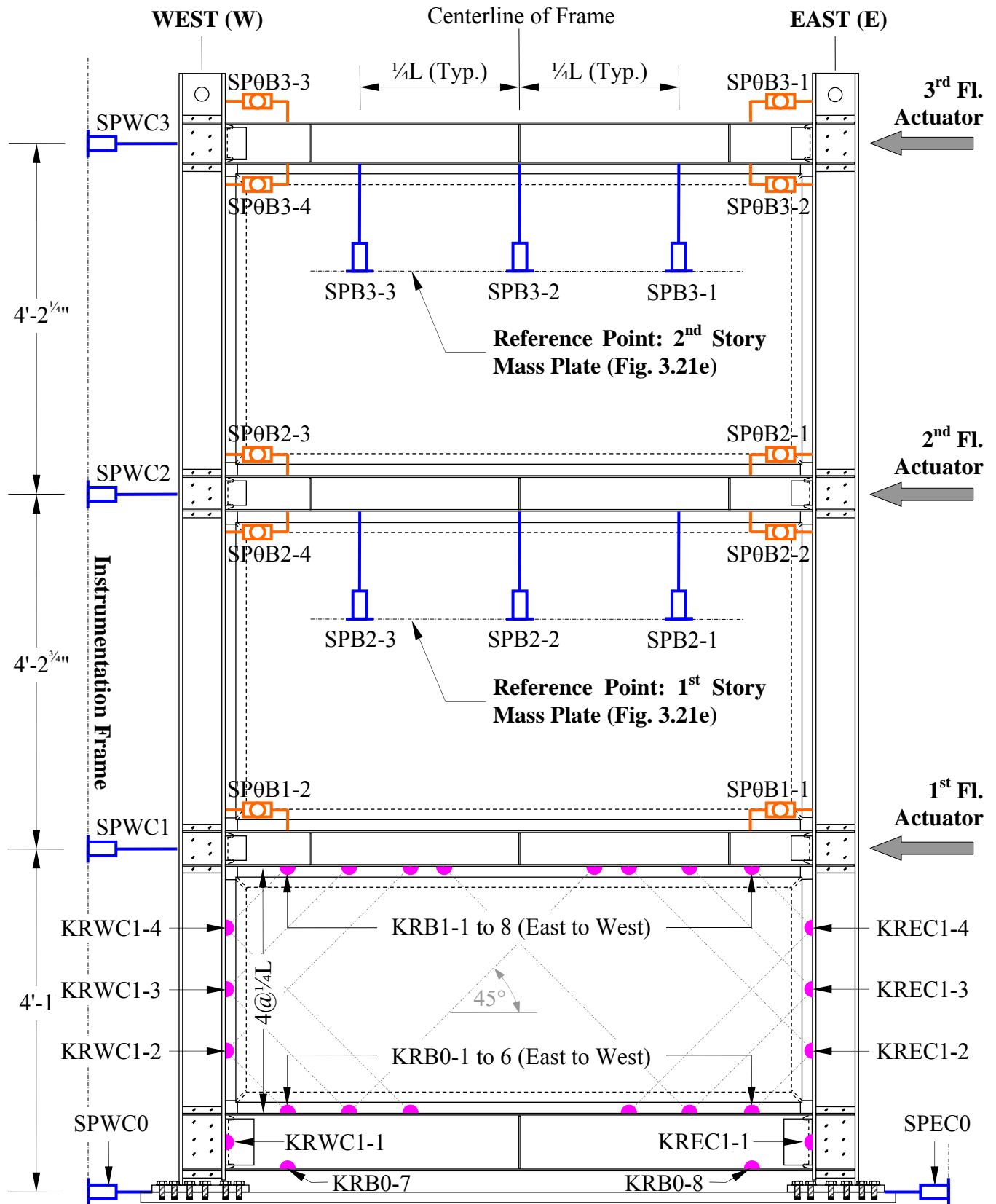
Figure 3-21 Instrumentation Layout:
(a) String-Pots and Krypton for Deformation Measurements
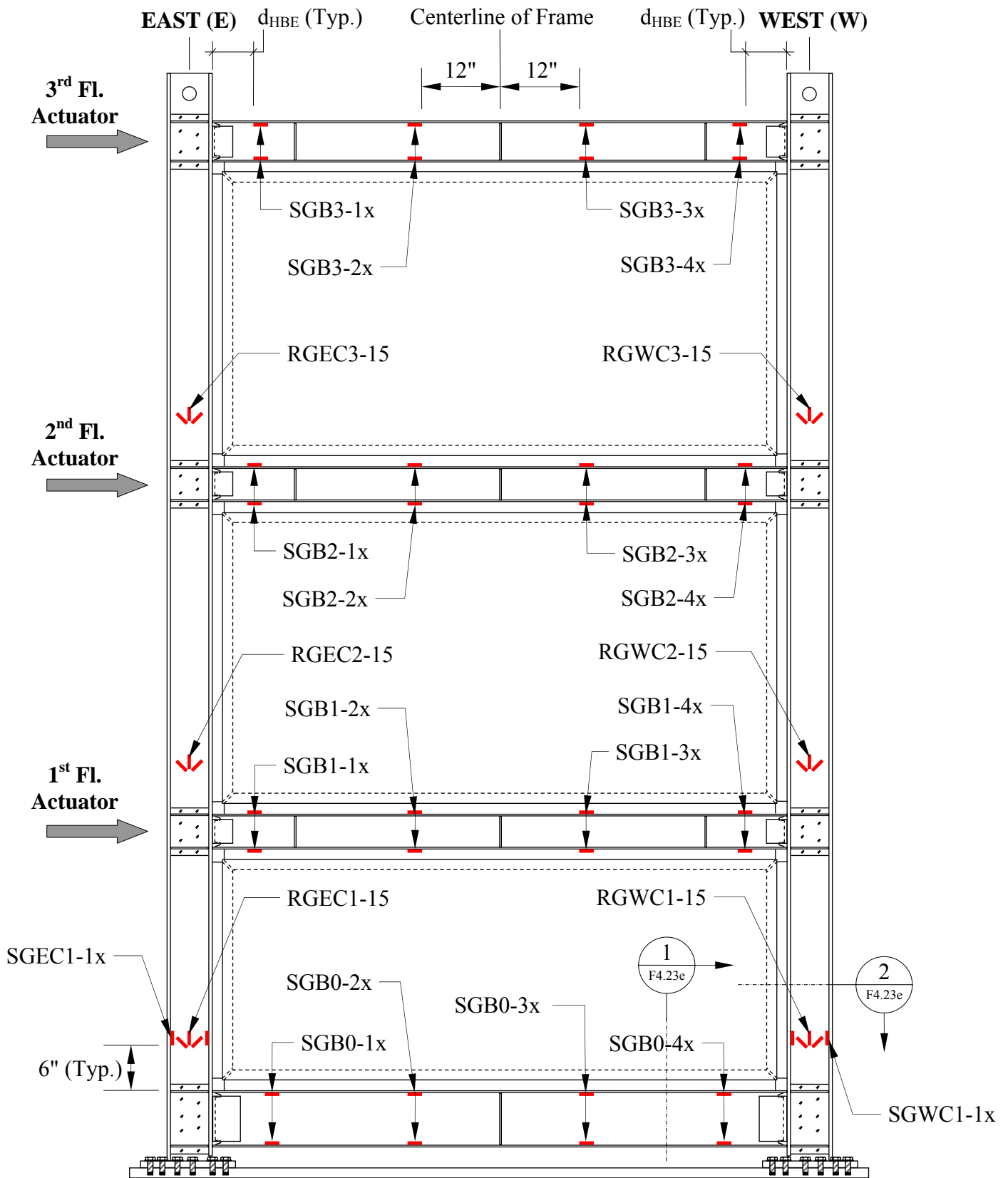
Figure 3-21 Instrumentation Layout – Cont'd:
(b) Strain-Gauges for Member Yielding Measurements
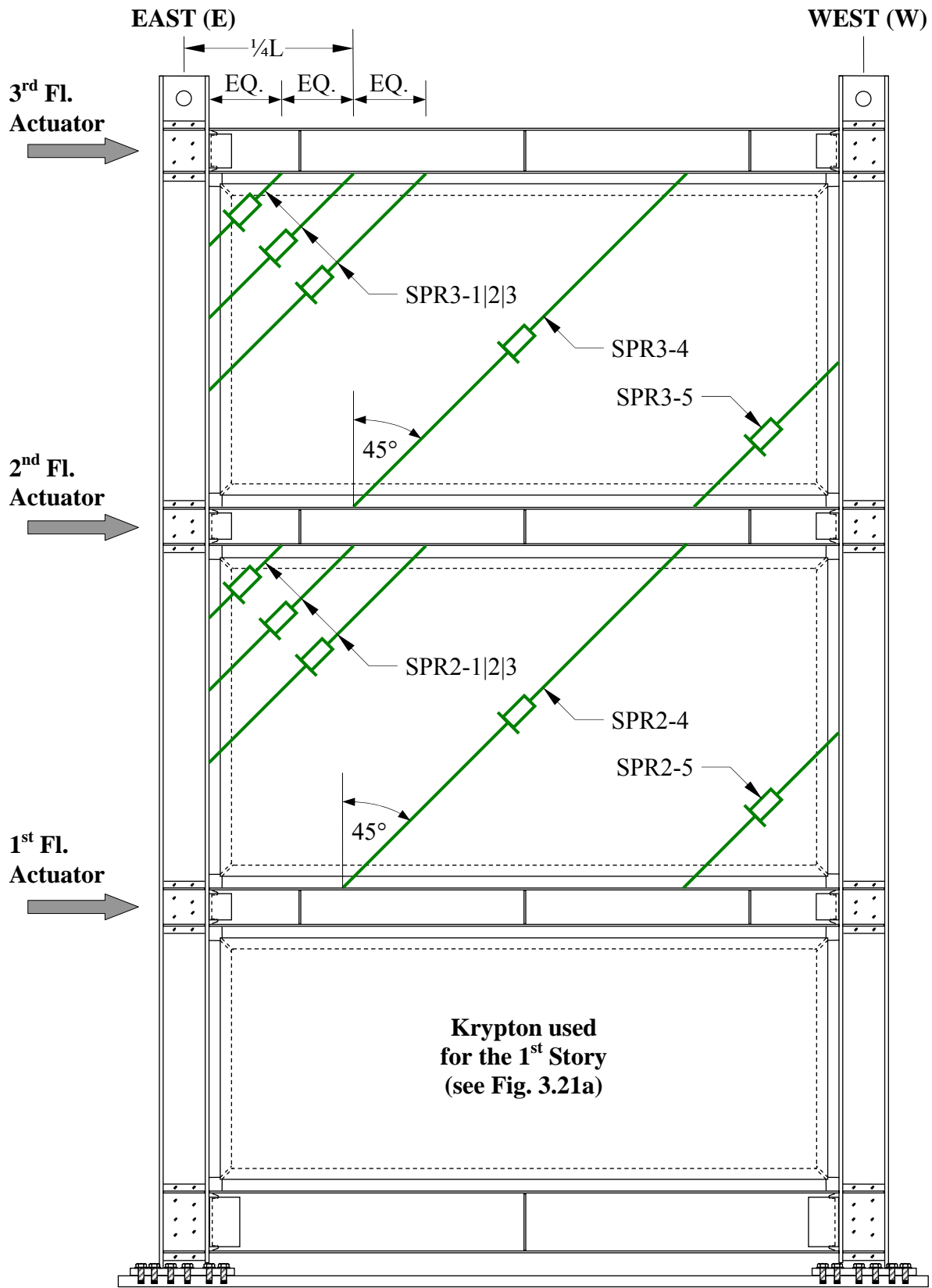
Figure 3-21 Instrumentation Layout – Cont'd:
(c) String Pots for Infill Plate Yielding Measurements in East to West Direction
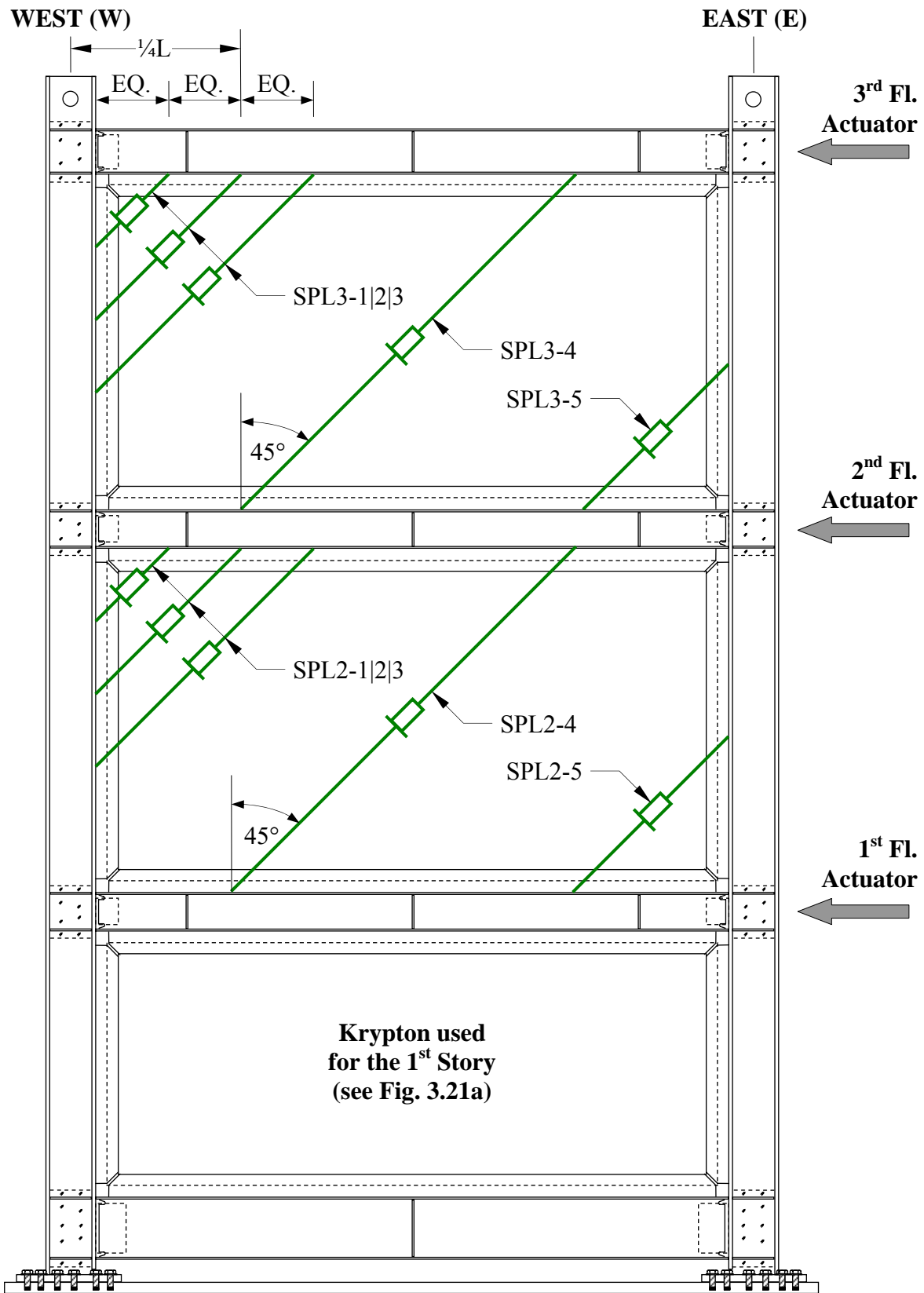
Figure 3-21 Instrumentation Layout – Cont'd:
(d) String Pots for Infill Plate Yielding Measurements in West to East Direction

92

3rd Fl. Mass Plate

SPG3

2nd Fl. Mass Plate — SPB3-x

SPG2

1st Fl. Mass Plate — SPB2-x

SPG1

Several Details are not shown for clarity

Strong Floor
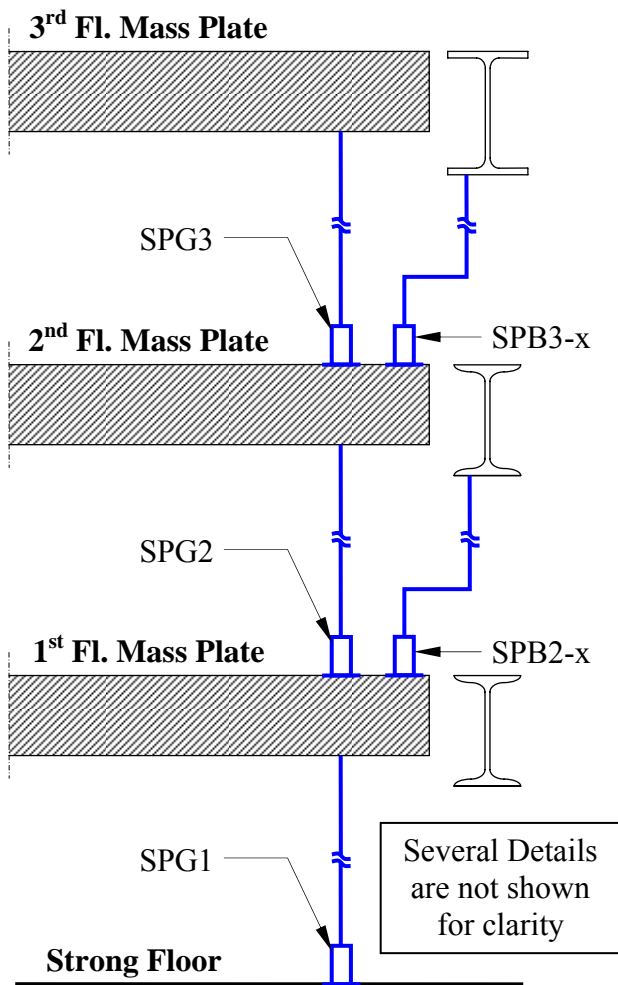
DETAIL 1

Instrumentation Nomenclature:

SG = Uni-axial Strain Gauge
RG = Rosette Strain Gauge
SP = String Pot
$SP\theta$ = String Pot for Rotation Measurement
KR = Krypton
B = Beam
EC = East Column
WC = West Column
G = Gravity mass plate
R = Right Leaning direction (toward West)
L = Left Leaning direction (toward East)

Instrumentation ID Convention:

First group = type of instrument
Second group = structural member
Third group = location/direction of instrument
Fourth group = instrumentation ID

Additional Information for Strain Gauges:

Sections for Beam = 1 to 4 → East to West
Sections for Column = 1 to 4 → Lower to Upper
Strain Gauges 1 & 2 = Top flange
Strain Gauges 3 & 4 = Bottom flange
Strain Gauges 5 = Web

LEGEND

SOUTH (S) | **NORTH (N)**

SGB0-41 — SGB0-42

SGB0-43 — SGB0-44

SECTION 1 (Typical)

SGWC1-12 — SGWC1-14

SOUTH (S)
NORTH (N)

SGWC1-11 — SGWC1-13

RGWC1-15
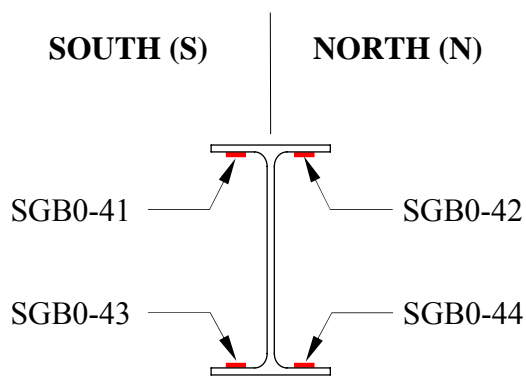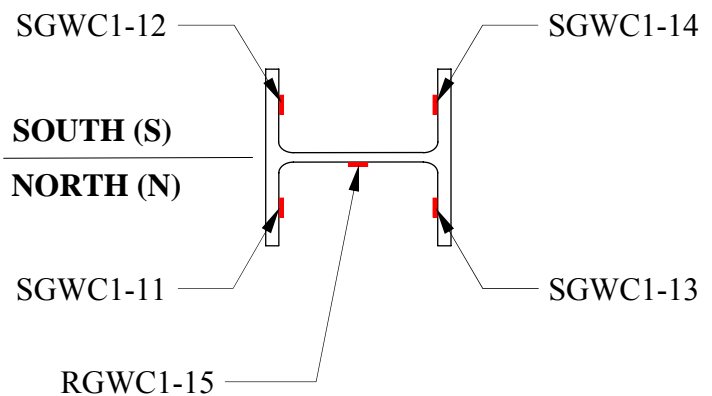
SECTION 2 (Typical)

Figure 3-21 Instrumentation Layout – Cont'd
(e) Legend of Symbols, Details, and Sections

Except for the intermediate beams, due to their sloping inside faces, all the strain gauges were located on the inner face of the flanges to protect them from possible damage during installation of the specimen. In addition, triaxial Rosette strain gauges were added at each story base, affixed to the web of the East and West columns. Secondary measurement of story shear forces (as a back up to that from the actuator load cells) can be obtained from these Rosette strain gauges. A total of 78 uniaxial and Rosette strain gauges were used for this experimentation and their layout is presented in Figure 3-21b.

A pair of displacement transducers positioned on the top and bottom flanges at selected beam ends were used to calculate cross-section rotations at those locations. For this purpose, two string pots, adjusted to be capable of recording small displacements of the order of 10^{-2} in. were used and positioned at a distance equal to an expected plastic hinge length of 6 in. from the face of the columns. In this case, cross-section rotation θ_b is determined as follows:

$$\theta_b = \left(\frac{\delta_t - \delta_b}{h_{sp}} \right)$$
(3-2)

where δ_t and δ_b are recorded displacements of the top and bottom string pots, respectively; and h_{sp} is the distance between the two string pots. The possibility of using clip gauges for the same purpose was investigated in the preliminary design of the instrumentation, but not used since they were not readily in stock at the SEESL facilities and would have had to be fabricated from scratch. A total of 10 adjusted string pots (labeled as SPθB) and 6 Krypton sensors (labeled as KRB) were used to measure cross-section rotations of 8 beam-to-column joints and their layout is presented in Figure 3-21a.

Buckling orientations and yielding distributions on each infill plate during testing were captured qualitatively by the deformation of the visible grid on its surface. Quantitative measurement of infill plate yielding was made by means of 5 string pots per panel side per floor. The string pots were placed at a 45° angle from the vertical and were distributed as shown in Figures 3-21c and 3-21d. Incidentally, linear variable differential transformers (LVDTs) were originally planned for this purpose, but there were not enough available LVDTs at the SEESL facilities to provide the 20 instruments needed for this purpose. The series of string pots on each side of the panel were

intended to provide information on the yielding distribution across the infill plates in both directions of loading. Like the instrumentation arrangement for measuring beam vertical deformations, Krypton sensors were used around the first story infill plate to capture the yielding distribution.

As mentioned already, the Krypton camera system (i.e., K600 series) was used in this experiment. The Krypton system measures 3D displacements using 3 built in cameras to locate the position of an infrared LED in space by triangulation principles. The Krypton can detect displacement of a single point at 3.5 m distance from the camera within 0.06 mm accuracy (Krypton Manual 2003). Key features of the Krypton system consist of a camera, a DAQ System, and LED sensors, as shown in Figure 3-22. A total of 27 Krypton LED sensors were used in this experiment. One sensor was affixed to the ground as a reference point, 2 sensors were affixed to the South gravity mass plate of the first story of each located adjacent to the East and West rocking columns, and 24 of them were affixed to the specimen where shown in Figure 3-21a.

In addition to the aforementioned instruments, 6 video cameras were used to record global behavior of the specimen and local behaviors of joints, beams, and lateral support components. Adding the 78 strain gauges, 71 displacement transducers (i.e., string pots and Krypton sensors), and 6 instruments for actuators, a total of 161 data acquisition channels were used to collect experimental data. A complete list of these channels is provided in Appendix A. These channels were divided into 4 different DAQ systems. Krypton sensors, actuators, and video feeds had separate DAQ system while all channels for strain gauges and string pots shared the same DAQ system. Among the four DAQ systems, only the data from Krypton sensors could not be viewed in real time during the test. A comprehensive discussion on the usefulness of this real time observation is presented in Section 5. In a nutshell, during testing, the real time display provided the ability to monitor the values of key parameters (e.g., base shear vs. top story displacement, beam vertical deformations, etc.) that were important to assess the performance of the specimen. As necessary, modifications of the planned loading protocol for the specimen could be made, based on the hysteretic curves observed in each particular cycle. The loading protocol used in this experiment is described in the following section.
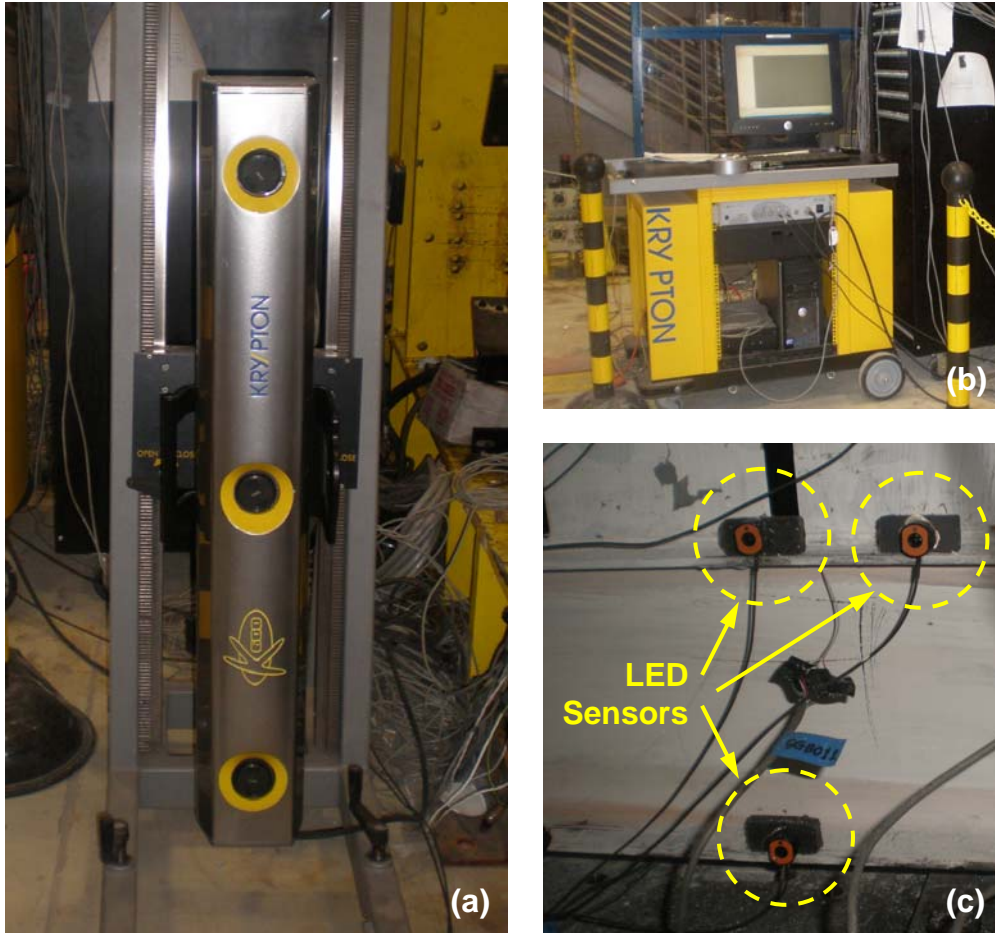
Figure 3-22 Krypton K600 Camera System: (a) Camera; (b) DAQ System; (c) LED Sensors

3.8 Development of Loading Protocol

As mentioned in Section 3.7.3, three dynamic actuators were used in this experiment, namely, one actuator at each story. In order to define a loading protocol, a force distribution among the three actuators needed to be decided in the first place. The force distribution used in the analytical model when designing and investigating behaviors of the specimen was the inverted triangular vertical distribution (similar to an idealized first mode shape) specified in the ASCE 7-10 document (ASCE 2010). Fraction of forces for each actuator F_i relative to the total base shear V_t was estimated based on the vertical distribution coefficient C_{vi} term expressed in (12.8-12) of the ASCE 7-10 document. Here, the amount of forces with respect to the total base shear applied at the third, second, and first actuator, respectively, were:

96

$$F_i = C_{vi} V_t = \begin{Bmatrix} 0.502 \\ 0.334 \\ 0.164 \end{Bmatrix} V_t \qquad (3\text{-}3)$$

In other words, the amount of forces for the first and second story actuators (i.e., denoted as F_1 and F_2) were about 1/3 and 2/3 of the forces applied on the third actuator (i.e., denoted as F_3), respectively.

In the SAP2000 (CSI 2007) model used to analyze those loading distributions on the specimen, half of the forces were applied to each of the beam-to-column joints at the East and West sides (i.e., applying a two-point loading transfer mechanism at each floor), and a displacement-controlled target (e.g., up to 4% or 5% top story drift) was defined at the third story level (i.e., denoted as Scheme I). As expected, the analytical results showed that the story force distribution followed the ratio given in (3-3). Plotting the results in Figure 3-23a, the ratio of story forces to the base shear was the same at the onset of the first strip yielding, when reaching the effective yielding (further defined in Section 3.8.1), 1% top drift, and 4% top drift. However, the displacement shape at an early stage (e.g., at 1% top story drift) was slightly different from the idealized first mode shape, though at a later stage (e.g., at 4% top story drift), a good agreement was observed between both displacement shapes (Figure 3-23b). Note that an eigenvalue analysis was also conducted to compare the idealized first mode shape based on the ASCE 7-10 document and the actual first mode shape of the specimen model. Comparable displacement shapes were observed between the two results. In addition, to imitate the three-point loading transfer mechanism used at each floor in this experimentation (Section 3.7.3), another analytical model of the specimen was developed considering that 1/3 of each estimated story forces in (3-3) was applied at each point of the three points on their respective floor (as applied to the actual specimen during the test). Insignificant differences in terms of the distribution of story forces and displacement shapes were observed between the two- and three-point loading transfer mechanisms.

In an early development of the loading protocol for this experimentation program, it was suspected that the displacement-controlled scheme used in the SAP2000 model would be intricate to replicate in an experimental setting. Specifically, assigning the inverted triangular load

97
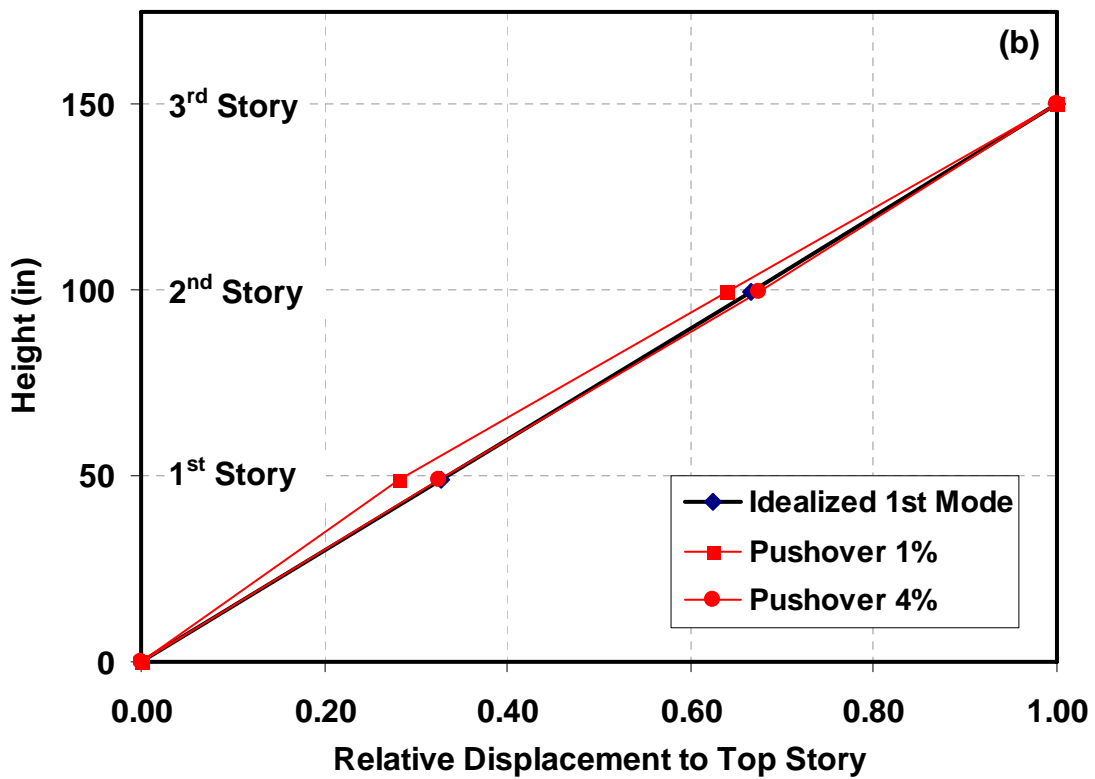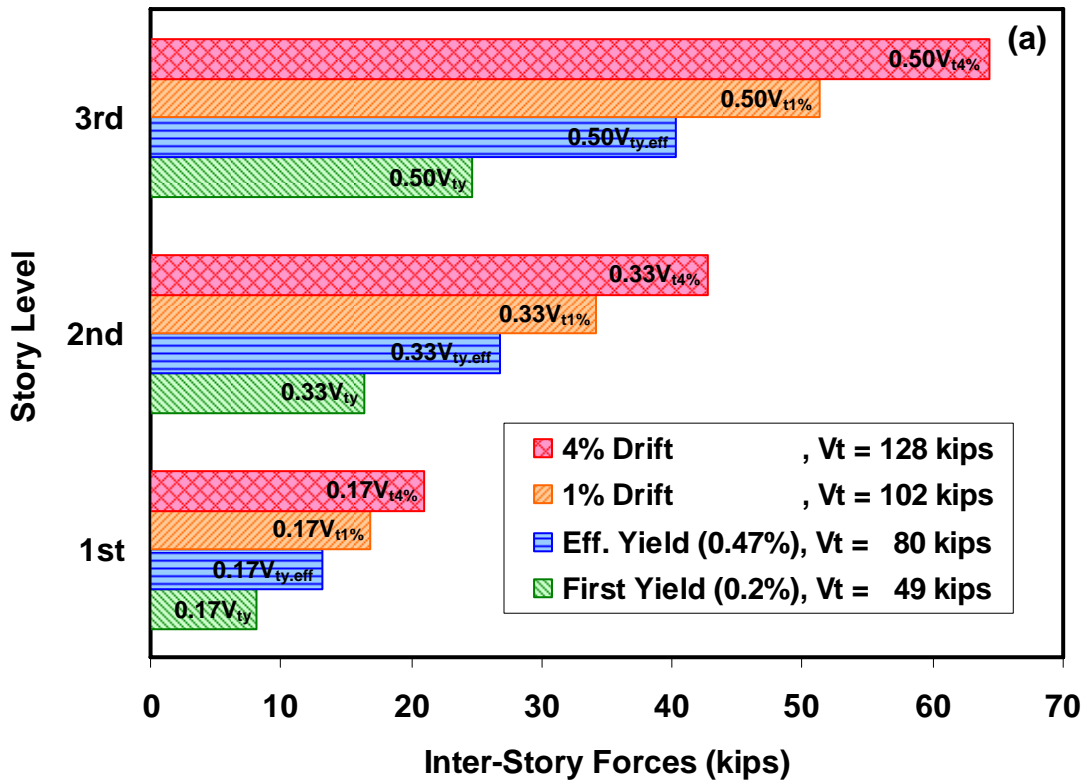
Figure 3-23 Development of Loading Protocol (Scheme I): (a) Inter-Story Force Distribution; (b) Displacement Shape

distribution among the three actuators according to the ratio given in (3-3) together with one displacement target at the third story actuator would be somewhat challenging. Incidentally, a uniform lateral load distribution among multiple actuators with one of them acting as a master actuator to reach a specified target displacement had been tried in past SPSW experiments (e.g., Driver *et al.* 1997; Lubell *et al.* 2000; and Behbahanifard *et al.* 2003). This uniform load distribution, however, could generate structural damage predominantly concentrated at the first story level, as reported in these respective documents. Hence, the inverted triangular load distribution was actually preferred here because it served the purpose of observing structural damage distributed throughout the height of the specimen.

For the above reason, it was decided instead to investigate whether a scheme relying on three-independent displacement-controls could be applied to simulate the SAP2000 displacement-control scheme. Magnitudes of these three displacement histories are related to each other (i.e., similar to a first mode deformed shape) though each of them would be independently specified to the respective actuator. This scheme is similar to the setting of two actuators used in the pseudodynamic test of two-story SPSW specimen by Qu *et al.* (2008), in which each actuator had its own displacement history.

To investigate the consequences of this displacement-control scheme (i.e., denoted as Scheme II), a SAP2000 model was created by adding a rigid column along the wall height, adjacent to the SPSW, and rigidly connected to it at each floor level. The rigid column was arbitrarily taken to be a W36×210 assigned a 100 times higher modulus of elasticity compared to that of regular A572 Grade 50 W-sections. That column was connected to the main structure using the "Equal Constraints" in SAP2000, to achieve the same lateral deformation at each level for the rigid column and the mid-point of the beam at each story level. The analytical results are summarized in Figure 3-24. The resulting story shear force distributions obtained were significantly different from that those observed in Scheme I. In particular, at the early stage of loading, the first story shear force was found to be acting in a different direction than that at the upper floor. In an experimental setting, this condition would require the first story actuator to pull while the other two would be pushing the specimen in the direction of loading. In a later stage, however, all actuators were observed to push the specimen in the same direction, as also observed in the
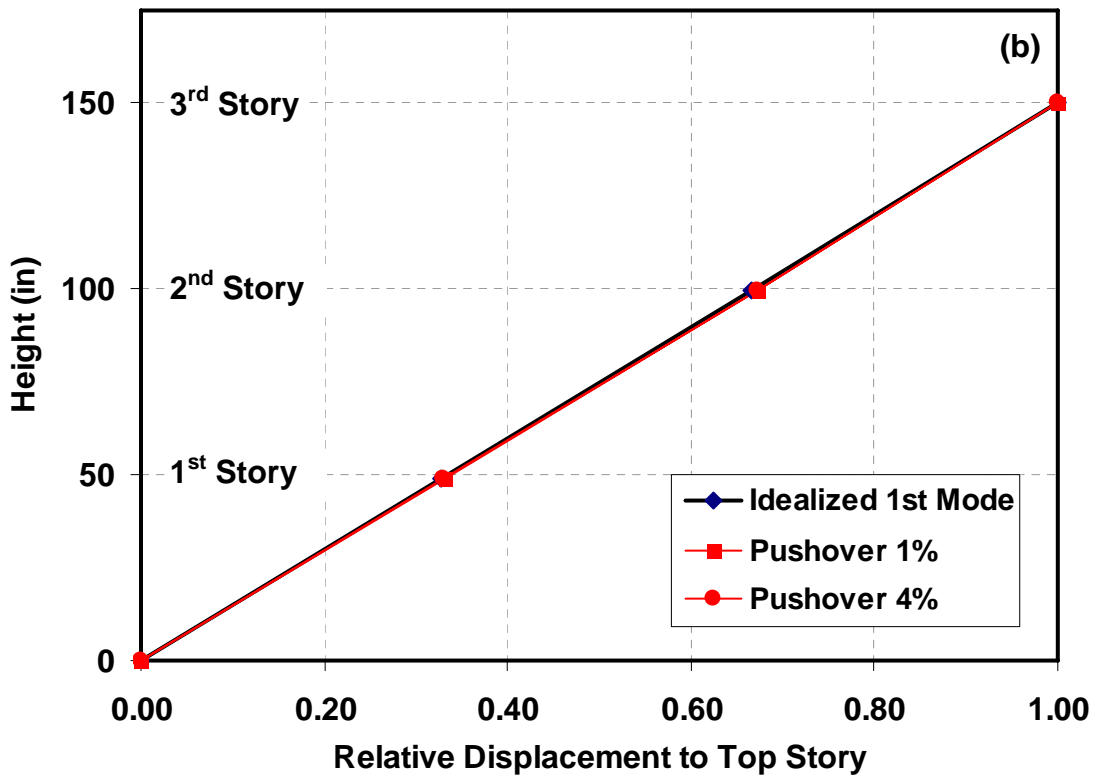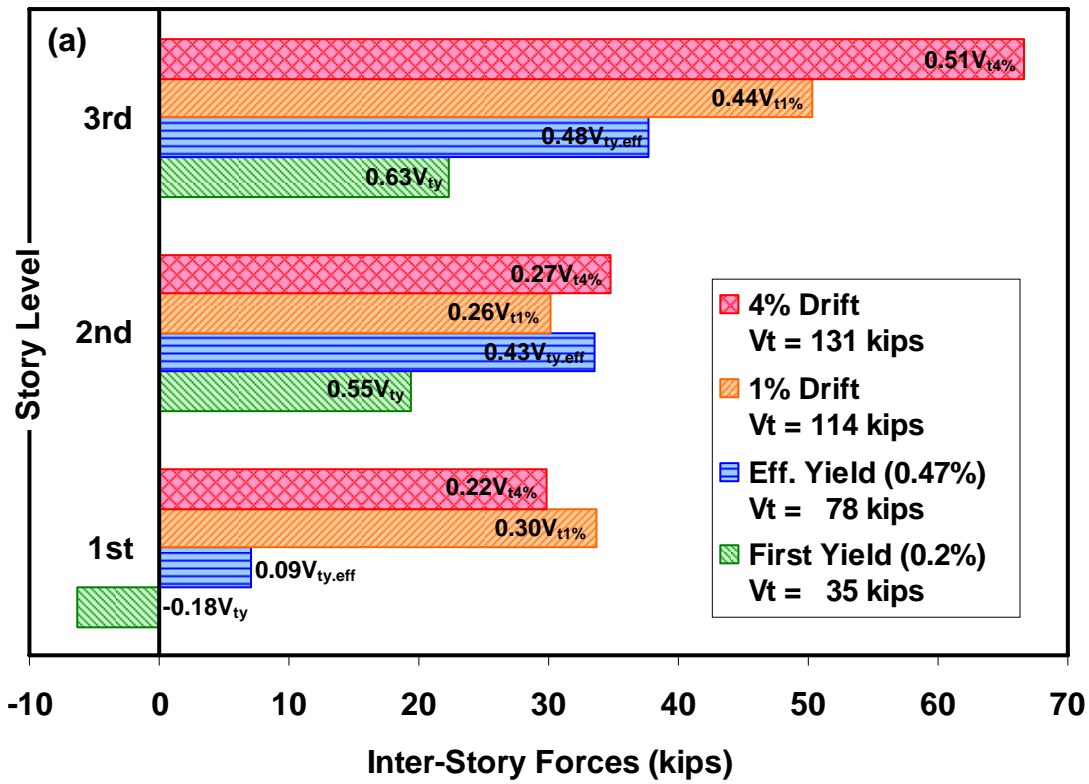
Figure 3-24 Development of Loading Protocol (Scheme II): (a) Inter-Story Force Distribution; (b) Displacement Shape

previous loading scheme. Also note in Figure 3-24 that, for this rigid column model, the displacement shapes at 1% and 4% top story drift practically matched the idealized first mode shape.

As mentioned several times, a close collaboration with the SMART Walls research project by Dowden and Bruneau (2014) somewhat molded the setting of this experimental program. In their first set of self-centering three-story SPSW tests, each actuator was assigned a different displacement history and a displacement-control scheme was applied to all three actuators. The researchers observed significant differences between their expected theoretical and experimental results. Unsynchronized push and pull modes among the three actuators to achieve three different displacement histories primarily contributed to this significant discrepancy. A comprehensive explanation of the observed phenomenon can be found in the respective report. Moreover, the researchers investigated a similar loading protocol to that described in this section as Scheme I. In this case, the third story actuator was set up in a displacement-control mode, while the other two actuators were in a force-control mode. Based on their successful approach during their tests, the same scheme was therefore followed in this experimental program. In other words, the first and second story actuators were slaved to the third story actuator, which acted as the master actuator and underwent a specified cyclic displacement history described in Section 3.8.2. The amount of forces applied by the first and second story actuators to the specimen at a particular time step in the loading history respectively were 1/3 and 2/3 of the forces recorded in the third story actuator within the previous time step. Given the relatively slow quasi-static testing (i.e., 2 to 5 minutes/cycle), this scheme worked well and minor delays in the control loop between the actuators did not affect the overall testing outcomes.

3.8.1 Effective Yield Force and Displacement

To estimate the effective yield displacement and corresponding lateral force values at that point (because this information is needed for the loading history described in Section 3.8.2), a monotonic pushover analysis was performed on the specimen analytical model. The specific model used for this purpose was the analytical strip model with actual material properties obtained from the tensile coupon tests; cross-section properties of HBEs that included the attached 1 in. wide fish plates; to which was applied an inverted triangular load distribution along

the height of the specimen, with the third story lateral displacement as a controlled point (displacement target), and two-point loading transfer mechanism at each floor. Note that the material properties defined in the SAP2000 model matched the average material properties obtained from the tensile coupon tests. To define similar stress-strain curves to that shown in Figure 3-8, average stress was sampled at the yield point, as well as at 2, 5, 10, 15, and 30% strains. Stresses beyond the 30% strain were excluded for simplicity (which, in the SAP2000 model, was interpreted as a constant stress value beyond 30% strain). The resulting pushover curve is displayed in Figure 3-25.
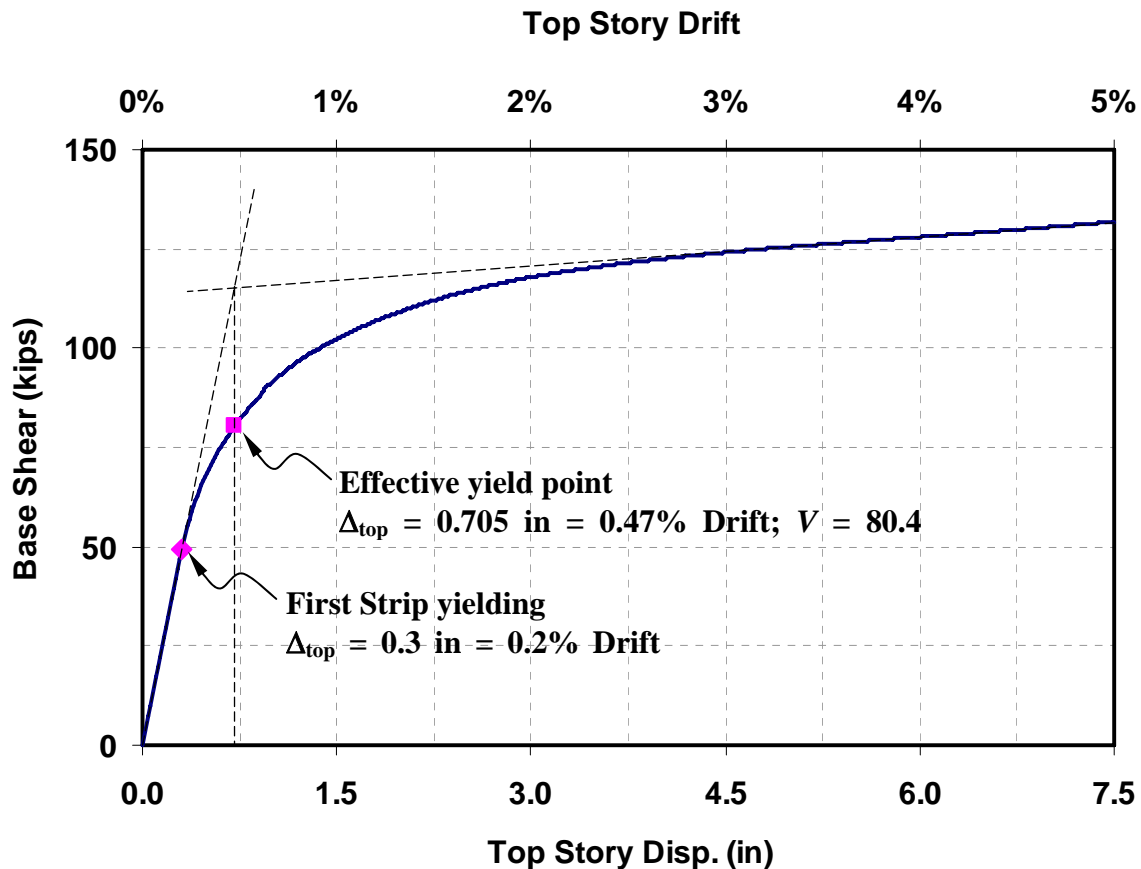
Figure 3-25 Estimation of Effective Yield Force and Displacement

The effective yield displacement was determined as the point where the elastic and inelastic tangents intersected to each other. As illustrated in Figure 3-25, the resulting effective top story yield displacement was 0.705 in., corresponding to a drift of 0.47%. The effective yield force, defined as equal to the base shear when the specimen reached the effective yield displacement, was 80.4 kips. Note that the first strip yielding occurred at a 0.3 in. top story displacement (or

102

0.20% top story drift), corresponding to a 49.3 kips total base shear. This indicated that at the effective yield point, significant yielding occurred in the infill plates of specimen.

3.8.2 Cyclic Displacement Loading History

The loading protocol for this experimental program was developed as a combination of the ATC-24 protocol (ATC 1992) and the AISC Seismic Provisions (AISC 2010b) requirements. Specifically, the first half of the loading protocol followed the loading sequences specified in the ATC-24 formulated as a function of ductility ratio (μ), defined here as the ratio of top story displacement (Δ_3) to the specimen effective yield displacement (δ_y), while its second half followed the AISC requirements that are in terms of top story drift.

Displacement targets for the first three displacement steps (amplitudes) were set to be 1/6, 1/3, and 2/3 of the estimated effective yield displacement (Section 3.8.1), and three cycles were to be conducted at each of these amplitudes. These multiple small steps were intended to allow observation of the specimen behavior within the elastic range. Afterward, the amplitude of the displacement target was increased to be equal to the effective yield displacement followed by multiples of δ_y until reaching a ductility of four. Again, three cycles were to be conducted at each of these amplitudes, except for the $4\delta_y$ displacement step which consisted of 2 cycles. Beyond this point, displacement targets were controlled by top story drifts. Starting with a target of 2.5% top story drift, subsequent displacement steps of 0.5% drift increment were chosen until the specimen top story reached 4% drift. At these large excursions, two cycles for each displacement step were considered. If the specimen could still resist loading beyond the 4% top story drift, the displacement amplitudes would be increased by 1.0% drift until completion of the test. A complete cyclic displacement loading history for this experimental program is summarized in Table 3-3 and graphical representation of the complete loading protocol is shown in Figure 3-26. A total of 13 displacement steps and a cumulative 32 cycles were designed in this experiment.

3.9 Preliminary Nonlinear Static Analysis of Specimen

A cyclic pushover analysis of the specimen numerical model was conducted prior to executing this experimental program to predict idealized specimen response. All modeling features

Table 3-3 Cyclic Displacement Loading History

Displacement Step	Number of Cycles	Cumulative Number of Cycles	Ductility Ratio Δ_3/δ_y	Top Story Drift (%)	Top Story Displacement Δ_3 (in)	Estimated Level 3 Act. Force F_3 (kips)	Estimated Level 2 Act. Force F_2 (kips)	Estimated Level 1 Act. Force F_1 (kips)	Estimated Base Shear V (kips)
1	3	3	0.17	0.08	0.12	9.9	6.6	3.2	19.8
2	3	6	0.33	0.16	0.24	19.9	13.2	6.5	39.6
3	3	9	0.67	0.31	0.47	33.5	22.2	10.9	66.6
4	3	12	1.00	0.47	0.71	40.4	26.8	13.2	80.4
5	3	15	2.00	0.94	1.41	50.6	33.6	16.5	100.7
6	3	18	3.00	1.41	2.12	55.6	36.9	18.1	110.7
7	2	20	4.00	1.88	2.82	58.6	39.0	19.2	116.8
8	2	22	5.32	2.50	3.75	61.0	40.6	19.9	121.5
9	2	24	6.38	3.00	4.50	62.3	41.5	20.4	124.2
10	2	26	7.45	3.50	5.25	63.4	42.1	20.7	126.2
11	2	28	8.51	4.00	6.00	64.3	42.8	21.0	128.0
12	2	30	10.64	5.00	7.50	66.2	44.0	21.6	131.8
13	2	32	12.77	6.00	9.00	68.1	45.3	22.2	135.6

Note:

Actuator Rate : 2 minutes/cycle (Displacement Steps 1 to 5)   Loading Protocol : Displacement Controlled at Level 3 Actuator (Master)
           : 3 minutes/cycle (Displacement Steps 6 to 13)   : Force Controlled at Level 2 & 1 Actuators (Slaves)
                                                           which $F_2 \approx 2/3F_3$ and $F_1 \approx 1/3F_3$
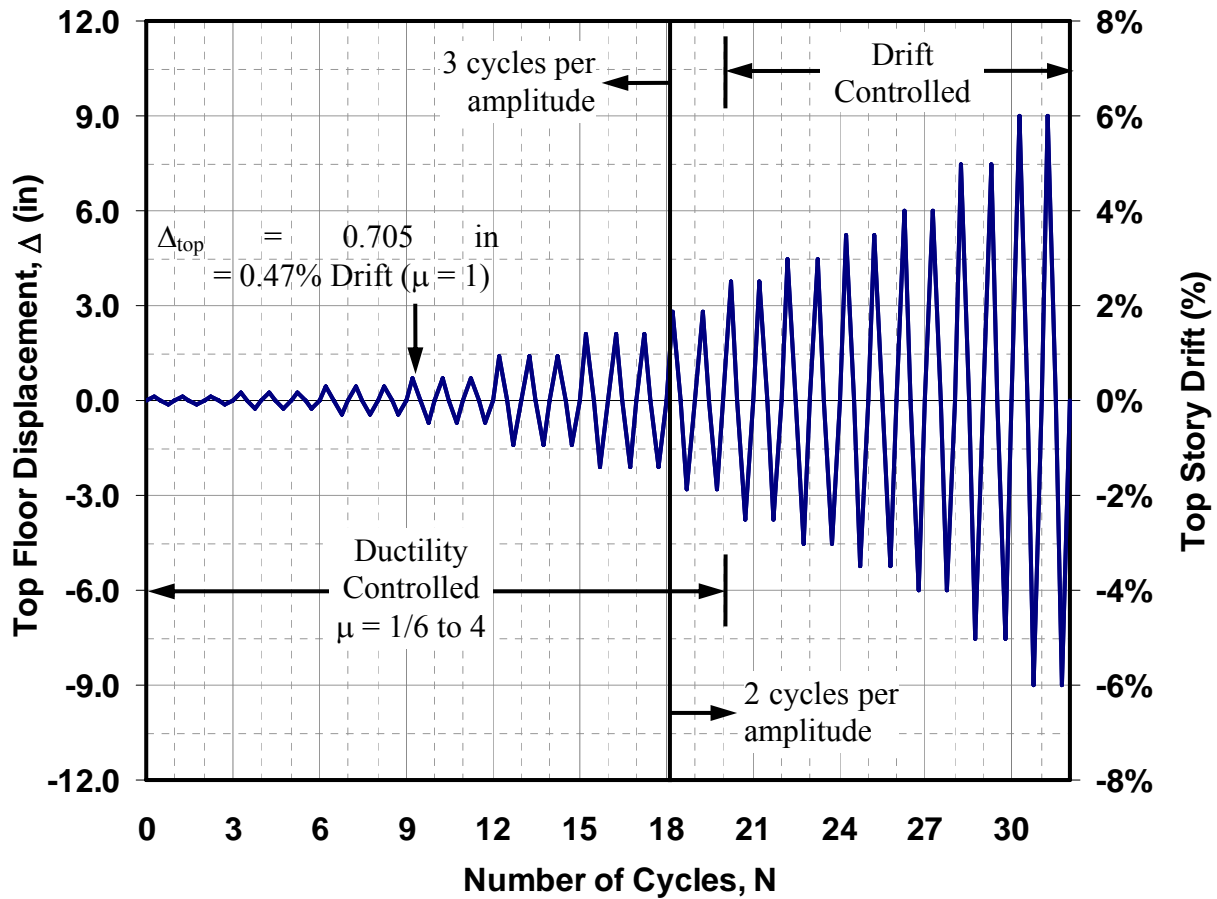
Figure 3-26 Cyclic Displacement Loading History

presented in Section 3.8.1 were included in this numerical model and the cyclic displacement loading history formulated in Section 3.8.2 (up to 4% top story drift), except that only one cycle of loading history was applied at each of the target displacement levels because no material degradation was included in the numerical model for cycles at the same displacement magnitude (defined as "in-cycle" degradation in the FEMA 440a). In addition, the elastic displacement steps (i.e., $1/6\delta_y$, $1/3\delta_y$, and $2/3\delta_y$ steps) were excluded from this analysis for expediency. The resulting overall cyclic hysteresis curve, HBE vertical displacement histories, moment-rotation relationships, and plastification distribution are presented in Figures 3-27a to 3-27d, respectively.

These results predicted a total base shear of 128 kips at 4% top story drift for both the positive and negative excursions. At the same drift level, the maximum vertical deformations of HBE0, HBE1, HBE2, and HBE3 were predicted to reach 1.5, 0.4, 1.1, and 1.2 in., respectively. All HBEs exhibited downward vertical deformations, except HBE0, which experienced upward
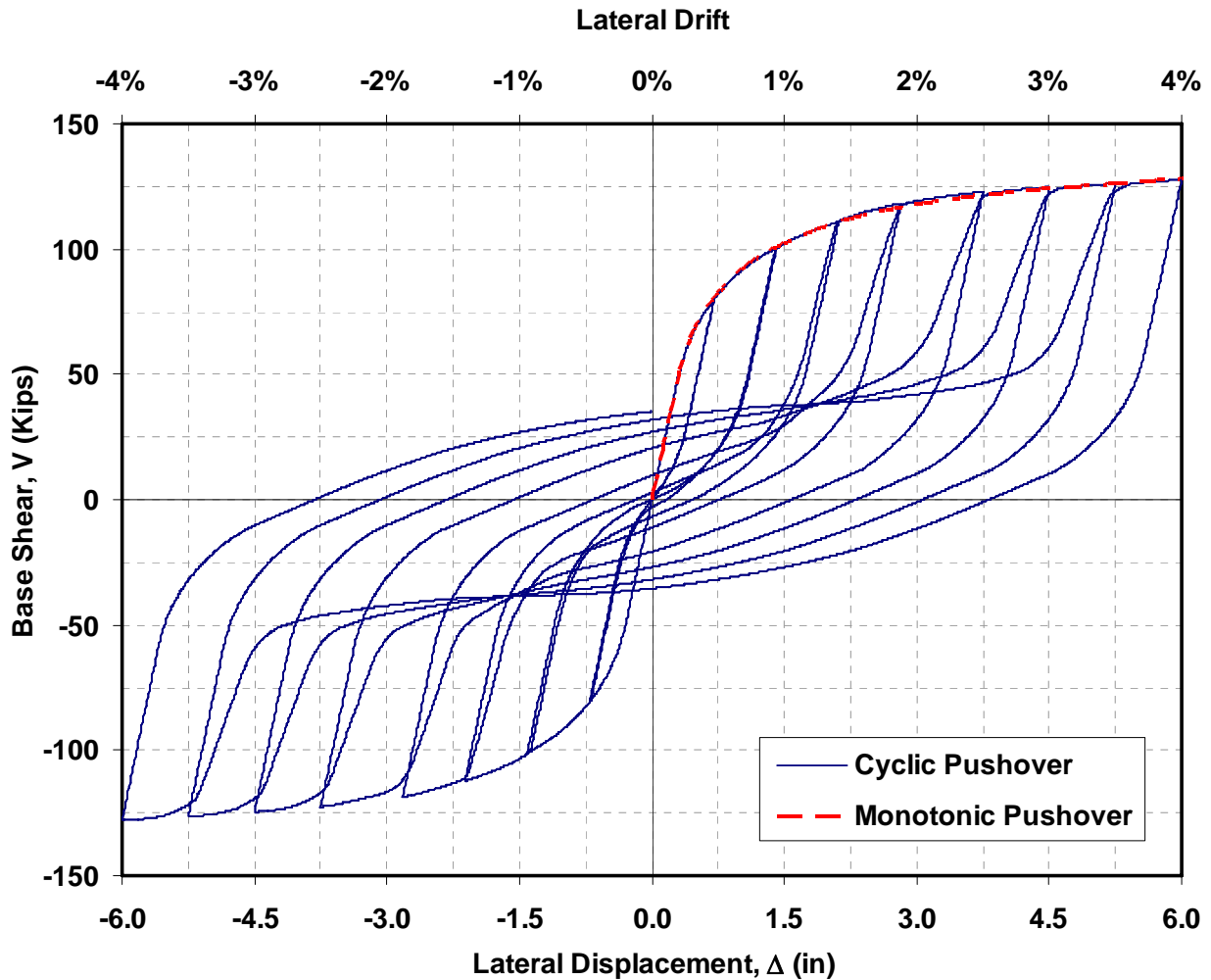
Figure 3-27 Nonlinear Static Analysis Results:
(a) Base Shear versus Top Floor Lateral Displacement

deformations. The maximum cross-section rotations at the East HBE-to-VBE joints were expected in excess of 0.054, 0.039, 0.065, 0.063 radians for HBE0 to HBE3, respectively. In addition to plastification at HBE ends, at the end of 4% drift cycle, in-span plastification was predicted to occur at the top two HBEs and the bottom anchor beam in excess of 0.02 and 0.051 radians, respectively. Lastly, compared to the infill plates in all other stories, the first story infill plate yielded less; this was attributed to the relatively large HBE0 vertical deformations, which diminished the first story infill plate elongations.
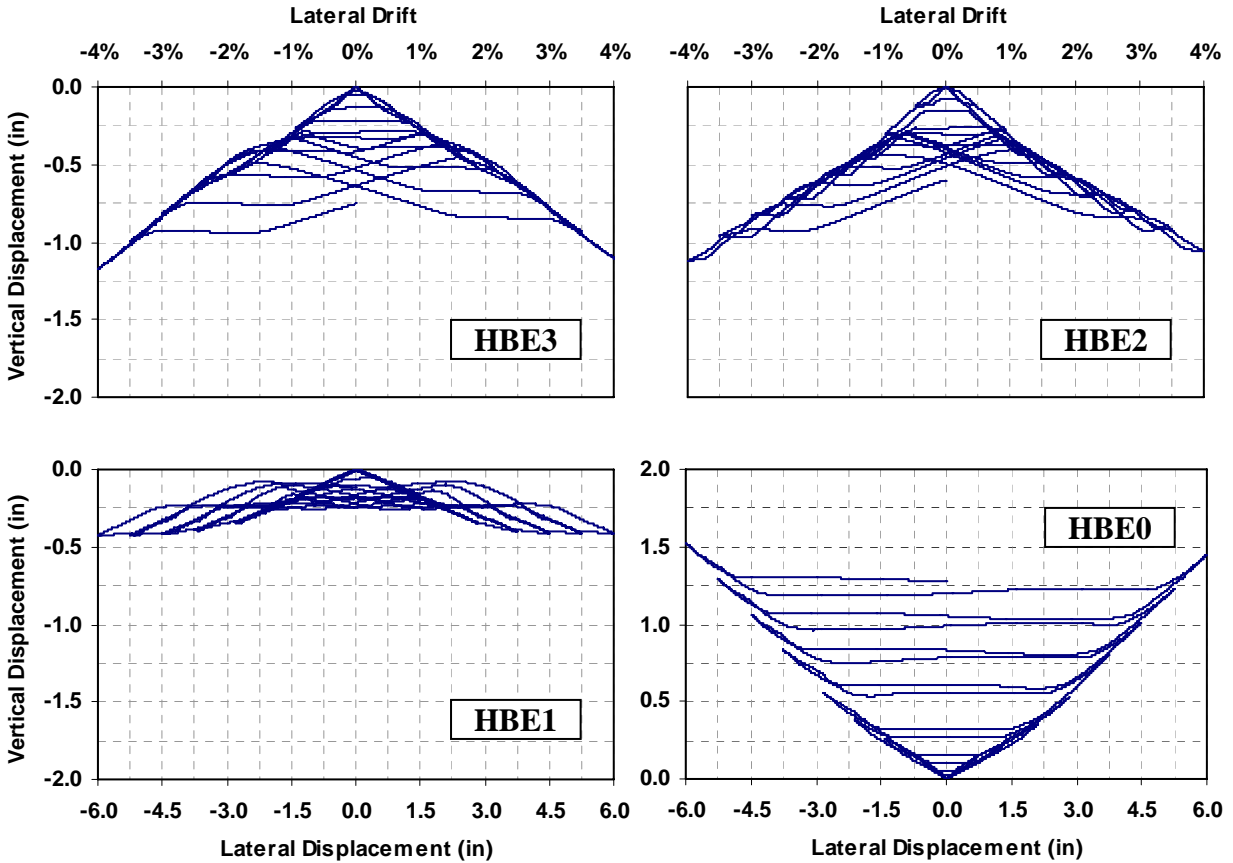
Figure 3-27 Preliminary Nonlinear Static Analysis Results – Cont'd:
(b) Top Story Lateral Displacement versus HBE Vertical Displacement

3.10 Summary

A three-story SPSW specimen was developed to experimentally investigate the impact of in-span hinges on the seismic behavior of steel plate shear walls. The specimen roughly corresponded to a 1/3-scale model of a SPSW that could be implemented in the three-story SAC model building (FEMA 355-C). Prior to obtaining a final design, several design considerations were examined to ensure that the experimental objectives were met. Design modifications considered were related to constraints in the experimental setting, variations on material yield strength and strain hardening, material availability, and impact of fish plate on HBE cross section properties.

Detailed information related to the specimen fabrication process at the local steel fabricator and final preparation at the Structural Engineering and Earthquake Simulation Laboratory (SEESL) of
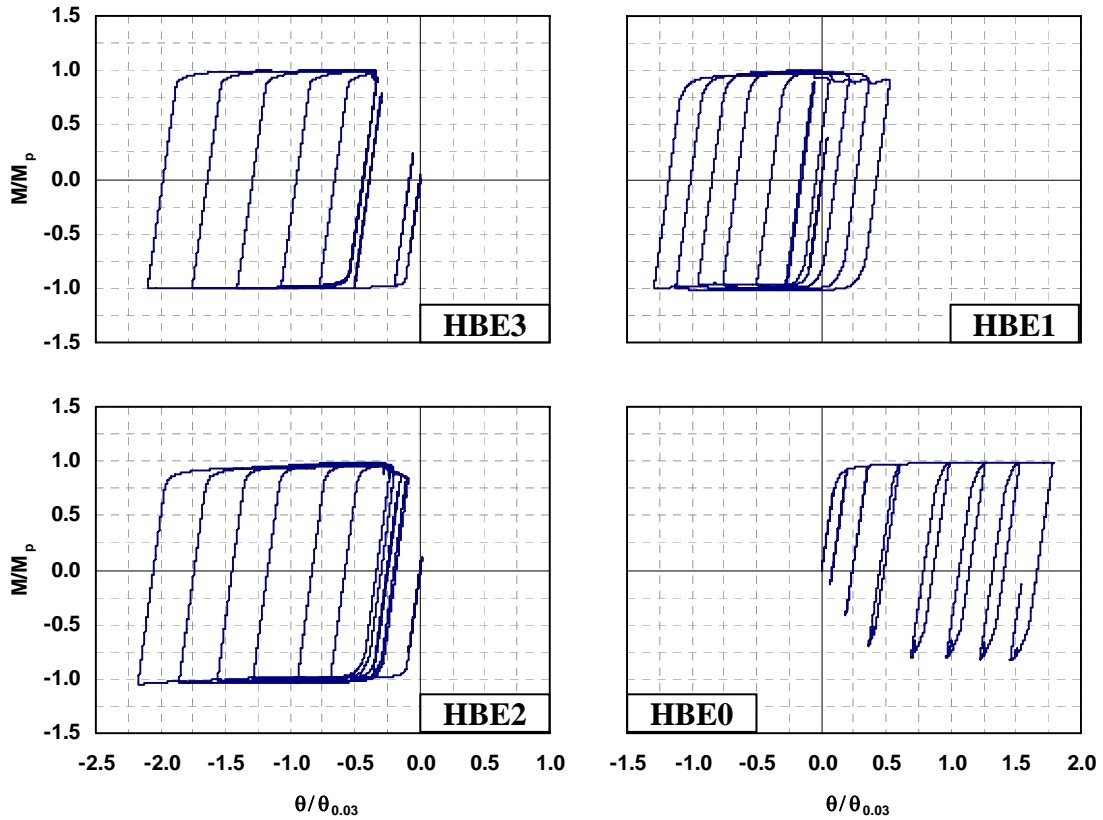
Figure 3-27 Preliminary Nonlinear Static Analysis Results – Cont'd:
(c) Normalized Moment Hysteresis at HBE West End
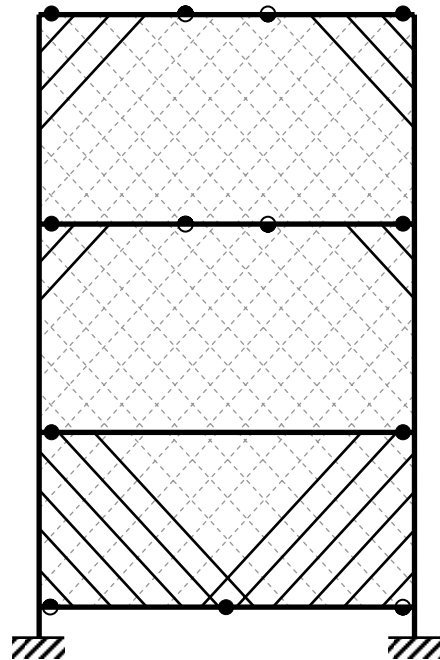
Figure 3-27 Preliminary Nonlinear Static Analysis Results – Cont'd:
(d) Plastic Hinge and Strip Yielding Distributions at the End of 4% Drift Loading

the University at Buffalo was presented, including information on the limited nondestructive testing of several special-moment resisting connections in the specimen, as well as on specimen instrumentation and preparation. Minor modifications to the specimen were explained.

Issues related to experimental setting were presented, which explained how the specimen, gravity column and lateral support systems, actuators, and instrumentation were assembled together for the purpose of achieving the experimental objectives. Moreover, development of the loading protocol was explained, and more specifically, how force distribution among three dynamic actuators was defined.

Finally, preliminary nonlinear cyclic pushover analysis, using a numerical model of the specimen with actual material properties, was presented. Experimental results and observations during the experimental program will be presented in Section 4.

SECTION 4

EXPERIMENTAL OBSERVATIONS AND RESULTS

4.1 General

This section describes experimental observations and results for the cyclic pushover testing of the three-story steel plate shear walls (SPSW) specimen designed in Section 3. Several minor adjustments to the planned loading protocol presented in the preceding section are discussed first. Reasons for such adjustments are explained when presenting in detail the behavior of the three-story SPSW specimen during testing. Based on adjustments in the loading protocol and to the experimental load transfer mechanism, observations made on specimen behavior are presented in three different loading sequences. Observations on behavior of the specimen subjected to the initial part of the originally planned load transfer mechanism are first presented, followed by observations after the load transfer mechanisms were modified and the specimen was subjected to a revised displacement sequence. During this stage of testing, modified loading transfer mechanisms failed, leading to other modifications. Observations on specimen behaviors following these repairs up to the completion of the experimental program are finally presented.

Following the discussion of specimen behavior, results from a revised analytical investigation are presented as an attempt to rationalize the above modifications on the load transfer mechanism. This analytical investigation is also intended to resolve discrepancies observed between results obtained during the first loading sequence of the experimental program and those predicted by the preliminary analysis conducted before testing (Section 3.9). For this purpose, non-linear static analysis results considering six different scenarios of load application and boundary conditions are reviewed.

The section ends with a review of several key experimental results to investigate whether the objectives of this experimental program previously discussed in Section 3.1 have been achieved. Global behavior is first reviewed, in terms of hysteric behavior of story shear versus specimen lateral displacement, followed by local behavior, such as plastic hinge and infill plate yielding distributions, HBE vertical deformations, and moment-rotation hysteresis.

111

4.2 Adjustment to Loading Protocol

Based on monitoring of a real time data display in the control room and visual observations on specimen behaviors throughout the testing, several minor adjustments to the loading protocol presented in Section 3.8 were introduced as testing unfolded. First, the displacement step at 1/6 of the yield displacement, δ_y, (corresponding to 0.08% top story drift) had to be repeated due to malfunction of the data acquisition system (DAQ system) during the first three cycles. Second, for reasons explained in the following section, displacement Step 6 at $3\delta_y$ (= 1.41% top story drift) was repeated for an additional 4 cycles, followed by conducting displacement Steps 7 and 8 for two cycles each as initially intended. Failures of the loading transfer mechanism within the last two displacement steps required repeating these displacement steps to establish specimen behaviors in those steps. Here, 6 additional cycles within the range of 1.88% up to 2.5% top story drift were repeated. Due to problems that developed in the experimental set-up, the testing program concluded after having conducted 6 and 8 cycles of displacement Steps 9 and 10, respectively.

In spite of these unforeseen difficulties, at the conclusion of the experiment, the specimen had been pushed and pulled up to a maximum top story lateral drift of 3.3%, corresponding to a ductility ratio of 7.09. Note that the maximum drift attained was slightly lower than the initial 3.5% top story drift targeted in displacement Step 10 (Section 3.9). In addition, one should note that the maximum target displacement defined at every displacement step was the displacement imposed by the third story actuator.

A complete actual cyclic displacement loading history for this experimental program is summarized in Table 4-1 (shaded rows in that table correspond to the additional displacement steps added to the initially planned ones) and graphically shown in Figure 4-1. Though the actual total number of different displacement amplitudes is less than originally planned (i.e., 10 instead of the 13 planned), the actual cumulative number of cycles applied to the specimen is larger (i.e., 48 cycles compared to the 32 cycles planned). Observations on specimen behaviors within each displacement step are explained in the following section.

Table 4-1 Experimental Cyclic Displacement Loading History

Displacement Step	Number of Cycles	Cumulative Number of Cycles	Ductility Ratio Δ_3/δ_y	Top Story Drift (%)	Top Story Displacement Δ_3 (in)	Estimated Level 3 Act. Force F_3 (kips)	Estimated Level 2 Act. Force F_2 (kips)	Estimated Level 1 Act. Force F_1 (kips)	Estimated Base Shear V (kips)
1	3	3	0.17	0.08	0.12	9.9	6.6	3.2	19.8
1a	2	5	0.17	0.08	0.12	9.9	6.6	3.2	19.8
2	3	8	0.33	0.16	0.24	19.9	13.2	6.5	39.6
3	3	11	0.67	0.31	0.47	33.5	22.2	10.9	66.6
4	3	14	1.00	0.47	0.71	40.4	26.8	13.2	80.4
5	3	17	2.00	0.94	1.41	50.6	33.6	16.5	100.7
6	3	20	3.00	1.41	2.12	55.6	36.9	18.1	110.7
6a | 6b | 6c	1 | 2 | 1	24	3.00	1.41	2.12	55.6	36.9	18.1	110.7
7	2	26	4.00	1.88	2.82	58.6	39.0	19.2	116.8
8	2	28	5.32	2.50	3.75	61.0	40.6	19.9	121.5
7a | 7b	2 | 2	32	4.00	1.88	2.82	58.6	39.0	19.2	116.8
8a	2	34	5.32	2.50	3.75	61.0	40.6	19.9	121.5
9	2	36	6.38	3.00	4.50	62.3	41.5	20.4	124.2
9a | 9b	2 | 2	40	6.38	3.00	4.50	62.3	41.5	20.4	124.2
10	1	41	6.74	3.17	4.75	62.7	41.7	20.5	124.9
10a | b | c | d	1 | 1 | 3 | 2	48	7.09	3.33	5.00	63.0	41.9	20.6	125.5

Actuator Rate : 2 minutes/cycle (Displacement Steps 1 to 5)   Loading Protocol : Displacement Controlled at Level 3 Actuator (Master)

         : 3 minutes/cycle (Displacement Steps 6 to 7a)   : Force Controlled at Level 2 & 1 Actuators (Slaves)

         : 5 minutes/cycle (Displacement Steps 7b to 10d)   which $F_2 \approx 2/3F_3$ and $F_1 \approx 1/3F_3$
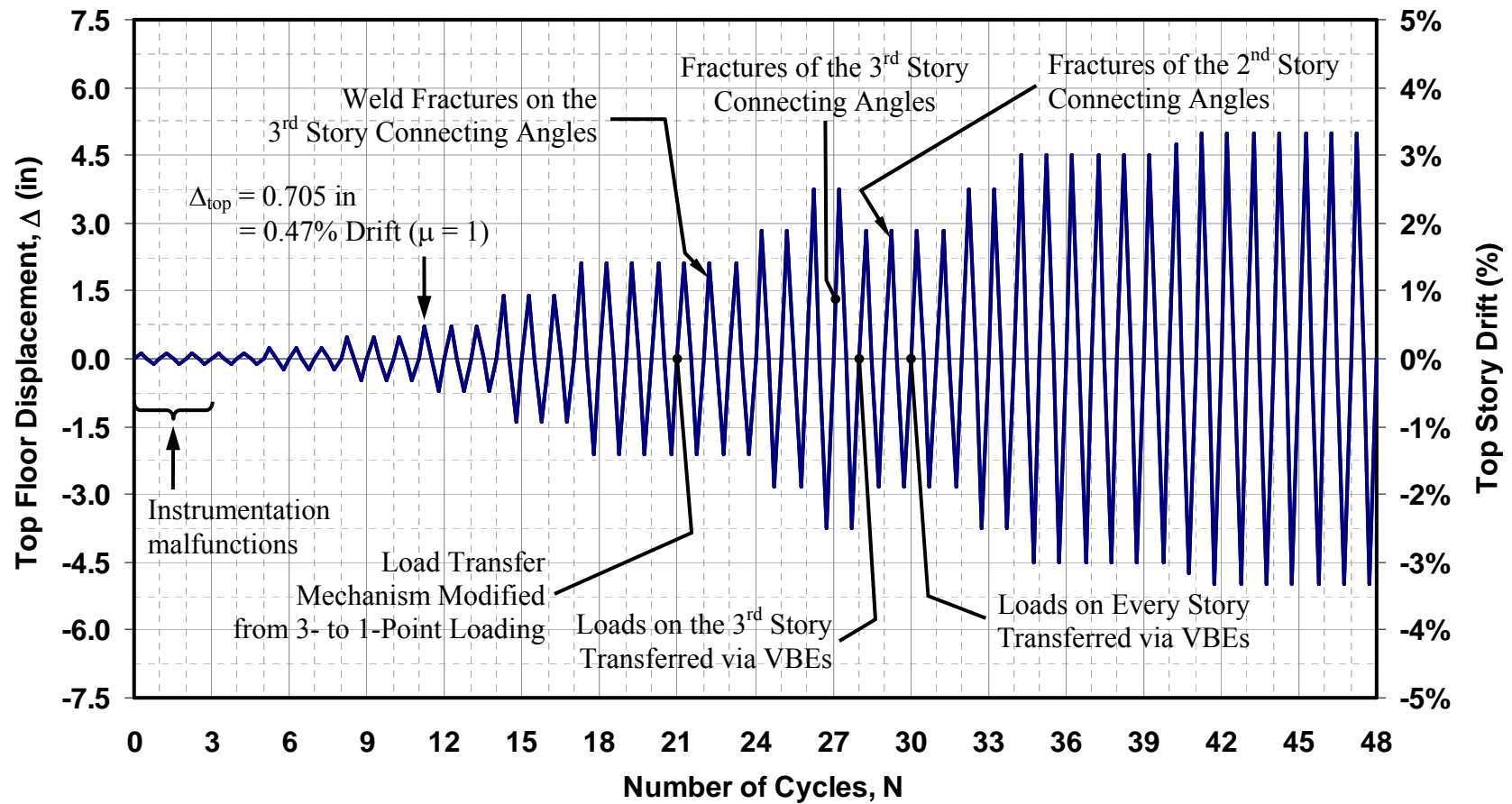
Figure 4-1 Cyclic Displacement Loading History

4.3 Experimental Observations

This section describes in detail the behavior of the three-story SPSW specimen during the cyclic pushover testing. Observations on specimen behavior are divided into three sub-sections, each focusing on one of the loading sequences described above. Adjustments to the loading protocol and the experimental setting are described. In the first sub-section, corresponding to displacement Steps 1 to 6a, the experimental setting (i.e., the loading transfer mechanism) was similar to what was presented in Section 3.7.3. In the second sub-section, covering displacement Steps 6b to 7a, focus is mostly on describing the modified load transfer mechanism used, problems that arose, and solutions to allow testing to proceed forward. In the third sub-section, for displacement Steps 7b to 10d, as will be explained later, loads are transferred to the specimen through its VBEs instead of through its HBEs, and the test is continued until unfixable problems arose with the experimental set-up. Note that, as an arbitrary convention in this experimental program, "pushing" and "pulling" refer to specimen displacements in the West and East directions, respectively. Hysteretic plots of specimen base shear versus top story specimen and actuator displacements for all displacement steps are shown in Figures 4-2 and 4-3, respectively.

4.3.1 Displacement Steps 1 to 6a

The experimental program began with 3 cycles with a target of 0.12 in. maximum displacement at the top story (called here the "actuator displacement", which also equals the mass plate lateral displacement). This target displacement corresponded to ductility ratio and top story drift of 1/6 and 0.08%, respectively. As mentioned previously, this first displacement step however was repeated for two additional 2 cycles because a significant number of strain gauges and string pots data were not recorded in the first 3 cycles. As expected, elastic buckling of the infill plates and a practically linear force-displacement relationship was observed during the first displacement step. The same elastic behavior (Figure 4-2a) continued in displacement Step 2 (top story drift amplitudes of 0.16% $=1/3\delta_y$), with a maximum base shear (i.e., total forces applied by the 3 actuators) of 48.5 kips. Interestingly, this base shear value was somewhat higher than the estimated base shear of 39.6 kips. During Step 2, no effort was made to explain this difference, considering it was still in the early stages of testing. It was also observed that the top story specimen displacement (called here the "wall displacement") measured by the string pot attached
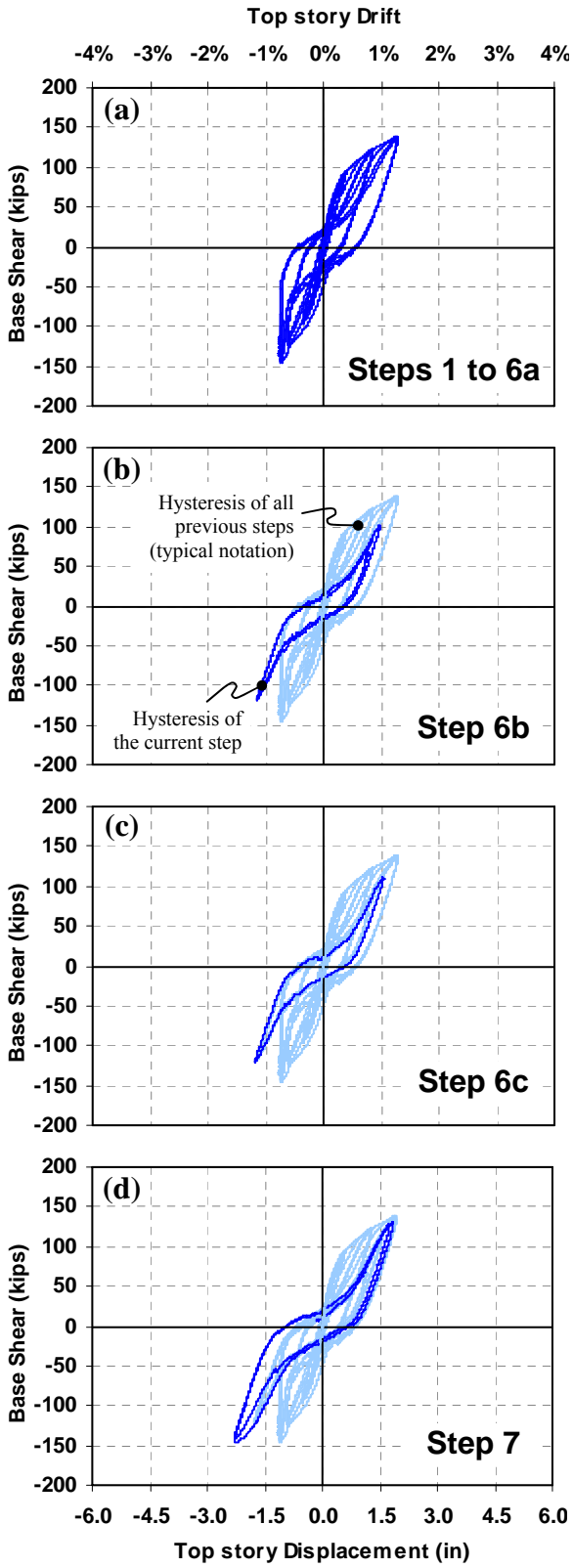
Figure 4-2 Base Shear versus Top Story Displacement
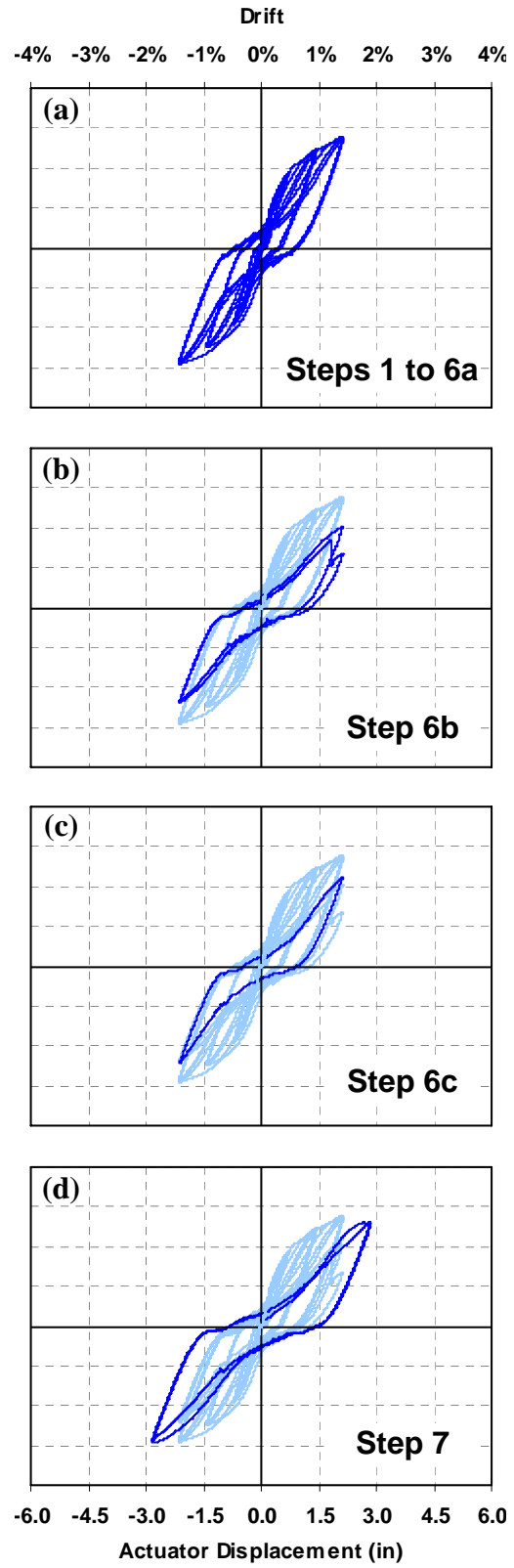
Figure 4-3 Base Shear versus Top Story Actuator Displacement

116
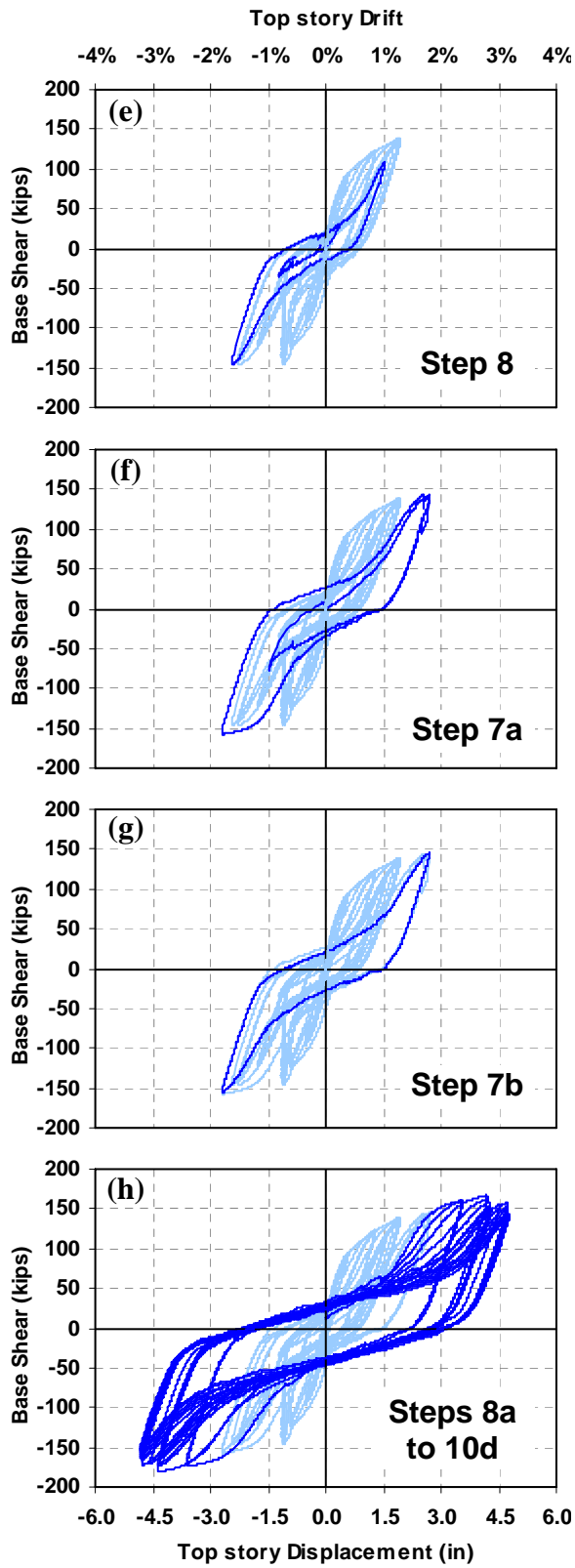
Figure 4-2 Base Shear versus Top Story Displacement – Cont'd
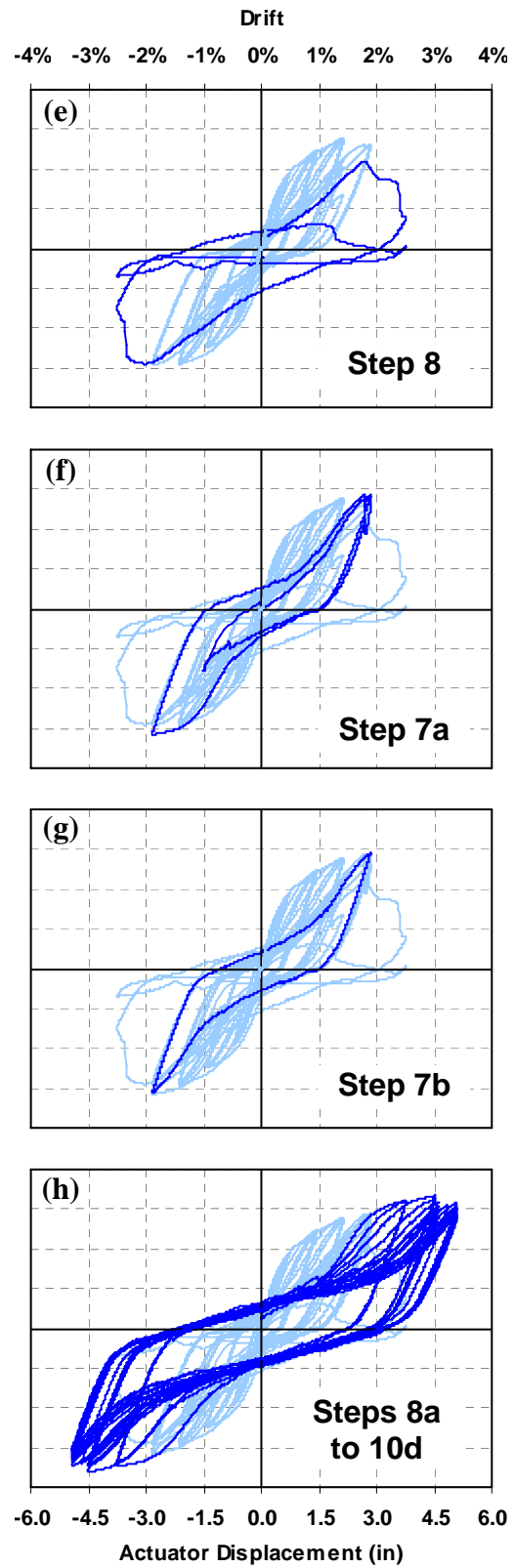
Figure 4-3 Base Shear versus Top Story Actuator Displacement – Cont'd

117

to the specimen (i.e., SPWC3, Figure 3-21a) was slightly lower than the actuator displacement (comparing displacement records in Figure 4-2a and Figure 4-3a). The difference between the two measurements was less than 0.1 in., which was within the range of tolerance provided in the oversize slotted holes of the angles used for the load transfer mechanism (Figure 3-18), in addition to possible small slips in other parts in reaction set-up. Therefore, it was considered acceptable.

Early sign of yielding was observed in displacement Step 3 when the maximum displacement at the top story reached 2/3 of the effective yield displacement (defined in Section 3.9). Though no sign of whitewash flaking was observed yet in this step, the force-displacement curve (i.e., base shear versus top story displacement) exhibited slight hysteretic behavior (Figure 4-2a). The infill plates remained slightly buckled when the specimen returned to its original position (after it was pushed and pulled up to a maximum top story drift of 0.31%); and there was negligible residual top story displacement at the end of Step 3. Noticeable signs of yielding were observed in the subsequent displacement step, when the specimen reached an expected effective yield displacement of 0.71 in. (= 0.47% top story drift). Flaking of whitewash was noted around the bases of both columns, on the outer side of their flanges at the level of the top continuity plates. Flaking of whitewash did not occur on the infill plates despite the fact that the permanent buckling of the infill plates was more pronounced in displacement Step 4 than in the previous step. The specimen deformed shape after it went through three full cycles at 0.47% drift is shown in Figure 4-4. The hysteretic force-displacement curve was somewhat fatter (Figure 4-2a) compared to what had been obtained in the previous displacement step, suggesting that yielding of the specimen has taken place. A residual displacement of approximately 0.08 in. was observed at the top story at the end of displacement Step 4.

When the specimen reached 0.47% top story drift, the resulting base shear reached 95.8 kips, which was significantly higher than the estimated base shear of 80.4 kips at the effective yield level. This discrepancy raised a concern as to whether the experimental program should be postponed to allow further analytical investigations to potentially explain (and resolve if needed) the causes of this phenomenon. One option was to re-analyze the specimen using the maximum values obtained from the tensile coupon tests instead of the average value for all the coupons (as
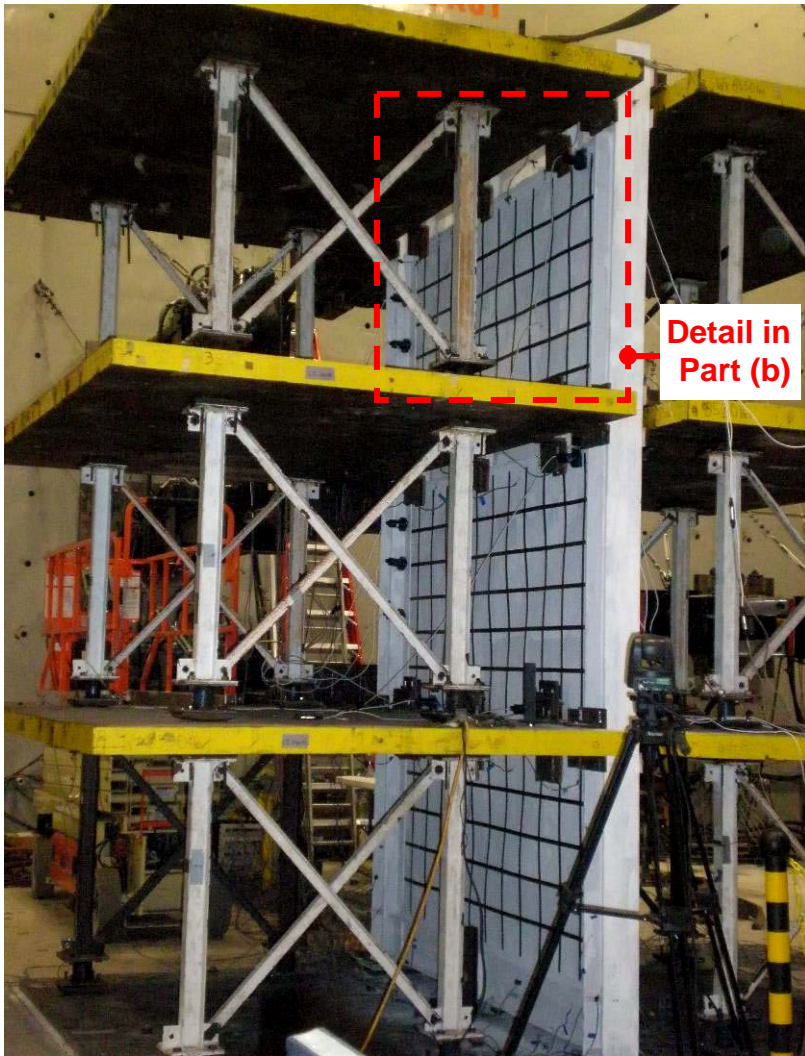
(a)
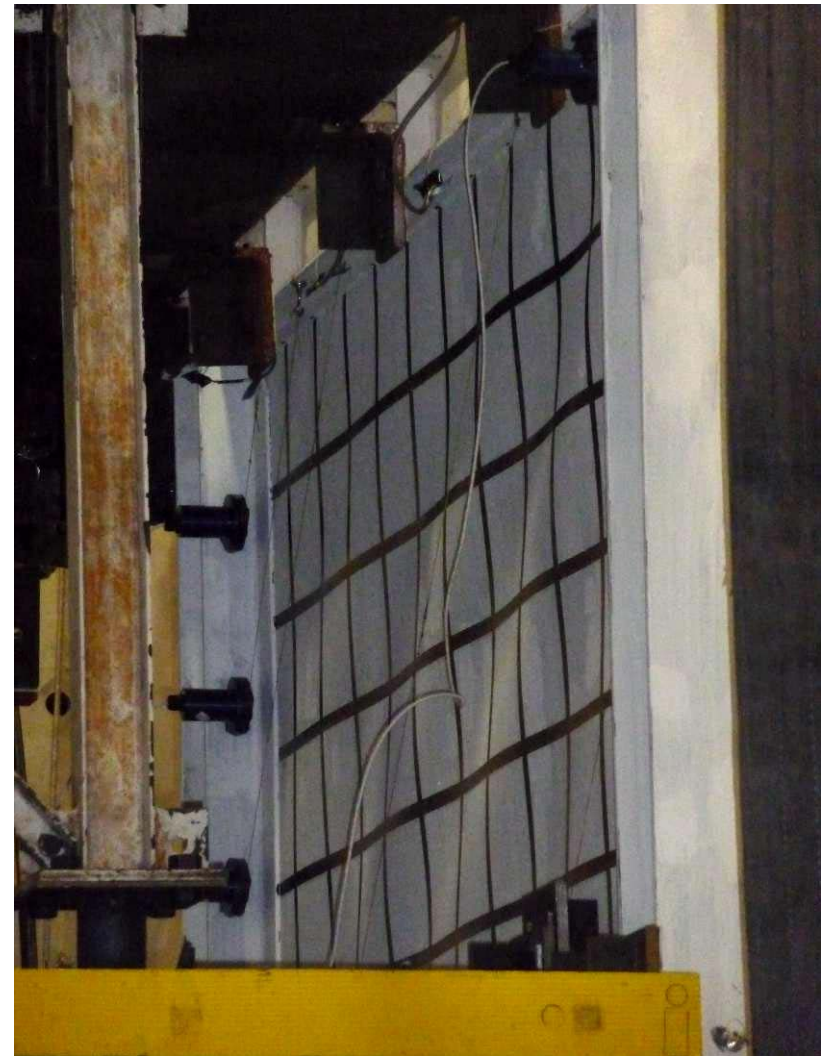
(b)

Figure 4-4 Specimen Condition at the End of Displacement Step 4 ($\Delta_3 = 1\delta_y = 0.47\%$ Drift): (a) Deformed Shape Overview; (b) 3rd Story Infill Plate Buckled (North Side)

was done in the preliminary analyses presented in Section 3.9). Note that there was a 5% difference between these average and the maximum yield strength values for the ASTM Grade 50 Steel used for boundary elements, and 10% for the light-gauge steels used for the infill plates. However, the monitored results showed that the HBE3 and HBE2 vertical displacements were somewhat lower than their predicted values, in spite of the higher base shear obtained. In this case, the actual HBE3 and HBE2 vertical displacements were 0.07 and 0.05 in., respectively, while their estimated vertical displacements at 0.47% top story drift were 0.16 and 0.13 in. for the same respective HBEs (Figure 3-27b). These results could not be explained by material property variability. At this point, it was speculated that the high-strength bolts used in the connecting angles to transfer actuator loads from the gravity mass plate to the specimen might have been stuck and that, as a consequence, the HBEs were not completely free to move vertically. Such unintended restraints would have made the specimen became more rigid than anticipated by designed, and additional forces beyond what was expected would have been required to push the specimen to the specified displacement target.

The two suggested potential causes of higher base shear certainly deserved further investigation. However, rather than postponed the test, it was decided to continue for two more displacement steps, to see if the trend continued. Obtaining additional test data from the next two displacement steps was considered necessary to be able to decide how to proceed for the remaining of the test. Before continuing the experimentation program with displacement Steps 5 and 6, the snug tight bolt connections at every load transfer angle was double-checked to not be over tight; in addition, to facilitate the intended sliding of the bolts along the edges of the vertically slotted holes in the angles (Figure 3-17), grease was added at these locations.

During displacement Step 5, at $2\delta_y$ (= 0.94% top story drift), flaking of whitewash appeared predominantly on the second story infill plate and at several spots on the first story infill plate (Figures 4-5c to 4-5e). Yielding around the bases of columns spread to a larger area, with new whitewash flaking appearing at the level of the bottom continuity plates for both columns and at the West column connection to the base plate (Figure 4-5b). Yield lines were visible on the flanges and web of HBEs. Two examples of HBE flange and web yielding are shown in Figures 4-5f and 4-5g, respectively. Concentrations of yield lines on the inner side of the HBE
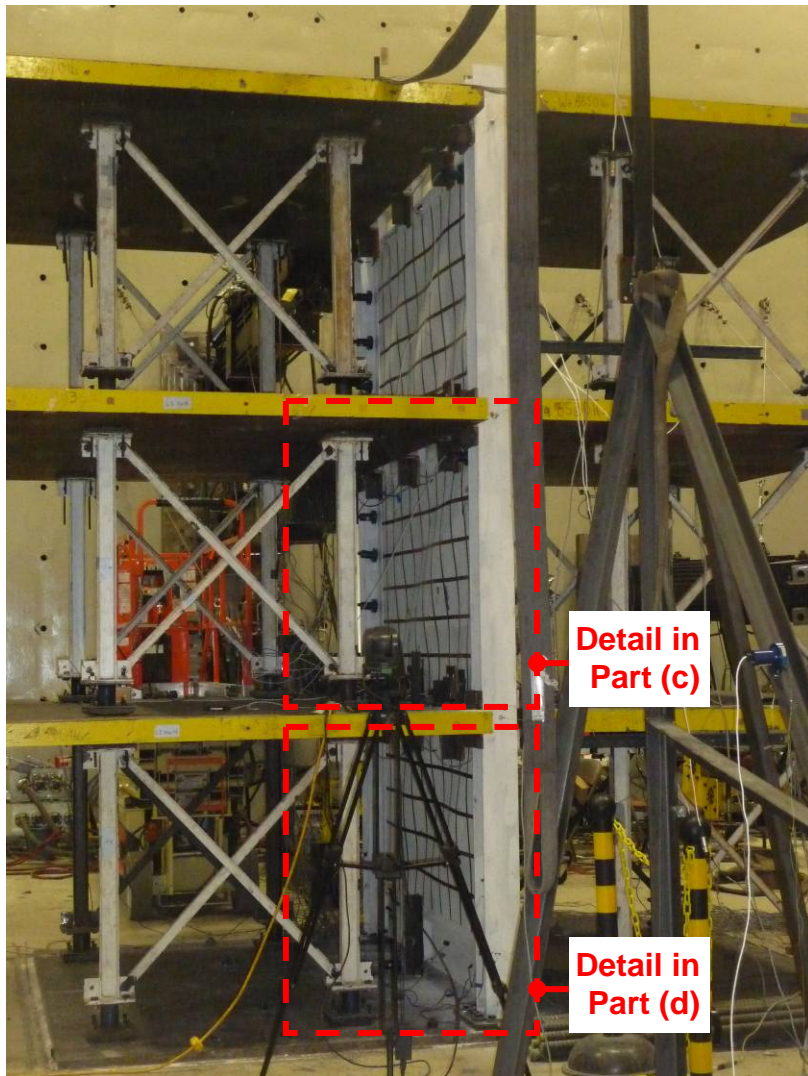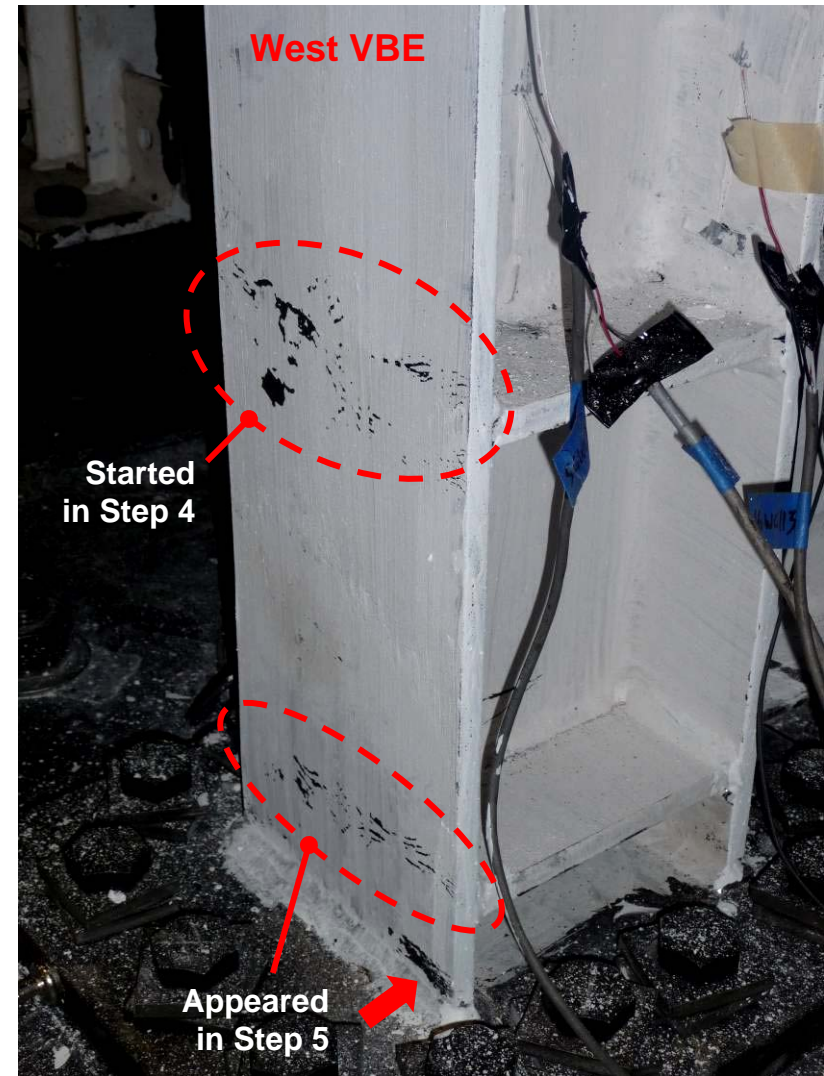
Figure 4-5 Specimen Condition at the End of Displacement Step 5 ($\Delta_3 = 2\delta_y = 0.94\%$ Drift): (a) Deformed Shape Overview; (b) Yielding around Column Base

121
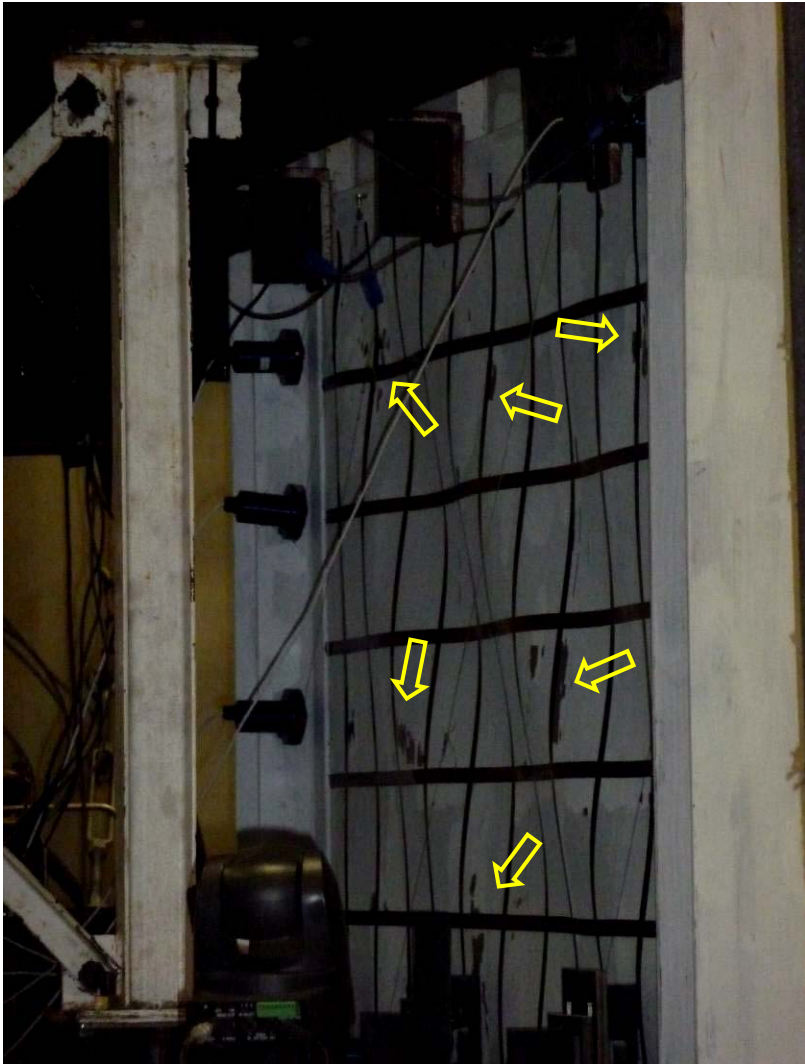
(c)
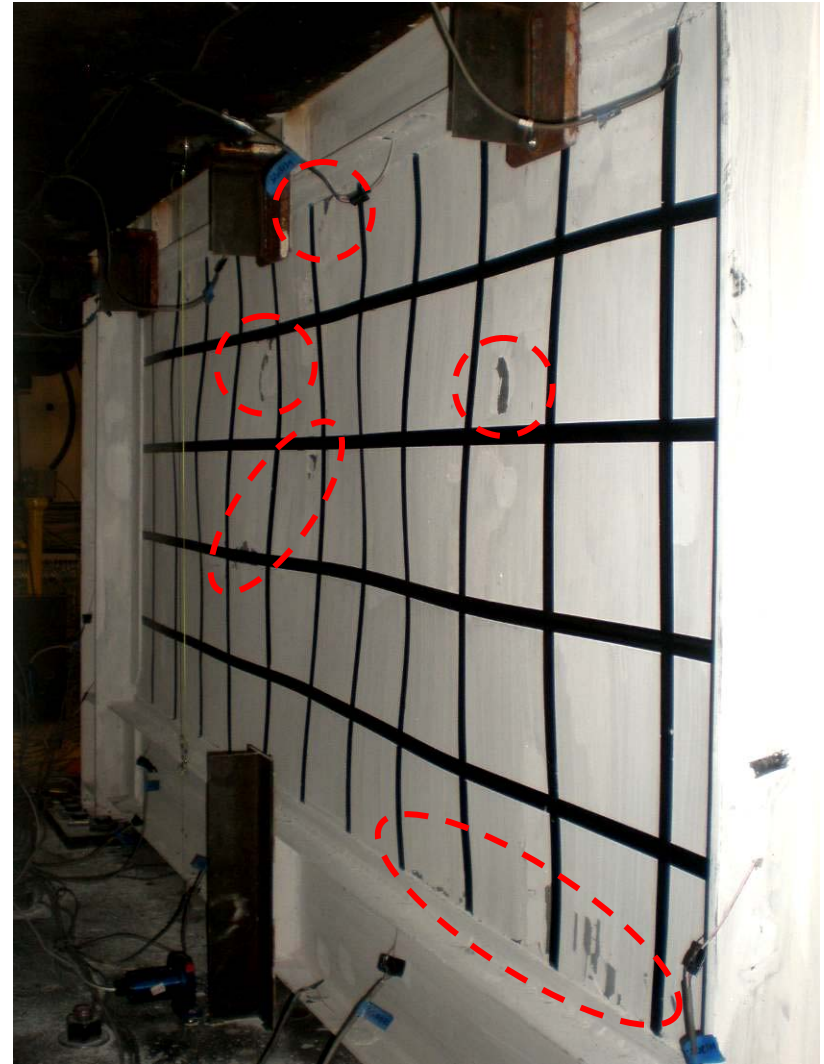
(d)

Figure 4-5 Specimen Condition at the End of Displacement Step 5 ($\Delta_3 = 2\delta_y = 0.94\%$ Drift) – Cont'd: (c) Yielding on the 2nd Floor Infill Plate (North Side); (d) Yielding on the 1st Floor Infill Plate (North Side)
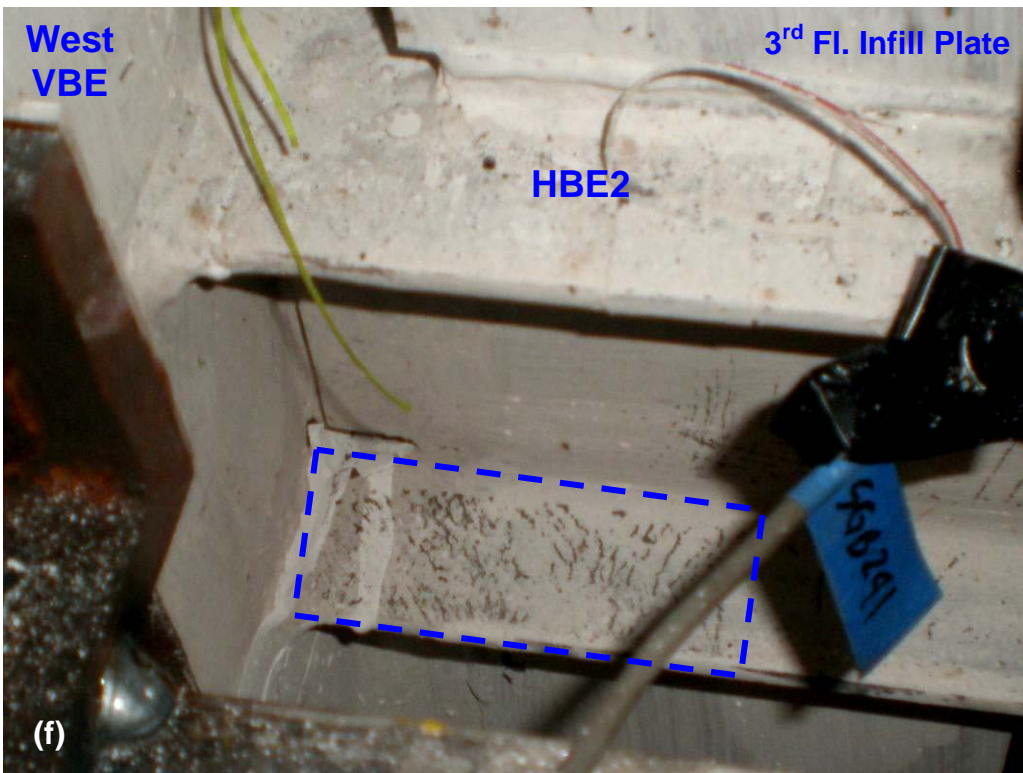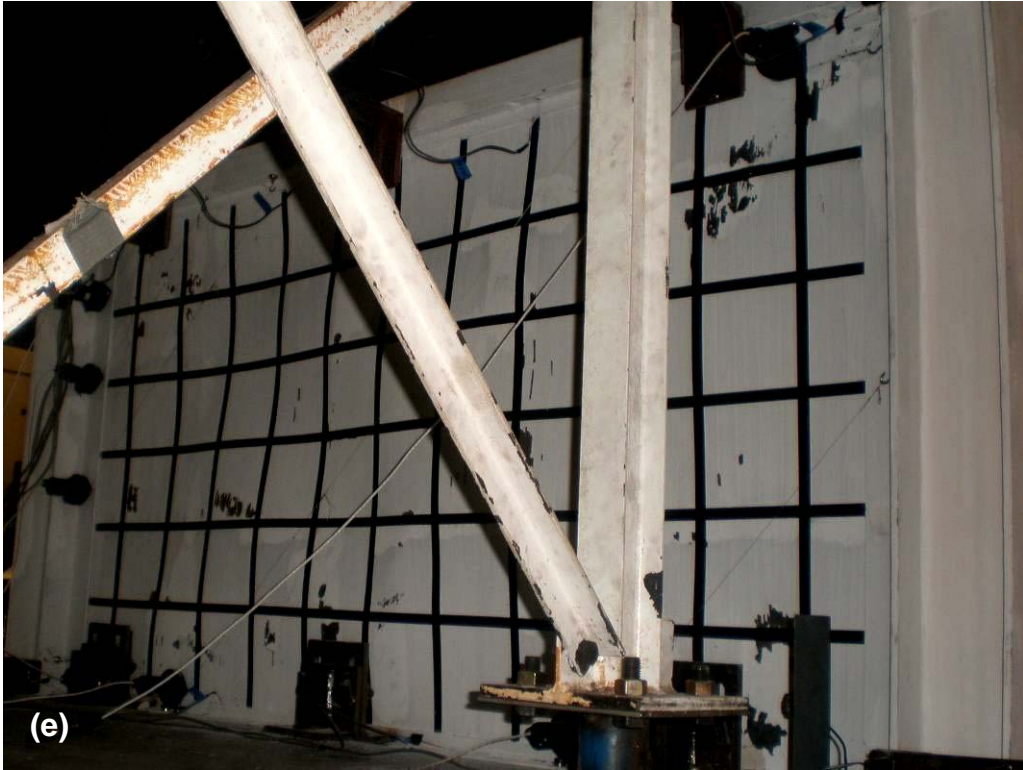
Figure 4-5 Specimen Condition at the End of Displacement Step 5 – Cont'd:
(e) North-West View of Yielding on the 2nd Floor Infill Plate; (f) Beam Flange Yielding

(g)

(h)
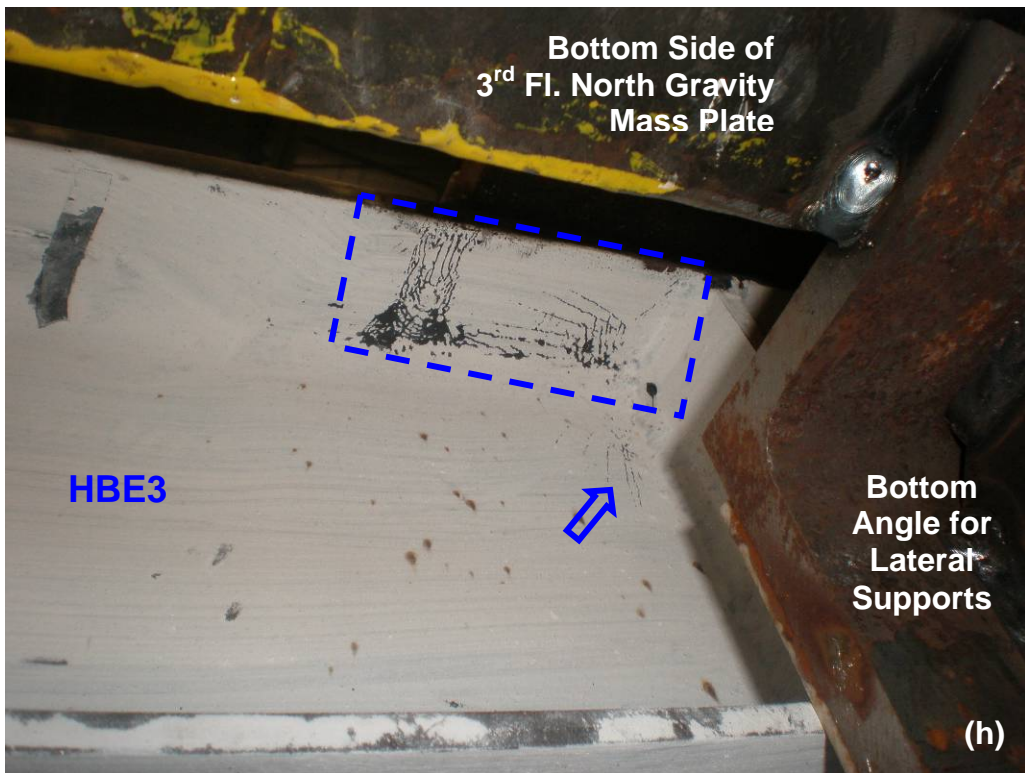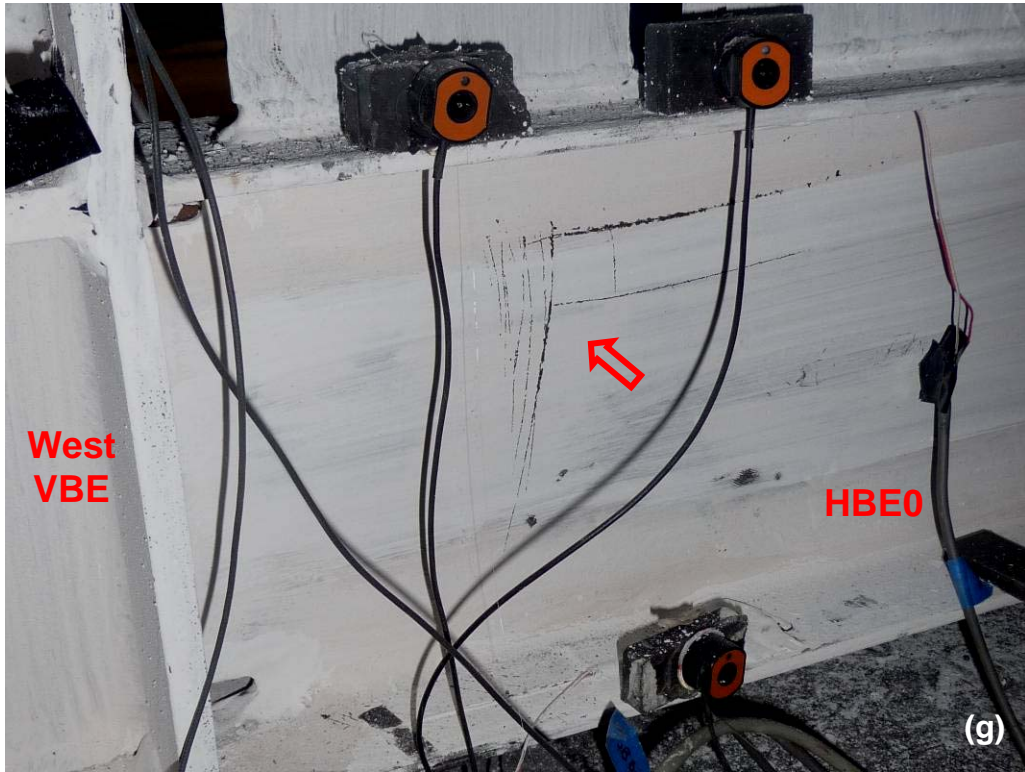
**Figure 4-5 Specimen Condition at the End of Displacement Step 5 – Cont'd:
(g) Beam Web Yielding; (h) Flange Yielding beneath Load Transfer Angles**

top flange, below the location where load transfer angles were welded (Figure 4-5h), suggested that the angles had prevented the HBEs from freely moving downward. This kind of yielding pattern was observed near all the connected angles, to various degrees of yielding. Comparing the deformed shape of the web plates presented in Figures 4-5a and 4-4a, it is seen that out of plane buckling increased after the specimen went through three full cycles at 0.94% drift. However, no tearing on the infill plates was found. The maximum base shear achieved was 123.2 kips when the actuator displacement was 1.42 in. to the West direction (Figure 4-3a). Note that the wall displacement was 1.28 inches in the West direction (Figure 4-2a), and even reached a lower displacement (i.e., 0.92 in) when the actuator pulled the specimen up to 1.42 in. to the East direction, though nearly the same maximum base shear was obtained (i.e., 124.7 kips). It was observed at this point that this discrepancy between the wall and actuator displacements has been present since displacement Step 2. In addition, the previously observed phenomena of higher base shears and lower HBE vertical displacements compared to the values predicted by the preliminary analysis continued to be exhibited in this displacement step, but with a larger discrepancy.

Nonetheless, the experimental program continued to displacement Step 6 with three cycles at $3\delta_y$ (= 1.41% top story drift). Note that prior to this step, the actuator operating rate was 2 minutes per cycle; and starting at this step, it was changed to 3 minutes/cycle. In this step, yielding in the specimen spread to an even larger area. For example, flaking of whitewash appeared at every infill plate (Figures 4-6a and 4-6b show the condition for the 2nd and 1st floor infill plates, respectively, while yielding on the 3rd floor infill plate was confirmed by a recorded video feed), at column bases (Figures 4-6c and 4-6d), on the inner side of the HBE top flange below the location where the load transfer angles were welded (Figures 4-6e and 4-6f), and at HBE-to-VBE connections (Figures 4-6g and 4-6h). In addition, several new yielding patterns appeared during this displacement step. First, yield lines at various angles (from 30° to 45° angles) spread along the web of both intermediate HBEs (Figures 4-7a and 4-7b) and at a few locations on the HBE3 web. New yield lines also spread along their flanges (Figure 4-7c). Interestingly, yielding was also observed on the outer flanges of columns at the level of the second and third story continuity plates (Figures 4-7d and 4-7e). This yielding was unexpected, considering that the columns and the panel zones at these levels were designed to remain elastic throughout the intended cyclic displacement loading history.

Figure 4-6 Specimen Condition at the End of Displacement Step 6 ($\Delta_3 = 3\delta_y = 1.41\%$ Drift): (a) Yielding on the 2nd Floor Infill Plate; (b) Yielding on the 1st Floor Infill Plate

126
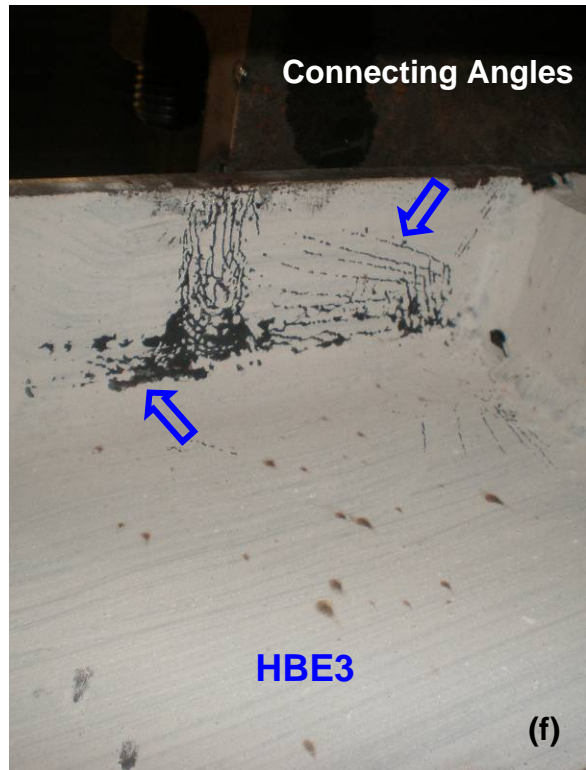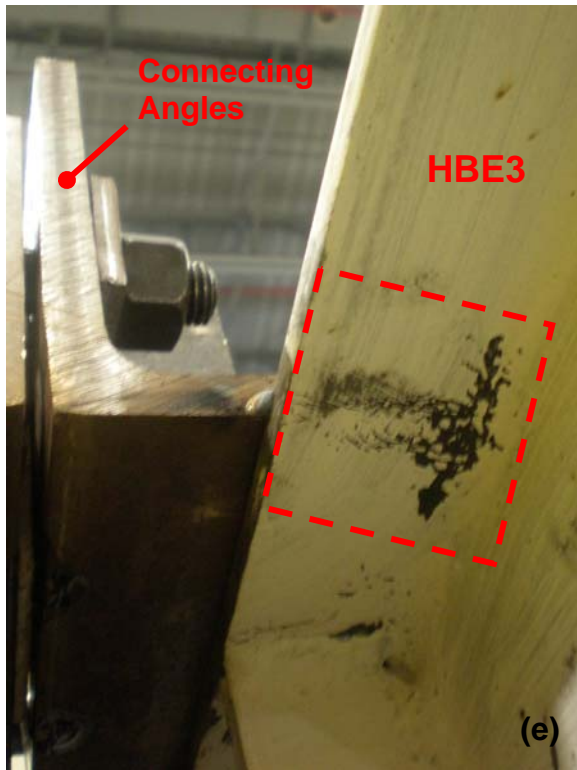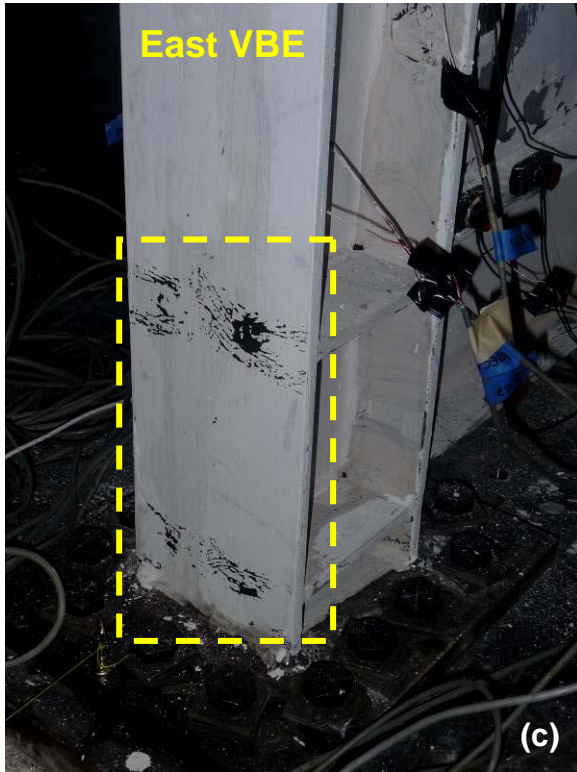
**Figure 4-6 Specimen Condition at the End of Displacement Step 6 – Cont'd:
(c) & (d) Yielding around Column Base (Ref. Part (d) to Fig. 5.5b); (e) & (f) Flange Yielding
beneath Load Transfer Angles (Ref. Part (f) to Fig. 5.5h)**
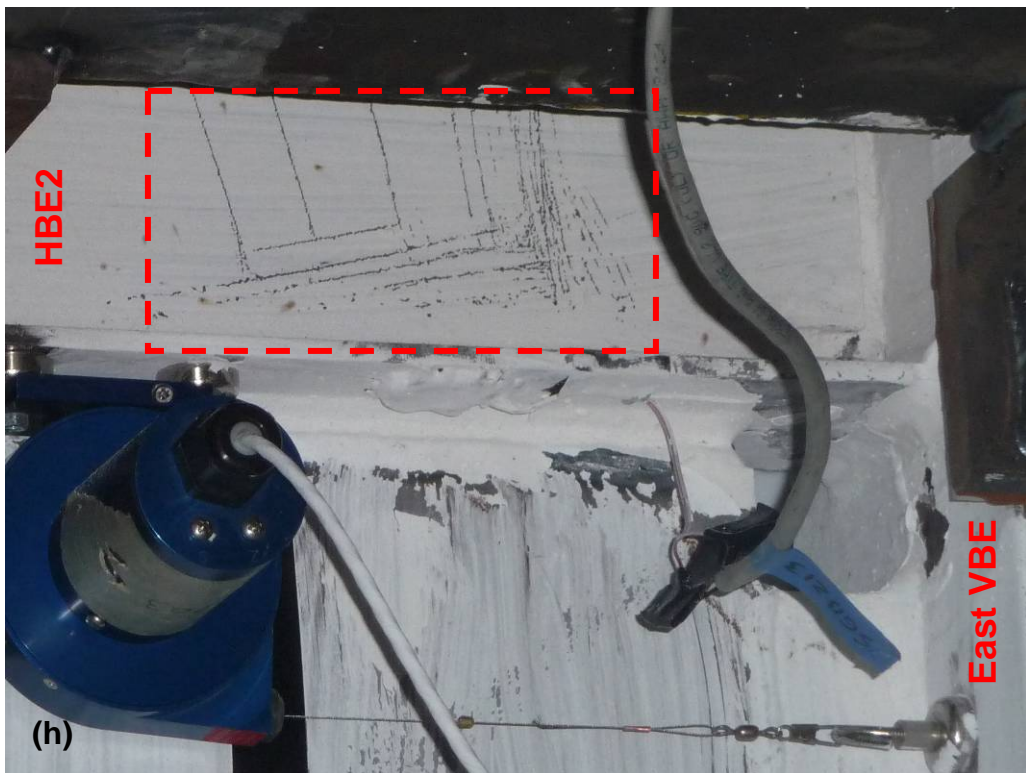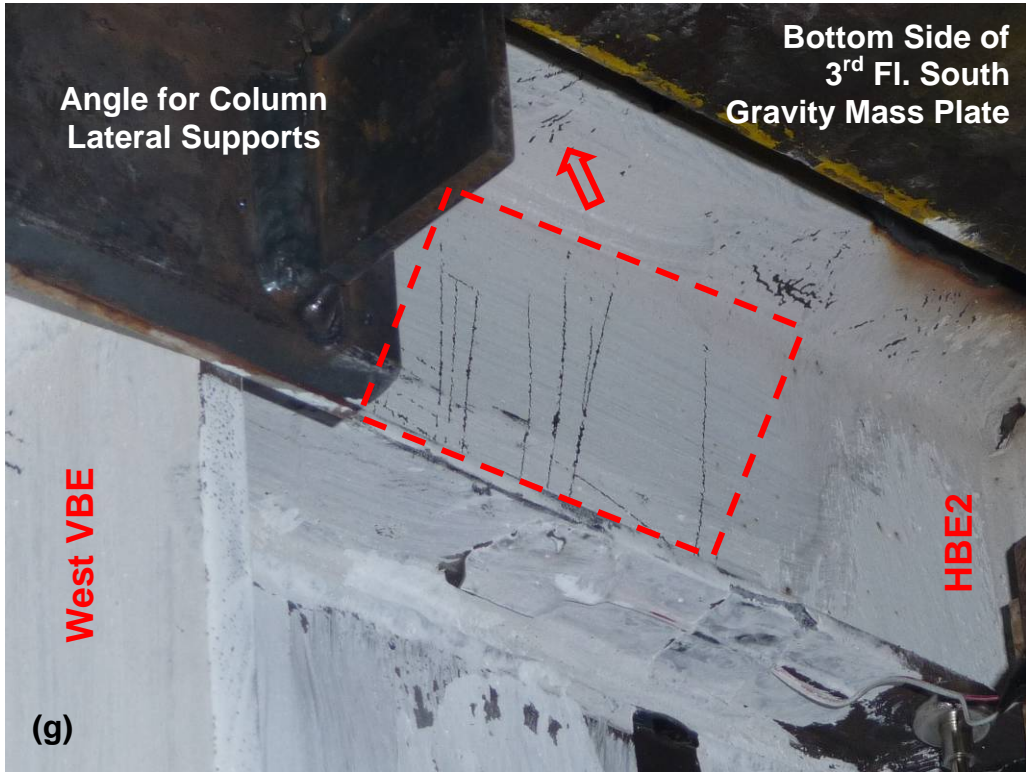
**Figure 4-6 Specimen Condition at the End of Displacement Step 6 – Cont'd:
(g) Beam Web and Flange Yielding; (h) Beam Web Yielding**

128
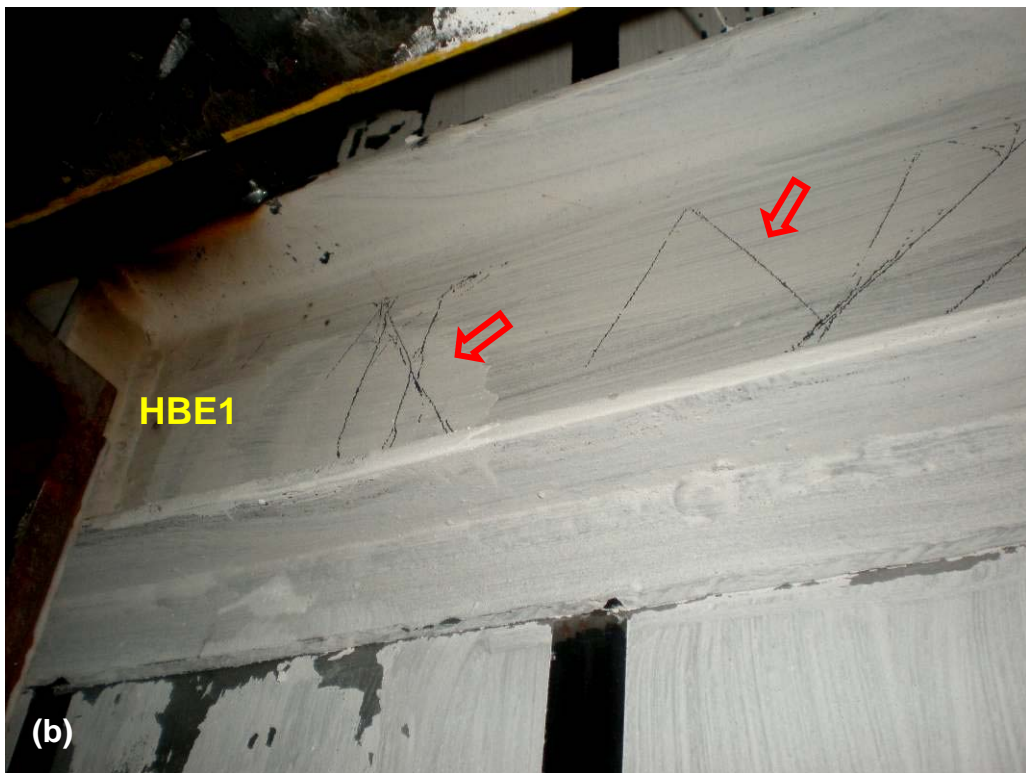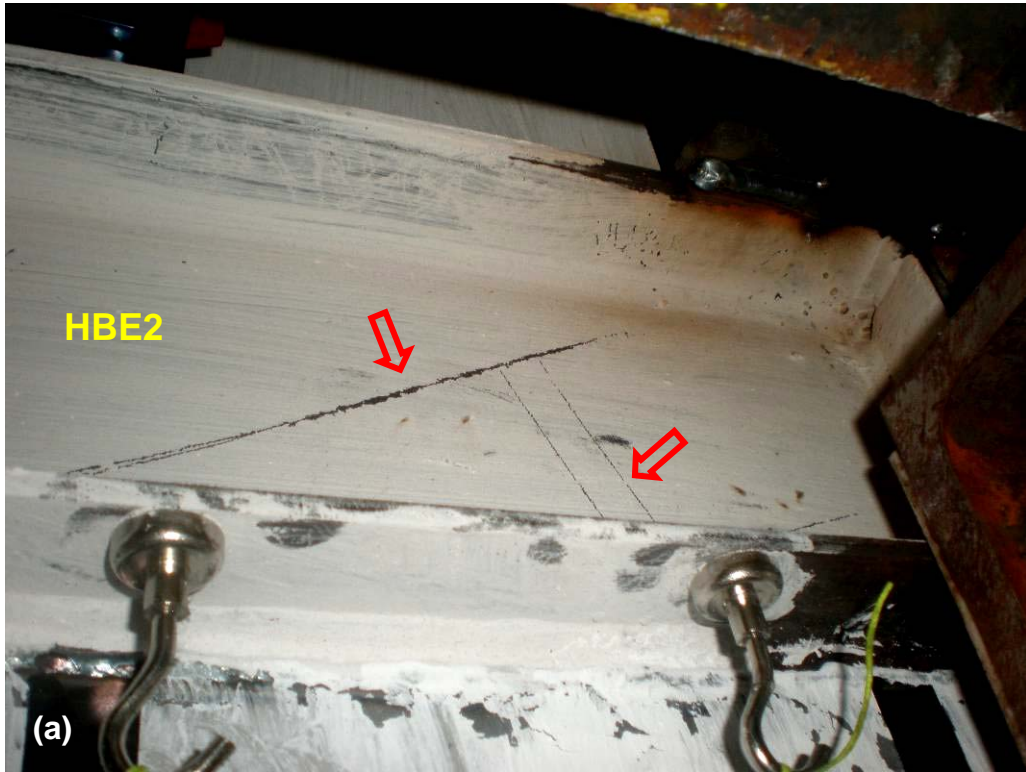
Figure 4-7 New Yielding Pattern Emerged in Displacement Step 6 ($\Delta_3 = 3\delta_y = 1.41\%$ Drift): Yield Lines at a Distinct Angle on (a) HBE2 Web; (b) HBE1 Web
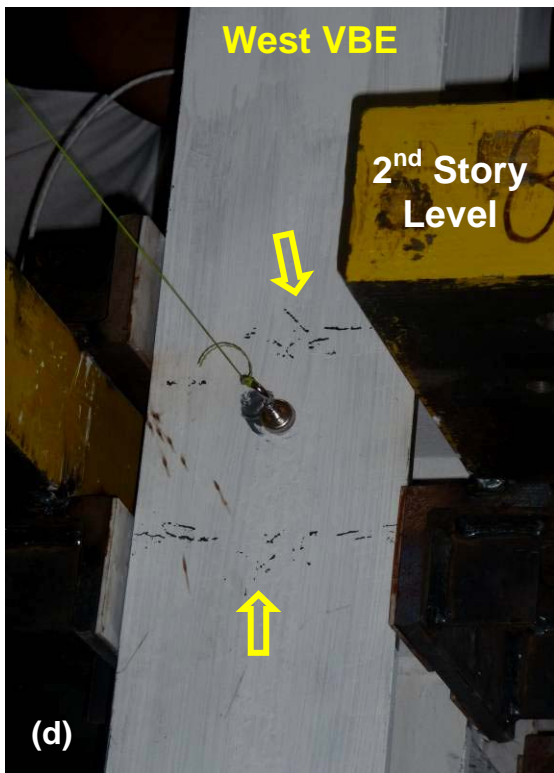
**Figure 4-7 New Yielding Pattern Emerged in Displacement Step 6 – Cont'd:
(c) Distributed Flange Yielding; (d) & (e) Upper Column Flange Yielding**

A more intriguing behavior at that stage was the increasing differences between the actuator and wall displacements. When the level 3 actuator pushed and pulled the specimen to the 2.12 inches target in displacement Step 6 (Figure 4-3a), the specimen only moved by 1.93 and 1.12 inches in the West and East excursions, respectively (Figure 4-2a). At that time, the cause for the significant difference of the wall displacements in the West and East excursions was unclear. The maximum base shear obtained was 34.3 kips higher than the estimated value (i.e., 145 kips versus 110.7 kips), yet the HBE vertical displacements were significantly lower than what was expected. By the end of displacement Step 6, HBE3 and HBE2 theoretically should have been deformed downward by approximately 0.43 in. However, the actual maximum deformation on these HBEs was no more than 0.20 in. As a result, the accumulation of plastic incremental deformations on the HBEs was not as pronounced as originally predicted.

Out of curiosity, to more carefully visually observe the specimen behavior in search of an explanation, an additional cycle with the same displacement target of $3\delta_y$ (= 1.41% top story drift, denoted as displacement Step 6a) was applied. Observers were positioned at three strategic locations in the laboratory (at a safe distance from the specimen) seeking to identify any unforeseen behavior that might explain the previous unexpected responses. No unusual response could be observed visually. In light of these persisting differences between predicted and experimentally obtained behaviors, it was decided to postpone the continuation of testing until some explanations for the observed behavior could be formulated. Testing could only be stopped for three days due to the laboratory's pressing schedule.

Experimental data recorded up to Step 6a and video feeds from Step 6 were reviewed. In addition, a limited analytical investigation was conducted. Based on the data and video feeds reviewed as well as analytical results obtained, several adjustments to the experimental setting were introduced. First, because it was believed that the multiple connection points along the HBE were "fighting each other" in preventing the beam rotations needed for experimental behavior to match the predicted one, bolts at the quarter- and third quarter-span of every HBE were taken out, leaving only 4 bolts at the mid-span of each HBE to transfer actuator forces to the specimen. The A325 bolts previously used were replaced by higher strength A490 bolts of the same ¾ in. bolt diameter to increase the bolts' safety factor from 1.5 to 1.8 when they sustained 66 kips story

shear forces that would be expected to develop at 5% drift. Second, displacement transducers (i.e., combination of linear variable differential transformer (LVDT) and string pots) were added to the bases of East and West columns to measure possible uplift at those points. Third, string pots were added to measure the difference in horizontal displacements between the actuator shoes and the mid-span point of each HBE as an attempt to study the cause of the significant difference between the actuator and wall displacements. Figure 4-8 shows the layout of these additional instruments. An insert photo in the figure shows the setting for the uplift measurements at the East column. The string pot measured column uplifts relative to the floor plate, while the LVDT measured floor plate uplifts relative to the strong floor. Details of this analytical investigation and modifications to the experimental setting are further discussed in Section 4.4. To maintain the flow of the presentation, experimental observations during the remaining displacement steps are presented first in the following sub-sections.

4.3.2 Displacement Steps 6b to 8

The experimental program resumed with 2 cycles at the same target displacement as in the previous step (i.e., $\Delta_3 = 3\delta_y = 1.41\%$ drift). While the actuators reached the same specified displacement target (Figure 4-3b), the maximum base shear recorded in the first cycle of displacement Step 6b was actually smaller than before, namely 119 kips compared to 145 kips in the previous step. The reason for this behavior was because the specimen actually experienced smaller displacements in this step compared to those in the previous step. As shown in Figure 4-2b, the wall displacements were 1.5 and 1.9 in. for displacement Step 6b and Step 6a, respectively, for the same actuator displacement between these two steps of 2.1 in. (Figure 4-3b). The significant difference between the actuator and wall peak displacements remained noticeable in this step (comparing displacement records in Figure 4-2b and Figure 4-3b). Its magnitude was increased to approximately 0.7 in. from the previous value of 0.2 in. The new string pot added to measure the magnitude of the displacement discrepancy between the actuator shoes and the mid-span point of HBE3 recorded a difference of 0.52 in. Knowing that the recorded top story force at this point was 56.6 kips, the recorded data confirmed that the axial deformation of HBE3 was not the main cause for this significant discrepancy (the 7 ft. long W8×13 used for HBE3 would only elongate 0.04 in. under this applied force). At this point, no obvious explanation was found to explain the observed discrepancy. It was speculatively suggested that the connecting angles
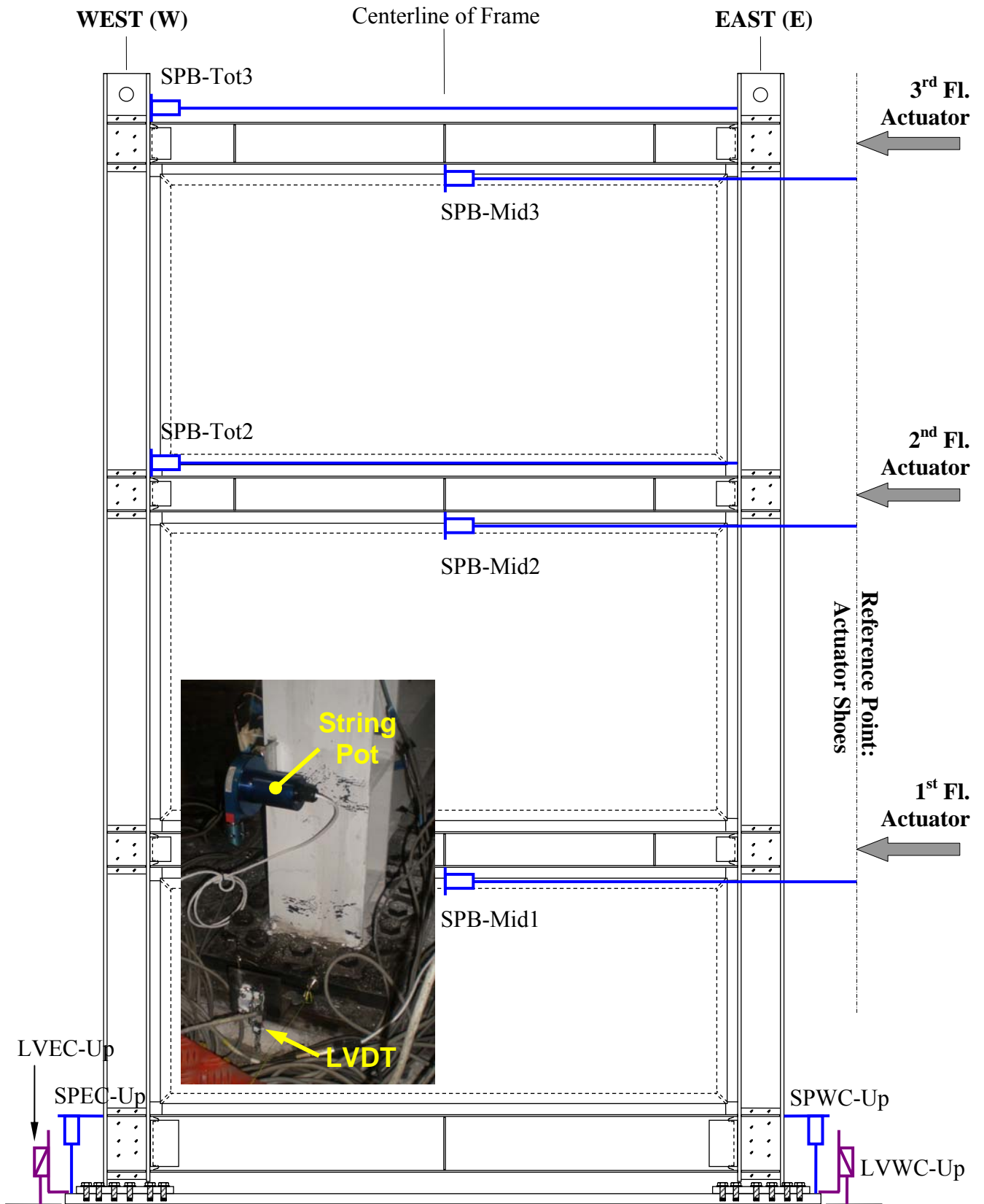
Figure 4-8 Layout of Additional Instruments

played a significant role in this case, which yet had to be observed in the subsequent displacement steps.

During the second cycle of Step 6b, when the top story actuator reached 1.81 in. (= 1.21% drift) in the West direction, a drop of 17.8 kips base shear was observed (Figure 4-3b) and a relatively loud bang was heard. The applied displacement, however, continued in the East direction up to the target value. Subsequent inspection after completion of the second cycle revealed weld fractures on the North connecting angle at the top floor (i.e., the 3rd floor), as shown in Figures 4-9a and 4-9b. Despite the weld fracture, the maximum base shear reached in the East direction was the same as that in the previous cycle (Figure 4-3b). After removing the fractured welds, re-welding, and reinforcing all angles with additional welds (Figure 4-9c), displacement Step 6c was conducted in the following day.

It was decided to repeat one cycle of the same displacement target in Step 6c to ensure that the repaired connecting angles performed well and that other aspects of the experimental setting worked properly. The resulting hysteretic loop followed somewhat the same pattern obtained in the previous step (Figures 4-2c and 4-3c). Specimen condition at the end of this step is shown in Figure 4-10. Recorded maximum vertical deformations of HBE3 and HBE2 in this step were 0.24 and 0.21 in., respectively, which was approximately 8% higher than the values obtained in displacement Step 6b. These marginal differences were reasonable because the specimen was pushed to the same displacement target.

This additional cycle also provided a chance to review the displacement difference between the East and West columns (corresponding to HBE axial deformation), as two additional string pots were added to measure these displacement prior to the start of the Step 6c cycle (Figure 4-8). These string pots recorded differential displacement of columns at the 2nd and 3rd story level. At the maximum target displacement during this cycle, HBE2 and HBE3 axial deformations were measured to be 0.04 and 0.03 in., respectively, confirming that HBE axial deformation played an insignificant role in explaining the considerable difference between the actuator and the specimen lateral displacements.
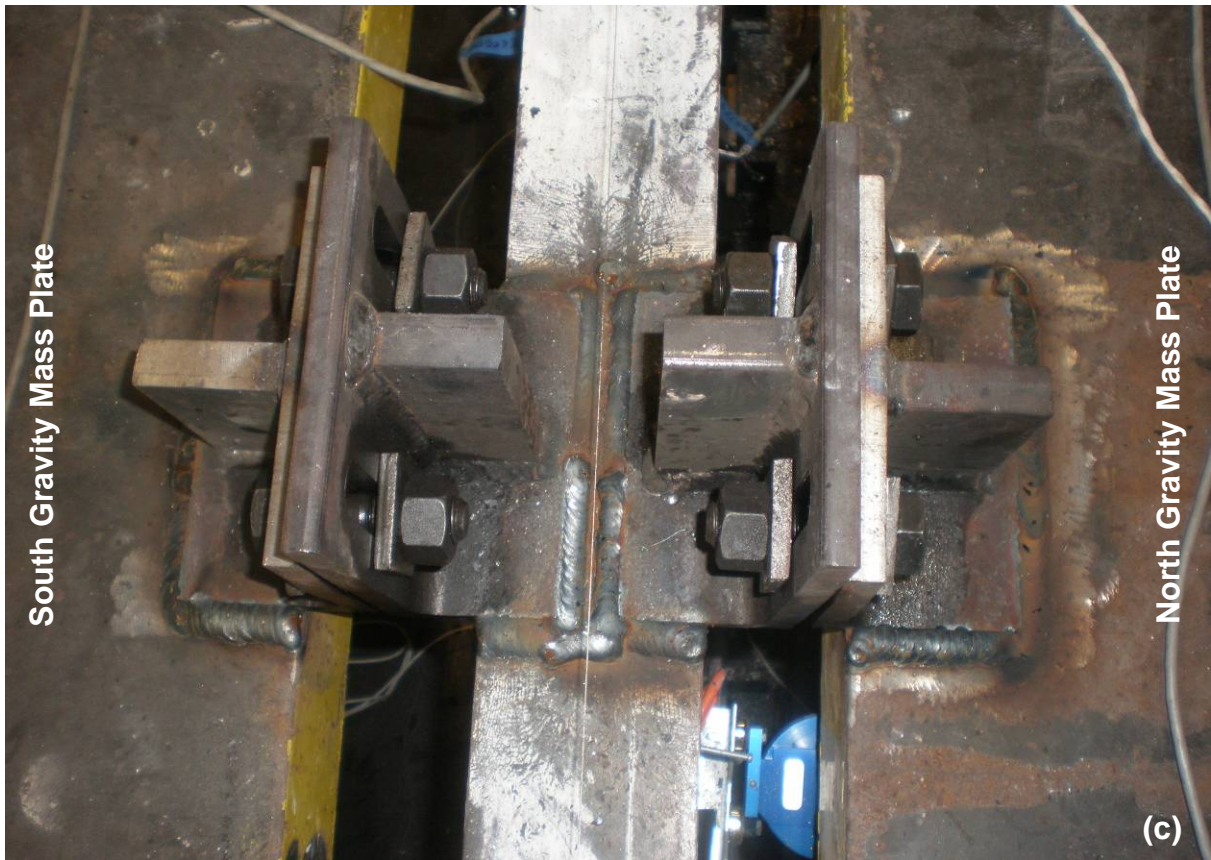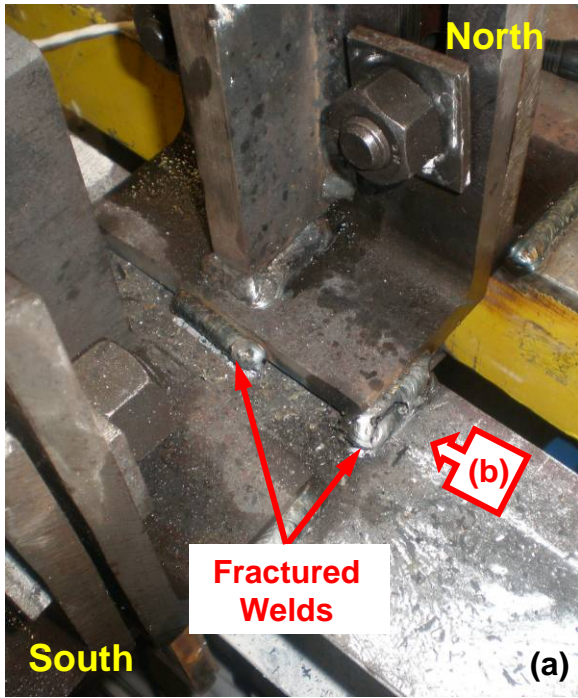
Figure 4-9 Third Story Connecting Angles: (a) Fractured Welds in Step 6b; (b) Detail Fracture of Part (a); (c) Retrofitted Connecting Angles

Figure 4-10 Specimen Condition at the End of Displacement Step 6c ($\Delta_3 = 3\delta_y = 1.41\%$ Drift): (a) Deformed Shape Overview; (b) Yielding on the 2nd Floor Infill Plate (North View)

Upon completion of displacement Step 6c, the experimental program continued with two cycles at the higher target displacement in Step 7 (i.e., $\Delta_3 = 4\delta_y = 1.88\%$ drift). For those cycles, using only two sets of angles at the mid-span of each HBE to transfer loads to the specimen, no evidence of increased yielding was observed in the upper VBEs (i.e., at the level of the 2nd and 3rd story panel zones, as first observed in Step 6); however, more evidence of yielding was observed at the VBE bases, which in this step was observed to have also progressed to the panel zone area of both the East and West VBEs. With bolts at the quarter- and third-quarter span angles removed, the mid-span connecting angles were able to substantially slide along the vertically slotted holes, which facilitated the downward movement of HBEs as lateral loading progressed (Figure 4-11). The maximum HBE3 vertical deformation recorded in Step 7 was 0.33 in. while that in HBE2 was 0.26 in., although these values remained significantly below the estimated values of more than 0.55 in. for both HBEs.

According to the revised nonlinear static analysis (conducted before modifying the test set-up, and presented later in Table 4-4), cross section rotation at the mid-span within this displacement step was expected to be relatively small (i.e., less than 0.01 radians). As such, it was expected that as the load progressed, the connecting angles would vertically slide with only minor rotations following the downward movement of the HBEs at those mid-span locations. However, the result shown in Figure 4-11d indicates a different behavior. The relatively flexible HBE flanges (particularly compared to the connecting angle flange) were considered as the contributing factor to this somewhat large angle rotation. As a result, yielding beneath the mid-span connecting angles had been progressed to the webs of both HBE3 and HBE2. Figure 4-12a shows an example for HBE3 web. Moreover, progression of yield lines at various angles (from 30° to 45° angles) spread along the web of both intermediate HBEs in this displacement step. Showed in Figure 4-12b is an example for HBE2. The maximum base shears obtained were 130.7 and 147 kips during the West and East excursion, respectively (see Figure 4-2d or 4-3d), which were respectively 13.9 and 30.3 kips higher than the estimated values.

Furthermore, at a peak displacement target of 2.82 in., the differences between the actuator and wall displacements were 0.98 and 0.53 in. during the West and East excursions, respectively. Figure 4-11 provides an example of this observation. The angles for lateral supports at the East
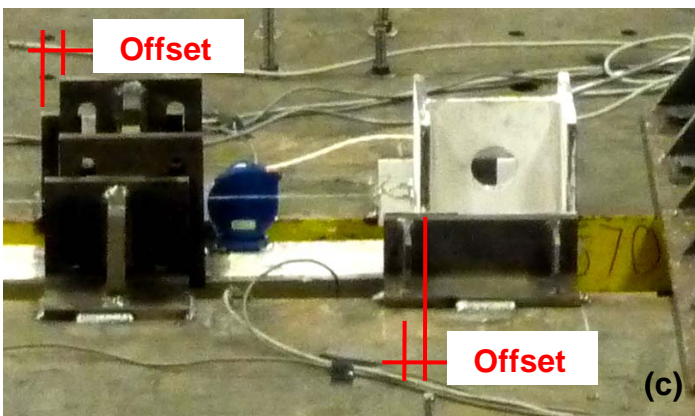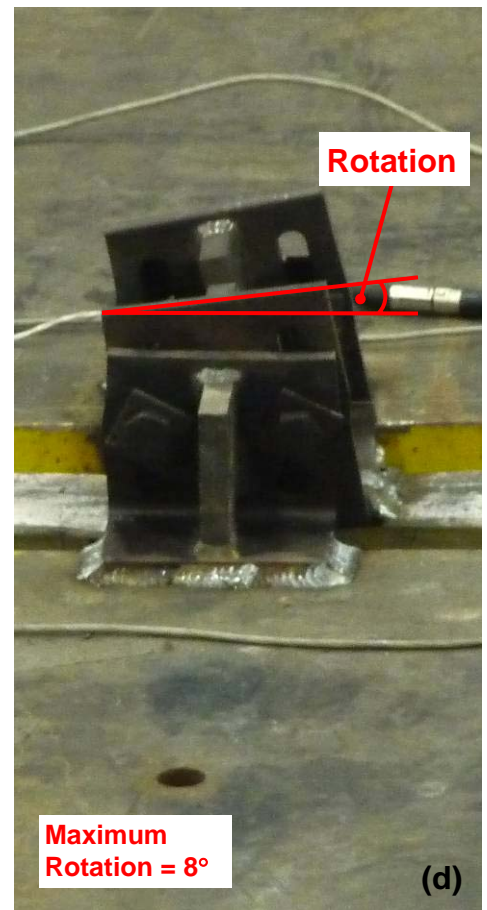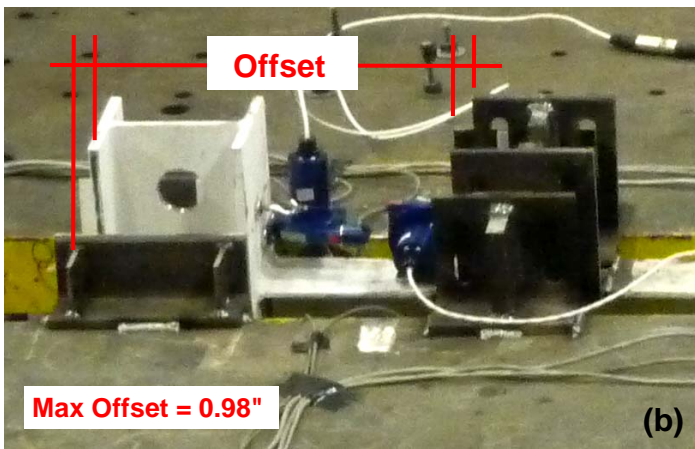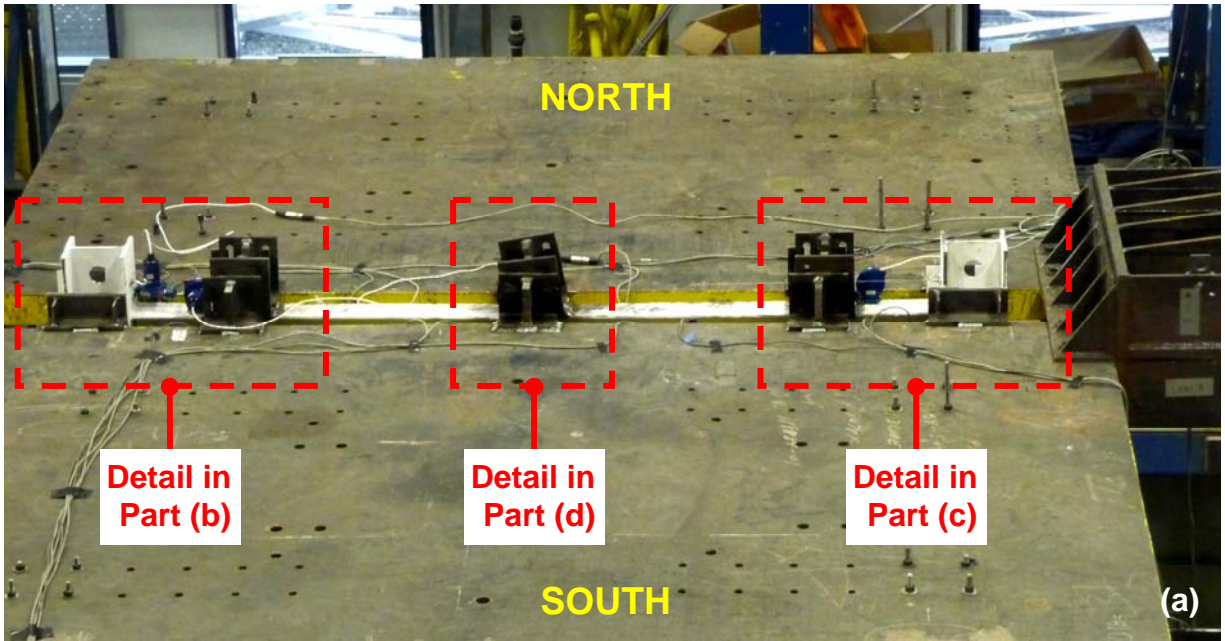
Figure 4-11 Lateral Support and Connecting Angle Conditions in Displacement Step 7
$(\Delta_3 = 4\delta_y = 1.88\%$ **Drift): (a) Overview; Detail of (b) East Side; (c) West Side; (d) Mid-Span**

138
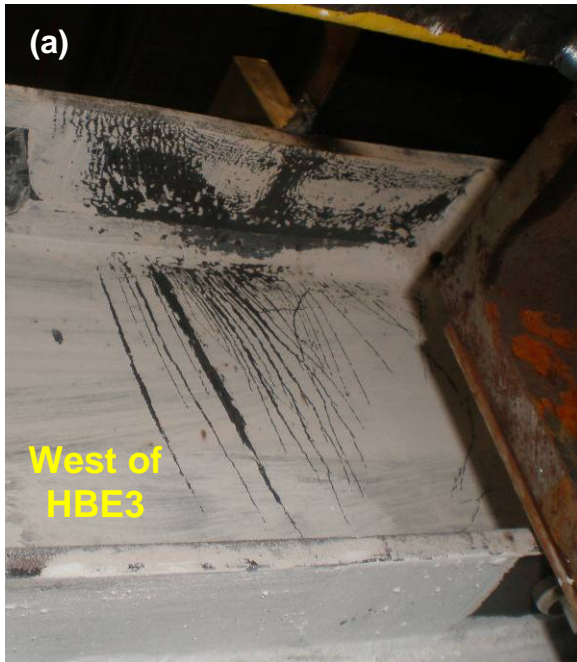
Figure 4-12 Yielding in Displacement Step 7 ($\Delta_3 = 4\delta_y$ = 1.88% Drift): (a) Beneath HBE3 Connecting Angles Overview; (b) Yield Lines at a Distinct Angle along HBE2 Web

and West column locations were significantly offset from their original locations at the centerline of the column (Figures 4-11b and 4-11c). Somewhat the same results were obtained when comparing the actuator displacement and the specimen displacement at the midpoint of HBE3 (i.e., 0.92 and 0.55 in. for the same respective excursions), indicating that HBE3 axial deformation made an insignificant contribution to these discrepancies. The significant rotation of the connecting angles instead caused these discrepancies. In other words, some of the lateral displacements imposed by the actuators rotated the connecting angles, explaining the lower lateral displacements experienced by the specimen compared to actuator displacement. To provide some perspectives, the angles rotated 8° and 5° during the West and East excursions of this cycle, respectively.

The experimental program continued with two cycles at the higher target displacement in Step 8 of 2.5% top story drift (= $5.32\delta_y$), as specimen displacements could still be measured in spite of the problems described above. Note that starting in this step, the loading protocol was switched from ductility- to drift-controlled. During the first excursion in the West direction, when the actuator displacement reached 2.7 in. (= 1.8% drift), base shear started to drop from 109.8 kips to 38.2 kips when reaching the specified target displacement of 3.75 in. (Figure 4-3e). Strangely, the specimen started to "rebound" toward the East direction (Figure 4-2e). In other words, as the actuator displacement progressed from 2.7 to 3.75 in., the wall displacement reduced from 1.5 to 1.1 in. While this phenomenon was observed in the real time data display, suggesting that fractures were possibly underway, the nature of this failure could not be ascertained from the experimental control room (observers were not allowed within proximity of the specimen during the cycles of loading, for safety reasons). The pre-programmed cycles of loading continued and the actuators started to push the specimen toward the East direction for the same target displacement. When the actuator displacement reached 3.0 in. (= 2.0% drift), the base shear was 145.1 kips and dropped to 74.6 kips at the target displacement while the wall displacement "rebounded" from 2.4 to 2.0 in. The pre-programmed displacement cycles continued. When returning to the West direction for the second excursion at 1.4 in. displacement (= 0.9% drift) with corresponding base shear of 31.5 kips, a loud bang was heard. Subsequent inspection after the completion of the second cycle revealed fractures of both connecting angles on the top floor (Figure 4-13b). Significant cyclic rotations experienced by these connecting angles (Figure 4-13a)

140
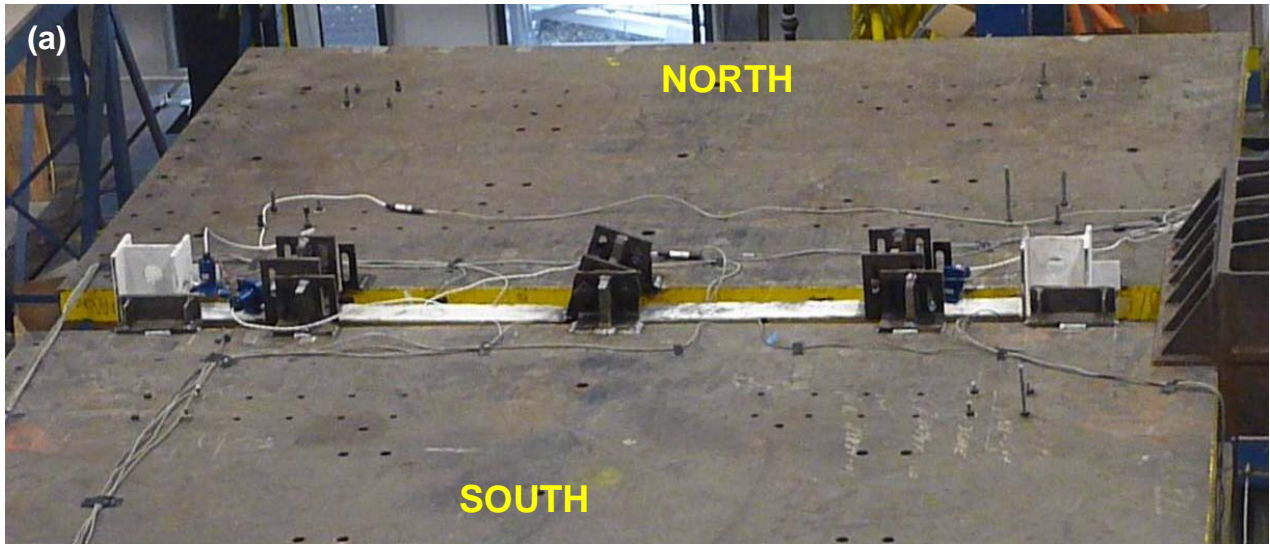
Figure 4-13 HBE3 Connecting Angle Condition in Displacement Step 8 (Δ₃ = 2.5% Drift = 5.32δ_y): (a) Connection Prior to Fracture; (b) & (c) Fracture of Both Connecting Angles; (d) Installation of Connecting Channels; (b) Newly Completed Connection at East Column

within the previous four cycles (i.e., Steps 6c to 8) contributed to these low fatigue fractures of the base metal, which started from heat affected zone (HAZ) on the East side of the angles and propagated to the West side.

Constrained by the laboratory's pressing schedule, a relatively quick and simple solution to fix the 3rd story load transfer mechanism was developed to be able to proceed with the experimental program within the following day. It was decided to change the mechanism by transferring the loads via the columns. Using ready in-stock steel materials in the SEESL facilities, two MC6×16.3 channels were welded (Figure 4-13d) on both sides of each column in parallel to the direction of loading and additional stiffeners were added to the columns. The new completed loading transfer mechanism is shown in Figure 4-13e. The welded connection on each channel of approximately 12 in. total length, made of ¼ in. thick fillet welds (E70XX, F_y = 70 ksi), was capable of transferring shear forces of 83.7 kips.

Having the new loading transfer mechanism installed, it was considered necessary to repeat the previous two displacement steps (i.e., Steps 7 and 8) to ensure that the connecting channels as well as the connecting angles at the lower stories could perform well before proceeding to a higher displacement target. For this reason, Step 7a of 4δ_y target displacement (= 1.88% drift) was repeated for two cycles. The first excursion reached peak base shears of 143 and 157.7 kips for the West and East directions, respectively, which was approximately 12 and 11 kips higher than that in Step 7 for the same respective directions (Figure 4-2f). This can be understood because the specimen actually experienced larger lateral displacement in Step 7a compared to that in Step 7 as a result of the connecting channels providing more direct load transfer from the mass plates to the specimen (resulting in closer agreement between the specimen and actuator displacements at that level). As a result of replacing the load transfer mechanism to the columns, the actuator and wall displacements at the 3rd floor level were comparable for the first time. In this case, when the level 3 actuator reached 2.82 in. target displacement, the recorded displacement on the specimen top floor was 2.71 in. (i.e. approximately a 0.1 in. difference between the two measurements).

During the second excursion in the West direction, when the top story actuator reached 2.7 in. displacement (= 1.8% drift), resulting in a base shear of 143 kips, a loud bang was heard and (at

the same time) a drop of 15.6 kips base shear was observed in the real time data display (Figure 4-3f). As the pre-programmed cycles continued, when the specimen returned an East direction displacement of 2.67 in. displacement (after reaching the West target displacement), another loud bang was heard and another drop of 18.7 kips base shear was noted. An observer monitoring the test from an observation deck vantage point closer to the specimen than the control room saw the second gravity mass plates displacing in the East direction, unrestrained by the specimen (Figure 4-14a), which happened because the lower actuators were in a force-control mode, and an emergency stop was triggered for safety precautions. Subsequent inspection revealed weld fractures of the connecting angles at the second floor (Figure 4-14b). To repair the specimen and provide a more direct load transfer mechanism once and for all, a similar connection to the one that had been previously installed at the third floor, but made of steel angles instead, was used for the first and second story load transfer mechanism (Figure 4-14c). In contrast to the channels on the top floor, for which welds were provided on the channel sides parallel and perpendicular to the loading direction, the L6×4×½ steel angles were only welded to the mass plate along their sides parallel to the loading direction. This was intentionally designed to allow free uplift of the columns (which had been observed in the previous displacement steps). The maximum uplifts recorded up to this step were 0.40 and 0.35 in. on the West and East column bases, respectively, when the specimen was pushed to the maximum target displacement (the uplifts elastically returned to almost zero when the specimen returned to its original position at 0% drift). Note that this photo was taken at the end of the experimental program since a similar photo of the steel angles right after they were welded was not available.

It took two working days to reconfigure the experimental set up (i.e., taking down all string pots on the first and second stories, preparing and installing four sets of connecting angles at the first and second stories on both South and North side of the specimen, and reinstalling the instrumentation). Note that the Rosette strain gauges on the first and second floor of both East and West column had to be removed because their locations coincided with the location of additional stiffeners for these connecting angles. Subsequently, displacement Steps 7b and 8a were conducted (as originally intended before the failure of the 2nd floor connecting angles) and observations during these steps leading to the completion of the experimental program are presented in the following sub-section.
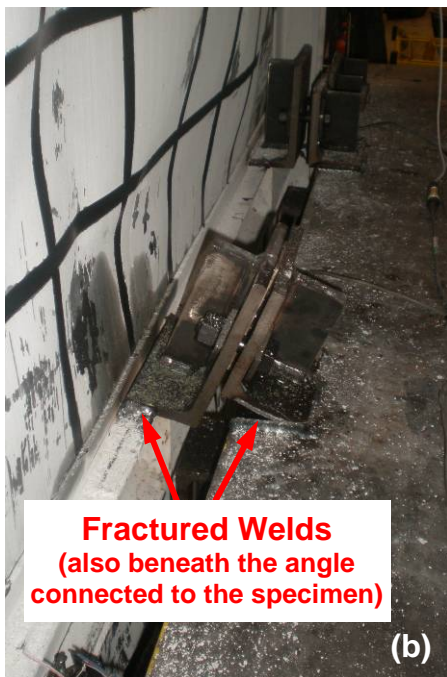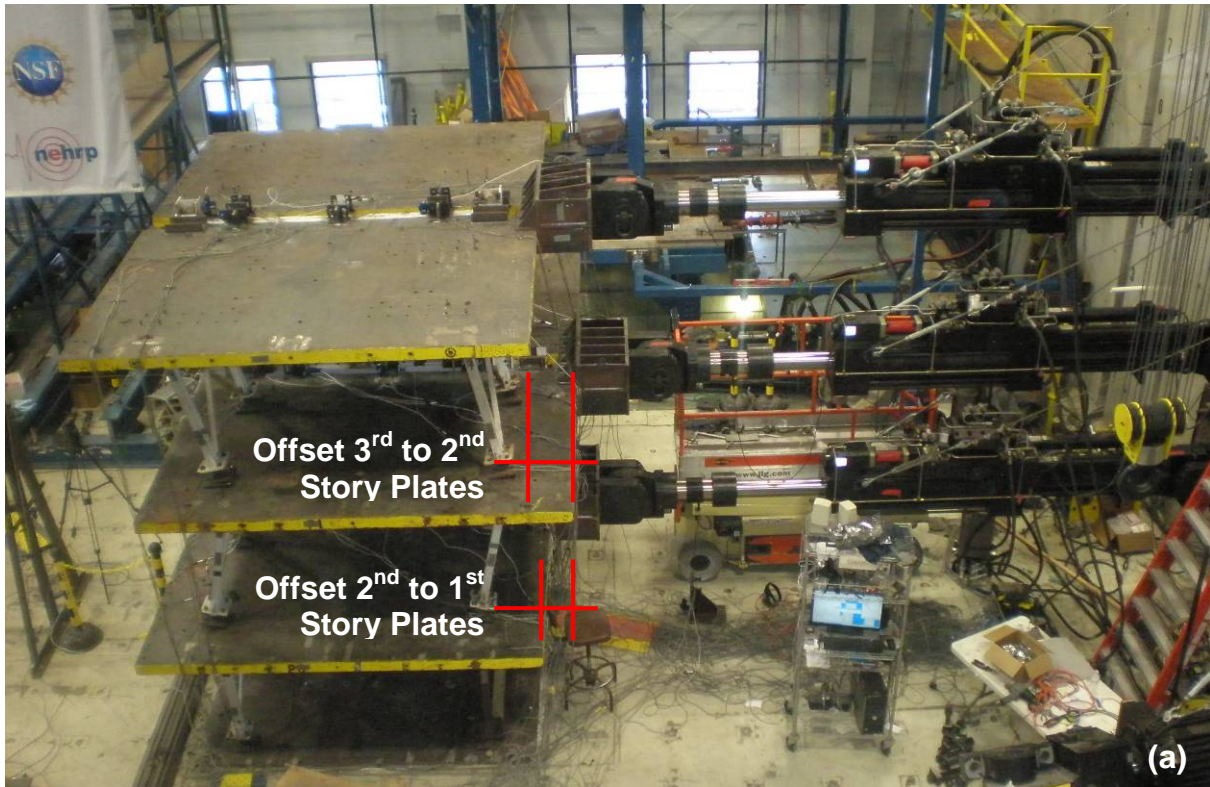
Figure 4-14 Failure and Replacement of Connecting Angles in Displacement Step 7a: (a) Vantage View at Failure; (b) Weld Fractures on Connecting Angles (South Side); (c) Load Transfer Connection at West Column (1st Story)

4.3.3 Displacement Steps 7b to 10d

The experimental program resumed, by first repeating two cycles at the same target displacement as in Step 7a (i.e., $\Delta_3 = 4\delta_y = 1.88\%$ drift). A slower loading rate of 5 minutes/cycle was selected to closely monitor performance of the new connecting angles as well as other parts in the specimen and reaction set-up.

As shown in Figures 4-2g and 4-3g, the resulting hysteretic loop of this displacement Step 7b follows the same path as in the first cycle of displacement Step 7a (i.e., the cycle before the 2nd story connecting angles fractured). The recorded peak base shears at the target displacement were 144.9 and 159.5 kips in the West and East directions, respectively. Similar to that in Step 7a, in which actuator loads were transferred through the columns, approximately 0.1 in. difference was observed in this step between the target displacement assigned to the top story actuator and the recorded displacement on the specimen top story (i.e., the actuator vs. wall displacements). Compared to displacement Step 7, yielding in all the previously reported locations essentially spread to larger area. It is important to reemphasize here that although the actuator displacement reached the same target displacement of 2.83 in. during both Steps 7 and 7b, the wall displacement were actually significantly different. In this case, the wall displacement in the West direction was 2.7 in. during displacement Step 7b compared to only 1.85 in. during displacement Step 7, showing the effectiveness of the final mechanism to transfer loads to the specimens. Specimen condition at the end of displacement Step 7b is shown in Figure 4-15. Examples shown in the figure are yielding condition for infill plates [Part (a) to (d)], HBE-to-VBE connections [Part (e) and (f)], and VBE bases [Part (g) and (h)]. Interestingly, the whitewash on the North side of the infill plates flaked more than on the South side on both the first and second story infill plates. However, this is mostly a random occurrence, as whitewash is not particularly effective at revealing yielding when it is used on light gauge steels having a smooth surface finish (compared to the mill scale of hot rolled steels). In addition, yielding at the base of the East column was more severe than that of the West column. Yield lines were observed above the panel zone area of the East column whereas those in the West column remained localized at its panel zone. Though not shown in Figure 4-15, yield lines were also observed on the inside faces of the East and West column flanges adjacent to their bases.

Figure 4-15 Specimen Condition at the End of Displacement Step 7b
($\Delta_3 = 4\delta_y = 1.88\%$ Drift): (a) & (b) 2nd Story Infill Plate; (c) & (d) 1st Story Infill Plate
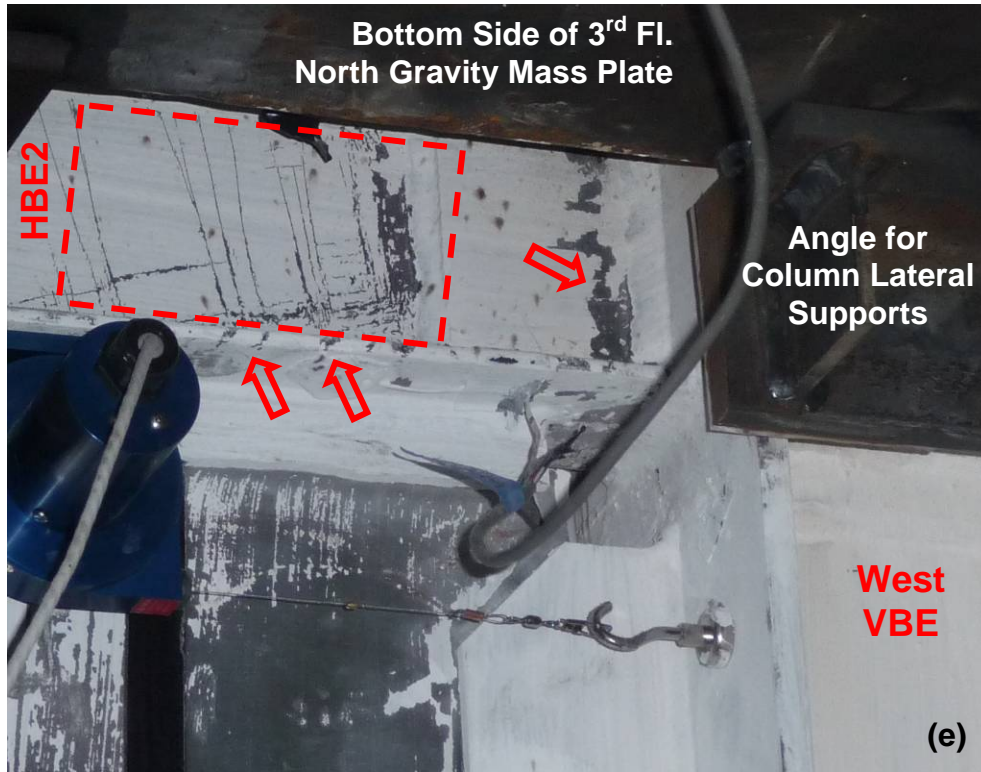
Figure 4-15 Specimen Condition at the End of Displacement Step 7b
($\Delta_3 = 4\delta_y = 1.88\%$ Drift) – Cont'd: (e) & (f) Yielding on HBE-to-VBE Connections
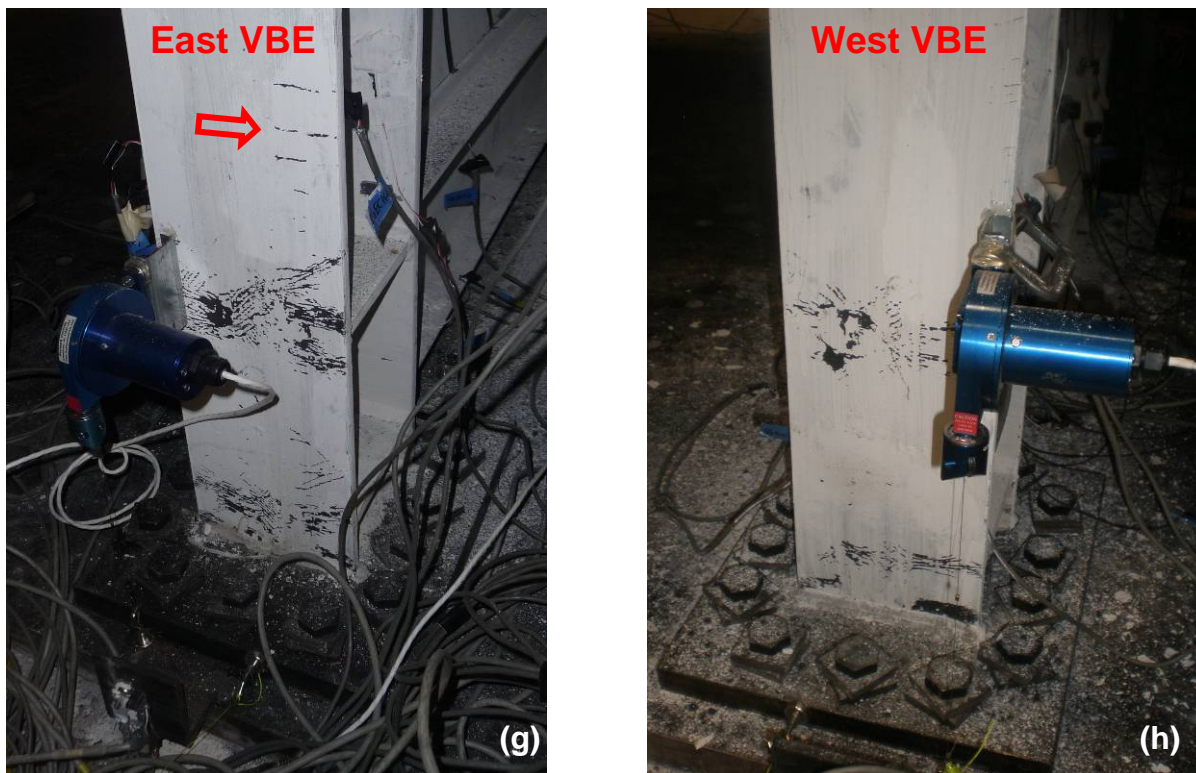
Figure 4-15 Specimen Condition at the End of Displacement Step 7b ($\Delta_3 = 4\delta_y = 1.88\%$ Drift) – Cont'd: (g) & (h) Yielding Around Column Bases

Upon completion of Step 7b, the experimental program continued by conducting two cycles at the same target displacement as in Step 8 (i.e., $\Delta_3 = 2.5\%$ drift = $5.32\delta_y$). Cycling at this 2.5% drift amplitude (i.e., denoted as displacement Step 8a) resulted in peak base shears on the specimen of 160.7 and 173.7 kips for the West and East excursions, respectively (Figures 4-2h and 4-3h). Note that this was the first step in which the specimen actually experienced 2.5% drift. Although the actuator reached the 2.5% drift target in the previous displacement Step 8, the specimen actually only experienced 1.0% and 1.6% drifts during the West and East excursions, respectively, due to the significant rotations of the connecting angles at HBEs mid-spans.

With this new test set-up, vertical deformations of the HBEs significantly increased. The maximum values recorded in Step 8a were 0.75 and 0.59 in. for HBE3 and HBE2, respectively. A snapshot of HBE3 with visible downward vertical deformation is shown in Figure 4-16 when the specimen was pushed to the West direction (only the top flange of the beam, between the two mass plates, is visible on that figure). The vertical deformation of HBE3 was somewhat larger
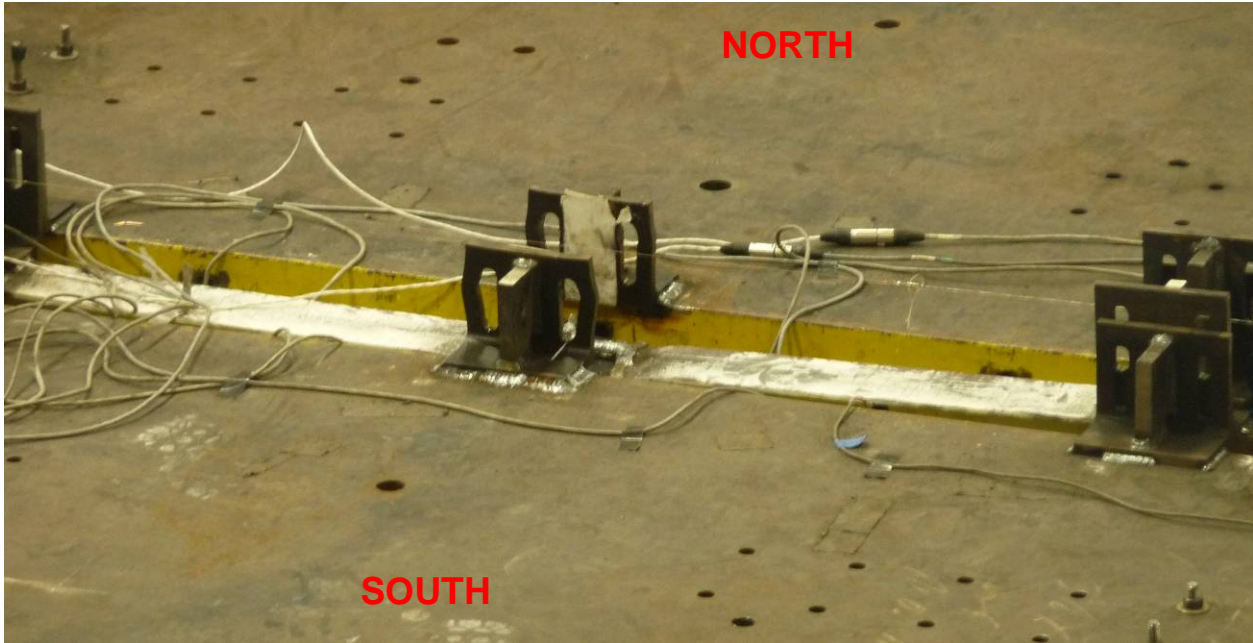
Figure 4-16 HBE3 Vertical Deformation during Displacement Step 8a
(Δ_3 = 2.5% Drift = 5.32δ_y)

than the estimated value of 0.65 in. while that of HBE2 approached its estimated value of 0.72 in. However, it is recognized that the plastic strength of HBE3 may have been reduced due to flange buckling where the connecting angle fractured in displacement Step 8, which may have also contributed to its larger vertical deformations. Figure 4-17 shows yielding at the mid-span of HBE3.

While the severity of yielding increased at the previously reported yielding locations (Figure 4-18), fish plate yielding, infill plate tearing, and HBE in-span plastification were observed for the first time in Step 8a. Yielding of fish plate occurred beneath the East and West shear tabs of HBE3 (Figures 4-19a and 4-19b, respectively). This type of yielding could not be caused by the pulling forces from the third story infill plate (which was considerably thinner and had a lower steel grade than the fish plate). It was attributed to the significant flexural rotations experienced by HBE3, in the perspective that fish plates contributed to the cross-section properties of boundary elements, as described in Section 4.6. Minor plate tearing occurred at the lower East and West cut-out corners of the third story infill plate. Figure 4-19c shows plate tearing for the lower East corner. Sign of in-span plastifications were observed on HBE0 located

Figure 4-17 Yielding beneath HBE3 Connecting Angles in Displacement Step 8a (Δ_3 = 2.5% Drift = 5.32δ_y): (a) Detail of West Side; (b) Detail of East Side
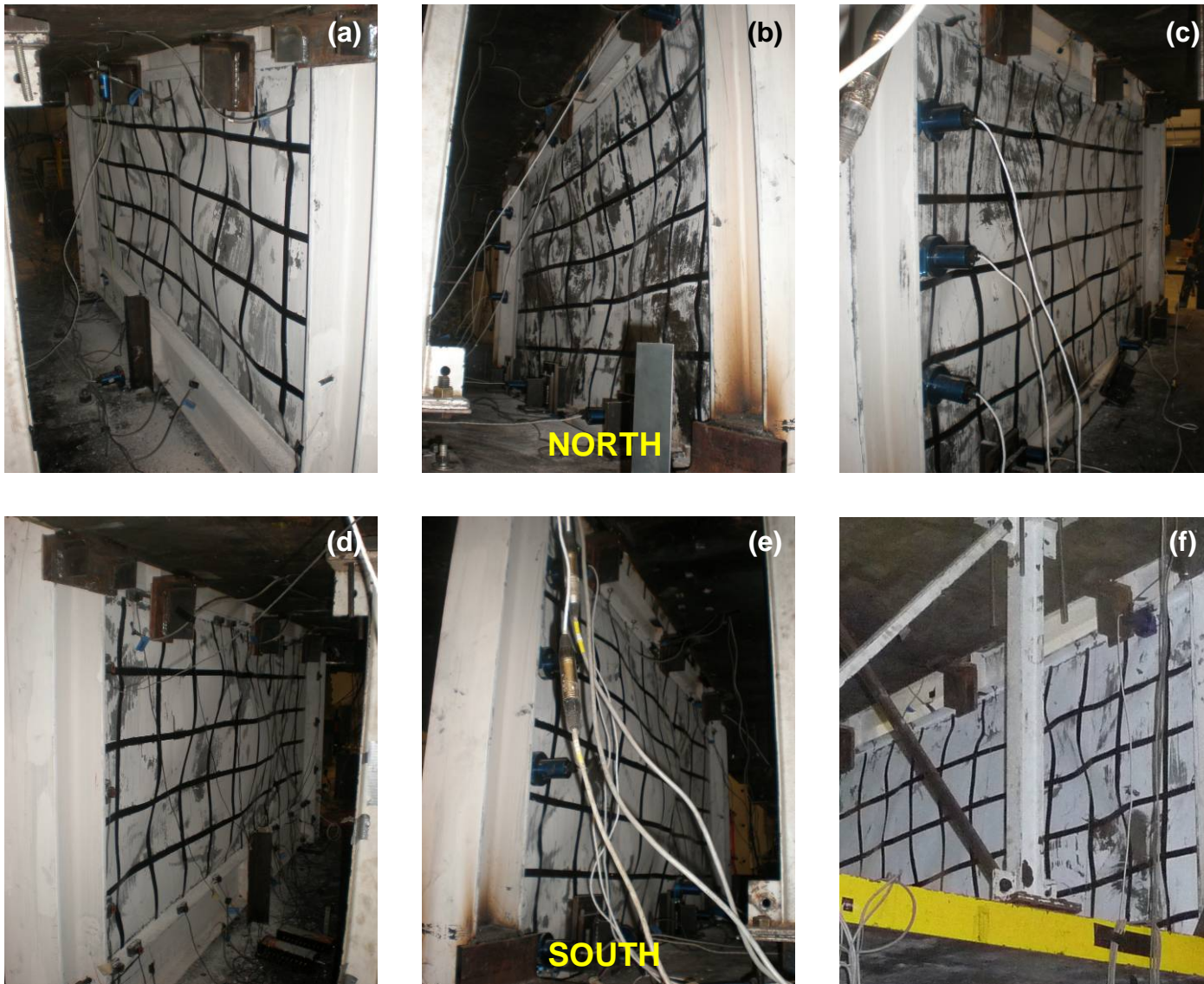
Figure 4-18 Specimen Condition at the End of Displacement Step 8a ($\Delta_3 = 2.5\%$ Drift $= 5.32\delta_y$): (a) & (d) 1st Story Infill Plate; (b) & (e) 2nd Story Infill Plate; (c) & (f) 3rd Story Infill Plate
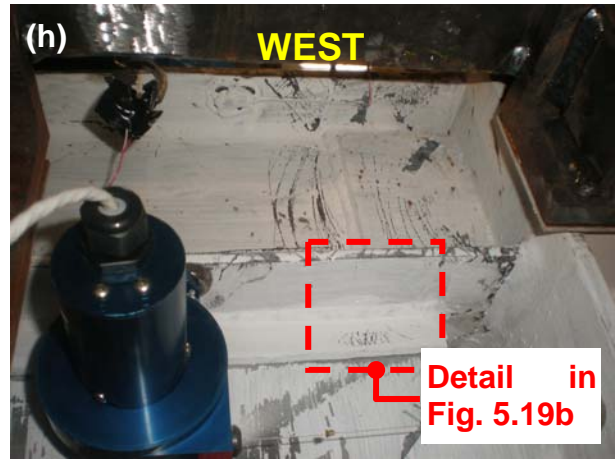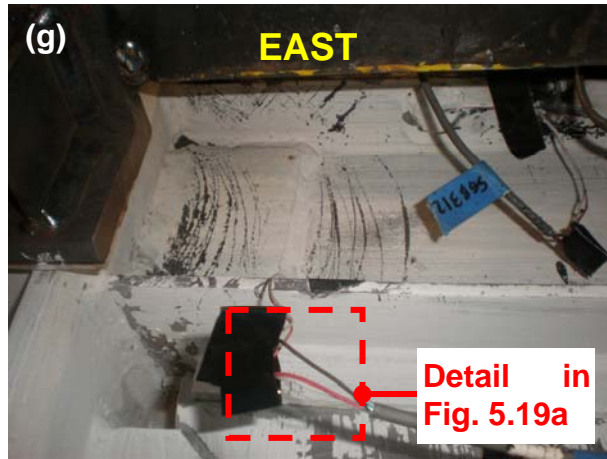
151

Figure 4-18 Specimen Condition at the End of Displacement Step8a – Cont'd:
(g) & (h) HBE3; (i) & (j) HBE2; (k) HBE1 (See Fig 5.20 for HBE0)
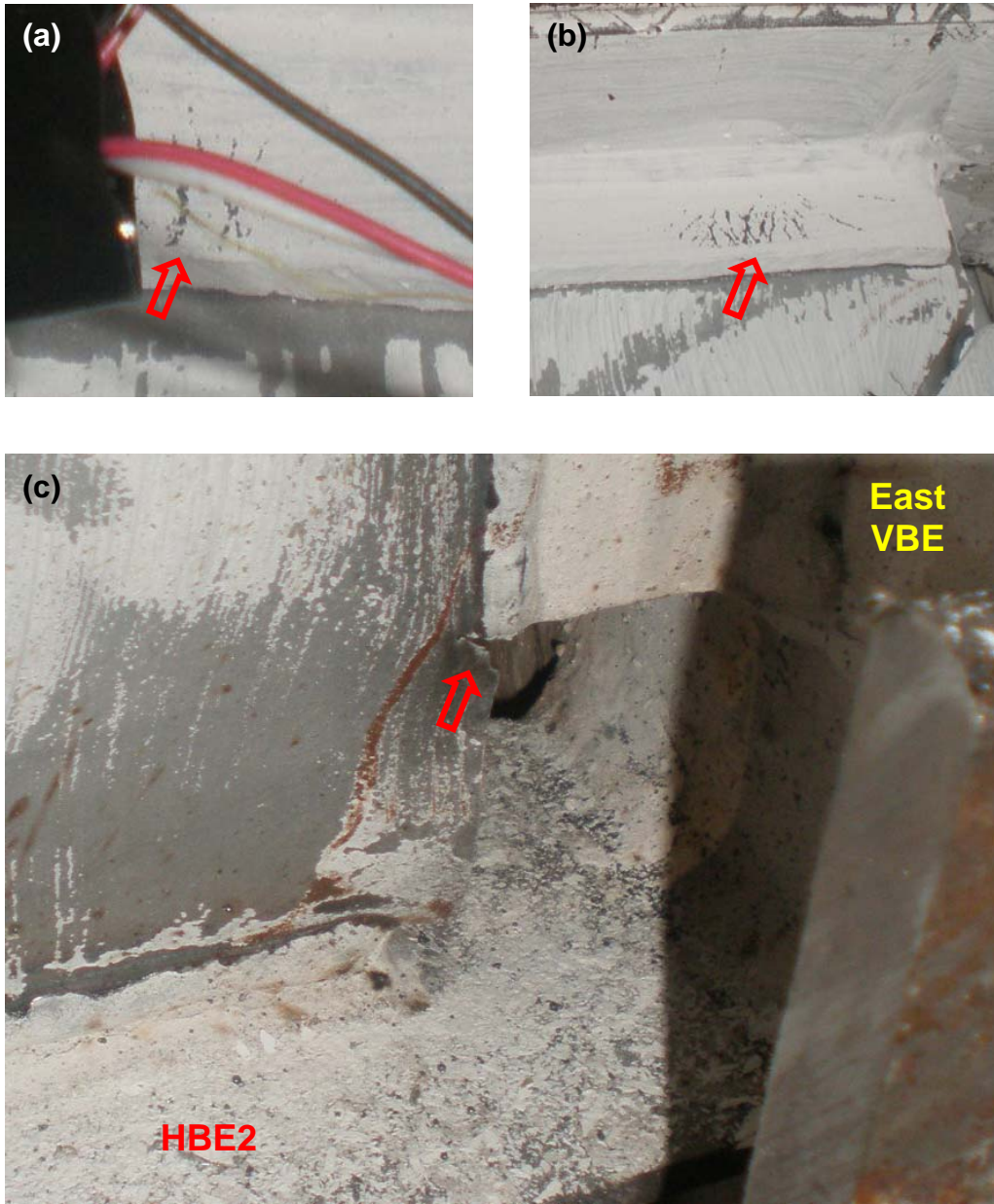
**Figure 4-19 Yielding Pattern at Displacement Step 8a (Δ_3 = 2.5% Drift = 5.32δ_y):
(a) & (b) Fish Plate Yielding (Detail of Fig. 5.18g & Fig. 5.18h); (c) Tearing of Infill Plate**

approximately 21 and 14 in. from the face of the East and West VBEs, respectively (Figure 4-20).
Slight flange local buckling and more whitewash flaking were observed on the East side
indicating that plastification was more severe there than that on the West side.

As the hysteretic curve showed no strength degradation, the experimental program continued
with two cycles at the higher target displacement in Step 9 (i.e., Δ_3 = 3.0% drift = 6.38δ_y). The
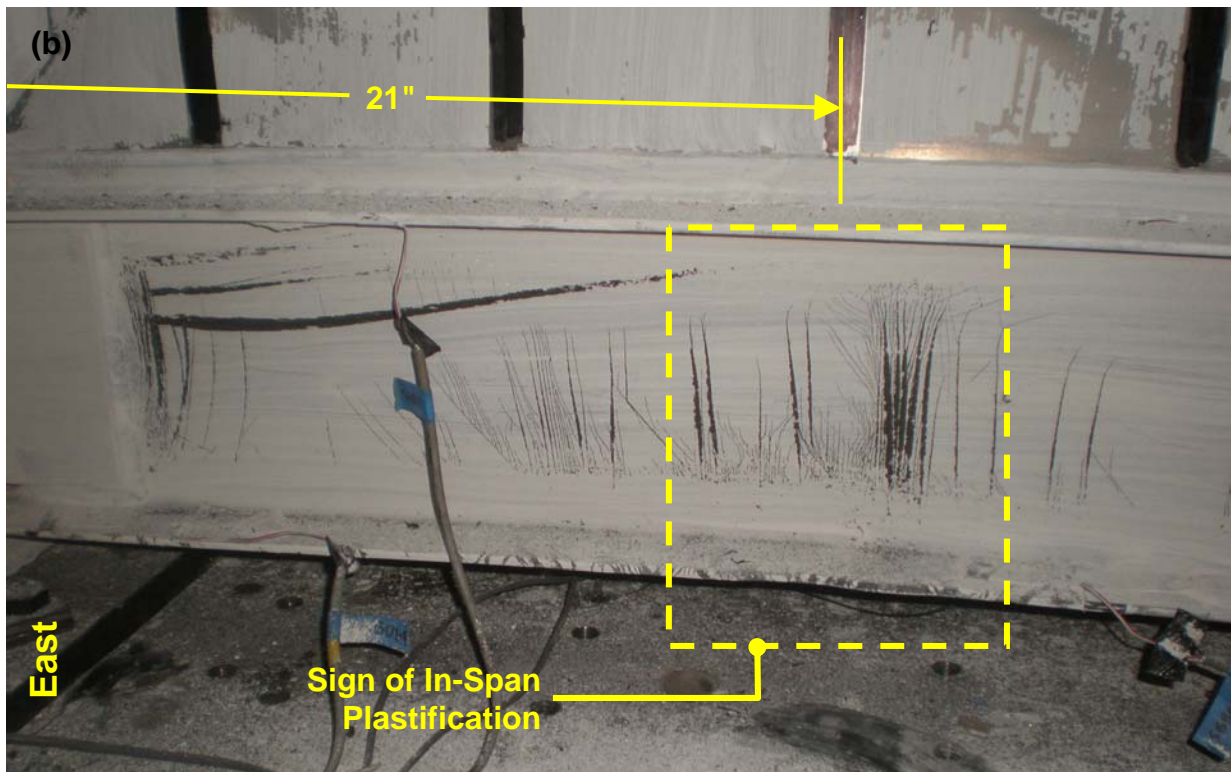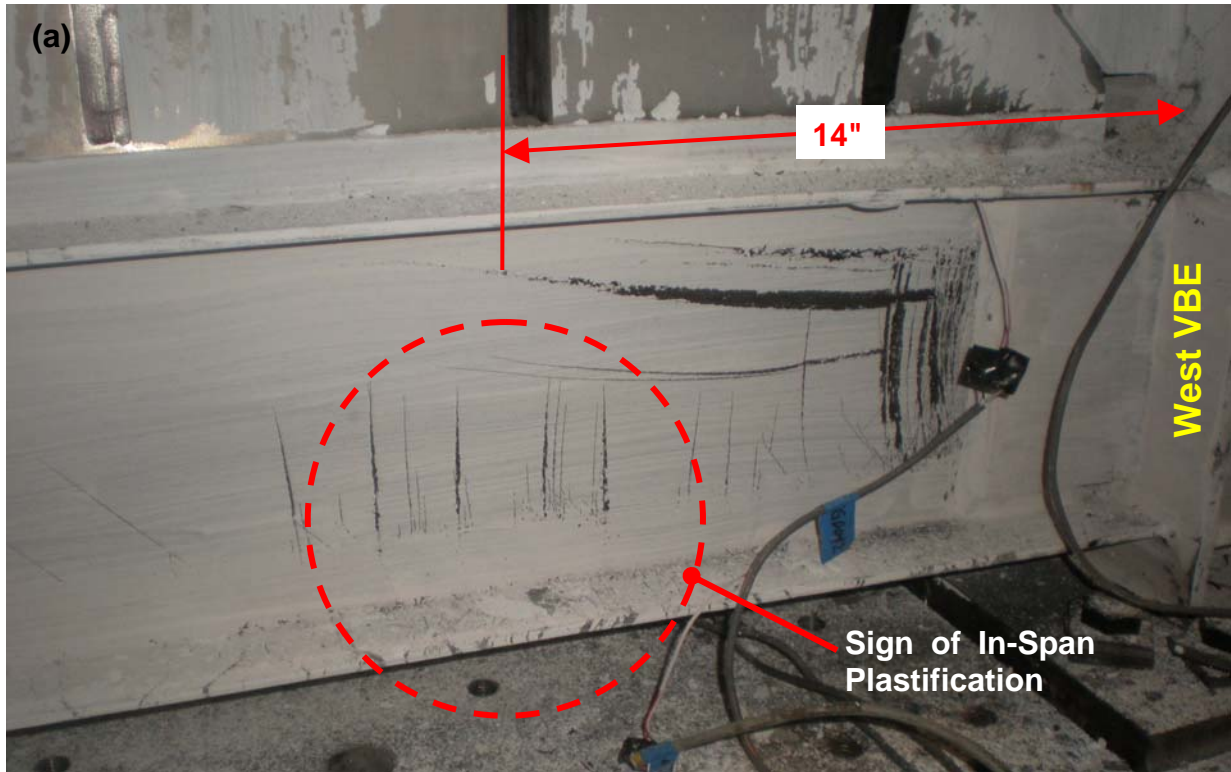
Figure 4-20 Sign of In-Span Plastification on HBE3 during Displacement Step 8a
$(\Delta_3 = 2.5\% \text{ Drift} = 5.32\delta_y)$**: (a) West Side; (b) East Side**

resulting peak base shears when cycling at 3.0% drift amplitude were 166.9 and 180.6 kips for the West and East excursions, respectively (an increase of 6.9 kips from the previous step). When the specimen was pushed beyond the maximum displacement of Step 8a (i.e., 3.75 in. top story displacement = 2.5% drift), tension field action developed anew in the infill plates to resist the applied lateral loads, as shown in Figures 4-21a and 4-21b during the West and East excursions, respectively. The magnitude of the "ridges" and "valleys" on the infill plate were quite significant by then (i.e., in comparison to displacement Step 4 in Figure 4-4b). When the specimen returned to its original position, significant residual out-of-plane buckling remained on every infill plate (Figure 4-22).

In displacement Step 9, cracks in the infill plates grew to approximately 0.5 and 0.25 in. on the first story infill plate (Figure 4-23a) and at the upper East corner of the second story infill plate, respectively. Plate tearing at the lower corners of the third story infill plate remained unchanged from what was previously observed in displacement Step 8a. Slight increase in yielding on the upper VBEs at the level of the first and second stories continuity plates was also noted in displacement Step 9 (Figure 4-23b). It was speculatively suggested that this behavior could be as a result of restraining the VBEs to the gravity mass plate through the connecting angles. Evidence of continued in-span plastification of HBE0 was more predominantly visible on its East side (Figures 4-23c and 4-23d). Lateral torsional buckling (LTB) and flange local-buckling were observed there (Figures 4-23e and 4-23f), on the bottom flange of HBE0 which is in compression when the tension forces generated by the yielding first story infill plate pull HBE0 upward.

After the displacement Step 9 cycles, relatively small gaps between the steel floor plate and the concrete strong floor were observed at the SPSW column locations. These residual uplifts at the East and West column locations were 0.17 and 0.01 in., respectively (when the specimen reached its target displacement, column uplifts were 0.57 and 0.65 in. at the same respective locations). Note that the actuators imposed approximately 30 kip forces at that point, to maintain the specimen at the zero-lateral-displacement position. When the actuators were brought back to zero loads, the floor plate residual uplifts became 0.11 and 0.04 in. residual uplifts, respectively. The steel floor plate is frequently used by SEESL; severe permanent inelastic damage to that plate was not permissible. The residual uplift values mentioned above were considered acceptable, but increases in these values were undesirable.
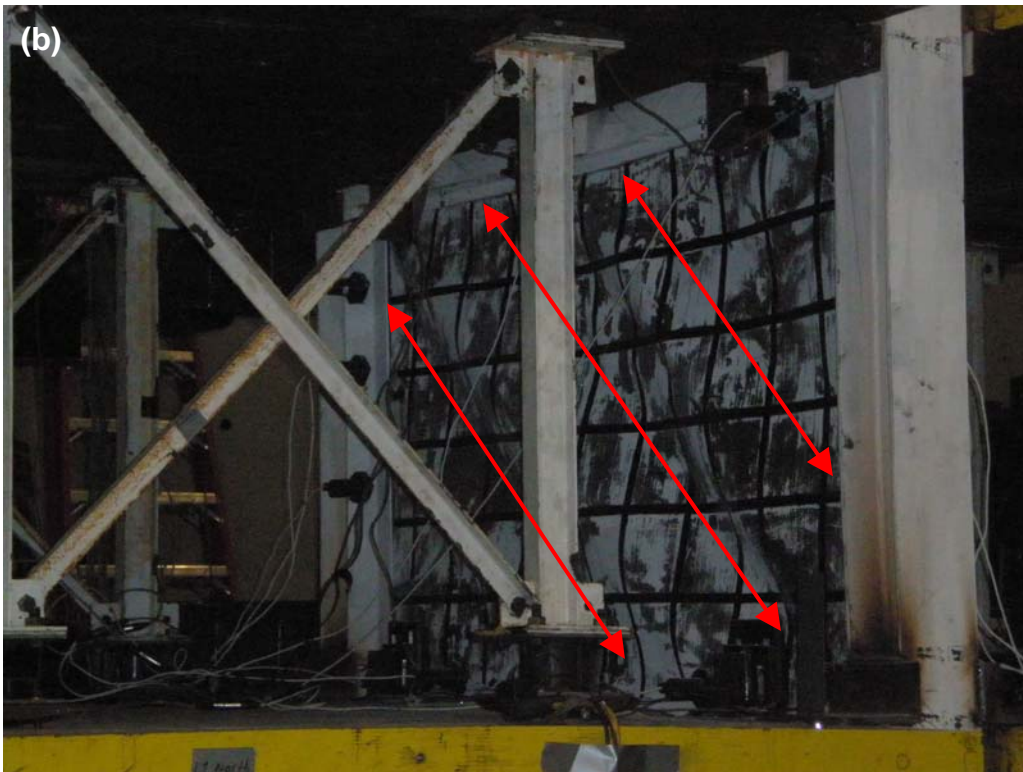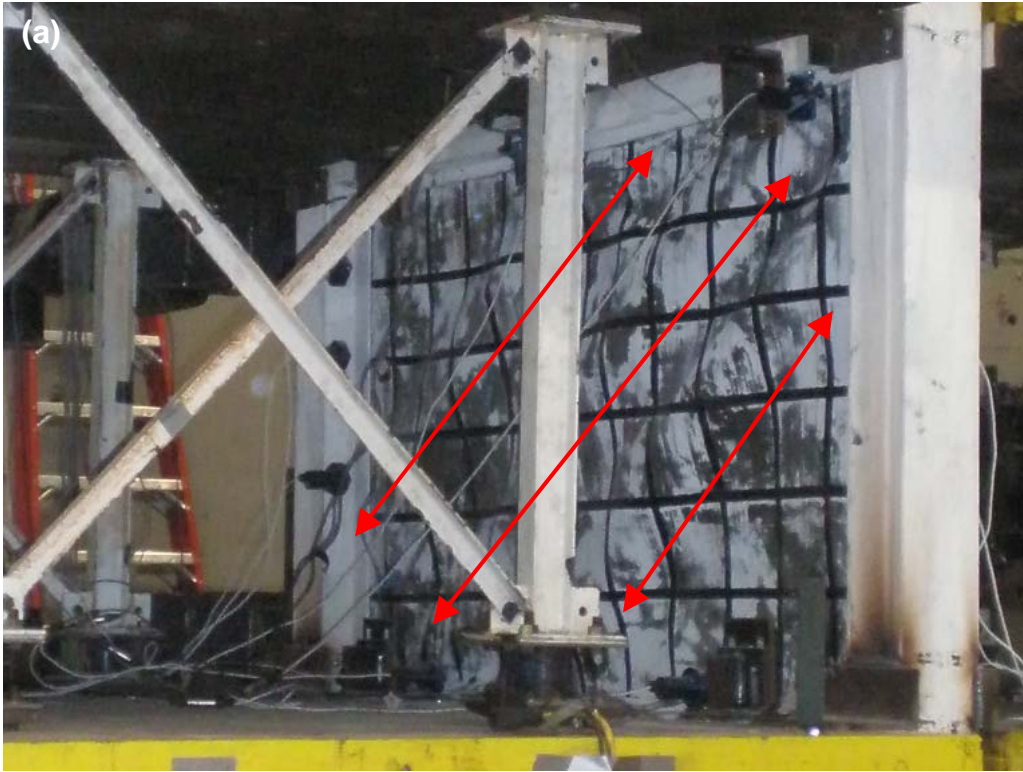
**Figure 4-21 Tension Field Actions during Displacement Step 9 (Δ_3 = 3.0% Drift = 6.38δ_y):
(a) West Excursion; (b) East Excursion**
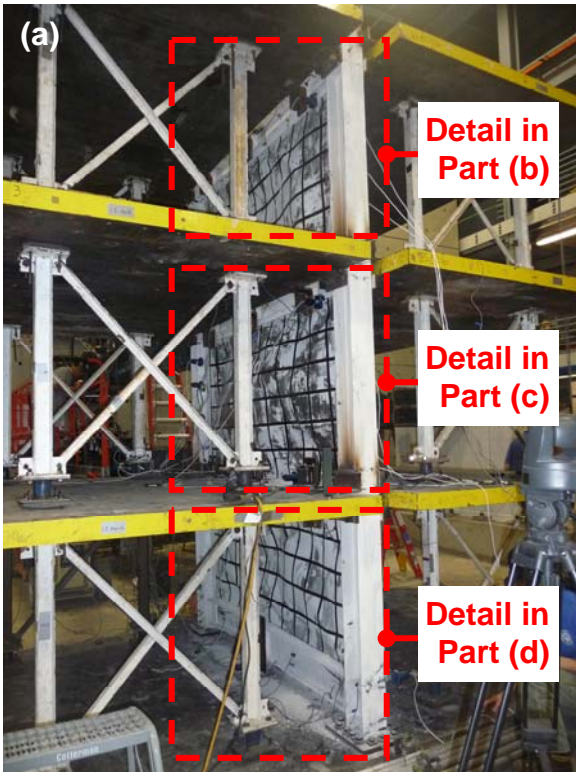
Figure 4-22 Infill Plate Out-of-Plane Buckling at the End of Displacement Step 9 ($\Delta_3 = 3.0\%$ Drift = $6.38\delta_y$): (a) Overview (North Side); (b) 3rd Floor; (c) 2nd Floor; (d); 1st Floor
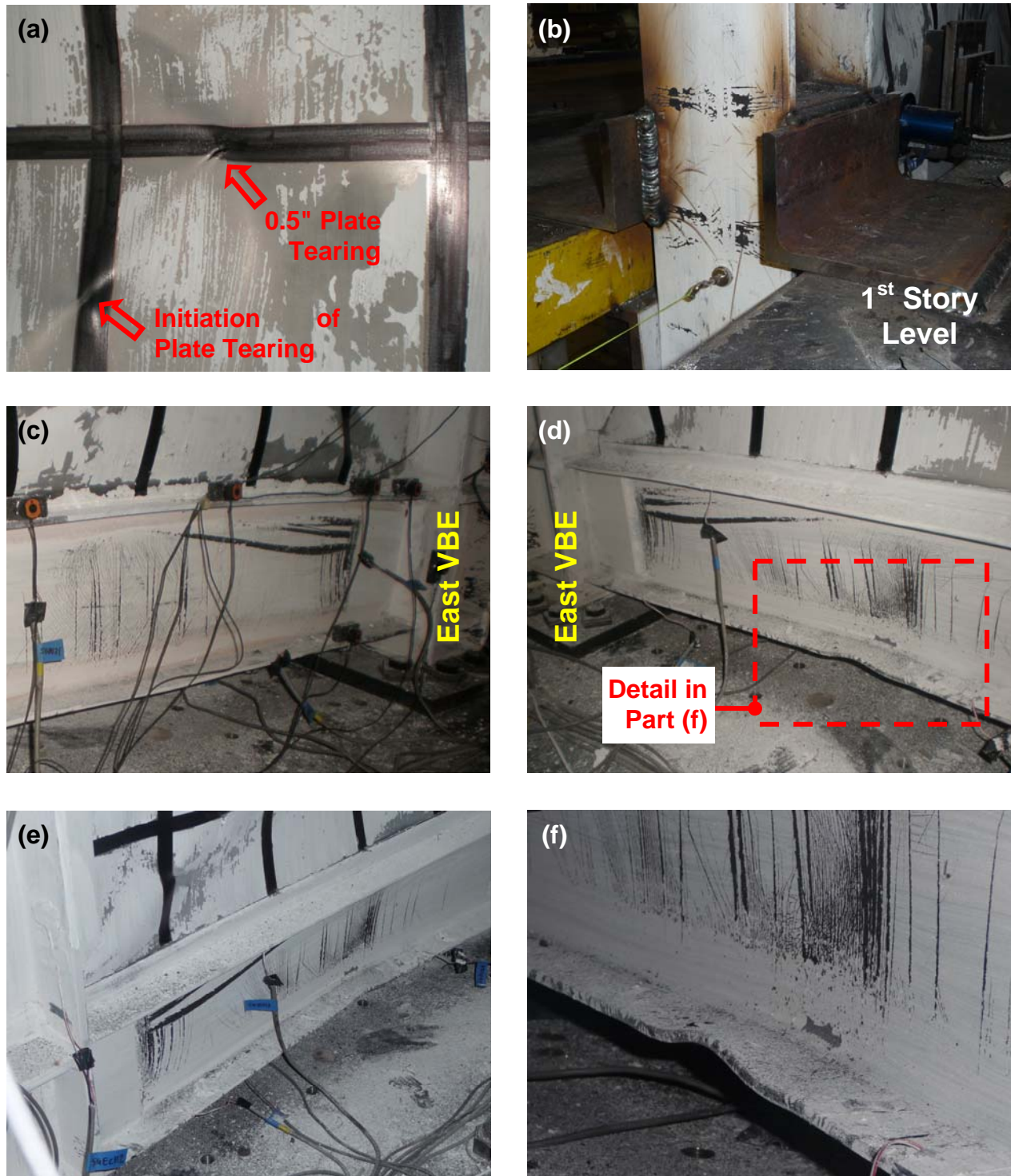
Figure 4-23 Specimen Condition at the End of Displacement Step 9
(Δ_3 = 3.0% Drift = 6.38δ_y): (a) Plate Tearing on the 1st Story Infill Plate; (b) Upper Column Flange Yielding; (c) In-Span Plastification (South View); (d)In-Span Plastification (North View); (e) Lateral Torsional Buckling; (f) Flange Local Buckling

In an attempt to prevent further permanent of uplifts, two additional cycles at the same displacement target of 3.0% top story drift (i.e., displacement Step 9a) were applied, in the expectation that strength degradation of the specimen would occur under this repeated loading (i.e. resulting in lower maximum base shear and lower uplift forces in the SPSW columns). The resulting peak base shears during the second displacement excursion were 153.4 and 164.5 kips in the West and East directions, respectively, which was 13.5 and 16.1 kips less than from that in displacement Step 9. The maximum and residual uplifts at the East and West columns remained practically the same as those observed in Step 9.

These cycles also allowed observation on the progression of HBE0 in-span plastification and the growth of plate tearing on the first and second story infill plates. Significant flange local buckling and yielding of the HBE bottom flange and web were observed (Figure 4-24a) at the location where LTB occurred (Figure 4-24b). Two new plate cracks developed: on the first story infill plate (Figure 4-24c) across the previous plate tearing observed in Step 9 and at the lower East corner of the second story infill plate (Figure 4-24d). Yielding at the previously reported locations (e.g., HBE-to-VBE connections, infill plates, and VBE bases) was not observed to be more significant than in the previous cycles.

Another two additional cycles were applied at the same 3% top story drift target (i.e., displacement Step 9b) in an attempt to further decrease the peak base shear. The resulting peak base shears were 148.5 and 159.5 kips for the second West and East excursions, respectively, which was 18.4 and 21.1 kips less than those in displacement Step 9 for the same respective excursions. The residual uplifts remained at the same magnitude (i.e., 0.17 and 0.01 in. at the East and West column locations, respectively) while the maximum uplifts slightly reduced (i.e., from 0.57 and 0.65 in. during displacement Step 9 to 0.55 and 0.62 in. within this step at the same respective column locations). Another 1.5 in long crack developed on the first story infill plate within this step (Figure 4-25).

The experimental program then continued to the displacement target of 3.17% drift (= 6.74δ_y, denoted as displacement Step 10). While closely monitoring floor plate uplifts, a first displacement cycle was applied. The peak base shear in this step was 10.1 kips higher than the

159
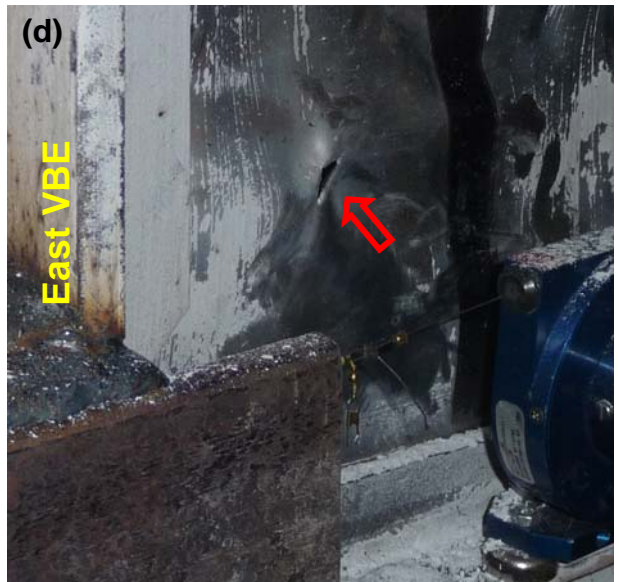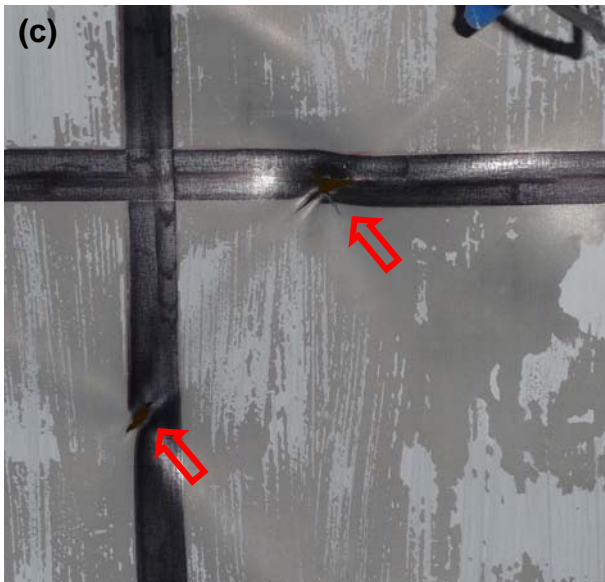
Figure 4-24 Specimen Condition at the End of Displacement Step 9a
($\Delta_3 = 3.0\%$ Drift $= 6.38\delta_y$): (a) Flange Local Buckling (South Side); (b) Lateral Torsional Buckling Observed from South Side); (c) Plate Tearing on the 1ˢᵗ Story Infill Plate; (d) Plate Tearing at Lower East corner of the 2ⁿᵈ Story Infill Plate

Figure 4-25 New Plate Tearing on the 1ˢᵗ Story Infill Plate (Displacement Step 9b)

maximum reached in the previous step, but still below that obtained during displacement Step 9 (during which residual floor plate uplifts first appeared). Residual floor plate uplifts remained at approximately the same magnitude as in the previous two displacement steps. Subsequently, the experimental program continued with one cycle of displacement (Step 10a) at a slightly higher displacement target (i.e., $\Delta_3 = 3.33\%$ drift $= 7.09\delta_y$). The resulting peak base shear remained 7.6 kips below that obtained in displacement Step 9. Again, to lower the maximum base shear (and corresponding uplift forces in the SPSW columns), another cycle of 3.33% drift amplitude was conducted in displacement Step 10b. It slightly lowered the peak base shear, to approximately 13 kips less than that in Step 9.

At the end of displacement Step 10b, fracture initiation was observed on the bottom flange of HBE2 at its connection to the East VBE (Figure 4-26). Residual uplifts at the East column slightly increased from 0.17 in. during displacement Step 9 to 0.20 in. within this step. At the West column, however, residual uplifts remained the same at 0.01 in. Maximum uplifts, when the specimen reached the target displacement, were 0.6 and 0.65 in. for the East and West column,
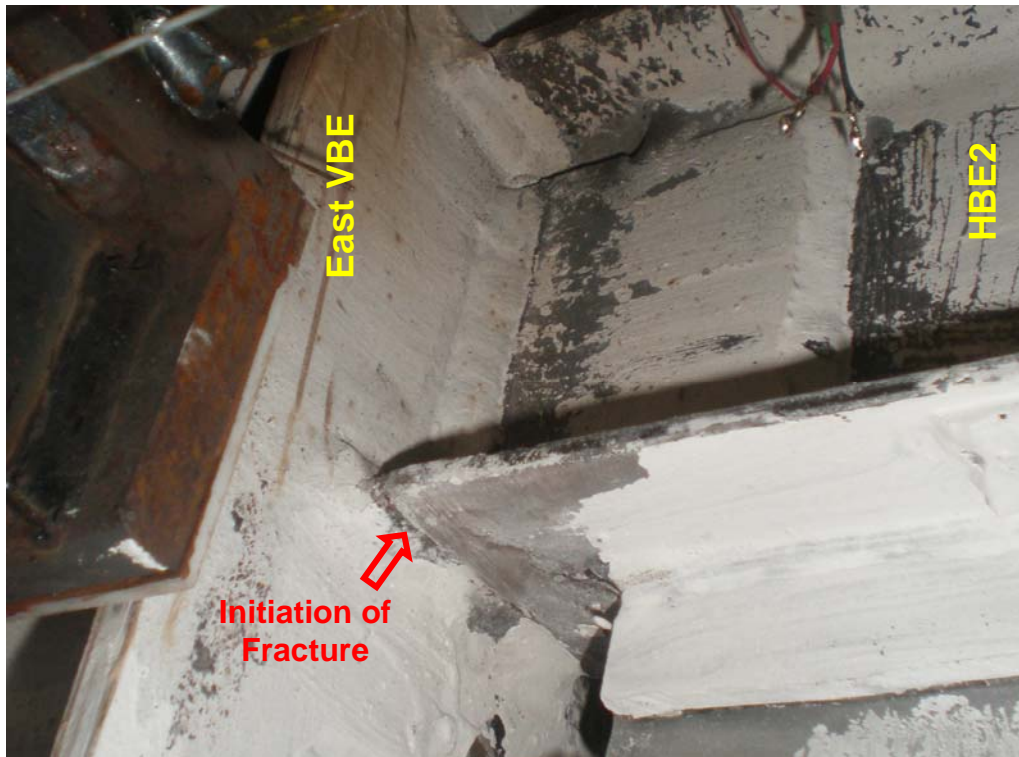
Figure 4-26 Initiation of fracture in Displacement Step 10b (Δ_3 = 3.33% drift = 7.09δ_y)

respectively. Subsequent inspection of the four tension rods adjacent to each column base and connecting the steel floor plate to the lab floor (Figure 3-14a) revealed various levels of looseness on the tension rods, indicating that they had lost their pre-tension, probably as a consequence of having yielded. Tightening or replacing these yielded tension rods was considered as a possible option to alleviate the floor plate uplifts. However, since the location of the maximum uplift (i.e., at the East-to-West centerline of the column base plate) was 12 in. away from each of these tension rods (Figure 3-14a), this plan would not have significantly solved the uplift problem. In other words, when the specimen would have been pushed to higher displacement targets, the uplift would have developed and yielded the replaced tension rods again. Hence, it was decided to leave the yielded tension rods in place, expecting pulling forces from the specimen to distribute to a larger area of floor plate (i.e., 48 in. by 24 in footprint).

The experimental program continued with three cycles at 3.3% drift (i.e., denoted as displacement Step 10c). The first excursion to 3.33% drift (= 7.09δ_y) reached peak base shears of 150.4 and 164.3 kips for the West and East excursions, respectively. At the end of the third cycle, the peak

162

base shears were down to 144.6 and 158.1 kips for the same respective excursions. Note that the peak base shears reached in displacement Step 9 were never reached again in the subsequent steps. Maximum and residual uplifts recorded at both East and West column locations remained approximately the same as that in the previous steps. The flange fracture of HBE2 progressed further (Figure 4-27a), and two other fractures developed, namely at the top flange of HBE1 at its connection to the East VBE (Figure 4-27b) and on the outer flange of the West VBE at its connection to the base plate (Figure 4-27c). In addition, plate tearing was noted at several new locations on the first and second stories.

Despite the above fractures at the boundary element connections, the extensive yielding at other connected locations, the significant yielding of each infill plate (Figure 4-28a), and the progression of in-span plastification and LTB (Figure 4-28b), it was unclear whether testing should continue or end at this stage; pushing the specimen to substantially larger drifts would have likely resulted in a maximum base shear exceeding the values reached in Step 9, and therefore risk damaging the expensive floor plate. However, it was judged worthwhile to check whether major damage would occur in the specimen and to record video feeds of the progression of fractures in the boundary frame. For this purpose, two additional cycles at the same target displacement (i.e., $\Delta_3 = 3.33\%$ drift = $7.09\delta_y$, denoted as displacement Step 10d) were applied to the specimen. The maximum uplifts during the last displacement step were 0.57 and 0.62 in. for the East and West column, respectively. The residual uplift displacements were 0.19 and 0.02 in. at the same respective locations.

After the displacement Step 10d cycles, the experimental program was concluded for several considerations, namely: (1) the specimen practically exhibited the same behavior within the last several displacement steps (i.e., Steps 10a to 10d with a total 7 cycles at 3.33% target drift), and no new behaviors would have been observed if the same displacement targets had been further repeated; (2) it was judged prudent to not push the specimen beyond the current displacement target to prevent damage to the floor plate; (3) there was a concern that, because the lower two floor actuators were acting in a force control mode, extreme damage to the specimen at the first or second story could lead to an uncontrolled behavior, resulting in an unexpected collapse and damage to the laboratory equipment; and (4) many other projects were in queue, waiting to use the same laboratory space and testing equipment, which put pressure on the project to conclude.
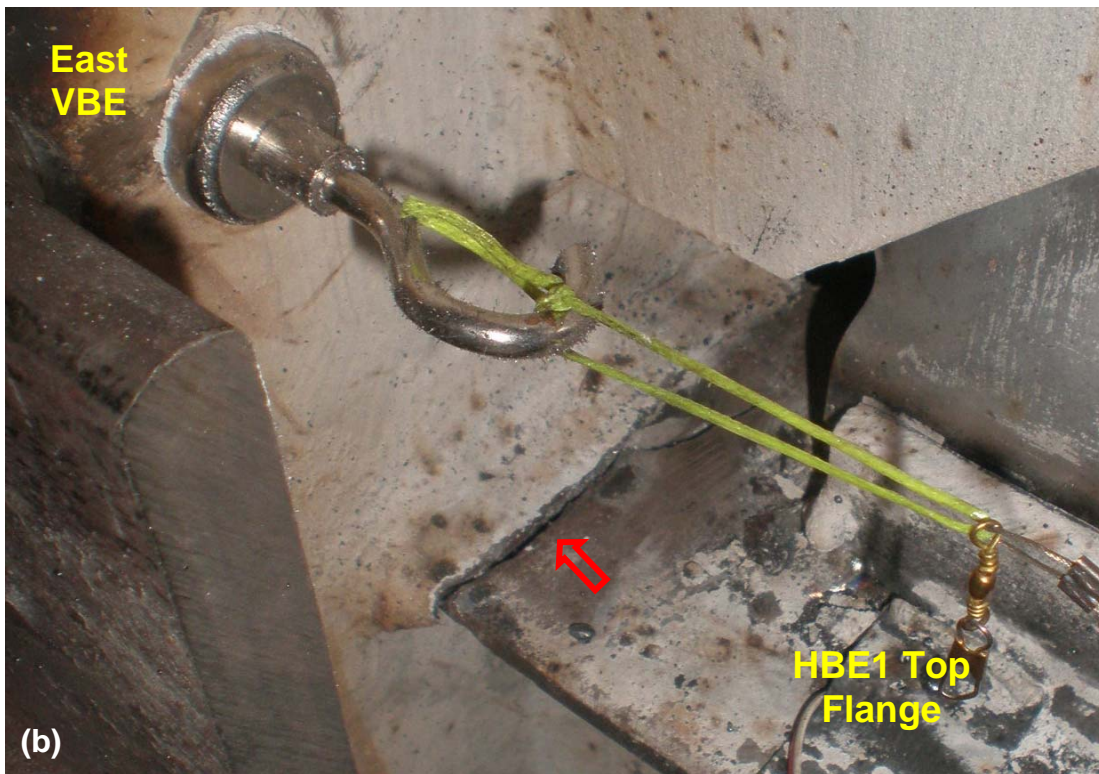
Figure 4-27 Special-Moment Resisting Connection Fractures in Displacement Step 10c
$(\Delta_3 = 3.33\% \text{ drift} = 7.09\delta_y)$**: (a) East Joint of HBE2; (b) East Joint of HBE1**

Figure 4-27 Special-Moment Resisting Connection Fractures in Displacement Step 10c
(Δ_3 = 3.33% drift = 7.09δ_y) – Cont'd: (c) Base of West VBE
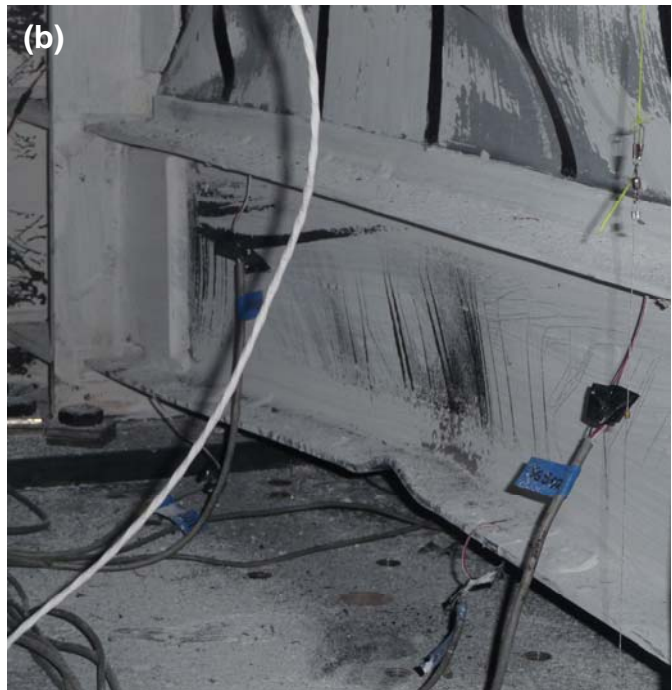
Figure 4-28 Specimen Condition at the End of Displacement Step 10c (Δ_3 = 3.33% Drift
= 7.09δ_y): (a) Infill Plate Yielding (North Side); (b) Lateral Torsional Buckling

After completion of the test, the gravity column system was removed, and a series of photos were taken to record the specimen's final condition. Figure 4-29 presents an overview of specimen final condition on both North and South views while Figures 4-30 and 4-31 present several detailed snapshots taken from the North and South sides, respectively. For the North side, details taken from the East to West side are presented, from left to right in Figure 4-30, while the order is reversed for the South side in Figure 4-31 (i.e., photos from left to right correspond to details taken from West to East side). For both figures, details for HBE3 are presented first, followed by each subsequent lower HBEs. With removal of the gravity column system, additional inelastic behaviors could be observed that had not been noticed during testing. First, in addition to yielding of panel zones at the level of HBE0 first reported in displacement Step 7, yielding of panel zones was also observed at the level of HBE3 (Figures 4-30a and 4-30e). Second, sign of in-span plastification was also observed on HBE3 (Figures 4-30b and 4-30d). Based on the extent and patterns of flaking of the whitewash, one could infer that this in-span plastification occurred in several displacement steps prior to conclusion of the test. It should have been reported as part of observations made in earlier displacement steps, but had been overlooked when the experiment progressed due to the difficulty of making observations at that location. In addition, these collections of snapshots provide full views of flange and web yielding across the span of HBEs. For example, this yielding on HBE2 is shown in Figures 4-30g to 4-30i).

For completion, several additional snapshots of boundary frame fractures and the final condition at column bases are shown in Figure 4-32. Particularly shown in Part (b) of this figure, the fracture of the HBE1 connection to the East VBE had progressed into the shear tab. Another flange fracture was observed at the HBE1 connection to the West VBE (Figure 4-32e). Schematic locations and dimensions of small tears in the infill plates are presented in Figure 4-33.

Measurements of residual deformations of each HBE were conducted and results at seven different locations for each HBE are presented in Table 4-2. Maximum residual deformations for top to bottom HBEs were 0.75, 0.5, less than 0.25, and 0.875 inches, respectively; and permanent out-of-plane displacement of HBE0 bottom flange at the location where LTB occurred was 1.5 inches.

Figure 4-29 Specimen Final Condition (Step 10d: Δ_3 = 3.33% Drift = 7.09δ_y): a) North Side Overview; (b) South Side Overview
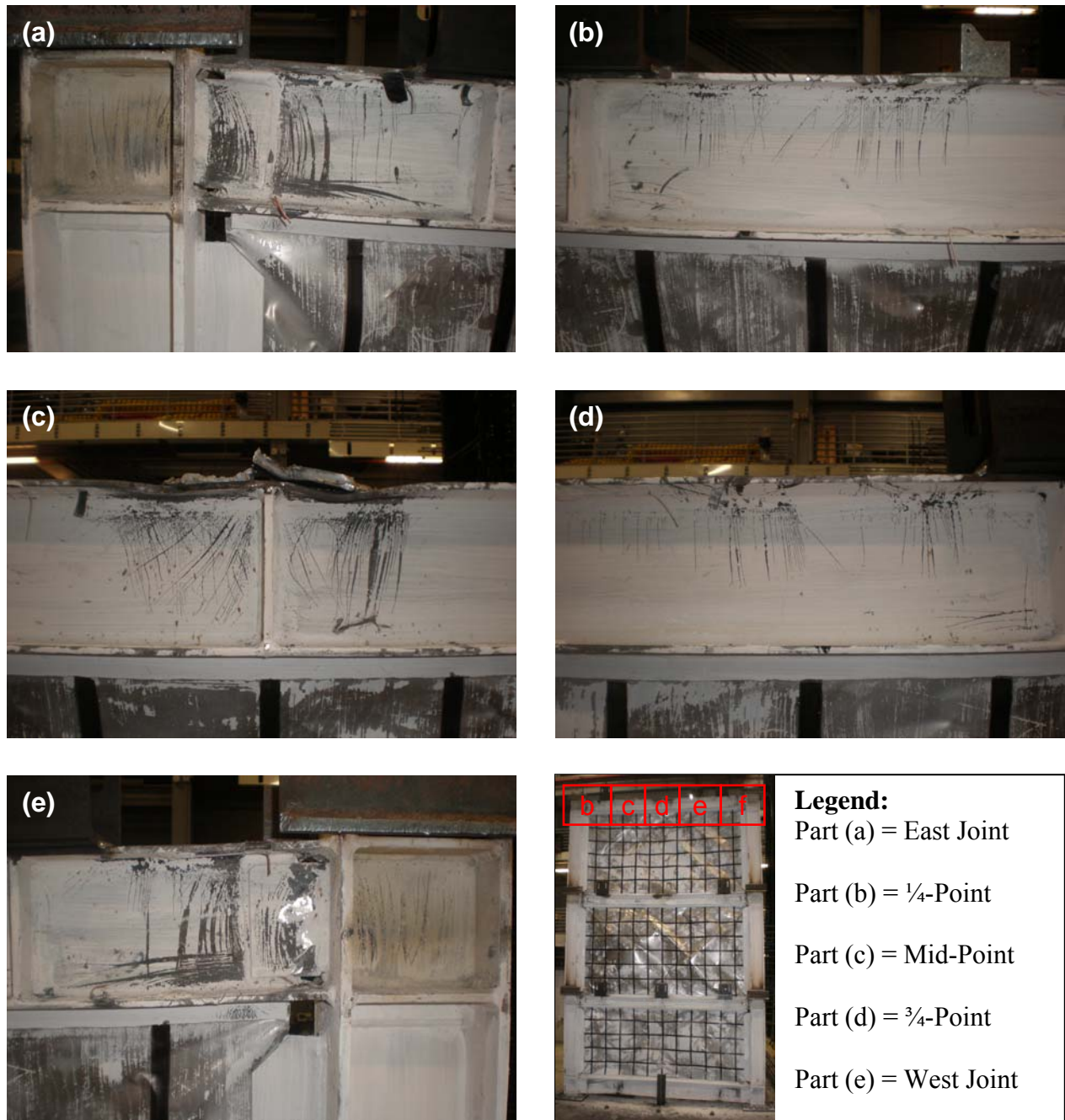
Figure 4-30 Details of Specimen Final Condition (Step 10d: $\Delta_3 = 3.33\%$ Drift $= 7.09\delta_y$): (a) to (e) HBE3 (North Side)

4.4 Revised Nonlinear Static Analysis of Specimen

When displacement Step 6a was concluded, many aspects of the specimen behavior were unexpected and required further explanation. Described in Section 4.3.1 throughout the first part
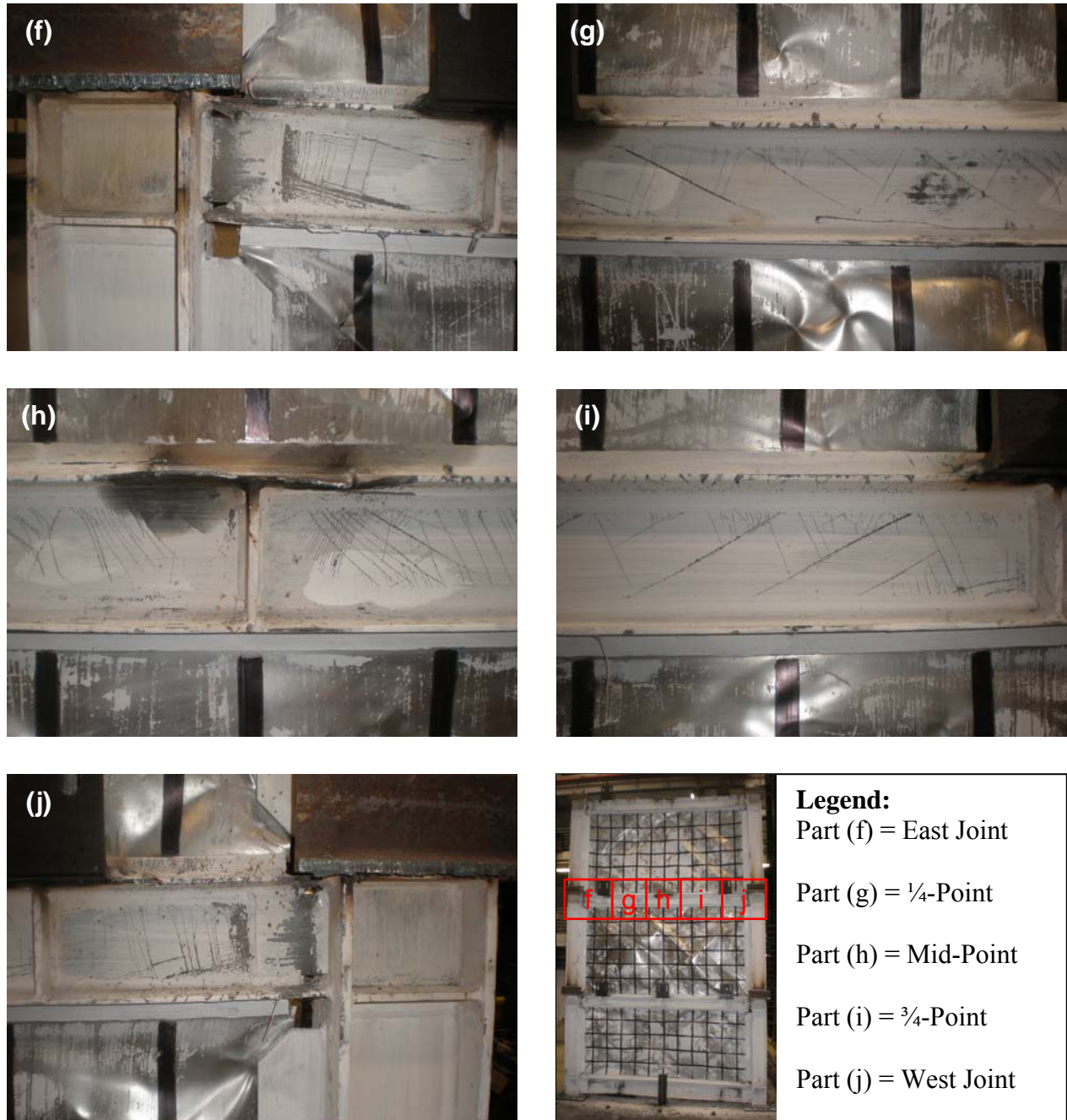
Figure 4-30 Details of Specimen Final Condition – Cont'd: (f) to (j) HBE2 (North Side)

of the experimental program, the recorded maximum base shear was always higher than the maximum value predicted. Moreover, in spite of the higher base shear obtained, the actual specimen lateral displacement was smaller than what the actuator imposed and HBE vertical displacements recorded were less than the estimated values, indicating that the accumulation of plastic incremental deformations on the HBEs was not as pronounced as originally predicted. At
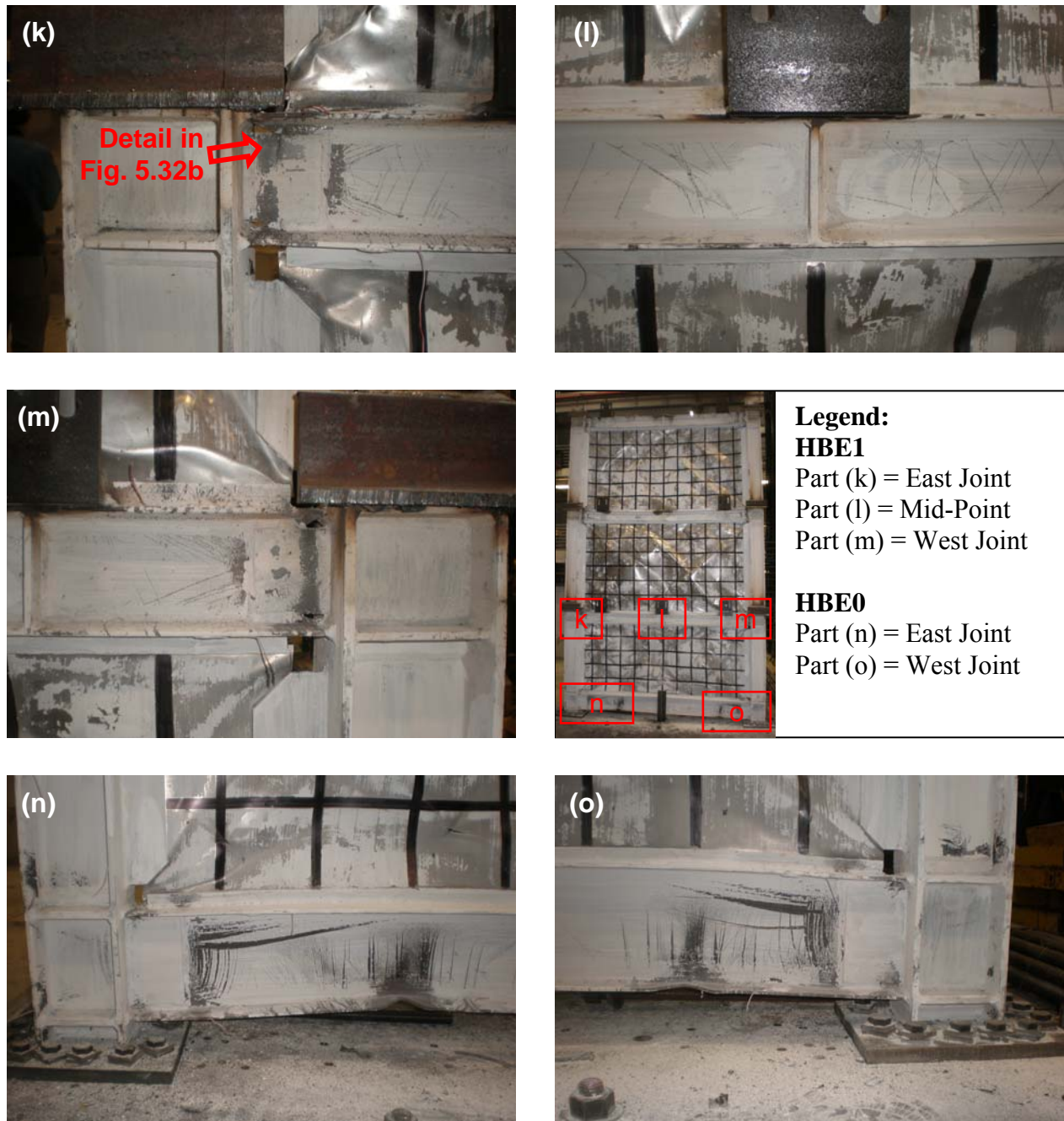
Figure 4-30 Details of Specimen Final Condition – Cont'd: (k) to (m) HBE1 (North Side); (n) & (o) HBE0 (North Side)

that point, it was speculated that the connecting angles used for load transfer mechanism (Section 3.7.3) at three locations for each floor might have been responsible for modifying the behavior from what was originally intended, possibly because they might not have been actually free to move upside down as the frame displaced laterally. As a result, the angles might have
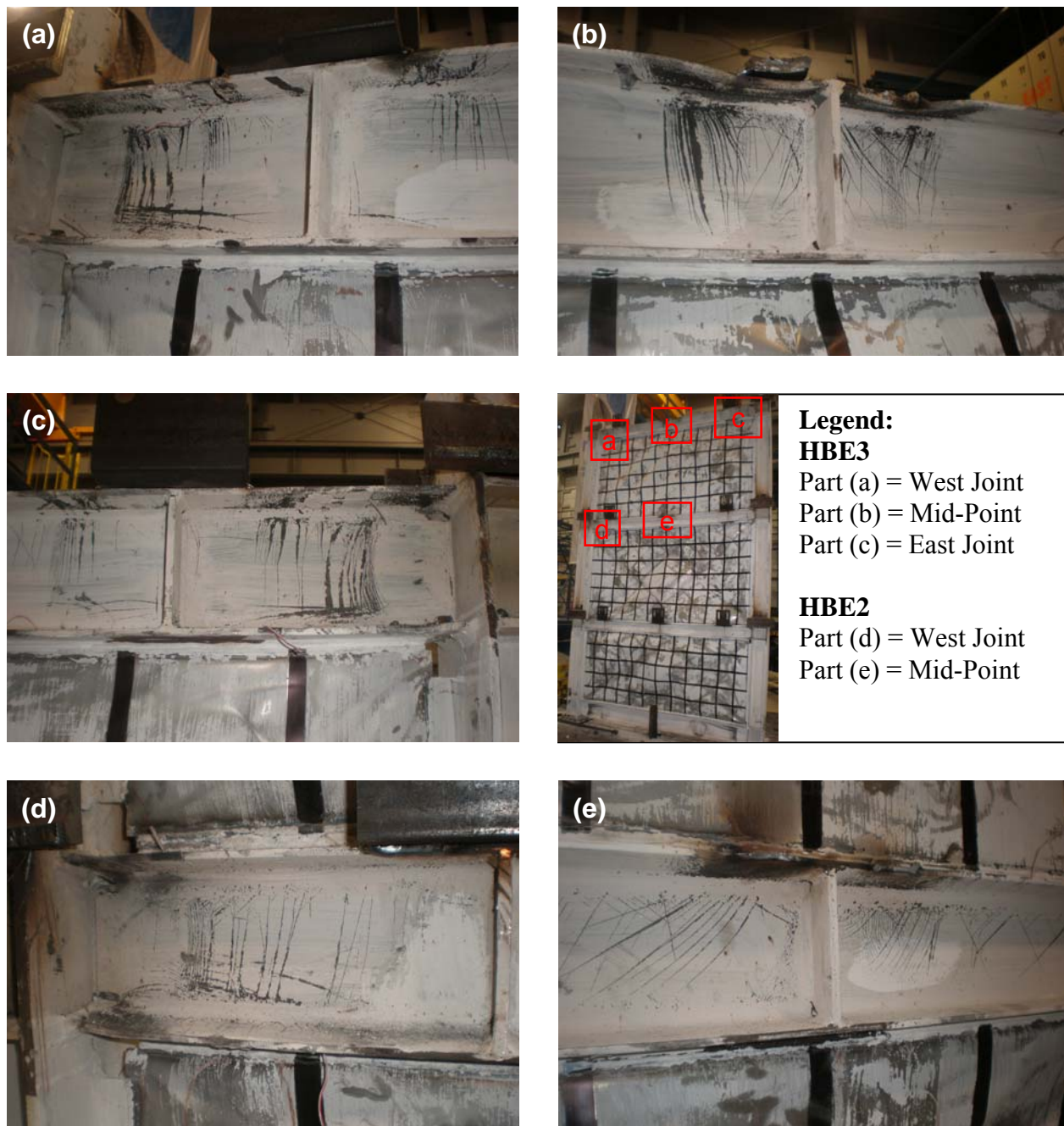
Figure 4-31 Details of Specimen Final Condition (Step 10d: Δ_3 = 3.33% Drift = 7.09δ_y):
(a) to (c) HBE3 (South Side); (d) & (e) HBE2 (South Side)

created unexpected additional restraints at every floor, resulting in a more rigid specimen than what was considered during design. It is the purpose of this section to present the analyses conducted to investigate this hypothesis, which eventually supported the decisions taken during the testing program.

Legend:
HBE2
Part (f) = East Joint

HBE1
Not available

HBE0
Part (g) = West Joint
Part (h) = Mid-Point
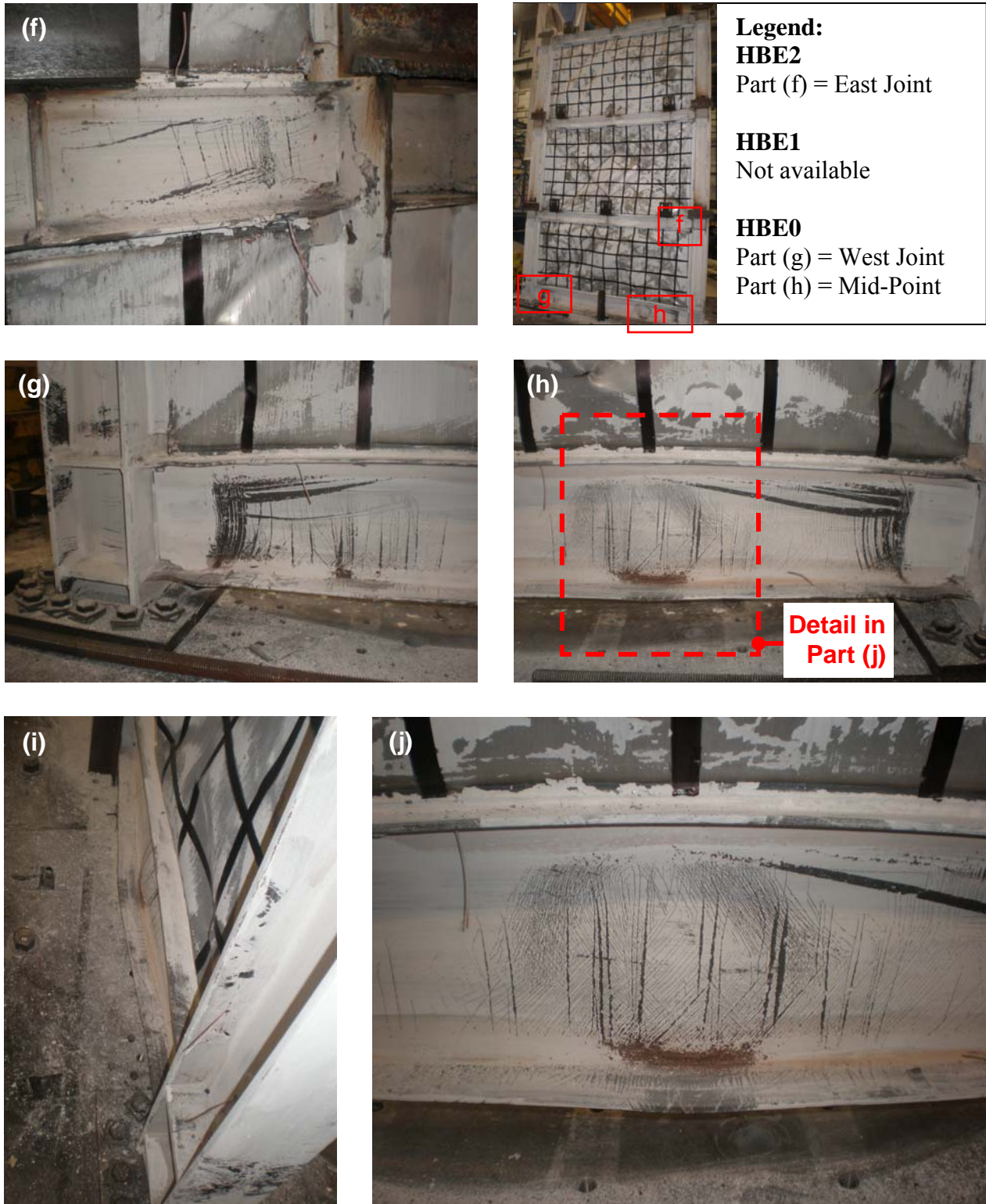
Figure 4-31 Details of Specimen Final Condition – Cont'd: (f) HBE2 West Joint (South Side); (g) & (h) HBE0 (South Side); (i) Lateral Torsional Buckling on HBE0; (j) Plastification at LTB Location

**Figure 4-32 Boundary Frame Final Condition (Step 10d: $\Delta_3 = 3.33\%$ Drift $= 7.09\delta_y$):
(a) Fracture at HBE2 Bottom Flange; (b) Shear Tab Fracture at HBE1**
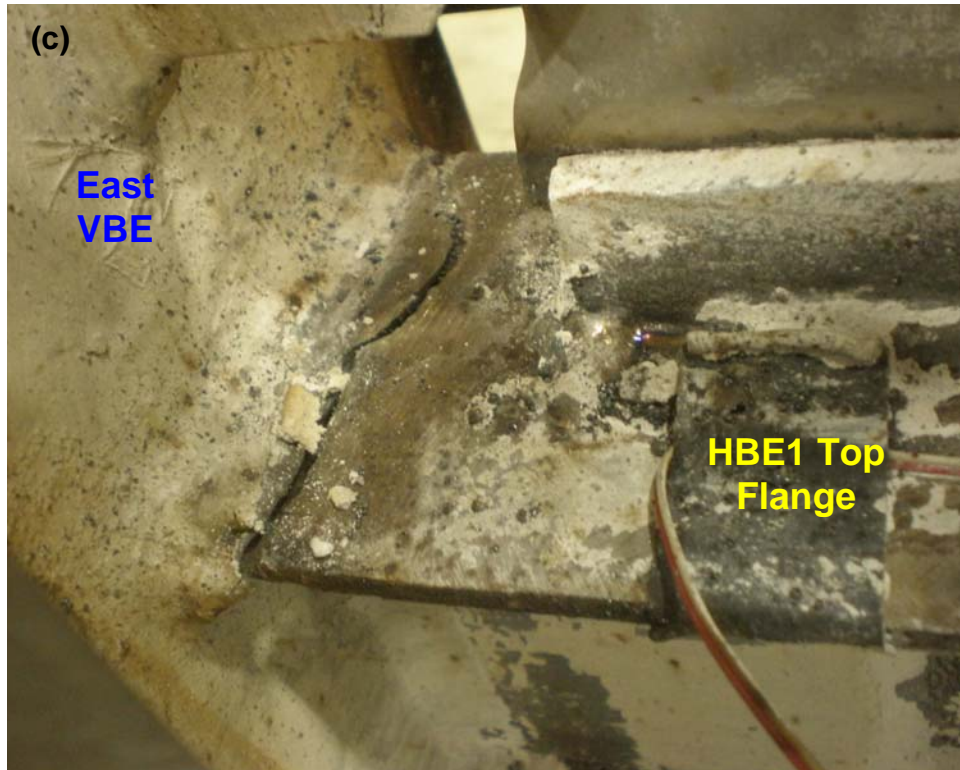
Figure 4-32 Boundary Frame Final Condition – Cont'd: (c) Fracture at HBE1 Top Flange (North View); (d) Fracture at HBE1 Top Flange (South View)

Figure 4-32 Boundary Frame Final Condition – Cont'd: (e) Fracture at HBE1 Top Flange at its Connection to West VBE; (f) & (g) Column Bases
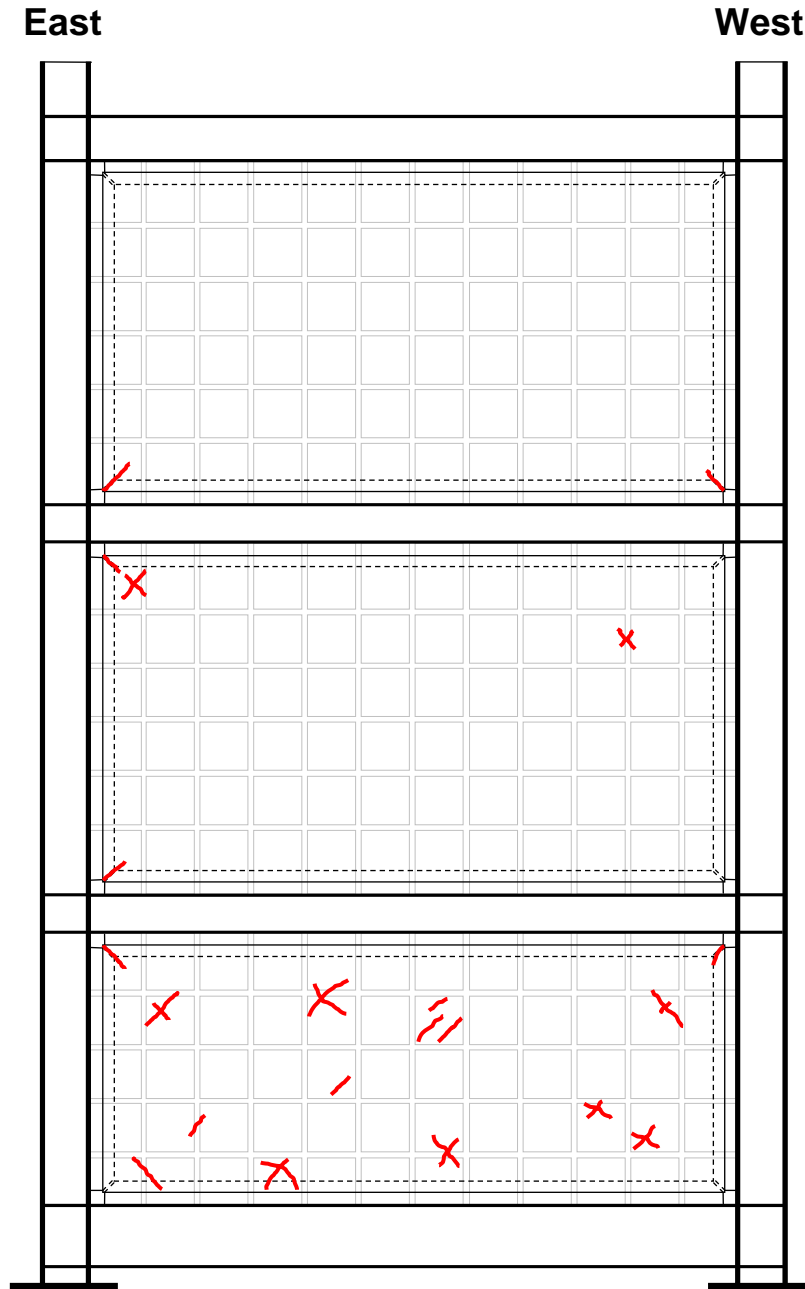
Figure 4-33 Infill Plate Final Condition (Step 10d: Δ_3 = 3.33% Drift = 7.09δ_y)

A limited analytical investigation was conducted using nonlinear static analysis. For this purpose, all features of the Case 10 numerical model presented in the previous section (i.e., Section 3.4) were carried over, with one additional modification. In the original Case 10 model, lateral forces for each story were distributed at three points along the respective HBE span and applied through its centerline. Considering that story forces actually transferred to the specimen via the HBEs' top

Table 4-2 Measurements of HBE Residual Deformations

HBE	Residual Deformations (in.)[1]						
	A	B	C	D	E	F	G
3	3/8"	5/8"	11/16"	3/4"	11/16"	9/16"	3/8"
2	1/4"	3/8"	1/2"	1/2"	1/2"	3/8"	1/4"
1	1/16"	1/16"	3/16"	3/16"	3/16"	1/16"	1/16"
0	1/4"	1/2"	5/8"	7/8"	3/4"	5/8"	3/8"

Note: [1] Locations of measurement along HBE span are schematically shown in the figure below.
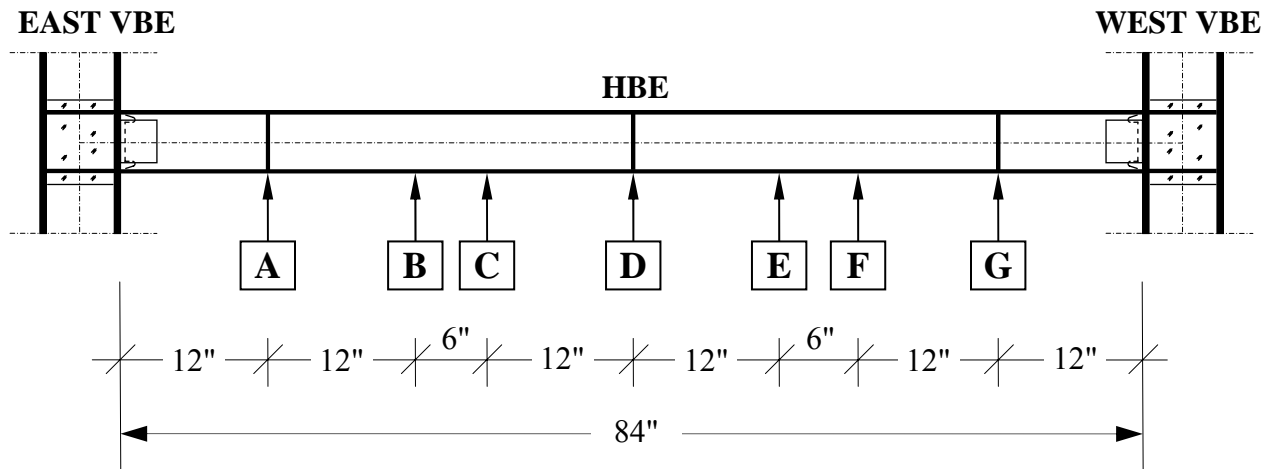
flange during the experiment, the story forces in the modified model were applied to the specimen at an offset equal to half of the HBE depth above its centerline. In the SAP2000 framework used for this analytical investigation, the "*Equal Constraint*" option was used to rigidly link the three offset points, where the story forces were applied, to their corresponding points in the frame elements located at the centerline of HBEs. For clarity, the current model is denoted as "Case 11"; subsequent models, investigating other alternative scenarios of restraints and constraints as further explained in the following paragraph, are labeled with subsequent numbers.

Using Case 11 as a benchmark, five different scenarios were investigated. Variations from one analytical model to another are summarized in Table 4-3. As the benchmark, the three offset points in Case 11 model are free to move (unrestrained) and independently from one another (i.e., no constraints are introduced). To reflect the fact that the gravity mass plates used to transfer the

Table 4-3 Variations of Analytical Models in SAP2000

ID	Restraints (u_x, u_y, r_z)	Lateral Constraint $(u_{x1} = u_{x2} = u_{x3})$	Schematic
Case 11	0, 0, 0	No	
Case 12	0, 0, 0	Yes	
Case 13	0, 1, 0	Yes	
Case 14	0, 0, 1	Yes	
Case 15	0, 1, 0	No	
Case 16	0, 1, 1	Yes	

actuator forces to the specimen are essentially rigid, a constraint in the lateral direction is imposed in the "Case 12" model, basically enforcing synchronized lateral movement of the three offset points (i.e., $u_{x1} = u_{x2} = u_{x3}$). In the SAP2000 framework, this can be done by applying the "Diaphragm Constraint" for these points.

In the two subsequent models, the impact of restraining vertical translation and rotation is investigated in "Case 13" and "Case 14" models, respectively, while the constraint in the lateral

178

direction imposed in Case 12 is carried over to both models. Case 13 provides a way to verify the previous assumption discussed in Section 4.3.1, which suggested that the high-strength bolts used in the connecting angles used to transfer actuator loads from the gravity mass plate to the specimen might have been stuck, preventing the HBEs from freely moving vertically. Moreover, the need to investigate Case 14 is schematically illustrated in Figure 4-34. In an unrestrained

(a) Deflected Shape of Unrestrained HBE

(b) Deflected Shape of Restrained HBE
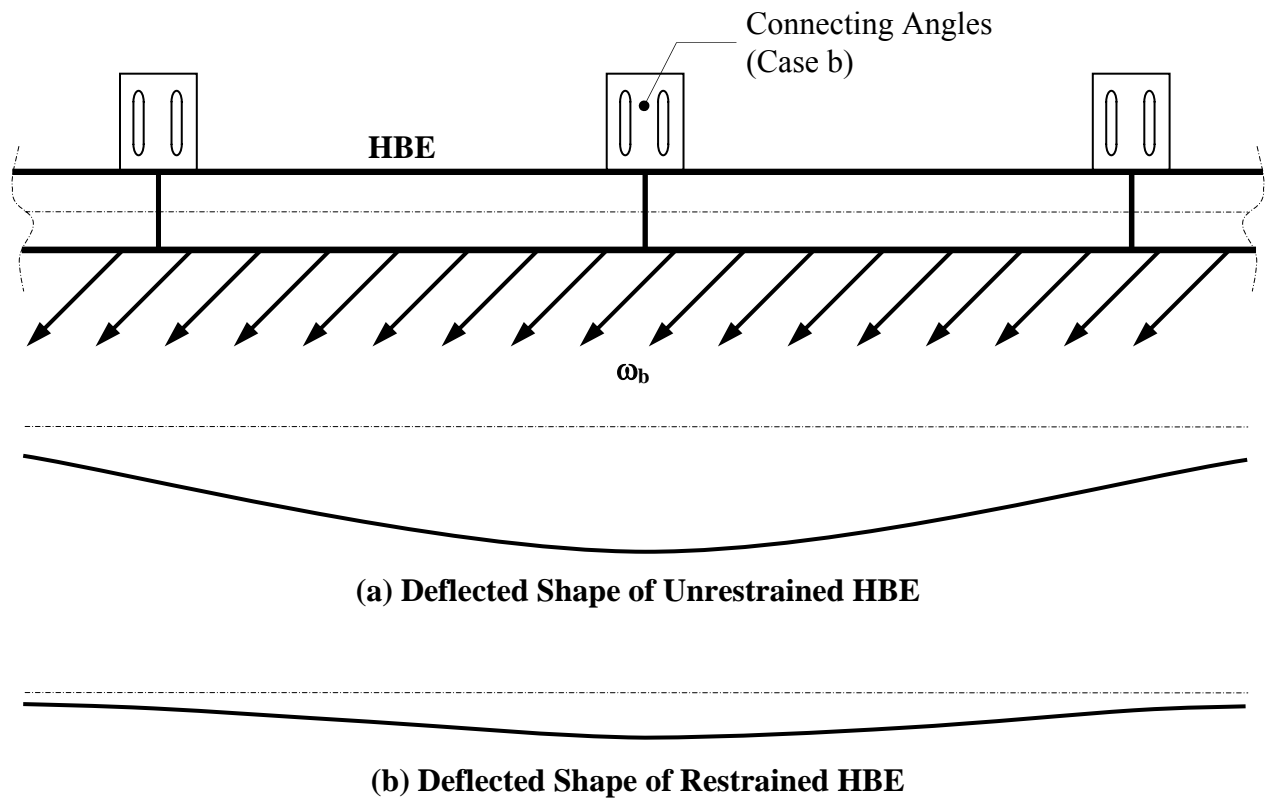
Figure 4-34 Illustration of Case 14

HBE (Figure 4-34a), tension forces generated by the yielded infill plate pull the HBE in the direction of the forces and cause a single-curvature deflection shape on the HBE. Accordingly, connecting angles at the quarter- and third-quarter-span of the HBE should allow the corresponding beam rotations to develop along its length. However, the bolts that connect these angles to another set of angles on the gravity mass plate (which itself doesn't rotate) may lock the angles against rotation (Figure 4-34b), modify the beam deflected shape, and consequently limit HBE deflections at the connecting points. For completeness, a variation of Case 13 which the tree offset points (where the loads are applied) restrained in the vertical translation but free to move independently from one another (unrestrained) in the lateral direction is investigated, denoted as

"Case 15". In the last model considered, denoted as "Case 16", the impact of combining the restraints and constraints imposed in Cases 13 and 14 is investigated. This last model provides corresponds to the extreme condition when the three loading transfer points for each HBE are restrained from moving vertically and from rotating. A monotonic pushover analysis was conducted for all six cases and their results are displayed in Figure 4-35 up to a 5% top story drift in the West direction (i.e., positive excursion).
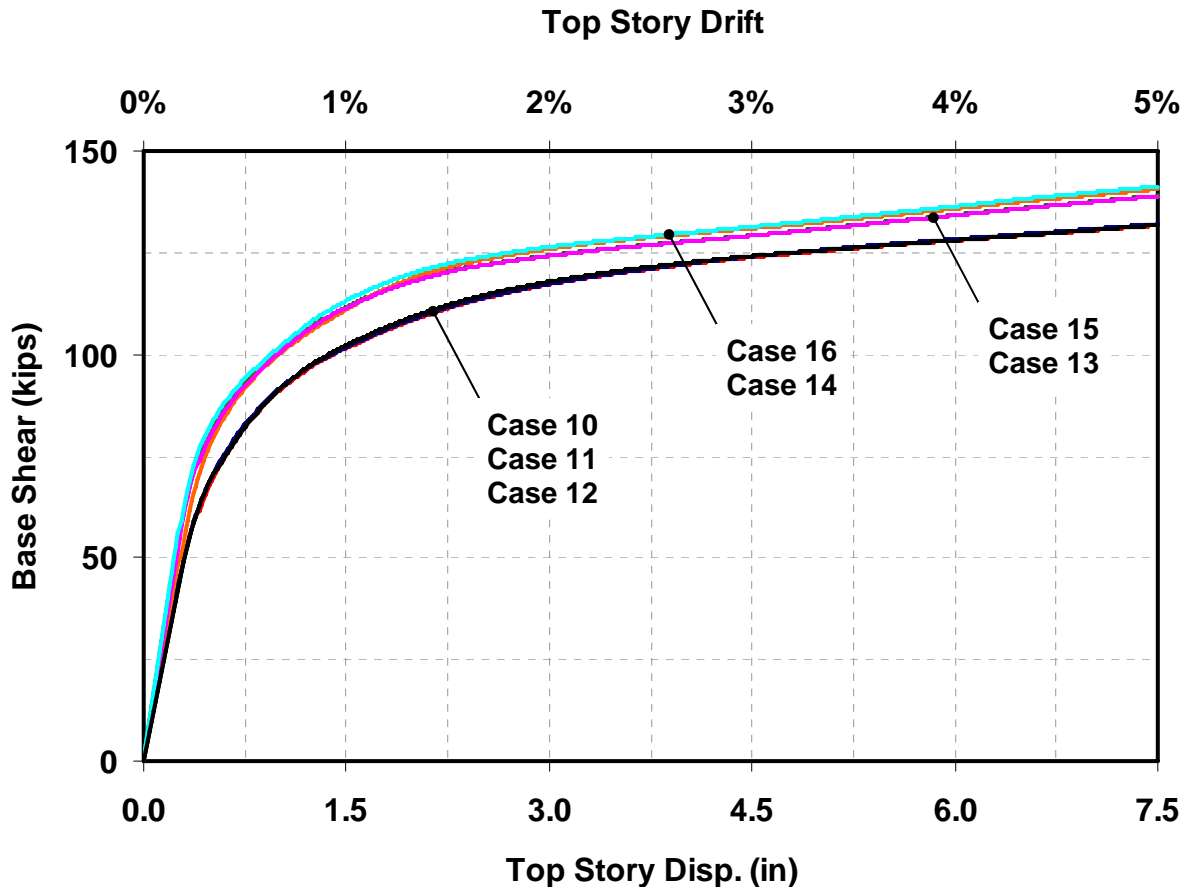
Figure 4-35 Pushover Curve for Several Scenarios

Several observations from these results are provided as follows.

- Changing the location of the applied story forces, from the HBEs centerline to their top flange, did not impact the specimen response. When comparing the results of Case 11 in this figure with that of Case 10, a negligible difference is obtained between the two.

- The same observation is made when comparing the impact of constraints. The un-constrained and constrained results (i.e., Case 11 versus Case 12 and Case 13 versus Case 15) were practically the same, irrespective type of restraints assigned. In other words,

180

retaining or allowing relative displacements along the HBE direction between the points where story force is applied does not impact the results.

- In contrast to the above cases, significant result differences were obtained when restraints were provided either along the vertical DOF, about the rotation DOF, or on both DOFs. However, only marginal differences were observed among these restrained cases (i.e. Cases 13 to 16). When the specimen experienced 1.41% top story drift (equal to the target displacement of Step 6a), the base shear for the restrained cases was as high as 11 kips above that for the unrestrained cases (i.e., Case 11 and Case 12). This increase for the restrained cases was caused by yielding of strips adjacent to the upper-East corners of the second and third story infill plates, which in the unrestrained cases remained elastic. In other words, as a result of restraining the vertical movement or/and rotation of upper HBEs at three locations of load transfer joints, complete yielding of the first and second story infill plates was observed in the restrained cases while partial yielding was observed in the unrestrained cases.

Nonetheless, the increase of base shear by 11 kips in the modified analytical model could only account for 1/3 of the base shear discrepancies between the results initially predicted by the analytical model (Case 10) and the obtained experimental results at displacement Step 6a. A 23 kip difference between the two remained. Changing the material properties in the analytical model from the average values to the maximum possible values obtained from the tensile coupon tests was another possible option to be investigated. When considering this modified material properties into Case 13 model, with 5 to 10% increases from the average to the maximum yield strength values of the steels used (Section 4.3.1), only 5% increases above the 11 kip base shear were obtained and did not resolve the remaining 23 kip base shear discrepancies.

Furthermore, HBE maximum vertical deformation in the restrained cases was significantly lower than that in the unrestrained cases. When the specimen model experienced 1.41% top story drift, HBE3 and HBE2 of the unrestrained models deformed of approximately 0.4 in., while the same HBEs in the restrained models only experienced less than 0.1 in. deformations. When the model experienced 4% top story drift, the maximum vertical deformations were approximately 1.0 and 0.2 in. for the same HBEs in the unrestrained and restrained models, respectively. This result

181

provided an insight as to why the progression of plastic incremental deformations on the HBEs was not as pronounced as originally predicted. If the loading transfer setting actually used in displacement Step 6a would have been continued up to 4% drift, the maximum deformation of the upper two HBEs (predicted by the restrained cases) would only have reached approximately 0.2 in. Note that this was the main motivation for changing the load transfer mechanism starting in displacement Step 6b by removing the bolts at the quarter- and the third-quarter-span connecting angles, leaving only 4 bolts at the mid-span of each HBE to the transfer actuator forces to the specimen. In other words, this modified transfer mechanism was basically an attempt to allow the HBE vertical deformation to progress while the actuator load increased, as shown by the unrestrained models. Observation on HBE rotations at the load transfer points provided additional support for this modification. As shown in Table 4-4 for Case 11 model, when the specimen reached 1.5 and 4% drift, HBE rotations were relatively large at the quarter- and the third-quarter-span points, while negligible rotation was observed at the mid-span.

Table 4-4 HBE Rotation at Load Transfer Points (Case 11)

HBE	Rotations when Specimen at 1.5% Top Story Drift (radians)			Rotations when Specimen at 4.0% Top Story Drift (radians)		
	¼-Point	Mid-Point	¾-Point	¼-Point	Mid-Point	¾-Point
3	0.012	0.001	0.008	0.028	0.004	0.017
2	0.014	0.0004	0.010	0.032	0.007	0.020
1	0.009	0.003	0.004	0.018	0.003	0.007

4.5 Discussion of Experimental Results

Several key experimental results are presented in this section and reviewed in light of the objectives of this experimental program (outlined in Section 3.1). The global behavior is presented first in terms of hysteretic behavior of story shear versus specimen lateral displacement followed by presentation of selected local behavior results, such as plastic hinge and infill plate yielding distribution, HBE vertical deformations, and moment-rotation hysteresis. Complementing the qualitative experimental observations presented in Section 4.3, recorded strain gauge

and string pot data on the boundary frame and the panel, respectively, are presented to quantitatively describe plastic hinge and infill plate yielding distributions. Recorded HBE vertical deformation can substantiate the accumulation of plastic incremental deformations. Assessment of the performance of special-moment resisting connections is conducted by reviewing moment-rotation data. Comparison to the preliminary nonlinear static analysis (Section 3.9) is presented wherever applicable.

4.5.1 Hysteretic Behavior: Story Shear versus Specimen Lateral Displacement

Hysteretic plots of story shear versus inter-story displacement are presented in Figure 4-36, from the third to the first story levels in parts (a) to (c), respectively. For completeness, the base shear versus top story displacement hysteresis (previously displayed in Figure 4-2h) is presented in Figure 4-36d. In general, each hysteretic loop resembles that expected for an unstiffened thin steel plate shear wall and reported in past experimental research; this hysteretic curve exhibits pinching, stable and ductile behavior when undergoing large lateral drifts, and a relatively small strength degradation between cycles at the same displacement step (i.e., defined as "in-cycle" strength degradation per FEMA-440a). Specific to this experiment, strength degradation beyond the maximum story shear is not observed because the experimental program was concluded before that behavior could substantially develop (Section 4.3.3).

During the last cycles of the experiment, maximum inter-story drifts of 3.73, 3.61, and 3.27% were reached at the first, second, and third story panels, respectively. These values were comparable to the maximum top story drift (i.e., third story displacements divided by the specimen total height) of 3.22% recorded at the end of displacement Step 10d. The corresponding maximum story shears were 180.6, 147.9, and 93.3 kips for the first, second, and third story, respectively. In contrast with the upper story hysteretic curves, the first story hysteretic curve displays significant un-symmetric maximum displacement obtained during the positive and negative excursions. The maximum inter-story drift reached within the West excursion was 2.67% while within the East excursion 3.73% inter-story drift was achieved.

Two other parameters can be identified from the hysteretic plots, namely: the elastic stiffness and energy dissipated per cycle (EDC). Elastic stiffness was calculated using results from
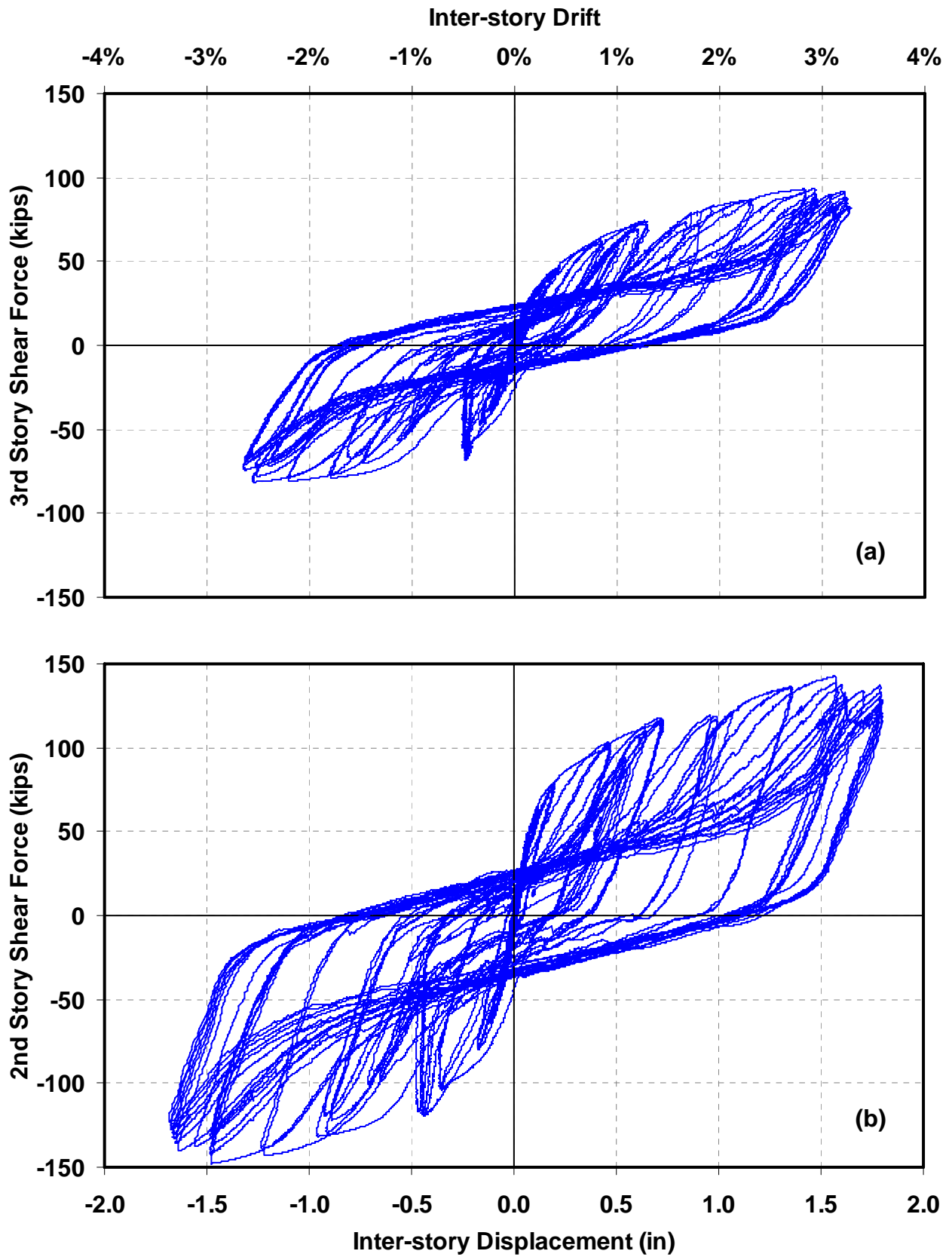
Figure 4-36 Story Shear Force versus Inter-Story Displacement: (a) 3rd Story; (b) 2nd Story
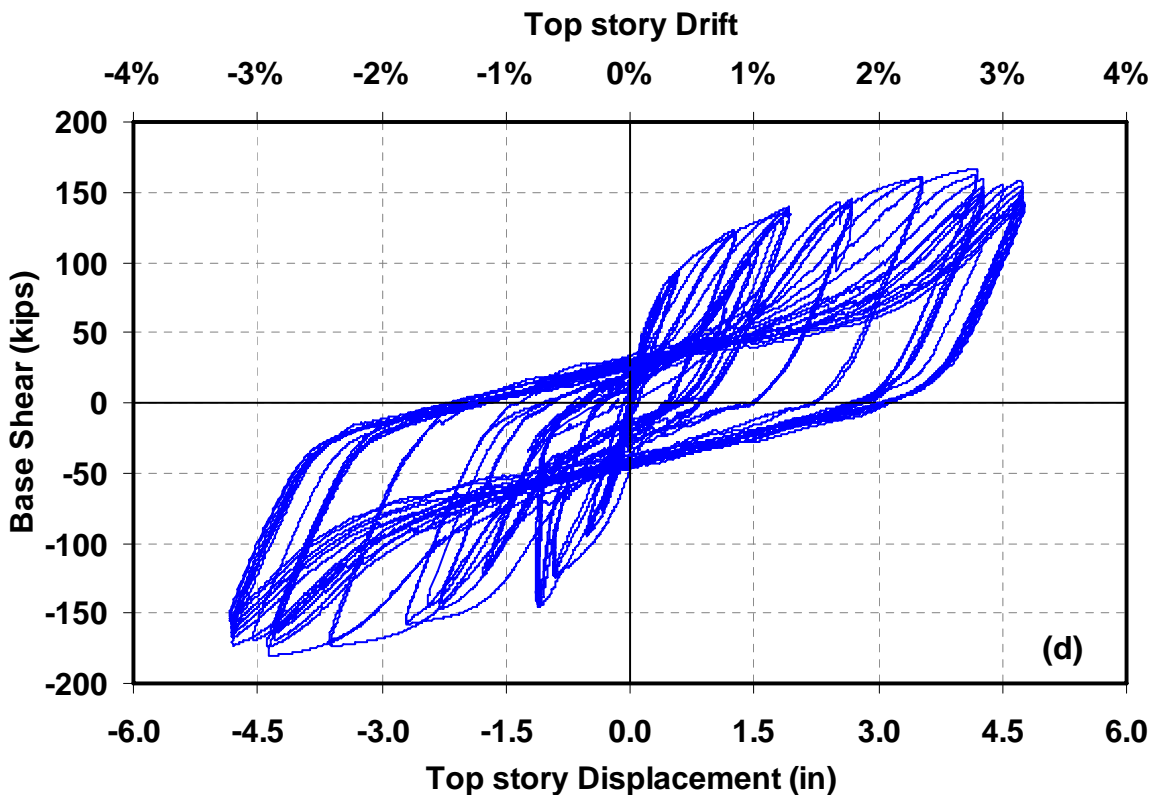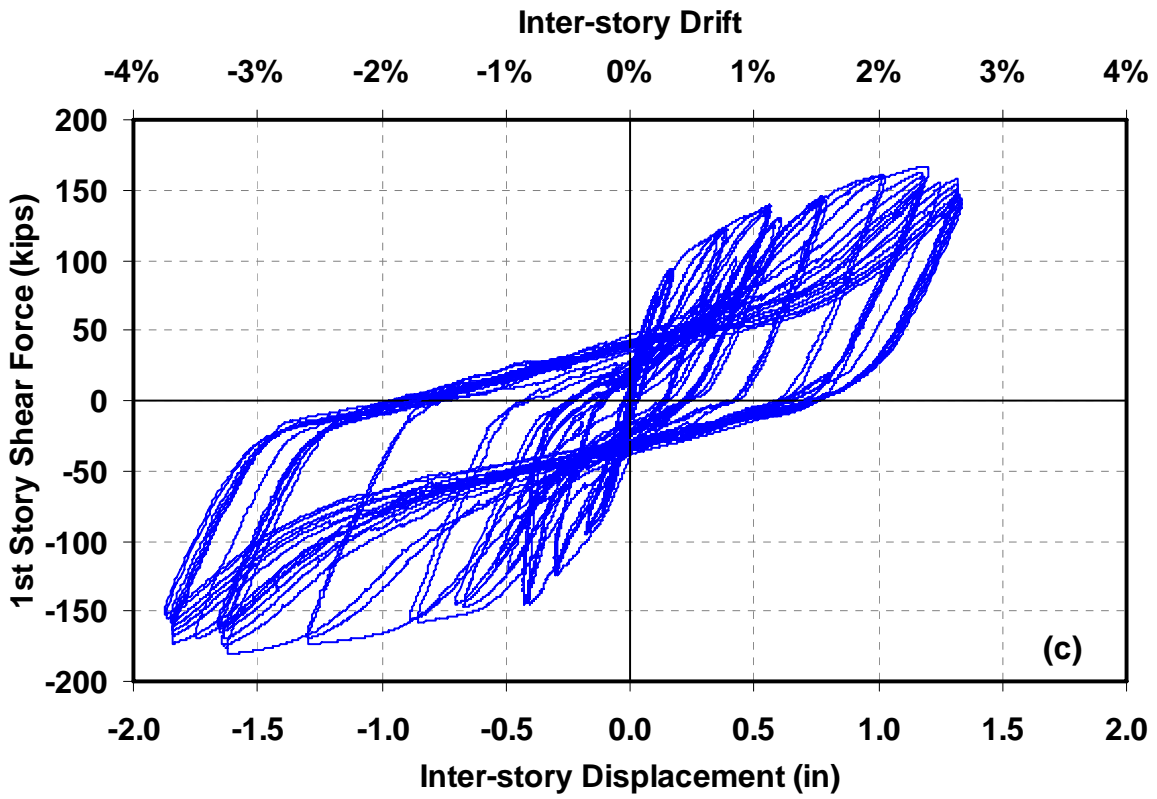
Figure 4-36 Story Shear Force versus Inter-Story Displacement – Cont'd: (c) 1st Story; (d) Base Shear versus Top Story Displacement

displacement Step 3 when maximum displacement at the top story reached 2/3 of the effective yield, using the following equation.

$$K = \frac{\left|V^+_{max}\right| + \left|V^-_{max}\right|}{\left|\Delta^+_{max}\right| + \left|\Delta^-_{max}\right|} \tag{4-1}$$

where Δ^+_{max} and Δ^-_{max} are the maximum positive (West) and negative (East) displacements and V^+_{max} and V^-_{max} are the story shears corresponding to Δ^+_{max} and Δ^-_{max}, respectively. The resulting elastic stiffness for the first, second, and third story panels are 1031, 793, and 394 kips/in, respectively. The EDC was calculated by integrating the area enclosed by a hysteretic loop in one full cycle of loading. For example, the EDC calculated from the first cycle of displacement Step 10d is 184, 171, and 84 kips-in for the first to third story panels. This trend of decreasing elastic stiffness and EDC from the lower to the upper story is expected in this SPSW specimen which thicker infill plate used on the first story and progressively decreasing infill plate thickness going toward the upper story.

4.5.2 Plastic Hinge and Infill Plate Yielding

Inspection of the specimen after the test (Figure 4-30) showed (using whitewash flaking as a qualitative indication) that plastic hinges developed at both ends of each HBE and at the base of each VBE. Strain-gauges data at these locations confirmed this behavior quantitatively, which will be further addressed in Section 4.5.4 when presenting moment-rotation hysteresis results. As for the development of in-span plastic hinge, several discrepancies were observed between the results obtained from the preliminary nonlinear static analysis and the experiment. In this case, numerical models predicted that in-span plastic hinge should have occurred on HBE0 and at the upper two HBEs (Figure 3-27d), while experimentally, evidence of in-span plastic hinge was only observed on HBE0 (more significantly at the quarter-span point from the East VBE (Figure 4-30n) and to a lesser extent at the third-quarter-span point (Figure 4-30o) and on HBE3 (Figures 4-30b and 4-30d). The actual location of in-span plastic hinge was not at HBE0 mid-span as initially predicted by the numerical model but slightly closer to the one-quarter-span. Moreover, yield lines distributed along HBE flange (Figures 4-30g and 4-30i) indicated that plastification of the upper two HBEs was not localized within a finite length as in the case of HBE0 but rather distributed within a longer span. Moments estimated from strain-gauge data (i.e.,

186

SGBx-2x and SGBx-3x in Figure 3-21b) confirmed that yield moment had been reached at these locations.

From the final condition of the infill plates presented in Section 4.3.3, qualitative indication suggested that complete infill plate yielding occurred in each panel. Flaking of whitewash was noted roughly over the entire surface of each panel (Figure 4-29). Quantitative measurements of infill plate yielding distributions are presented in Figure 4-37 for both North and South sides. The figure provides information of plate yielding at 5 measurement locations for the upper two infill plates (i.e., measured by 5 string pots per each direction per floor as shown in Figures 3-21c and 3-21d) and at 7 locations for the first story infill plate (i.e., measured by Krypton sensors as shown in Figure 3-21a). Interestingly, plate yielding did not develop simultaneously (i.e. at the same stages of loading), but rather progressively, from the first occurrence of yielding in displacement Step 3 (= 0.31% top story drift) to the last one in displacement Step 9b (= 3.0% top story drift). This is because in-span plastification of HBE0 contributed to the delay of plate yielding at the lower corners of the first story infill plate. However, at the conclusion of the test, it appeared that the entire infill plate had yielded, as data recorded from the string pots installed diagonally to measure plate elongation (Figure 4-37) indicated strains in excess of the yield strain (string pot displacement divided by measured span). Therefore, the theoretically predicted incomplete yielding of the infill, with the upper corners of the second and third story infill plate as well as at the lower corners of the first story infill plate (Figure 3-27d) remaining elastic, seems to not have happened.

The initial load transfer setting in the first part of the experimental program contributed in part to this behavior especially at the upper infill plates. When vertical movements of the upper two HBEs were limited, infill plates adjacent to the panel corners could elongate beyond its yield displacements.

4.5.3 Deformation of Boundary Frame

Recorded vertical deformations for each HBE during this cyclic pushover testing are presented in Figures 4-38 to 4-41 for HBE3 to HBE0, respectively. Results shown for the upper two HBEs were taken from the string pots attached to the mid-spans of HBE3 and HBE2 (i.e., data recorded

187
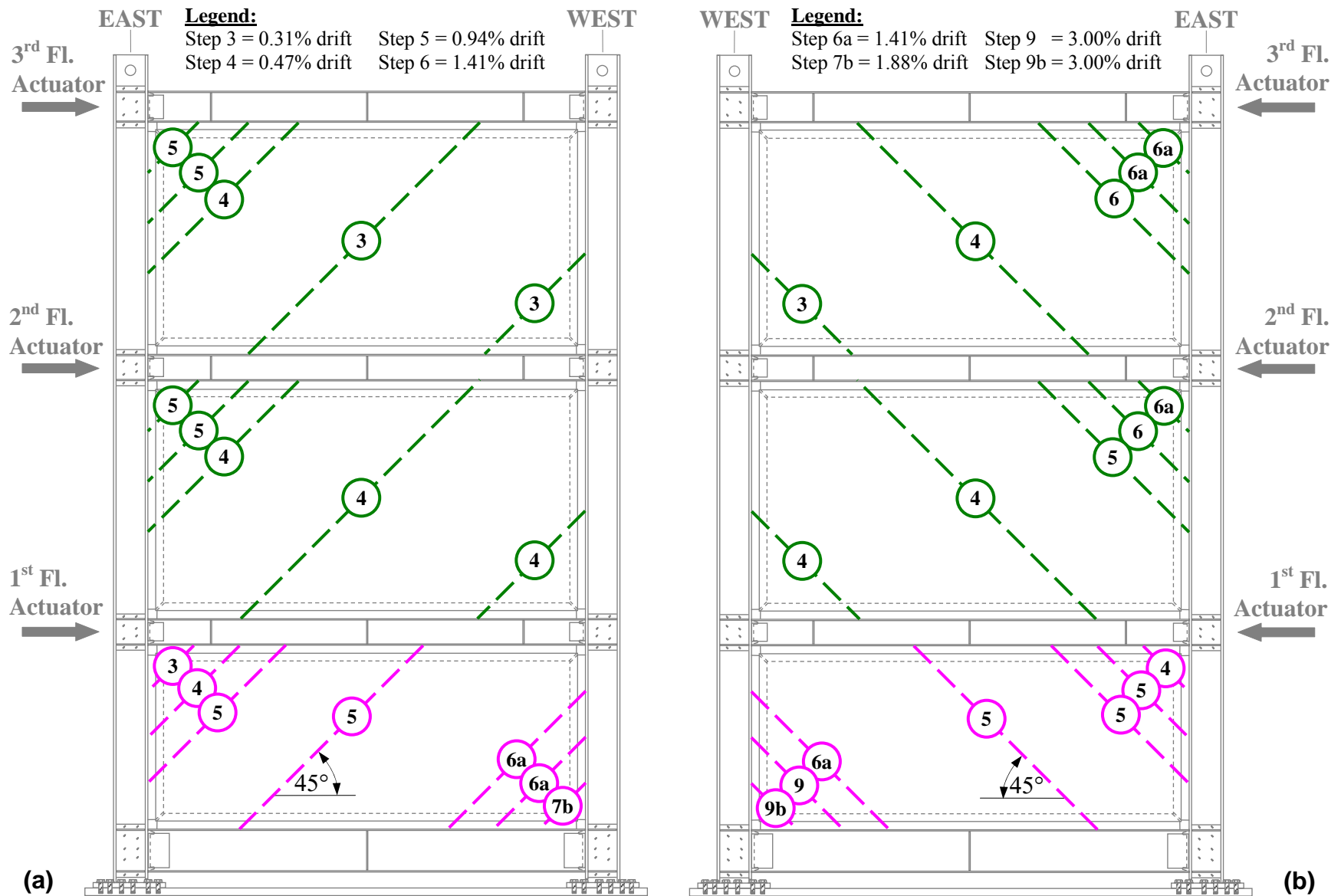
Figure 4-37 Infill Plate Yielding Distributions: (a) North Side; (b) South Side
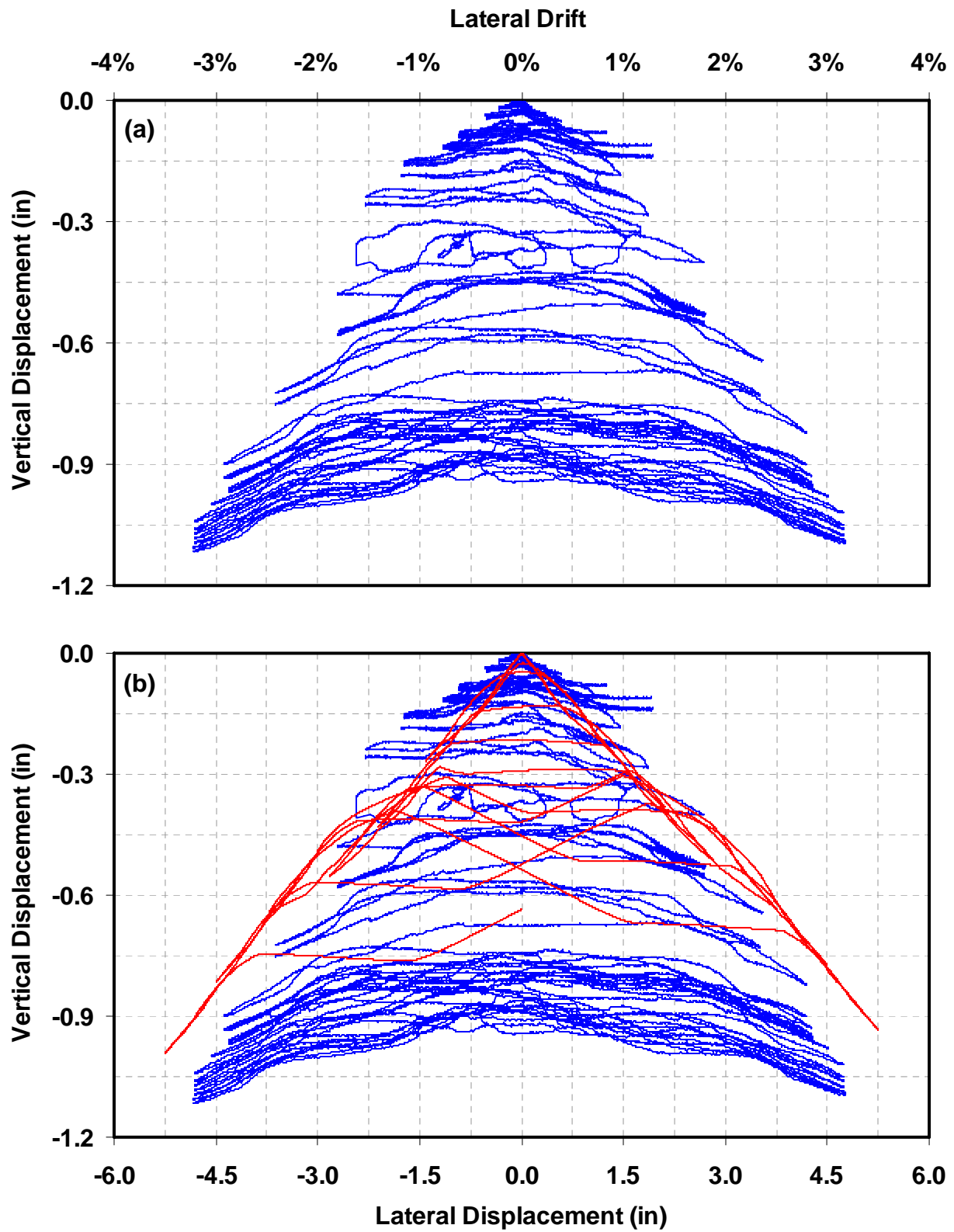
Figure 4-38 HBE3 Vertical Displacement: (a) Experimental Results;
(b) Experiment vs. Theoretical Comparison

189
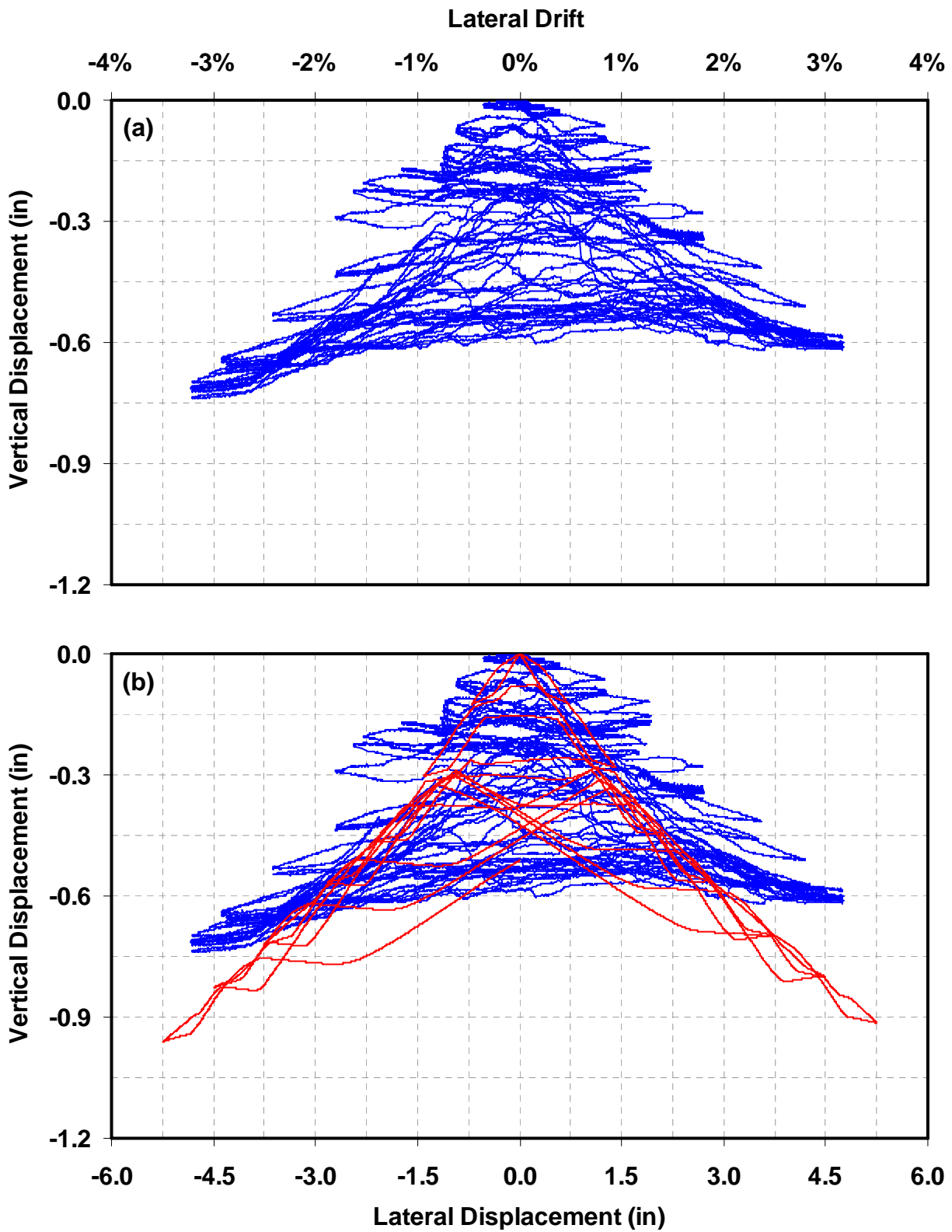
**Figure 4-39 HBE2 Vertical Displacement: (a) Experimental Results;
(b) Experiment vs. Theoretical Comparison**
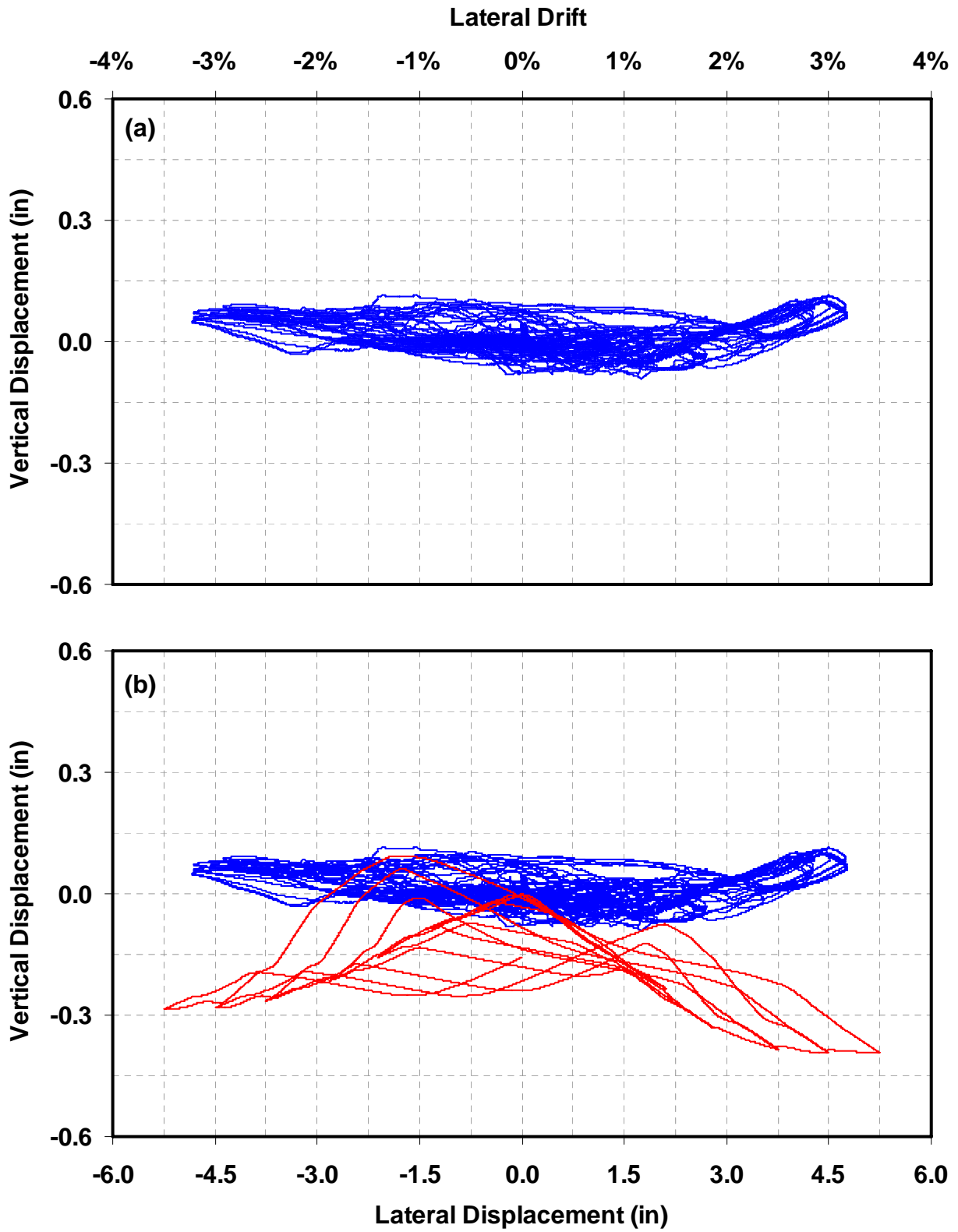
**Figure 4-40 HBE1 Vertical Displacement: (a) Experimental Results;
(b) Experiment vs. Theoretical Comparison**
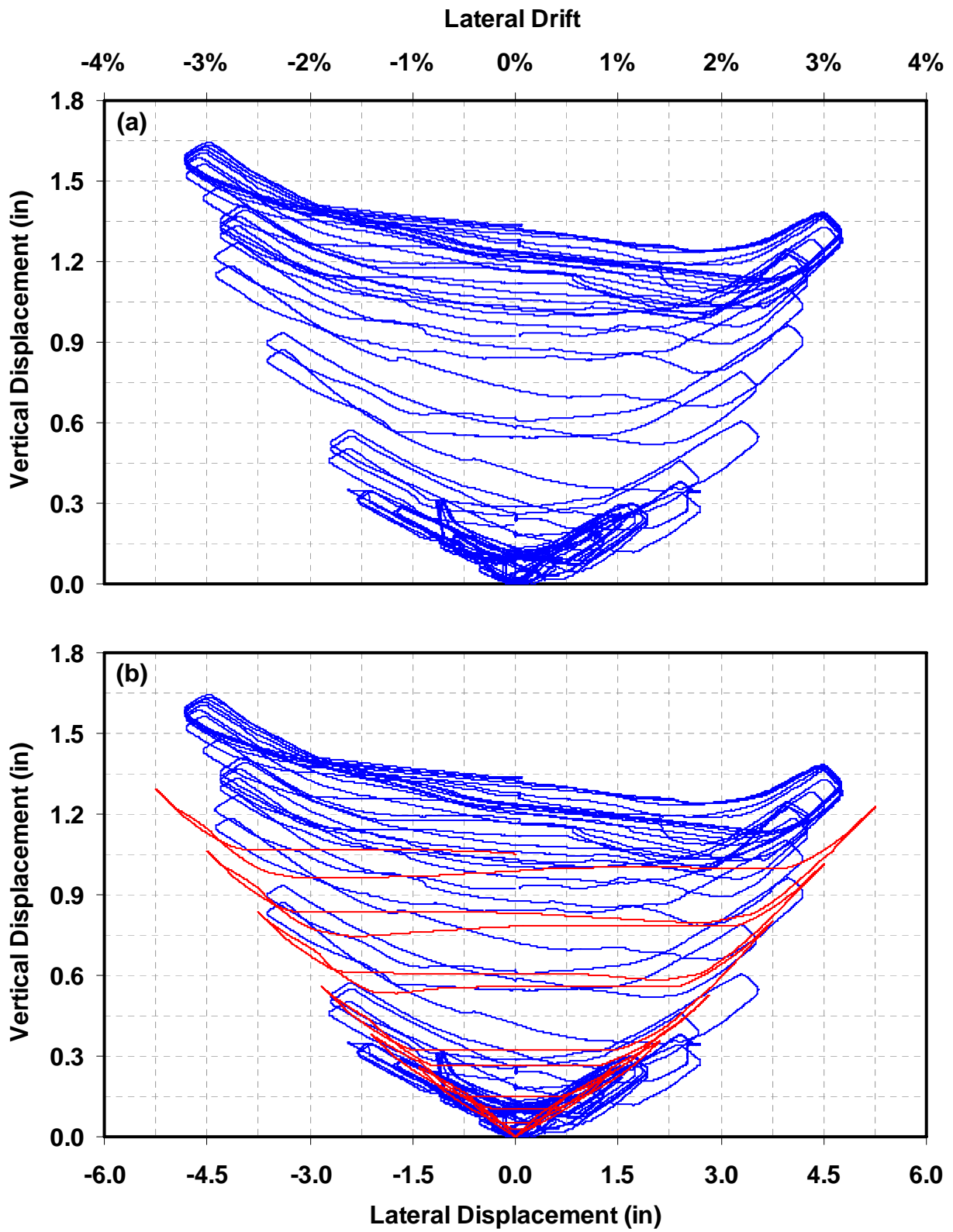
Figure 4-41 HBE0 Vertical Displacement: (a) Experimental Results; (b) Experiment vs. Theoretical Comparison

by SPB3-2 and SPB2-2, Figure 3-21a) while that for the lower two HBEs were taken from the Krypton sensors adjacent to the mid-spans of HBE1 and HBE0 (i.e., data recorded by KRB1-4 and KRB0-3, Figure 3-21a). Note that Krypton sensors were not available to record HBE1 and HBE0 vertical deformations at their mid-spans because the angles used to provide lateral supports at these locations (Figure 3-18c) blocked the view of the beam at that location. However, the deformation profile along the span of these HBEs is presented toward the end of this section. As mentioned in Section 3.7.4, the string pots attached to the upper two HBEs measured relative movements of these HBEs in respect to the gravity mass plates. Additional string pots added to monitor rigid body movements of the mass plate in respect to each other and the ground (Figure 3-21e) confirmed that the vertical movements of the mass plate were insignificant (e.g., maximum values of 0.14 in. when reaching 3.33% top story drift within displacement Step 10d). Hence for simplicity, the results shown in Figures 4-38 and 4-39 are the displacement records taken directly from the string pots that attached to the mass plates (i.e., not corrected to account for the negligible the mass plate vertical deformations relative to the ground). With respect to HBE3 vertical deformations, data from the second cycle of displacement Step 7a were excluded because the displacements recorded during this cycle have been affected by the large displacement of the gravity column system that occurred relative to the SPSW specimen when the second story connecting angles fractured (Section 4.3.2), and are therefore not reliable.

Although evidence of in-span plastic hinge (inferred from yield line in the whitewash) was only visible on HBE0, the results in those figures indicate that accumulation of plastic incremental deformations were apparent not only on HBE0 but also on HBE2 and HBE3. The "backbone" displacements (defined as the displacement when the structure reached the maximum target drift of every cycle) progressively increased from practically zero in the first displacement step to 1.64, 0.76, and 1.11 in. respectively for HBE0, HBE2, and HBE3 in the last displacement step (when the specimen was cycled up to 3.33% top story drift amplitude). The same trend was also observed on the progression of the "residual" displacement (defined as the displacement when the structure returned to its original position at 0% drift). After the last displacement step, the residual displacements were 1.34, 0.63, and 0.91 in. for the same respective HBEs. In contrast with the other three HBEs, HBE1 has relatively small vertical deformation, as predicted by the

preliminary nonlinear static analysis of the specimen (Section 3.9) which indicated that in-span plastification was not expected to develop on HBE1.

The accumulation of plastic incremental deformations predominantly occurred in the third part of the experimental program (i.e., displacement Steps 7b to 10d). For example, the backbone displacement of HBE3 at the end of the 21 cycles in the first part of the loading program (i.e., displacement Step 6a) was 0.14 in., which is approximately 13% of the maximum value obtained at the conclusion of the experimental program. During the second part of the test (over a total of 9 cycles), the backbone displacement progressively increased from 0.22 in. at the end of displacement Step 6b, to 0.48 in. at the end of displacement Step 7a. At this point, the backbone displacement reached approximately 43% of the maximum value obtained at the end of the test. The remaining 57% of the total plastic deformation accumulations occurred within the 18 cycles applied during the last part of the experimental program. Obviously, those large lateral drift targets imposed in the third part of the testing program (i.e., from 1.88 to 3.33% top story drift) occurred after the load transfer mechanism was modified to ensure development of the HBE vertical movement, which was apparently not free to deflect during the first part of the test. This effect becomes clearer when comparing the experimental results to the theoretically predicted ones. The two are plotted together in Figure 4-38b. The backbone deformations for both cases are somewhat the same for each HBE. In contrast with the backbone deformation, accumulation of residual deformations was actually faster during the experimentation program compared to that predicted by the nonlinear static analysis because the numerical model did not consider material fatigue life and degradation. This indicates that HBEs were actually less likely to rebound after they reached a maximum target displacement and returned to their original position at 0% drift. This was especially true when the specimen experienced a large displacement step. Note that plastification of the top HBE was affected due to rotation of the load-transfer mid-span connecting angles (Figures 4-9 and 4-12); this also influenced the HBE3 vertical deformations reported in Figure 4-38a, but the actual contribution of this effect to the total HBE3 plastic deformations was difficult to quantify.

Moreover, the actual HBE2 vertical deformation was smaller than the predicted value. At the last cycle of displacement Step 10d, when the specimen reached the negative peak (i.e., East

excursion) at 3.33% top story drift, HBE2 experienced approximately 0.75 in. downward displacement, while the numerical model predicted 0.90 in. However, when the specimen returned to the initial position at 0% drift, both theoretical and experimental results have comparable values of residual vertical deformations. Interestingly, HBE1 vertical deformation obtained from the analytical and experimental results are significantly different (Figure 4-40b). Note that slight adjustments were introduced on the theoretical HBE1 vertical deformations. The one plotted in Figure 3-27b was measured at its mid-span while that in Figure 4-40 was taken from the same locations where the Krypton sensors located (i.e., at 0.375L). This was done for an accurate comparison.

For the bottom HBE, relatively small accumulation of plastic incremental deformations was also observed in the first part of the test (Figure 4-41), even though the HBE was unrestrained by angles in this case: HBE0 was completely free to move vertically throughout the entire test. This can be understood because, during the first part of the test, the specimen actually experienced significantly smaller lateral drifts compared to those imposed by the actuators (Section 4.3.1) such that HBE0 sustained relatively smaller pulling force from the first story infill plate. The actual vertical deformation on HBE0 was larger than that predicted by the SAP2000 model. Damage on the location where lateral torsional buckling occurred on HBE0 during the experiment contributed to this behavior, which the numerical model did not simulate.

A number of Krypton sensors had been installed around the perimeter of the first story panel (Figure 3-21a). Data from those sensors allows observation of HBE0 and HBE1 vertical deformations along their spans as the cyclic load progressed. Figures 4-42 and 4-43 show deformation profiles of HBE0 and HBE1, respectively. In each figure, the results are presented at the positive and negative peaks (i.e., West and East excursions, respectively) of the last cycle for selected displacement steps. Note that the impact of changing the load transfer mechanism (i.e., from the three-point loadings connected to HBEs to the two-point loadings connected to VBEs) on HBE vertical deformations can be observed in Figure 4-43. Krypton sensors recorded somewhat the same deformations at every point along the HBE span within displacement Step 1a to Step 6. Once that HBE became completely un-restrained (i.e., Steps 7b to 10d), the HBE deformation profiles changed significantly.
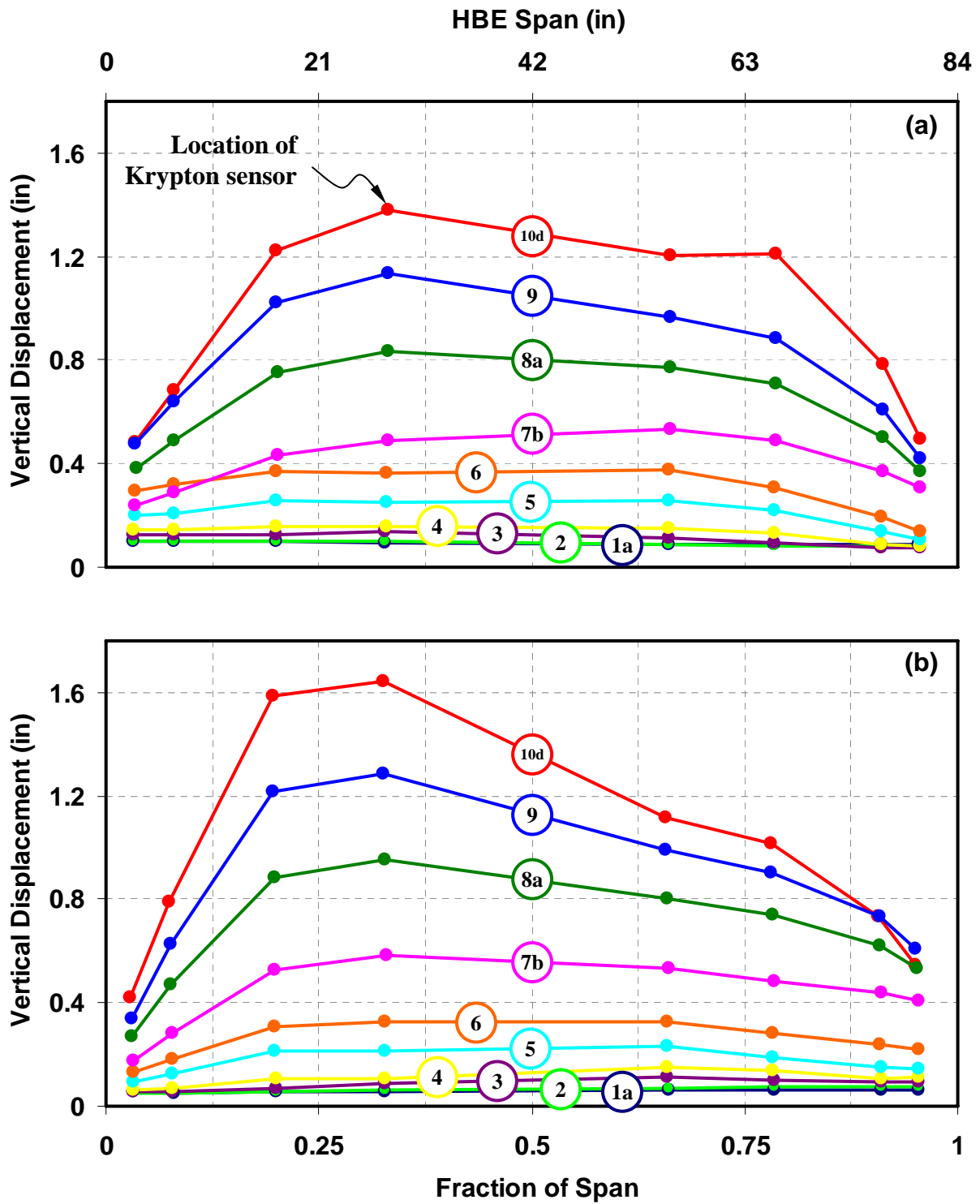
Figure 4-42 Profile of HBE0 Vertical Displacement: (a) West Excursion; (b) East Excursion
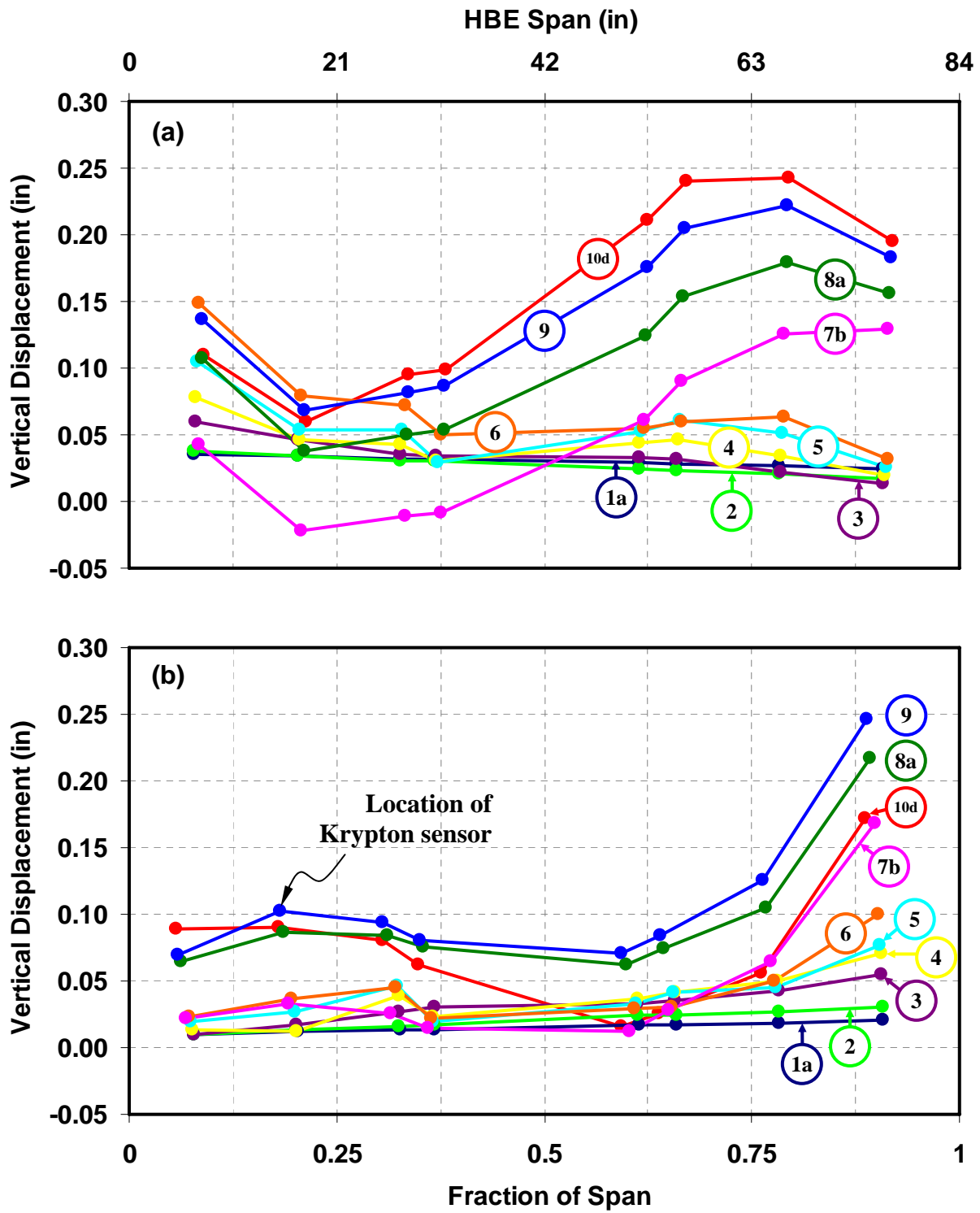
Figure 4-43 Profile of HBE1 Vertical Displacement: (a) West Excursion; (b) East Excursion

Figure 4-44 shows deformations of the west VBE at both the positive and negative peaks of selected displacement steps measured by the string pots. At the early step of loading (i.e., Step 1a to Step 5) toward the West excursion, the column deformation profile was similar to an inverted triangular shape, indicating comparable relative deformations between stories. However, as the load progressed to higher displacement steps, the first story underwent less inter-story displacements compared to the upper stories, as shown by a 'kink' on the column profile (marked as circular area A in the figure). A similar kinked column deformation profile, but to a lesser magnitude, is also observed at the second story within the East excursion (marked as circular area B in the figure). This profile provides insights on the possible cause for the flange yielding patterns observed on the upper VBEs (Figure 4-7 and Figure 4-23a). Lastly, the significant difference of the top story displacement during the East and West excursions (reported in Section 4.5.1 when presenting the hysteretic behavior) can also be observed in this column deformation profile (marked as gap C in the figure).
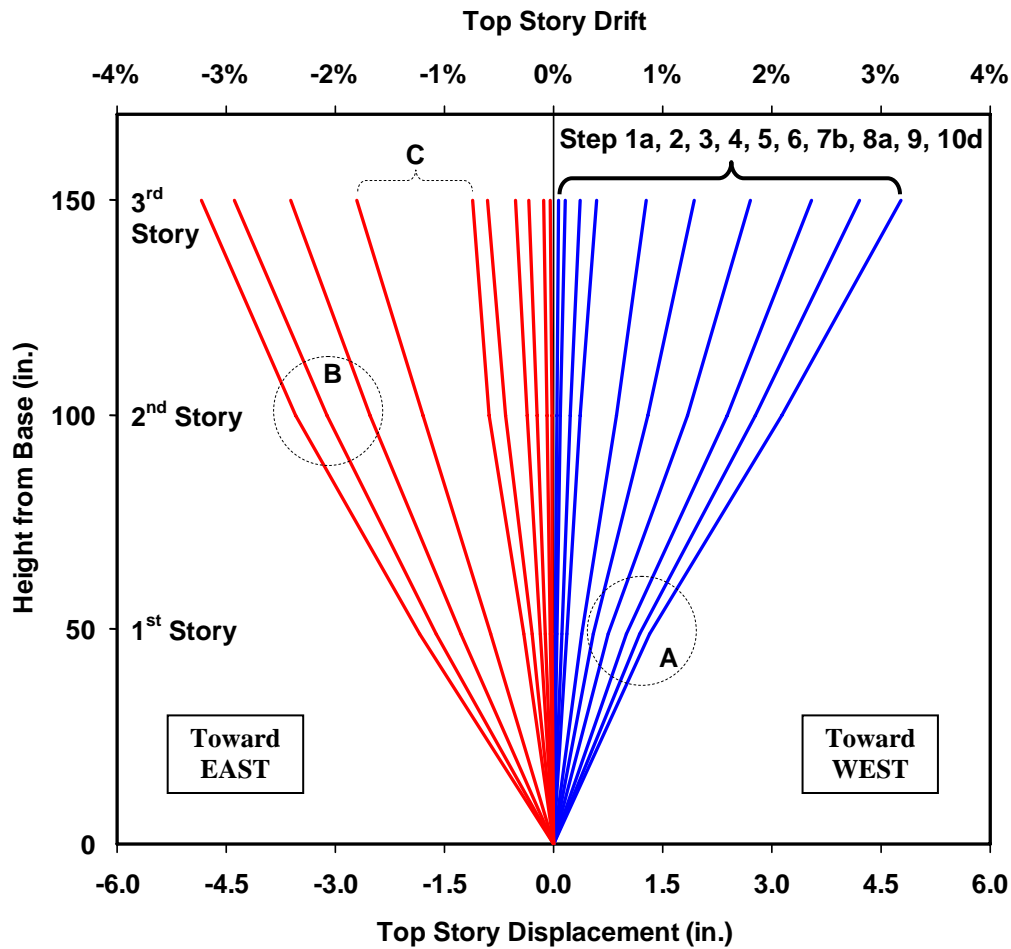
Figure 4-44 Profile of West VBE at the Maximum Displacement of Selected Steps

4.5.4 Moment-Rotation Hysteresis

Experimental data is used to investigate the performance of the special-moment resisting connections used in the specimen, in terms of moment-rotation hysteretic curves. As reported in Section 4.3, after cycling the specimen for a total of 48 cycles up to a maximum top story drift of 3.33%, HBE-to-VBE connection fractures occurred at both ends of HBE1 and at the East end of HBE2 (Figure 4-32). The procedure used to estimate moments and rotations indirectly from strain-gauges and string pots data is first described.

As presented in Figure 3-21b, four strain-gauges were clustered at four critical sections along the span of each HBE. Moments at one particular section were indirectly estimated from data recorded by these four strain-gauges. The following procedure outlines steps to calculate boundary element internal moments as follows:

1. Based on the position of strain gauges affixed to boundary elements, each strain-gauge records at the same time strains generated by internal axial forces and moments. To obtain flexural strains, axial strains must be excluded from the total strains. Axial strains at one particular cross-section are estimated using the following equation.

$$\varepsilon_{\text{axial}} = \frac{\varepsilon_1 + \varepsilon_2 + \varepsilon_3 + \varepsilon_4}{4} \tag{4-2}$$

   where ε_1 to ε_4 are the strains recorded by the first to the fourth strain gauges (Figure 3-21e).

2. Ideally, for this specimen, the remaining strains after excluding the axial strains are flexural strains generated by strong axis bending. However, unexpected weak axis bending generates additional strains. To separate flexural strains caused by strong axis bending (ε_{fx}) from those caused by weak axis bending (ε_{fy}), the following relationship is assumed:

$$\varepsilon_{\text{f\_}i} = \varepsilon_{\text{fx\_}i} + \varepsilon_{\text{fy\_}i} \tag{4-3a}$$

   together with the following equalities:

$$\varepsilon_{\text{fx1}} = \varepsilon_{\text{fx2}} = -\varepsilon_{\text{fx3}} = -\varepsilon_{\text{fx4}} \tag{4-3b}$$

$$\varepsilon_{\text{fx2}} = \varepsilon_{\text{fx4}} = -\varepsilon_{\text{fx1}} = -\varepsilon_{\text{fx3}} \tag{4-3c}$$

3. Once strong bending flexural strains are obtained, cross-section curvature can be estimated using the following equation

$$\phi = \frac{\varepsilon_{\text{fx}}}{h/2} \tag{4-4}$$

4. Finally, moment at a particular cross-section can be estimated using the following normalized moment curvature equations taken from Bruneau *et al.* (2011).
a. When y* is located in the flange:

$$\frac{M}{M_y} = \frac{\phi}{\phi_y}\left(1 - \frac{bd^2}{6S}\right) + \frac{bh^2}{4S}\left[1 - \frac{1}{3}\left(\frac{\phi}{\phi_y}\right)^2\right] \tag{4-5}$$

b. Otherwise, when y* is located in the web:

$$\frac{M}{M_y} = \frac{M_p}{M_y} - \left(\frac{t_w d^2}{12S}\right)\left(\frac{\phi}{\phi_y}\right)^2 \tag{4-6}$$

where y* is the distance from the cross section neutral axis to the location where strain reaches the yield point ε_y; b is the flange width; d is the total depth of boundary element section; h is the web length or the distance between top and bottom flanges; t_w is the web thickness; S is the elastic section modulus about the strong axis; M_y and ϕ_y are the yield moment and yield curvature, respectively; and M_p is the plastic moment. Values of the last three variables are calculated as follows:

$$M_y = F_y S \, ; \; M_p = F_y Z \, ; \; \phi_y = \frac{M_y}{EI} \tag{4-7}$$

where F_y is the steel yield strength (obtained from the coupon test); Z is the plastic section modulus about the strong axis, E is the Young's modulus of elasticity; and I is the strong axis moment of inertia.

When processing strain gauges data in the second step of the above procedure, the resulting flexural strains in the weak axis bending on the South and North flange were not symmetric. No substantial effort however was given to resolve this phenomenon. It was considered that unidentified factors contributed to this outcome and their impacts would not significantly affect the intended observations of this sub-section. Moreover, cross-section rotations were calculated

using (3-2). String pot data were used to estimate cross-section rotations for HBE3 and HBE2, while Krypton readings were used for HBE1 and HBE0. However, the string pot attached to the top flange of HBE3 adjacent to its connection to the East VBE either failed to record experimental data or recorded string elongations so unreasonably high that they were deemed incorrect during post-processing. Both string pots adjacent to HBE2's East connection worked well only during displacement Step 1a to 7a (they appeared to work during displacement Step 7b to Step 10d, but post-processing showed that no experimental data but noises were recorded instead). It was also found out during post-processing that the Krypton readings did not provide reasonable data. Hence, cross-section rotations were only available for HBE3 and HBE2 at their connections to the West VBE. Their normalized moment-rotation hystereses are shown respectively in Figures 4-45 and 4-46 compared to their theoretical counterparts previously presented in Figure 3-27.

While the results confirm the initially predicted un-symmetric hysteretic curves, some behavioral differences are observed between the experimental and theoretical observations. First, although the predicted HBE3 maximum rotation is comparable to that obtained from the experimental program, their "rotation ranges" were somewhat different. Here, rotation range is defined as the absolute difference between rotations at the positive and negative extremes of one particular displacement step/cycle. When the specimen was cycled up to the maximum target drift of 3.33% within the last displacement step, HBE3 maximum rotation reached 0.054 radians (i.e., corresponding to a normalized rotation $\theta / \theta_{0.03}$ of 1.80, where $\theta_{0.03}$ is defined as the required plastic rotation capacity of a special moment resisting frame) compared to 0.052 radians obtained from the cyclic pushover analysis. However, HBE3 rotation range of 0.023 radians were recorded in the 3% cycle, compared to the analytical value of 0.032 radians. The same condition was observed in the subsequent 3.3% cycle as shown in Table 4-5. A second comparison was conducted on HBE2 moment-rotation hysteresis. When the specimen model reached 3.33% target drift, the predicted HBE2 maximum rotation was 0.055 radians, which was 0.015 radians higher than that actually recorded during the experimental program. HBE2 rotation range was also higher in the cyclic pushover analysis than that in the experimental program (e.g., 0.043 versus 0.034 radians in the 3% cycle as shown in Table 4-5).
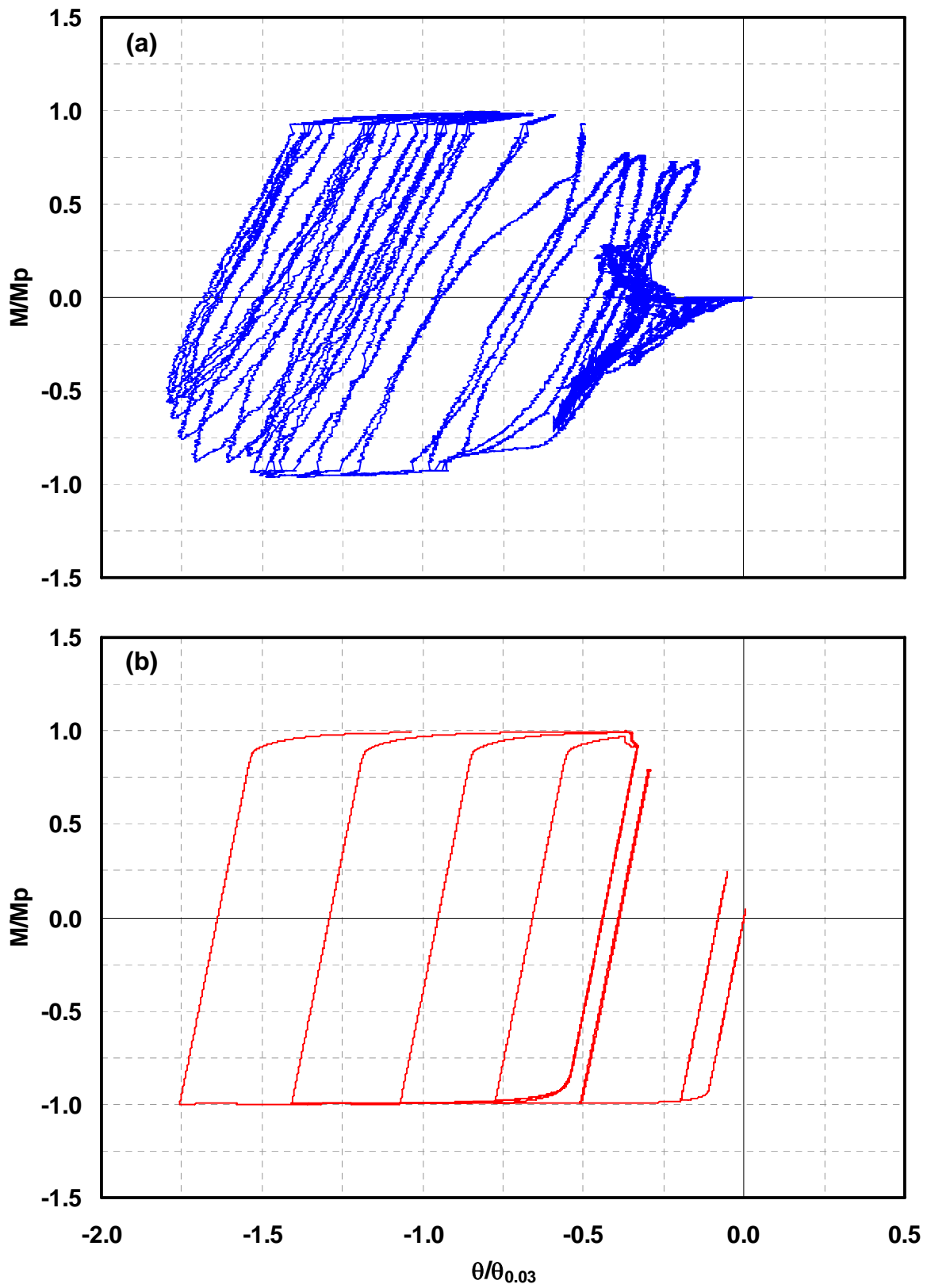
Figure 4-45 HBE3 Normalized Moment-Rotation Hysteresis:
(a) Experimental Result; (b) Analytical Result
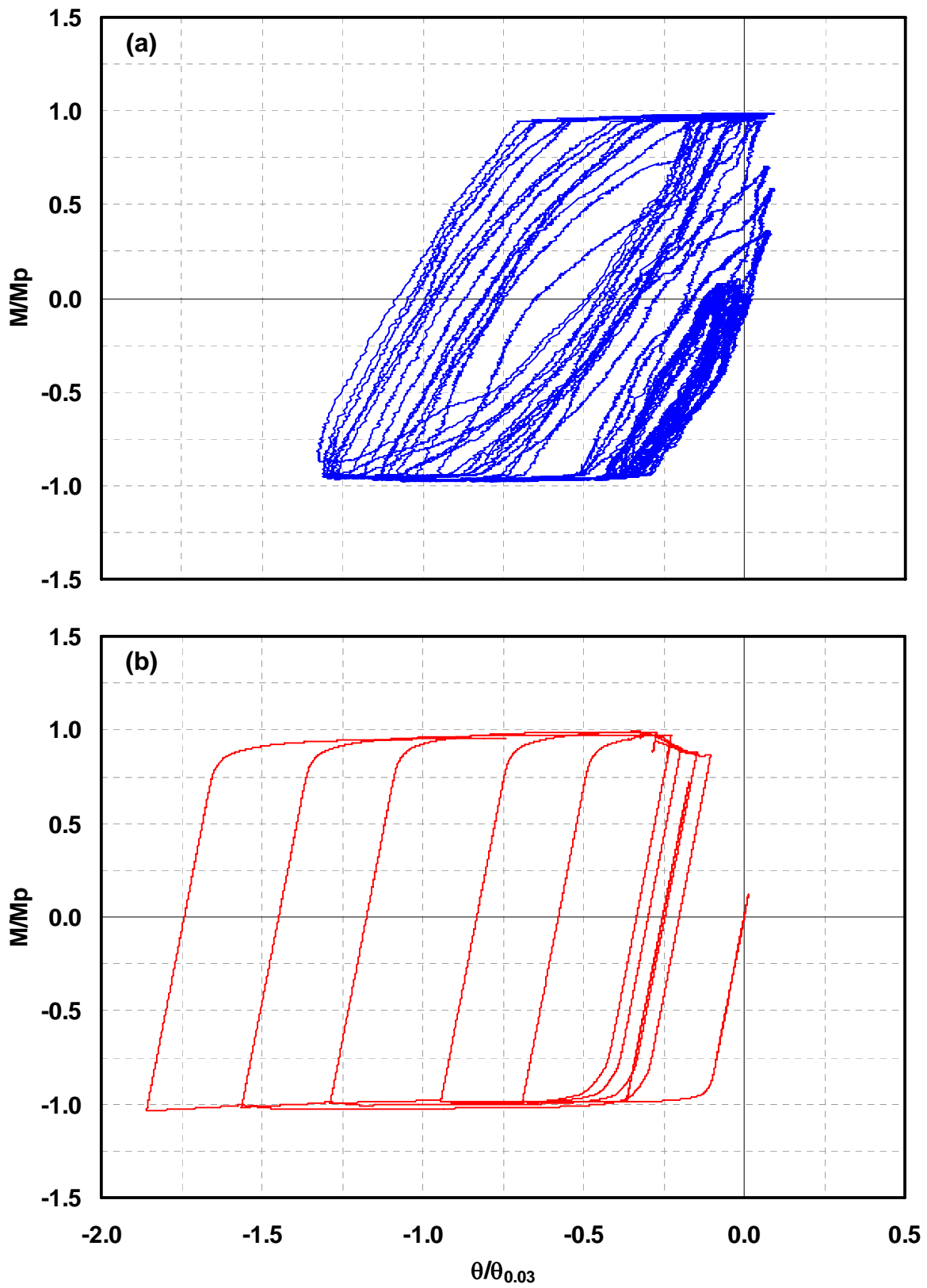
**Figure 4-46 HBE2 Normalized Moment-Rotation Hysteresis:
(a) Experimental Result; (b) Analytical Result**

Table 4-5 Maximum Rotation and Rotation Range in HBE3 and HBE2

HBE	Experiment Result			Analytical Result		
	θ_{max} at 3.3% Drift	θ_{range} at 3.0% Drift	θ_{range} at 3.3% Drift	θ_{max} at 3.3% Drift	θ_{range} at 3.0% Drift	θ_{range} at 3.3% Drift
3	0.054	0.023[a]	0.031[b]	0.052	0.032[e]	0.042[f]
2	0.040	0.034[c]	0.042[d]	0.055	0.043[g]	0.052[h]

Note: (Unit: radians)
[a] Rotation range: –0.014 to –0.037
[b] Rotation range: –0.023 to –0.054
[c] Rotation range: +0.002 to –0.032
[d] Rotation range: +0.002 to –0.040

[e] Rotation range: –0.010 to –0.042
[f] Rotation range: –0.010 to –0.052
[g] Rotation range: –0.004 to –0.047
[h] Rotation range: –0.003 to –0.055

In spite of higher maximum rotation recorded at HBE3 compared to that of HBE2 (i.e., 0.054 versus 0.040 radians), HBE3-to-VBE3 special moment connections remained intact up to the conclusion of the experimental program. In contrast, HBE2 which experienced lower maximum rotation suffered connection fracture at its connection to the VBE2. The significantly higher rotation range recorded on HBE2 compared to that of HBE3 (i.e., 0.042 versus 0.031 radians within 3.3% drift cycle) was considered playing important role to the fracture of HBE2 connection.

4.6 Summary

A cyclic pushover test of a three-story SPSW specimen was conducted. Throughout the displacement loading history, several modifications to the loading protocol and experimental setting were necessary to ensure that the experimental objectives could be achieved. A limited analytical investigation was conducted between test stages to rationalize such modifications and to resolve discrepancies between behavior observed in the first part of the experimental program and that initially predicted by analyses.

Experimental investigation on the three-story SPSW specimen, for which in-span plastic hinging was predicted to develop, demonstrated the development of in-span plastification and

accumulation of plastic incremental deformations in HBE0, HBE2 and HBE3. Note that in-span plastification was not localized within a finite length but rather distributed within a longer span. As a result of the accumulation of plastic incremental deformations, plate yielding did not develop simultaneously, but progressively. However, at the conclusion of the test, it appeared both from qualitative and quantitative measurements that the infill plates had yielded entirely. The theoretically predicted incomplete yielding of the infill, with the upper corners of the second and third story infill plate as well as at the lower corners of the first story infill plate remaining elastic, seems to not have happened.

The initially predicted un-symmetric hysteresis was indeed confirmed during this experimental investigation. Several special moment connections that exhibited this behavior were found to remain intact up to the conclusion of the experimental program in spite of its higher maximum rotations. In contrast, other special moment connections that experienced lower maximum rotations suffered connection fractures. Higher rotation range in the latter connections compared to that in the former ones in large part contributed to the fracture of these connections.

SECTION 5

FINITE ELEMENT INVESTIGATION OF TESTED SPSW SPECIMEN

5.1 General

This section describes the modeling and analysis of the three-story SPSW specimen (Figure 3-2) using the finite element software ABAQUS/Standard (Dassault Systèmes 2009b). Geometry modeling and meshing algorithm, element and material definitions, boundary conditions, constraint, loading input, and techniques to maintain numerical stability are first described in the following section. Results from eigenvalue buckling analysis, monotonic pushover analysis, and cyclic pushover analysis are presented afterward. The effectiveness of the finite element model developed simulating the experimental results is discussed.

5.2 Description of Finite Element Model

5.2.1 Geometry Modeling and Meshing Algorithm

ABAQUS/CAE, a graphical preprocessor program, was utilized to define a Finite Element Model (FEM) of the specimen described in Section 3.2. Geometry modeling started using the *Part Module* by defining each "plate" of the specimen, i.e. boundary element flanges and webs, panel zones, continuity plates, stiffeners, and infill plates independently in its own coordinate system (however, plates that have the same dimensions and material properties only needed to be defined once). The resulting model consisted of 26 such parts.

As a consequence of selecting relatively small W-sections for the specimen HBEs, the attached fish plates and shear tabs significantly affected the ultimate capacity of the HBEs (Section 4). Therefore, they were included in this finite element model. Instead of creating new parts for the fishplates and shear tabs, they were simply modeled directly as *Partitions* of the infill plates and HBE webs, respectively. The same approach was also applied for the doubler plate extension (of 1 in. beyond panel zones as shown in Figure 3-3), which in this case was defined as a partition of

the VBE webs. These partitions were assigned different thicknesses from the rest of their respective plates/parts, following the geometric properties shown in Figures 3-3 and 3-5.

Using the *Assembly Module* tools, the parts were then positioned, relative to each other in a global coordinate system, thus creating one final assembly (note that some parts were used more than once). At this point, the parts are not yet connected to each other, although one part may touch other parts (e.g. HBE flanges and its web). Two approaches are possible to connect the parts: the *Tie Constraints* option allows effectively merging the interface nodes, whereas the *Merge/Cut Instances* tool allows creating a single combined mesh by assembly of compatible meshes between the parts (Dassault Systèmes 2009a). The latter option was chosen for the models described here. This option merged the various parts into one single model and removed any duplicated nodes along intersecting boundaries of adjacent parts. This option also eliminated the need for tie constraints that are more computationally demanding (Dassault Systèmes 2009a).

Meshes were then generated on the merged model within the *Mesh Module* after "seeding" every edge by specifying an average element size desired along that edge (*Edge by Size* rule, Dassault Systèmes 2009a). Here, an average dimension of 1×1 in. per shell element was selected. Using the *Structured Meshing Technique*, the models were meshed entirely using quadrilateral shell elements. To reduce mesh distortion, the *Minimizing the Mesh Transition* option was applied where ABAQUS/CAE automatically creates internal partitions that divide the region into simple "structured" mesh regions and then automatically determines the number of elements (i.e., seeds) along the boundaries of the smaller regions. In general, the mesh so created is not guaranteed to match the number of elements that was previously specified (i.e., "seeded") along the boundaries of the principal region (Dassault Systèmes 2009a). The resulting finite element model, which contained 24,000 shell elements, is shown in Figure 5-1 in solid and wire-mesh views.

5.2.2 Element Definitions

The entire infill plate and boundary elements (HBEs and VBEs) were meshed using the isoparametric S4R shell elements, a four-node doubly curved general-purpose conventional shell element with reduced integration and hourglass control. Each node has six degrees of freedom, three translations (u_x, u_y, u_z) and three rotations (θ_x, θ_y, θ_z). Reduced integration together with
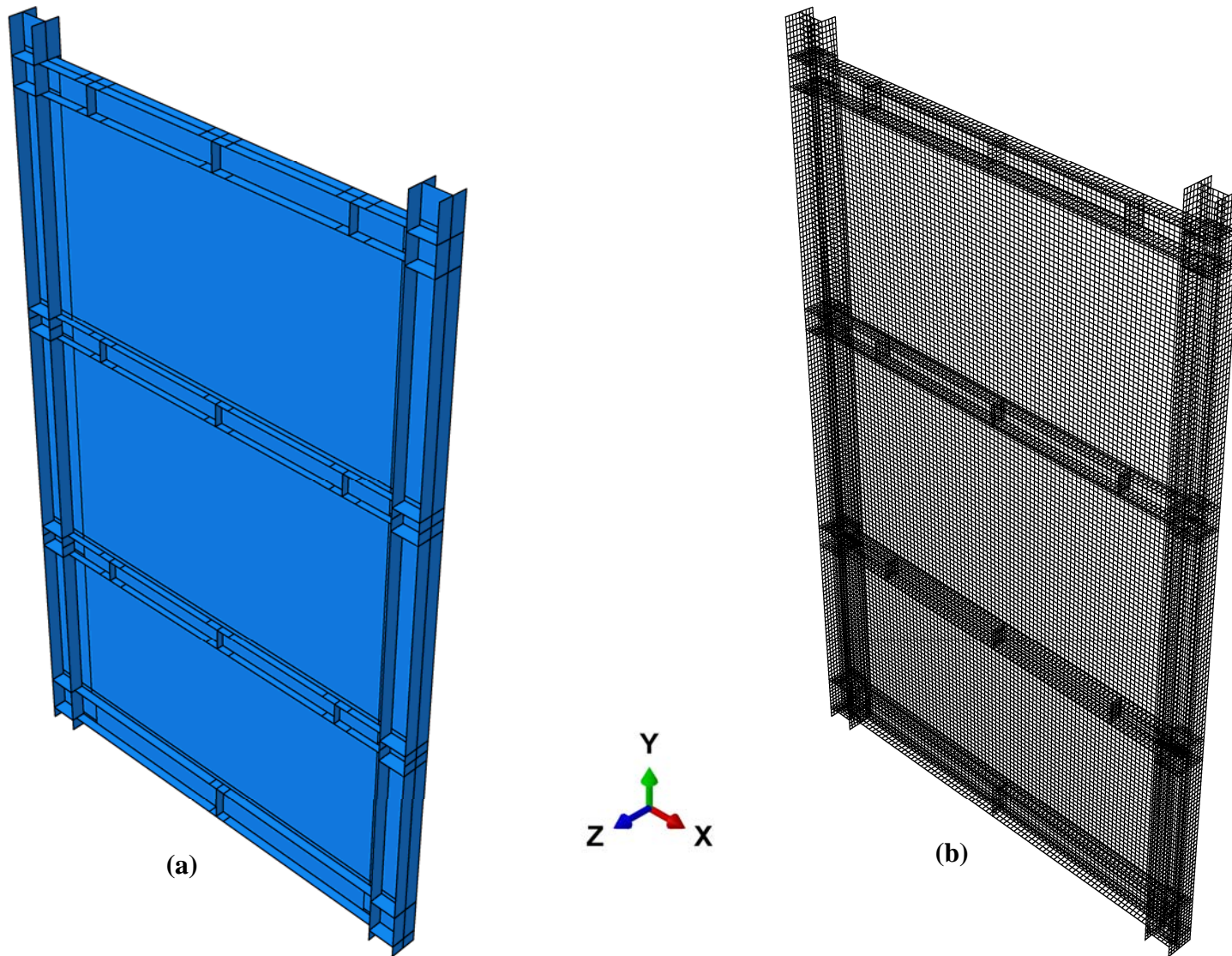
Figure 5-1 Finite Element Model of the 3-Story SPSW Specimen: (a) Solid View; (b) Wire-Mesh View

hourglass control can provide more accurate results compared with fully integrated S4 shell elements, as long as the provided elements are not distorted (relatively close to being square in shape), and significantly reduce running time especially in three dimensions. If hourglass occurs, a finer mesh may be required or concentrated loads must be distributed over multiple nodes (Dassault Systèmes 2009b).

This element allows transverse shear deformation by applying thick shell theory as the shell thickness increases. Conversely as the thickness decreases, it becomes discrete Kirchhoff thin shell element with transverse shear deformation becoming very small. Moreover, this element also accounts for finite (large) member strains and large rotations, geometric and material nonlinearities, and changes in thickness by inputting a specific Poisson's ratio $\nu = 0.3$ for steel (Dassault Systèmes 2009b).

The transverse shear calculation is performed at the center of the element and assumed constant over the element thickness. Hence, transverse shear strain, force, and stress will not vary over the area of the element (Dassault Systèmes 2009b). Nevertheless, in ABAQUS/Standard, the default output points through the thickness of a shell section are the points that are on the bottom and top surfaces of the shell section for integration with Simpson's rule (Dassault Systèmes 2009b). Nine integration points were used through a single layer shell and output was taken at the top surfaces.

5.2.3 Material Definitions

ABAQUS/Standard defines stress-strain material properties in terms of "true" stress (Cauchy stress) and logarithmic plastic strain, σ_{true} and $\varepsilon_{\ln}^{pl}$, respectively. The specified nominal stress (σ_{nom}) and nominal strain (ε_{nom}) values obtained from coupon tests (Section 3) were therefore converted using the following relationships (Dassault Systèmes 2009b):

$$\sigma_{true} = \sigma_{nom} \cdot \left(1 + \varepsilon_{nom}\right) \tag{5-1}$$

$$\varepsilon_{\ln}^{pl} = \ln\left(1 + \varepsilon_{nom}\right) - \frac{\sigma_{true}}{E} \tag{5-2}$$

where E is Young's modulus. Note that these equations are valid only for an isotropic material. To define the inelastic (hardening) behavior, the *Combined Hardening* model was used. This

hardening model is a nonlinear combination of *Isotropic Hardening* and *Kinematic Hardening* models. The Von Mises yield criteria was used.

As described in Section 3, several groups of coupons were cut from light gauge steels used for the infill plates and from W- and S-sections used for boundary elements. To define material properties for each steel component in the finite element model, its stress-strain data was selected from the coupon in every group whose mechanical properties were the most similar to the average material properties of that corresponding group (Table 3-2). For other plates for which data from coupon tests were not available (i.e., doubler plates, continuity plates, fish plates, and stiffener plates), their stress-strain properties were assumed to be the same as that of the HBE-B3 coupon (i.e., one of the coupons taken from the flanges of the bottom anchor beam), as its mechanical properties were comparable to that of a typical ASTM A572 Gr. 50 (F_y = 50 ksi) steel.

5.2.4 Boundary Conditions, Constraints, and Loading

In the experiment setup, the angles connecting the gravity mass to the specimen (Figures 3-17 and 3-18) served both to provide out-of-plane lateral support and as a load transfer mechanism. In the FE model however, these roles have to be separated to avoid conflict of constraints in several nodes (i.e., know as the *Overconstraint* condition in ABAQUS term). This was done by restraining the exterior nodes of HBE flange and stiffener elements at the locations of the angles against out-of-plane movement (Figure 5-2a) and assigning nodes at the centerline of HBE top flange (again at the angle locations) to transfer the load to the specimen (Figure 5-2b). As for VBEs, the exterior nodes around the perimeter of panel zones (i.e., nodes of VBE flange and continuity plate elements) were restrained against out-of-plane movement and nodes at VBE web at the level of HBE top flange were selected to transfer the load (Figures 5-2a and 5-2b). Note that the gravity mass frame was not included in the FE model.

The above approach also simplified the modeling process when considering changes in the load transfer mechanism. Recall (from the information presented in Section 4.3) that the load transfer mechanism was changed from a three- to one-point load transfer through HBEs during the first two sequences of loading in the experiment, and from transferring the load through HBEs to
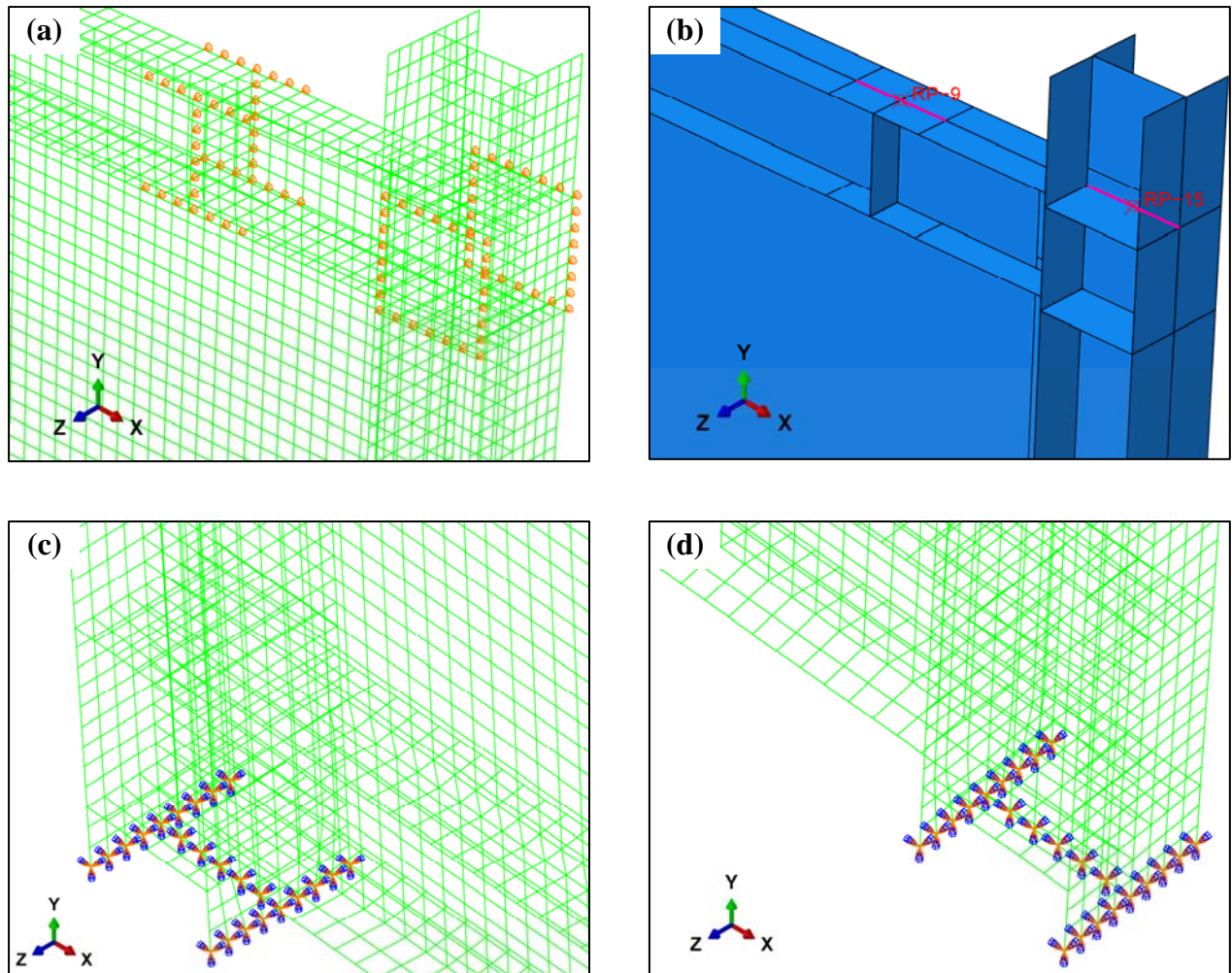
Figure 5-2 Boundary Conditions and Constraints: (a) Typical Boundary Conditions on HBE & VBE; (b) Typical Constraints to Transfer Load; (c) & (d) Fixed Support

doing so through VBEs in the last sequence of the experiment. Here, out-of-plane restraint for the nodes at the specified locations remained the same throughout the analysis sequences, while the node locations where the load transferred were changed accordingly following the loading sequence applied in the experiment (Figure 5-3).

As a first case in this finite element investigation, the floor plate to which the frame was connected at its base (Figure 3-14) was excluded from the FE model. The model was assumed to have a fixed support for simplicity. Here, translational and rotational motion of all nodes at the base of the East and West VBEs were restrained (Figures 5-2c and 5-2d, respectively). This
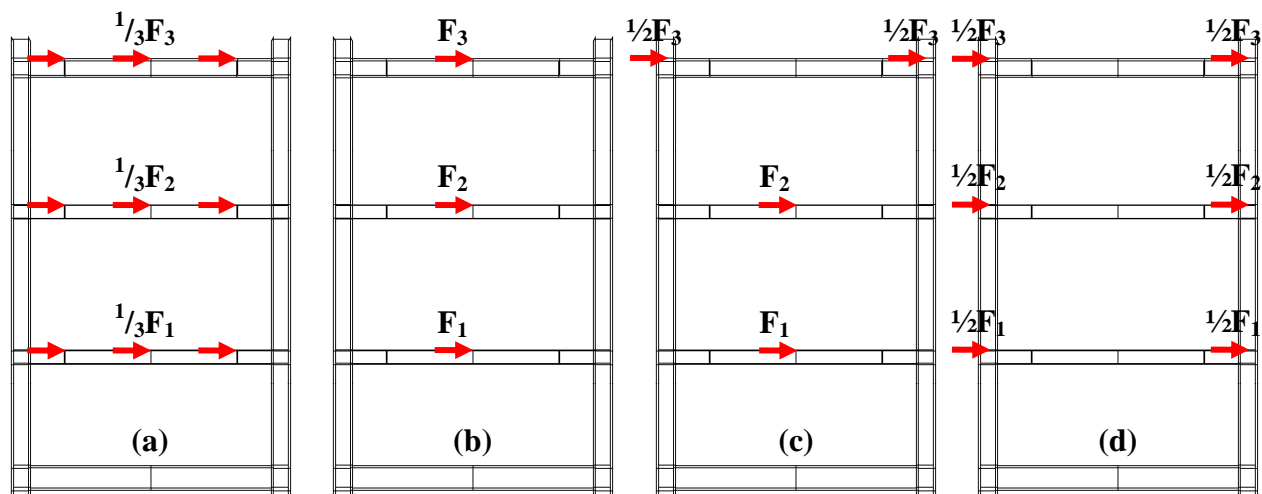
Figure 5-3 Loading Configuration: (a) Step 1-6a; (b) Step 6b-8; (c) Step 7a; (d) Step 7b-10d

assumption will be revisited in a later section by explicitly modeling the floor plate to enable simulation of column uplifts observed during the experiment.

Five references points (RP) per floor were defined for possible locations of pushover displacement (Figure 5-3): One reference node at each location of the connecting angles and one at each West and East panel zones. A *Kinematic Coupling Constraint* was used to constrain both the translational and rotational motion of the coupling nodes to their corresponding reference point. The coupling nodes are defined as the nodes where the load is transferred to the FE model (Figure 5-2b), typically 3 in. away from the left and right of the reference points. Table 5-1 summarizes the peak story displacement recorded during the experiment. These story displacements were applied to the reference nodes according to the experimental sequences shown in Figure 5-3. Note that in the experiment (Section 3.8), the third story actuator was set up in a displacement-control mode, while the other two actuators were in a force-control mode. Having displacement records for each story available, an independent displacement-control for each story could be applied in the FE model to simulate the loading protocol applied in the experiment.

5.2.5 Nonlinear Numerical Stability

Geometric non-linearities mainly arise, in this model, from the large-displacements exhibited in the infill plate and local buckling of the infill plate may lead to unstable conditions. Although the

Table 5-1 Peak Displacement Summary for Finite Element Analysis

Analysis Step[1]	Number of Cycles	"Time" Step[2]	Cumulative "Time" Step	Story Displacement (in.)		
				Δ_1	Δ_2	Δ_3
1a	1	3	3	0.02	0.05	0.07
2	1	3	6	0.05	0.10	0.16
3	1	3	9	0.11	0.22	0.36
4	1	3	12	0.17	0.37	0.59
5	1	3	15	0.38	0.86	1.28
6	1	3	18	0.55	1.29	1.93
6c	1	3	21	0.51	1.05	1.55
7	1	3	24	0.60	1.25	1.85
8	1	3	27	0.49	1.04	1.53
7a	1	3	30	0.78	1.78	2.69
8a	1	3	33	1.01	2.38	3.54
9	1	3	36	1.18	2.78	4.20
9b	1	3	39	1.15	2.80	4.28
10	1	3	42	1.22	2.96	4.51
10d	1	3	45	1.31	3.13	4.77

Note:
[1] To reduce computational complexities, several steps in the experiment (i.e., Step 6a, 6b, 7b, 9a, 10a, 10b, 10c) were not included in the finite element analysis.
[2] In the FE model, one displacement cycle conducted in the experiment was simulated in 3"time" steps

S4R shell elements described in Section 5.2.2 are able to accommodate large-displacements, instability of the entire model may still occur. ABAQUS/Standard can overcome this unstable condition using the *Stabilize* option in which the program provides an additional artificial damping to the model during a nonlinear static analysis. The artificial damping factor is determined in such a way that the extrapolated dissipated energy for the step is a small fraction of the extrapolated strain energy. The fraction is called the *dissipated energy fraction* (DEF) and has a default value of 2.0×10^{-4} (Dassault Systèmes 2009b).

ABAQUS/Standard then uses Newton's method to solve the nonlinear equilibrium equations. The solution is usually obtained as a series of "time" increments from 0.0 to 1.0, with iterations to obtain equilibrium within each increment. The program can automatically adjust the time increment to permit convergence of results without unstable responses due to the higher degree of nonlinearity in the system, in this case related to infill plate buckling. In addition, for models having very thin infill plates, the increment should be defined small to ensure that any obtained solution is not too far from the equilibrium state that is being sought (Dassault Systèmes 2009b). Here, the minimum and maximum increments were set to 1.0×10^{-5} and 0.0125, respectively.

When using the stabilization feature, one should ensure that the ratio between the viscous damping energy (ALLSD – *ABAQUS definition*) and the total strain energy (ALLSE) does not exceed the DEF value or any reasonable value (Dassault Systèmes 2009b). Though detailed results are not presented here, it was confirmed that after running the FEM model, ALLSD was significantly smaller than ALLSE over the entire time increments/period.

5.3 Eigenvalue Buckling Analysis and Initial Imperfections

Many researchers in the past (Section 2.2.2) reported that including initial imperfections of infill plates was important to help initiate panel buckling and development of tension field action (TFA) in finite element models; and excluding the initial imperfections resulted in a stiffer finite element (FE) model compared to the actual "imperfect" structure. Hence, this finding was considered in the FE model described here. ABAQUS offers three methods to define an imperfection, namely: as a linear superposition of buckling eigenmodes, from the displacements of a static analysis, or by specifying the node number and imperfection values directly (Dassault Systèmes 2009b). The first of these options was chosen for the model described here.

An eigenvalue buckling analysis was first run on the "perfect" structure to request the first eight eigenmodes of every panel (i.e., total 24 eigenmodes). The resulting eigenmodes of each story panel were somewhat similar and thus those of the second story panel were arbitrarily selected to represent the results in Figure 5-4. Shown in parts (a), (b), and (c) of the figure are the 1st, 3rd, and 6th mode shapes, respectively. The other requested modes are not plotted in Figure 5-4 because
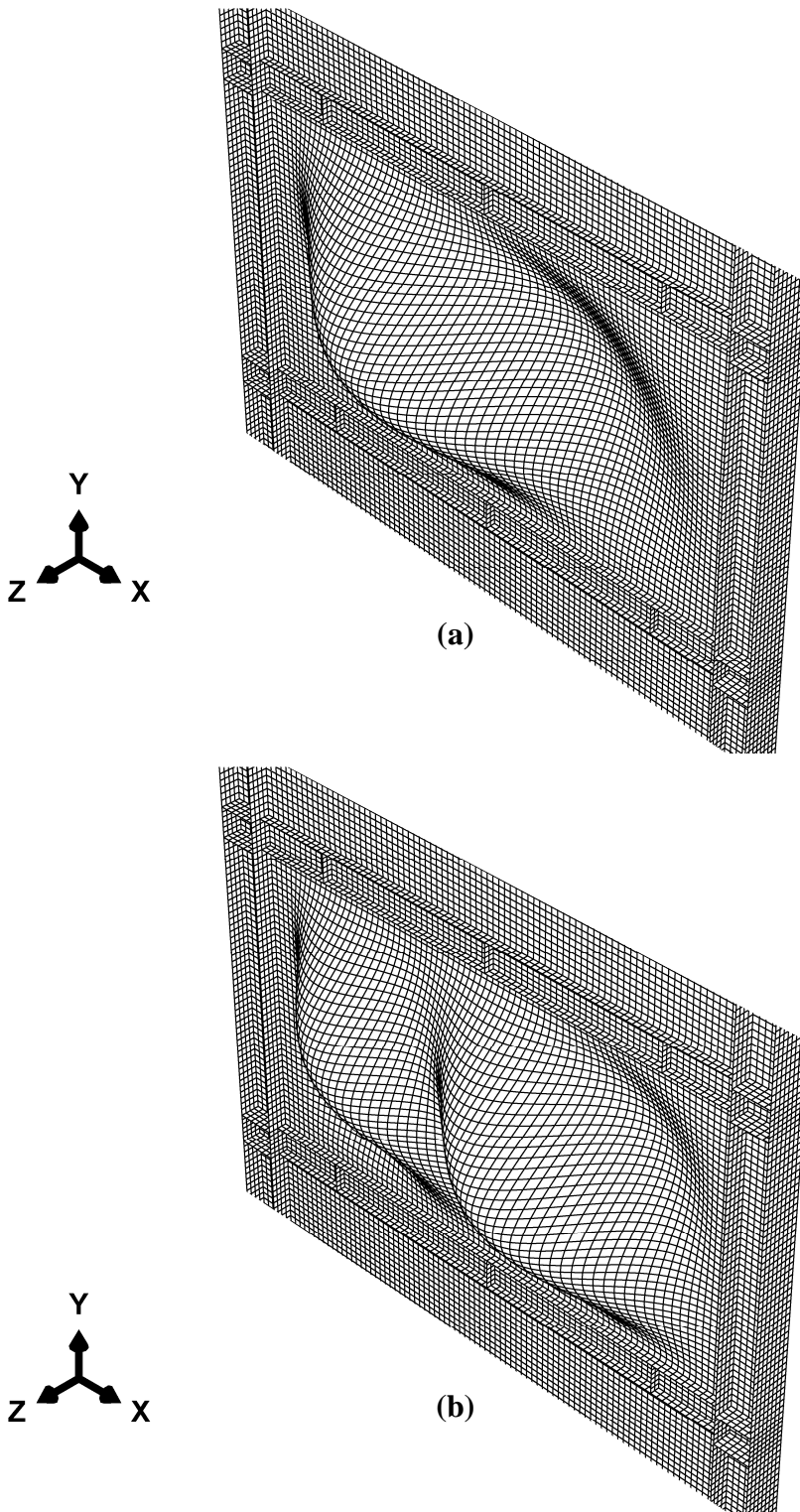
Figure 5-4 Buckling Modes of the 2nd Story Panel: (a) 1st Mode; (b) 3rd Mode
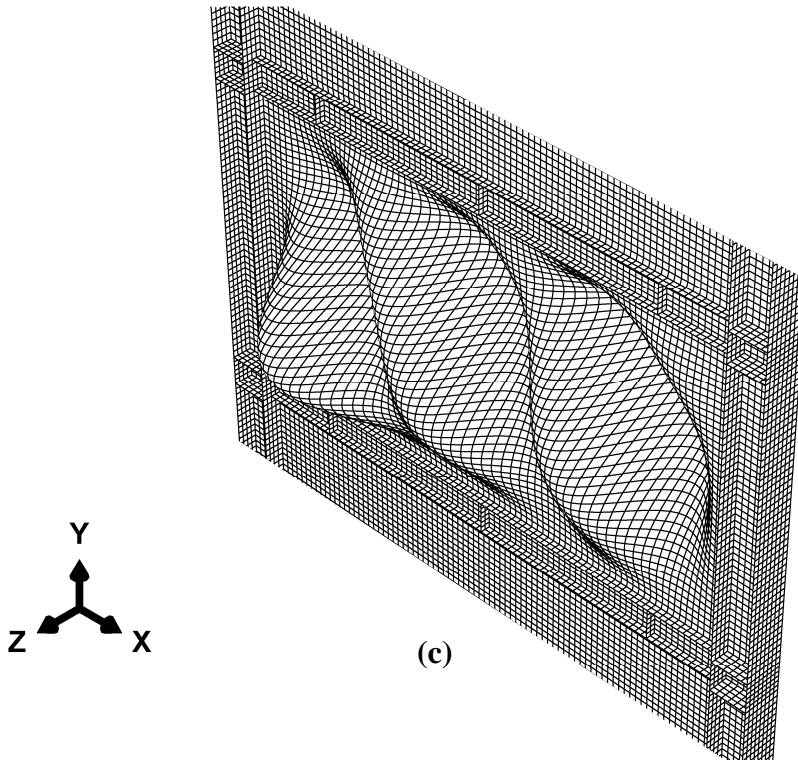
Figure 5-4 Buckling Modes of the 2nd Story Panel: (c) 6th Mode

they have similar eigenmodes (or closely spaced eigenvalues) to these three modes (i.e., the 2nd mode is similar to the 1st mode; the 4th and 5th modes are similar to the 3rd mode; the 7th and 8th modes are similar to the 6th mode).

Postbuckling analysis was subsequently run after introducing imperfections in the geometry by adding these buckling modes to the "perfect" geometry where ABAQUS interprets the imperfection data through nodal displacements. The imperfection thus has the form

$$\Delta x_i = \sum_{i=1}^{M} \omega_i \, \phi_i \tag{5-3}$$

where ϕ_i is the ith mode shape and ω_i is the associated scale factor (Dassault Systèmes 2009b). The lowest buckling modes are frequently assumed to provide the most critical imperfections, so usually a higher scale factor is assigned to the lowest eigenmodes, progressively decreasing for the higher eigenmodes. In addition, a similar scale factor is assigned to the closely spaced eigenvalues. Based of recommendations of a previous study (i.e., Purba and Bruneau 2007), scale

factors equal to 1, ½, and ¼ were selected respectively for the first and second modes, the third to fifth modes, and the sixth to eight modes of each panel. The resulting imperfection magnitudes corresponded to only a small percent of the shell thickness, as shown in Figure 5-5.
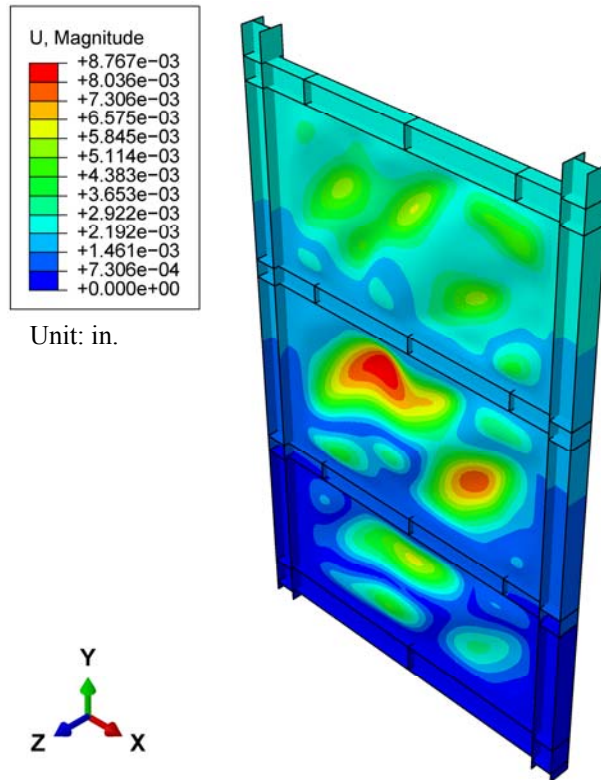
Figure 5-5 Initial Imperfections of Infill Plates

5.4 Finite Element Monotonic Pushover Analysis of Tested Specimen

Prior to performing a cyclic pushover analysis, a finite element monotonic pushover analysis of the tested specimen was conducted. This analysis was intended to verify whether the FE model developed (Figure 5-1) could simulate the cyclic envelope of the force displacement hysteresis recorded in the experiment (Figure 4-36d). The FE monotonic pushover analysis was conducted toward the positive direction (which simulating the specimen pushed toward the West direction in the experiment).

As shown in Table 5-1, the maximum story displacement of displacement Steps 6a to 8 was smaller than that of Step 6. Problems on the load transfer mechanism during the experiment (as presented in Section 4) contributed to this condition. The maximum story displacement recorded

in Step 6 (e.g., 1.93 in. at the top floor) was not surpassed until displacement Step 7a (e.g., 2.69 in. at the top floor). In principle, the target displacement of a monotonic pushover analysis has to be continuously increased. Hence, displacement Steps 6a to 8 were excluded from this monotonic pushover analysis. Here, the FE model was pushed at each story level using the loading configuration shown in Figure 5-3a until the first, second, and third story reached story displacements of 0.55, 1.29, and 1.93 in., respectively. Following this analysis "time" step, the loading configuration shown in Figure 5-3d was used and the FE model was pushed until the respective stories reached story displacements of 1.31, 3.13, and 4.77 in.

Incidentally, one can also divide the above target displacements into several smaller targets following the displacement steps summarized in Table 5-1. For example, instead of reaching the specified displacement target of 1.93 in. at the top floor in one "time" step from 0.0 to 1.0, the analysis can be conducted in six "time" steps from 0.0 to 6.0 in which successive steps have displacement targets of 0.07, 0.16, 0.36, 0.59, 1.28, and 1.93 in. at the top floor. A preliminary finite element analysis showed an insignificant difference in results obtained from both approaches. The small difference was caused by the slightly different time increment in both cases, which ABAQUS automatically adjusted to permit convergence of results. Consequently, the former approach was selected to expedite subsequent pushover analyses.

5.4.1 Results and Comparison

Figure 5-6a presents the resulting pushover curve. Interestingly, an abrupt drop of base shear in the pushover curve occurred when the loading configuration changed from the three-point loading (Figure 5-3a) to the two-point loading (Figure 5-3d). No substantial effort was invested to resolve this phenomenon. Instead, two additional monotonic pushover analyses were conducted. In the first analysis, the FE model was pushed all the way to the maximum recorded story displacements (i.e., until the first, second, and third story reached story displacements of 1.31, 3.13, and 4.77 in., respectively) using the three-point loading configuration. The same analysis was then repeated but in this case the FE model was pushed using the two-point loading configuration. Their resulting pushover curves are also plotted in Figure 5-6a with a less than 4% difference between the ultimate base shears obtained; and the initial pushover curve lies between these two pushover curves.
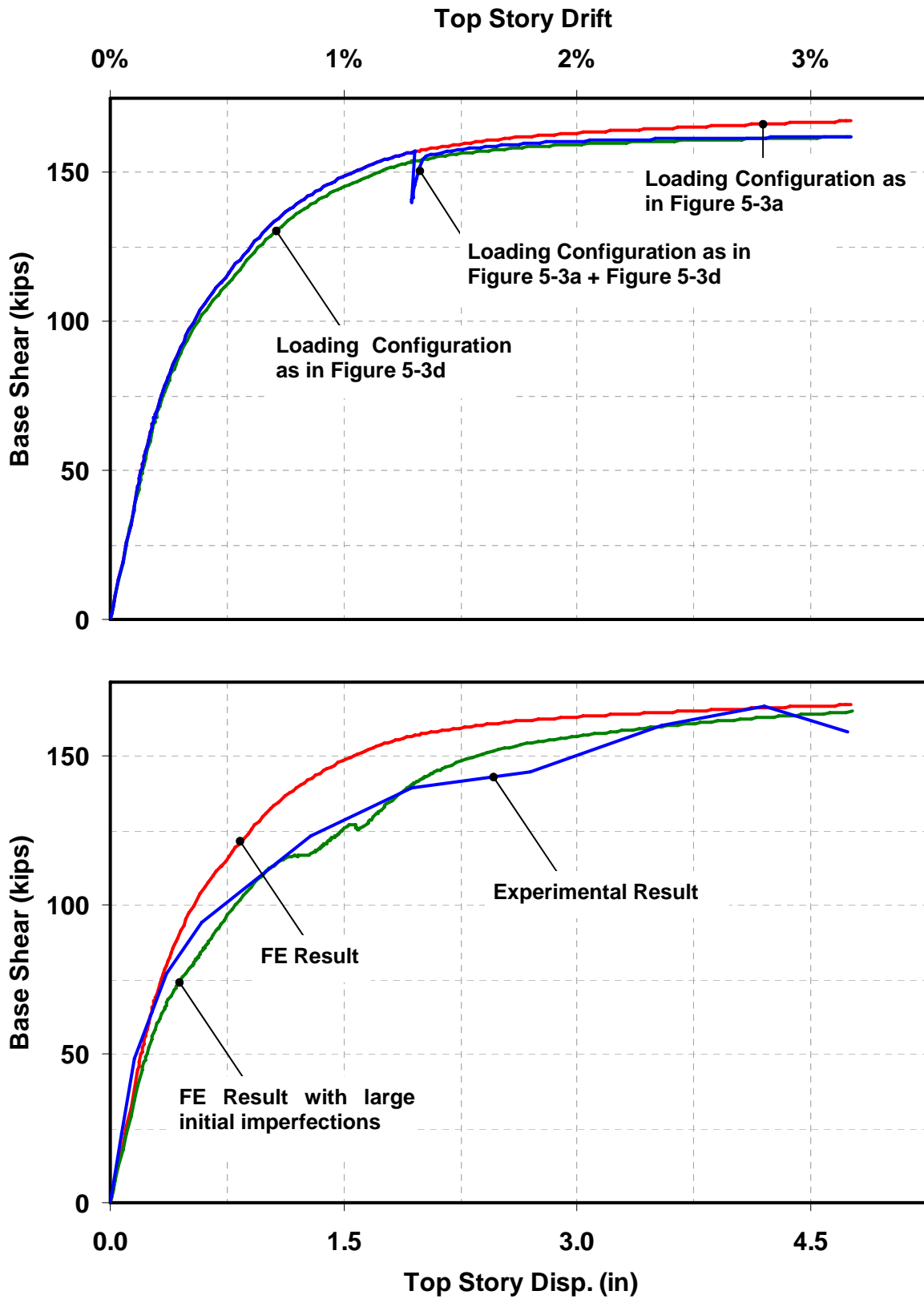
Figure 5-6 Finite Element Monotonic Pushover Analysis: (a) Results for Three Analysis Scenarios; (b) Analytical versus Experimental Results

The monotonic pushover curve with the three-point loading configuration used through the entire pushover loading was selected to represent the finite element result and compared to the experimental result in Figure 5-6b. While the initial stiffness of the analytical model is in good agreement to that observed in the experiment, after reaching the inelastic stage, the FE model significantly overestimated the experimental strength. For example, the experimental base shear strength was 123 kips when the specimen experienced 1.28 in. displacements at the top floor, while the FE model at the same point has a base shear strength of 142 kips, which overestimates the experimental results by 15.3%. Interestingly, the ultimate base shear obtained from the FE analysis is similar to that recorded during the experiment.

5.4.2 Attempts to Resolve Analytical and Experimental Discrepancies

Several attempts were made to resolve the above discrepancies between the analytical and experimental results at the inelastic stage prior to reaching the ultimate strength. First, the influence of mesh refinement was investigated. The previous FE model, meshed with an average 1×1 in. size of shell element (Figure 5-1), was refined to obtain shell elements with half that average size. The resulting finite element model contained 86,088 elements, which are approximately 4 times more elements than that of the original FE model. It was found that the resulting monotonic pushover curve (not shown here) was practically similar to that of the FE model with coarse mesh.

In a second attempt, the initial imperfections defined in Section 5.3 were revisited. Here, a larger initial imperfection was defined to obtain a less stiff FE model. For this purpose, the same definition of initial imperfection expressed in (5-3) was again followed but all eight eigenmodes considered were assigned the same scale factor of 1.0. While assigning the same scale factor for all considered eigenmodes is uncommon (i.e., seems to contradict the typical practice explained in Section 5.3), it is instructive to also investigate the consequences of this option providing cautious assessment of the obtained results is exercised.

The resulting monotonic pushover curve is shown in Figure 5-6b. Both the analytical pushover curve and the backbone of cyclic hysteretic curve from the experiment apparently are in a good agreement. However, one might question reliability of the analytical result given the unusual

jaggedness in the pushover curve. Several variations of scale factors and different combinations of considered eigenmodes to define the initial imperfections were tried, yet no satisfactory results were obtained. Either the discrepancy between the analytical and experimental results remained or an apparent agreement existed between the two curves but with a jagged analytical pushover curve observed. These results lead to the conclusion that the discrepancy between the analytical and experimental results more likely was not caused by an inaccurate definition of initial imperfections, and the initial imperfections defined in Section 5.3 were deemed sufficient to help initiate panel buckling and development of tension field action without causing an unintended stiffer finite element model.

As a last attempt, the floor plate at the base of the frame (Figure 3-14) was explicitly included in the finite element model developed. This was because the use of fixed supports (Figures 5-2c and 5-2d) was not particularly accurate to model the bases of East and West columns considering the column uplifts observed in the experiment. In other words, the FE model with fixed supports is relatively stiffer than the actual specimen. Modifications on the current FE model to accommodate this change and findings of this investigation are presented in the following section.

5.5   Finite Element Model with Floor Plate Included

To reiterate information presented in Section 3.7.1, the SPSW specimen was anchored to an existing 9 ft. by 12 ft., 1.5 in. thick floor plate using high-strength bolts on each column base plate. The existing floor plate was anchored to the concrete strong floor using 22 high strength tension rods (i.e., $F_y = 130$ ksi; $F_u = 150$ ksi) of $1^1/_8$ in. diameter, which were uniformly distributed through out the floor plate footprint with a corresponding tributary area of 24 in. by 24 in. per rod (Figure 3-14a).

Instead of modeling the entire floor plate, only a portion of it was included in the finite element model developed, as shown in Figure 5-7. A 7 ft. wide portion of floor plate in the direction perpendicular to the specimen model was considered adequate to simulate the uplifts observed in the experiment. When modeling the floor plate in ABAQUS/CAE, a new part was added to the original FE assembly (Figure 5-1). This floor plate part was then partitioned to model the base
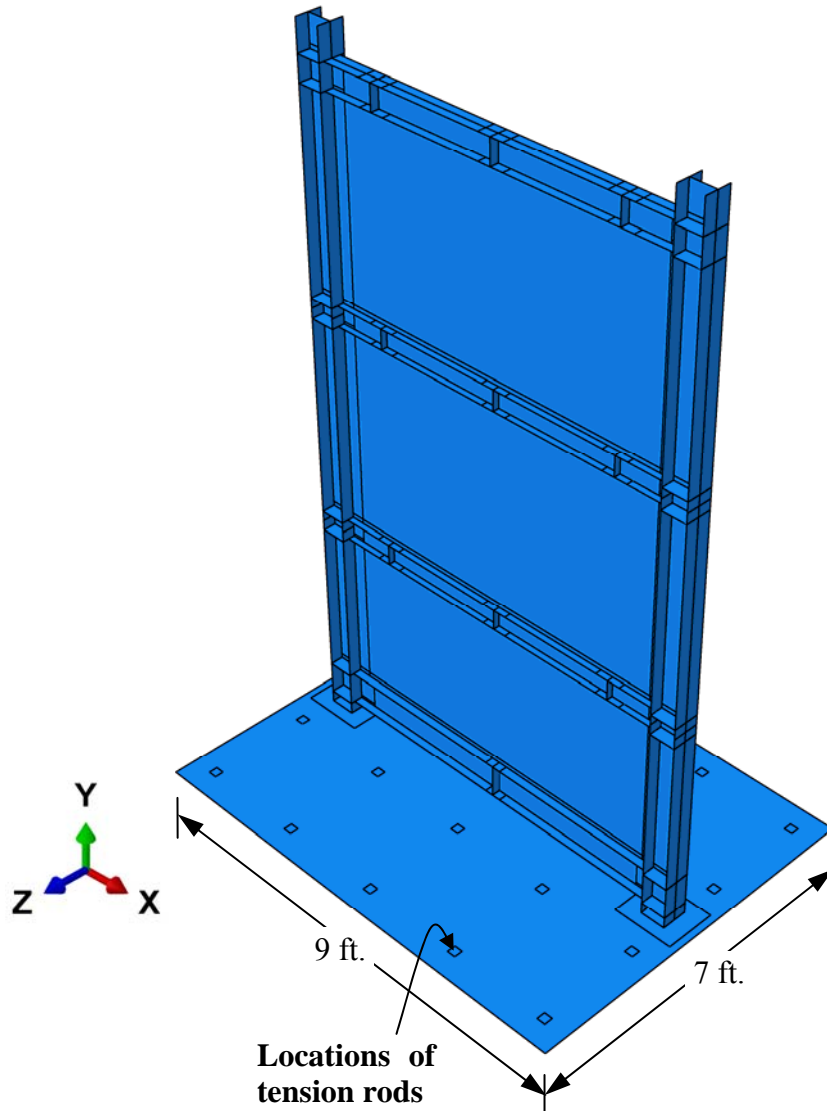
Figure 5-7 Finite Element Model of the 3-Story SPSW Specimen with Floor Plate

plates and locations where the tension rods connected the floor plate to the concrete strong floor; and subsequently was merged to the SPSW model into one single FE model using the *Merge/Cut Instances* tool. The base plate partitions, due to their complexity caused by I-shape columns connected to it, were meshed using the *Free Meshing Technique*, while the rest of the floor plate was meshed using the *Structured Meshing Technique*. To reduce the mesh distortion within the free meshing region, the *Medial Axis Control Algorithm* together with the *Minimizing the Mesh Transition* option were applied. The entire floor plate was meshed using the isoparametric S4R shell elements with an average dimension of 1×1 in. per shell element. The resulting SPSW and floor plate model contained 33,288 shell elements.

ASTM A572 Gr. 50 (F_y = 50 ksi) and ASTM A36 (F_y = 36 ksi) steels were used for the base plate and the floor plate, respectively. Like other plates in the specimen model that were made of ASTM A572 Gr. 50 steel but for which data from coupon tests were not available (Section 5.2.3), the stress-strain data for the base plate was assumed to be the same as that of the HBE-B3 coupon. As for the floor plate, an elasto-perfectly plastic material model was used to idealize the ASTM A36 steel. The concrete strong floor was not explicitly modeled; instead an analytical rigid surface was defined in the FE model beneath the floor plate (not shown in Figure 5-7). Upon activating the *General Contact* feature in ABAQUS/Standard, the program automatically detected contact between the floor plate surface and the rigid surface as a result of their proximity. Mechanical properties of this contact were defined by the default 'hard' contact relationship in ABAQUS/Standard, which basically allowed the program to consider the two surfaces to be in contact when clearance between them reduced to zero, at which point any contact pressure can be transmitted from one surface to another; once the contact pressure reduces to zero, the two surfaces are considered acting as separate surfaces (Dassault Systèmes 2009a). The tension rods connecting the floor plate at the specified locations to the ground were modeled using the *Axial Connector* with an elasto-perfectly plastic behavior.

For the purpose of defining initial imperfections, an eigenvalue buckling analysis was run on the modified FE model (Figure 5-7) to request the first eight eigenmodes of every panel. The resulting eigenmodes for the modified FE model were similar to that presented in Figure 5-4. Subsequently, the modified FE model was pushed using the three-point loading configuration (Figure 5-3a) until the first, second, and third story reached story displacements of 1.31, 3.13, and 4.77 in., respectively. The resulting pushover curve is shown in Figure 5-8. Though the analytical model still overestimated the experimental strength at the onset of yielding, an improved result was observed when compared to the previous result for the FE model with fixed supports (presented in Figure 5-6b, and now superposed in Figure 5-8). The discrepancy between the analytical and experimental results was down from 15.3% to less than 5% when the specimen experienced 1.28 in. displacements at the top floor. The elastic stiffness of the FE model with floor plate, however, was lower than the experimental stiffness; and the FE model underestimated the experimental ultimate base shear by approximately 3%. Moreover, the overall specimen behavior is well represented by the FE model, as shown in Figure 5-9a. In particular, the FE
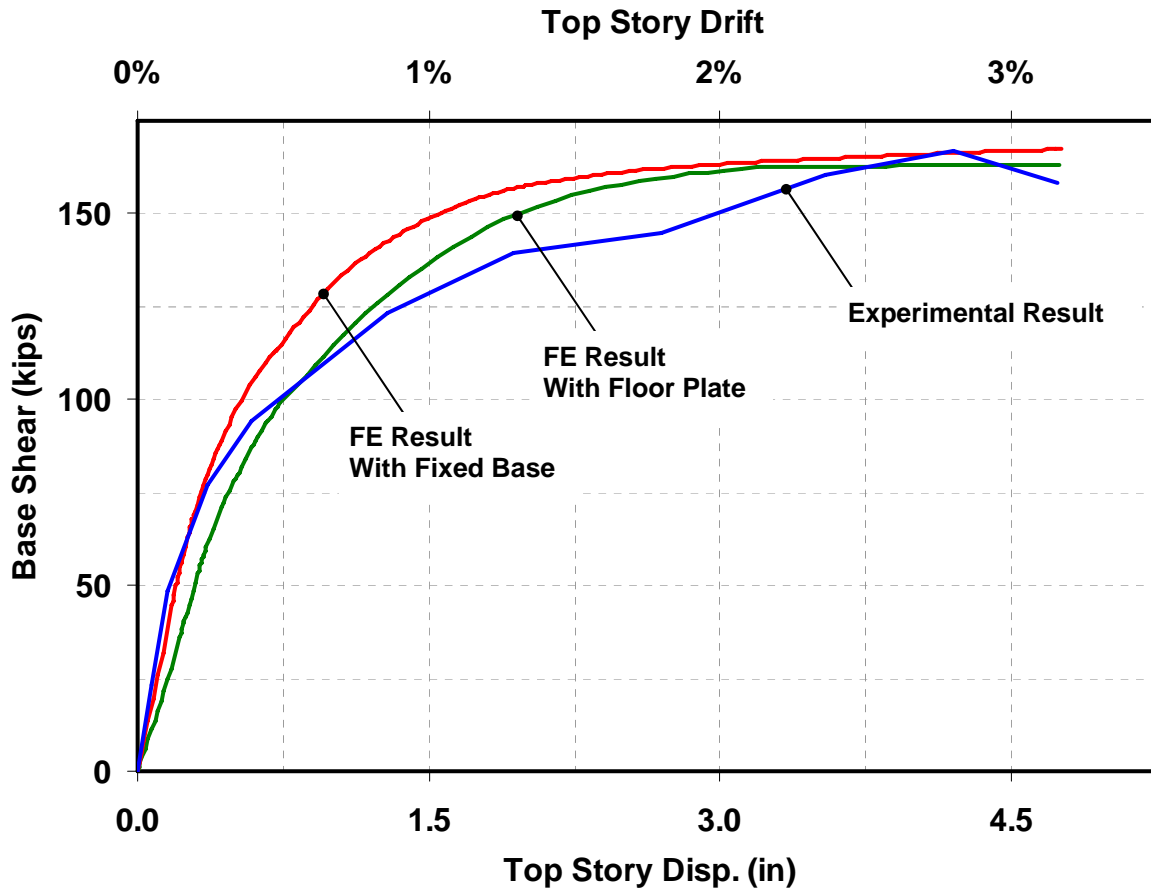
Figure 5-8 Experimental Results versus Finite Element Monotonic Pushover Analysis

model results show inelastic buckling of the infill plates and that plastification occurred not only localized at the HBE-to-VBE connection but also spread over a greater length on HBEs.

While the FE model can simulate the overall behavior of the specimen, it did not accurately simulate the interaction between the floor plate and the analytical rigid surface. Specifically, the floor plate at the location of the column that was in compression (i.e., at the West column) freely penetrated the rigid surface, as shown in Figure 5-9c. Here, a downward deformation of 0.46 in. was recorded at the tip of the floor plate (Figure 5-9d). Except for the direction of plate deformation, the floor plate at this location did not behave differently from the other portion at the location of the column that was in tension (i.e., East column), as shown in Figure 5-9b and 5-9d. To resolve this problem (defined as the *Overclosure* problem in ABAQUS term), several available options in ABAQUS/Standard to simulate the interaction between the two surfaces were tried such as: (1) defining a contact initialization algorithm to remove small initial surface
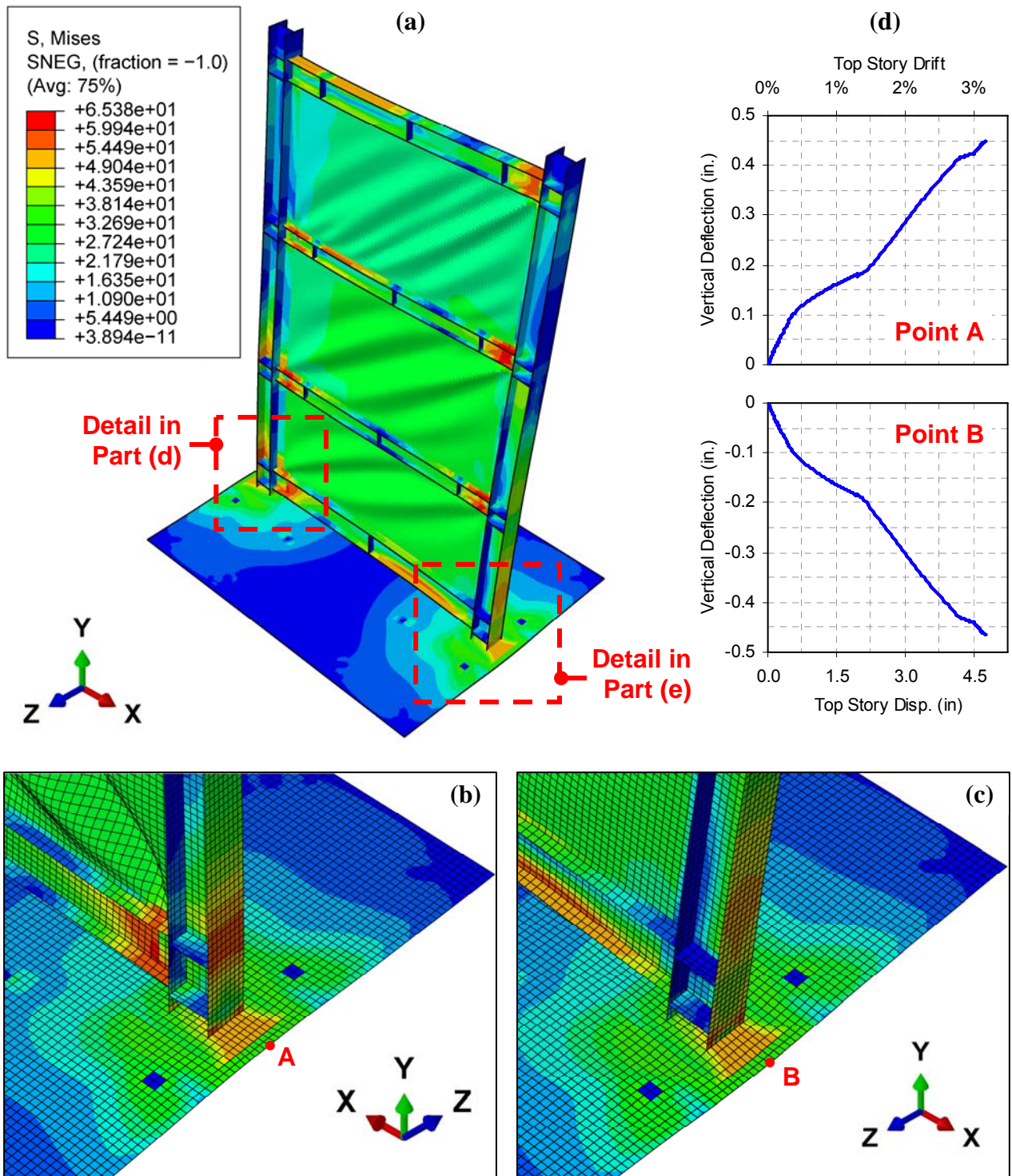
Figure 5-9 Finite Element Model of the 3-Story SPSW Specimen with Floor Plate

overclosures between the floor plate and the rigid surface that might exist during mesh generation; (2) including the offset of 0.75 in. between the centerline of the floor plate and the rigid concrete

surface; and (3) revising the contact definition from the *General Contact* to the *Surface-to-Surface* option. However, no satisfactory results were obtained and the overclosure problem remained unresolved.

The above results led to subsequent investigations in which the floor plate was modeled using the general three-dimensional C3D8R continuum elements (an 8-node solid element with reduced integration and hourglass control) in contact with the rigid surface; and the rigid floor modeled using solid element (with modulus of elasticity 100 times larger that that of normal concrete) was in contact with the floor plate modeled using shell element. No satisfactory results were obtained either. The rigid floor failed to prevent penetration of the floor plate by the column in compression. Consequently, it was decided to use the model shown in Figure 5-7 for the subsequent cyclic pushover analysis assuming that the incorrect local behavior would only have an insignificant impact to the overall results.

5.6   Finite Element Cyclic Pushover Analysis of Tested Specimen

The cyclic pushover analysis was conducted following the displacement history presented in Table 5-1. Here, several steps performed during the experiment (i.e., Step 6a, 6b, 7b, 9a, 10a, 10b, 10c) were excluded from the finite element analysis to reduce computational complexities. For the same reason, it was decided to perform only one cycle per analysis step instead of the 2 or 3 cycles conducted during the experiment. Though slight differences in the displacement histories in the positive and negative directions were observed during the experiment, all displacement excursions were taken as symmetric in the finite element analysis and the values shown in Table 6-1 correspond to the displacement history in the positive direction. The loading configuration followed the experimental sequences shown in Figure 5-3.

Figure 5-10 shows the resulting hysteresis of base shear versus lateral displacement at the top floor. The finite element analysis results with this model capture the experimental strength well in the positive direction while it slightly underestimates that in the negative direction. However, the pinching behavior obtained in the analysis is not as severe as that observed during the experiment. The analytical deformed shape with stress contours shown in Figure 5-11 displays
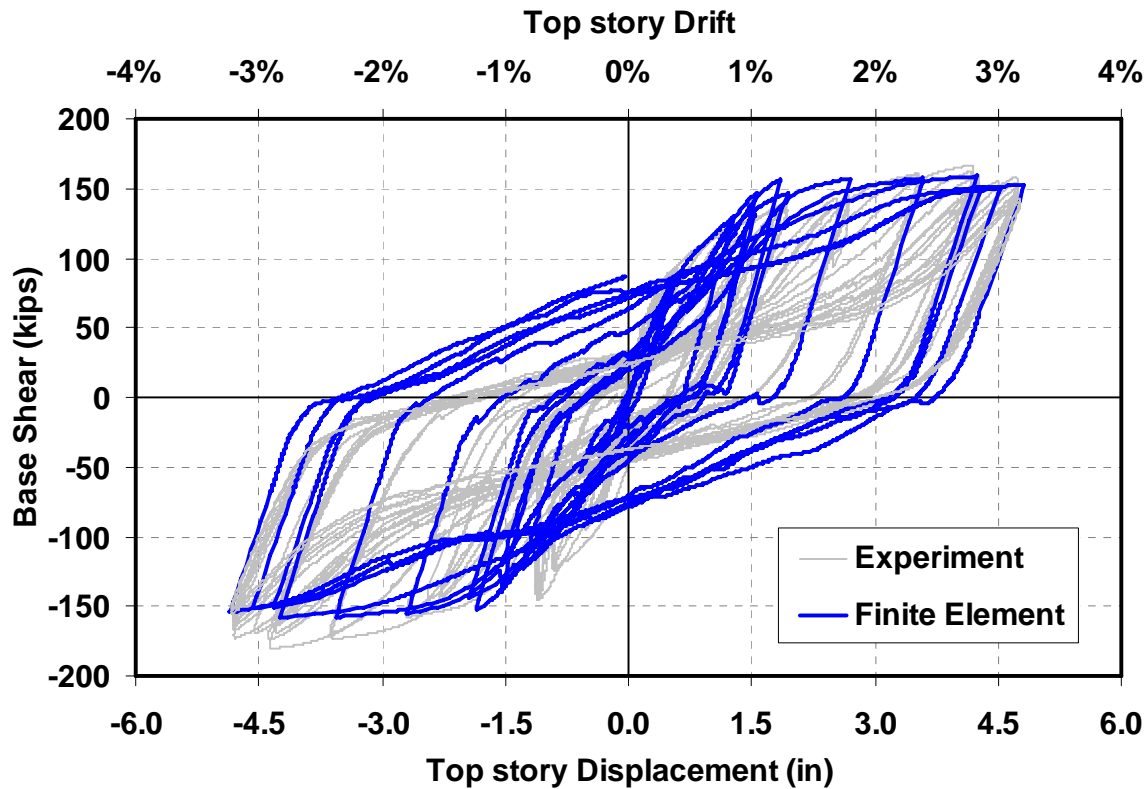
Figure 5-10 Base Shear versus Top Story Displacement

the amount of yielding in the FEM model at 3.33% drift. Plastification of the horizontal boundary elements is observed not only at the HBE ends but also along their spans. Figure 5-12 presents close up views of the HBE plastification and compares it to the specimen condition at the end of the test. The finite element results resemble the specimen behavior observed during the experiment.

HBE vertical deformations obtained from the finite element analysis are presented in Figure 5-13 and compared to those recorded during the experiment. Overall, the finite element results show the accumulation of plastic incremental deformation on HBE0, HBE2, and HBE3 similar to that was observed during the experiment. However, their magnitudes were significantly smaller compared to those recorded during the experiment. In the last displacement cycle (when the FEM model was cycled up to 3.33% top story drift amplitude), the vertical deformations were 0.56 (upward), 0.36, and 0.39 in. for HBE0, HBE2, and HBE3, respectively. In contrast, the vertical deformations recorded during the experiment for the same respective HBEs were 1.64 (upward), 0.74, and 1.12 in.
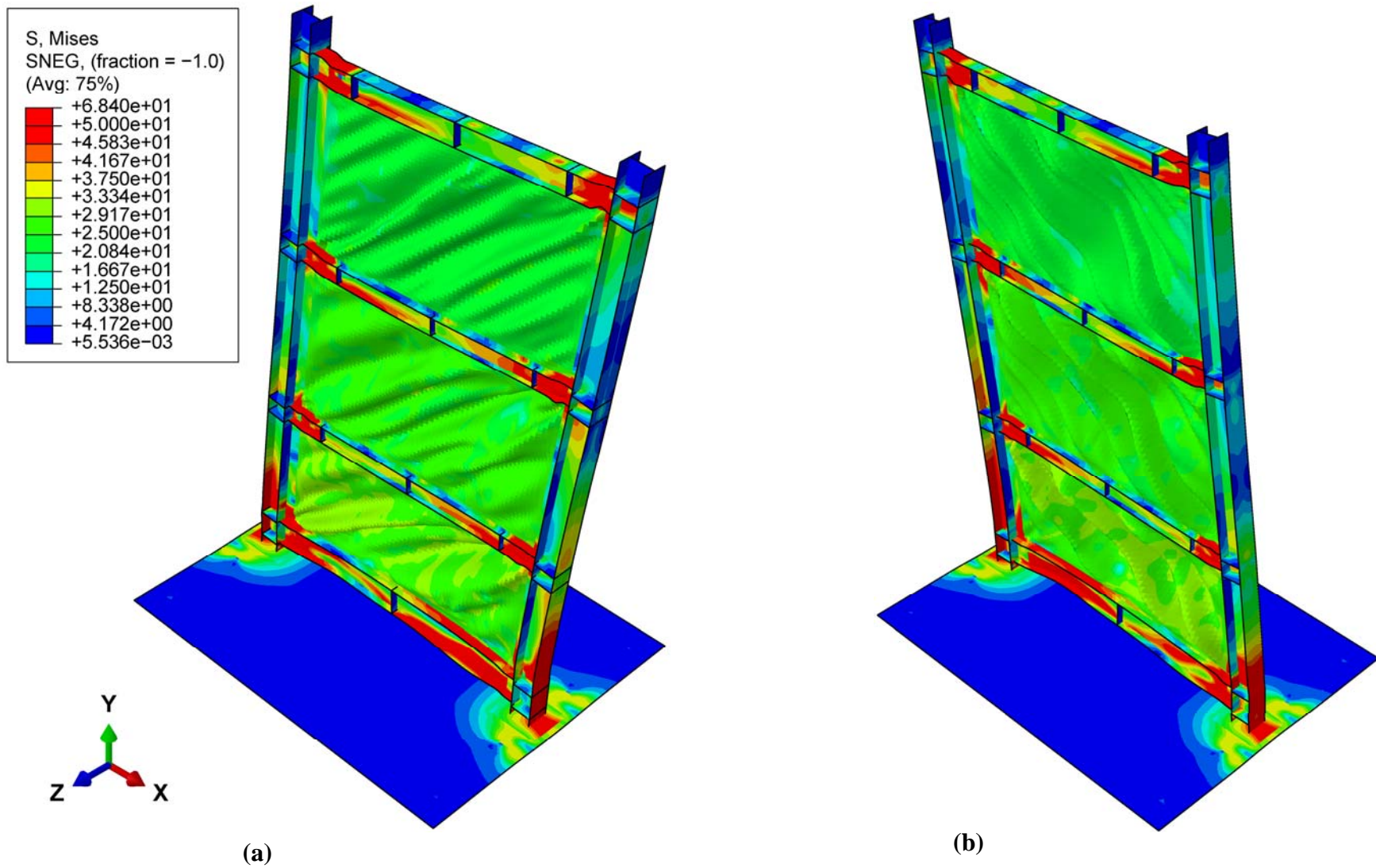
Figure 5-11 Analytical Deformed Shapes with Stress Contours: (a) at +3.33% Drift; (b) at –3.33% Drift
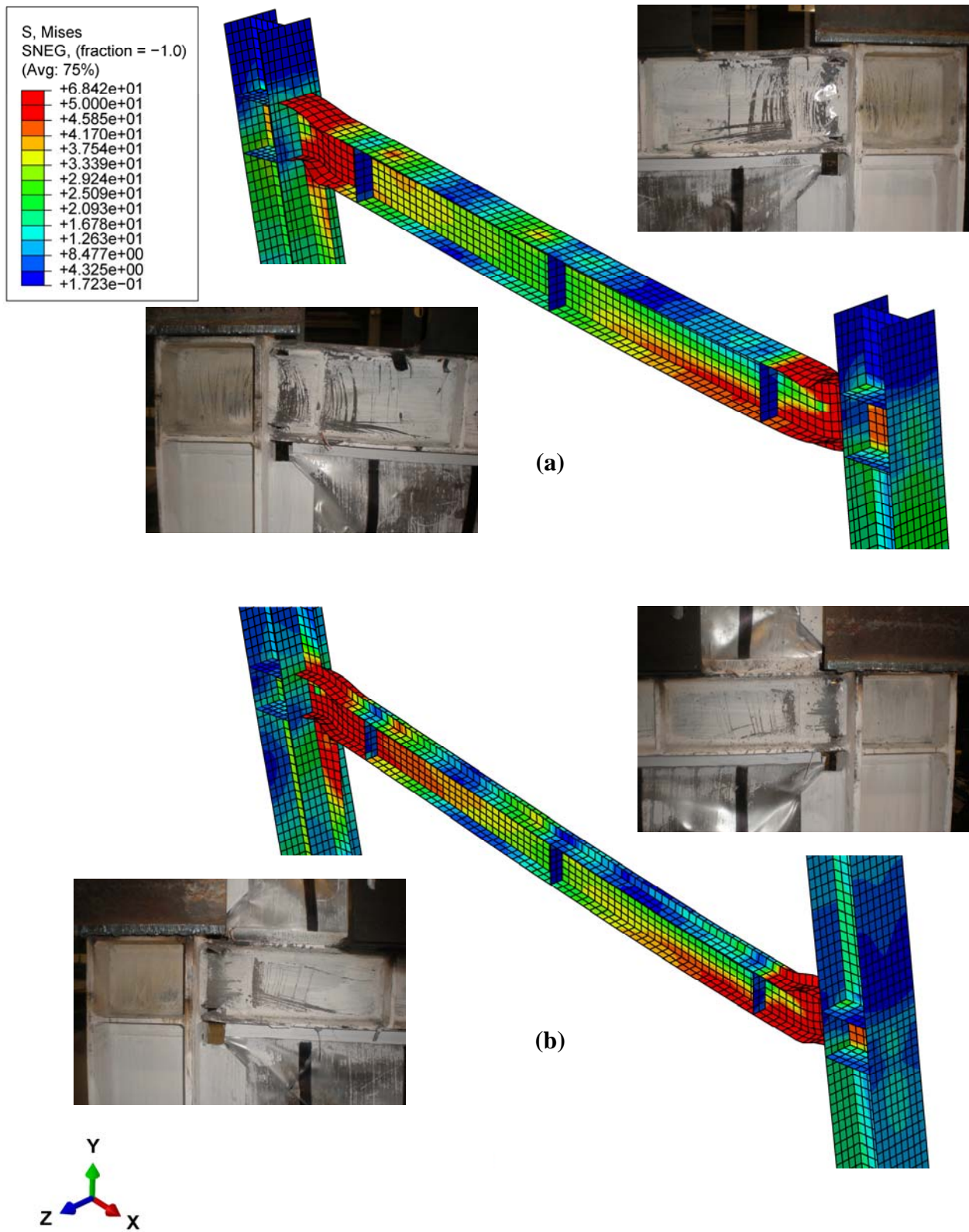
Figure 5-12 Analytical Deformed Shapes with Stress Contours of HBEs at –3.33% Drift: (a) HBE3; (b) HBE2
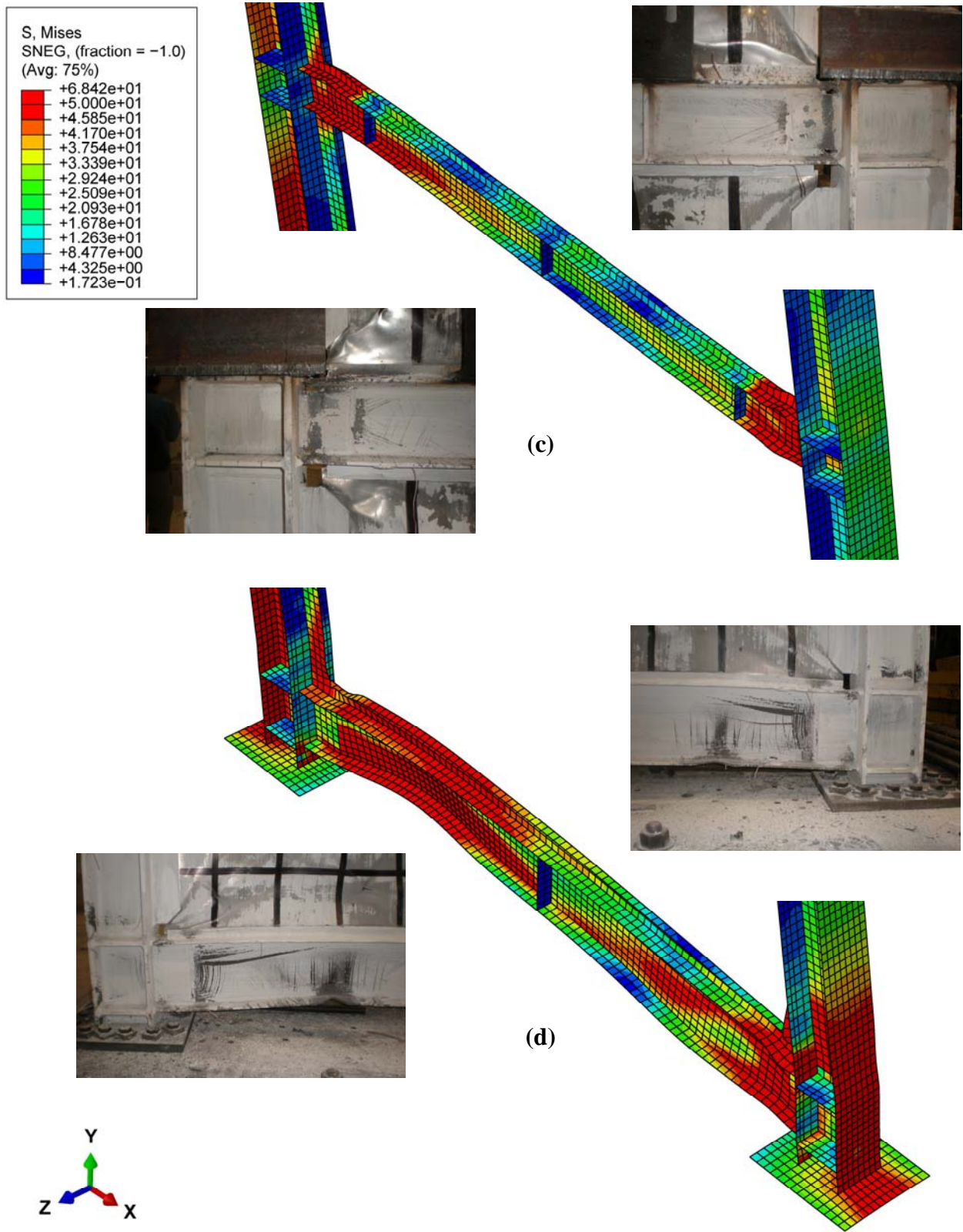
Figure 5-12 Analytical Deformed Shapes with Stress Contours of HBEs at –3.33% Drift: (c) HBE1; (d) HBE0

231
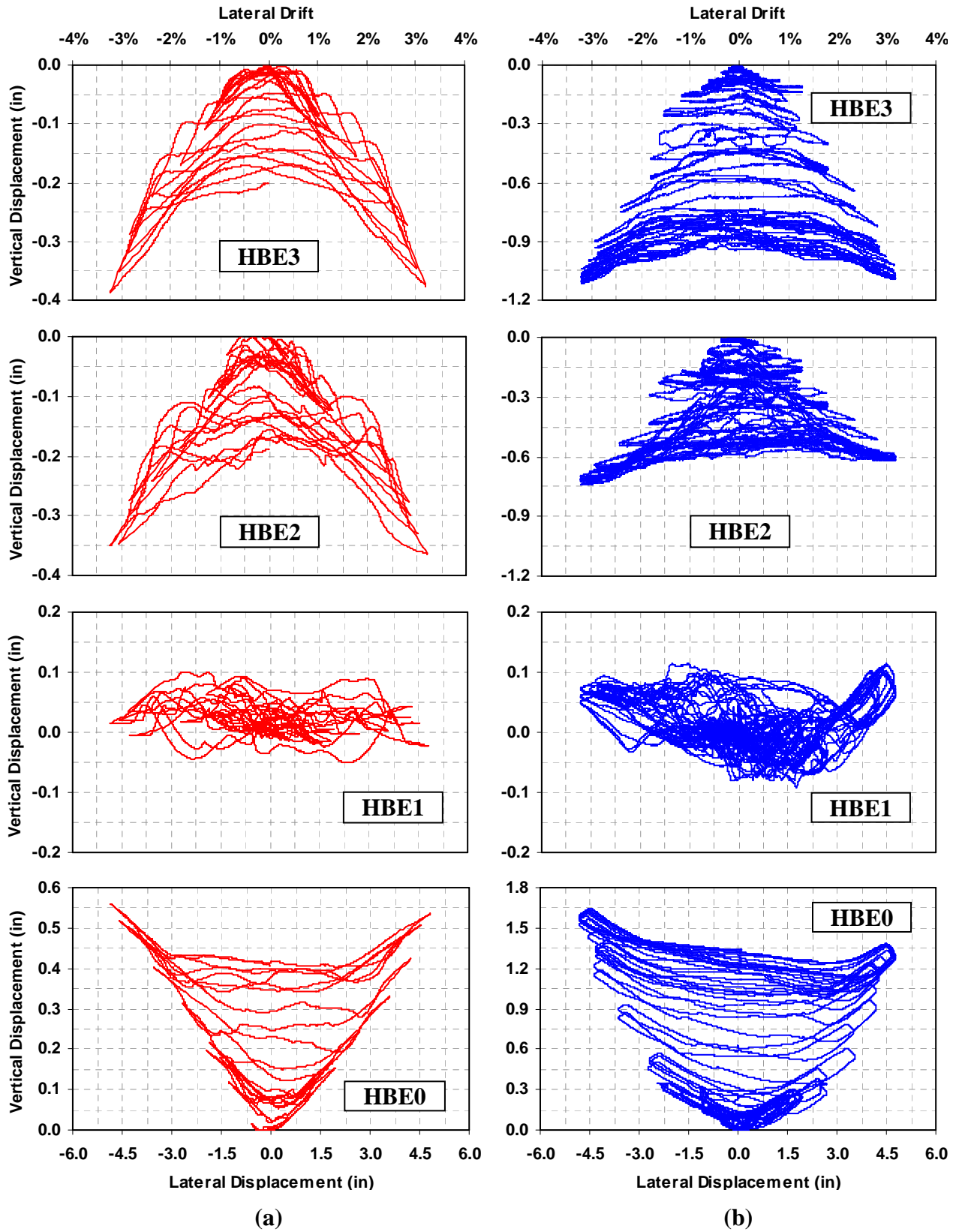
Figure 5-13 HBE Vertical Displacement Structure versus Lateral Displacement (a) Finite Element Analysis; (b) Experiment

232

Figure 5-14 shows the resulting moment-rotation hysteresis compared to those recorded during the experiment. Note that the moment-rotation hysteresis for the bottom two HBEs were not available from the experiment due to instrumentation limitation. While the finite element results confirm the observed un-symmetry of the experimentally obtained hysteretic curves, the rotation magnitude for HBE2 and HBE3 were also smaller compared to those recorded during the experiment. For example, when the FE model was cycled up to the maximum target drift of 3.33%, HBE3 maximum rotation reached 0.035 radians (i.e., corresponding to a normalized rotation $\theta/\theta_{0.03}$ of 1.17, where θ and $\theta_{0.03}$ are the angle of rotation and the required plastic rotation capacity of a special moment resisting frame) compared to 0.054 radians recorded during the experiment. It is suspected that the decision to exclude several displacement steps from the analysis and to conduct only one cycle per displacement step; as well as the fact that the FEM model was not developed to consider material fatigue life, contributed to these discrepancies as well as to the discrepancies in the accumulation of plastic incremental deformation. It was also observed that the finite element results exhibited more severe local buckling at the ends of the HBE than observed experimentally (Figure 5-12), which explains the drop in flexural strength noted in the analytically obtained experimental curves (Figure 5-14). The reasons for this discrepancy are unclear but partly attributable in some cases to the detailing used for load transfer to the specimen. This may have contributed to all of the above discrepancies, but in a manner that is unquantifiable given the constraints in the available experimental data. Hopefully, future researchers, benefiting from the knowledge generated during this experimental program, will be able to generate additional experimental data tailored for validation by finite analysis results to further investigate the causes for the above discrepancies.

5.7 Summary

A finite element investigation of the tested SPSW specimen was conducted using the finite element software ABAQUS/Standard (Dassault Systèmes 2009b). Specific finite element features to capture the SPSW specimen behavior were described. Among them were geometry modeling and mesh algorithm, element and material definitions, boundary conditions, constraints, loading sequences simulating the experimental setting, and nonlinear numerical stability. Eigenvalue buckling analysis was performed to introduce initial imperfections in the finite element (FE)
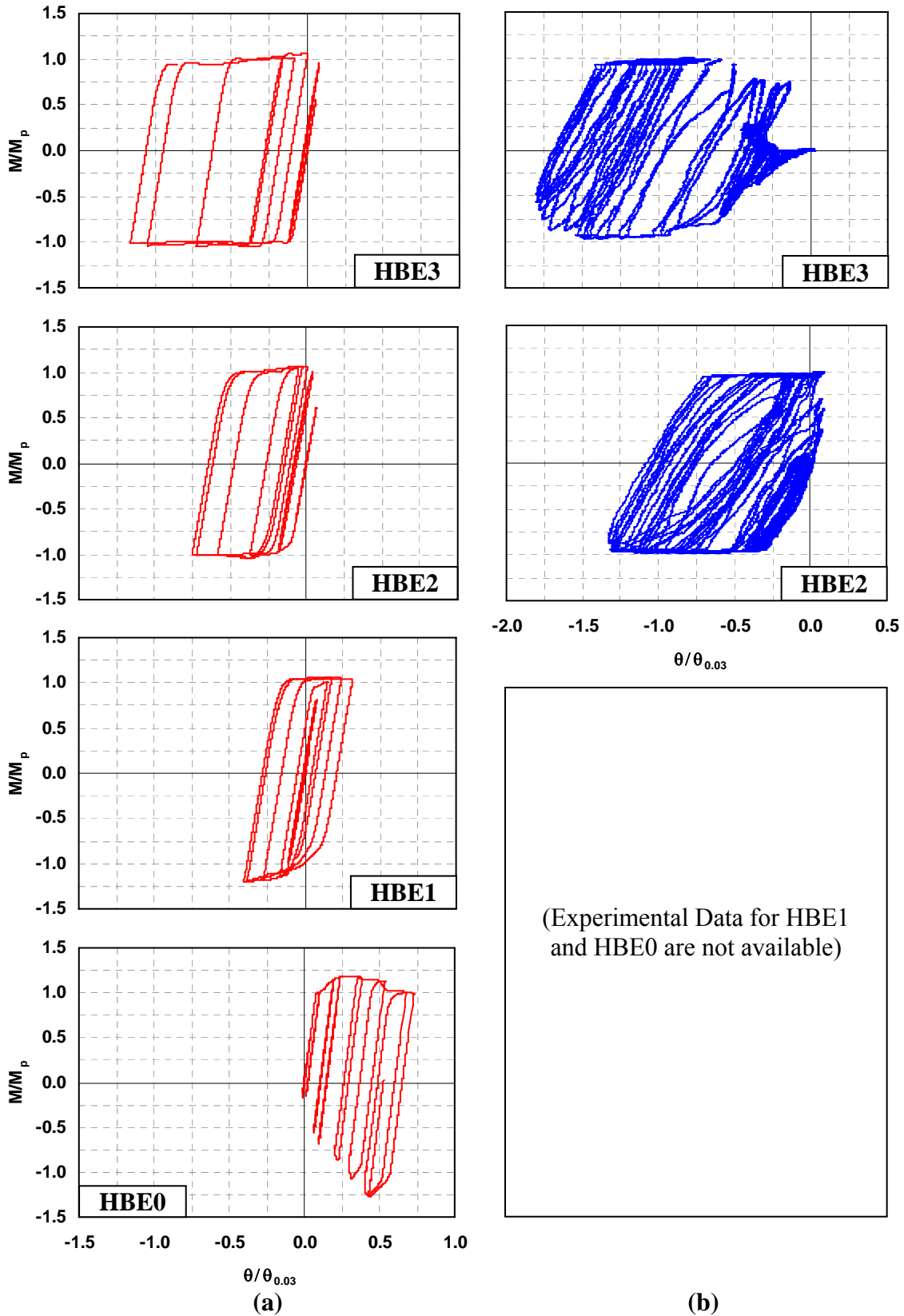
**Figure 5-14 Normalized Moment Rotation Hysteresis at East HBE-to-VBE Joints
(a) Finite Element Analysis; (b) Experiment**

model. A finite element monotonic pushover analysis with a fixed support at the base of columns was first conducted. Discrepancies between results from the analytical pushover curve and the corresponding cyclic envelope of the force displacement hysteresis recorded in the experiment led to a subsequent analysis using a revised FE model with floor plate included. The revised model, however, did not consider the interaction between the floor plate and the rigid concrete floor discussed in the previous two sections. Though the analytical model still overestimated the experimental strength at the onset of yielding, an improved result was observed when compared to the previous result for the FE model with fixed supports. Afterward, a finite element cyclic pushover analysis was conducted. Results were presented in terms of the hysteresis of base shear versus lateral displacement at the top floor, plastification in the FE model, HBE vertical deformations, and moment-rotation hysteresis at HBE connections to VBEs. Overall, the finite element results resemble the specimen behavior observed during the experiment.

SECTION 6
DETERIORATION MODEL DEVELOPMENT FOR COLLAPSE ASSESSMENT OF STEEL PLATE SHEAR WALLS

6.1 General

One of the research objectives outlined in Section 1 was to quantify seismic performance factors (SPF) for steel plate shear walls (SPSW). The FEMA P695 methodology was selected to accomplish this objective. As briefly reviewed in Section 2, this methodology provides a rational basis for establishing SPF for seismic-force resisting systems through assessing the system risks against collapse under maximum considered earthquake (MCE) ground motions. One of the key elements of this assessment depends on the accuracy of the structural numerical models to simulate component strength deterioration that would lead to global collapse of the system. This section describes development of component strength deterioration models for collapse assessment of SPSW, focusing on stress-strain or force-deformation relationships for infill plates and boundary elements. Development of global structural numerical models and results of the collapse assessment will be presented in the two subsequent sections.

Deterioration and failure modes identified from 36 SPSW tested specimens are presented first. Cyclic deformation capacities of these SPSWs when reaching their ultimate strength, failure points, and rate of strength degradations are statistically quantified. Based on these statistical results, initial deterioration models for SPSW components (i.e., infill plates and boundary elements) are presented. Prior to calibration of these initial models, implementation of these deterioration material models in OpenSees (Mazzoni *et al.* 2009) is presented followed by a brief summary of results obtained for various case studies conducted. Using nonlinear static analysis, these case studies are intended to examine several possibilities of degradation models for infill plates and boundary elements, namely: (1) different rate of strength deterioration for both components; (2) different deterioration parameters for corner and middle "strips", when referring to strips in modeling walls (i.e., severe and moderate strength degradations for corner and middle strips, respectively); and (3) strength degradation only occurring on either one of the SPSW

components (i.e., elasto-plastic material for infill plates and degradation material model for boundary elements, and vise versa).

The chosen deteriorated material models for infill plates and boundary elements are then calibrated to four selected SPSW specimens varying from one- to four-story, with aspect ratio ranging from 1.0 to 2.2. Final deterioration models obtained from this calibration are described, and will be used for collapses assessment of steel plate shear walls in Section 8.

6.2 Deterioration and Failure Modes of Steel Plate Shear Walls

A literature review of past research on modeling strength degradation of structural components was presented in Section 2.3. As described in that section, in order to correctly model collapse of structures, it is important to quantify plastic deformations of structural components when reaching the point of maximum strength before strength degradation starts to occur (i.e., defined as the capping point in the FEMA P695 document), rate of degradation (post-capping stiffness), and residual strength. To quantify these degradation parameters for SPSW components (namely, for the boundary elements and infill plates), a detailed literature review of SPSW experimental results from research in the past thirty years was conducted. This review was intended to investigate three specific objectives, namely: (1) identify the deterioration modes associated with loss of strength and the failure modes that occurred at the end of each test, (2) statistically quantify at what story drift the capping and failure points occurred, and (3) statistically quantify rate of degradation, which is defined as the ratio between strength drop and drift range from the failure to the capping points.

The aforementioned review was limited to conventional unstiffened slender-web steel plate shear walls for which testing data was adequately reported and accessible to the author at the time of this writing. While the terms "unstiffened" and "slender-web" are self explanatory, the term "conventional" deserves some additional explanation. In this research, conventional SPSWs are defined as SPSWs with flat infill plates as opposed to corrugated infill plates (e.g., Berman and Bruneau 2005), without openings or slits in the infill plates for which the standard Strip Model would not be not applicable (e.g., Roberts and Sabouri-Ghomi 1992; Hitaka and Mitsui 2003),

without steel restrainers used to prevent or reduce the free development of infill plate out-of-plane buckling (e.g., Lin and Tsai 2004; Li *et al.* 2010), without concrete restraints intended to prevent buckling of infill plates or create composite SPSWs (e.g., Zhao and Astaneh Asl 2004), with infill plates fully connected to steel boundary frames as opposed to partially connected only to horizontal boundary elements or connected to concrete boundary frames (e.g., Choi and Park 2009; 2011), and with horizontal boundary elements with full continuous moment connections to vertical boundary elements (as opposed to post tensioned rocking connections as used in self-centering SPSWs such as those considered by Dowden *et al.* 2012; Clayton *et al.* 2012).

In addition, coupled walls (Choi and Park 2009; Neagu *et al.* 2011) were excluded from this study because no sufficient research evidence existed at the time of this writing to suggest that coupled walls behave similarly (in terms of peak strength and failure modes as a function of drift) to conventional SPSWs. Lastly, only specimens tested using an incremental pushover loading to simulate earthquakes were included because the aforementioned degradation parameters were relatively simple to identify in this type of loading protocol compared to that in other kind of loadings. In other words, specimens tested using shake table testing (e.g., Rezai 1999), pseudo-dynamic testing (e.g. Tsai *et al.* 2006, Qu *et al.* 2008), and blast loadings (e.g., Warn and Bruneau 2009) were also excluded from this study. It should be emphasized that the perforated SPSW and corner cut-out SPSW tested by Vian and Bruneau (2005) were included in the review because these specimens demonstrated comparable behaviors to those with solid infill plate and their design and behavior is similar to conventional SPSWs.

Based on the above categories, 36 SPSW specimens were examined, varying from single-story to four-story SPSWs with aspect ratios ranging from 0.7 to 2.2. Both welded and bolted connections were used in these walls, either connecting infill plates by means of fish plates to boundary frames or connecting horizontal to vertical boundary elements. Findings from this literature review are discussed in the following two sub-sections.

6.2.1 Identification of Deterioration and Failure Modes

Inferred from the experimental data considered here, the possible causes of deterioration of structural components that lead to failures of steel plate shear walls can be classified into 3

modes. As summarized in Table 6-1, they are deteriorations associated with web tearing, flexural or shear failure of boundary elements, and instability of boundary elements. Each deterioration mode is described in detail as follows.

Table 6-1 Possible Deterioration and Failure Modes of Steel Plate Shear Walls

Failure Mode	Description
Web Tearing (WT)	Fractures or tearing of the infill plates that result in failure of plate to develop tension field action (TFA) and cause degradation of SPSW strength to sustain story shear forces. Web tearing can occur either at infill plate connections to fish plates, at the corners of web panels, across the infill plates where right- and left-leaning yield lines intersect, or at several of these locations.
Failure of Boundary Elements (FBE)	**Flexural Failure** Flexural failure observed in past experiments is characterized by the following damages. 1. Plastic hinge development at boundary element ends with excessive yielding and localized flange or web buckling. 2. Weld fracture at the connections either between HBE and VBE or between VBE and the base. 3. Fracture of the boundary elements away from the connections (i.e., at the center line of plastic hinge). Especially in SPSWs with reduced beam section (RBS) connections, fractures can occur at its reduced flange center line. 4. Shear tab failure that leads to HBE web and flange fractures. **Shear Failure** Shear failure is characterized by shear yielding of a significant length across the web of VBEs, resulting in lower expected VBE plastic moments and significant VBE inward deformations (i.e., hour-glass shape deformations) from the pulling forces of yielded infill plates.
Instability of Boundary Elements (IBE)	Instability of boundary elements is associated with global out-of-plane (weak-axis) buckling of VBEs or lateral-torsional buckling of HBEs. In general, SPSWs with this type of failure mode have significantly low capacity to sustain loads.

6.2.1.1 Web Tearing

As the main component of SPSWs to dissipate energy during earthquakes, infill plates (webs) are designed to experience large inelastic elongations. As a result of web inelastic buckling during development of tension field action (TFA) and repeated cycles of loadings, low-cycle fatigue fracture or tearing of the webs is unavoidable. Reported repeatedly in past experiments, web tearing can occur either at the corners of web panels (Figure 6-1a), at infill plate connections to fish plates (Figure 6-1b), or at the intersection of right- and left-leaning yield lines across the infill plates where plate kinking frequently takes place upon repeated cyclic loading (Figure 6-1c). In general, web tearing occurs at several locations rather than exclusively at one of these locations.
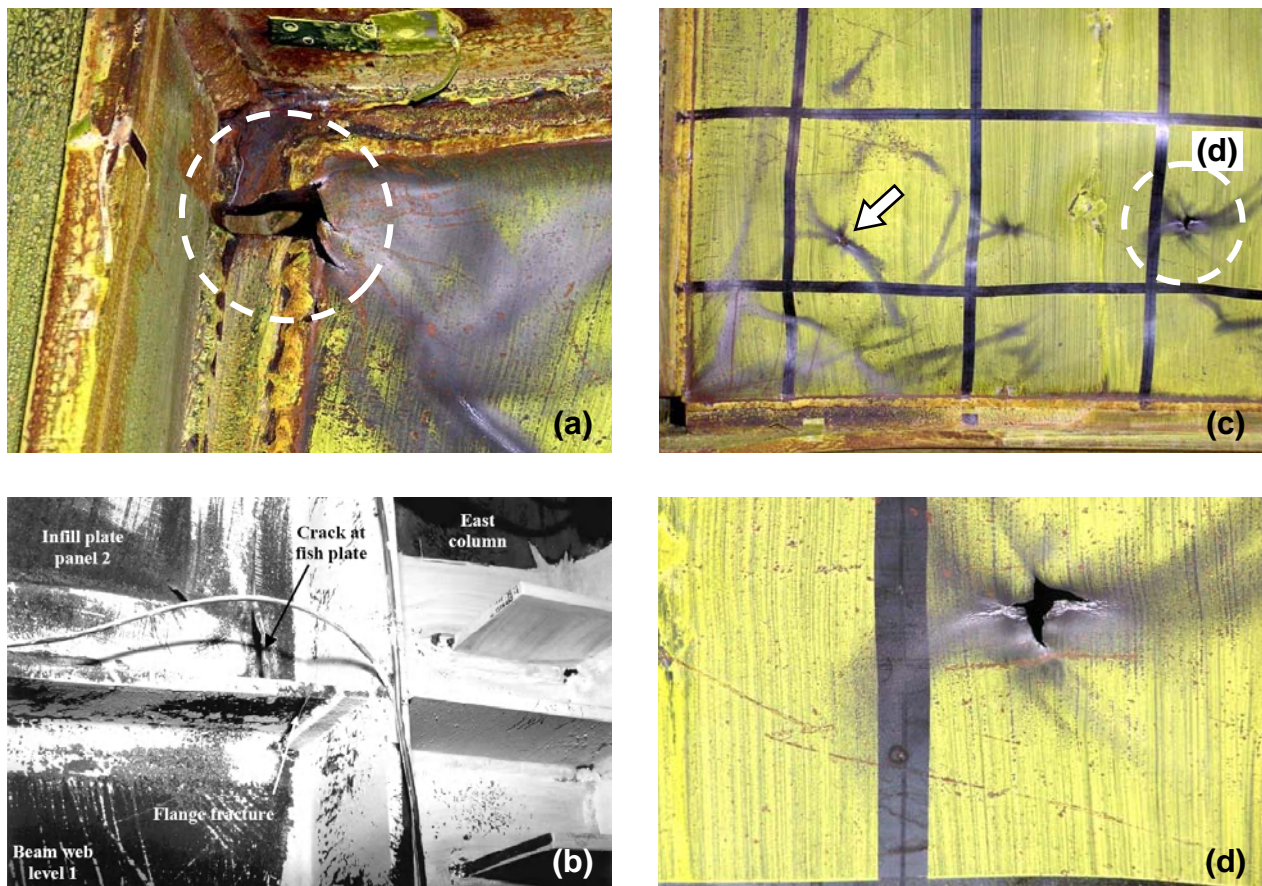
Figure 6-1 Common Locations of Web Tearing: (a) at the Corner of Web Panel (Vian Bruneau 2005); (b) Connection to Fish Plate (Behbahanifard *et al*. 2003); (c) and (d) Across Infill Plates (Vian and Bruneau 2005)

It should be emphasized here that not every web tearing situation can be attributed to deterioration of SPSW strength. A relatively small fracture of infill plates (and as long as it remains at somewhat the same size through out loading histories) has insignificant degrading impact on the structure's ultimate strength. Since infill plates provide high redundancy to transfer tension forces to surrounding boundary elements, cracks in one part of a plate strip may only locally disturb the "regularity" of the tension stress flows. As such, stresses can flow around and re-distribute tension stresses to adjacent un-cracked part of the infill. Figure 6-2 illustrates how a crack strip maintains TFA for the three possible types of locations of fractures. This phenomenon by which infill plates can maintain TFA throughout the loading history even though cracks have occurred at several locations was reported in past experiments (e.g., Lubell et. al. 2000, Astaneh-Asl and Zhao 2002, Vian and Bruneau 2005, Li *et al*. 2010). Strength degradation reported in these reports was typically associated with another deterioration mode (i.e., failure of boundary elements) which will be explained in a later paragraph.
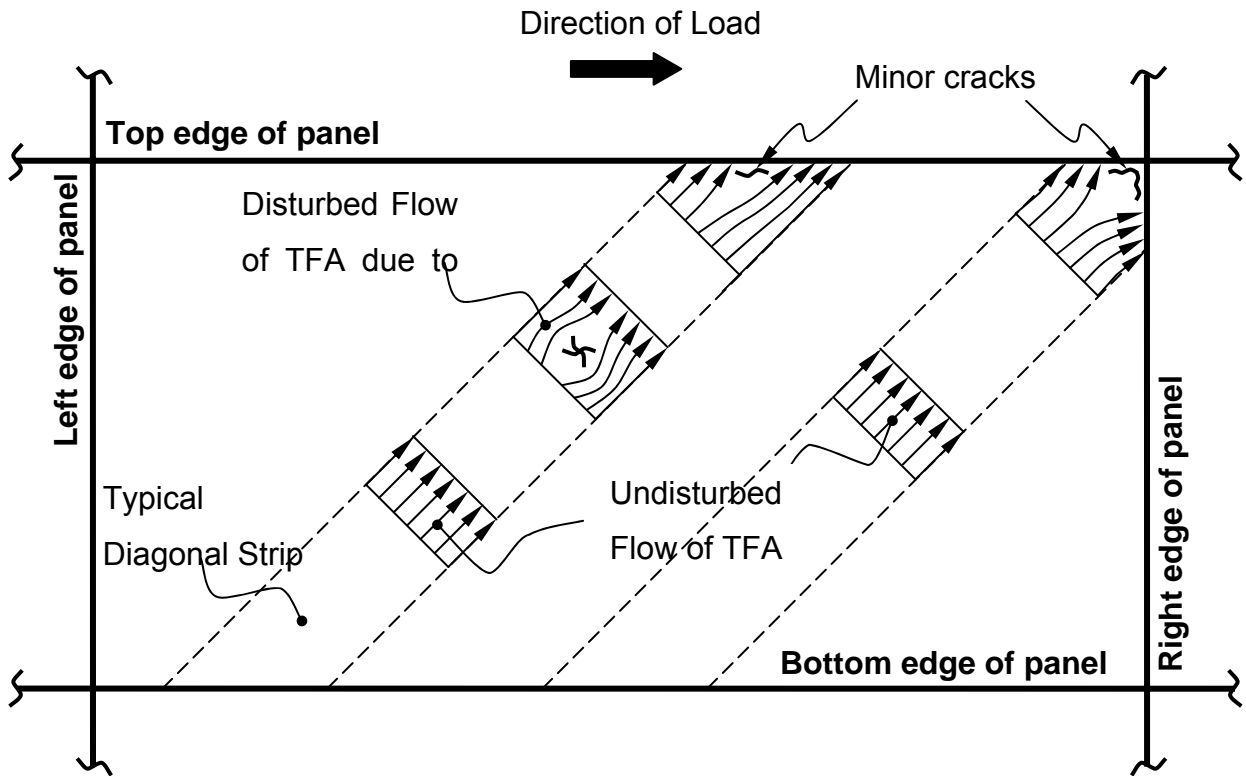
Figure 6-2 Re-orientation of Tension Field Action (TFA)

Web tearing can be attributed to deterioration of SPSW strength only if fractures of infill plates propagate to significant lengths, which can then cause parts of the infill plates (corresponding to their plate strips in computer models) to be unable to develop TFA. As a result, infill plates progressively lose their capacity to sustain loads. Examples of this deterioration mode are shown in Figure 6-3. In the first example, the cracks initially occurred at the corner of the panel and then propagated to the connections of infill plates with vertical and horizontal fish plates; while in the second example, the cracks also initially occurred at the same location as the first one, but this time propagated to the middle part of the infill plates.
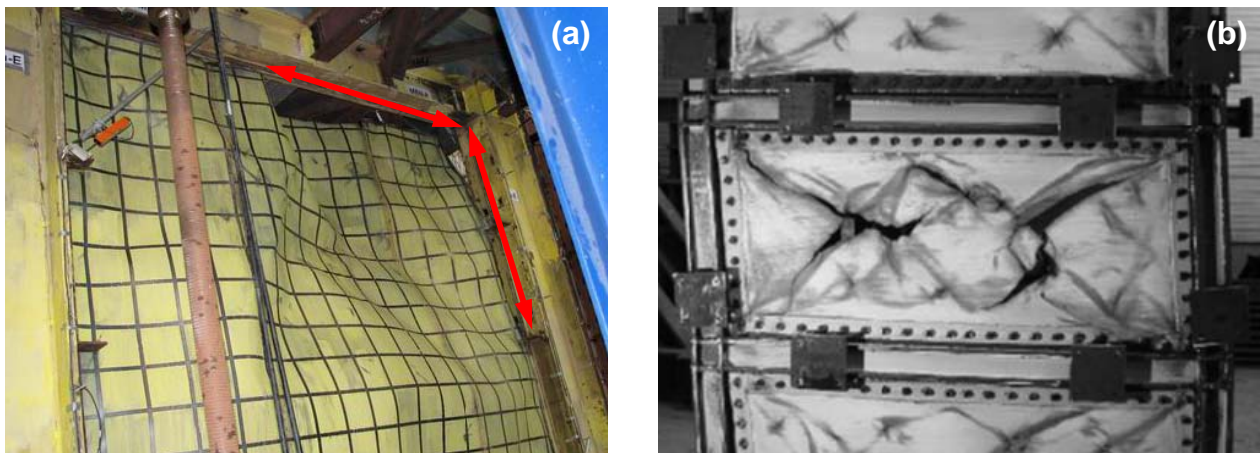
Figure 6-3 Web Tearing Creating Strength Deterioration: (a) Web Tearing along Vertical and Horizontal Fish Plates (Qu and Bruneau 2008); (b) Web Tearing across the Infill Plates (Choi and Park 2009)

To distinguish the above two kinds of web tearing for the purpose of quantifying deterioration parameters in Section 6.2.2, they are respectively referred to as *non-deteriorated web tearing (nWT)* and *web tearing (WT)* attributed to deterioration of SPSW strength.

6.2.1.2 Failure of Boundary Elements

In the early development of SPSW, simple HBE-to-VBE connections and relatively large sections for boundary elements were sometimes used, with the objective of ensuring that boundary elements essentially remain elastic under the maximum tension forces from the yielded infill plates. Consequently, failures of boundary elements were not reported in these early experiments. While boundary elements remain relatively large in the more recent SPSW research as well as in implementations in real buildings, moment connections have replaced simple connections to

provide additional redundancy and overstrength to the system. As a result, failures of boundary elements have been more frequently reported in research (when testing was conducted to failure after satisfactory seismic performance was achieved). Hence, it is important to investigate the failure of boundary elements in order to correctly model deteriorations for collapse assessment of steel plate shear walls.

Failures of boundary elements (FBE) can be classified as either flexural failure or shear failure. Flexural failure observed in past experiments can be classified into the following types of damage, namely: (1) plastic hinge development at boundary element ends with ductile strength degradation due to localized flange or web buckling; (2) weld fracture at the connections between HBE and VBE or between VBE and their base; (3) fracture of the boundary elements away from the connections (i.e., at the center line of plastic hinge, particularly in HBEs with reduced beam section (RBS) connections where fractures have been observed to occur at mid-length of the reduced flange segment), and; (4) shear tab failure that leads to HBE web and flange fractures. Shear failure is characterized by shear yielding of a significant length across the web of VBEs, which causes lower-than-expected VBE plastic moments and can result in significant VBE inward deformations (i.e., hour-glass shape deformations) due to the pulling forces from yielded infill plates (Qu and Bruneau 2010). Note that in some instances in past research, specimens were specifically designed to trigger specific failure modes. For example, two specimens that developed shear failure were intentionally designed to have non-compact VBE sections. Excessive flange local buckling was reported in that case, which accentuated the VBE inward deformations (Park *et al.* 2007). Several examples of flexural and shear failures are shown in Figures 6-4 and 6-5, respectively.

While flexural failure is desirable to dissipate earthquake energy, shear failure should be avoided for the reason described above. This can be achieved by designing boundary elements with seismically compact sections and by ensuring that the shear demand, V_u, on boundary elements is less than their nominal shear strength V_n estimated as:

$$V_n = 0.6 f_y A_w \tag{6-1}$$

where f_y is the yield stress of boundary elements and A_w is the web area of boundary elements. Consequently, shear failure can be prevented in properly designed SPSWs, and it is therefore ruled
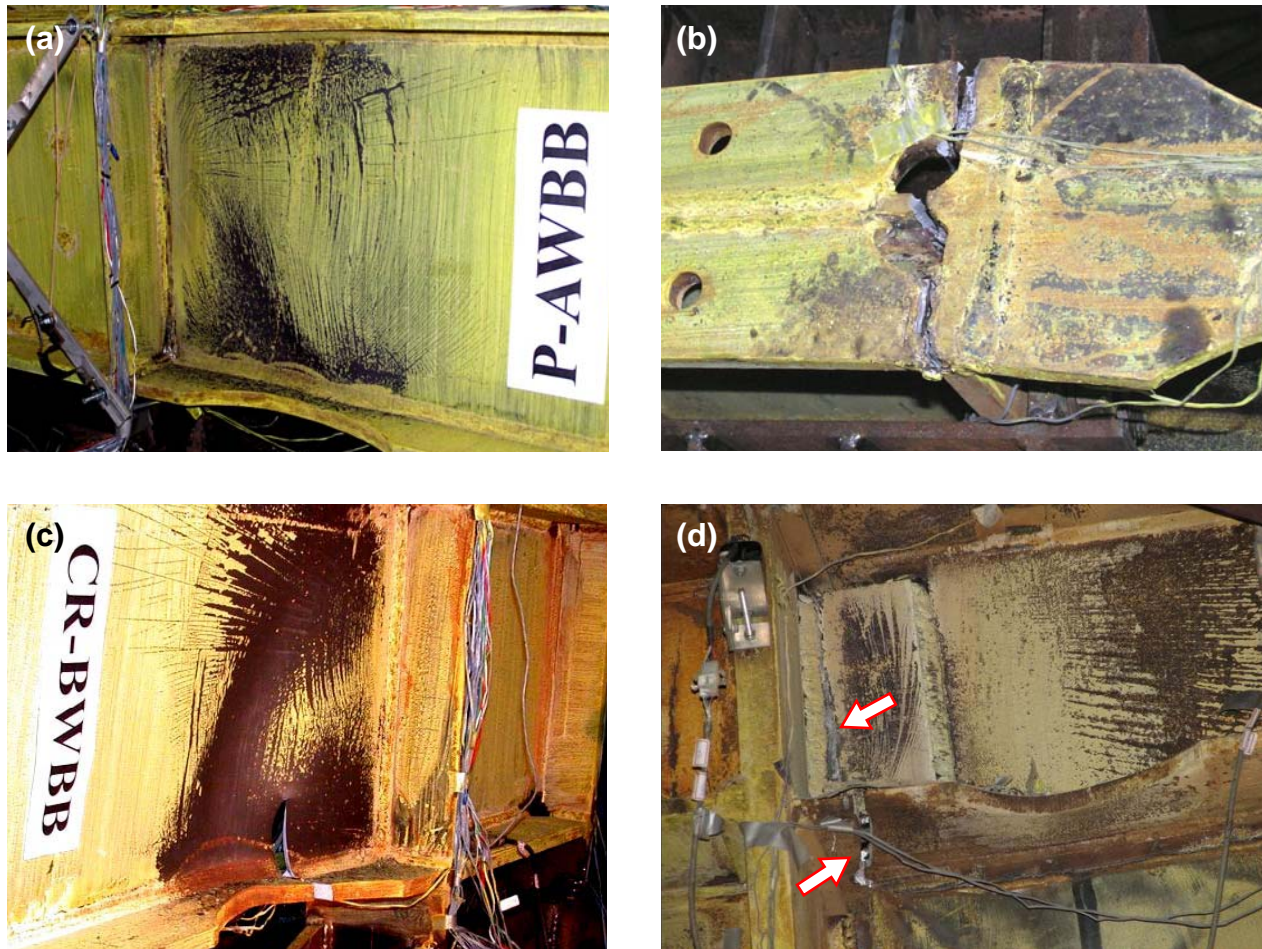
Figure 6-4 Flexural Failure of Boundary Elements: (a) Plastic Hinge Development; (b) Weld Connection Fracture; (c) Fracture at RBS Connection (the first three photos from Vian and Bruneau 2005); (d) Shear Tab Fracture (Qu and Bruneau 2008)

out as one of the limit states to be considered in applying the FEMA P695 methodology and in developing deterioration models for collapse assessment of steel plate shear walls.

6.2.1.3   Instability of Boundary Elements

A deterioration mode associated with instability of boundary elements (IBE) has been occasionally reported in past experiments. Among 36 SPSW specimens examined, only 3 specimens exhibited this deterioration mode, compared to 8 and 25 specimens that exhibited the first two deterioration modes, respectively (Sections 6.2.1.1 and 6.2.1.2). Global instability reported in these 3 specimens was associated with out-of-plane (weak-axis) buckling of VBEs or lateral-torsional buckling of HBEs; and occurred in the early stages of loading (i.e., as early as 1% drift). Figure 6-6 presents examples of IBE deterioration mode.

245
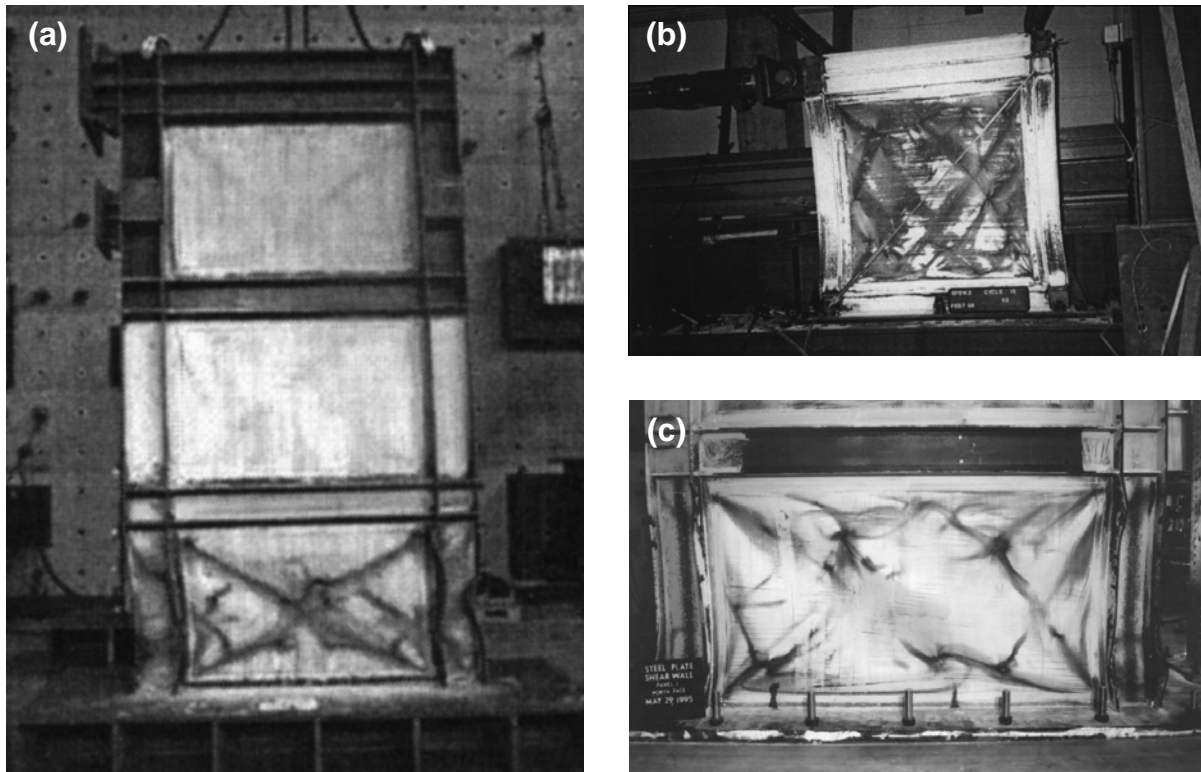
Figure 6-5 Shear Failure of Boundary Elements: (a) Shear Yielding with Excessive Local Buckling (Park *et al*. 2007); (b) Hour-Glass Shape Deformation (Lubell *et al*. 2000); (c) Shear Yielding at the Base of 4-Story Specimen (Courtesy of Driver R. G.)
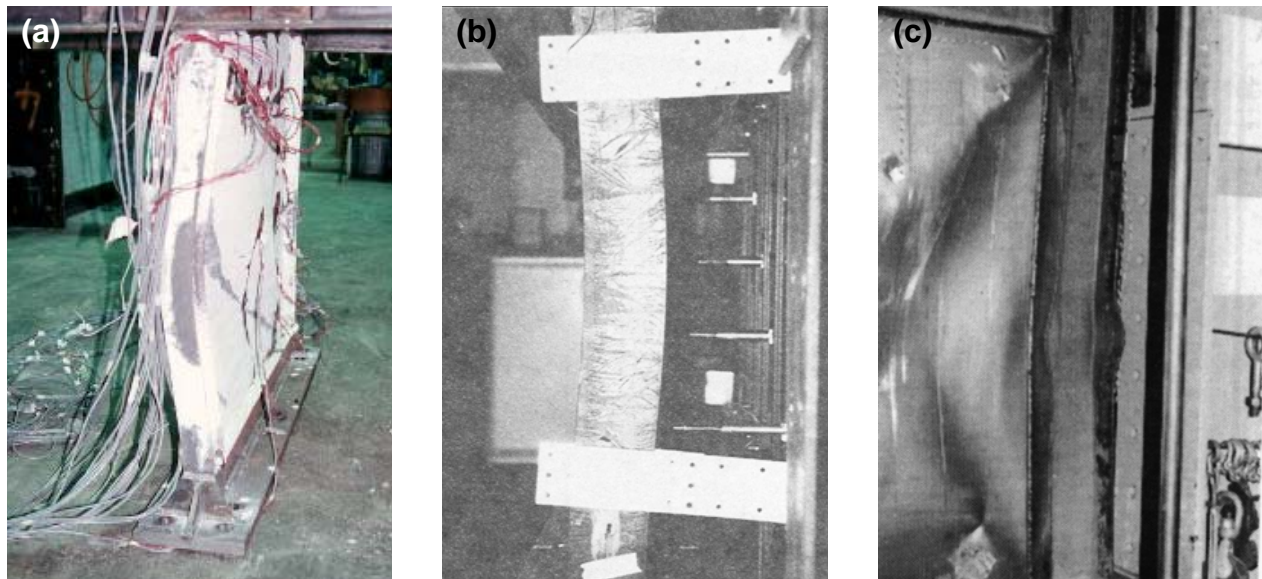
Figure 6-6 Instability of First Story Vertical Boundary Elements: (a) Out-of-plane Buckling in 4-Story SPSW Specimen (Courtesy of Ventura C. E.); (b) Out-of-plane Buckling in 3-Story SPSW Specimen (Caccese *et al*. 1993); (c) VBE Local Buckling in 2-Story SPSW Specimen that Lead to Global Instability (Elgaaly 1998)

246

This undesirable failure mode is mainly ascribed to insufficient flexural stiffness of boundary elements (Montgomery and Medhekar 2001). For this reason, to ensure adequately stiff boundary elements in designs, the Canadian and American standards for seismic design of steel structures specify that moment of inertia of boundary elements $I_{HBE,\,VBE}$ should satisfy the following limit:

$$I_{HBE,VBE} \geq 0.00307 \frac{t_w h_s^4}{L} \tag{6-2}$$

where t_w is the infill plate thickness; h_s and L are the center-to-center distances of story height and bay width, respectively. Recent work by Qu and Bruneau (2010), however, suggested that there is no correlation between satisfying this specified limit and preventing global instability of boundary elements. Instead, IBE deterioration mode can be prevented by designing boundary element sections with sufficient out-of-plane buckling strength.

IBE is unlikely to occur in a well-designed SPSW, because it can be prevented by designing boundary elements according to the capacity design principle. Therefore, as for the previously described shear failure mode, the IBE failure mode also can be ruled out as one of the limit states to be considered in applying the FEMA P695 methodology and for deterioration model development. Hence, only the web tearing (WT) and failure of boundary elements (FBE) are considered in this research for quantification of deterioration parameters in SPSW and the results are presented in the following sub-section.

6.2.2 Statistical Estimation of Cyclic Deformation Capacity

Among 36 SPSW specimens examined, large variability of experimental outcomes was observed. To avoid a bias interpretation of cyclic deformation capacity at the ultimate (capping) and failure points, those specimens were first classified into four groups according to whether the ultimate strength of the specimen had been reached or not, and whether brittle or ductile strength degradation occurred for the specimens that had reached their ultimate strengths, as summarized in Table 6-2. The first group in the table consists of specimens for which ultimate strength was not yet reached during the experiments. Instability of boundary elements, brittle weld fractures at column connections to base plates, and decisions of researchers (that might be related to some experimental limitations) were some of the factors reported to have caused these experiments to conclude before specimens reached their ultimate strengths. Specimens classified into the second

Table 6-2 List of Steel Plate Shear Walls Tested Specimens

Researcher	Spec. ID	No. of Stories	Geometric Properties			Type of Connection[1]		Condition at Ultimate			Condition at End			μ
			L_p (mm)	H_s (mm)	Aspect Ratio	Frame	Infill	Mode[2]	V_{max} (kN)	Drift (%)	Mode[2]	V_{end} (kN)	Drift (%)	
Group 1: Tests stopped before specimen reached its ultimate strength (7 SPSWs)														
Timler and Kulak (1983)	–[a]	1	3750	2500	1.5	P+W	W	–	–	–	nWT	2698[b]	1.12[i]	2.8[c]
Tromposch and Kulak (1987)	–[a]	1	2750	2200	1.3	P	W	–	–	–	nWT	3000[b]	0.77[h]	5.7
Caccese et al. (1993)	M22	3	1245	838	1.5	W	W	–	–	–	FBE	169	2.00[j,e]	6.7
Elgaaly (1998)	SWT11	2	1473	1156	1.3	P	P	–	–	–	IBE	369	2.09[e]	4.2
	SWT12	2	1473	1156	1.3	P	P	–	–	–	FBE	387	2.09[e]	4.2
	SWT13	2	1473	1156	1.3	P	P	–	–	–	FBE	343	1.79[e]	3.6
Lubell et al. (2000)	SPSW4	4	900	900	1.0	W	W	–	–	–	IBE	175	1.5[d]	1.5
Group 2: Tests stopped approximately at the ultimate point (6 SPSWs)														
Caccese et al. (1993)	M14	3	1245	838	1.5	W	W	FBE	334	2.00[e]	–	–	–	4.0
	S22	3	1245	838	1.5	P	W	FBE	142	1.8[e]	–	–	–	6.0
	S14	3	1245	838	1.5	P	W	FBE	356	1.7[e]	–	–	–	3.4
Lubell et al. (2000)	SPSW1	1	900	900	1.0	W	W	FBE	210	4.00[h]	–	–	–	4.0
Park et al. (2007)	SC4T	3	1750	1100	1.6	W	W	FBE	2532	2.6[e]	–	–	–	4.4
	SC6T	3	1750	1100	1.6	W	W	FBE	3021	2.6[e]	–	–	–	4.0
Group 3: Tests conducted beyond the ultimate point with brittle degradation (6 SPSWs)														
Caccese et al. (1993)	M12	3	1245	838	1.5	W	W	FBE	376	1.00[e]	IBE	360	1.7[e]	2.4
Elgaaly (1998)	SWT14	2	1473	1156	1.3	P	W	IBE	405	1.19[e]	IBE	343	1.79[e]	3.6
	SWT15	2	1473	1156	1.3	P	P	FBE	432	2.09[e]	IBE	426	2.39[e]	4.8
Vian and Bruneau (2005)	S2	1	4000	2000	2.0	W+RBS	W	FBE	2115	3.0	FBE	1692	3.0	10
Park et al. (2007)	WC4T	3	1750	1100	1.6	W	W	FBE	1526	0.9[e]	IBE	1000	2.5[e]	5.8
	WC6T	3	1750	1100	1.6	W	W	FBE	1682	0.8[e]	IBE	800	2.5[e]	5.4

Table 6-2 List of Steel Plate Shear Walls Tested Specimens – Cont'd

Researcher	Spec. ID	No. of Stories	Geometric Properties			Type of Connection[1]		Condition at Ultimate			Condition at End			μ
			L_p (mm)	H_s (mm)	Aspect Ratio	Frame	Infill	Mode[2]	V_{max} (kN)	Drift (%)	Mode[2]	V_{end} (kN)	Drift (%)	
Group 4: Tests conducted beyond the ultimate point with ductile degradation (17 SPSWs)														
Driver et al. (1997)	– [a]	4	3050	1776	1.7	W	W	WT	3080	2.2[d]	FBE	2618	4.0[d]	9.0
Lubell et al. (2000)	SPSW2	1	900	900	1.0	W	W	FBE	250	4.00	FBE	175	5.0	7.5
Astaneh-Asl and Zhao (2002)	UCB-1	2	– [f]	3100	– [f]	W	W	FBE	4005	3.3[d]	FBE	2403	4.0[d]	5.7
	UCB-2	3	– [f]	2067	– [f]	W	W	FBE	5451	2.2[d]	FBE	4066	3.0[d]	4.3
Behbahanifard et al. (2003)	– [a]	3	3050	1678	1.8	W	W	FBE	3500	2.62[d]	WT	2850	3.7[d]	7.9
Berman and Bruneau (2005)	F2	1	3658	1829	2.0	P	W	WT	620	3.0	WT	420	3.7	12
Vian and Bruneau (2005)	P	1	4000	2000	2.0	W+RBS	W	FBE	1790	2.0	FBE	1650	3.0	10
	CR	1	4000	2000	2.0	W+RBS	W	FBE	2050	2.5	FBE	1340	4.0	13.3
Park et al. (2007)	SC2T	3	1750	1100	1.6	W	W	FBE	1663	2.6[e]	FBE	1338	3.8[j]	7.0
Qu et al. (2008)	– [a]	2	4000	4000	1.0	W+RBS	W	FBE	4245	3.3[d,g]	WT	2387	5.2[d,g]	10.4
Choi and Park (2008)	FSPW1	3	1650	1075	1.5	W	W	FBE	1392	3.6[e]	FBE	1364	5.2[j]	8.1
	FSPW2	3	2350	1075	2.2	W	W	FBE	1817	4.5[e]	WT	1776	5.6[j]	11.8
	FSPW3	3	2350	1075	2.2	W	W	FBE	1565	2.7[e]	FBE	1100	5.4[j]	10.6
Choi and Park (2009)	BSPW1	3	2350	1075	2.2	W	P	WT	1882	3.6[e]	WT	1200	5.3[e]	11.8
	BSPW2	3	2350	1075	2.2	W	P	WT	1961	3.3[e]	FBE	1055	5.3[e]	11.0
Li et al. (2010)	N	2	2140	3250	0.7	W+RBS	W	FBE	1300	4.0[j]	FBE	1105	5.0[j]	12.5
	S	2	2140	3250	0.7	W+RBS	W	FBE	1070	3.0[j]	WT	910	5.3[j]	12.5

Note: [a] No specimen identification available   [b] Two-single story SPSW tested in tandem. Value shown is capacity of one single-story SPSW
[c] μ = $\Delta_{end}/\Delta_{yield}$ (Group 1, 3, 4); μ = $\Delta_{max}/\Delta_{yield}$ (Group 2)   [d] First story drift   [e] Top story drift   [f] Not available
[g] Information from phase II (i.e., cyclic test)   [h] At the end of the first loading phase (i.e., cyclic pushover loading)
[i] Result from monotonic pushover loading   [j] Maximum inter-story drift
[1] P = Pin (simple) or partial welded connection; W = Welded (rigid) connection; RBS = Reduced Beam Section
[2] nWT = non-deteriorated; WT = deteriorated Web Tearing; FBE = Failure of Boundary Elements; IBE = Instability of Boundary Elements

group were tested up to their ultimate strength and the experiments concluded either at that point, or shortly thereafter. Typically, in such tests, a nearly flat pushover curve (i.e., force-displacement relationship) toward the end of a test was deemed to be an indication that the specimen had reached its ultimate strength and the experiment stopped.

The last two groups in Table 6-2 consist of the specimens that were pushed beyond the ultimate point and strength degradations were recorded. These two groups are differentiated by how strength degradations occurred. Specimens that could only sustain one displacement step beyond the ultimate point before major failure caused experiments to terminate are listed together in the third group. By contrast, strength degradation in specimens in the last group were subjected to several displacement cycles beyond the ultimate point. Stable degradation and gradual strength drop with respect to the ultimate strength were generally exhibited in those specimens.

Here, these two types of strength degradations (corresponding to specimens in the third and fourth groups of Table 6-2) are labeled as brittle and ductile degradations, respectively. In the former case, excessive inelastic deformation that caused instability of boundary elements and shear failure of boundary elements were two factors that caused specimens to fail abruptly in the displacement step beyond the ultimate point. By contrast in the latter case, gradual tearing (fracture) of web or boundary elements as the load progressed resulted in stable and ductile degradations.

Table 6-2 provides information on all 36 specimens reviewed, with respect to specimen number of stories, geometric dimensions (for multi story specimens, the first story height and width are used), panel aspect ratio, types of connections used for infill plate-to-boundary frames and HBE-to-VBE, base shear and corresponding drifts when the specimen reached the ultimate point and at conclusion of the test, and displacement ductility ratio (measured as specimen displacement at the conclusion of the test divided by reported effective yield displacement).

To statistically estimate cyclic deformation capacities at the capping and failure points, the following considerations were exercised.

1. Since the specimens in Group 1 did not reach their ultimate point, they were excluded from these statistical calculations.

2. Cyclic deformation capacity at the capping point was estimated considering the specimens in Groups 2, 3, and 4 of Table 6-2.

3. Only the specimens in Group 4 were considered to statistically quantify the cyclic deformation capacity at the failure point and rate of degradation.

Frequency distribution (histogram) and lognormal cumulative distribution function (fragility curve) for statistical estimation of cyclic deformation capacity when specimens reached the ultimate strength are shown in Figure 6-7. On average, SPSW specimens reached their ultimate strength at 2.6% drift when all specimens in Group 2, 3, and 4 are considered. The average cyclic capacity is slightly higher when only specimens in Group 4 are considered (i.e., 3.1% drift). This seems reasonable considering the lower cyclic capacities of several specimens in Group 2 and 3 compared to that in Group 4. As shown in Table 6-2, these lower cyclic capacities for several specimens in Group 3 were attributed to either IBE failure mode or shear failure of boundary elements. Similar results can also be obtained from the fragility curve (Figure 6-7b). The median of cyclic capacity at the ultimate point (corresponding to a 50% probability of occurrence) are 2.4% and 3.0% for the same respective groups for which statistical calculations are conducted. Based on these statistical results, one can make a general statement to the effect that SPSWs are most likely to reach their ultimate strength between 2.5 and 3% drift.

As for the condition at the failure point (at the conclusion of the test), cyclic deformation capacity and percentage of strength degradation need to be estimated. Two approaches were conducted to statistically estimate these values. In the first approach, both parameters were treated as two independent statistic variables. The resulting histograms and fragility curves (not shown here) revealed that the average SPSW cyclic capacity at the failure point was 4.5% drift. In other words, statistically, when cycling displacements of the specimens reached 4.5% drift, substantial web tearing, failure of boundary elements, or combination of both deterioration modes had occurred and the test had to be concluded. A similar result was also obtained when specimen cyclic capacities at the failure point ($\Delta_{failure}$) were first normalized by their respective capacities at the capping point (Δ_{max}) prior to conducting the statistical calculation. As shown in Figure 6-8a,
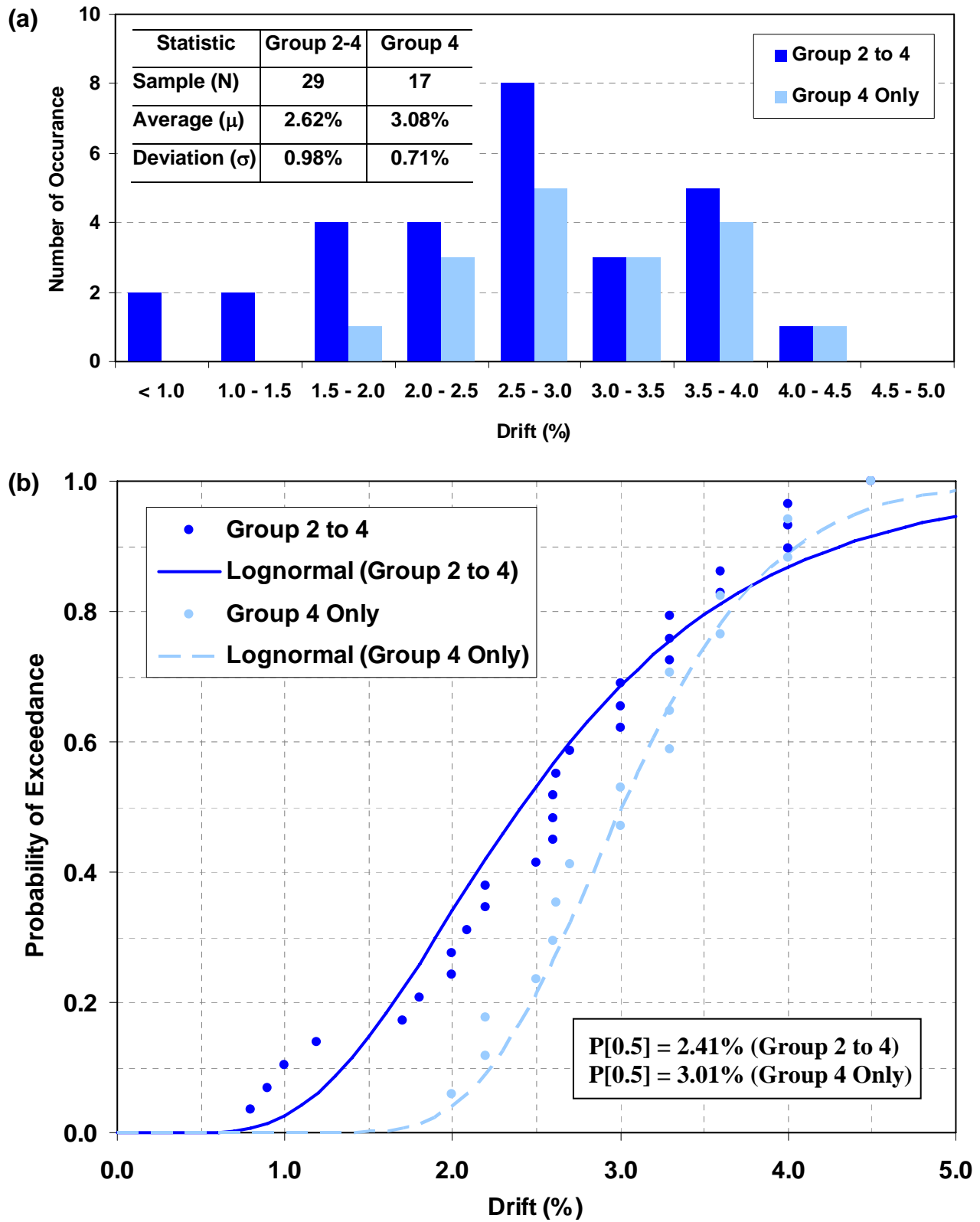
Figure 6-7 Cyclic Deformation Capacity at the Ultimate Point: (a) Frequency Distribution; (b) Cumulative Distribution Function
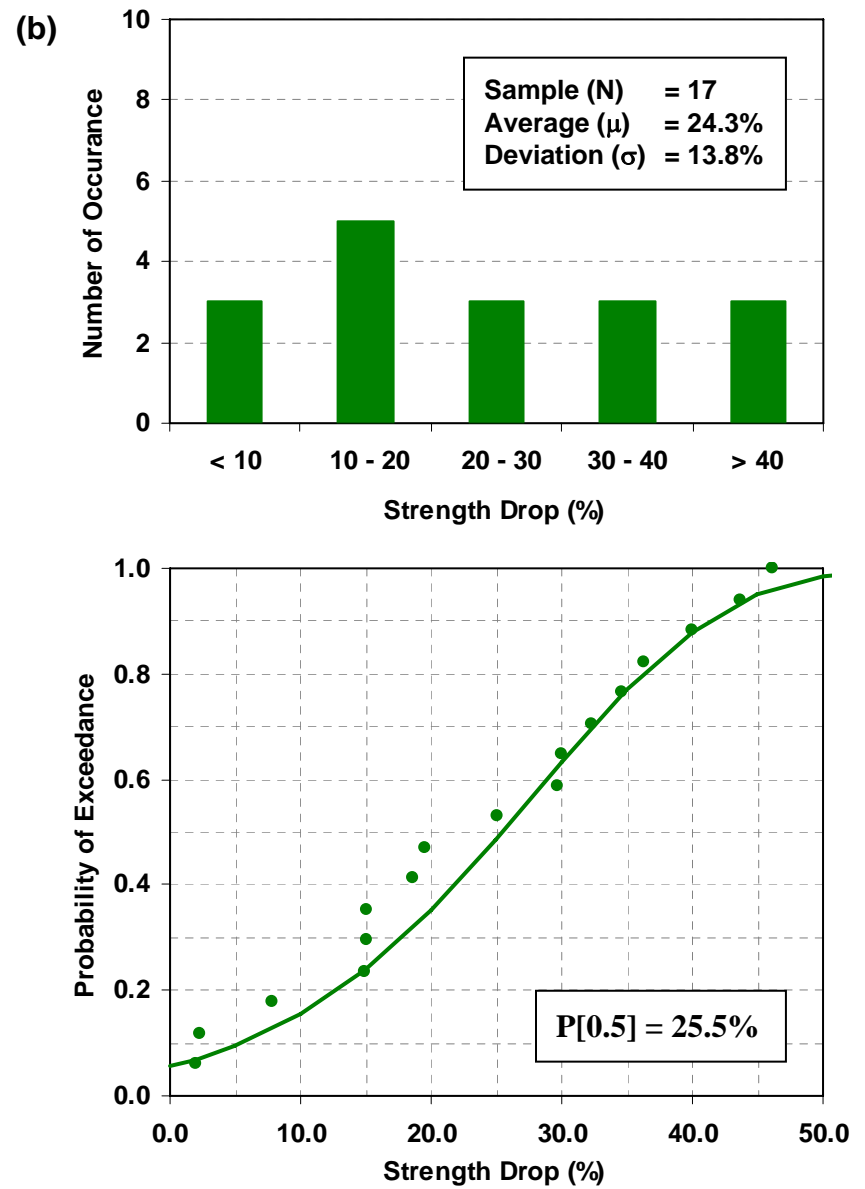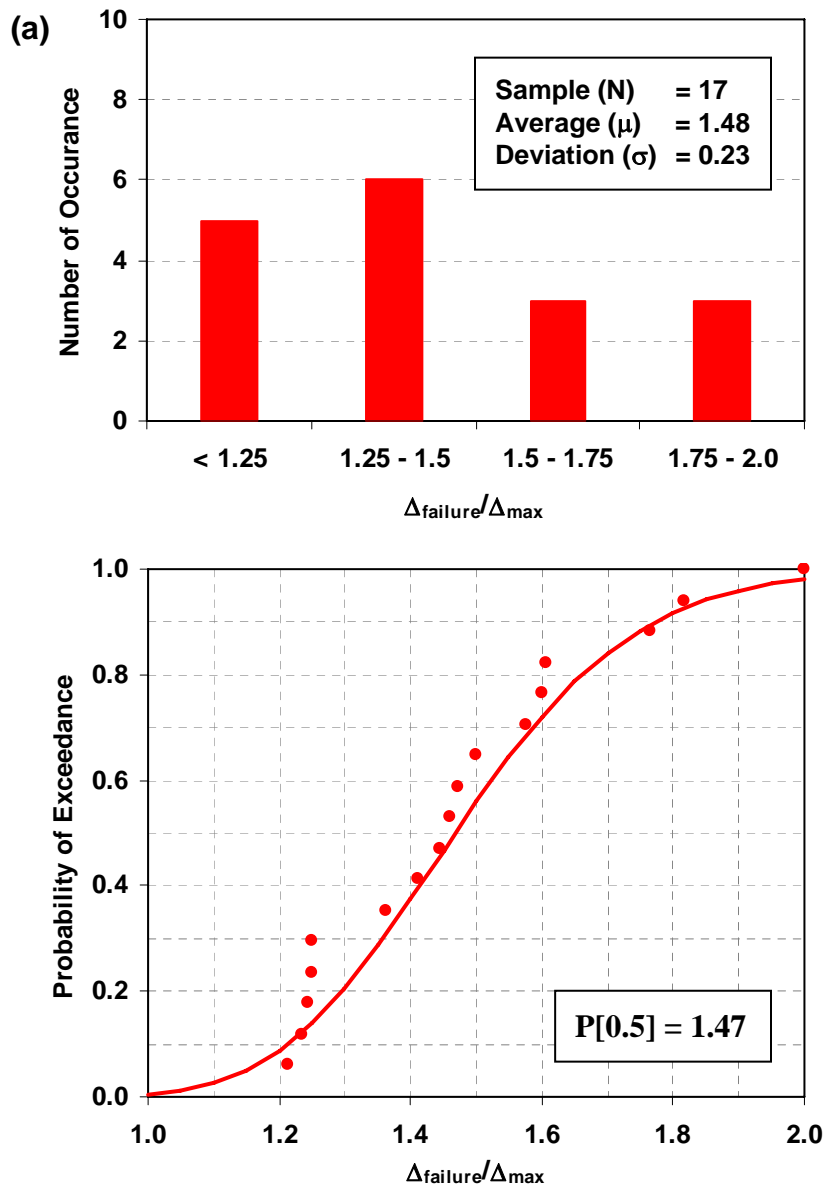
Figure 6-8 Histogram and Cumulative Distribution Function at the Failure Point (a) Estimation of Cyclic Deformation Capacity; (b) Estimation of Strength Drop

253

the average ratio between Δ_{failure} and Δ_{max} is approximately 1.5. Given that the average cyclic deformation capacity at peak strength is 3% drift for the specimens in Group 4, global failure occurs at approximately 4.5% drift (i.e., after specimens experience cyclic deformations of 1.5 times beyond that at the capping point). Moreover, Figure 6-8b presents statistical distribution for estimation of strength degradation when reaching the failure point. On average when this occurred, SPSW specimens have lost approximately 25% of their ultimate strengths at the failure point. In other words, many tests were stopped after a substantial drop in strength was observed (on average 25%), and the actual rate of progression of further damage that would have occurred beyond that point is not known for those specimens.

On the second approach, both parameters were treated as two related statistical variables. The process started by preparing a normalized backbone curve of the cyclic hysteresis for each specimen from the ultimate to the failure points. In this case, base shear strength and drift were normalized by the strength and the corresponding drift at the capping point, respectively. For a certain percentage of strength degradation beyond the capping point, the corresponding normalized story drift at this degradation level was recorded for each specimen; then, for all specimens, average and standard deviation values were calculated. A 5% strength degradation interval was chosen to obtain a relatively large number of data points. Note that since each specimen has a different level of strength degradation when reaching the failure point (Table 6-2), statistical calculation at every degradation level considered a different number of specimens. In other words, the number of data points considered in the statistical calculations decreased for higher level of strength degradation. For example, at the level of less than 5% strength degradation, data was available for 17 specimens, but data for only 3 specimens was available at the level of larger than 60% strength degradation. Figure 6-9 presents the resulting normalized story drift for each level of strength degradation considered, superimposed with the polynomial and linear regression curves for the data points considered, and indicating the number of data points available at each degradation level. While a polynomial regression (solid line) would provide a better correlation with the actual degradation behavior, the linear regression (dash line) provides a simpler approach to simulate strength degradation. Based on this result, to obtain reliable estimation of strength degradation and drift at the failure point, it was decided to only consider the cases for which at least 9 data points are available (which correspond to deterioration
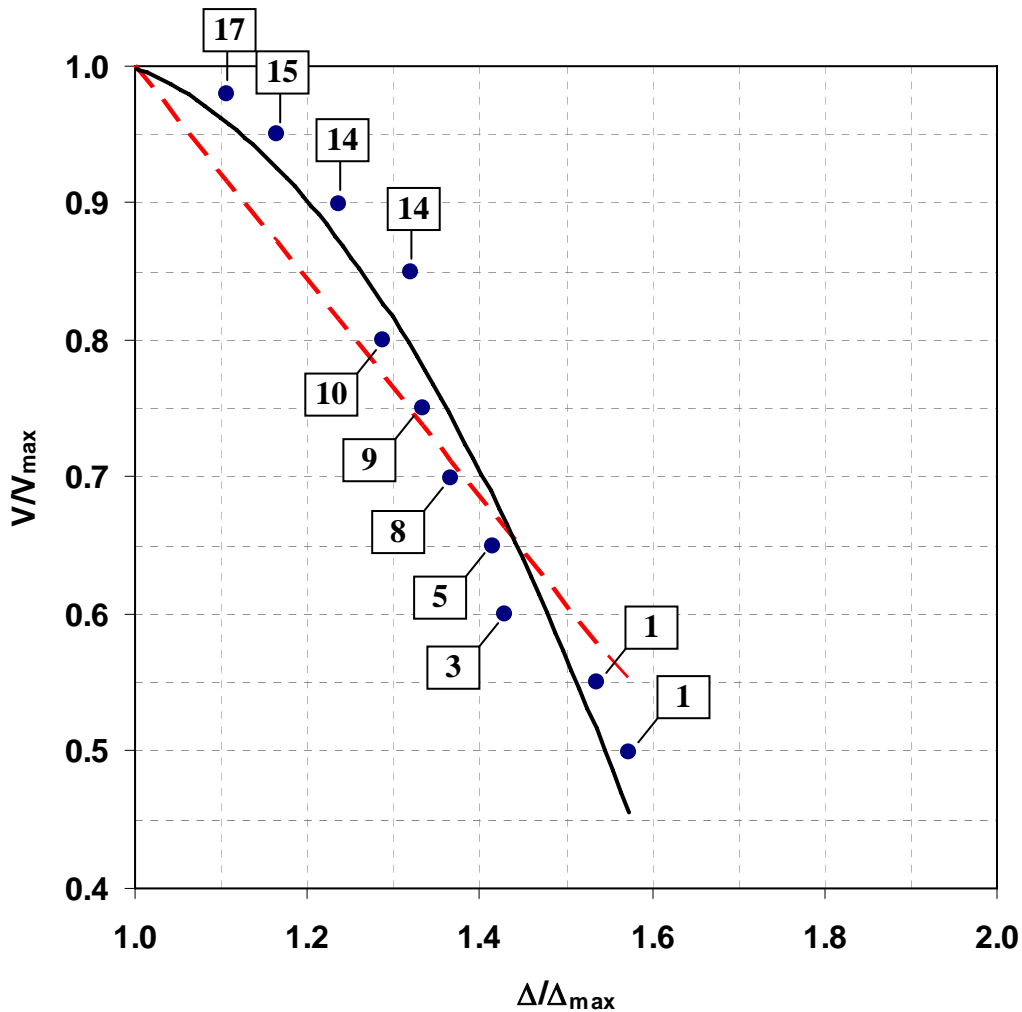
**Figure 6-9 Normalized Base Shear Strength versus Normalized Drift
from Capping to Failure Points**

levels where data is available for more than half of the total number of specimens in Group 4). On that basis, 25% strength degradation and approximately 4.0% drift (i.e., 1.33 times the average drift at the ultimate point of 3%), respectively, were obtained from the statistical calculation of 9 data points. Interestingly, results from this somewhat more elaborate approach are only marginally different from those obtained using the first approach.

Though detailed information is not presented in this report, similar outcomes were also obtained when the same procedure was conducted using actual drifts instead of their normalized values. In this case, half of the specimens were found to have lost 25% of their strength when they reached 4.1% drift. In addition, similar statistical outcomes would probably be obtained using a reversed

procedure which for a certain increase of normalized drift beyond the capping point, the corresponding strength degradation is calculated for each specimen. However, it was not tried in this study.

All the above statistical results suggest that, generally, SPSWs most likely would experience global failure when cycled up to 1.5 times beyond the displacement at which peak strength is reached. Therefore, since peak strength is typically reached at 3% drift, global failure would approximately occur at between 4.0 and 4.5% drift.

It is worth emphasizing here that several other factors might affect cyclic deformation capacities of specimens when reaching the capping and failure points, such as panel aspect ratio, specimen scales that dictate boundary element sizes, boundary element compactness, types of connections between SPSW components as well as between specimens and their bases. In addition to these factors related to specimen geometric properties, the design approaches used to size the SPSWs (e.g., elastic design, plastic design or capacity design principles, designing specimens as shear-type structures, as flexural-type structures, or combination of both) and loading protocol imposed during experiments (e.g., level of axial loads imposed, distribution of lateral loads along the specimen height for multi story specimens) might affect specimen capacities to resist earthquake loads. However, in light of the relatively few number of SPSW specimens tested at the time of this writing, the effect of these factors on specimen cyclic deformation capacities cannot be statistically investigated, and is considered to be beyond the context of this research. As new data becomes available, the effect of these factors and relationships between one factor and another could be quantified.

6.3 Initial Deterioration Model and Selection of Structural Analysis Software

Cyclic deformation capacities estimated in the previous section for the capping and failure points were capacities at the structural level. To model deterioration for SPSWs using structural analysis software, similar information needs to be developed at the component level. In other words, assuming that the degradation pattern at the structural level is an expression of behavior at the component level, moment-rotation and axial force-deformation degradation models are required

for boundary elements and infill plates, respectively. These models usually are developed from past component tests or from past assembly of structural system tests that reported these local behaviors. However, since neither of these sources is available for SPSWs at the time of this writing, it was decided to develop initial deterioration models for boundary elements and infill plates indirectly from the structural level. This can be done by first developing numerical models of several selected specimens, performing monotonic pushover analysis, and recording local behaviors when the structure experienced 3% and 4% interstory drift (i.e., corresponding to the capping and global failure points).

For that purpose, the specimens selected were Vian and Bruneau (2005), Qu and Bruneau (2008), Choi and Park (2009), and Driver *et al.* (1997) specimens. Detailed information and the rationale for selecting these single- to four-story specimens are addressed later in Section 6.6. Strip models were developed in SAP2000 for each specimen, similarly to what was previously presented in Purba and Bruneau (2010), with the *Axial-hinge* and *Fiber-hinge* chosen to define the inelastic behavior of the infill plates and the boundary elements, respectively. In the analysis of the strip models, both steels used for boundary elements and infill plates were represented by an idealized elasto-perfectly plastic stress-strain material. A monotonic pushover analysis was then conducted for each specimen up to 5% drift, and maximum cross-section rotations of boundary elements and maximum axial elongations of infill plates were recorded at 3 and 4% drifts as summarized in Table 6-3. The average values at 3 and 4% drifts were chosen as the degradation parameters at the capping and failure points, respectively. To consider strength degradation, yield strengths of both steels used for boundary elements and infill plates were assigned a 25% strength drop at the failure point based on the statistical results presented in Section 6.2.2. The resulting initial degradation models are shown in Figure 6-10 for boundary elements and infill plates. Note that the degradation models are defined at the material level. For the boundary elements, the extreme fiber strain corresponds to the capping and failure points can be estimated as follows:

$$\varepsilon = \frac{0.5h}{L_p} \times \theta \qquad (6\text{-}3)$$

where h is the cross-section depth; L_p is the plastic hinge length; and θ is the cross section rotations, which are 0.03 and 0.04 radians for point C and D, respectively.

Table 6-3 Parameters of Initial Degradation Models for Boundary Elements and Infill Plates

Model Based on Specimen	Number of Stories	Boundary Element Rotation (radians)		Strip Elongation (δ/δ_y)	
		at 3% Drift	at 4.0% Drift	at 3% Drift	at 4.0% Drift
Vian & Bruneau 2005	1	0.035	0.045	15.0	21.1
Qu and Bruneau 2008	2	0.029	0.037	14.2	18.3
Choi and Park 2009	3	0.029	0.039	9.4	12.5
Driver *et al.* 1997	4	0.030	0.040	5.8	7.6
	Average =	**0.030**	**0.040**	**11.1**	**14.9**

(a)   **(b)**
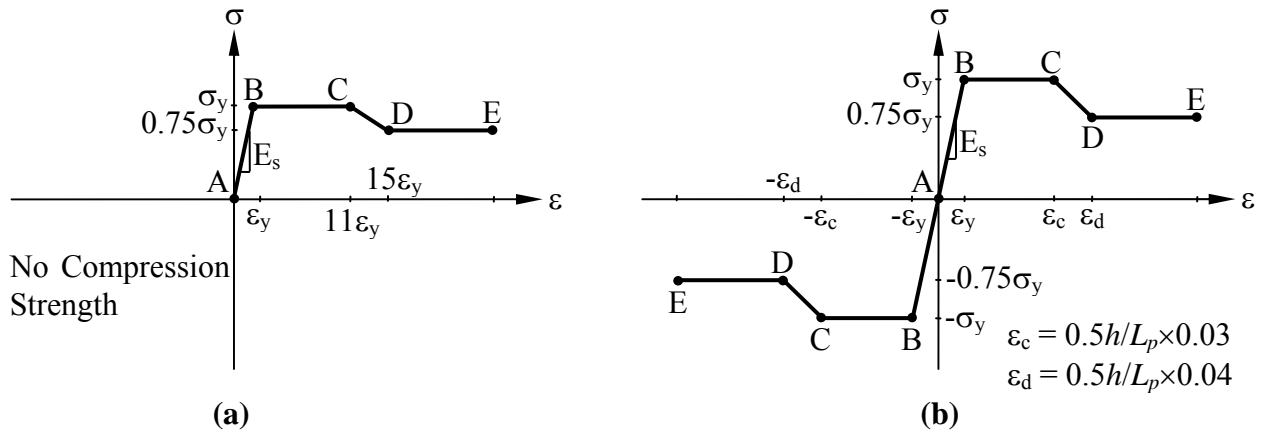
Figure 6-10 Initial Degradation Models: (a) Strips; (b) Boundary Elements

To verify that the strip model with deteriorated boundary elements and infill plates behaved as intended, monotonic pushover analysis (up to 5% drift) and cyclic pushover analysis (progressively increasing cyclic displacement history up to 6% drift) were conducted on the single story SPSW specimen of Vian and Bruneau (2005). Two unexpected numerical outcomes were observed. First, monotonic pushover results indicated that global system strength degradation rate was relatively slower than that of the material model. When reviewing the moment-rotation relationship at one expected location of plastic hinge in a boundary element, it was found out that the reduction in end moment after the cross-section rotation reached 0.04 radians (i.e. the specified value at Point D in Figure 6-10), was only approximately 15% as opposed to 25% strength degradation. Note that this problem did not occur in the force-deformation relationship for the strip, as the axial-hinges exhibited as-expected degradation

behavior. Second, during the cyclic pushover analysis, the structure did not accurately follow the specified cyclic displacement loading history once strength degradation started to occur. In this particular strip model of the Vian and Bruneau (2005) specimen, when the structure had reached the ultimate point during the positive excursion and strength degradation had occurred (marked as point A in Figure 6-11), the structure supposedly should have undergone into a negative excursion following the specified cyclic displacement loading history (marked by the dash arrow in the figure). However, the structure instead maintained the same positive excursion as if a monotonic loading history had been imposed. In a 'loose' analogy, this behavior shows similarity to a "snap-through" phenomenon. Interestingly, after reaching Point D (when structural components reach their "stable" residual strengths), normal cyclic hysteretic behavior as exhibited in earlier cycles reemerged. Consequently, the cyclic pushover curve was significantly biased toward the positive direction, even though the cyclic displacement loading history was symmetric in both positive and negative directions.
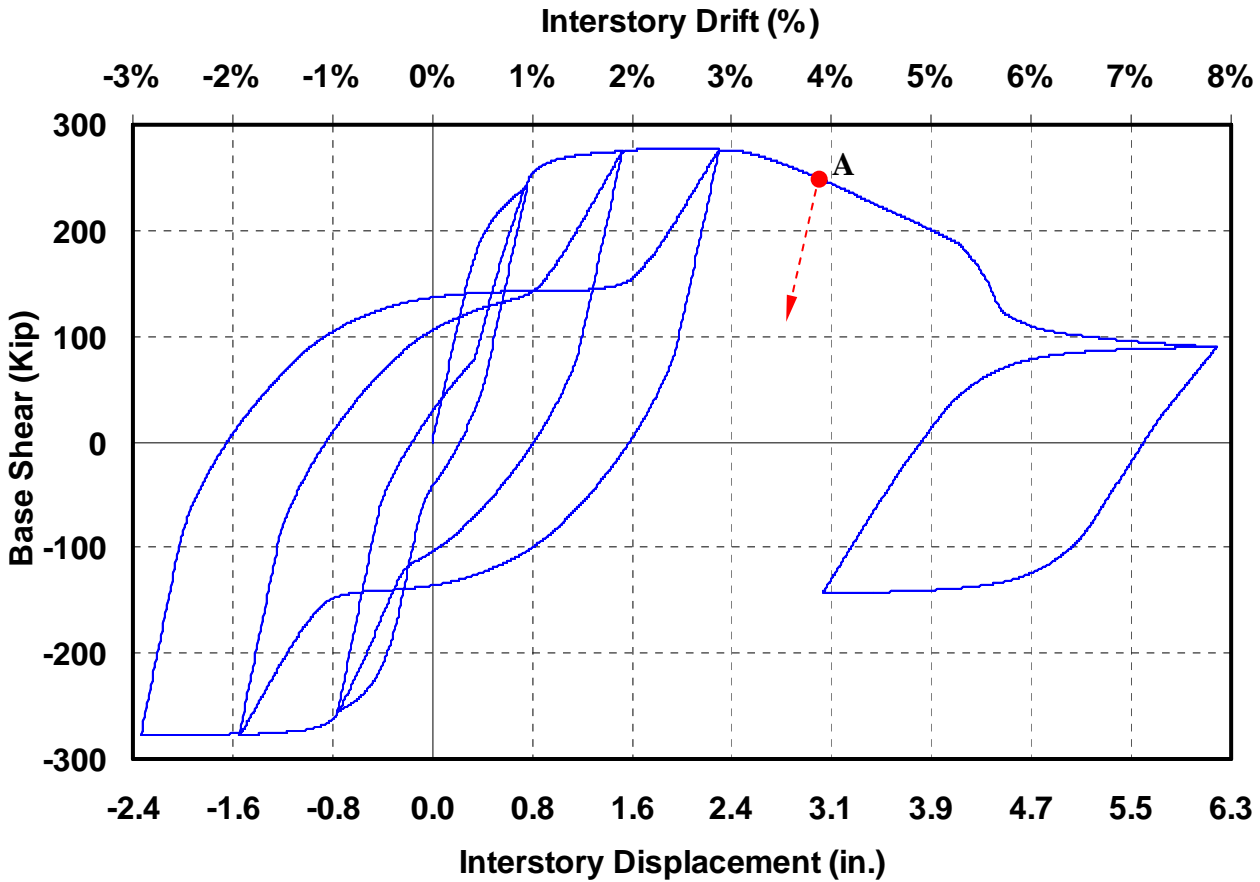
Figure 6-11 Incorrect Cyclic Pushover Analysis Result in SAP2000

259

The aforementioned slower strength degradation can be understood through the mechanics of fiber-elements. In a fiber-element, each fiber has its own stress-strain relationship. Hence, when the fiber element is subjected to flexure, stress-strain distribution varies from one fiber to another depending on its location in respect to the plastic neutral axis. When the furthest fiber from the plastic neutral axis reaches the yield point, all other fibers remain in the elastic range. Consequently, when stress of the furthest fiber starts to decrease after reaching a specified strain for degradation, all other fibers have not reached this level yet (i.e., stress at the plateau level). Several fibers close to the plastic neutral axis even remain elastic. Consider a cross section with degradation model as shown in Figure 6-10 as an example. When cross-section rotation reaches 0.04 radians, not every fiber has lost 25% of it strength; therefore, degradation of moment capacity is less than 25%. Fibers have to experience larger strains, beyond 0.04 radians, for a 25% stress degradation to develop in most of the fibers, and thus achieve a 25% degradation of moment capacity. Hence, the slower degradation rate observed in those analyses is a consequence of having selected fiber-hinges to model the inelastic behavior of boundary elements.

In light of this result, one might suggest using another structural element with zero-length plastic hinge to model the boundary elements. Unlike fiber-hinges which require a finite length of plastic hinge, the entire cross-section of an element with zero-length plastic hinge presumably could reach any particular level of internal force-deformation at the same time, and could eliminate the above issue of incorrect degradation behavior. However, experience shows that fiber-element remains the better option when modeling SPSWs inelastic behavior, because fiber-element inelastic hinges automatically account for the interaction between the axial forces and moments that occurs in the HBEs and VBEs (Purba and Bruneau 2010), a phenomenon that cannot be accommodated reliably by other elements such as zero-length plastic hinges. This is particularly true given the highly fluctuating axial forces in boundary elements, which depends on the tension forces developed in the infill plates. Given the other problems encountered in the past when attempting to model SPSWs to account for the effect of axial forces using other methods, it was decided to keep the fiber-element but adjust it in a way to capture the correct strength degradation behavior of boundary elements.

From a numerical modeling standpoint, the target fiber-element degradation behavior can be achieved by specifying larger stress degradation to fibers, such that when the cross-section experiences the specified rotations for Point D, the resulting deteriorated moment capacity matches the desired specified value. To estimate level of stress degradation on the fibers that has to be specified in order to obtain the desired moment degradation at a particular cross-section rotation, a case study on plastic analysis at the cross-section level was conducted. As an example, to obtain the deterioration behavior shown in Figure 6-10b, approximately 70% stress degradation at 0.022 strains has to be specified for the fibers in the W18×65 HBE in the Vian and Bruneau (2005) specimen; a resulting 25% moment degradation was thus achieved when cross-section rotations reached 0.04 radians with this approach.

As for the second unexpected numerical outcome, another case study was conducted to review SAP2000 ability to perform cyclic pushover analysis on a structure having strength degradation defined for its components. The results indicated that the axial-hinge used to model the inelastic behavior of strips did not properly "rebound" toward the opposite direction once strength degradation has taken place (i.e., between Points C and D). When in the strength degradation range, the strip force-displacement curves continued elongating toward Point D even when a reversed global displacement was applied. Detail explanations of this case study are presented in Appendix B.

Substantial effort was invested to debug the axial-hinge error, including consultations with SAP2000 technical supports. Upon unsuccessful outcomes, subsequent development of the degradation model for steel plate shear walls was conducted using the Open System for Earthquake Engineering Simulation (OpenSees) framework. As shown in Appendix B, OpenSees allowed the successful performance of nonlinear analysis with degradation material. Incidentally, the robust finite element software ABAQUS also could have been used for this purpose. However, OpenSees was preferred as it also allowed development of many archetypes with various structure configurations in a relatively short time (further discussed in Section 7). The following section presents the degradation models for the infill plates and boundary elements implemented in OpenSees framework.

6.4 Deterioration Models for SPSW Components

6.4.1 Unstiffened Infill Plates

Using OpenSees v. 2.3.0 (Mazzoni *et al*. 2009), unstiffened infill plates were modeled as series of *Truss Elements* oriented in the direction of the tension field. The *Hysteretic Uniaxial Material* model was selected to define the inelastic behavior of these truss elements. In a general configuration, this uniaxial material model can construct bilinear hysteretic behavior with pinching on both force and deformation as well as simulate cyclic strength degradation, "in-cycle" strength degradation, and unloading stiffness degradation (Mazzoni *et al*. 2009). To simulate tension-only truss element, the pinching factor for stress during reloading was set to a small value (i.e., 10^{-5}) and the last two model parameters (i.e., "in-cycle" strength degradation and unloading stiffness degradation) were set to zero. Use of this small pinching factor forced the strip to have practically zero strength during compression, return to the compression onset point before taking tension, and to reload in tension elastically up to the peak plastic strain reached in previous cycles before yielding anew (Clayton 2012). As discussed in Section 2.3.2, the decision to set the last two model parameters equal to zero was based on the assumption that "in-cycle" strength degradation and unloading stiffness degradation did not play a significant role in the deterioration of steel plate shear walls reported in past experiments.

A typical resulting tension-only hysteretic behavior of a strip with strength degradation is shown in Figure 6-12. Unlike typical results of SAP2000 which report only plastic deformations, elastic deformations are included in the OpenSees results. Note that the resulting hysteresis is actually a combination of force-displacement outputs of two truss elements, whose positions mirror each other in the model. Detailed explanations of the tension-only truss element with hysteretic uniaxial material model are presented in Appendix B.

6.4.2 Horizontal and Vertical Boundary Elements

OpenSees has three possible elements that can be used to model horizontal and vertical boundary elements (HBE and VBE), namely: (1) using the *Force-Based Beam-Column Element* (Figure 6-13a) which is also called the *Nonlinear Beam-Column* (NLB) *Element* in OpenSees; (2) using the *Beam with Concentrated Hinge* (BCH) *Element* ((Figure 6-13b), and (3) using a combination
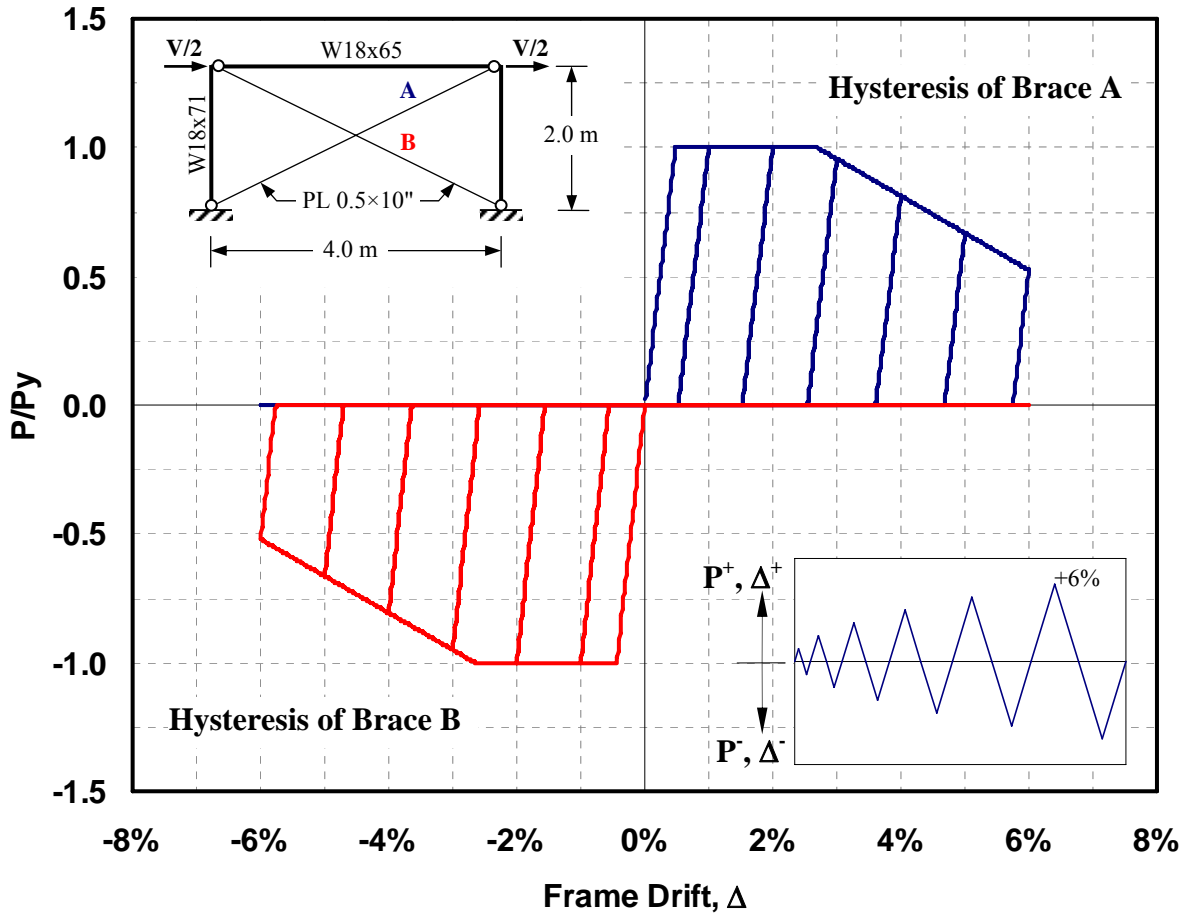
Figure 6-12 Typical Force-Displacement Hysteresis of Tension-only Truss Element Obtained from OpenSees Analysis
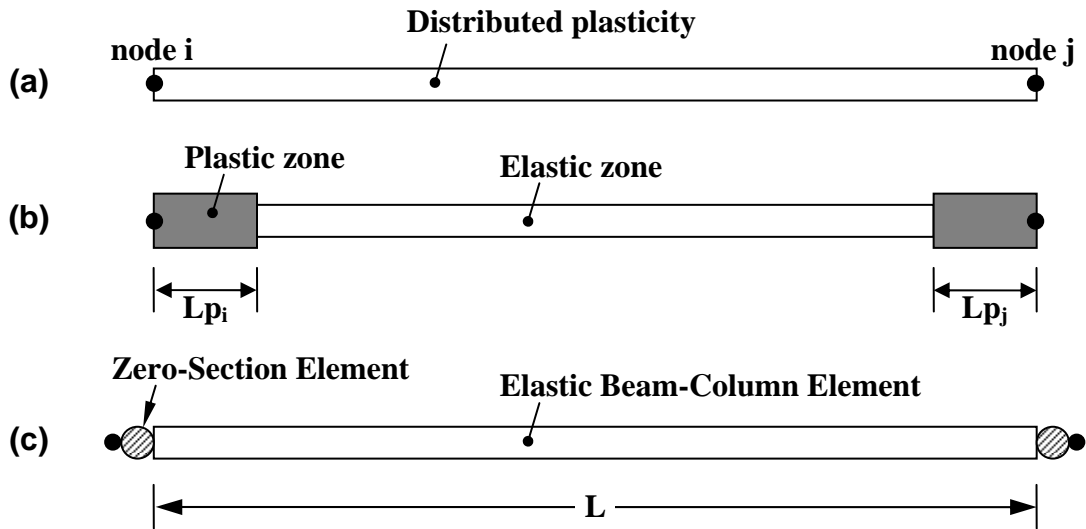
Figure 6-13 OpenSees Elements to Model Boundary Elements: (a) Nonlinear Beam-Column (b) Beam with Concentrated Hinge; (c) Zero Section + Elastic Beam Column

of the *Zero-Length Section* (ZLS) *Element* located at a member's ends and the *Elastic Beam-Column* (EBC) *Element* at its middle part (Figure 6-13c). All of these can accommodate fiber cross sections and have been verified to accurately match the theoretical P-M interaction behavior, as presented in Appendix B. In addition, the hysteretic uniaxial material model can be applied to define the inelastic behavior of each fiber. Unlike that in the truss element, pinching factor for strain during reloading was set to a small value (i.e., 10^{-5}) in these elements to simulate the 'fat' hysteresis behavior of boundary elements. Note that the ZLS element available in OpenSees is slightly different from the zero-length plastic hinge structural members commonly used in the simple plastic analysis. Stress-strain relationship at the material level can be defined in the ZLS element while in the zero-length plastic hinge member (which also available in OpenSees) cross-section properties can only be defined in terms of moment-rotation relationship.

In terms of simulating accurate strength degradation however, the BCH element is simpler to use compared to the other two elements. Derived from the Gauss-Radau quadrature rule, the BCH element assumes that plasticity is concentrated over a certain length at the ends of beam-column members, and the user has flexibility to specify that length (Scott and Fenves 2006). By contrast, the NLB element is developed based on distributed plasticity concept. Plastic hinge length in the NLB element is defined as the length of the first integration point according to the Gauss-Lobatto rule. In other words, the plastic hinge length is a function of the number of integration points specified. Contrary to its impact on the numerical integration accuracy, a larger number of integration points results in a decreasing length of plastic hinge. As a result of smaller plastic hinge length, strain-softening (localization issue) could occur in NLB elements with deteriorated material properties, while plastic strains quickly increase and rapid strength degradation occurs (Coleman and Spacone 2001), as shown in Figure 6-14a. The figure presents results of a case study on a simple cantilever column modeled with BCH, NLB, and ZLS+EBC elements under a horizontal pushover load at its tip. Having no definition of plastic hinge length in ZLS elements, one can 'loosely' infer the ZLS element to be a special case of the NLB element with a considerably small plastic hinge length.

The straightforward definition of plastic hinge length in BCH elements plays a key role in their ability to adequately simulate the nonlinear deteriorating material response of beam-column
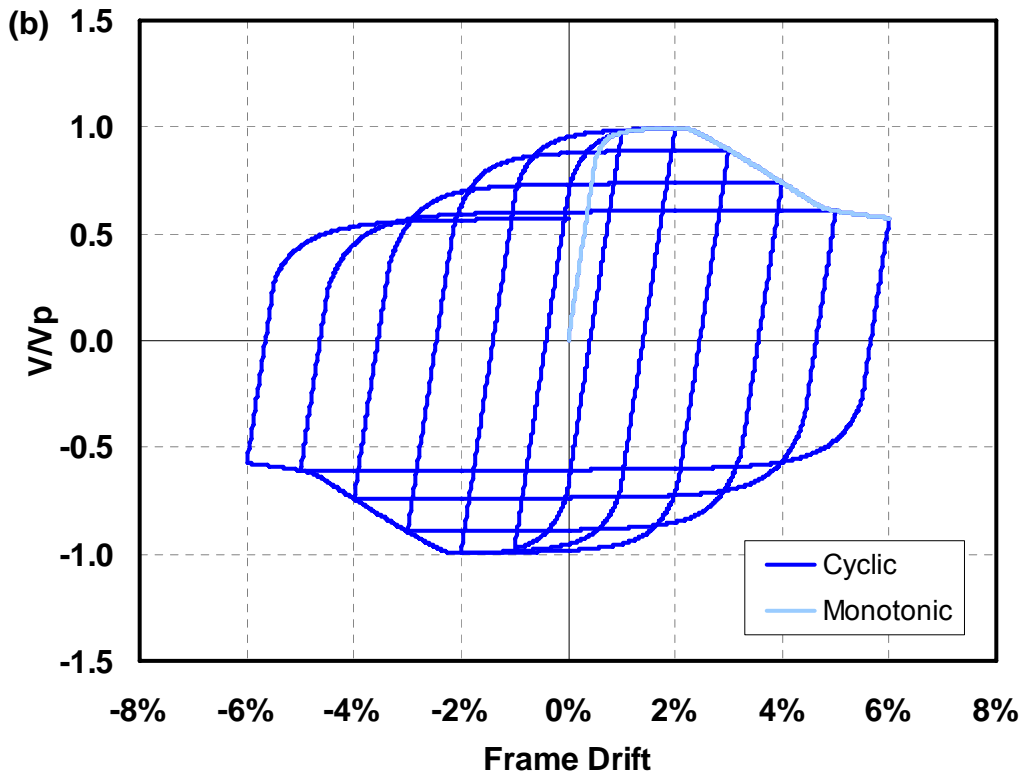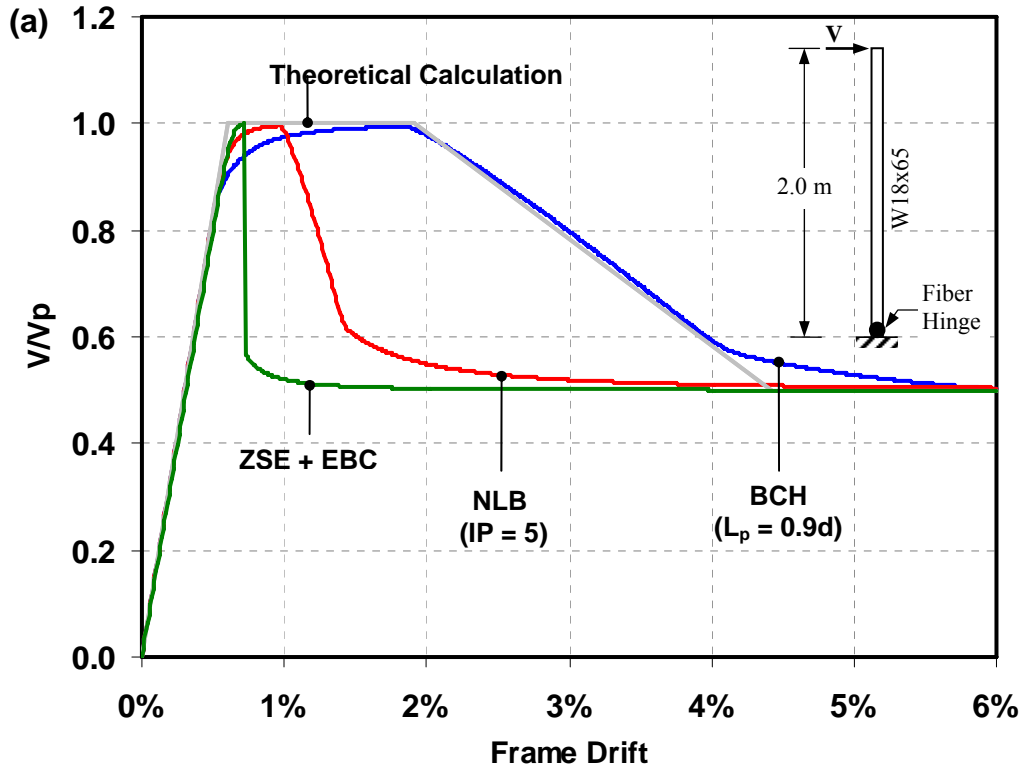
Figure 6-14 Modeling Boundary Elements in OpenSees Framework: (b) Monotonic Results for 3 elements; (b) Typical Hysteresis of Beam with Concentrated Hinge (BCH) Element

members. As shown in Figure 6-14a, the BCH element result is in a good agreement with that of the theoretical prediction. With several modifications however, the other two elements can simulate the same behaviors as well. Coleman and Spacone (2001) developed a regularization technique to resolve the localization issue for the NLB element which requires modification of its material stress-strain behavior to maintain constant fracture energy at the onset of degradation and selection of a correct number of integration points such that the length of the first integration points equals the expected plastic hinge length. Full compliance with this technique to model SPSW boundary elements would require the development of a new strain modification factor, since the factor proposed by those researchers was developed based on the compression fracture energy of concrete. Hence, it was not investigated in this case study. Partial application of this technique, however, was investigated and results are presented in Appendix B. By reducing the number of integration points, the NLB results approached those of BCH. Moreover, in a complete SPSW model, in which boundary elements are "sliced" into shorter members to match the distance between strips, this technique of reducing the number of integration points might not be applicable (and is not practical). The smallest number of integration points (i.e., 3 points) might be too small for short elements and would sacrifice numerical integration accuracy. As for the ZLS element, modification on material stress-strain behavior can be used. After multiplying strains by an expected plastic hinge length (L_p), the ZLS results approached those obtained with the BCH element. This approach is equivalent to specifying material properties as a stress versus (strain $\times L_p$) relationship rather than in the standard stress-strain relationship. To simulate the actual flexural stiffness of beam-column element, further modification on flexural stiffness of combined ZLS and elastic beam-column elements are required (Ibarra and Krawinkler 2005).

On the basis of that fundamental knowledge, boundary elements were modeled using BCH elements with fiber sections and hysteresis uniaxial material model. A typical moment-rotation hysteresis obtained using BCH element with strength degradation is shown in Figure 6-14b. To deal with shorter HBEs and VBEs in a complete SPSW model, smaller plastic hinge length was assigned to the end of BCH element where plasticity was not expected to occur and elastic material properties were specified to this zone. In this research, the plastic hinge length of this zone was taken as one-tenth of plastic hinge length at the other end.

6.5 Behavior of SPSW Considering Various Deterioration Models

Up to this point, web tearing (WT) and flexural failure of boundary elements (FBE) have been identified as the two main sources that cause SPSW capacity to deteriorate in strength and stiffness, and these two failure modes have been considered in the development of deterioration models (Figure 6-10). Though both deterioration modes generally take place once SPSW specimens are cycled to relatively large lateral displacements (or drifts), as confirmed by the results of past experiments (Table 6-2), it was reported in many cases that infill plates could continue to dissipate energy even after failure of boundary elements occurs. In such cases, infill plates exhibited non-deteriorating web tearing (Section 6.2.1) with significant inelastic deformations. Hence, one might be tempted to consider modeling deteriorating SPSWs by implementing strength deterioration model only for the boundary elements, while providing elasto-perfectly plastic model without deterioration for infill plates. The problem with that approach is that when significant web tearing occurs, as observed in a number of other tests, it would give incorrect results.

Another legitimate question is whether the residual strength defined for infill plates in Figure 6-10a is appropriate considering that once significant tears starts to propagate across the infill, the corresponding strip plate used in the model at this location should lose its entire strength to sustain loads (i.e., the stress it carries should completely drop to zero when that tears start to propagate). Furthermore, given that web tearing that is correlated to strength degradation generally starts from one of the panel corners, an accurate model should presumably account for the fact that strips attached closer to the panel corner would lose strength faster than the others. It is unclear what would be the impact of using different deterioration models for strips depending on their location from the panel corner.

To investigate the above concerns, a series of monotonic pushover analyses were conducted with various deterioration models assigned to boundary elements and infill plates. More specifically, these analytical investigations were intended to compare the global SPSW deterioration behavior obtained when deterioration models were assigned to both infill plates and boundary elements with the case when a deterioration model was only assigned to either boundary elements or the infill plates. In addition, impact of severe and moderate deterioration models assigned

267

respectively to corner and middle strips was investigated and compared with the case with uniform deterioration models. Lastly, different deterioration rates for infill plates were investigated, considering abrupt drop to zero stress at a certain specified strain level, as well as gradual drop to zero stress at various rates. Details of these case studies and outcomes are presented in Appendix B. However, a few key findings resulting from these parametric are important to highlight here:

1. **Different Deterioration Models for Boundary Elements and Strips**. When a deteriorating material model was assigned to boundary elements while an elasto-plastic was assigned to strips, strength degradation was less pronounced and convergence was relatively easy to achieve compared to the reverse scenario, where a deteriorating material model was assigned to strips while an elasto-plastic was assigned to boundary elements. To provide a general SPSW model that is capable to simulate both deterioration modes in boundary elements and strips, it is necessary to assign deteriorating material models to both components.

2. **Different Deterioration Models for Corner and Middle Strips**. Due to the flexibility of boundary elements when resisting tension force from yielded strips, strips attached closer to the panel corner (i.e., corner strips) elongated and deteriorated significantly faster than other strips (i.e., middle strips). Assigning different deterioration model for strips depending on their location from the panel corner resulted in a more realistic deterioration behavior (i.e., smoother force-displacement pushover curve) compared to the somewhat jagged pushover curve that was obtained when defining uniform deterioration for all strips. For simplicity, however, the last option was selected and the same deterioration model was assigned to all strips.

3. **Deterioration Rate for Strips**. It seems reasonable to assume that once deterioration due to severe web tearing occurs and TFA is unable to develop, the corresponding strip plate in the analytical model should lose its entire strength. In other words, no residual strength should be assigned to a strip once strength degradation occurs. This would be consistent with the fact that strength degradation was reported to be relatively fast once severe web tearing occurred in past experiments. Hence, a relatively stiff deterioration slope should be assigned for strips in the numerical model to simulate the behavior observed in experiments. However, it was found from the case studies conducted that using an abrupt

drop in deteriorating model for strips created numerical convergence problem during the analysis, and therefore, a gradual deterioration was used (i.e., setting strips to lose 100% of their strength within once or twice the specified displacement increment beyond the capping point).

4. **Plastic Hinge Location in VBEs**. Per capacity design principle, plastic hinges in VBEs are expected to develop only at the base of SPSW, while VBEs over the rest of the wall height are expected to remain elastic. However, the case studies conducted revealed that plastic hinges could also possible to develop at the ends of VBEs in the upper stories. This condition occurs when significant numbers of strips in a particular story lose their entire strength to resist story shear forces (given that these strips are modeled without residual strength once strength degradation occurred) and the VBEs progressively contribute more (replacing the strips) in sustaining the story shear forces. As a result, plastification at the ends of VBEs at any story could take place. Hence, in the SPSW strip model, plastic hinges need to be defined at the ends of every VBE to simulate the possibility to develop soft-story mechanism at any story level.

Those findings are considered when conducting calibration of the proposed deterioration model in the following section.

6.6 Calibration of Proposed Deterioration Model

Two failure modes have been identified as the main sources of strength deterioration for steel plate shear walls and initial models for boundary elements and infill plates were proposed in Figure 6-10. However, analyses using these initial models did not match experimental results well (see Section 6.3). To improve the analytical results over the strength-degradation range of response, it was therefore decided to modify and calibrate those models to available experimental data. By matching the results of analyses using these numerical models to their corresponding experimental results, key deterioration model parameters (i.e., the capping Point C and the residual strength Point D in Figure 6-10) for boundary elements and infill plates could be estimated. This section presents the details of this calibration of the proposed deterioration models.

269

Calibration of the proposed deterioration models was conducted using 4 selected specimens that represent single- to four-story SPSWs, with panel aspect ratio ranging from 1.0 to 2.2. Each specimen has a unique characteristic for which observation of different scenarios of strength degradation can be made. The Vian and Bruneau (2005) single-story specimen exhibited fractures of boundary elements but no fractures of its infill plates that contributed to the specimen strength degradation (i.e., the infill plates exhibited significant plastic deformations instead). The reverse scenario was observed in the three-story specimen tested by Choi and Park (2009), where strength deterioration was attributed to web tearing in absence of significant damages to boundary elements. A case for which both fracture of boundary elements and deterioration due to web tearing was reported by Qu and Bruneau (2008) for a two-story specimen. While both deterioration modes were also observed in the Driver *et al.* (1997) four-story specimen, strength degradation rate and magnitude of this degradation were not as severe as that in the two-story specimen.

Prior to presenting the calibration results, the procedure used for the calibration process is first explained (Section 6.6.1). Based on the calibration outcomes (Sections 6.6.2 to 6.6.5), a final deterioration model is defined to represent general strength deterioration behavior for boundary elements and infill plates (Section 6.6.6). That general model is then used for the collapse assessment of steel plate shear walls in Section 8.

6.6.1 Calibration Procedure

The following calibration procedure was applied to all specimens considered to estimate the general deterioration model parameters at the capping Point C and the failure Point D for both boundary elements and strips. Additional considerations and engineering judgments specific to each specimen will be explained in the subsequent sections when presenting specimen-specific calibration results.

1. **Strip Model Development**. Based on documented experimental information reported for each specimen (e.g., geometric and section properties, material properties, presence of gravity loads, lateral load distributions, cyclic pushover displacement loading histories), a strip model of the entire SPSW was developed in OpenSees for each specimen.

2. **Preliminary Analysis**. Prior to performing cyclic pushover analysis to simulate the actual experimental program, a series of monotonic pushover analyses were conducted to obtain a monotonic pushover force-displacement curve that would match the backbone of the force-displacement hysteretic curve obtained in the experiment. As an initial start, monotonic pushover analysis was conducted on the strip model with both the steels used for boundary elements and strips represented by an idealized elasto-perfectly plastic stress-strain material. This initial monotonic push-over analysis, conducted up to the maximum drift to which each considered specimen was tested, served two purposes, namely: (a) to observe whether the resulting analytical elastic stiffness and the onset of effective yielding matched that reported in the corresponding experiment; and (b) to obtain rough estimates of cross-section rotations in boundary elements and axial elongations in strips when the strip model reached displacements that corresponded to the specimen's ultimate and failure points (i.e., Point C and D).

3. **Matching the Capping Point**. As a result of excluding strain-hardening from the material models in the above initial analysis, obviously, the resulting ultimate strength obtained in Step 2 above was less that the reported ultimate strength of each tested specimen. To match the actual ultimate strength observed in the experiment, subsequent analysis considered a strain hardening of 2% up to Point C and an assumed zero-slope plateau of no strain hardening beyond this point. Even though strain hardening would likely be more substantial in boundary elements than in infill plates, for simplicity, strain hardening was assigned to be identical for the steels used for the boundary elements and strips. More specifically, the above 2% strain hardening model was assigned to the stress-strain material property of the axial hinges, as well as to each fiber in the boundary element plastic hinge model, which translated to an effective 2% strain hardening at the cross-section level (i.e., in terms of moment-rotation or axial force-deformation relationship). Note that assigning 2% strain hardening up to the capping point (i.e., Point C) for the materials in the numerical model results in a greater strain hardening rate than that typically reported in the material properties obtained from coupon tests. However, this approach was deemed acceptable considering that strain hardening typically develops faster in cyclic tests.

4. **Identifying Deteriorated Components**. Once a good match between the numerical and experimental results up to the capping point was obtained (Step 3), material properties for both boundary elements and strips at Point C can be established. To obtain the same result at the failure point, one must identify which SPSW components deteriorated during each experiment.

5. **Defining Strength Deterioration.** For the components identified in the previous step, the drift at which this deterioration started to take place and the amount of strength drop that occurred at the structural level due to this local deterioration were quantified. The percentages of strength degradation were estimated based on severity of damages reported in the experiment. For example, fracture of one flange in a W-section could result in approximately 40% strength degradations in that boundary element, and significant tearing of infill plates such that TFA could not be developed should be modeled in the numerical model as strips losing their entire strength (i.e., 100% strength degradations). The rate of strength degradation, as a function of element deformations was also quantified. From experiment step-by-step results and observations (e.g., drift levels when fracture started to occur and when degradation stabilized or ended), one can define parameters for Point D. In other words, degradation rate observed at the global structural level was assumed to be proportionally correlated to the degradation rate in the material level. Because each specimen exhibited different scenarios of strength degradation, different deterioration models (i.e., values for Point C and D) were assigned to boundary elements and strips for each specimen. Using this information, a deterioration model was created for every component which was damaged during the experiment (i.e., replacing the previously used elasto-plastic with strain hardening model defined as in step 3). Note that, as mentioned in Section 6.2.1, only WT and FBE deterioration modes were considered.

6. **Performing Cyclic Pushover Analysis**. Once a good match between the resulting monotonic pushover curve and the backbone of hysteretic curve from the experiment was obtained, cyclic pushover analysis was conducted following the actual displacement loading histories imposed during each experiment. In this calibration process, only one cycle of loading history was applied at each displacement increment level, because no in-cycle material degradation was included in the numerical model.

Several iterations were typically required to obtain a good match between the numerical and experimental results, which included revising parameters at Point C and D defined for both boundary elements and strips, slightly increasing yield strength of steels used for boundary elements and strips by a factor 5 to 10%, and re-analyzing the strip model under monotonic and cyclic pushover analysis. Note that the slight increase of material strength above the reported value was deemed necessary to obtain a better match between the numerical and experimental results. This increase is within the range of material property variability obtained from coupon tests, and was therefore it deemed acceptable. As addressed later in the following sub-sections, the numerical model generally underestimated the onset of effective yielding observed in the experiment. No substantial effort was invested to resolve this discrepancy in the calibration process because underestimating the onset of effective yielding was considered not to critically affecting the collapse prediction of steel plate shear walls.

6.6.2 Single Story SPSW: Vian and Bruneau (2005) Specimen

The first calibration was conducted on the single-story cutout corner SPSW specimen tested by Vian and Bruneau (2005). The centerline dimensions of this one-half scale specimen were 4000 mm wide by 2000 mm high, as schematically shown in Figure 6-15. Special moment resisting HBE-to-VBE connections with reduced beam section (RBS) on the HBEs, reinforced quarter-circle cutouts of 500 mm radius at the upper corners of the infill plate, and real hinge supports located 850 mm below the intersection point of the VBE and lower HBE working lines, were implemented. Fish plates were added to facilitate welded connection of the infill plates to the surrounding frame. W18X65 and W18X71 were used for HBEs and VBEs, respectively, and low yield steel (LYS) was used for the 2.6 mm thick infill plate. Boundary elements were made of steel equivalent to ASTM A572 Grade 50 (F_y = 345 MPa) and infill plate from LYS with yield and ultimate stresses of 165MPa and 305MPa, respectively. Cyclic displacement history applied to the actuators attached to the mid-span of top HBE is shown in Table 6-4.

Bottom flange fractures at both RBS locations of the lower HBE occurred at 3.0% interstory drift and caused a strength degradation of 17.5% from the specimen ultimate strength of 2060 kN, which was reached in the previous displacement cycle of 2.5% interstory drift. Note that the

(a)

HORIZONTAL LOADING BEAM

W18x65 (345MPa)

233

2000

W18x71 (345MPa)

W18x71 (345MPa)

R 500 TO MID-THICKNESS OF FLANGE

2.6mm LYP STEEL INFILL PANEL

850

5mm DOUBLER PLATE PLUG-WELDED TO COL WEB

W18x65 (345MPa)

2000

2000

4000

(b)

W18x71 COLUMN

W18x65 BEAM

250

50

193

CONTINUITY PLATE DIMS TO MATCH BEAM FLANGE

R 250
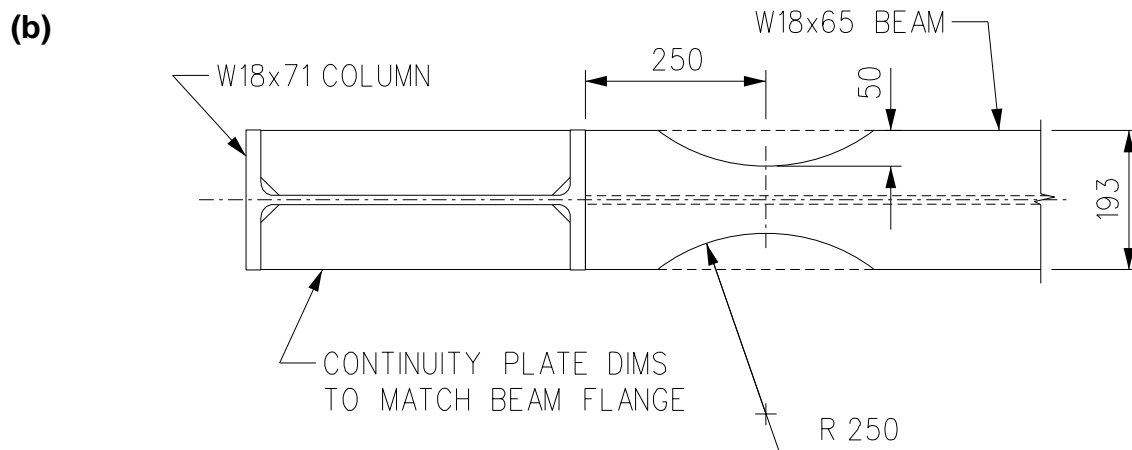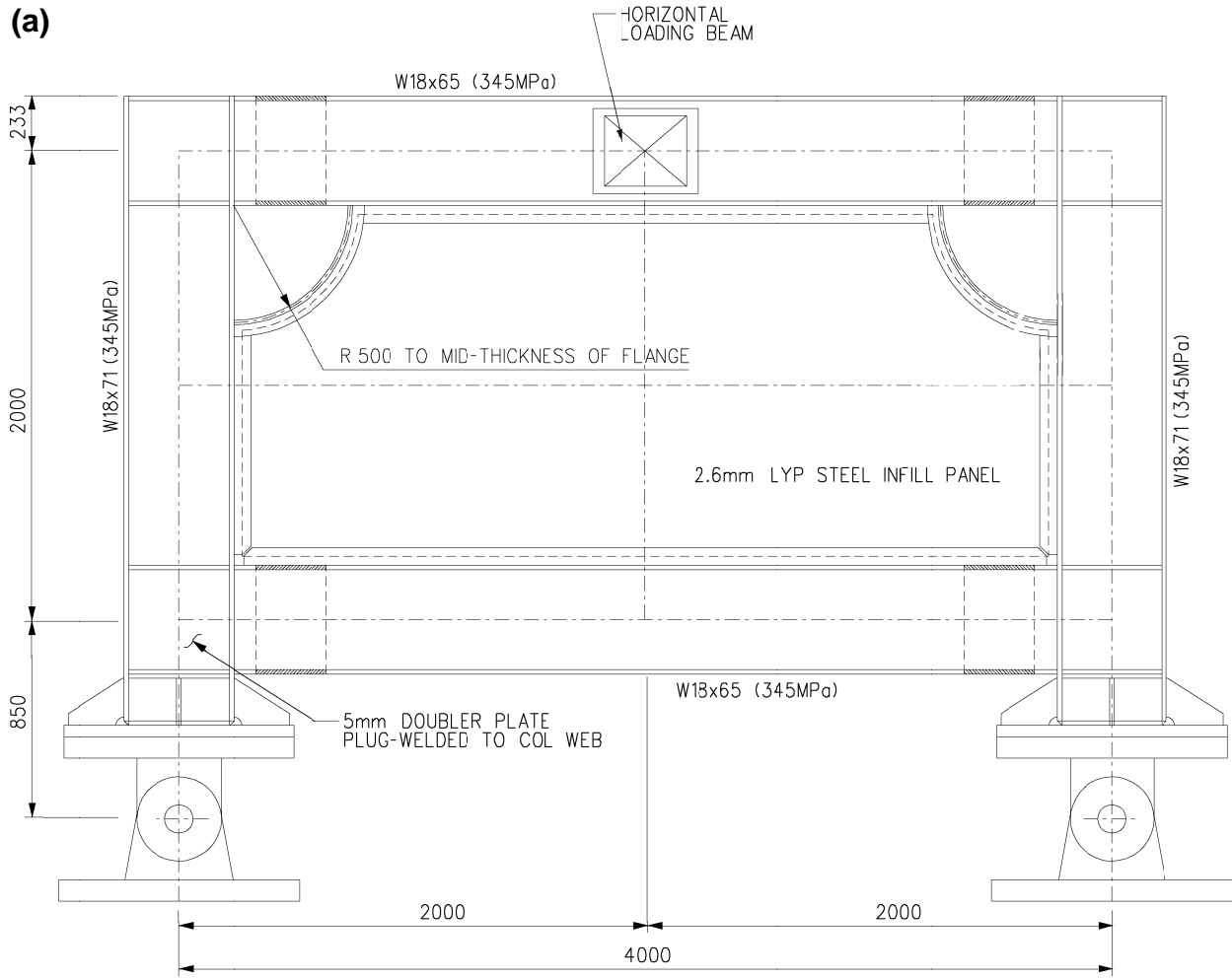
**Figure 6-15 Single Story SPSW Specimen (Vian and Bruneau 2005):
(a) Schematic of Specimen; (b) Reduced Beam Section (RBS) Detail**

274

Table 6-4 Cyclic Displacement History for Single Story SPSW (Vian and Bruneau 2005)

Displacement Step	Number of Cycles	Cumulative Number of Cycles	Ductility Ratio Δ/δ_y	Top Drift (%)	Top Displacement Δ (mm)
1	3	3	0.33	0.14	3.9
2	3	6	0.67	0.26	7.3
3	3	9	1.00	0.37	10.4
4	3	12	2.00	0.68	19.5
5	3	15	3.00	1.00	28.5
6	2	17	4.00	1.32	37.6
7	2	19	5.00	1.64	46.7
8	2	21	6.67	2.16	61.6
9	2	23	8.33	2.66	75.9
10	2	25	8.33	2.65	75.5
11	2	27	10.00	3.22	91.7
12	2	29	13.33	4.27	121.6

initiation of these fractures actually occurred during the third cycle of the 2.5% interstory drift. Moreover, fractures at the connection of the upper HBE to the VBE (i.e., which started at the welded connection between the top continuity plates to the VBE flange and progressed to the VBE web) occurred at 4.0% interstory drift and caused a strength degradation of 24% from the specimen's ultimate strength. Snapshots of these fractures at the boundary elements are shown in Figure 6-16. These boundary element fractures occurred during the positive excursion of the respective displacement cycles. Compared to the aforementioned strength degradation recorded during the positive excursion, strength degradation was larger in the subsequent negative excursion of the same displacement cycle. During the negative excursion, the values were 27% and 35% strength degradations at 3% and 4% interstory drifts, respectively. As for the infill plate, noticeable plastic deformations and minor cracks were observed (Figure 6-17) but these had insignificant impact on the overall deterioration behavior of the specimen.

In the strip model developed for this specimen (Figure 6-18), a deteriorating material model was assigned to the HBEs (indicated by solid circular marker in the figure) while an elasto-plastic
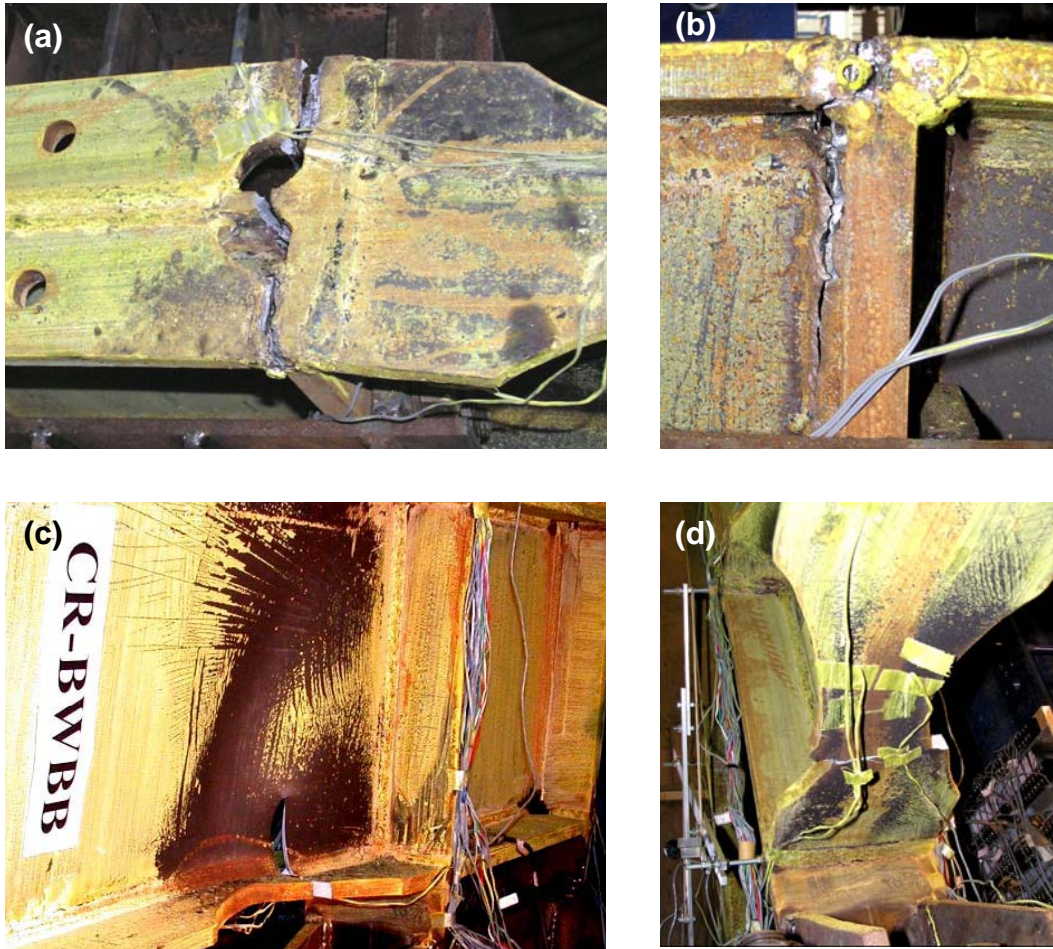
Figure 6-16 Failure of Boundary Elements in Single Story SPSW Specimen (Vian and Bruneau 2005): (a) Fracture at VBE Connection to Upper HBE; (b) Side View of Part (a); (c) Fracture at RBS Location of Lower HBE; (d) Bottom View of Part (c)
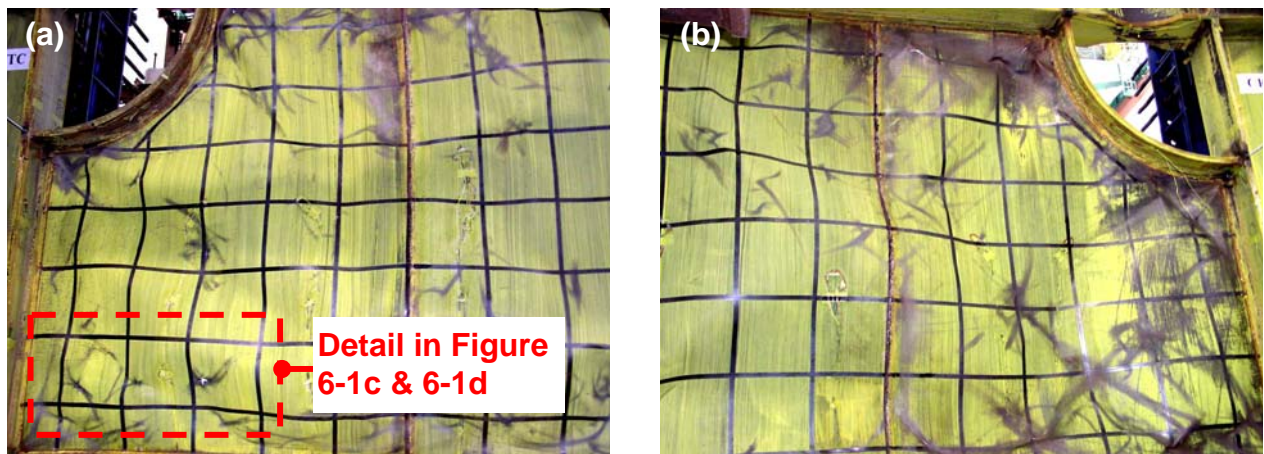
Figure 6-17 Plastic Deformations and Minor Cracks in Single Story SPSW Specimen (Vian and Bruneau 2005): (a) Left Part; (b) Right Part
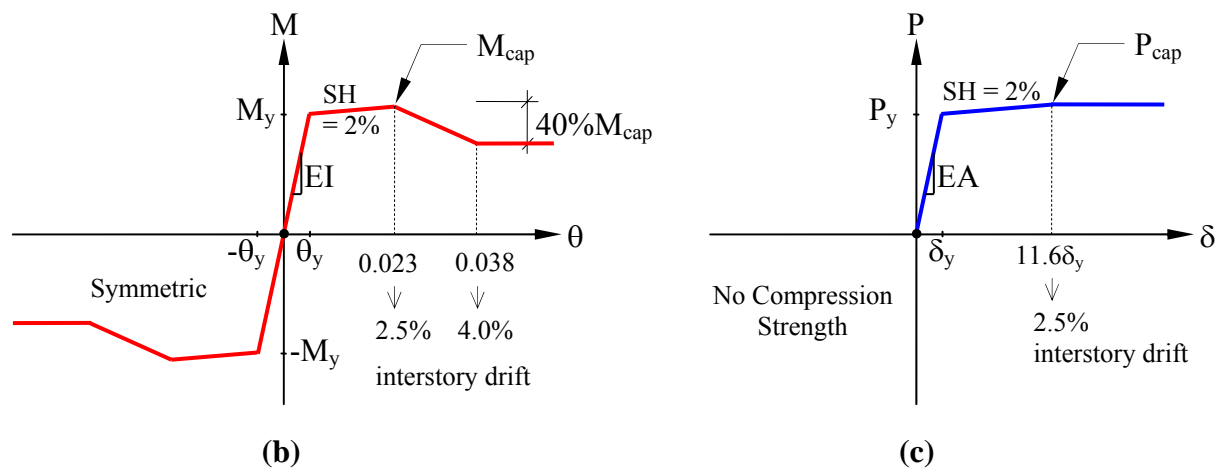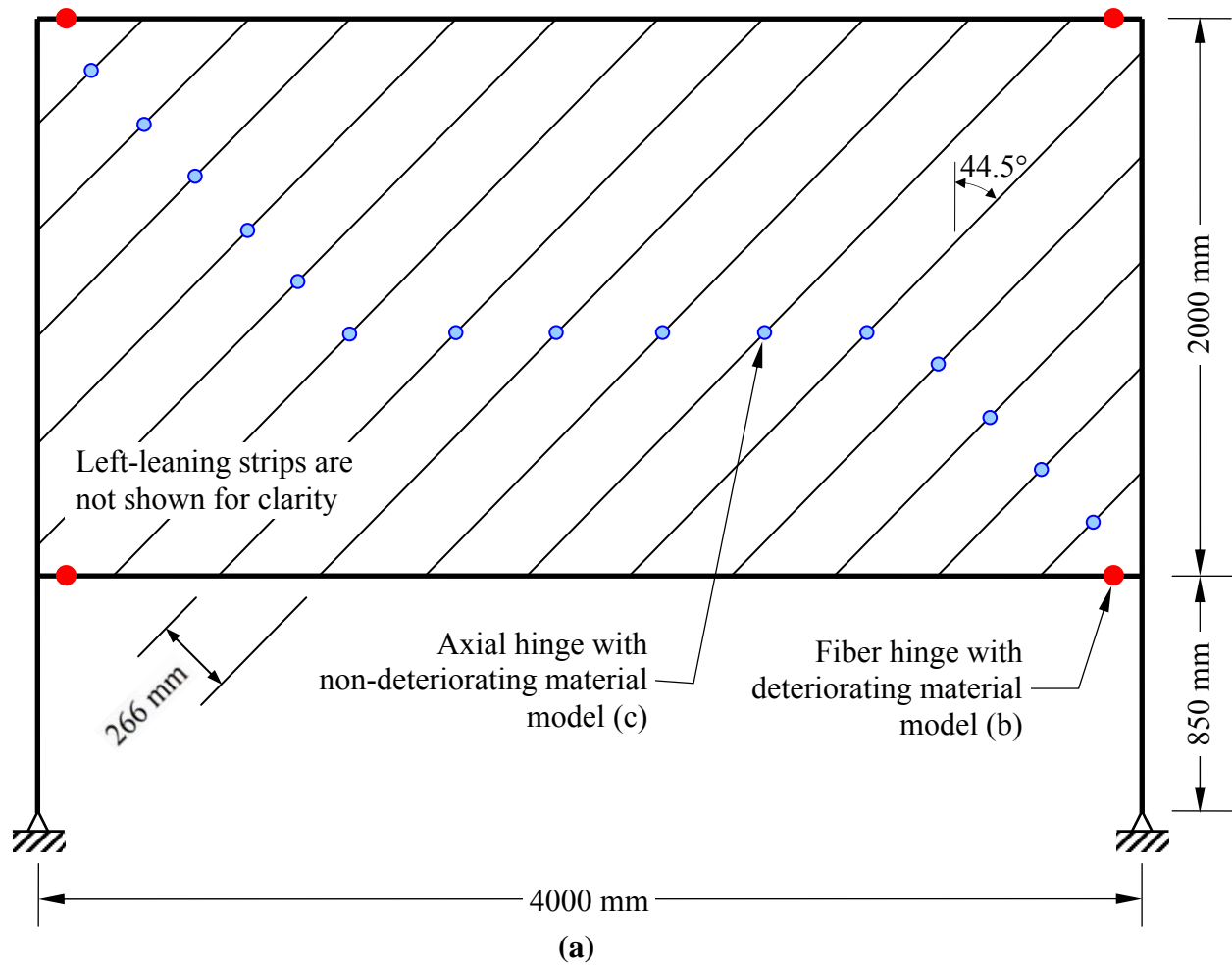
Figure 6-18 Strip Model for Single Story Vian and Bruneau (2005) Specimen: (a) Overview; (b) Material Model for Boundary Elements; (c) Material Model for Strips

material model was assigned to the infill plates (indicated by light-color circular marker in the figure). A 2% strain hardening up to the capping point was assigned to both material models. Though fractures occurred at the upper HBE located at its connection to VBEs, for simplicity, fiber hinges were assigned at the center of RBS similar to that of lower HBE. In addition, both HBE0 and HBE1 were assigned a similar deteriorating material model (Figure 6-18b) even though fractures actually occurred sooner on HBE0 (i.e., recorded at 3.0% drift cycle) compared to that on HBE1 (i.e., recorded at 4.0% drift cycle). Lastly, the quarter-circle cutouts at the upper corners of the infill plate were not included in the strip model. Hence, strips used to model the plates which were welded to the cutout stiffeners during the experiment (Figure 6-17) were connected directly to the boundary elements in the numerical model.

The resulting force-displacement hysteresis of the strip model is shown in Figure 6-19, plotted together with that of the cyclic pushover test. Overall, the analytical hysteresis is in a good agreement with that from the experiment. The hysteresis has a better match with the capping point and the degradation backbone up to the completion of the test in the positive excursion compared to that in the negative excursion. This can be understood because in-cycle strength degradation was not considered in the material model (Section 6.6.1). Moreover, the strip model exhibited more severe pinching behavior compared to that observed during the experiment. This discrepancy is attributed to the material model assigned to the infill plate that can only yield in tension and has no strength in compression, which will be further addressed in Section 6.6.6.

6.6.3 Two-Story SPSW: Qu and Bruneau (2008) Specimen

Qu and Bruneau (2008) conducted an experimental program on a full-scale, two-story steel plate shear wall with RBS connections and composite floors. Schematic of the specimen and the experiment setup are shown in Figure 6-20. The centerline dimensions of the specimen were 8000 mm total high by 4000 mm wide. Wide-flange section H532×314×25×40 was selected for VBEs at each story while H458×306×17×27, H350×252×11×19, and H446×302×13×21 were selected for the bottom, intermediate, and top HBEs, respectively. Note that the designation for H shapes sequentially refers to section overall depth, flange width, web thickness, and flange thickness. Hot-rolled steels of 3.2 and 2.3 mm thick were selected for the first and second story infill plates, respectively. Material properties of boundary elements and infill plates are

278
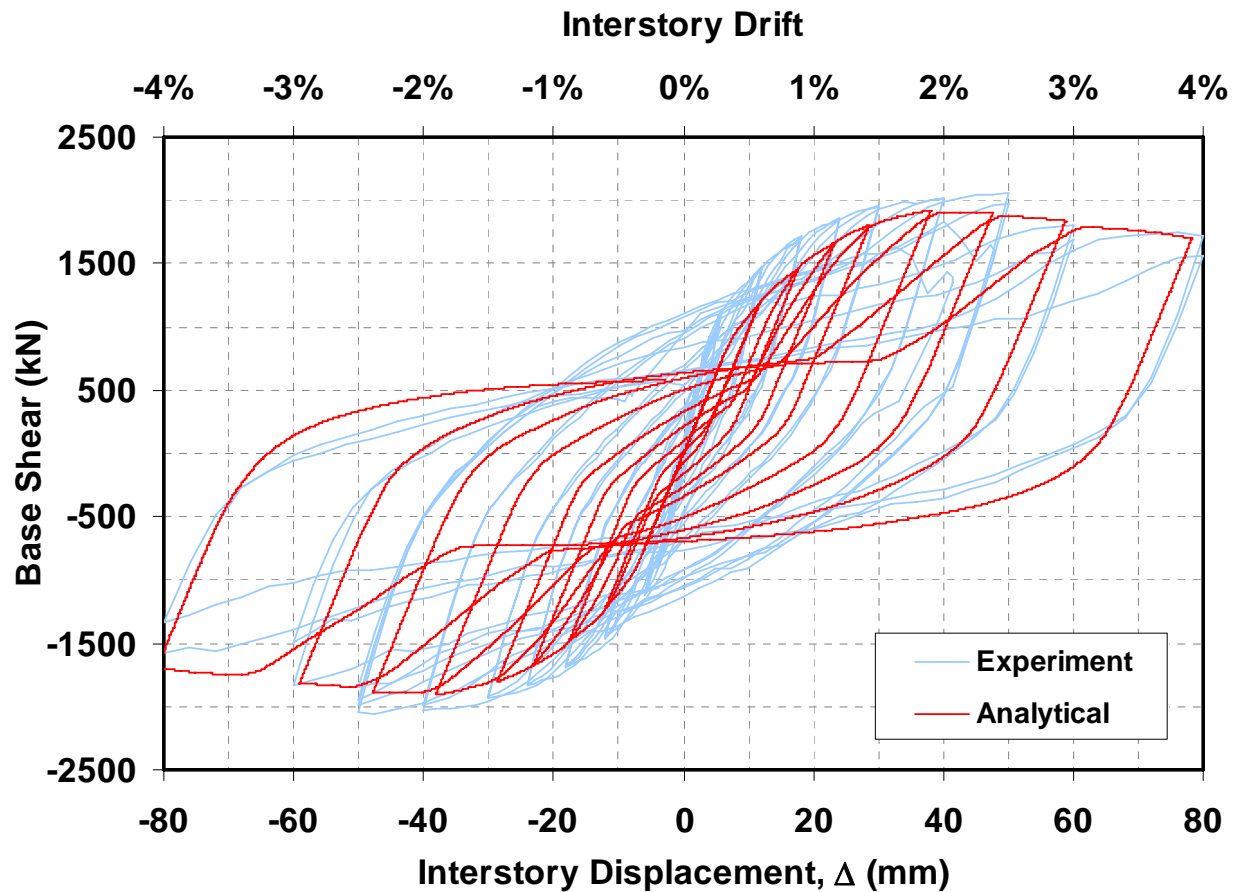
Figure 6-19 Single Story SPSW Specimen Hysteresis

summarized in Table 6-5. A vertical load of 1,400 kN was applied at each column to simulate gravity loads. In the first half of the experiment, two series of pseudo-dynamic tests were conducted, followed by a cyclic pushover test up to the failure of the specimen. Prior to conducting the second series of pseudo-dynamic tests, buckled infill plates were replaced by new plates and damaged shear tab at the intermediate HBE were replaced by a new one prior to the cyclic pushover test. For practical purposes, the calibration process for this specimen focused on matching the force-displacement hysteresis obtained from the cyclic pushover test with that from numerical analysis of this specimen using strip model (i.e., results from the pseudo-dynamic tests were excluded from the analysis).

When reaching the capping point at 3.0% first story drift, the maximum base shear recorded was 4245 kN. At the conclusion of the experiment after the specimen was cycled up to a maximum first story drift of 5.2%, the base shear strength dropped approximately 44% from its ultimate
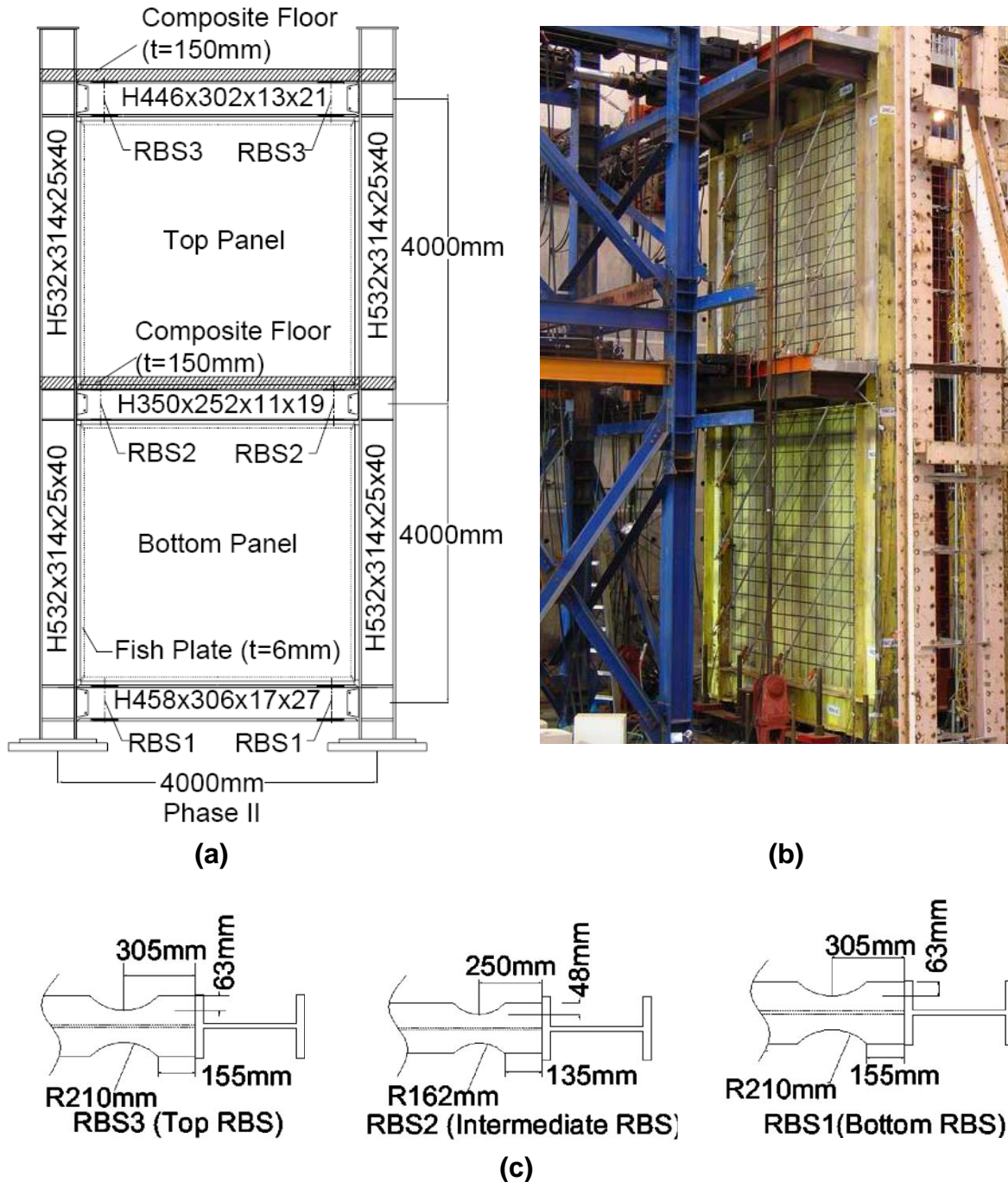
Figure 6-20 Two-Story SPSW Specimen (Qu and Bruneau 2008):
(a) Schematic of Specimen; (b) Experiment Setup; (c) Reduced Beam Section (RBS) Details

strength as a result of significant web tearing in the first story infill plate and fracture of the intermediate HBE (Figure 6-21). Interestingly, except for insignificant tearing at the corners of the second story infill plate, no major fractures were reported either in the infill plate or boundary

Table 6-5 Material Properties of Two-Story SPSW Specimen (Qu and Bruneau 2008)

Component	Nominal Thickness (mm)	Actual Thickness (mm)	Yield Strength (MPa)	Ultimate Strength (MPa)	Ultimate Strain (%)
HBE0 Flange	27	28	335	496	24
HBE0 Web	17	19	290	500	25
HBE1 Flange	19	19	470	589	18
HBE1 Web	11	12	475	608	19
HBE2 Flange	21	22	350	519	20
HBE2 Web	13	13	290	467	25
VBE Flange	40	40	357	548	18
VBE Web	25	25	370	505	19
1st Fl. Infill Plate	3	3.2	310	435	15
2nd Fl. Infill Plate	2	2.3	285	368	20

Figure 6-21 Failure Modes in Two-Story SPSW Specimen (Qu and Bruneau 2008): (a) Intermediate HBE Fracture; (b) First Story Web Tearing

elements of the upper story and no strength deterioration occurred in that story. Hence, in the strip model developed for this specimen, as shown in Figure 6-22, deteriorating material models were only assigned to most of the first story strips and intermediate HBE while an elasto-plastic material model with 2% strain hardening up to the capping point was assigned to the remaining members. The same circular markers to distinguish components with deteriorating and

(a) 354 mm · 42.7° · 4000 mm · 4000 mm · 4000 mm · Left-leaning strips are not shown for clarity · 11 · 12 · 10 · 9 · 8 · 7 · 4 · 2 · 1 · 3 · 6 · 5

(b) M · M_cap · M_y · SH = 2% · EI · 40%M_{cap} · $-\theta_y$ · θ_y · 0.031 · 0.045 · θ · Symmetric · 3.0% · 3.7% first story drift · $-M_y$ · For non-deteriorating boundary elements

(c) P · P_{cap} · SH = 2% · P_y · EA · δ_y · $7\delta_y$ · δ · No Compression Strength
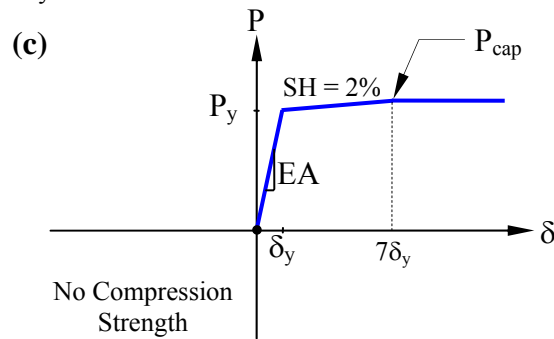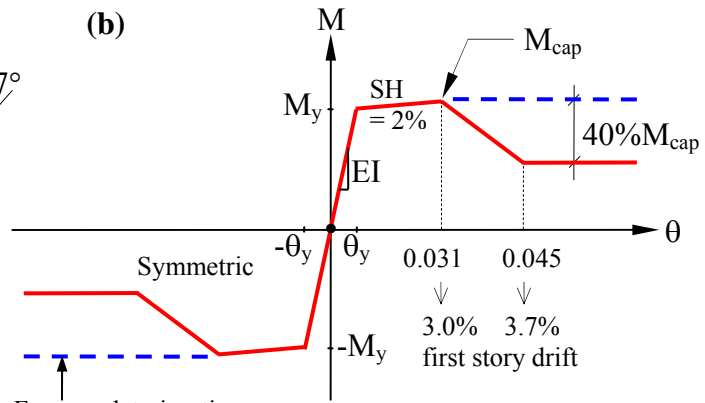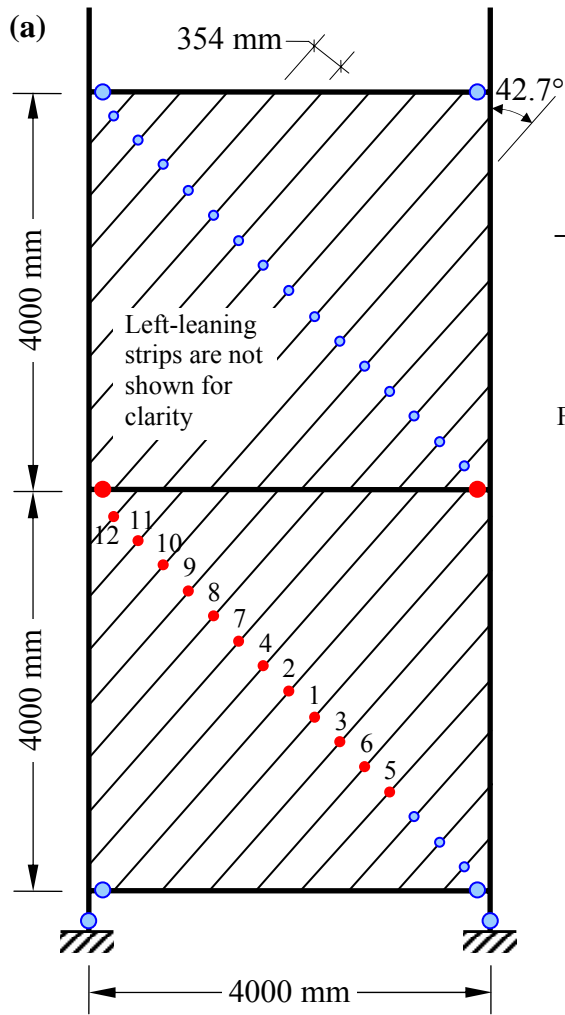
Legend:
○|● = Fiber Hinge with non-deteriorating | deteriorating material model
○|• = Axial Hinge with non-deteriorating | deteriorating material model

(d) P · P_{cap} · SH = 2% · P_y · EA · δ_y · δ_C · δ_D · δ · No Compression Strength · Δ_C · Δ_D
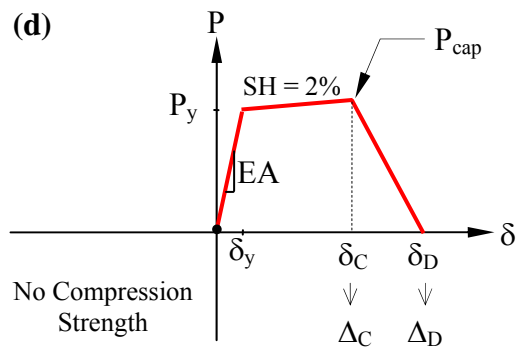
δ_C | δ_D = Strip elongation at the capping | failure point

Δ_C | Δ_D = Corresponding first story drift when reaching the capping | failure point

Seq.	δ_C	δ_D	Δ_C	Δ_D
1	$7.6\delta y$	$8.1\delta y$	3.0%	3.2%
2	$8.0\delta y$	$8.6\delta y$		
3	$7.6\delta y$	$9.0\delta y$	3.2%	3.7%
4	$9.0\delta y$	$10.6\delta y$		
5	$7.1\delta y$	$9.1\delta y$	3.7%	4.3%
6	$8.2\delta y$	$10.2\delta y$		
7	$10.4\delta y$	$12.8\delta y$		
8	$10.2\delta y$	$12.6\delta y$		
9	$12.0\delta y$	$13.9\delta y$	4.3%	4.8%
10	$10.8\delta y$	$13.0\delta y$		
11	$8.4\delta y$	$10.3\delta y$		
12	$1.6\delta y$	$2.4y$		

Figure 6-22 Strip Model for Two-Story Qu and Bruneau (2008) Specimen: (a) Overview; (b) Material Model for Boundary Elements; (c) Material Model for Non-Deteriorating Strips; (d) Material Model for Deteriorating Strips

282

non-deteriorating material models introduced in the previous section are also used in Figure 6-22. Inferred from the experimental step-by-step observations reported in Qu and Bruneau (2008), fracture of the intermediate HBE occurred at the onset of the 3.0% first story drift and strength degradation stabilized at 3.7% first story drift. In addition, web tearing in the first story infill plate started at the upper North corner when the specimen experienced 3.0% first story drift and progressed toward the upper South corner and the bottom North corner at 4.8% first story drift. At the conclusion of the test, the first story infill plate was practically torn away from the intermediate HBE. In the numerical model, the sequence of strips losing their capacity to sustain lateral loads is schematically shown in Figure 6-22d.

Furthermore, fiber hinges in the model were located at the center of the RBSs. Composite slabs were not included in the numerical model, but their contribution to global behavior was taken into account by increasing the thickness of the top flange of the intermediate and top HBEs such that their resulting plastic cross-section properties were the same as that of the actual composite beams. One should note that even though no shear studs were installed over the length of the RBSs, composite action was considered to be effective as a consequence of the presence of shear studs outside the RBS locations (as if assuming that RBS length was comparable to the stud spacing needed to develop composite action). Incidentally, excluding composite action in the numerical model developed for this specimen resulted in a poor match between the analytical and experimental force-displacement hysteresis. In principle, under negative flexure case (i.e., with tension in the concrete slab), the composite action was incorrectly considered by this approach. However, this approximation has negligible impacts when simulating the global behavior of this two-story SPSW specimen, as demonstrated by the results presented later.

Cyclic displacement histories applied to each actuator at the first and second story levels are shown in Table 6-6. Note that the cyclic displacement histories became unsymmetrical beyond 3.2% and 3.0% at the first and second story, respectively. This was because the actuators had reached their maximum stroke in the negative direction. As a result, increasing cyclic displacement in the subsequent cycles only occurred in the positive direction. In OpenSees, these two separate displacement histories were defined using the *Time Series* command and the *Penalty-Method Constraint* was used to force each story to follow its assigned displacement

history. The analysis was conducted using the *Load Control Integrator*. It should be emphasized that the term "load" in this case refers to its broader definition which includes "displacement" as one type of loads. In other words, though the analysis was conducted under a load controlled scheme, the target actually was displacements assigned to the first and second stories.

Table 6-6 Cyclic Displacement History for Two-Story SPSW (Qu and Bruneau 2008)

Displacement Step	Number of Cycles	Cumulative Number of Cycles	1st Floor		2nd Floor	
			Positive Drift (%)	Negative Drift (%)	Positive Drift (%)	Negative Drift (%)
1	2	2	1.2	-1.2	1.0	-1.0
2	2	4	2.4	-2.4	2.0	-2.0
3	2	6	3.0	-3.0	2.5	-2.5
4	2	8	3.2	-3.2	3.0	-3.0
5	2	10	3.7	-3.2	3.5	-3.0
6	2	12	4.3	-3.2	4.0	-3.0
7	2	14	4.8	-3.2	4.5	-3.0
8	0.25	14.25	5.2	n.a.	5.0	n.a

The resulting force-displacement hysteresis of the strip model is shown in Figure 6-23, plotted together with that from the cyclic pushover test. Overall, the analytical hysteresis is in good agreement with that from the experiment. It matches the capping point and the degradation backbone up to completion of the test. While the analytical hysteresis is noticeably fatter compared to that recorded in the experiment in the early stages of the hysteretic behavior, this discrepancy is because the inelastic excursions recorded during the pseudo-dynamic test prior to the cyclic pushover test were not accounted for in the numerical analysis (i.e., the infill plate contribution to strength of the SPSW up to the drift reached during the pseudo-dynamic tests could not be mobilized until drift exceeded these drifts in the cyclic tests).

284
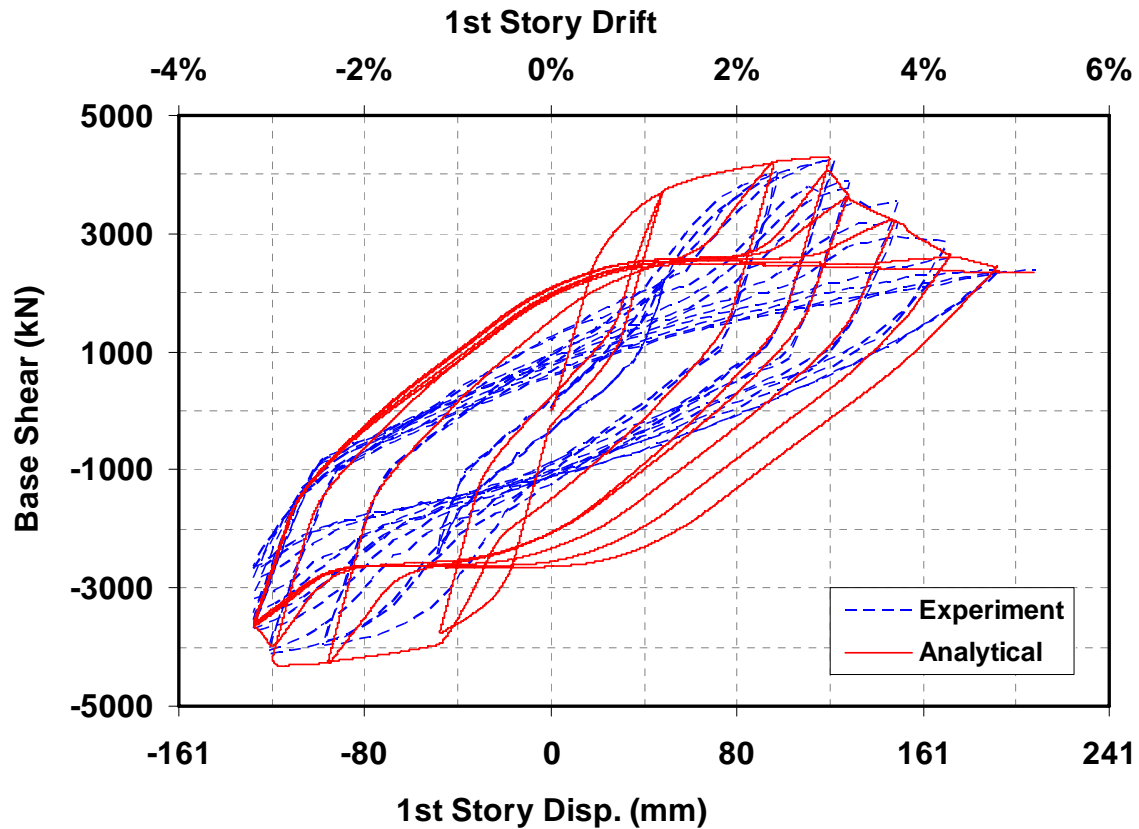
Figure 6-23 Two-Story SPSW Specimen Hysteresis

6.6.4 Three-Story SPSW: Choi and Park (2009) Specimen

One of Choi and Park (2009) three-story SPSW specimens (i.e., denoted as BSPW2) was selected for this calibration process. Shown schematically in Figure 6-24a, this one-third-scale specimen has overall height and width of 3550 and 2500 mm, respectively. Built-up wide-flange sections H150×150×22×22, H150×100×12×20, and H250×150×12×20 were selected for VBEs, intermediate HBEs, and top anchored beam (i.e., HBE3), respectively. The bottom side of the first story infill plate was connected via fish plates directly to a steel strong floor. In other words, no bottom anchor beam was provided. A hot-rolled steel plate 4 mm thick was selected for all infill plates. Special moment resisting connections were designed for all HBE-to-VBE and VBE-to-the strong floor connections, while bolts at 100 mm spacing were used to connect the infill plate (via fish plates) to the surrounding vertical and horizontal boundary elements. Material properties of boundary elements and infill plates are summarized in Table 6-7. Cyclic displacement history applied to the single actuator attached to the specimen top story is shown in Table 6-8.
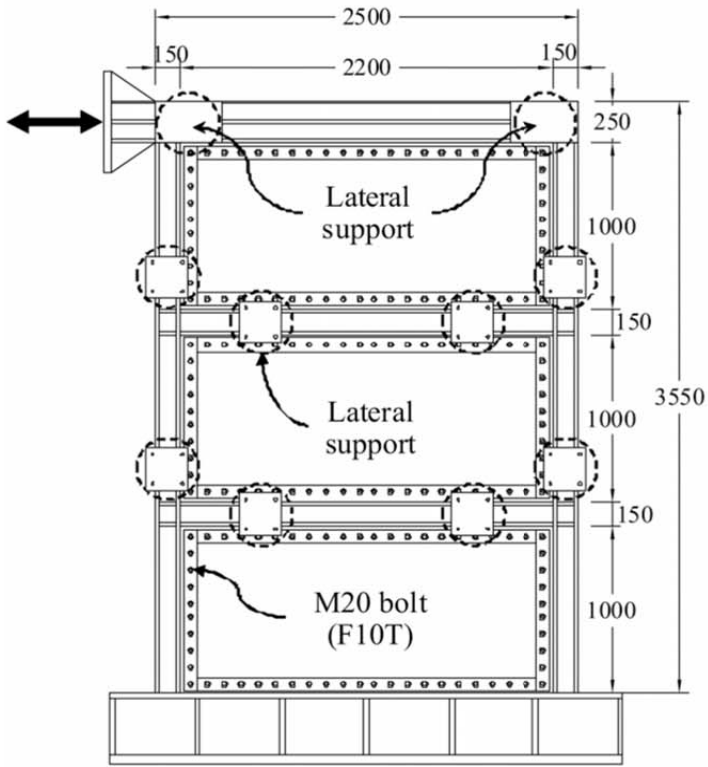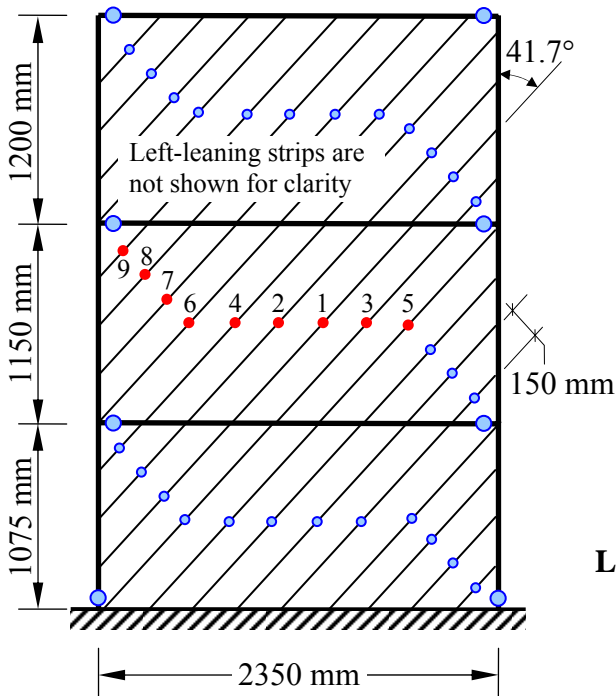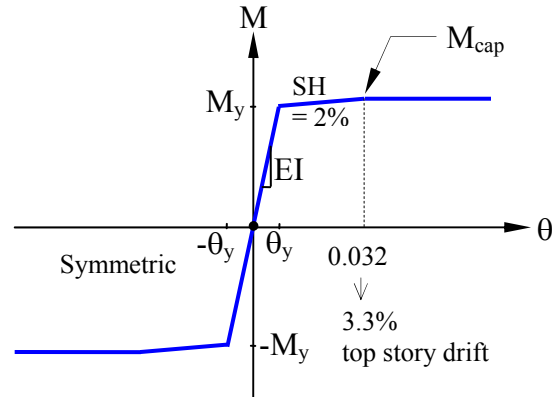
Figure 6-24 Three-Story SPSW Specimen Tested by Choi and Park (2009): (a) Schematic of Specimen; (b) Failure Modes; (c) Strip Model; (d) Material Model for Boundary Elements

(e)

P ↑
P_{cap}
$SH = 2\%$
P_y
For non-deteriorating strips (SH up to $8\delta_y$)
EA
No Compression Strength
δ_y δ_C δ_D → δ
Δ_C Δ_D
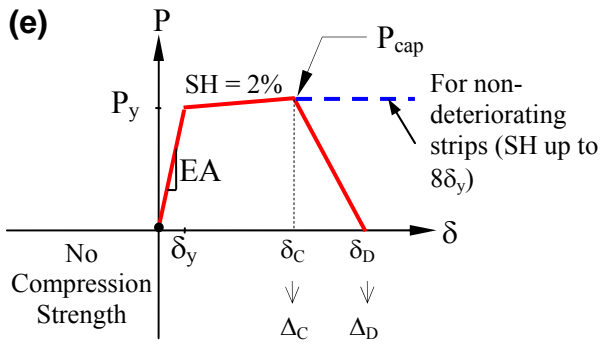
$\delta_C \mid \delta_D$ = Strip elongation at the capping | failure point

$\Delta_C \mid \Delta_D$ = Corresponding top story drift when reaching the capping | failure point

Seq.	δ_C	δ_D	Δ_C	Δ_D
1	$11.9\delta y$	$14.9\delta y$		
2	$11.9\delta y$	$14.9\delta y$	3.3%	3.7%
3	$11.7\delta y$	$14.9\delta y$		
4	$11.7\delta y$	$14.9\delta y$		
5	$17.8\delta y$	$19.6\delta y$	4.4%	4.8%
6	$17.7\delta y$	$22.8\delta y$		
7	$14.4\delta y$	$25.8\delta y$		
8	$16.7\delta y$	$25.3\delta y$	4.6%	5.3%
9	$17.0\delta y$	$27.5\delta y$		

Figure 6-24 Three-Story SPSW Specimen Tested by Choi and Park (2009) – Cont'd: (e) Material Model for Strips

Table 6-7 Material Properties of Three-Story SPSW Specimen (Choi and Park 2009)

Component	Nominal Thickness (mm)	Actual Thickness (mm)	Yield Strength (MPa)	Ultimate Strength (MPa)
HBE Flange	20	20.1	353	538
HBE Web	12	12.1	377	527
VBE	22	21.7	348	522
Infill Plate	4	3.9	299	372

The ultimate base shear recorded during the experiment in the positive and negative excursions were somewhat the same. When reaching the capping point at 3.3% top story drift in the positive excursion, the maximum base shear was 1961 kN. Even though initiation of web tearing was observed in the first and second story infill plates prior to reaching the capping point, it did not affect the overall capacity of the structure to sustain lateral loads. The base shear strength significantly dropped to 1524 kN in the subsequent displacement step of 4.4% top story drift when major plate tearing occurred in the second story infill plate. As shown in Figure 6-24b, which documents the specimen condition at completion of the test, web tearing had propagated to almost the entire area of the second story infill plate, causing the base shear strength to drop by

Table 6-8 Cyclic Displacement History for Three-Story SPSW (Choi and Park 2009)

Displacement Step	Number of Cycles	Cumulative Number of Cycles	Ductility Ratio Δ/δ_y	Top Drift (%)	Top Displacement Δ (mm)
1	3	3	0.2	0.09	3.0
2	3	6	0.4	0.18	6.0
3	3	9	0.6	0.26	9.0
4	3	12	0.8	0.35	12.0
5	3	15	1.0	0.44	15.0
6	3	18	1.5	0.66	22.5
7	3	21	2.0	0.88	30.0
8	3	24	3.0	1.31	45.0
9	3	27	4.0	1.75	60.0
10	3	30	6.0	2.63	90.0
11	3	33	8.0	3.50	120.0
12	3	36	10.0	4.38	150.0
13	1	37	12.0	5.26	180.0

approximately 46%, to 1055 kN at 5.3% top story drift. Based on this failure mechanism, in the strip model developed for this specimen (Figure 6-24c), deteriorating material models were assigned to most of the strips at the second story. Minor plate tearing and plate kinking in the first and third story infill plates were considered to be non-deteriorating web tearing (nWT) and therefore an elasto-plastic material model with 2% strain hardening up to the capping point was used at these stories instead of a deteriorating material model. Moreover, flange fracture at the upper end of the second story VBE occurred in the last cycle of displacement loading. However, since no indication reported that this fracture initiated at an earlier cycle of displacement loading, all boundary elements were considered to have non-deteriorated material model similar to the strips at the first and third stories.

As in the calibration process for the Qu and Bruneau (2008) specimen, strips at the second story of the Choi and Park (2009) specimen lost their capacity to sustain lateral loads sequentially. As schematically shown in Figure 6-24e, it started from middle strips at the onset of 3.3% top story

drift and gradually propagated toward strips adjacent to upper left and lower right corners at 5.3% top story drift. The resulting force-displacement hysteresis of the specimen model is shown in Figure 6-25, plotted together with that from the cyclic pushover test. Overall, the two hystereses are in a good agreement with negligible discrepancies at the onset of effective yielding, at the capping point, and the degradation backbone up to completion of the test. However, the two hystereses have slightly different pinching behavior. As for the calibration results for the Vian and Bruneau (2005) case, the strip model exhibited severe pinching behavior as opposed to the moderate pinching behavior observed during the experiment.
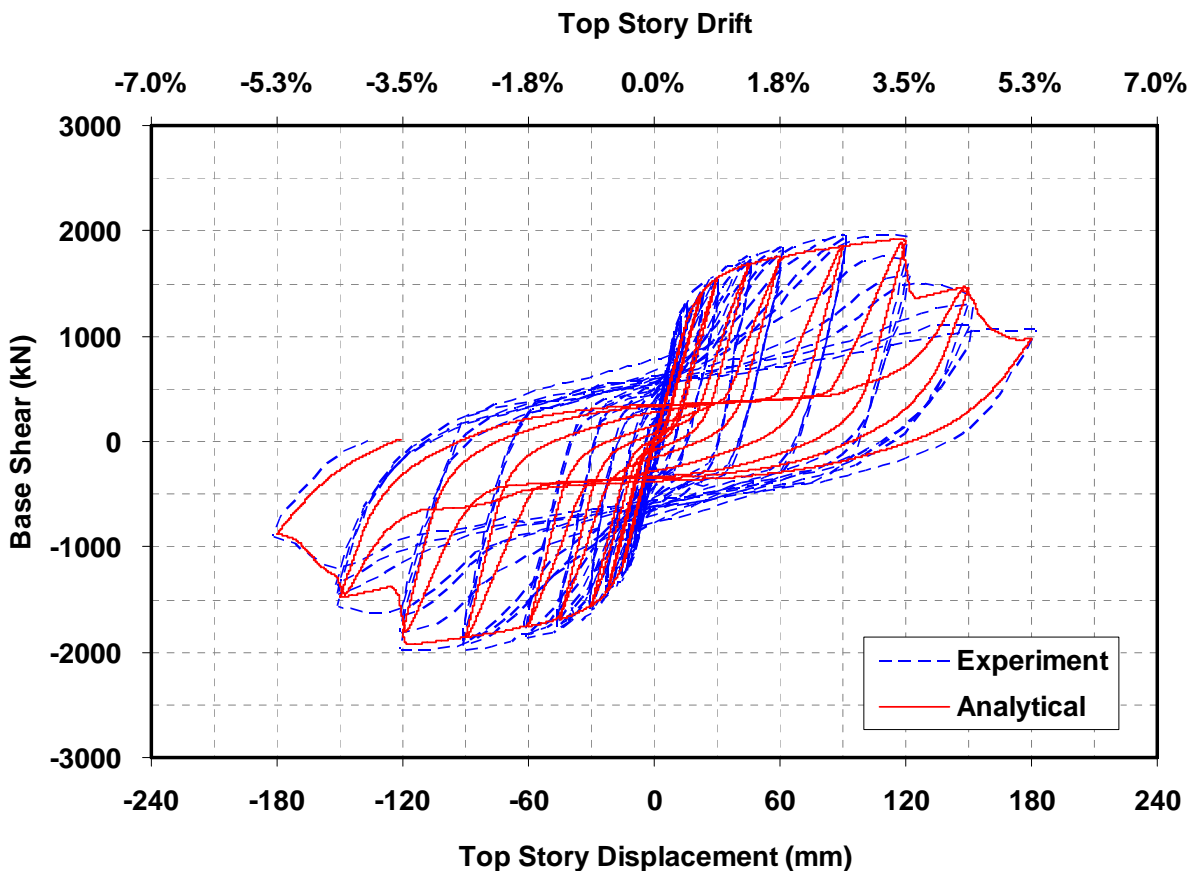
Figure 6-25 Three-Story SPSW Specimen Hysteresis

6.6.5 Four-Story SPSW: Driver *et al.* (1997) Specimen

The specimen tested by Driver *et al.* (1997) is the only four-story SPSW specimen (at the time of this writing) tested up to the specimen ultimate capacity and that exhibited stable hysteretic behavior and strength degradation behavior. Schematic of this one-half scale specimen is shown in Figure 6-26a. It had an overall height of 7421 mm and center-to-center bay width of 3050 mm.

(a) Schematic of Specimen labels:

Level 4
W530 x 82
Panel 4
3.4 mm Plate
Level 3
W310 x 60
Panel 3
3.4 mm Plate
Level 2
W310 x 60
Panel 2
4.8mm Plate
Level 1
W310 x 60
Panel 1
4.8mm Plate

East   West

W310 x 118   W310 x 118

1836
1829
1829
1927
7421
3050

(b) Strip Model:

42.3°
Left-leaning strips are not shown for clarity
265 mm
See Figure 6-22 for legend definitions
3050 mm

(c) Material Model for Boundary Elements:

M
M_{cap}
M_y
SH = 2%
$40\%M_{cap}$
EI
$-\theta_y$ θ_y 0.021   0.037
Symmetric
$-M_y$
2.2%   4.0%
first story drift
θ
For non-deteriorating BEs

(d) Material Model for Strips:

P
P_{cap}
P_y
SH = 2%
For non-deteriorating strips (SH up to $8\delta_y$)
EA
No Compression Strength
δ_y $3.7\delta_y$ $7.6\delta_y$
δ

Figure 6-26 Four-Story SPSW Specimen (Driver *et al*. 1997): (a) Schematic of Specimen; (b) Strip Model; (c) Material Model for Boundary Elements; (d) Material Model for Strips

290

The entire four stories used W310×118 (SI equivalents to standard United States shape of W12×79) steel for VBEs. A relatively deep and stiff beam W530×118 (W21×55) was used at the roof level to anchor the tension field forces generated by yielded infill plates, while a smaller beam W310×60 (W12×40) was used for the intermediate HBEs. Similarly to the three-story Choi and Park (2009) specimen, no bottom anchored beam was provided. For the infill plates, 4.8 mm and 3.4 mm hot-rolled steel plates were used for the first two stories and the next two stories, respectively. These infill plates were welded to fish plates on the surrounding boundary elements. Like the other three specimens, special moment resisting connections were designed for all HBE-to-VBE connections. Material properties of boundary elements and infill plates are summarized in Table 6-9.

Table 6-9 Material Properties of Four-Story SPSW Specimen (Driver *et al*. 1997)

Component	Elastic Modulus (MPa)	Yield Strength (MPa)	Ultimate Strength (MPa)	Ultimate Strain (%)	Rupture Strain (%)
All VBEs	202991	313	482	15.5	26.3
Intermediate HBE	203947	332	478	16.8	26.2
Top HBE	206092	349	493	15.5	26.9
Panel 1 & 2	208835	341	456	20.1	34.2
Panel 3	210898	257	344	20.0	42.5
Panel 4	203079	262	375	17.7	34.1

A uniform lateral load distribution along the height of the specimen was applied (one point load per story level) and displacement of the first story was used as a controlled point. A vertical load of 720 kN was applied at each column to simulate gravity loads. Prior to conducting a displacement controlled test, the first 10 cycles were conducted under a force-controlled scheme by pushing the specimen to gradually reach a base shear of 1950 kN. Table 6-10 shows the applied cyclic displacement history up to 9 times the first story yield displacement (i.e., $9\delta_y = 76.5$ mm = 4% drift). The actual cyclic displacement history however became unsymmetrical beyond $5.48\delta_y$ (= 46 mm) because the actuator at the third story had reached its maximum stroke in the negative direction (pulled to the East direction). Consequently, increasing cyclic displacement in the subsequent cycles only occurred in the positive direction (pushed to the West direction).

Table 6-10 Cyclic Displacement History for Four-Story SPSW (Driver *et al*. 1997)

Displacement Step	Number of Cycles	Cumulative Number of Cycles	Ductility Ratio Δ/δ_y	First Story Drift (%)	First Story Displacement Δ (mm)
1[a]	3	3	1.0	0.44	8.5
2	3	6	2.0	0.88	17.0
3	3	9	3.0	1.32	25.5
4	2	11	4.0	1.76	34.0
5	2	13	5.0	2.21	42.5
6[b]	2	15	6.0	2.65	51.0
7	2	17	7.0	3.09	59.5
8	2	19	8.0	3.53	68.0
9	1	20	9.0	3.97	76.5

Note: [a] Prior to conducting displacement controlled test, the first 10 cycles were conducted under a force-controlled scheme by pushing the specimen to gradually reach a base shear of 1950 kN.

[b] Starting Displacement Step 6, maximum displacement in the negative direction was maintained at $5.48\delta_y$ (= 2.42% = 46 mm) because the actuator at the third story had reached its maximum stroke.

The maximum base shear of 3080 kN was reached at 2.2% first story drift (= $5\delta_y$). Minor web tearing at the top West corner of the first story infill plate and flange local buckling at both ends of the East VBE1 (i.e., below HBE1 and near the base) as well as at the upper end of the West VBE1 were reported in earlier cycles prior to reaching the capping point. As the web tearing propagated to a larger size and the severity of VBE flange local buckling increased (Figure 6-27), the lateral strength of the specimen started to deteriorate. The degradation rate however was relatively slow compared to that of the other three specimens considered above. In this case, the specimen base shear strength only dropped 15% from the maximum base shear at the end of 4.0% first story drift cycle (= $9\delta_y$). Structural damage predominantly concentrated at the first story level as a result of the uniform loading distribution selected.

In the strip model developed for this specimen (Figure 6-26b), deteriorated material models were only assigned to VBE1 and several strips in the first story infill plate while an elasto-plastic material model with 2% strain hardening up to the capping point was assigned to the remaining members.
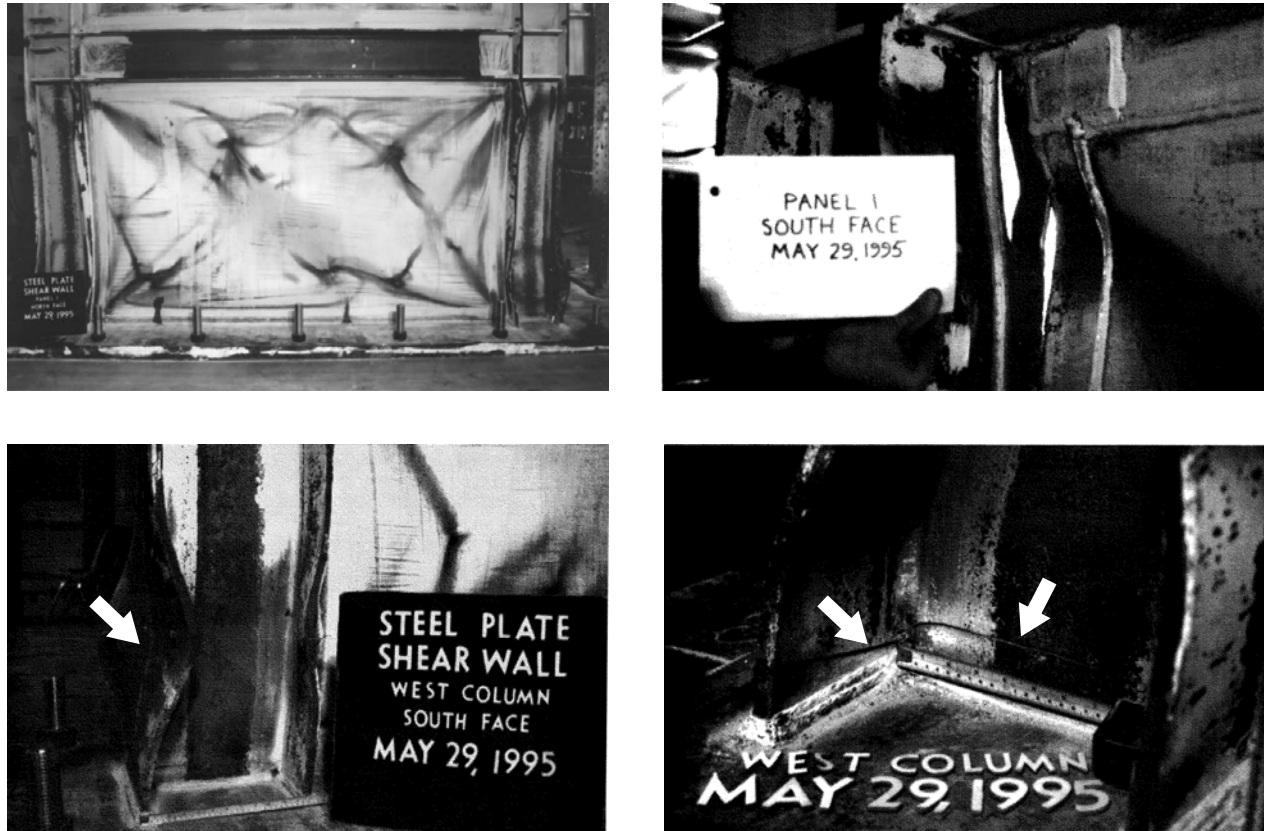
Figure 6-27 Failure Modes in Four-Story SPSW Specimen: (a) Damage at the First Story Level (Courtesy of Driver R. G.); (b) Web Tearing at the Corner of Panel (Driver *et al*. 1997); (c) VBE Flange Local Buckling; (d) Fracture of VBE at the Base (Driver *et al*. 1997)

It was considered that the aforementioned minor web tearing and VBE flange local buckling prior to the capping point have insignificant impacts on the overall strength of the specimen. As such, strength degradation in the strip model was set to start at 2.2% first story drift. For practical reasons, the first 10 cycles under the force-controlled condition were excluded in the nonlinear analysis of the strip model.

The resulting force-displacement hysteresis of the strip model is shown in Figure 6-28, plotted together with that from the cyclic pushover test. As with the other three calibration results, the resulting analytical hysteresis of the four-story specimen is in a good agreement with that from the experiment, which matches the capping point and the degradation backbone up to the completion of the test. As a consequence of excluding in-cycle strength degradation in the material model however, numerical strength degradation remained at the same level after the

$5.4\delta_y$ excursion in the negative direction. Again, the strip model exhibited more severe pinching behavior compared to that observed during the experiment, which is attributed to the fact that the material model assigned to the infill plates can only yield in tension and has no compression strength.
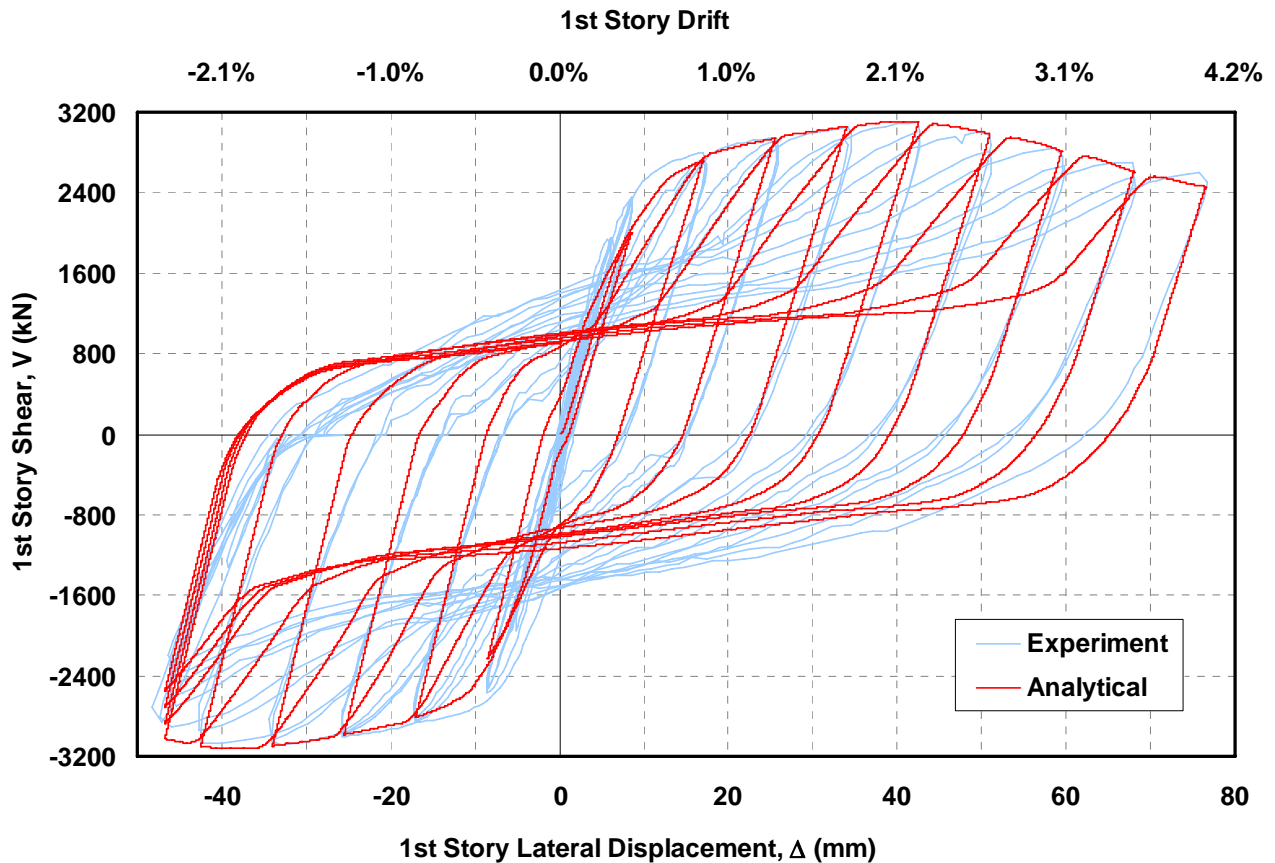
Figure 6-28 Four-Story SPSW Specimen Hysteresis

6.6.6 Interpretation of Calibration Results

Even though, in all cases, the calibration process successfully matched the capping point and the backbone of the degrading hysteresis, discrepancies in pinching behavior were observed between the numerical and experiment results. One possible explanation for this underestimation of the experimental pinching behavior may be because the strip material models exclude the compressive strength that can develop during loading reversal. This assumption is reasonably correct to simulate infill plate behavior in earlier cycles. However, it has been observed in some cyclic tests that after SPSWs undergo substantial inelastic elongation, the, infill plates can exhibit a significant compressive strength during load reversal, as reported in Clayton *et al*. (2012).

When including compressive strength during reversal of loading in the material model for the infill plates, Choi and Park (2010) successfully simulated the pinching behavior observed in the Driver *et al*. (1997) experiment. However, their numerical model failed to simulate the deteriorating hysteresis behavior after the capping point. During the calibration process, no effort was made to resolve the underestimated pinching behavior because it was considered that it would have a marginal impact on the overall collapse performance of steel plate shear walls. Furthermore, recent tests by Dowden and Bruneau (2014) showed that the effect of this compressive strength was insignificant in shake table tests (as opposed to cycling testing). Hence, compressive strength of the strip was excluded from the final strip deterioration model.

In light of the above calibration results, particularly the fact that different models were used to replicate each of the four experimental results, one might ask which of the above degradation parameters should be selected to capture, in a general sense, the degradation of boundary elements and infill plates in any specific SPSW. Since only a limited number of specimens were calibrated, the approach selected here was to take the worst degradation parameters from the above cases, as opposed to the average values of all four specimens. Hence, for the collapse assessment of steel plate shear walls, degradation models for boundary elements and infill plates were selected from the calibration results of the two-story Qu and Bruneau (2008) SPSW specimen.

6.7 Behavior of Selected SPSW Specimens with Final Deterioration Models

To examine the impact of selecting the most conservative deterioration models (i.e. model with the most severe degradation, as identified in Section 6.6.6), another set of analyses were conducted on all calibrated specimens. Boundary elements and every strip at every floor were modeled according to the deterioration models shown in Figures 6-29a and 6-29b, respectively. Note that the model presented in Figure 6-29a for boundary elements calibrated to the Qu and Bruneau (2008) specimen was at the condition when HBE1 experienced axial loads P equal to 493 kips (i.e., P = 16%Py). To apply the model to other specimens, the model first was modified to the condition at zero axial loads. The updated rotation capacities (obtained from a cross-section analysis in OpenSees) for the capping point and the point corresponding to 40% degradation of moment capacity for boundary element model are also shown in Figure 6-29a.
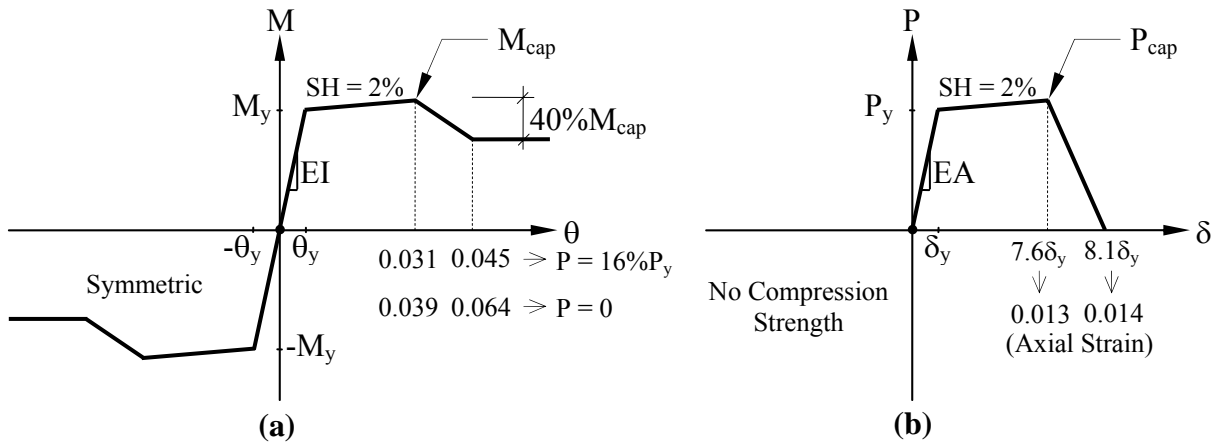
Figure 6-29 Conservative Degradation Models Selected from the Calibration of Qu and Bruneau (2008) Two-Story Specimen: (a) Boundary Elements; (b) Strips

The resulting hysteresis for all calibrated specimens using the conservative deterioration models are shown in Figure 6-30. As expected, since the conservative deterioration models were selected from the Qu and Bruneau (2008) specimen, the analytical result obtained (i.e., denoted as the "conservative case" in Figure 6-30b) is close to the calibration result of the experimental hysteresis (i.e., denoted as the "matching case" in Figure 6-30b). All additional drops in strength in the conservative case were attributed to partial strength degradation of the second floor panel predicted by the model, which in the actual experimental did not happen and was not considered in the matching case. In Vian and Bruneau (2005) specimen (Figure 6-30a), the conservative model actually delayed degradation which had started at 2% interstory drift in the experiment to 3.3% interstory drift in the analysis. However, beyond this point, strength degradation was significant and abrupt. In other words, deterioration of infill plates and boundary elements occurred somewhat at the same time. Significant differences were observed in the Choi and Park (2009) specimen. As shown in Figure 6-30c, strength degradation started to occur at 2.7% drift, which is sooner than observed in the actual experiment where it happened at 3.5% drift. In addition to boundary element deterioration, all strips lost strength by 3.5% drift compared to the fact that only the second story infill plate lost strength at 5.3% drift in the actual experiment. The remaining strength of the specimen observed in the conservative case beyond 3.5% is attributed to the residual strength of boundary elements. Lastly, for the Driver *et al.* (1997) specimen shown in Figure 6-30d, similar response to that reported in the actual experiment is observed in this specimen up to 2.1% top story drift. Beyond this point however, faster strength degradation is
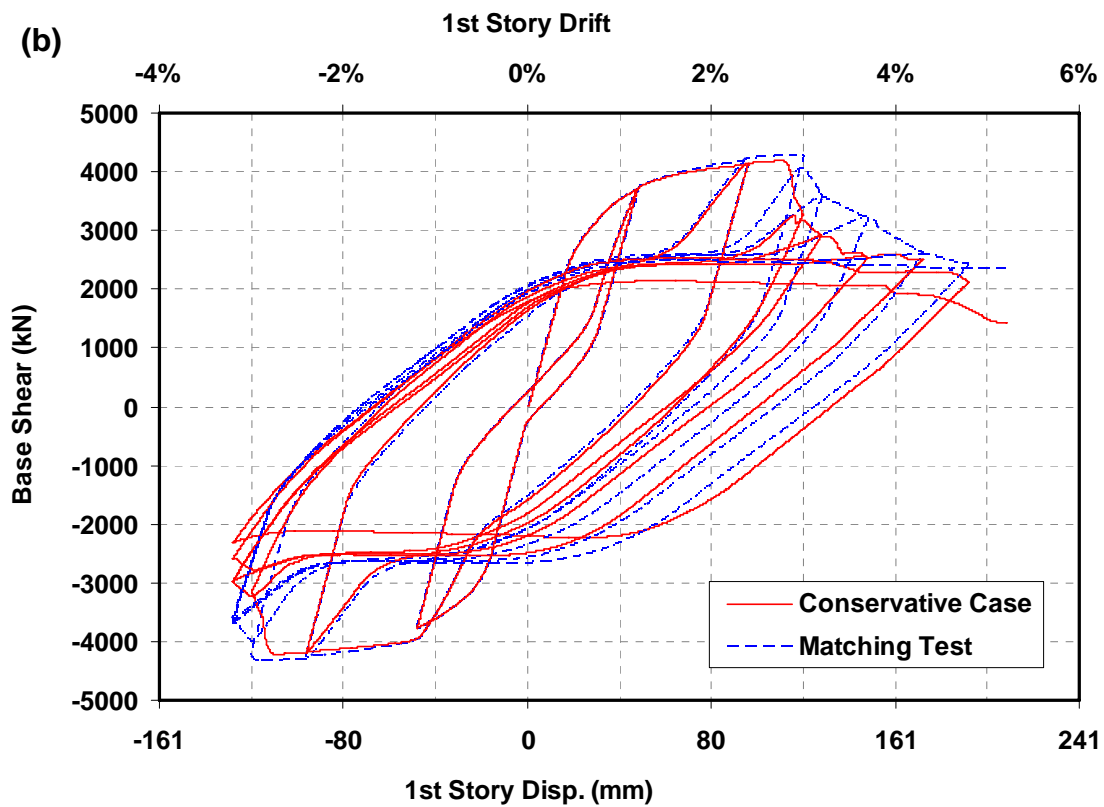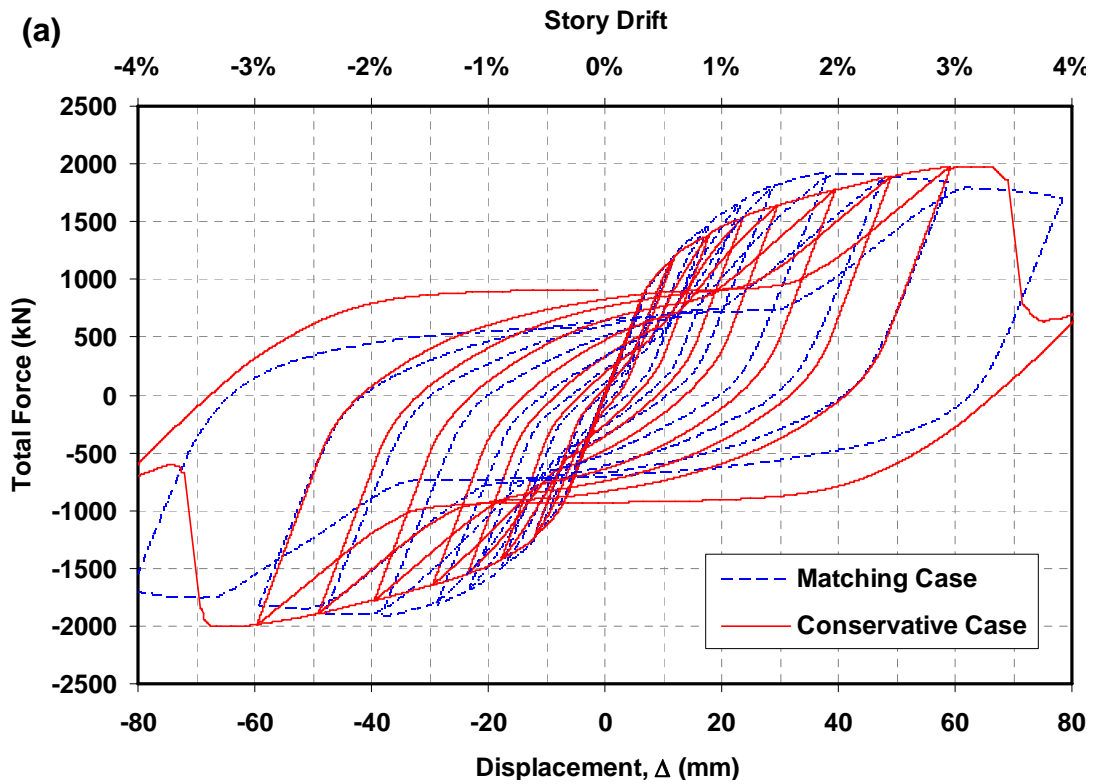
296

Figure 6-30 SPSW Specimen Hysteresis with Conservative Degradation Models: (a) Vian and Bruneau (2005); (b) Qu and Bruneau (2008)
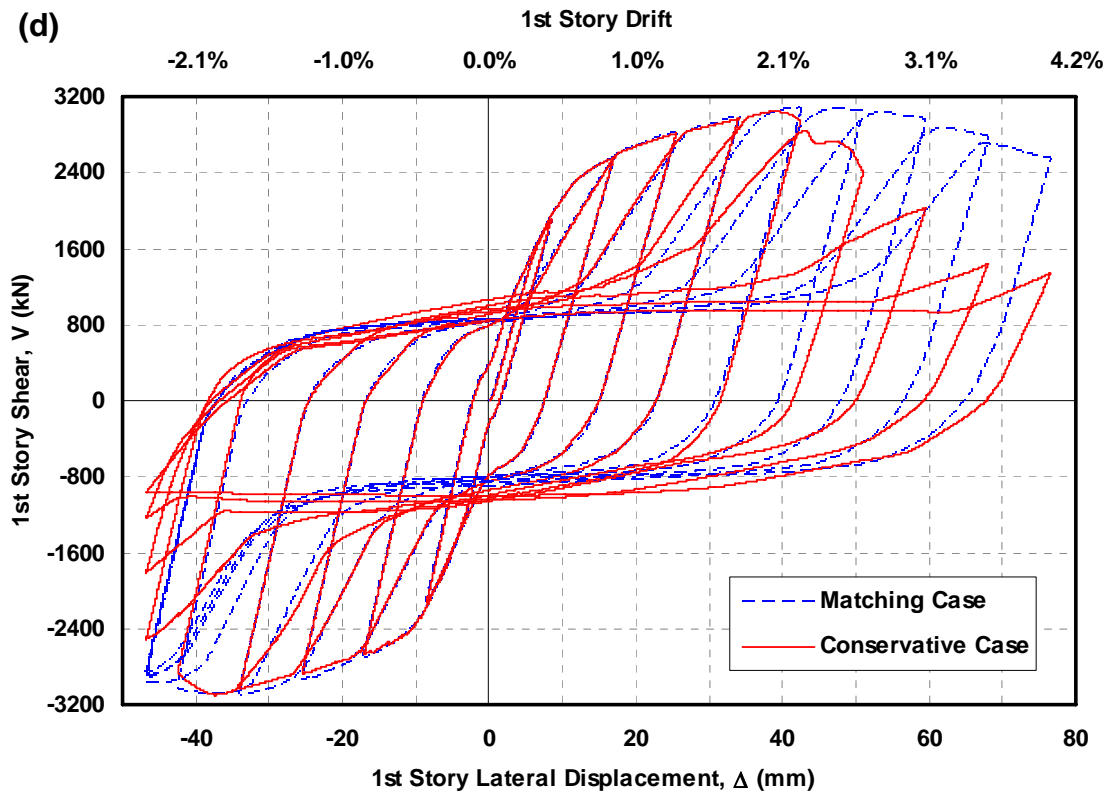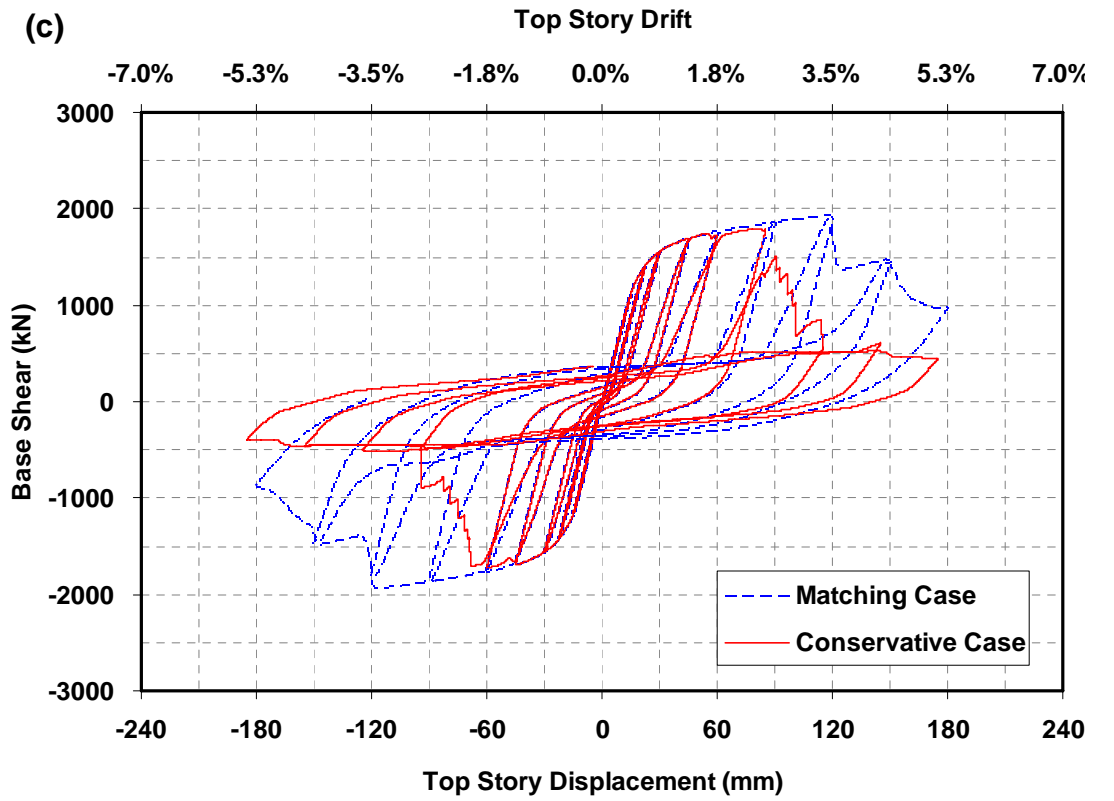
Figure 6-30 SPSW Specimen Hysteresis with Conservative Degradation Models – Cont'd: (c) Choi and Park (2009); (d) Driver *et al*. (1997)

observed in the conservative case within the positive excursion while that in the negative excursion remained the same. At the conclusion of the analysis, the specimen had lost 67.5% of its strength, down to only 1000 kN. This outcome is a consequence of the fact that, in the model, all strips and HBEs at each floor contributed to the degradation compared to only the first floor elements in the actual experiment.

Furthermore, the conservative strip model selected from the calibration of the Qu and Bruneau (2008) specimen (Figure 6-29b) was based on result of its first strip to deteriorate. As shown in Figure 6-22, 15 strips were used to model the first story infill plate degradation behavior. Each of them has different degradation parameters (i.e., deformation capacities at the capping and failure points) in order to match the experimental results. On average, the deformation capacities of these strips at the capping and failure points were $9\delta_y$ and $10.7\delta_y$, respectively (corresponding to 1.5 and 1.8% axial strain, respectively). Marginal differences were observed in the two- and three-story SPSW specimens (detailed results are not reported here) when using these average results for the infill plate deterioration models as opposed to using the conservative model in Figure 6-29b. Nevertheless, these average values were selected for the final deterioration model for strips, as shown in Figure 6-31a. This was necessary to avoid an overly conservative deterioration model for strips in a general case of SPSWs.

At the time of this writing, no SPSW specimens have been tested up to extreme drifts (i.e., 10% drift). Among the currently available experimental data (Table 6-2), the maximum drift to which SPSW specimens have been tested is 5.6% drift. For collapse assessment of SPSW using incremental dynamic analysis (Section 8), it is important to investigate specimen behaviors up to such extreme drift as it may "condition" the results. For this purpose, another set of analyses were conducted on all calibrated specimens up to 10% drift. The loading protocol up to the last point of the experiment was selected to remain the same except that the unsymmetrical loading histories in the Qu and Bruneau (2008) as well as in the Driver et al. (1997) specimens was modified to be symmetric. Beyond the last point of experiment, the loading protocol was then increased progressively by 1% drift until reaching 10% drift. The deterioration of boundary element was modeled to linearly decrease down to zero strength when cross-section rotation reaches 0.103 radians. At the fiber level, this corresponds to 0.057 strains in the farthest fiber from the neutral axis.
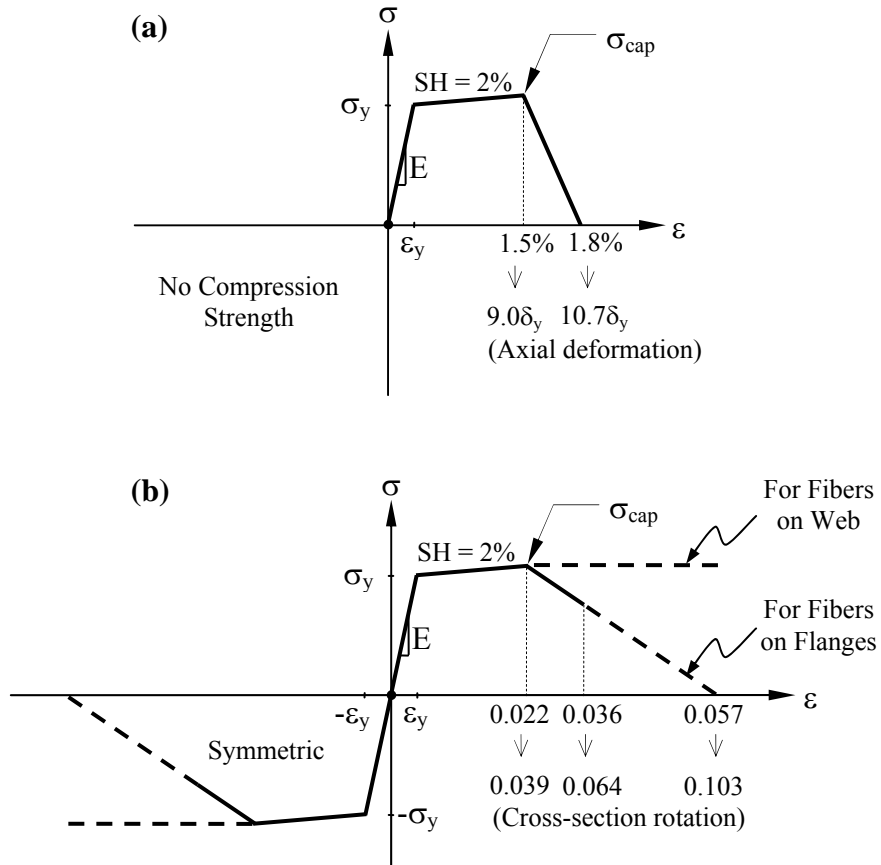
Figure 6-31 Final Degradation Models: (a) Strips; (b) Boundary Elements

During the first analysis of the Qu and Bruneau (2008) specimen subjected to such an extreme drift, a numerical convergence problem developed after the specimen experienced 6% drift. Further investigation revealed that the main source of the problem was the inability of boundary elements modeled with fiber-element to sustain axial loads once most of the fibers had lost their flexural strength at large drift. To solve this problem, it was decided to assign an elasto-plastic material model for fibers on the web of boundary elements and a deteriorating material model for the fibers located on the bottom and top flange of the cross section, as shown in Figure 6-31b. This technique made it possible for the analyses to execute fully when the structures experienced drifts of up to 10%. In other words, this approach was equivalent to having the fibers on the web of a cross section "reserved" to sustain axial loads when all other fibers have lost their capacity due to significantly large cross-section rotations. As a consequence of this approach, boundary elements actually have a residual flexural strength when reaching 0.103 radians, as opposed to the zero strength originally intended. However for W-sections commonly used in North America, the

web of W-shapes contributes on average approximately up to 20% of a section total plastic moment. Therefore, the above approach was deemed acceptable, particularly considering that during incremental dynamic analysis, gravity leaning columns would cause global structural collapse once a structure undergoes significant lateral displacements at relatively small residual strength. Figure 6-32 presents the resulting hysteresis for each calibrated specimen (i.e., denoted as the "extended case" in the figure) using the final deterioration models (Figure 6-31). At the end of the 10% drift cycle, all specimens have lost a significant amount of their ability to sustain lateral loads, and the remaining residual strengths observed are the contribution of the boundary elements (from the bi-linear elasto-plastic fibers in their webs).

6.8   Summary

Deterioration models for infill plates and boundary elements were developed for the purpose of assessing the risk of SPSW collapse under MCE ground motions. Based on a review of 36 specimens of conventional unstiffened slender-web SPSWs tested in past experiments, deterioration and failure modes in SPSW were identified, namely: deteriorated web tearing (WT), shear and flexural failures of boundary elements (FBE), and instability of boundary elements (IBE). In well-designed SPSWs, shear failure and instability of boundary elements can be avoided if boundary elements are designed according to capacity design principles. Hence, among these failure modes, only web tearing and flexural failure of boundary elements were considered in the development of deterioration models. From reviewed SPSW specimen data, cyclic deformation capacities at the capping and failure points as well as percentage of strength degradation were statistically quantified. Based on these statistical results, initial deterioration models for infill plates and boundary elements were developed. These initial models were then calibrated to four selected specimens that represent one- to four-story SPSWs, with panel aspect ratio ranging from 1.0 to 2.2.

Initially, the calibration process was intended to be performed in SAP2000. However, OpenSees was used instead, due to the inability of the axial-hinge used in SAP2000 to model the inelastic behavior of tension-only strips under cyclic deformations once strength degradation has taken place. Hence, implementation of deterioration material models for infill plates and boundary
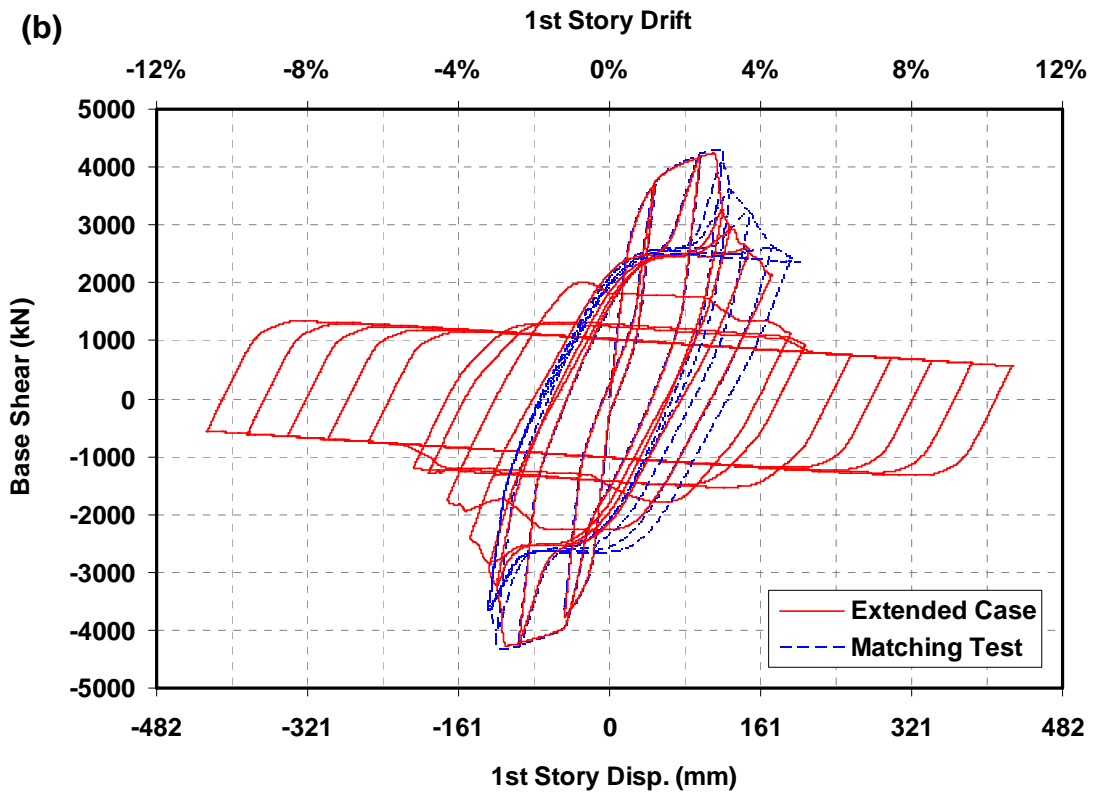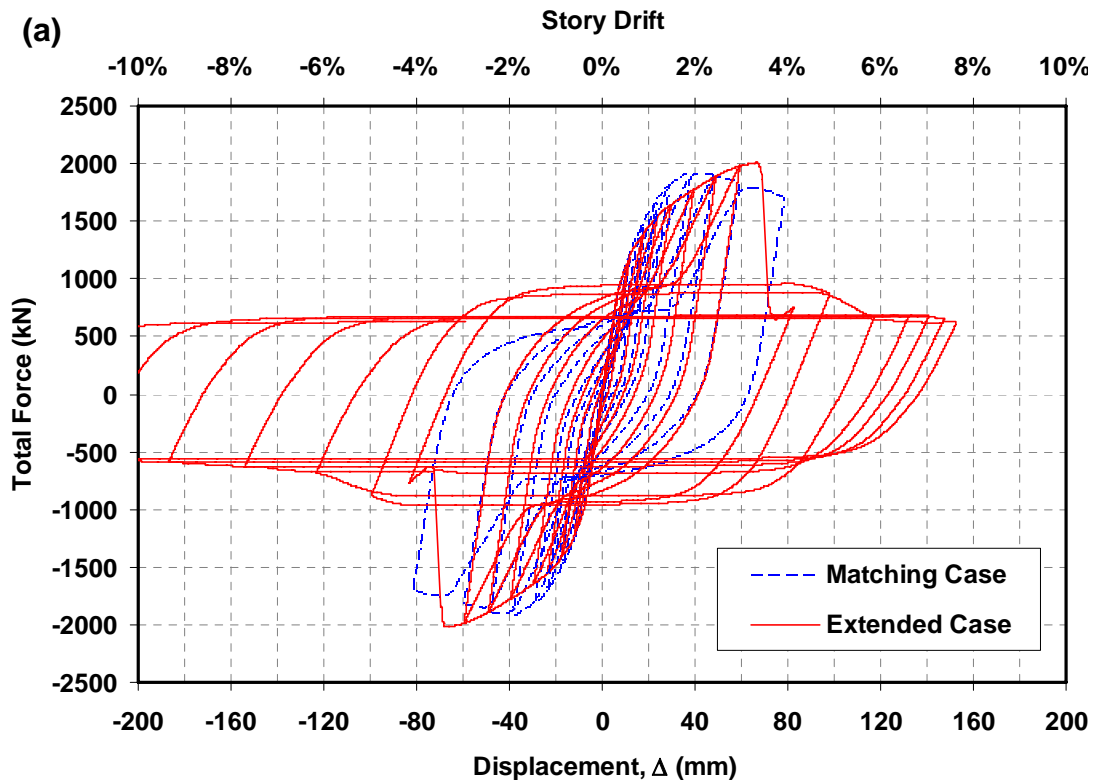
Figure 6-32 SPSW Specimen Hysteresis with Final Degradation Models: (a) Vian and Bruneau (2005); (b) Qu and Bruneau (2008)

(c)
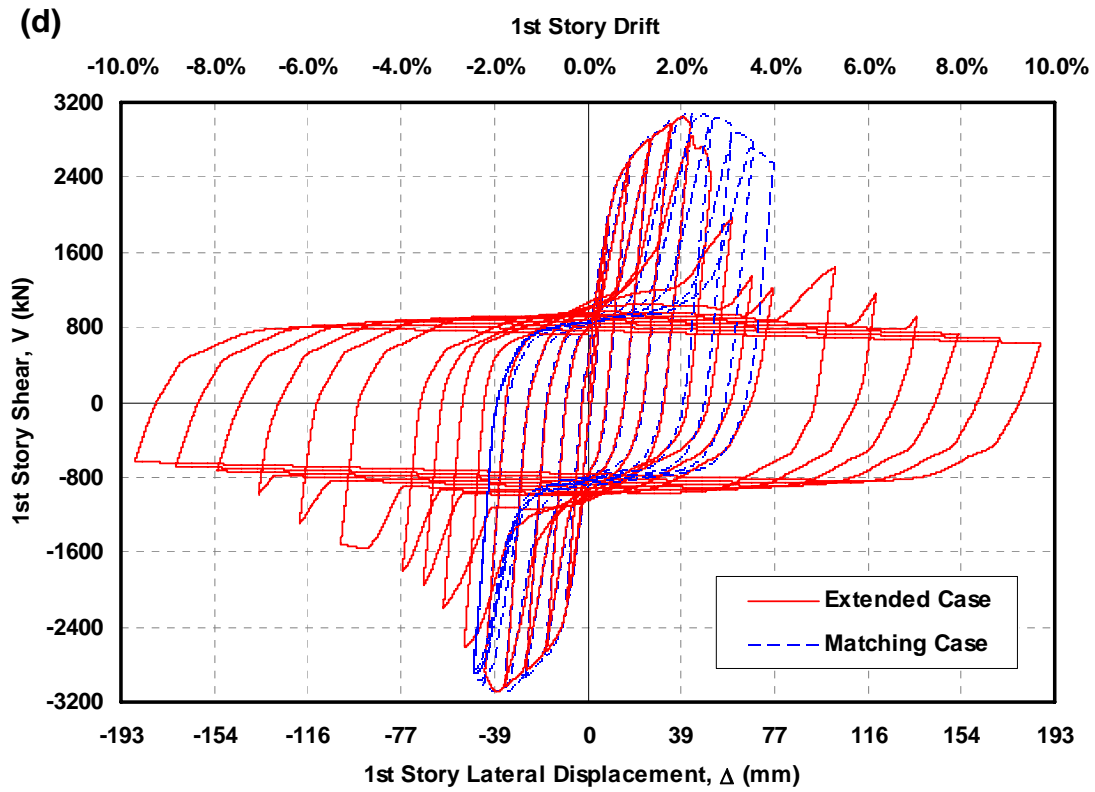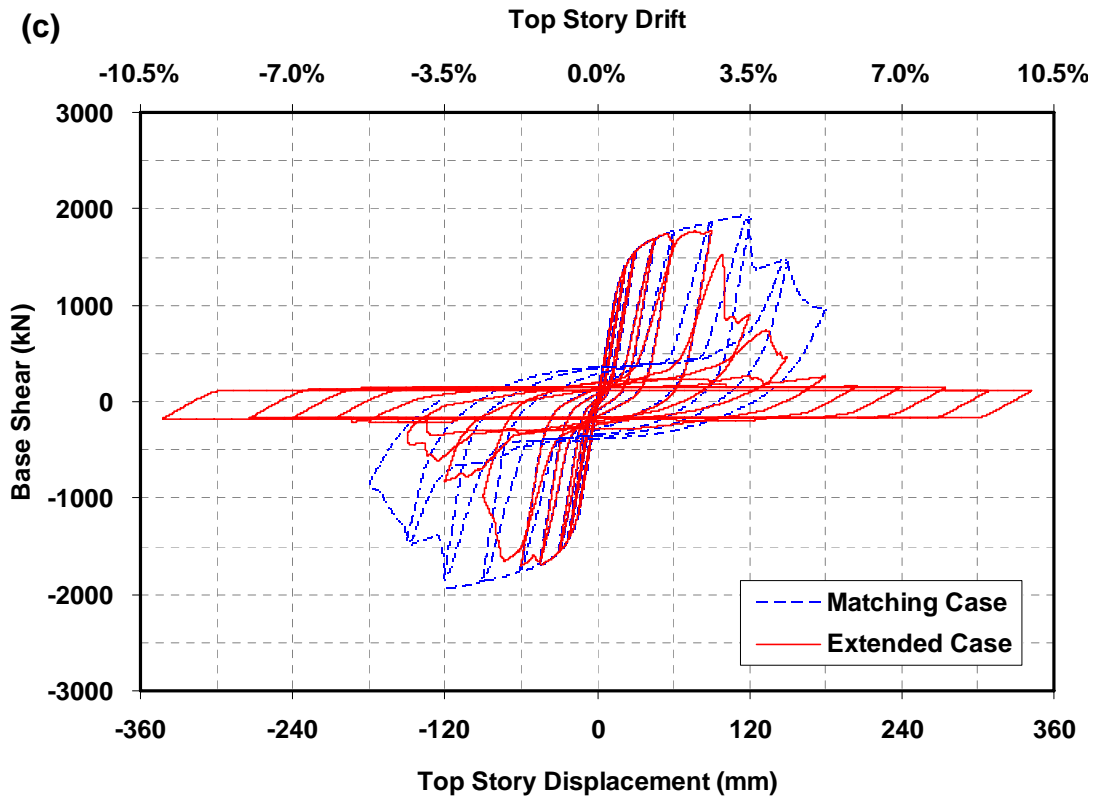
Figure 6-32 SPSW Specimen Hysteresis with Final Degradation Models – Cont'd:
(c) Choi and Park (2009); (d) Driver *et al*. (1997)

elements in OpenSees framework was investigated. Unstiffened infill plates were modeled as series of *Truss Elements* oriented in the direction of the tension field. Boundary elements were modeled using the *Beam with Concentrated Hinge Element* (BCH) elements with fiber sections. The *Hysteretic Uniaxial Material* model was selected to define the inelastic behavior of these truss and BCH elements. To obtain a specified degradation of moment capacity in one cross-section, when plastic hinges are modeled using a fiber element, fiber stress-strain relationship need to be modified to account the effect of variation of stress level along the depth of the hinge at a certain strain level.

A brief presentation of various case studies conducted to obtain satisfactory degradation models was addressed. The case studies included investigation of different deterioration behaviors for corner and middle strips based on sequence of infill plate fractures observed in past experiments (i.e., severe and moderate strength degradations for corner and middle strips, respectively), and with strength degradation only occurring in a few SPSW components (i.e., elasto-plastic material for infill plates and degradation material model for boundary elements, and vice versa).

Lastly, final deterioration models for infill plates and boundary elements were proposed. The deterioration model for boundary elements were characterized with strain hardening of 2%, reaching the capping point at 0.04 radians, and gradually losing their entire strength at 0.10 radians. This deterioration material model however was only applied to fibers at the bottom and top flanges, while those on the webs were modeled with no degradation allowed to maintain numerical stability during the analysis when boundary elements sustained axial forces. As for the infill plates, strips were modeled to start to deteriorate at 1.5% axial strain (i.e., $9.0\delta_y$) and lost their capacity to sustain loads due to plate tearing rather quick at 1.8% axial strain (i.e., $10.7\delta_y$). All strips were set to have the same deterioration model irrespective of the location of strips (i.e., corner or middle strips) and the same for every floor. Using these deterioration models, global structural models and results of collapse assessment will be developed and presented respectively in the two subsequent sections.

SECTION 7

DEVELOPMENT OF ARCHETYPES AND NONLINEAR MODELS FOR COLLAPSE ASSESSMENT OF STEEL PLATE SHEAR WALLS

7.1 General

The methodology described in the FEMA P695 document for collapse assessment of a proposed seismic-force resisting system requires the consideration a series of system archetypes. FEMA P695 defines an archetype as "a prototypical representation of a seismic-force-resisting system configuration that embodies key features and behaviors related to collapse performance when the system is subjected to earthquake ground motions." This section describes the development of archetypes for collapse assessment of steel plate shear walls (SPSW). These collapse assessments will be conducted (in Section 8) for two types of SPSWs having infill plates designed to sustain different levels of lateral loads. In the first group of SPSWs, infill plates are designed to resist the entire lateral loads, without considering the possible contribution from surrounding boundary frame moment resisting capacities, whereas in the second group of SPSWs, infill plates are designed to resist a portion of lateral loads and the boundary frame resists the remaining portion of the lateral loads.

Prior to presenting the archetype development for those two types of SPSWs, some issues related to the behavior of SPSW considering boundary frame moment resisting action are presented, first by reviewing research results by Qu and Bruneau (2009) and, second, through a limited case study. Based on observed behaviors in this case study, considerations for selecting a "balanced" distribution of lateral loads to design the infill plates and boundary frame of the second group of SPSWs are presented, followed by an outline of the range of design parameters considered for the archetypes specifically developed for this research. The capacity design approach used to design SPSW-CD in Purba and Bruneau (2010) is applied to design all of the archetypes. Subsequently, member sections for each archetype are presented. Toward the end of this section, nonlinear models used for collapse assessment of SPSWs are presented.

305

7.2 Behavior of Steel Plate Shear Walls Considering Boundary Frame Moment Resisting Action

In the current Canadian Standard (i.e., CSA 2009) for the design of steel structures, it is specified that infill plates of SPSW must be designed to resist the entire lateral loads, without considering the possible contribution from the surrounding boundary moment resisting frame. Such a statement is not explicitly included in the American Seismic Provisions (i.e., AISC 2010b); one of possible interpretations of the design specifications could lead to the same design approach. In this approach, horizontal and vertical boundary elements (HBEs and VBEs) are designed to resist the tension field forces generated by the fully yielded infill plates, and the resulting boundary frame moment resisting action contributes to the global plastic lateral strength of SPSW by adding overstrength (i.e., lateral load resistance above the specified story-shear force).

As reported in past experiments, this overstrength in conventional SPSWs can be quite significant. For example, Driver *et al*. (1997) reported that boundary frame moment resisting action contributed about 25% of the global plastic strength of their four-story SPSW specimen. The same observation was also made by Berman and Bruneau (2005), who indicated that the boundary frame of their single story SPSW specimen contributed 38% to the total strength of the wall. Qu and Bruneau (2009) demonstrated that boundary frame moment resisting action can contribute up to 50% of the total strength of a SPSW with aspect ratio of 2.0 when its boundary elements are designed per the capacity design principles described in Purba and Bruneau (2010). In such a case, the total lateral strength of the SPSW is twice that needed to resist the total specified lateral loads.

While the SPSW design procedures have been developed, verified, and validated for buildings having a few stories, SPSWs have been implemented in a number of high-rise buildings. Examples of SPSW implementations in high-rise buildings can be found in Bruneau *et al*. (2011). In a recent application, SPSWs were used as the main lateral load resisting system for a 56 story building in Los Angeles (AISC 2008). In such large structures, there is a particularly significant incentive to reduce overstrength by explicitly considering boundary frame moment resisting action as contributing to the SPSW overall lateral strength (even though this incentive exists to some degree in all SPSW designs).

7.2.1 Review of Balanced SPSW Design Concept by Qu and Bruneau (2009)

Qu and Bruneau (2009) proposed a procedure to consider and quantify the contribution of boundary frame moment resisting action in the design of SPSWs. As illustrated in Figure 7-1 for the case of multiple-story SPSWs, a percentage of the total design story shear forces $\kappa_i F_{Di}$ is assigned to the infill plates (Figure 7-1b) while the remaining design story shear forces $(1-\kappa_i)F_{Di}$ are resisted by the boundary frame (Figure 7-1c). In addition to resisting its portion of the design story shear forces in Figure 7-1c, the boundary elements must have sufficient strength to resist the tension forces generated by yielded infill plates in Figure 7-1b. The required infill plate thickness to resist these reduced story shear forces can be estimated using the standard AISC equation. Here, a κ_i factor equal to 1 means 100% of the design story shear forces at the i-th story are resisted by the infill plate without considering the possible contribution from the surrounding boundary frame to resist a percentage of the specified lateral loads.
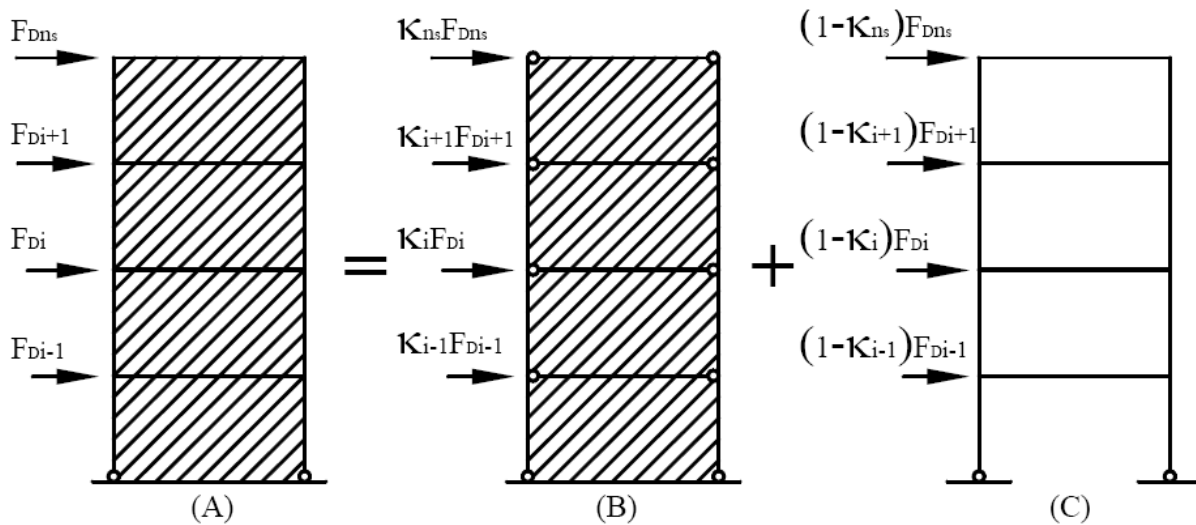
Figure 7-1 SPSW Design Considering Boundary Frame Moment Resistance (Qu and Bruneau 2009)

To select an optimum value of κ factor, it is important to estimate first how much overstrength is available in a given SPSW. For a uniform sway plastic mechanism developing in a SPSW, Qu and Bruneau (2009) derived the following relationship for overstrength of a SPSW at the i-th story.

$$\Omega_{\kappa i} = \frac{F_{pi}}{F_{Di}} = \kappa_i \left[1 + \frac{1}{2} \tan^{-1}(\alpha_i) \left(\frac{L}{h_i} \right) \right] \tag{7-1}$$

where Ω_κ is the overstrength, defined as the ratio of panel plastic strength, F_p, and design story shear force, F_D; κ is the percentage of the total design story shear forces assigned to the infill plate; α is the tension field inclination angle; L and h are the width and height of the panel, respectively. Note that all parameters correspond to the properties at the i-th story. Figure 7-2 shows a plot of this overstrength equation as a function of κ for different values of a SPSW panel aspect ratio (L/h). Results in this figure were plotted for an assumed tension field inclination angle of 45°.
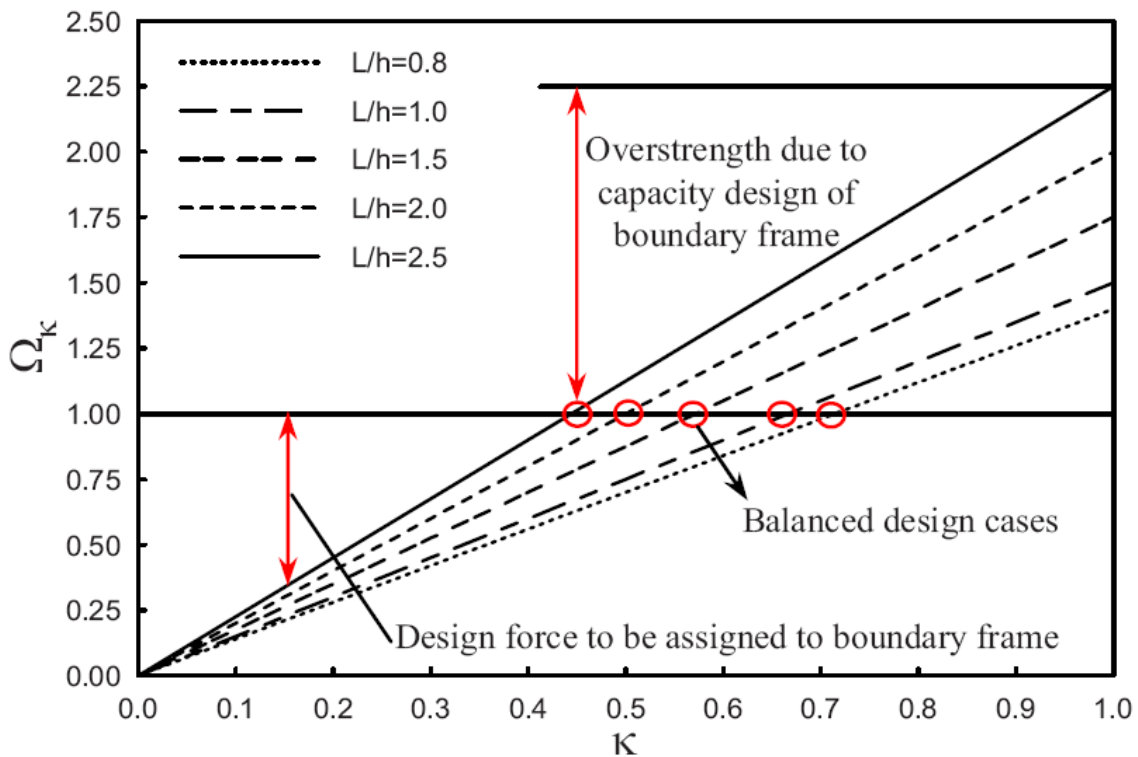
Figure 7-2 Relationship between Ω_κ and κ for Various Aspect Ratios (Qu and Bruneau 2009)

Based on the information presented in this figure, there are three possible SPSW design cases, as far as overstrength of the structural system is concerned, namely:

1. SPSWs having overstrength as a consequence of the lateral load resistance provided by boundary frame moment resisting action ($\Omega_\kappa > 1.0$). The case of SPSW-CD, described in Purba and Bruneau (2010), is an example of SPSWs in this category. SPSW-CD had an

308

aspect ratio *L/h* of 2.0 and that it was designed such that 100% of the specified story shear forces were resisted by the infill plates ($\kappa = 1.0$). Based on (7-1), or reading from the chart in Figure 7-2, SPSW-CD had an overstrength factor of 2.0. In other words, SPSW-CD can sustain lateral loads up to twice the design lateral loads.

2. SPSWs optimized to effectively eliminate overstrength such that the sum of the strength of boundary frame and infill plates is exactly equal to the required strength to resist the designed lateral loads. This optimum design was defined as the "balanced" design case by Qu and Bruneau (2009). In Figure 7-2, these design outcomes are shown by circular markers. For this balanced design case, overstrength equals unity ($\Omega_\kappa = 1.0$) and the percentage of shear forces resisted by the infill plate, $\kappa_{balanced}$, can be estimated as follows:

$$\kappa_{balanced\_i} = \left[1 + \frac{1}{2}\tan^{-1}(\alpha_i)\left(\frac{L}{h_i}\right)\right]^{-1} \qquad (7\text{-}2)$$

If redesigning SPSW-CD to become a balanced design case, 50% of the design story shear forces would be assigned to the infill plates, and the remaining 50% of the story shear forces would be resisted by the boundary frame. As a result of this design approach, boundary elements would be smaller than those used for SPSW-CD.

3. SPSW with weak infill plates. Qu and Bruneau (2009) defined this undesirable third design category ($\kappa < \kappa_{balanced}$, $\Omega_\kappa < 1.0$) as the case when the selected infill plate thickness is smaller than that in the corresponding balanced design case. If redesigning SPSW-CD to have weak infill plates, a percentage lower than 50% of design story shear forces would be assigned to the infill plates, and the remaining story shear forces would be resisted by the boundary frame. In other words, the boundary frame resulting from capacity design principles alone (i.e., designed only to resist forces from yielded infill plates) would have to be strengthened to provide sufficient strength to resist the design story shear forces.

As an introduction to the work ahead, it was deemed useful to examine the behavior of SPSWs that would correspond to each of the above three categories through a case study. Understanding better these behaviors prior to developing general archetypes for the purpose of quantifying seismic performance factors (SPF) for SPSWs was intended to provide guidance as to the percentage of lateral forces distributed to infill plates and boundary frame that should be selected

in the design of archetypes, and to investigate whether SPSWs designed considering boundary frame moment resistance (i.e., either with an arbitrary distribution of shear forces between infill plates and boundary frame, with the balanced case, or with the weak infill cases) would behave comparably to typical conventional SPSWs reported in Section 6. The following sub-sections present the details and results of this case study.

7.2.2 Description of Case Study

Using the three-story SPSW-CD described in Purba and Bruneau (2010) as a benchmark (Case 01), four other similar size SPSWs were designed but with different distribution of shear forces, namely: (a) Case 02: 75% of the specified story shear forces resisted by infill plates while 25% resisted by boundary frame; (b) Case 03: balanced design case ($\kappa = \kappa_{balanced}$); (c) Case 04: weak infill plate design with 37% and 63% of the specified story shear forces resisted by infill plates and boundary frame, respectively; and (d) Case 05: another weak infill plate design with 25% of the specified story shear forces resisted by infill plates and 75% resisted by boundary frame (which, incidentally, is the reversed shear force distribution of the one in Case 02). It should be emphasized for the balanced case (Case 03) that, to be exact, the panel at each story would have a different $\kappa_{balanced}$ factor, according to (7-2), depending on the tension field inclination angle of one particular story. However, considering that variation of this angle from one story to another story would be marginal, for practical reason, the same $\kappa_{balanced}$ value was selected for all stories, calculated using the average of tension field inclination angle of all panels (i.e., $\alpha_{average}$).

The resulting sizes of HBEs, VBEs, and infill plate thickness are summarized in Table 7-1 for all four design cases and the benchmark SPSW. In addition, the demand-to-capacity ratio for each element is displayed in parenthesis below the resulting section shape. Two sets of boundary frames are considered for the last two cases of SPSW having weak infill plates, namely results for the un-strengthened ('weak') and strengthened conditions. The strengthened case is obtained by increasing the strength of the boundary frame to match the strength required to resist the specified story shear (which happens to also be equivalent to the strength corresponding to the balanced condition) and was designed using the Method I described in Qu and Bruneau (2009), with the exception that different size HBEs were selected at each floor. In this Method I, the required

Table 7-1 Design Summary of SPSW Components for Case Study on the Behavior of SPSW Considering Boundary Frame Moment Resisting Action

SPSW Components	Case 01[a] (100%:0%)	Case 02 (75%:25%)	Case 03 (49%:51%)[b]	Case 04 (37%:63%)		Case 05 (25%:75%)	
				Weak	Strengthened	Weak	Strengthened
HBE-3	W18×76 (0.99)	W18×60 (0.99)	W18×40 (0.99)	W14×38 (0.97)	W16×67 (0.98)	W12×30 (0.94)	W18×60 (0.98)
HBE-2	W14×61 (0.99)	W18×40 (0.95)	W12×35 (0.98)	W12×26 (0.97)	W18×46 (0.99)	W10×22 (0.96)	W12×79 (0.99)
HBE-1	W12×45 (0.95)	W12×35 (0.98)	W10×26 (0.95)	W12×19 (0.96)	W18×60 (0.98)	W10×15 (0.91)	W24×62 (0.96)
HBE-0	W24×117 (0.98)	W27×84 (0.99)	W21×68 (0.98)	W18×60 (0.96)	W18×60 (0.94)	W16×45 (0.97)	W16×45 (0.94)
VBE-3	W16×89 (0.98)	W18×65 (0.98)	W14×53 (0.94)	W12×45 (0.99)	W14×82 (0.98)	W10×39 (0.95)	W21×57 (0.99)
VBE-2	W18×76 (0.99)	W18×60 (0.98)	W18×40 (0.98)	W12×40 (0.96)	W18×65 (0.97)	W10×30 (0.95)	W21×62 (0.96)
VBE-1	W24×146 (0.96)	W27×102 (0.99)	W24×76 (0.96)	W21×62 (0.98)	W21×68 (0.98)	W16×50 (0.99)	W21×62 (0.96)
t_{w3} (in)	0.036	0.027	0.018	0.013		0.009	
t_{w2} (in)	0.059	0.044	0.029	0.021		0.015	
t_{w1} (in)	0.072	0.054	0.035	0.026		0.018	

Note: [a] SPSW-CD as a benchmark (Purba and Bruneau 2010)
  [b] Balanced condition: $\kappa_{balanced} = 0.49$, $L/h = 2.0$, $\alpha_{average} = 44°$

plastic modulus of the HBE at each floor was determined by equating the external and internal work for the boundary frame by considering a sway collapse mechanism for the sub-frame from i-th story to the top story. Note that all SPSWs were designed using the same R factor of 7.0, even though it remains to be verified by the research whether this factor is applicable for SPSWs designed to consider boundary frame moment resistance. This topic will be addressed in the next section.

A monotonic pushover analysis was conducted on each SPSW until each structure reached a 5% lateral drift. In addition, a cyclic pushover analysis up to 3% drift was conducted on selected cases (i.e., Cases 03 and 04). For these analyses, strip model and load distribution along the height of the structure were similar to those described in Purba and Bruneau (2010) for SPSW-CD. The analyses for this case study were conducted in SAP2000 considering elasto-perfectly plastic material models for both infill plates and boundary elements. Note that the case study analyses presented here were conducted before the deterioration models presented in Section 6 (using OpenSees) were developed.

7.2.3 Case Study Results and Discussions

The resulting pushover curves for all five SPSWs considered are shown in Figure 7-3 and the overstrengths obtained from these SAP2000 analyses are compared to the theoretical overstrength calculation per (7-1) in Figure 7-4. As expected, base shear strength and overstrength decreased as the κ factor reduced as a consequence of thinner infill plates and smaller boundary element sizes selected for cases with κ factor smaller than 1.0. For example, in the 100% case ($\kappa = 1$, SPSW-CD benchmark design), the resulting base shear at 5% story drift is 477 kips, while for κ factors equal to 0.75 and 0.49 (i.e., $\kappa_{balanced}$), the base shears at the same 5% story drift are 359 and 234 kips, respectively.

Interestingly, the base shear strength of 234 kips for the balanced design case is actually larger than the design base shear of 176 kips. At first glance, this seemed to contradict the theoretical definition of the balanced design case for which there is supposed to be no overstrength ($\Omega_\kappa = 1.0$) in the structural system. However, this discrepancy is logical and is actually an artifact of an overstrength inherent to the design equation specified in the current AISC 2010 to calculate
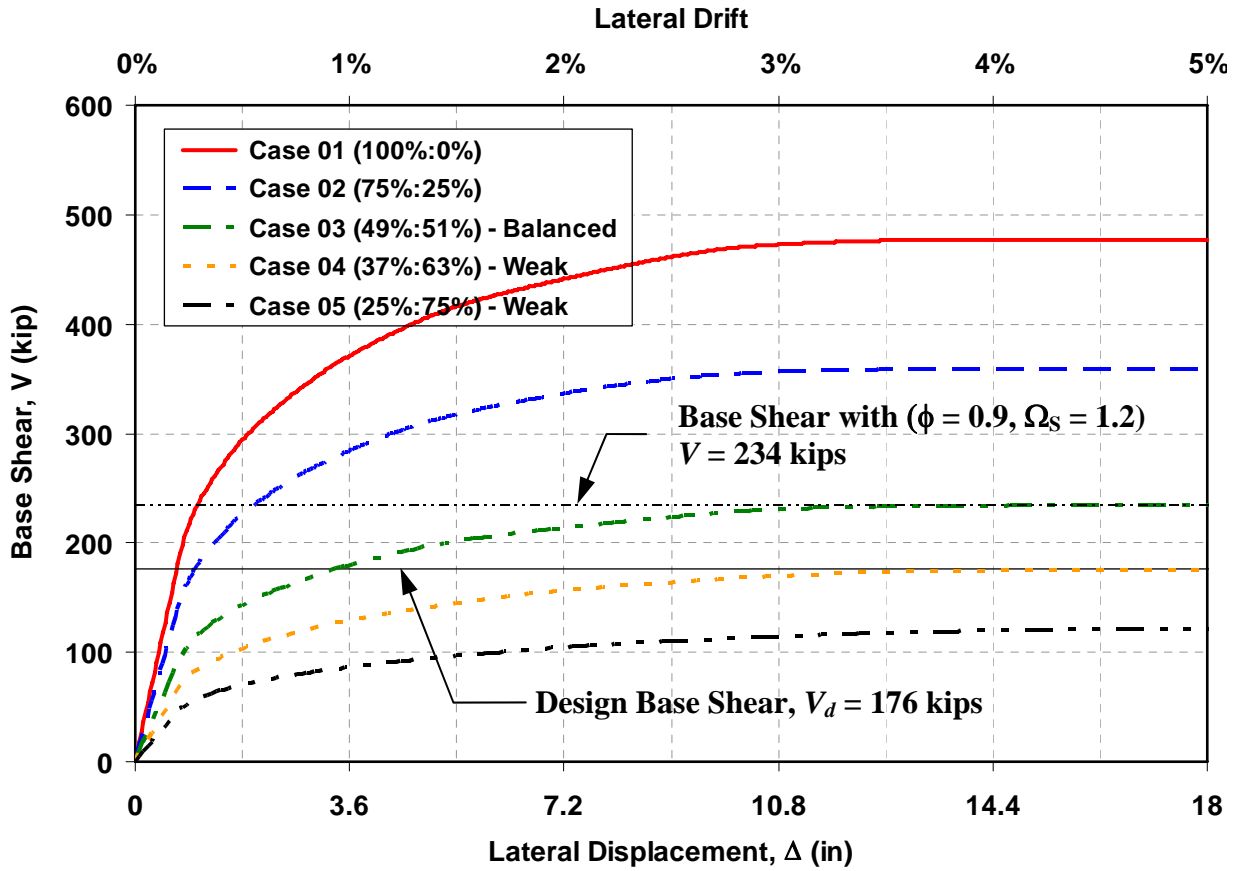
Figure 7-3 Monotonic Pushover Curves for Five Design Cases
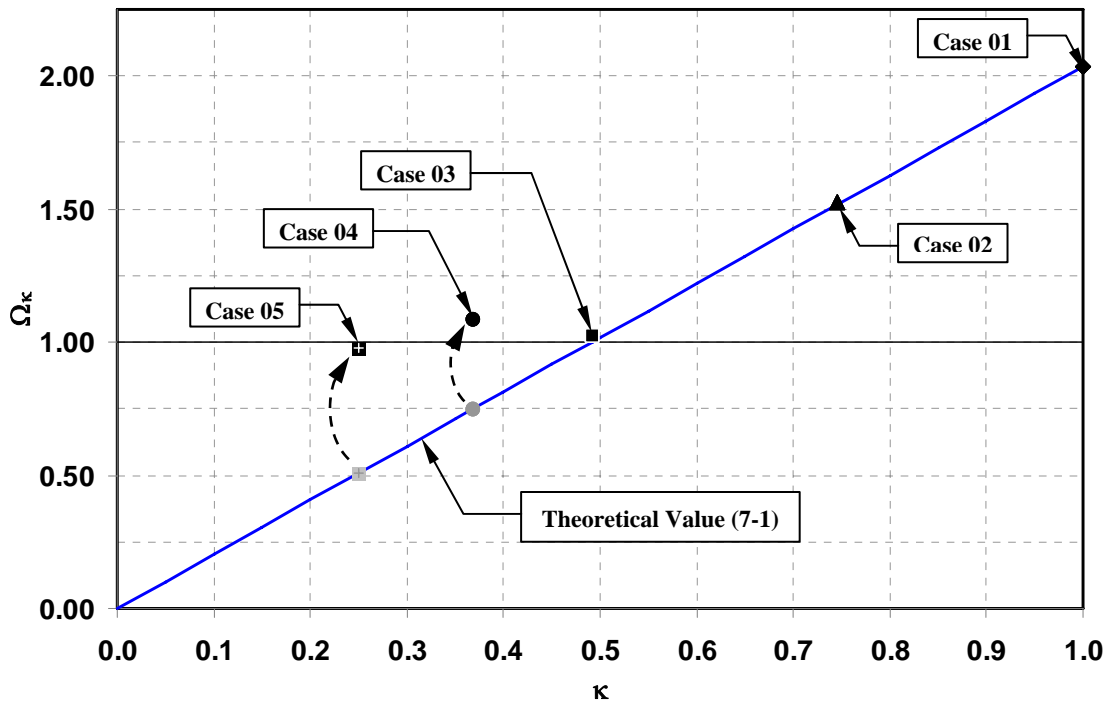
Figure 7-4 Theoretical Overstrength versus Overstrength observed in SAP2000 Model

plastic strength of infill plates. In accordance with Eq. (F5-1) of the 2010 AISC Seismic Provisions, an implicit system overstrength Ω_s of 1.2 is embedded in the design equation, to which adds up the strength resistance/reduction factor ϕ of 0.9 considered in sizing the thickness of infill plates. The two factors combine to provide an inherent overstrength of 1.33. This value is equal to ratio between the SAP2000 results for the balanced design case (Case 03) and the theoretical design base shear. Therefore, here, the base shear strength of 234 kips (with its inherent overstrength per code equations) is considered as the balanced design case. Case 04 (i.e., 37% of design base shear resisted by infill plate) was originally selected to correspond to the case for which this inherent overstrength was excluded. As shown in Figure 7-3, the SAP2000 results for this case show ultimate strength that matches the theoretical design base shear. By comparison, the SPSW in Case 04 has ultimate strength of less than 234 kips (which is less than the value required by code), and therefore is considered as having a weak infill plate.

For the monotonic pushover curves, each curve plotted in Figure 7-3 exhibits somewhat the same pattern. When all curves are normalized by their corresponding ultimate strengths (not shown here), the elastic part of the curves are on top of one another and the transition part from the elastic to perfectly plastic conditions exhibits somewhat the same "curvature". However, once the boundary frames of weak infill cases were strengthened, their pushover curves were slightly different, as shown in Figure 7-5 (i.e., Cases 04 and 05 strengthened). In addition to changes in the original stiffness, changes in the shapes of the pushover curves after the yield point (and thus possibly the sequence of yielding) were observed in the pushover curves of strengthened cases, up to the ultimate strength.

To investigate this behavior, additional monotonic pushover analyses were conducted for the 100% case, the balanced design case, and the 37% strengthened case, except that the structures were separated in "parts" to be able to plot the individual pushover curves corresponding to infill plates and boundary frames separately. For this purpose, numerical models similar to those in Figures 7-1b and 7-1c were developed for all three cases to obtain pushover curve of infill plates and boundary frames (i.e., using bare frame model), respectively. Results are presented in Figure 7-6, superposed with the previous obtained pushover curves for the full walls. Key results are described as follows:
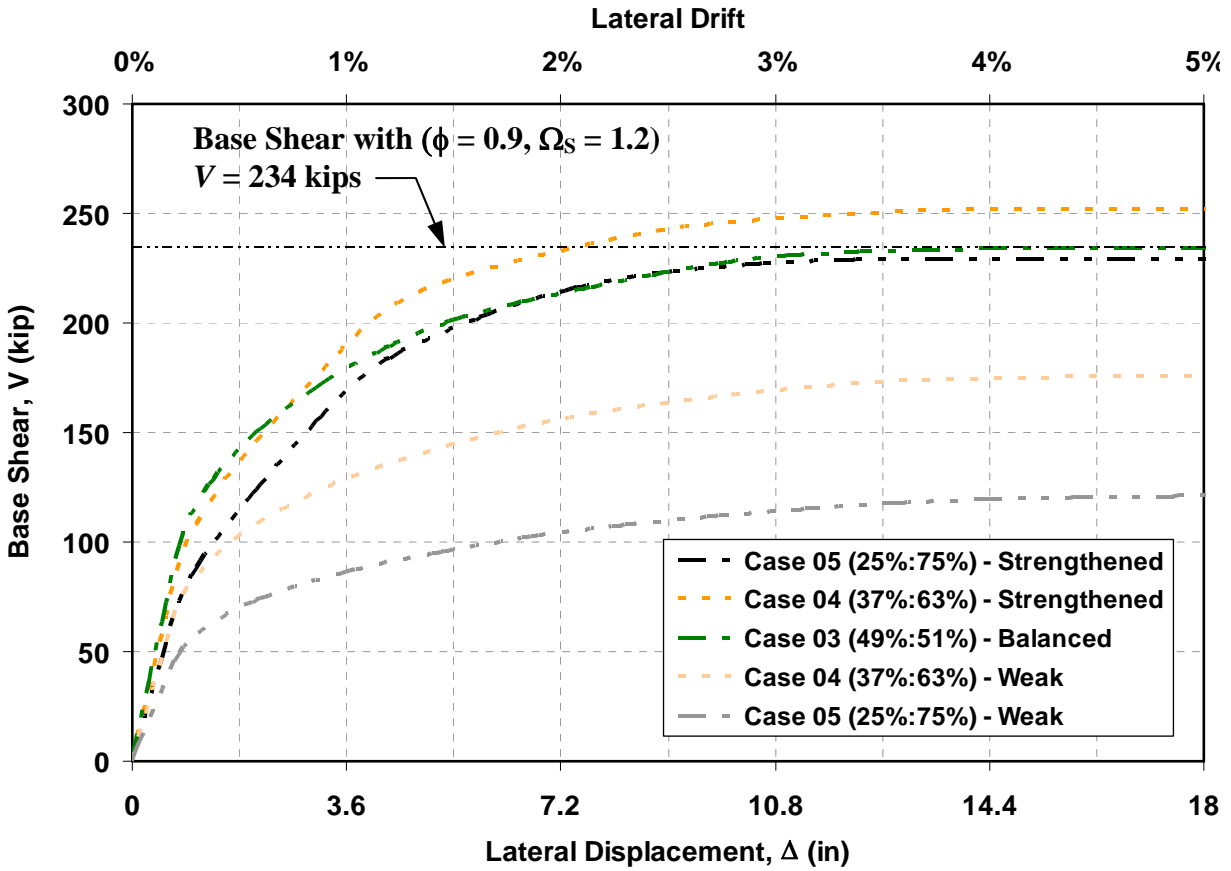
Figure 7-5 Monotonic Pushover Curves for Balanced and Weak Cases

1. For both the 100% and balanced design cases (Figures 7-6a and 7-6b), respective contributions of infill plate and boundary frame to the overall SPSW strengths were somewhat the same. For the 100% case, its infill plates and boundary frame contributed 52 and 48% to the overall strength, respectively, while for the balanced case, the respective contributions were 51 and 49%.

2. As a consequence of strengthening the boundary frame in Case 04 (Figure 7-6c), contribution of the boundary frame to the overall strength became significantly larger compared to that of the infill plates (i.e., 64% versus 36%).

3. Infill plates contributed significantly more to the elastic stiffness of SPSWs in both Cases 01 and 03, compared to Case 04 where infill plates and boundary elements contributed equally to SPSW elastic stiffness.

4. Infill plates in the first two cases started to yield at approximately 0.5% top story drift and reached complete yielding at 1.5% top story drift. By contrast, infill plates in Case 04

315
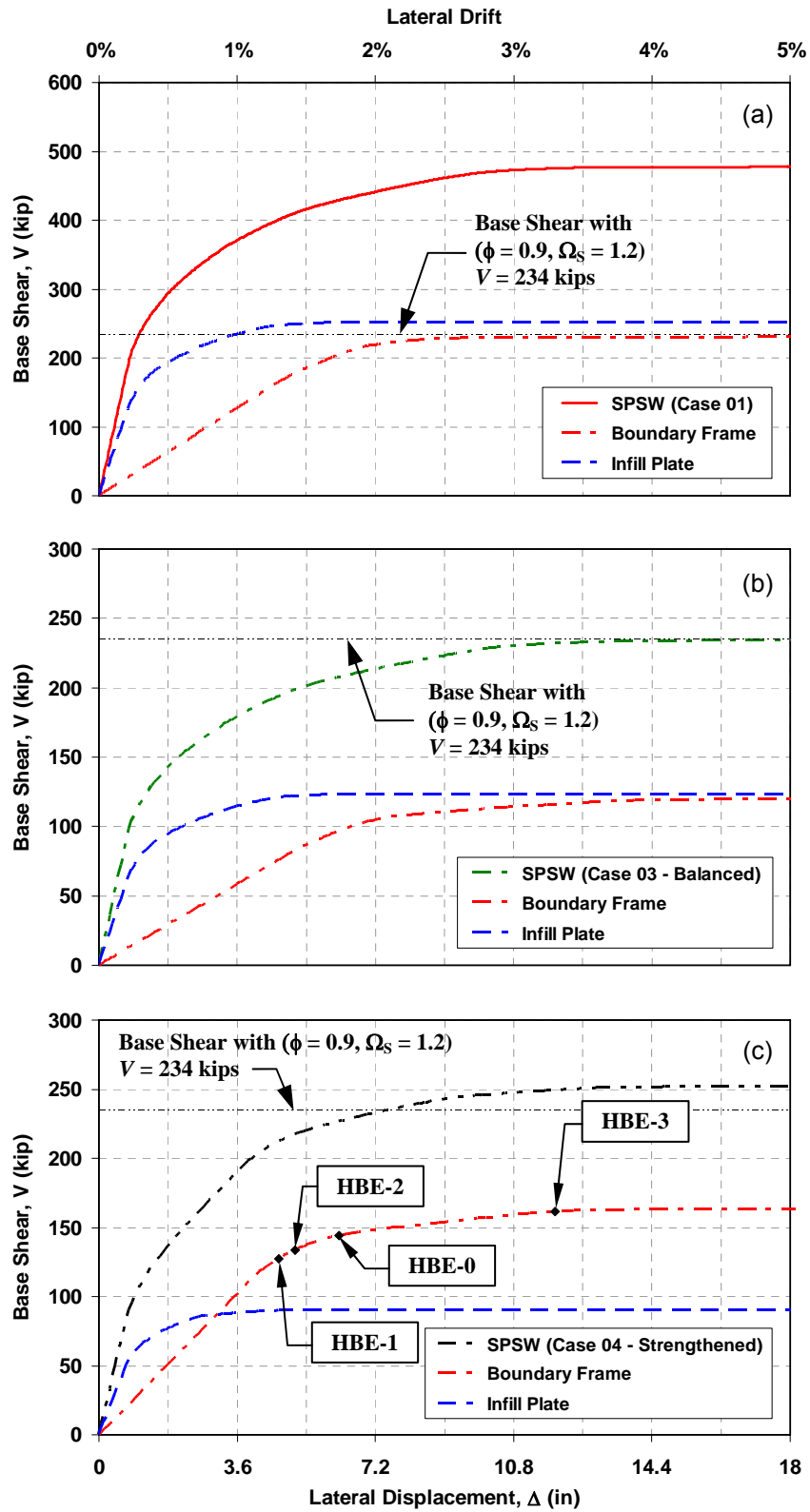
Figure 7-6 Monotonic Pushover Curves for SPSW Components: (a) Case 01 ($\kappa = 1.0$); (b) Case 03 ($\kappa = \kappa_{balanced} = 0.49$); (c) Case 04 Strengthened ($\kappa = 0.37$)

started to yield at approximately 0.25% top story drift and reached complete yielding at 0.75% top story drift. In all cases, complete yielding of infill plates occurred before plastification of boundary frame took place.

5. For Case 04, first HBE plastification occurred at 1.3% drift on HBE1 and the last plastic hinged developed on HBE3 at 3.2% drift. Hence, the slight kinks observed in the pushover curve of Case 04 correspond to the first yielding of infill plate, the first plastification of boundary frame, and the last plastification of boundary frame.

Several aspects of the pushover curves for SPSW components plotted in Figure 7-6 require further explanation. First, a slight discrepancy between the theoretical infill plate strength and SAP2000 results was observed in Case 01 (i.e., 234 versus 251 kips). This was found to be a consequence of a slight difference in strip width calculation for the strip model. In this case, the calculation of strip width was based on bay width (i.e., $S_{diag} = (L \cos \alpha + H \sin \alpha)/$ number of strips) while the theoretical calculation of infill plate strength [Eq. (F5-1) of the 2010 AISC Seismic Provisions] was based on clear width (L_p). Changing the clear width to bay width in the theoretical calculation resolved this discrepancy. The impact was marginal for the balanced design case (Case 03) because clear width and bay width were somewhat the same as a result of smaller sizes of VBEs compared to that in the 100% case. Second, the overall strength of the 37% strengthened case (Figure 7-6c) was slightly above the design base shear. This was found to be a consequence of the fact that the W-sections selected for the boundary elements have a strength that slightly exceeded the required strength (as a consequence of available W sizes). Incidentally, a reverse condition occurred for the 25% strengthened case (Case 05 in Figure 7-5), where the W-section selected for boundary elements resulted in a slightly lower SPSW overall strength compared to the design base shear. Third, the observed contribution of infill plates and boundary frame to SPSW overall strengths in Case 01 and Case 03 (i.e., each approximately contributing 50%) is only valid for SPSWs having an aspect ratio L/h of 2.0. Other SPSWs with different aspect ratios would have different proportions of infill plate and boundary frame resistance. This was verified in another SPSW (designed with $\kappa = 1.0$) with an aspect ratio of 1.0 (results not reported here). In that case, contributions of infill plate and boundary frame were 65% and 35%, respectively.

To further compare behavior of the SPSW with balanced design case and SPSW with weak infill plates to the benchmark SPSW-CD, cyclic pushover analysis was conducted to obtain hysteretic behavior and moment-rotation relationship at HBE ends. Figure 7-7 compares the resulting hysteretic behaviors for the balanced design and 37% strengthened cases. The balanced case hysteretic has a pinching behavior similar to the regular SPSW while the strengthened case exhibits significantly less pinching (i.e. an hysteretic behavior closer to that of moment resisting frames).
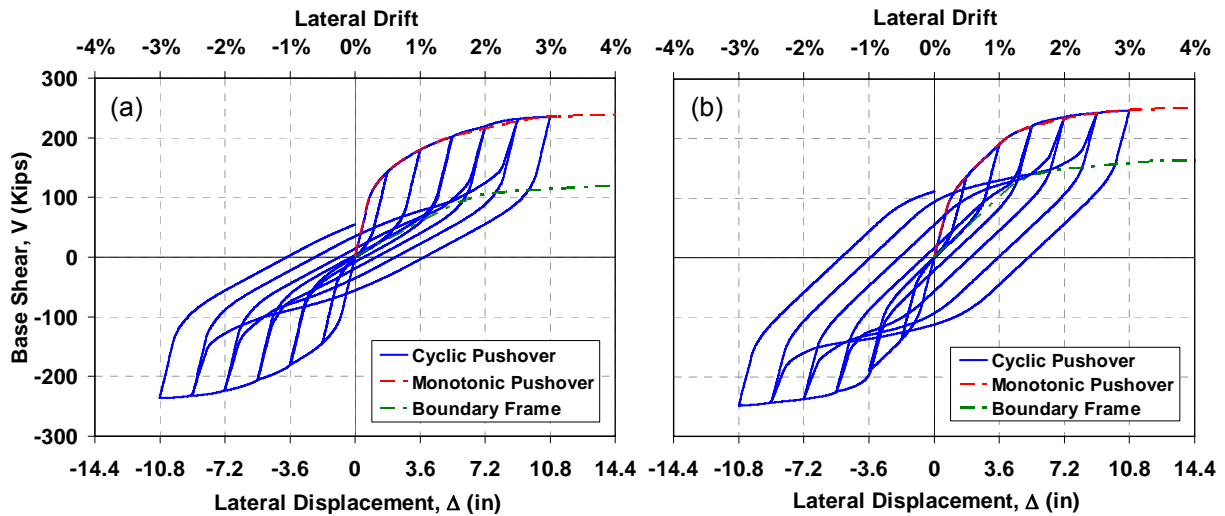
Figure 7-7 Cyclic Pushover Results: (a) Balanced Design Case; (b) 37% Strengthened Case

The same observation can be seen in the moment-rotation hysteresis, as shown in Figure 7-8. Showing results for HBE2 as a representative case, it is observed that the moment hysteretic curves for the balanced design case are biased toward one direction as previously observed in the moment-rotation relationship of SPSW-CD (Purba and Bruneau 2010), while that in the strengthened case is less biased, and closer (but not identical) to the symmetric hysteretic curve typically obtained for special moment resisting frames. These above observations are consistent with the fact that boundary frame plays a more significant role in SPSWs that fall below the balanced point (i.e., $\kappa < \kappa_{balanced}$), since the boundary frame in those cases must be strengthened beyond what is required to satisfy capacity design purposes, therefore increasing the moment resisting frame contribution to total behavior (the system effectively becoming a pure moment resisting frame for the case $\kappa = 0$). However, it must be recognized that this discussion is somewhat academic, since cases for which $\kappa < \kappa_{balanced}$ are not permissible.

318
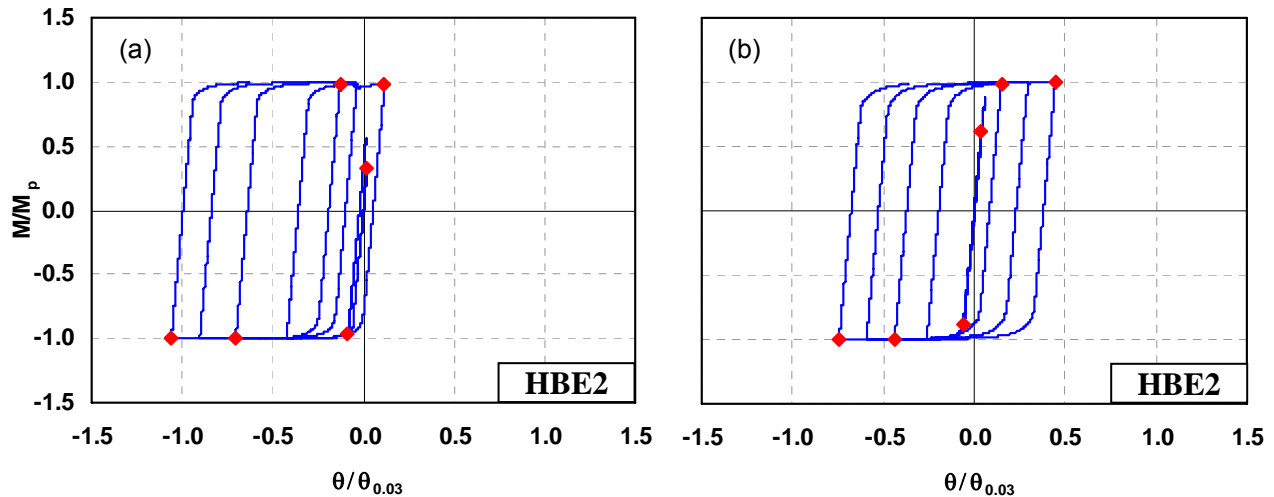
Figure 7-8 Moment-Rotation Hysteresis for HBE2 Left Joint: (a) Balanced Design Case; (b) 37% Strengthened Case

Table 7-2 summarizes total weight of steel required for each SPSW. As expected, the balanced design is the most optimum in terms of total weight of steel. The two strengthened cases required more steel than the balanced case for the same capacity.

Table 7-2 Comparison of Steel Weight of Five Design Cases

SPSW Compo-nents	Case 01 (100:0%)	Case 02 (75:25%)	Case 03 (49:51%)	Case 04 (37:63%)		Case 05 (25:75%)	
				Weak	Strength-ened	Weak	Strength-ened
HBE	5980	4380	3380	2860	4660	2240	4920
VBE	3110	2270	1690	1470	2150	1190	1810
Infill Plate	1369	1023	667	496	496	338	338
Total	**10459**	**7673**	**5737**	**4826**	**7306**	**3768**	**7068**

Unit: weight in pounds

Having established that cases $\kappa < \kappa_{balanced}$ are not cost-effective and behave differently than other conventional SPSWs, it was decided to develop SPSW archetypes for the collapse assessment investigations by considering the following two cases: the 100% case ($\kappa = 1.0$) and the balanced design case ($\kappa = \kappa_{balanced}$). Once seismic performance factors are established for these two cases,

319

the corresponding performance factors for SPSWs in between these two cases (i.e., $\kappa_{balanced} < \kappa < 1.0$) could be interpolated if so desired. Development of SPSW archetypes for the collapse assessment is discussed in the following section.

7.3 Development of Steel Plate Shear Walls Archetypes

7.3.1 Scope of SPSW Archetype Configurations

Archetypes are intended to represent a general configuration of a proposed seismic-force resisting system. They should encompass possible combinations of design parameters permitted by building codes and represent conditions in construction practice (FEMA P695). Several design parameters that are typically considered in developing archetypes include (but not limited to) functionality of buildings, minimum level of gravity and seismic loads, range of structure geometric properties (i.e., bay width, story height, and number of stories), to name a few. The following design parameters were considered here in the development of archetypes for steel plate shear walls.

1. **Type of Steel Plate Shear Walls.** Archetypes developed in this research represent configuration of conventional SPSWs defined previously in Section 6. Though several of conventional SPSWs in that section included SPSWs with simple HBE-to-VBE connections, archetypes developed in this research for collapse assessment were designed to have moment resisting HBE-to-VBE connections.

2. **Building Functionality.** In past applications, SPSWs have been designed as the main seismic-force resisting system for various buildings having different functionalities (e.g., residential, hospital, office, hotel, etc). In this research, archetypes were considered as part of typical office buildings. For convenience, their loading information, floor plans, and elevations were arbitrarily taken as similar to the SAC model building described in the FEMA 355-C document.

3. **Elevation and Plan Configuration.** Each SPSW archetype was designed to have building height representative of low- to mid-rise SPSWs (between 3 to 10 stories), one bay width, and aspect ratio varying from 1.0 to 2.0. Elevation and plan configuration were also taken as similar to the SAC model building described in the FEMA 355-C document. All archetypes have a typical story height of 13 ft with various bay widths depending on

320

the aspect ratio of one particular archetype. Note that a three-story SPSW was selected as the shortest archetype of interest here to allow observation of the behavior of top and bottom anchor HBEs as well as of intermediate HBE. To avoid unnecessary overstrength, the required infill plate thickness to sustain story shear forces were assumed available, and vary along the height of the building as a function of story shear force demands.

4. **Boundary Frame Moment Resisting Action.** SPSW archetypes are designed either for the case where the infill plates can resist alone 100% of the specified seismic load without considering boundary frame moment resistance (i.e., $\kappa = 1.0$) or for the balanced design case (i.e., $\kappa = \kappa_{balanced}$). Both design approaches use the capacity design principle outlined in the AISC 2010 Seismic Provisions to design HBEs and VBEs.

5. **HBE Plastic Hinges Location.** Archetypes are explicitly designed to avoid development of in-span hinges. This can be achieved by following the design procedure addressed in Purba and Bruneau (2010).

6. **Seismic Tributary Weight.** Two levels of seismic tributary weight are considered, namely low and high seismic weight. Number of SPSWs in one building is determined as a function of seismic weight. For a specified design seismic load, fewer numbers of SPSWs present in a building corresponds to high seismic tributary weight for each SPSW, and vice versa.

7. **Seismic Design Category.** Except for the 3-story SPSW archetypes (for reasons explained in Section 7.3.2), all archetypes are sized based on the Design Basis Earthquake (DBE) response spectra specified in the FEMA P695 document for high seismicity (i.e., SDC D_{max}), as shown in Figure 7-9.

7.3.2 Matrix of SPSW Archetypes

From a limited literature review conducted on the basic configuration of constructed SPSWs (Bruneau *et al.* 2011), it was found that low-rise SPSWs are more likely to have low aspect ratios (while recognizing that SPSWs having any aspect ratios can be, and have been, used for any given building height). This aspect ratio would gradually increase for taller SPSWs. The gray shaded cells in Table 7-3 are intended to reflect this trend, relating likely wall aspect ratio to number of stories. Here, it was decided to design SPSW archetypes with story aspect ratios
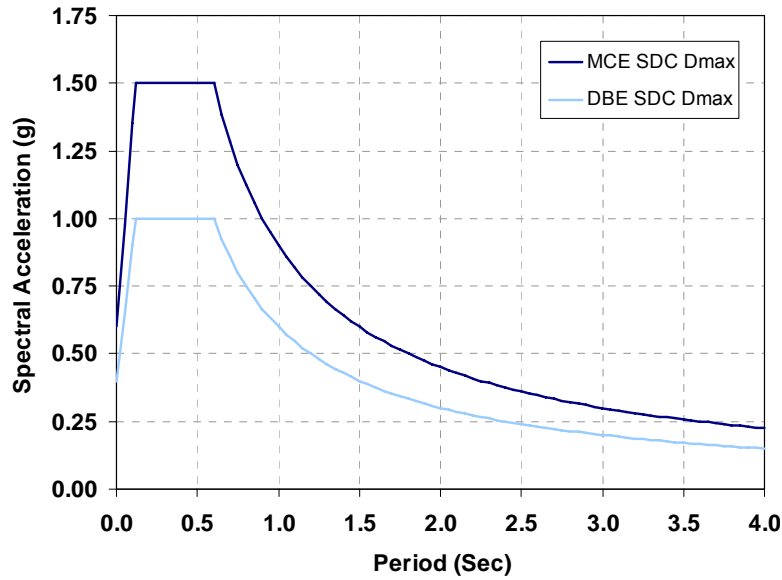
Figure 7-9 DBE and MCE Response Spectra for Collapse Assessment of SPSW Archetypes

Table 7-3 Basic Configuration of SPSW Archetypes

Basic Configuration		Number of Stories								
Type	Aspect Ratio[1]	3	5	7	10	14	17	20	25	30
Low Aspect Ratio	0.75	▨								
	1.0	✓	▨							
Moderate Aspect Ratio	1.5		▨	▨	▨					
	2.0	✓	✓	▨	✓	▨	▨	▨		
High Aspect Ratio	2.5			▨	▨	▨	▨	▨	▨	
	3.0						▨	▨	▨	▨

Note:

▨ = Possible configuration of low- to mid-rise SPSWs

✓ = Selected SPSW Archetypes

[1] Aspect ratio is defined as the ratio between the panel width and height (*L/H*)

322

similar to actual SPSWs; these archetypes are shown by the "check marked" entries in Table 7-3. This includes 3-story SPSW archetypes with aspect ratios of 1.0, 5- and 10-story SPSW archetypes with aspect ratio of 2.0. In addition, even though SPSW-CD (i.e., 3-story wall with aspect ratio of 2.0) falls outside the gray shaded zone, it was decided to include it as one of the archetypes for collapse assessment of SPSW because many important behaviors of SPSWs have been studied in the previous sections using this SPSW-CD. Considering here further extends its usefulness as a benchmark against which the behavior of other archetypes studied here can be compared (i.e., providing a reference point to benchmark level of tributary seismic weight, 100% design case vs. balanced design case, and different values of *R* factor used in designs). Structure description and the design of this 3-story SPSW was presented in Purba and Bruneau (2010).

Table 7-4 shows the matrix of SPSW archetypes used here to quantify seismic performance factors for SPSWs. Archetypes are divided in two basic configurations, namely: 100% case ($\kappa = 1.0$) and balanced case design ($\kappa = \kappa_{balanced}$). Each basic configuration considers two levels of panel aspect ratios (i.e., low and moderate aspect ratios). Archetypes can be categorized as part of short or long period domain, and low or high tributary seismic mass. Note that the FEMA P695 procedure defined short- and long-period archetypes on the basis of the transition period T_s, which is the boundary between the region of constant acceleration and constant velocity of the design response spectrum. For SDC D_{max}, T_s equals to 0.6 seconds (Figure 7-9). The fundamental period of archetype *T* was estimated as follows:

$$T = C_u \times 0.02 h_n^{0.75} \geq 0.25 \text{ seconds} \tag{7-3}$$

where the value of the coefficient C_u equals to 1.4 in high seismic regions for $S_{D1} \geq 0.4$ (ASCE 7-10, Table 12-8.1); and h_n is the building height in feet. In addition, archetypes designed with high tributary seismic mass sustained half of the story seismic mass while that designed with low tributary seismic mass sustained one-sixth of the story seismic mass.

One should note that total number of archetypes developed here is less than what is specified for a complete application of the FEMA P695 procedure (i.e., 48 archetypes would be required for two assumed basic structural configurations, high and low tributary seismic masses, two seismic design levels (e.g., SDC D_{max} and D_{min}), two period domains (short and long periods), and three archetypes for each performance group). In this research however, it was decided to investigate

selected archetypes that represent critical SPSW configurations. Hence, a total of 14 archetypes were prepared and their design outcomes are presented in the following sub-section.

Table 7-4 Matrix of Archetype Configurations for SPSW Collapse Assessment

Archetype ID[1]	Basic Configuration	Panel Aspect Ratio[2]	No. of Stories	Period Domain[3]	Tributary Seismic Mass[4]
SW310	**100% Story Shear Forces Resisted by Infill Plate** $(\kappa = 1.0)$	Low	3	Short	Low
SW320		Moderate	3	Short	Low
SW320G		Moderate	3	Short	High
SW520		Moderate	5	Long	Low
SW520G		Moderate	5	Long	High
SW1020		Moderate	10	Long	Low
SW310K	**Balanced Design Case** $(\kappa = \kappa_{balanced})$	Low	3	Short	Low
SW320K		Moderate	3	Short	Low
SW320GK		Moderate	3	Short	High
SW520K		Moderate	5	Long	Low
SW520GK		Moderate	5	Long	High
SW1020K		Moderate	10	Long	Low
SW320KR6		Moderate	3	Short	Low
SW320KR5		Moderate	3	Short	Low

Note: [1] ID Convention follows the following example
        SW320GKR6 = **S**teel **W**alls | **3** story Archetype | Aspect Ratio **2.0** | High Tributary Seismic Mass (High **G**ravity Loads on Leaning Column) | Design with $\kappa_{balanced}$ | Design with **R** factor of **6** instead of 7
[2] Low: $0.75 \leq AR \leq 1.0$; Moderate: $1.0 < AR \leq 2.0$; High: $2.0 < AR \leq 3.0$
[3] Short Period: $T < 0.6$ sec; Long Period: $T \geq 0.6$ sec.
[4] Low tributary: seismic weight equals $1/6$ of total weight.
   High tributary: seismic weight equals ½ of total weight.

7.3.3 Design of Steel Plate Shear Walls Archetypes

Story seismic weight for each archetype is shown in Table 7-5. Story seismic weight for archetypes with shorter than or equal to 65 ft (i.e., ≤ 5 story building) were chosen to match the seismic weight of the 3-story SAC model building while archetypes higher than 5-story buildings

Table 7-5 Story Weight and Design Base Shear of SPSW Archetypes

Archetype	Level	W_{SPSW} (kips)	$W_{P-\Delta}$ (kips)	W_{total} (kips)	V_d (kips)
SW310, SW310K	Roof	63.42	317.41	380.83	154.84
	Lower	58.61	292.99	351.60	
SW320, SW320K	Roof	126.94	253.89	380.83	175.87
	Lower	117.20	234.40	351.60	
SW320KR6	Roof	126.94	253.89	380.83	205.18
	Lower	117.20	234.40	351.60	
SW320KR5	Roof	126.94	253.89	380.83	246.22
	Lower	117.20	234.40	351.60	
SW320G, SW320GK	Roof	126.94	1014.55	1141.49	464.51
	Lower	117.20	937.83	1055.03	
SW520, SW520K	Roof	126.94	253.89	380.83	255.32
	Lower	117.20	234.40	351.60	
SW520G, SW520GK	Roof	126.94	1014.55	1141.49	765.95
	Lower	117.20	937.83	1055.03	
SW1020, SW1020K	Roof	136.00	256.30	392.30	680.88
	Lower	126.25	237.93	364.18	

Note:
W_{SPSW} = Gravity Loads on SPSW
$W_{P-\Delta}$ = Gravity Loads on P-Δ Leaning Column
W_{total} = Total Seismic Weight for Base Shear Calculation (= $W_{SPSW} + W_{P-\Delta}$)
V_{total} = Design Base Shear

matched the seismic weight of the 9-story SAC model building. Calculation of design base shear and distribution of story forces along the height of the building followed the procedure presented in the ASCE 7-10 document. The resulting design base shear for each archetype is shown in Table 7-5. In selecting the VBE and HBE sections, the same optimum design objective considered when designing SPSW-CD was followed (i.e., achieving a demand-to-capacity ratio close to 1.0, without exceeding it). The resulting sizes of VBEs, HBEs, and infill plate are summarized in Tables 7-6 to 7-8 for 3-, 5-, and 10-story archetypes, respectively. In addition,

Table 7-6 Design Summary of 3-Story SPSW Archetypes for Collapse Assessment

SPSW Components	100% Design Case ($\kappa = 1.0$)			Balanced Design Case ($\kappa = \kappa_{balanced}$)[1]		
	SW310	SW320[a]	SW320G	SW310K	SW320K[b]	SW320GK
HBE-3	W14×53 (1.0[c])	W18×76 (0.99)	W27×146 (0.96)	W12×40 (0.95)	W18×40 (0.99)	W21×93 (0.96)
HBE-2	W12×45 (0.99)	W14×61 (0.99)	W14×159 (0.96)	W10×33 (0.95)	W12×35 (0.98)	W18×71 (0.97)
HBE-1	W16×31 (0.98)	W12×45 (0.95)	W18×97 (0.97)	W12×22 (0.94)	W10×26 (0.95)	W14×48 (1.0)
HBE-0	W18×86 (0.94)	W24×117 (0.98)	W24×306 (0.97)	W18×55 (0.96)	W21×68 (0.98)	W21×166 (0.98)
VBE-3	W18×50 (0.96)	W16×89 (0.98)	W27×161 (0.98)	W16×36 (0.98)	W14×53 (0.94)	W14×132 (0.99)
VBE-2	W18×71 (0.98)	W18×76 (0.99)	W27×178 (0.95)	W16×45 (0.96)	W18×40 (0.98)	W21×93 (0.96)
VBE-1	W21×122 (1.0)	W24×146 (0.96)	W36×300 (1.0)	W18×86 (0.96)	W24×76 (0.96)	W21×201 (0.97)
t_{w3} (in)	0.071	0.036	0.101	0.044	0.018	0.047
t_{w2} (in)	0.115	0.059	0.163	0.071	0.029	0.078
t_{w1} (in)	0.141	0.072	0.203	0.087	0.035	0.094

Note: [a] Previously presented as SPSW-CD (Purba and Bruneau 2010) and Case 01 (benchmark) in Table 7-1
   [b] Previously presented as Case 03 in Table 7-1
   [c] Value in parenthesis is demand-to-capacity ratio
   [1] Balanced condition: $\kappa_{balanced} = 0.63$, $L/h = 1.0$, $\alpha_{average} = 41°$ (SW310K)
      $\kappa_{balanced} = 0.49$, $L/h = 2.0$, $\alpha_{average} = 44°$ (SW320K, SW320GK)

Table 7-7 Design Summary of 5-Story SPSW Archetypes for Collapse Assessment

SPSW Components	100% Design Case ($\kappa = 1.0$)		Balanced Design Case ($\kappa = \kappa_{balanced}$)[1]	
	SW520	SW520G	SW520K	SW520GK
HBE5	W18×97 (1.0[a])	W24×229 (0.96)	W16×57 (0.97)	W18×143 (0.98)
HBE4	W21×68 (0.97)	W24×176 (0.99)	W14×48 (0.96)	W27×84 (0.96)
HBE3	W14×74 (0.99)	W21×166 (0.99)	W14×38 (0.95)	W21×83 (0.98)
HBE2	W12×58 (1.0)	W27×114 (1.0)	W14×30 (0.97)	W24×62 (0.98)
HBE1	W12×45 (0.99)	W24×84 (0.98)	W10×22 (0.91)	W18×46 (1.0)
HBE0	W36×160 (1.0)	W40×431 (1.0)	W30×90 (0.96)	W36×232 (0.99)
VBE5	W21×93 (1.0)	W24×250 (0.96)	W18×55 (0.98)	W27×114 (1.0)
VBE4	W21×111 (0.98)	W30×261 (0.98)	W18×65 (1.0)	W27×146 (0.94)
VBE3	W27×84 (0.97)	W36×232 (0.96)	W21×50 (0.95)	W30×124 (0.97)
VBE2	W27×161 (0.97)	W40×397 (0.99)	W27×84 (0.96)	W33×201 (1.0)
VBE1	W33×221 (0.98)	W40×593 (1.0)	W27×129 (0.98)	W33×318 (0.99)
t_{w5} (in)	0.027	0.084	0.013	0.041
t_{w4} (in)	0.048	0.149	0.023	0.071
t_{w3} (in)	0.064	0.200	0.031	0.094
t_{w2} (in)	0.075	0.235	0.036	0.111
t_{w1} (in)	0.082	0.254	0.039	0.119

Note: [1] Balanced condition: $\kappa_{balanced} = 0.49$, $L/h = 2.0$, $\alpha_{average} = 44°$ (SW520K)

$\kappa_{balanced} = 0.48$, $L/h = 2.0$, $\alpha_{average} = 43°$ (SW520GK)

[a] Value in parenthesis is demand-to-capacity ratio

design outcomes for 3-story SPSW archetypes designed with different *R* factors are presented in Table 7-9.

7.4 Nonlinear Models for Collapse Simulation

Figure 7-10 shows an example two-dimensional nonlinear model for collapse simulation of 3-story SPSW archetypes. It incorporates an axial hinge at every strip and concentrated fiber plastic hinges (each with 65 fibers across the cross-section) at the ends of VBEs and HBEs. Panel

Table 7-8 Design Summary of 10-Story SPSW Archetypes for Collapse Assessment:
(a) Vertical and Horizontal Boundary Elements

Boundary Frame	SW1020	SW1020K[1]
HBE10	**W24×131** (0.97[a])	**W21×73** (0.94)
HBE9	**W27×102** (0.98)	**W21×62** (0.95)
HBE8	**W27×102** (0.94)	**W21×55** (0.95)
HBE7	**W24×94** (1.0)	**W18×55** (1.0)
HBE6	**W27×84** (0.99)	**W18×50** (1.0)
HBE5	**W21×83** (1.0)	**W18×46** (0.92)
HBE4	**W21×73** (1.0)	**W18×46** (0.95)
HBE3	**W21×62** (1.0)	**W14×38** (0.92)
HBE2	**W21×55** (0.94)	**W16×26** (0.94)
HBE1	**W12×53** (0.96)	**W14×22** (1.0)
HBE0	**W36×439** (0.98)	**W30×235** (0.99)
VBE10	**W30×124** (0.97)	**W21×83** (0.92)
VBE9	**W30×191** (0.93	**W24×104** (0.99)
VBE8	**W33×221** (0.96)	**W24×131** (0.91)
VBE7	**W33×241** (0.97)	**W27×129** (0.92)
VBE6	**W36×230** (1.0)	**W30×116** (0.96)
VBE5	**W36×230** (0.95)	**W30×116** (0.96)
VBE4	**W36×328** (1.0)	**W36×160** (0.97)
VBE3	**W36×439** (1.0)	**W36×210** (1.0)
VBE2	**W36×650** (0.89)	**W36×280** (0.97)
VBE1	**W36×798** (0.84)	**W36×328** (0.98)

Note: [1] Balanced condition: $\kappa_{balanced} = 0.47$, $L/h = 2.0$, $\alpha_{average} = 42°$
[a] Value in parenthesis is demand-to-capacity ratio

Table 7-8 Design Summary of 10-Story SPSW Archetypes – Cont'd: (b) Infill Plates

Infill Plate	SW1020	SW1020K[1]
t_{w10} (in)	0.044	0.020
t_{w9} (in)	0.081	0.037
t_{w8} (in)	0.114	0.052
t_{w7} (in)	0.142	0.065
t_{w6} (in)	0.166	0.077
t_{w5} (in)	0.185	0.085
t_{w4} (in)	0.201	0.094
t_{w3} (in)	0.213	0.100
t_{w2} (in)	0.221	0.103
t_{w1} (in)	0.226	0.104

Note: [1] Balanced condition: $\kappa_{balanced} = 0.47$, $L/h = 2.0$, $\alpha_{average} = 42°$

Table 7-9 Design Summary of 3-Story SPSW Archetypes Designed with Different *R* Factors

SPSW Components	SW320 ($R = 7.0$)	SW320KR5 ($R = 5.0$)	SW320KR6 ($R = 6.0$)	SW320K ($R = 7.0$)
HBE-3	W18×76 (0.99[a])	W14×68 (0.98)	W16×50 (1.0)	W18×40 (0.99)
HBE-2	W14×61 (0.99)	W14×43 (0.99)	W14×38 (0.97)	W12×35 (0.98)
HBE-1	W12×45 (0.95)	W14×30 (1.0)	W12×26 (0.97)	W10×26 (0.95)
HBE-0	W24×117 (0.98)	W24×84 (1.0)	W18×86 (1.0)	W21×68 (0.98)
VBE-3	W16×89 (0.98)	W18×60 (0.99)	W14×61 (0.94)	W14×53 (0.94)
VBE-2	W18×76 (0.99)	W18×55 (0.99)	W18×46 (0.99)	W18×40 (0.98)
VBE-1	W24×146 (0.96)	W27×94 (1.0)	W24×84 (1.0)	W24×76 (0.96)
t_{w3} (in)	0.036	0.025	0.021	0.018
t_{w2} (in)	0.059	0.041	0.034	0.029
t_{w1} (in)	0.072	0.050	0.042	0.035

Note: [a] Value in parenthesis is demand-to-capacity ratio
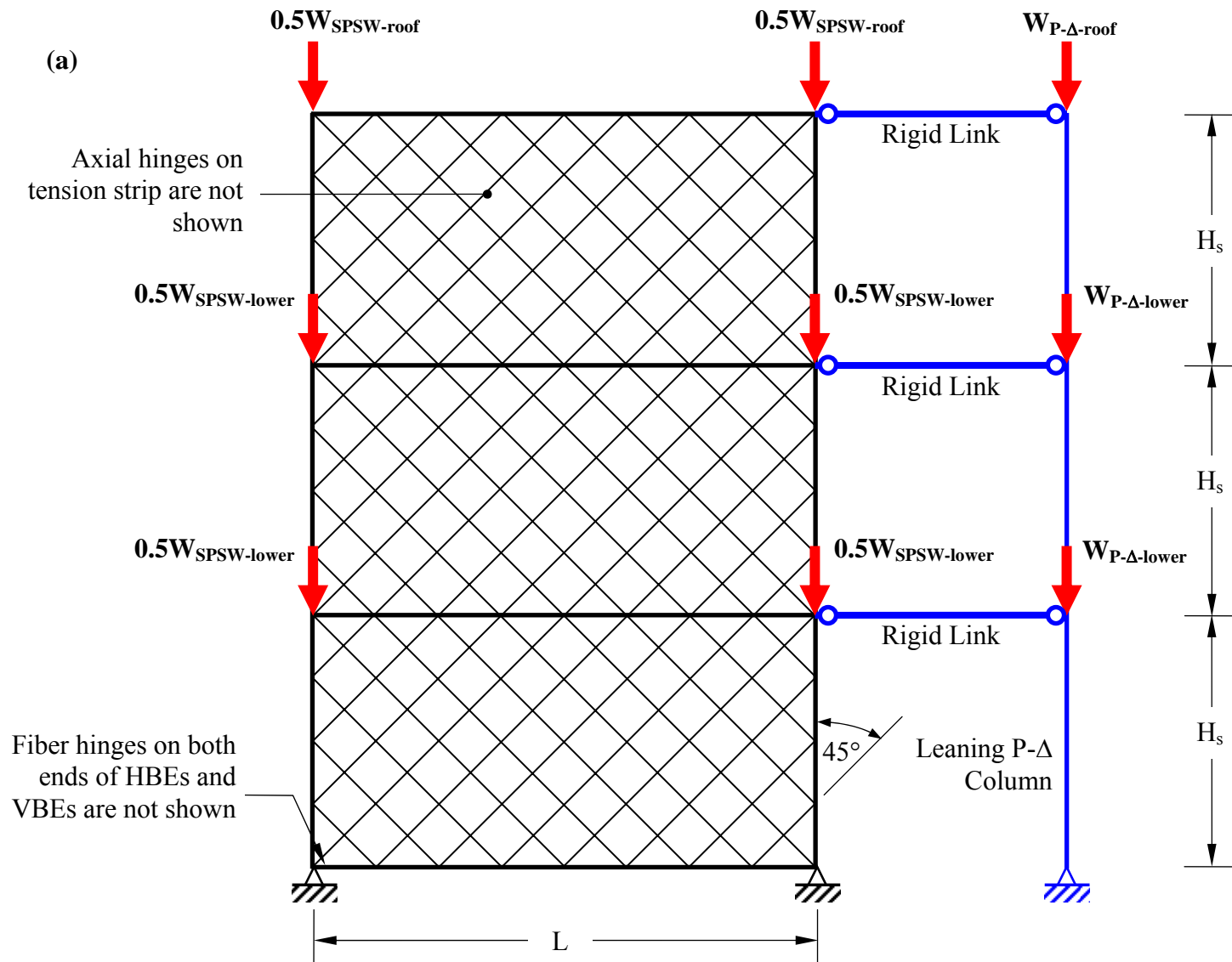
Figure 7-10 Nonlinear Model for Collapse Simulation: (a) Example Structural Model of 3-Story Archetype
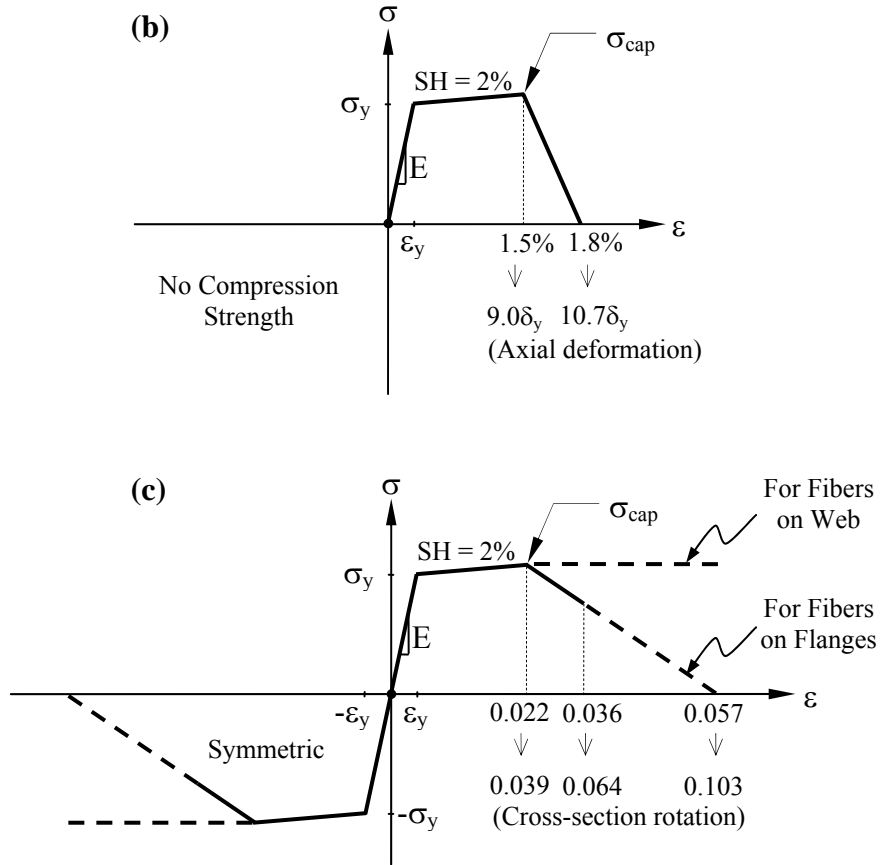
Figure 7-10 Nonlinear Model for Collapse Simulation – Cont'd: (b) Degradation Material Model for Strips; (c) Degradation Material Model for Boundary Elements

zones are not included in this model as their impacts on the global behavior of the model are insignificant. Deterioration material models for SPSW components (i.e., strips and boundary elements) have been presented in Section 6 and are re-plotted here for convenience in Figures 7-10b and 7-10c, respectively. All deterioration parameters have been defined in Section 6. The gravity leaning column elements are added to capture the P-Δ effects due to gravity loads that are not located on the SPSW. The values of gravity loads located on the SPSW and on the leaning column for each archetype are summarized in Table 7-5.

As addressed in Section 6, the nonlinear models were developed in the OpenSees framework. In this framework, there are at least two approaches to model leaning columns. First, a leaning column can be modeled using an *Elastic Beam-Column* (EBC) *Element* combined with a *Zero-length Element* (ZLE) at both ends of the column. Typically with this approach, moment of

inertia and cross section area of the EBC element are multiplied by the number of gravity columns present in the structure. However, since there is no definitive information on the number of gravity columns in the archetypes, their values are arbitrarily increased by 100 times their actual values to represent the aggregate effect of all the gravity columns. In addition, a significantly small flexural stiffness is assigned to the ZLE element to simulate moment release at both ends of the column. This approach was used in the degradation simulation of moment resisting frames performed by Eads (2012). Second, a leaning column can be modeled with only an EBC element with cross section area increased by 100 times the regular column cross section area, but with moment of inertia reduced to be 100 times smaller than the actual regular column moment of inertia. This approach basically defines an axially rigid leaning column with a significantly small flexural stiffness. It is comparable to the first approach but without the need to define ZLE elements at both ends of EBC element. This approach was used in the nonlinear analysis of self-centering SPSW conducted by Clayton *et al*. (2012) and was selected here to model the leaning column. Rigid links were used to connect the leaning column and SPSWs at every floor, and were modeled by using a *Truss Element* with cross section area arbitrarily increased to 100 times the HBE cross section at the corresponding floor. No seismic mass was applied on the leaning column; all of them were applied to the SPSWs and distributed equally to its left and right joints at every story.

7.5 Summary

Development and design of archetypes for the collapse assessment of steel plate shear walls was presented. Archetypes were categorized into two basic configurations. In the first group of archetypes, infill plates were designed to resist the entire lateral loads, without considering the possible contribution from the surrounding boundary moment-resisting frames. In the second group of archetypes, infill plates were designed to resist a portion of the lateral loads and the boundary frame resisted the remaining portion of the lateral loads. Review of previous research conducted by Qu and Bruneau (2009) was performed and a limited case study was conducted to develop an understanding of the behavior of archetypes in the second group, and to decide what percentage of lateral loads distributed between infill plates and boundary frame should be used in the design of these archetypes. The "balanced" distribution of lateral loads ($\kappa = \kappa_{balanced}$) was

selected for the design of the second group of archetypes because SPSWs designed per this approach exhibited similar behavior under monotonic and cyclic pushover analyses as the first group of archetypes designed per the AISC 2010 Seismic Provisions.

Archetypes developed were limited to low- and mid-rise SPSWs having low to high aspect ratio (i.e., 1.0 to 2.0). In-span hinges were explicitly prevented in HBEs of the archetypes. Low and high tributary seismic mass intensity were considered and all archetypes were designed to resist forces obtained from a design response spectra for high seismicity zone (i.e., SDC D_{max} of FEMA P695: $S_{DS} = 1.0g$ and $S_{D1} = 0.6g$). Archetype elevation and plan configuration were similar to the SAC model building. A total of 14 archetypes were considered.

Nonlinear models developed for collapse simulation featured a dual strip model with gravity leaning columns. The model incorporated an axial hinge at every strip, concentrated fiber plastic hinge at both ends of boundary elements, and material models that accommodated strength degradation. Added to capture the P-Δ effects of gravity loads that were not located on the SPSWs, the gravity leaning column was modeled in OpenSees using the *Elastic Beam-Column Element* with cross section area increased by 100 times the regular column cross section area, but with moment of inertia reduced to be 100 times smaller than the actual regular column moment of inertia. Rigid links modeled with the *Truss Element* (with cross section arbitrarily increased to 100 times the HBE cross section at the corresponding floor) were used to connect the leaning column and SPSW. No seismic mass was applied on the leaning column; all seismic masses were applied to the SPSW and distributed equally on the left and right of HBE-to-VBE joints at every story. Results of the collapse assessment analysis for each archetype are presented in the subsequent section.

SECTION 8

COLLAPSE ASSESSMENT OF STEEL PLATE SHEAR WALLS FOR QUANTIFICATION OF SEISMIC PERFORMANCE FACTORS

8.1 General

The two preceding sections addressed two key components required to perform collapse assessment of steel plate shear walls (SPSW). Using the strength degradation material model and nonlinear structural model developed in Sections 6 and 7, respectively, this section presents collapse assessment on SPSW archetypes designed in Section 7. The main objective of this assessment is to quantify seismic performance factors (SPF) for SPSWs. Specifically, it aims to quantify response modification coefficient (R factor), system overstrength factor (Ω_o factor), and deflection amplification factor (C_d factor) for two types of SPSWs with two different basic configurations. First, collapse assessment is conducted on SPSW archetypes designed neglecting the contribution of their boundary moment resisting frames to resist story shear forces. In other words, in those cases, infill plates are designed to resist the entire story shear forces (i.e., $\kappa = 1.0$). Collapse assessment is also conducted on a second group of SPSW archetypes designed considering the sharing of story shear forces between the boundary frames and infill plates, such that system overstrength is theoretically eliminated (i.e., $\kappa = \kappa_{balanced}$). SPFs for both types of SPSWs are identified and compared.

The methodology described in the FEMA P695 document is used for the above purpose. A brief summary of this methodology for quantification of SPF (e.g., step-by-step procedures, required nonlinear analyses, performance criteria, and other relevant assumptions) was reviewed in Section 2. One of the required nonlinear analyses specified in the methodology involves conducting incremental dynamic analysis (IDA) until global collapse of archetypes is obtained. Thus, the definition of collapse used in IDA is first presented in this section. Following this, the FEMA P695 methodology is explained in detail proceeding through examples of two 3-story SPSW archetypes that represent the two basic configurations (i.e., SPSW designed with $\kappa = 1.0$ and $\kappa = \kappa_{balanced}$). Results of nonlinear static (pushover) analysis and dynamic analysis (IDA),

collapse fragility curves, and collapse margin ratios between the two groups of archetypes are compared. Effect of different intensity measures, damage measures, and non-deteriorated material models on collapse margin ratios is addressed afterward. Building upon this understanding of collapse performance evaluation for the 3-story SPSW archetypes, collapse assessment on 10-story archetypes is then conducted. Local behaviors (e.g., infill plate yielding and plastic hinge distributions, cross section rotations, and interstory drifts) of the 3- and 10-story archetypes are compared to investigate why the taller archetypes are found to have larger collapse margin ratios.

Collapse fragility curves are then presented for all archetypes analyzed, considering various structural configurations (i.e., panel aspect ratio, seismic weight intensity, and number of stories). Closing this section, reviewing all results generated, the adequacy of existing seismic performance factors for SPSWs is assessed for both types of SPSWs considered, and possible adjustments are recommended.

8.2 Collapse Definition for Incremental Dynamic Analysis

Incremental dynamic analysis (IDA) is a series of time history analyses performed on a given structural model for which intensity of a given ground motion is gradually scaled up from low to high magnitude until the structure reaches a specified limit state. Spectral acceleration and peak ground acceleration (PGA) are the two most common parameters used to measure the ground motion intensity in this context; and top story drift, interstory drift, cross-section plastic rotation, or base shear are examples of parameters commonly used to assess seismic performance of the structural model (Vamvatsikos and Cornell 2002). To comply with the FEMA P695 methodology, IDA in this research is conducted until a given SPSW archetype is deemed to have reached collapse.

In a typical IDA curve that plots an intensity measure (IM) versus a damage measure (DM), a nearly flat line is an indicator of structural collapse (or dynamic instability), because in that case, a relatively small increase in ground motion intensity from that in the preceding IDA step causes excessive lateral deformations of the structure under consideration. An example that shows such

an indication of collapse point is presented in Figure 8-1a, which plots spectral acceleration (as the IM) versus maximum interstory drift (as the DM). After the last stable point (i.e., $S_a = 1.6g$, $\varDelta_{max}/h = 4.6\%$, where Δ_{max} is the maximum interstory displacement and h is the story height), DM moves toward 'infinity' (i.e., $\varDelta_{max}/h$ is greater than 100%) with an increase of 0.1g IM. Here, the collapse intensity, S_{CT}, equals 1.7g. In several cases however, a collapse point could be observed before DM moves toward infinity (i.e. be still visible in the plot for an arbitrary selected range of the horizontal axis, at a drift less than 15% interstory drift for the example shown in Figure 8-1b). In such cases, the collapse point is taken as the next point after the last stable point providing that the slope between these two points (i.e. the last stable point and the one after it, as annotated in Figure 8-1b) is significantly smaller than the slope over several earlier IDA steps (i.e., 'elastic' slope). For example, for the case in Figure 8-1b, with an increase of 0.1g from the last stable point (i.e., S_{CT} of 5.9g and Δ_{max}/h of 6.8%), the maximum interstory drift increased by more than 5% (i.e., at the collapse intensity, where S_{CT} equals 6.0g, the value of Δ_{max}/h jumped to 12.6%).

Vamvatsikos and Cornell (2002) described weaving and structural resurrection phenomena can sometimes be observed in IDA curves. Weaving is a phenomenon where an increase in the IM (e.g., spectral acceleration) is not followed by a larger DM (e.g., interstory drift). Structural resurrection is the condition by which an archetype reappears as a non-collapsing structure (as if it gains strength again) at a higher intensity level after global structural collapse (i.e., dynamic instability) occurs at a lower intensity level. These two phenomena are respectively illustrated in Figures 8-1c and 8-1d. In an event of weaving, the collapse point is the higher intensity after passing the weaving zone when the structure tends toward infinity (or exhibits a significant 'jump' of DM for a small increase of IM). For example, the collapse intensity, S_{CT}, for the IDA results shown in Figure 8-1c is 7.0g instead of 5.8g even though at this point the maximum interstory drift has reached 10%. As for structural resurrection, the collapse point is the lower intensity when the first dynamic instability occurs, as opposed to the second time after the resurrection. For example, the S_{CT} for the IDA results shown in Figure 8-1d is 2.7g as opposed to 4.4g. Determination of collapse in this study is done in compliance with the above rules.
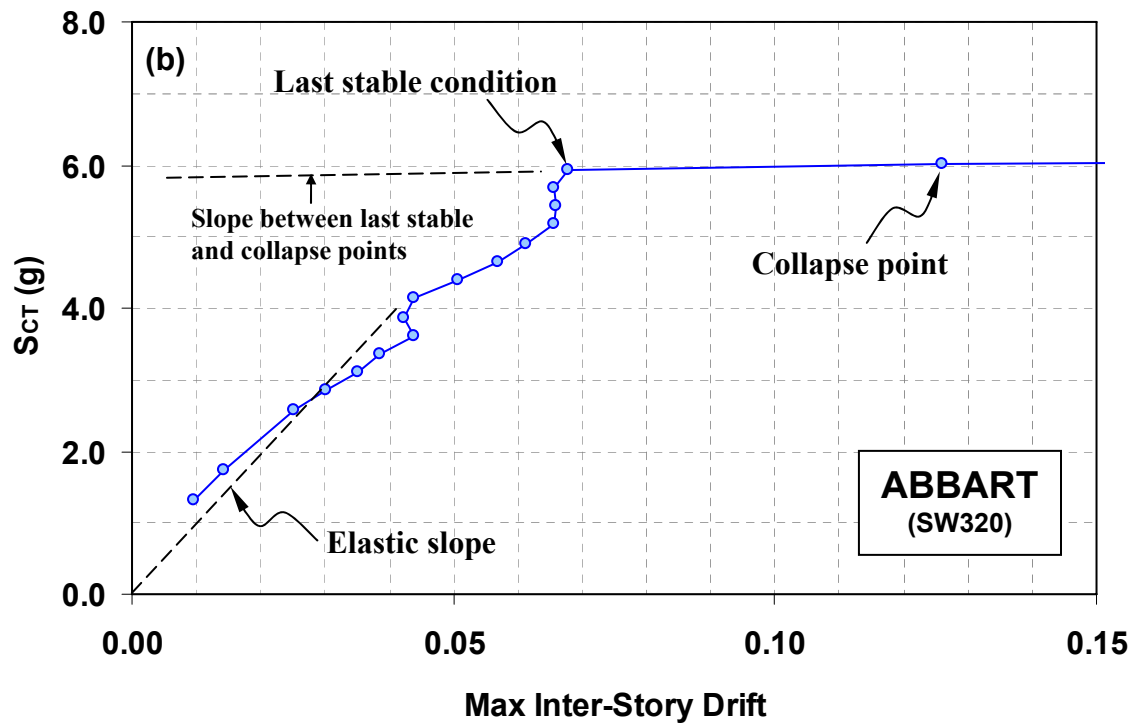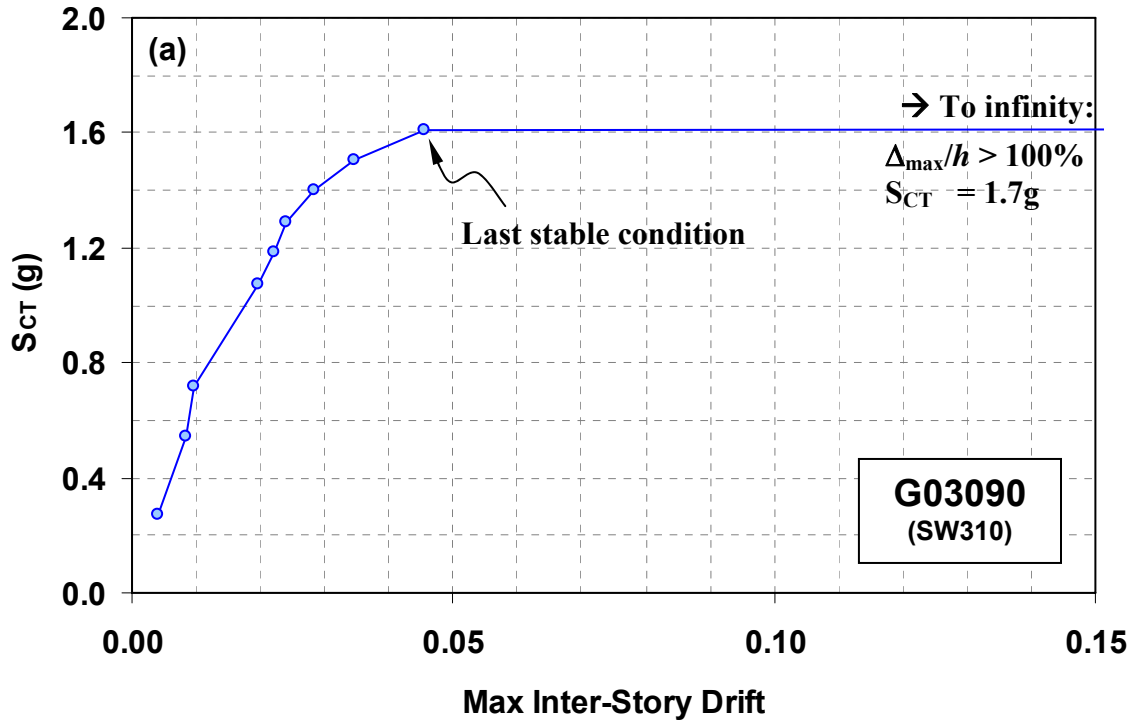
**Figure 8-1 Collapse Definition for Incremental Dynamic Analysis:
(a) Collapse Point Occurred at Infinity; (b) Collapse Point Based on "Tangent Slope" Rule**
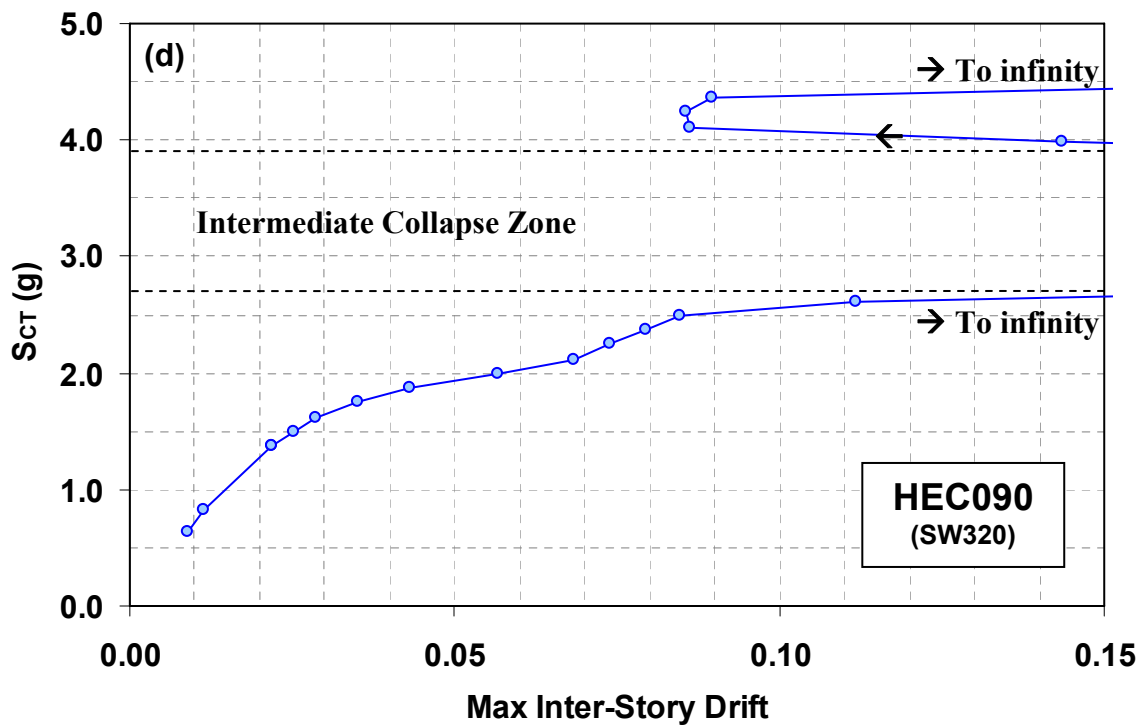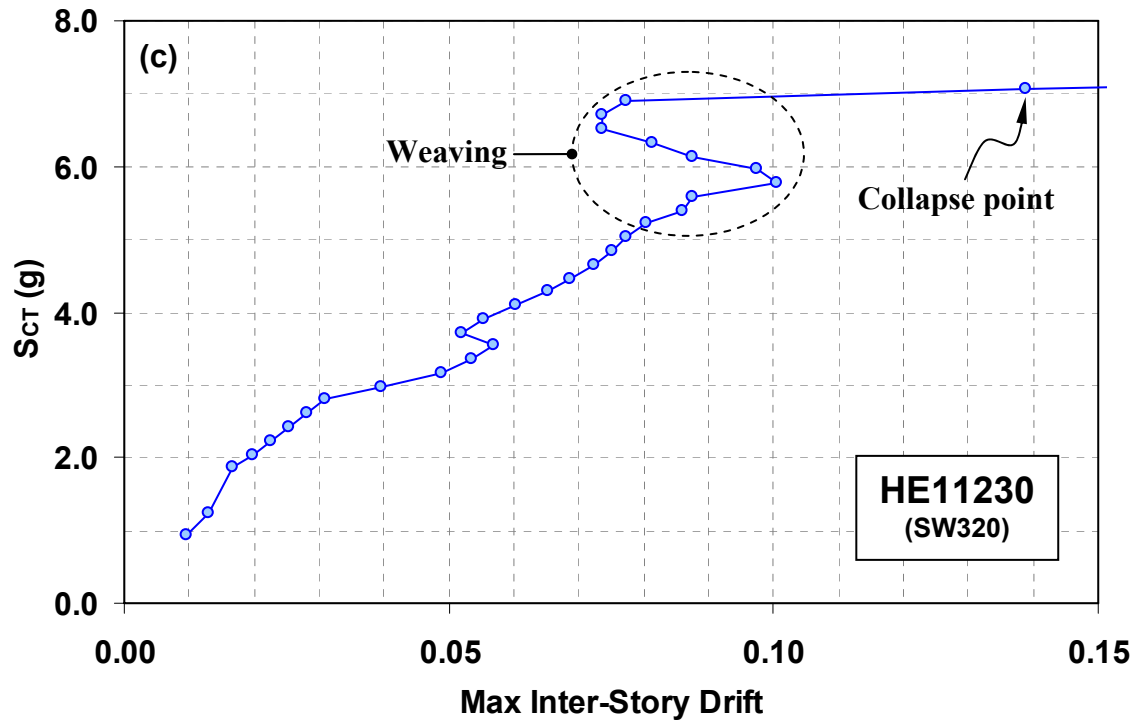
Figure 8-1 Collapse Definition for Incremental Dynamic Analysis – Cont'd: (c) Collapse Point in case of Weaving; (d) Collapse Point in case of Structural Resurrection

8.3 Application of FEMA P695 Methodology to 3-Story SPSW Archetypes

The FEMA P695 methodology, developed to provide a rational basis to quantify the global seismic performance factors (SPF) of seismic-force-resisting systems, was explained in Section 2.4. The following illustrates in detail application of this methodology to two 3-story SPSW archetypes. In this case, archetypes SW320 and SW320K are selected. The two archetypes represent the two basic SPSW configurations considered in this research (Section 7), namely: the design of SPSW with κ factor equals to 1.0 (i.e., SW320) and the balanced design case with κ factor set to be $\kappa_{balanced}$ (i.e., SW320K). Results for the two archetypes are compared in the following paragraphs.

8.3.1 Structural System Archetypes and Nonlinear Analytical Model

As summarized in Table 7-5, both SW320 and SW320K archetypes were designed to resist a design base shear of 176 kips. However, the amount of base shear sustained by their infill plates was different. In the case of SW320, the entire specified design base shear was resisted by its infill plates, while for SW320K, the infill plates only resisted 86 kips and the remaining base shear of 90 kips was sustained by its boundary frame. Member sizes for both archetypes were presented in Table 7-6. It was mentioned in Section 7 that a response modification coefficient (*R* factor) of 7 was used to design both archetypes, following the current value assigned to steel plate shear walls in ASCE 7-10. Moreover, nonlinear analytical models of both archetypes were conducted using the dual strip model shown in Figure 7-10. Detailed information on nonlinear analytical models was presented in Section 6.

For the purpose of performing performance evaluation (Section 8.3.3), uncertainty factors related to archetypes and nonlinear models need to be determined by rating the design procedures used to size the archetypes, the experimental data used to verify proposed strength degradation model, and the collapse modes incorporated in the nonlinear model according to the guidelines described in Tables 2-4 to 2-6. Each rating and corresponding uncertainty factor is described as follows.

Uncertainty Related to Design Requirements

In this research, the procedures used to design SPSW archetypes followed the current design procedures described in the AISC 2010 Seismic Provisions for SPSW. Developed based on

SPSW research conducted in the last 30 years, this provision provides sufficient design requirements to safeguard against unanticipated failures. Moreover, SPSWs have been used in several buildings as their main lateral-force resisting systems. Examples of SPSWs implementations both in low- and high-rise buildings can be found in Bruneau *et al*. (2011). However, no documented performance of SPSWs during earthquakes is available (at the time of this writing) to verify whether a well-designed SPSW is actually performed as intended. Hence, based on the guidelines outlined in Table 2-4, the current SPSW design requirements are rated as B (Good) and the corresponding uncertainty factor related to design requirements (β_{DR}) equals 0.2. Over time, as research on SPSWs continues and new understanding of SPSW behavior is obtained, this value could be revisited.

Uncertainty Related to Test Data

At the time of this writing, 36 conventional unstiffened slender-web SPSWs have been tested by various researchers (as summarized in Section 6.2). They varied from single- to four-story specimens with aspect ratios ranging from 0.7 to 2.2. This total number of tested SPSW specimens is relatively low in comparison to that of other lateral-force-resisting systems (e.g., special moment frames). In addition, all SPSW specimens tested focused on investigating global behavior of the system, and there is a lack of individual component tests. Hence, based on the guidelines outlined in Table 2-5, SPSW test data at the time of this writing is rated as C (Fair) and the corresponding uncertainty factor related to test data (β_{TD}) equals 0.35.

Uncertainty Related to Nonlinear Model

Based on past SPSW experimental research available at the time of this writing, common deterioration and failure modes in steel plate shear walls have been identified and addressed in Section 6. Among the failure modes identified, deteriorating web tearing and flexural failure of boundary elements are the primary factors that would contribute to collapse of SPSWs; these were considered in the development of nonlinear models used in this research (Section 6.7, Figure 7-10). The other two failure modes (i.e., instability and shear failure of boundary elements) can be avoided in a well-designed SPSW that complies with the AISC 2010 specification, and are therefore not modeled. However, the deteriorated material models presented in Section 6 were calibrated only to a limited number of SPSW specimens that have stable strength degradation behavior. Hence, based on the guidelines outlined in Table 2-6, the nonlinear analytical model

341

developed in this research is rated as B (Good) and the corresponding uncertainty factor related to the nonlinear model (β_{MDL}) equals 0.2.

8.3.2 Nonlinear Static and Dynamic Analyses

Nonlinear static (pushover) and dynamic (response history) analyses were performed with the OpenSees program (Mazzoni *et al*. 2009). Dynamic analyses of 44 specified ground motions were executed using the NEES-HUB supercomputer. Procedures and results of both analyses are presented as follows.

Nonlinear Static Analysis

Nonlinear pushover analysis was performed in accordance with the description presented in Section 2.4.3 and intended to estimate overstrength (Ω_o) and period-based ductility (μ_T) factors for both archetypes. The resulting monotonic pushover curves for both archetypes are presented in Figure 8-2. The ultimate base shear strengths for SW320 and SW320K are 495 and 226 kips, respectively. To obtain the overstrength factors for both archetypes (2-3), their ultimate strengths are divided by the design base shear of 176 kips. Hence, Ω_0 factors are 2.8 and 1.3 for SW320 and SW320K, respectively. Moreover, effective yield and ultimate top floor displacements (i.e., $\delta_{y,eff}$ and δ_u, respectively) are required to obtain the period-based ductility 2-4), which is later used for performance evaluation (Section 8.3). As indicated in Figure 8-2a for SW320, the effective yield and ultimate displacements are 1.8 and 8.9 in., respectively, while in Figure 8-2b for SW320K, the respective displacement values are 1.8 and 8.6 in. Hence, μ_T factors are 4.9 and 4.8 for SW320 and SW320K, respectively. Even though both archetypes have significantly different strength capacities, they have somewhat the same displacement capacities.

With respect to overstrength, it should be noted that in both cases, the resulting factors first include an inherent design overstrength factor of 1.33 as a consequence of complying with the current AISC design procedure for SPSW (i.e., using $\Omega_s = 1.2$ and $\phi = 0.9$, Section 7.2.3). The additional overstrength factor in SW320 of 2.1 (= 2.8/1.33) is attributed to boundary frame moment resisting action (that was not designed to resist story shear forces, but which unavoidably does), to material strain hardening developed in the boundary elements and infill plates, and to the strip model which was developed based on center-to-center dimensions as

342
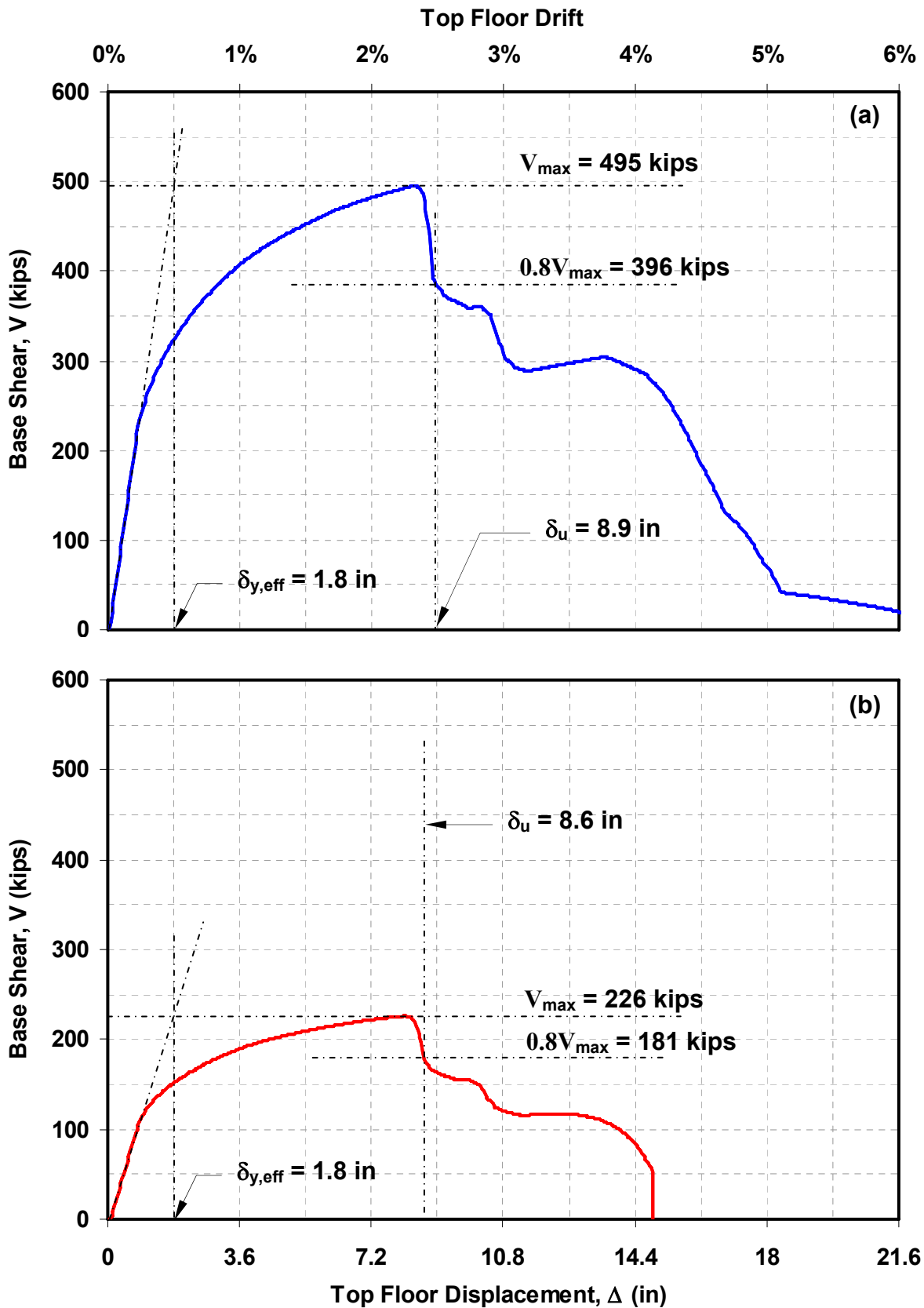
Figure 8-2 Monotonic Pushover Analysis Results: (a) SW320; (b) SW320K

opposed to the clear dimensions of the infill plates (Section 7.2.3). Obviously, among these three factors, the biggest contribution to overstrength comes from the first one. This can be observed in the balanced case archetype (SW320K), in which overstrength due to boundary frame was eliminated as it was explicitly designed to resist its share of the story shear forces. In this case, the resulting overstrength factor of 1.3 is attributed to the inherent design overstrength mentioned above, with marginal contributions to the overstrength due to material strain hardening and modeling. Interestingly, the resulting factor of 1.3 for SW320K is actually slightly less than the inherent design overstrength factor of 1.33, which at first appears illogical (considering the other two overstrength sources, the total overstrength factor should in fact be larger than 1.33). Closer scrutiny of SPSW response revealed that the difference is due to the fact that several strips in SW320K have started to deteriorate before fiber hinges in boundary elements reached a complete plastic condition; as a result, the ultimate strength of SW320K was slightly less than the theoretical ultimate strength which does not consider degradation in structural components.

Incremental Dynamic Analysis (IDA)

Theoretically, any arbitrary incremental scheme of ground motion intensity can be selected for incremental dynamic analysis (IDA). In this research project that considers the 44 ground motions specified in the FEMA P695, the IDA started with using the actual un-scaled recorded ground motions, followed by two subsequent increments for which all ground motions were scaled such that the median spectral acceleration of the 44 ground motions (at the fundamental period of a given archetype being analyzed) matched that at the Design Basis Earthquake (DBE) and at the Maximum Considered Earthquake (MCE) spectral acceleration levels (Figure 7-9), respectively. From there on, each motion was gradually scaled up in steps equal to one-tenth of the MCE level (i.e., $0.1S_{a\text{-}MCE}$), up to an intensity that caused structural collapse. Specific to SW320K, several ground motions actually caused collapse at intensities lower than the MCE level (as further shown in Figure 8-3). In those cases, considering the large intensity discrepancy between the DBE and MCE levels, 3 to 6 additional analyses were conducted between these two levels to refine assessment of the collapse intensity level for these ground motions.

Incidentally, increments equal to one-tenth of the median spectra beyond the MCE level actually resulted in relatively broad variation of increments among ground motions (since this was done in an average sense). Several of the ground motions ended up having an intensity increment of less

344

than 0.1g while several others had increments larger than 0.3g. To reduce the number of analysis for the former and maintain sufficient accuracy in determining collapse intensity level for the latter, in the subsequent series of IDA for the remaining archetypes (i.e., Sections 8.5 to 8.8), a uniform intensity increment of 0.1g was selected for all considered ground motions.

Figure 8-3 presents IDA results for SW320 and SW320K. The corresponding collapse fragility curves developed based on the collapse data points in Figure 8-3 are compared in Figure 8-4. The median collapse spectral acceleration intensity, $\hat{S}_{CT}$, is 3.6g and 2.3g for SW320 and SW320K, respectively. These results inform that at the same level of 50% collapse probability, the spectral acceleration intensity at which 22 ground motions caused collapse of SW320 is higher than that which caused SW320K to collapse. Note that these 22 ground motions are not the same for both cases (which is often the case in such FEMA P695 analyses). The collapse fragility curves in Figure 8-4 also indicate that when both archetypes are subjected to a set of ground motions having their median spectral acceleration scaled to the MCE response spectra level of 1.5g, SW320K has a higher probability of collapse compared to SW320. In this case, the collapse probabilities at the MCE level are 21.5% versus 2.8% for SW320K and SW320, respectively. The same information can be also obtained from IDA curves in Figure 8-3, where more collapses (i.e. flat lines) can be seen to occur below the S_{MT} level for the SW320K case compared to SW320. From these IDA results, a collapse margin ratio (CMR) can be estimated, which the FEMA P695 methodology defines as the ratio between $\hat{S}_{CT}$ and S_{MT} (2-5). Here, the CMR is 2.4 and 1.5 for SW320 and SW320K, respectively.

Note that above, the reported median collapse spectral acceleration intensities, $\hat{S}_{CT}$, were taken from their respective collapse fragility curves as the spectral acceleration intensities that corresponded to a 50% probability of collapse. These fragility curves (Figure 8-4) were obtained by fitting a lognormal distribution through the collapse data points of each archetype. Alternatively, an empirical $\hat{S}_{CT}$ could have been used, defined as the lowest spectral acceleration intensity when 22 ground motions caused collapse. The values of $\hat{S}_{CT}$ obtained by this alternative approach for SW320 and SW320K would have been 3.9g and 2.2g, respectively. This differs slightly from the values of 3.6g and 2.3g obtained from the lognormal fragility curves. In this research, the first definition of $\hat{S}_{CT}$ was used, since the fit to a lognormal distribution was
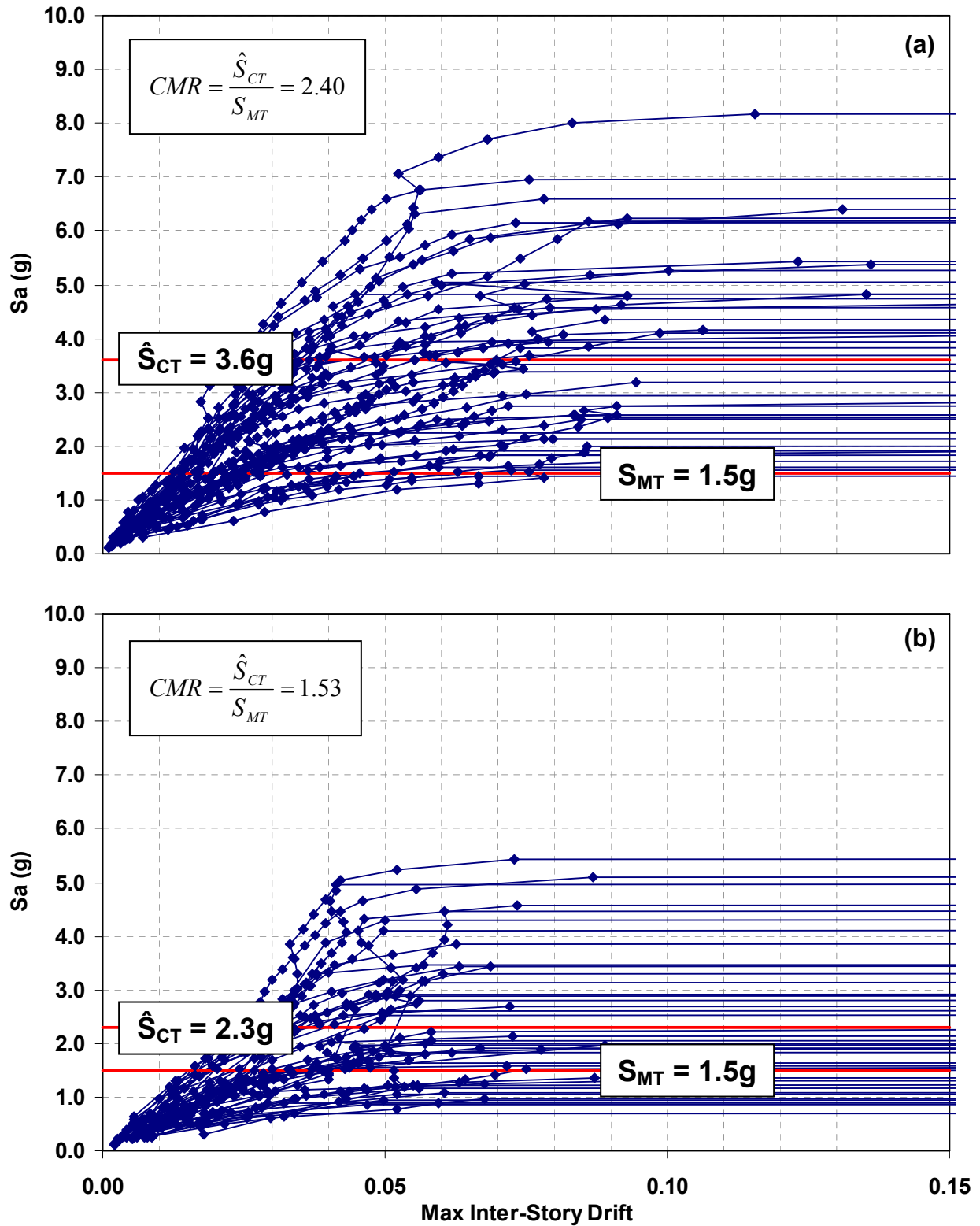
Figure 8-3 Incremental Dynamic Analysis (IDA) Results: (a) SW320; (b) SW320K

346
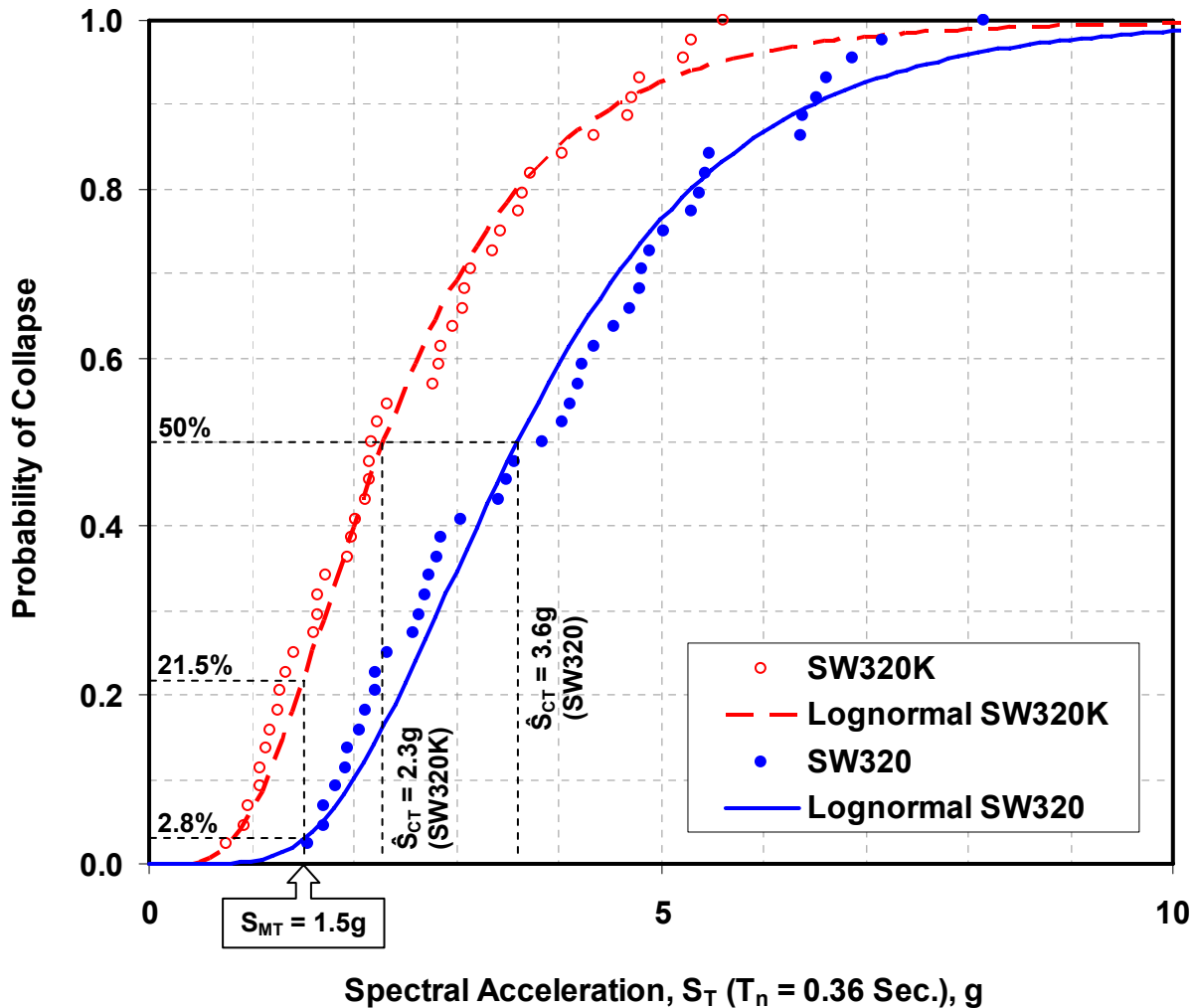
Figure 8-4 Collapse Fragility Curves for SW320 and SW320K

generally good, as shown in Figure 8-4. Note that using a normal distribution, instead of a lognormal one, would not have been acceptable, according to Kolmogorov-Smirnov test (Ang and Tang 2007); consequently, simply taking the average (arithmetic mean) of the collapse data points as $\hat{S}_{CT}$ is not an acceptable approach.

8.3.3 Collapse Performance Evaluation

Table 9-1 compares collapse performance evaluation for both archetypes, by summarizing design information, nonlinear static and dynamic analyses results, and evaluation of the seismic performance factors used for the original design. The performance evaluation starts by adjusting the CMR value obtained from the IDA to consider frequency content of the selected ground motion records (i.e., the effect of spectral shape). Spectral shape factor (SSF) values used to

347

Table 8-1 Summary of ATC-63 Methodology on 3-Story SPSW Archetypes

Parameter	SW320	SW320K	Note and Reference
1. Design Stage			
R	7	7	Initial value ASCE 7-10 Table 12.2-1
V_{design}	176	176	Table 8.5
2. Nonlinear Static (Pushover) Analysis			
V_{max}	495	226	Fig. 9.5
$\Omega = V_{max}/V_{design}$	2.81	1.29	Included SH = 2%, Ω_d = 1.2 and ϕ = 0.9
$\delta_{y,eff}$	1.80	1.80	Fig. 9.5
δ_u	8.86	8.64	
$\mu_T = \delta_u/\delta_{y,eff}$	4.92	4.80	Eq 2.2
3. Incremental Dynamic Analysis (IDA)			
S_{CT}	3.60	2.29	Fig. 9.6
S_{MT}	1.50	1.50	Fig. 8.9
$CMR = S_{CT}/S_{MT}$	2.40	1.53	Eq 2.3
4. Performance Evaluation			
T	0.36	0.36	Eq. 8.3
SDC	D_{max}	D_{max}	FEMA P695 (ATC63) Table 5-1
SSF (T, μ_T)	1.25	1.24	Table 2.1
ACMR = SSF (T, μ_T) x CMR	3.00	1.90	Eq. 2.4
β_{RTR}	0.4	0.4	Section 2.4.4
β_{DR}	0.2	0.2	Table 2-2: (B - Good)
β_{TD}	0.35	0.35	Table 2-3: (C - Fair)
β_{MDL}	0.2	0.2	Table 2-4: (B - Good)
$\beta_{tot} = $ sqrt $(\beta_{RTR}^2 + \beta_{DR}^2 + \beta_{TD}^2 + \beta_{MDL}^2)$	0.60	0.60	Eq. 2.5
$ACMR_{20\%} (\beta_{tot})$	1.66	1.66	Table 2-5
$ACMR_{10\%} (\beta_{tot})$	2.16	2.16	Table 2-5
$Status_i$	**Pass**	**Pass**	Eq. 2-6a
$Status_{PG}$	**Pass**	**NOT Pass**	Eq. 2-6b
5. Final Results			
R	**7**	**Try Again**	
Ω	**2.8**	**Try Again**	
μ_T	**4.9**	**Try Again**	
$C_d = R$	**7**	**Try Again**	

Units: kips, in, sec., g

modify the CMR to the adjusted collapse margin ratio (ACMR) are a function of the archetype fundamental period and period-based ductility (μ_T) obtained from pushover analysis. The fundamental period (*T*) calculated using (7-3) is 0.36 seconds for both archetypes. For *T* less than

0.5 seconds, μ_T values of approximately 5, and seismic design category (SCD) D_{max}, the value of SSF obtained from Table 2-3 is approximately 1.25 for both archetypes. Accordingly, the ACMR for SW320 and SW320K are 3.0 and 1.9, respectively. In Section 8.3.4, these values will be compared to acceptable ACMR values to justify whether the initial R factor used to design these archetypes satisfy the FEMA P695 requirements.

It should be emphasized that the analytical fundamental periods for SW320 and SW320K obtained from OpenSees eigenvalue analysis were different from the one reported above, and were 0.35 and 0.50 seconds, respectively. While the analytical fundamental period of SW320 is in good agreement with the theoretical fundamental period, that of SW320K is slightly higher. Even though the FEMA P695 methodology specifies the use of the theoretical fundamental period when estimating SSF values, it is noteworthy that the resulting SSF values for both archetypes would be the same if the analytical fundamental periods are used instead. As shown in Table 2-3, SSF values for archetypes with fundamental period less than 0.5 seconds are the same for a given period-based ductility; and for periods larger than 0.5 seconds, slightly different analytical and theoretical fundamental periods would either result in the same or marginally different SSF values, depending on μ_T values.

To estimate acceptable ACMR, total system collapse uncertainty (β_{TOT}) is required. As discussed in Section 2.4.4, the value of β_{TOT} is obtained by combining uncertainty factors related to record-to-record (β_{RTR}), design requirements (β_{DR}), test data (β_{TD}), and nonlinear modeling (β_{MDL}). For the selected ground motions used in the FEMA P695 methodology, a constant value of β_{RTR} equal to 0.4 is used, given that period-based ductility is larger than or equal to 3 ($\mu_T \geq 3$). The other three uncertainty factors have been presented in Section 8.3.1. Their values are 0.2, 0.35, and 0.2 for β_{DR}, β_{TD}, and β_{MDL}, respectively. Hence, the total system uncertainty calculated using (2-7) is 0.6. As presented in Table 2-7 for β_{TOT} of 0.6, the acceptable ACMR for 10% and 20% collapse probability under MCE ground motions (i.e., $ACMR_{10\%}$ and $ACMR_{20\%}$) are 2.16 and 1.66, respectively. A limited sensitivity analysis to examine the impact of different uncertainty factors on these acceptable ACMR is presented in Section 8.8.

The FEMA P695 methodology specifies that $ACMR_{20\%}$ and $ACMR_{10\%}$ are the acceptable threshold values to evaluate performance of individual archetype and average performance of several archetypes in one performance group, respectively. Hence as individual archetypes, both SW320 and SW320K pass the performance requirement. Here, SW320 has an ACMR significantly above $ACMR_{20\%}$ (i.e., 3.0 versus 1.66) while SW320K has an ACMR only slightly higher than the threshold value (i.e., 1.9 versus 1.66). However, the performance evaluation might have different outcomes within the performance group level. If both archetypes were part of different performance groups and their ACMR values were representative of that group, then SW320K would fail the requirement while SW320 would pass the requirement.

8.3.4 Evaluation of Seismic Performance Factors

For illustration purposes, if SPFs for SPSWs are judged solely based on the collapse performance evaluations of SW320 and SW320K, the initial *R* factor of 7 used to design archetypes in the first basic configuration (i.e., $\kappa = 1.0$) is adequate. The system overstrength factor (Ω_o) could be specified as high as 2.8 and deflection amplification factor (C_d) equal to 7, similar to the value of *R* factor (2-10). As for the second basic configuration (i.e., $\kappa = \kappa_{balanced}$), the initial *R* factor of 7 used to design these archetypes is not adequate. The collapse performance satisfied the individual performance criteria but does not satisfy the performance group criteria. Here, further iteration process is required to evaluate the collapse performance of balanced archetypes designed with a lower *R* factor (e.g., *R* = 6 or 5).

Final recommendations of SPF for SPSWs however are yet to be determined pending upon collapse performance evaluations of other archetypes, which will be addressed in Section 8.7. However, the information presented so far indicates that for SPSWs designed with a similar *R* factor of 7, SW320 seems to have a better seismic performance compared to SW320K. Impact of lower *R* factor on collapse performance will be addressed in Section 8.8.

8.4 Factors that Affect Collapse Margin Ratio

The CMR is key in determining whether a proposed SPF can satisfy the FEMA P695 performance criteria. Accordingly, an investigation on several factors that affect CMR is useful at

this stage. This section provides such a review, focusing on the impact of intensity measure, damage measure, and non-deteriorated material model.

8.4.1 Intensity Measure (IM)

The collapse margin ratios for SW320 and SW320K, presented in the previous section, were estimated based on spectral acceleration intensity when half of the considered ground motions caused these archetypes to collapse (by experiencing excessive lateral interstory displacements). However, PGA is another intensity measure (IM) commonly used in IDA (Vamvatsikos and Cornell 2002). Using this IM, comparison of CMR becomes independent of archetype fundamental periods. It was deemed of interest to investigate how results would change if using this IM instead.

Figure 8-5 shows IDA results for SW320 and SW320K using PGA as the selected intensity measure; the resulting corresponding collapse fragility curves are shown in Figure 8-6. Half of the ground motions caused SW320 to collapse at a PGA level of 1.7g, while a lower level of PGA of 1.1g was sufficient to do the same condition for SW320K. From a different perspective, by conducting a comparison of response at the MCE level (i.e., PGA = 0.6g), results show that SW320 has only 0.5% probability of collapse at that level, whereas SW320K has a 10.6% probability of collapse.

While those results exhibit the same trend as shown in Figures 8-3 and 8-4 (i.e., SW320K has a smaller margin to collapse, and higher probability of collapse), the resulting CMR for each archetype using PGA as the intensity measure is slightly higher than that using spectral acceleration. Here, the median collapse PGA intensity, PGA_{CT}, for SW320 and SW320K are 1.7g and 1.1g, respectively. Comparing to PGA intensity at MCE level (PGA_{MT}), CMR for respective archetypes are 2.76 and 1.76 (i.e., ACMR values are 3.44 and 2.2, respectively), which are approximately 15% larger than for results obtained when using spectral acceleration as the intensity measure. Accordingly, the SW320K, with its ACMR of 2.2, would satisfy the performance criteria of $ACMR_{20\%}$ or $ACMR_{10\%}$ if the evaluation was based on PGA as the IM.
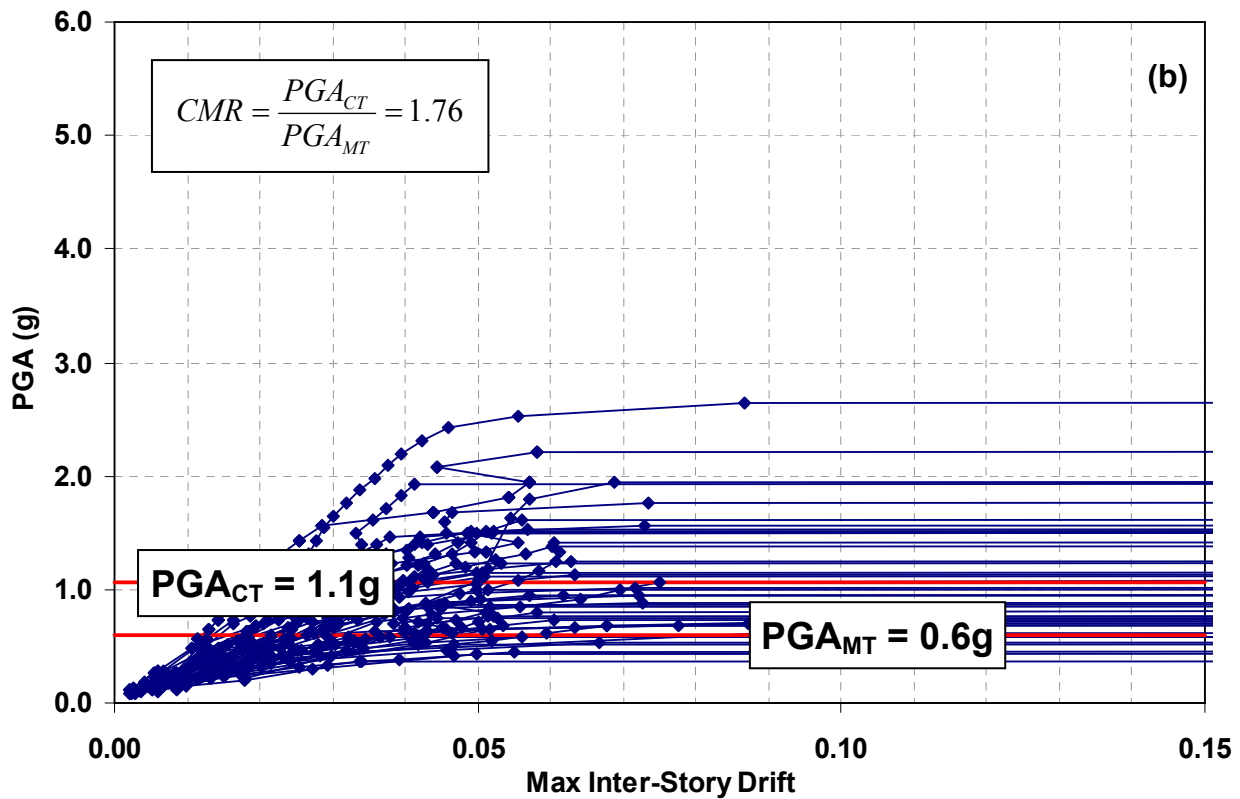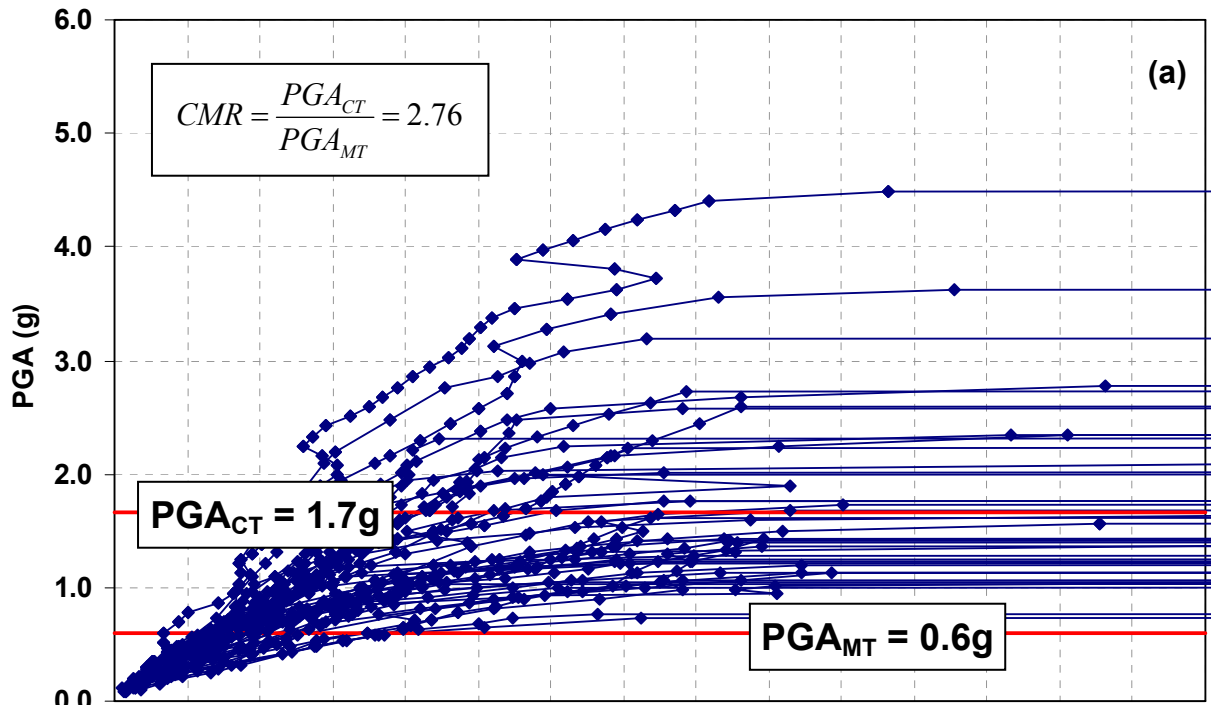
Figure 8-5 Incremental Dynamic Analysis (IDA) Results using PGA as Intensity Measure: (a) SW320; (b) SW320K
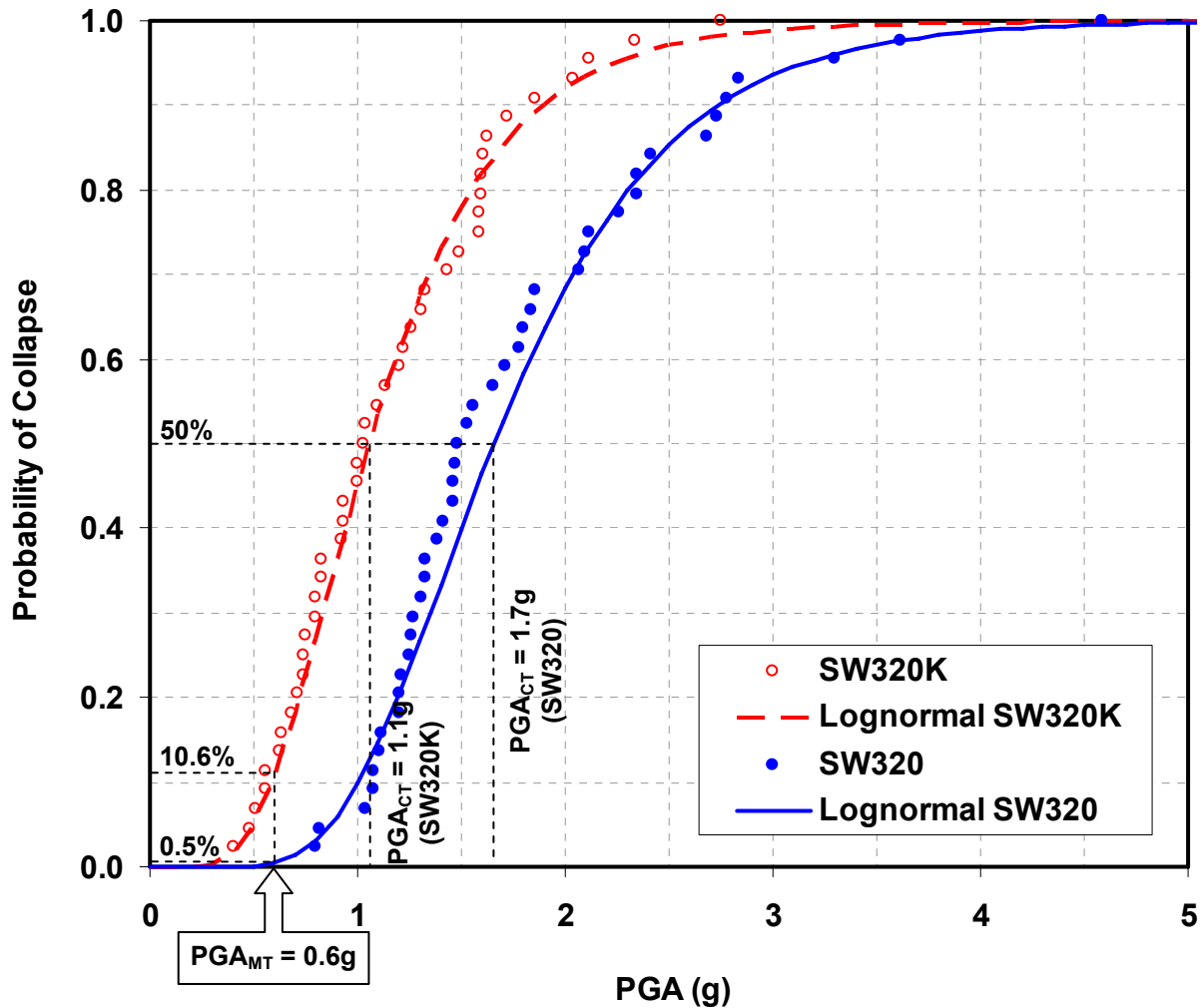
Figure 8-6 Collapse Fragility Curves for SW320 and SW320K using PGA as Intensity Measure

8.4.2 Damage Measure (DM)

The damage measure (DM) is a parameter used in IDA to characterize response of archetypes under specified ground motions (Vamvatsikos and Cornell 2002). The collapse point where excessive lateral interstory displacement occurred in archetypes is typically selected as a DM. In general though, the collapse point of an archetype occurs at a considerably large interstory drift. For example, consider the IDA results for SW320 and SW320K shown in Figure 8-7, expressed as an exceedance fragility curve of the interstory drift when collapse occurred. The median interstory drifts (i.e., corresponding to 50% probability of exceedance) when collapse occurred in SW320 and SW320K are 7.6% and 5.8%, respectively. Note that the range of obtained value is
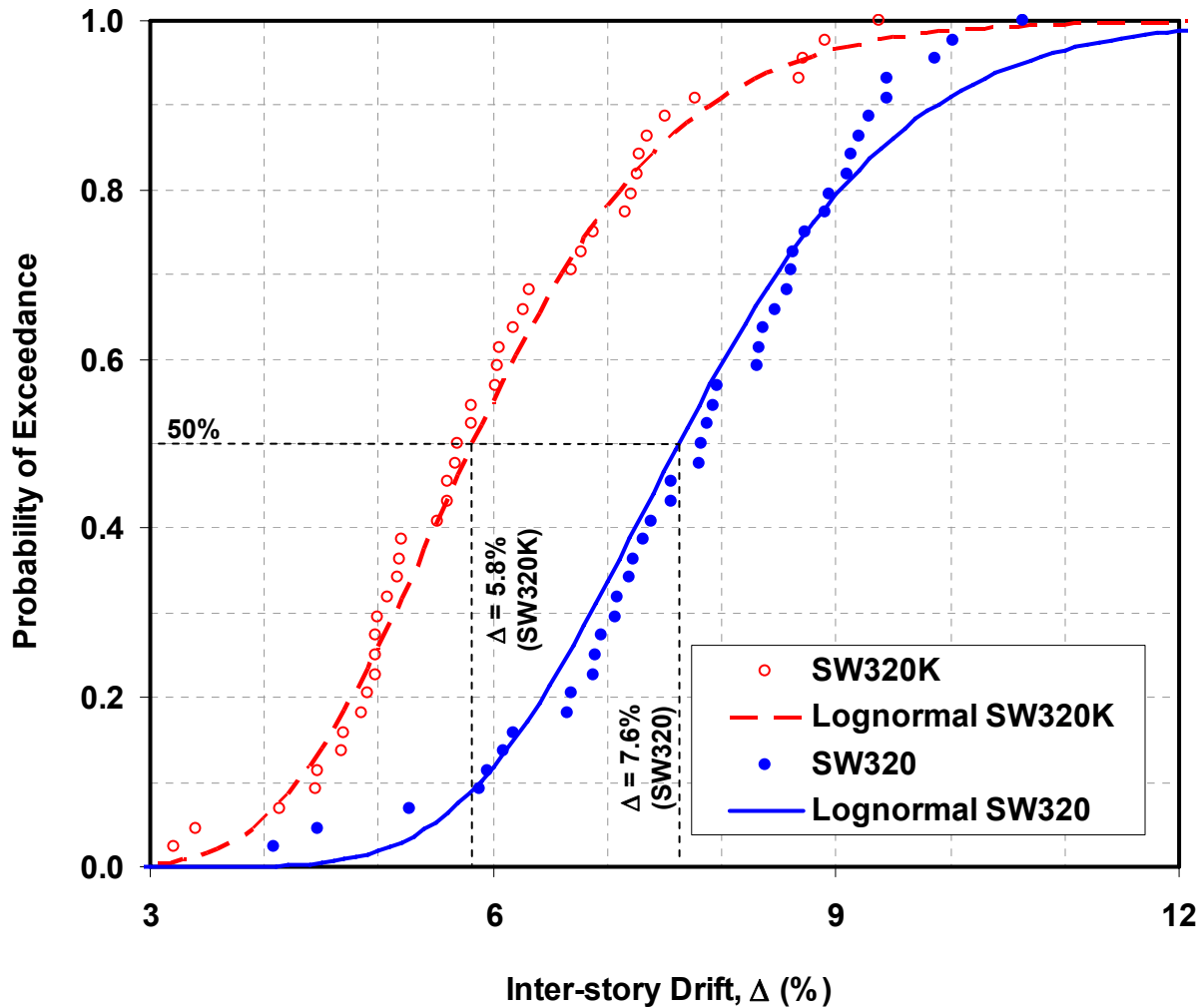
Figure 8-7 Exceedance Fragility Curves for SW320 and SW320K

significant, with the lowest and highest interstory drifts at collapse being approximately 4% and 11% for SW320 and 3% and 9% for SW320K. Incidentally, the median top story drifts (i.e. total drift) when collapse occurred are 5.1% and 3.9% for the same respective archetypes (fragility curve are not presented here), which are close to the top story drift values observed in the pushover results at the point when the archetypes lost their capacity to sustain loads (Figure 8-2).

It is also meaningful to interpret the IDA results in terms of drift demands. Specifically, fragility curves can be constructed for the probability of exceeding certain drift values in terms of spectral acceleration of the ground motions, for selected fixed values of interstory drifts up to the drift at the collapse. The resulting "drift-exceedance" fragility curves for SW320 and SW320K, using interstory drifts as DMs, are plotted in Figures 8-8 and 8-9, respectively. As a reference, the

354
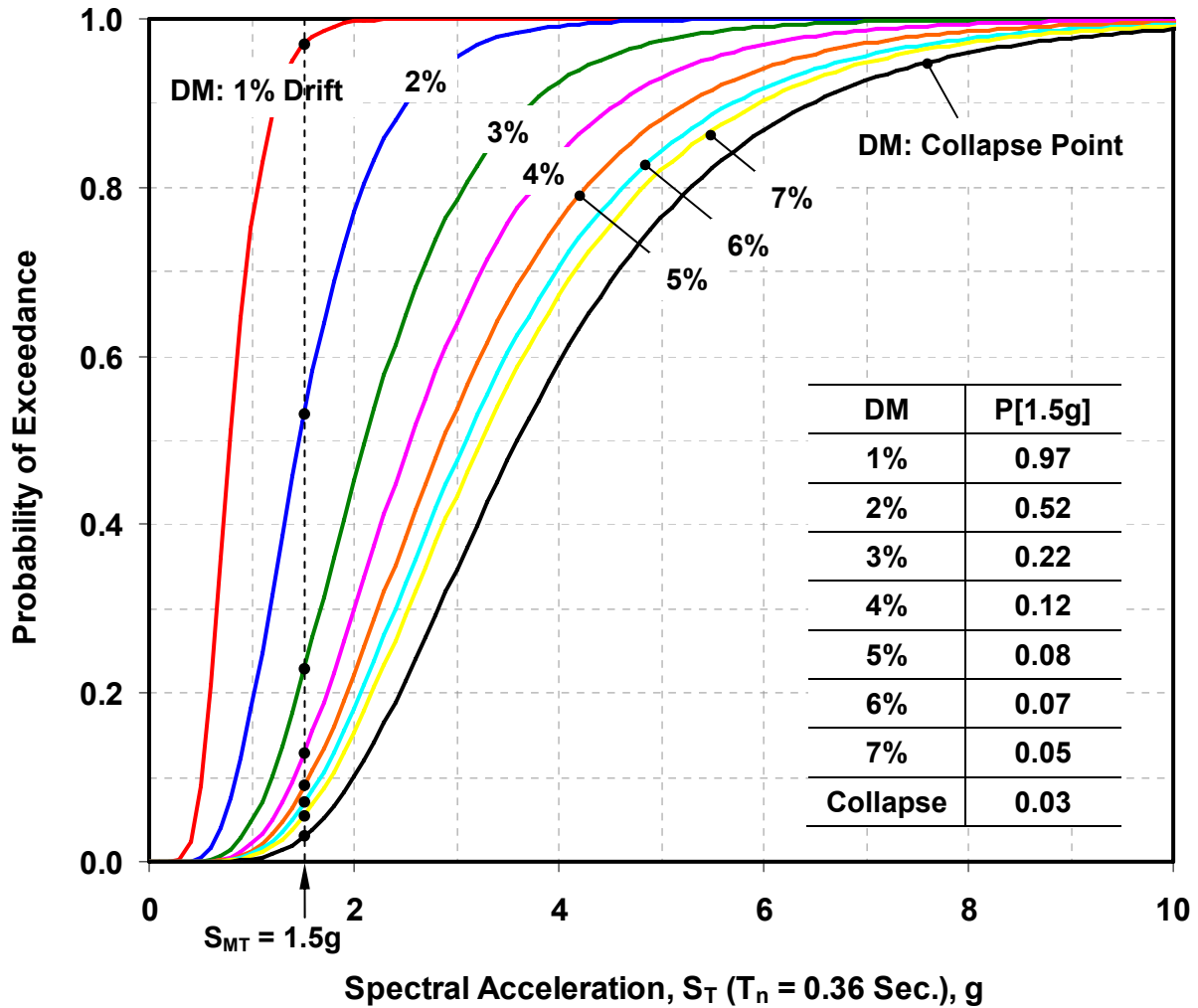
Figure 8-8 Exceedance Fragility Curves for SW320 using Various Levels of Inter-story Drift as Damage Measure

results from Figure 8-4 using the collapse point as the DM are superimposed in these curves. At the MCE level (i.e., S_{MT} = 1.5g), there is approximately a 50% probability that drifts will exceed 2% and 3.5% interstory drifts for SW320 and SW320K, respectively. More significantly at a 20% probability of exceedance, the respective archetypes will exceed 3% and 7% interstory drifts. Corresponding probabilities for other drift levels are tabulated in the figures. The results indicate that SW320K has higher probability to suffer significantly larger interstory drift, which can be associated with larger structural and non-structural damages.

By analogy with the collapse margin ratio concept, an exceedance margin ratio (EMR) can be defined as the ratio between the spectral acceleration intensity when half of the specified ground
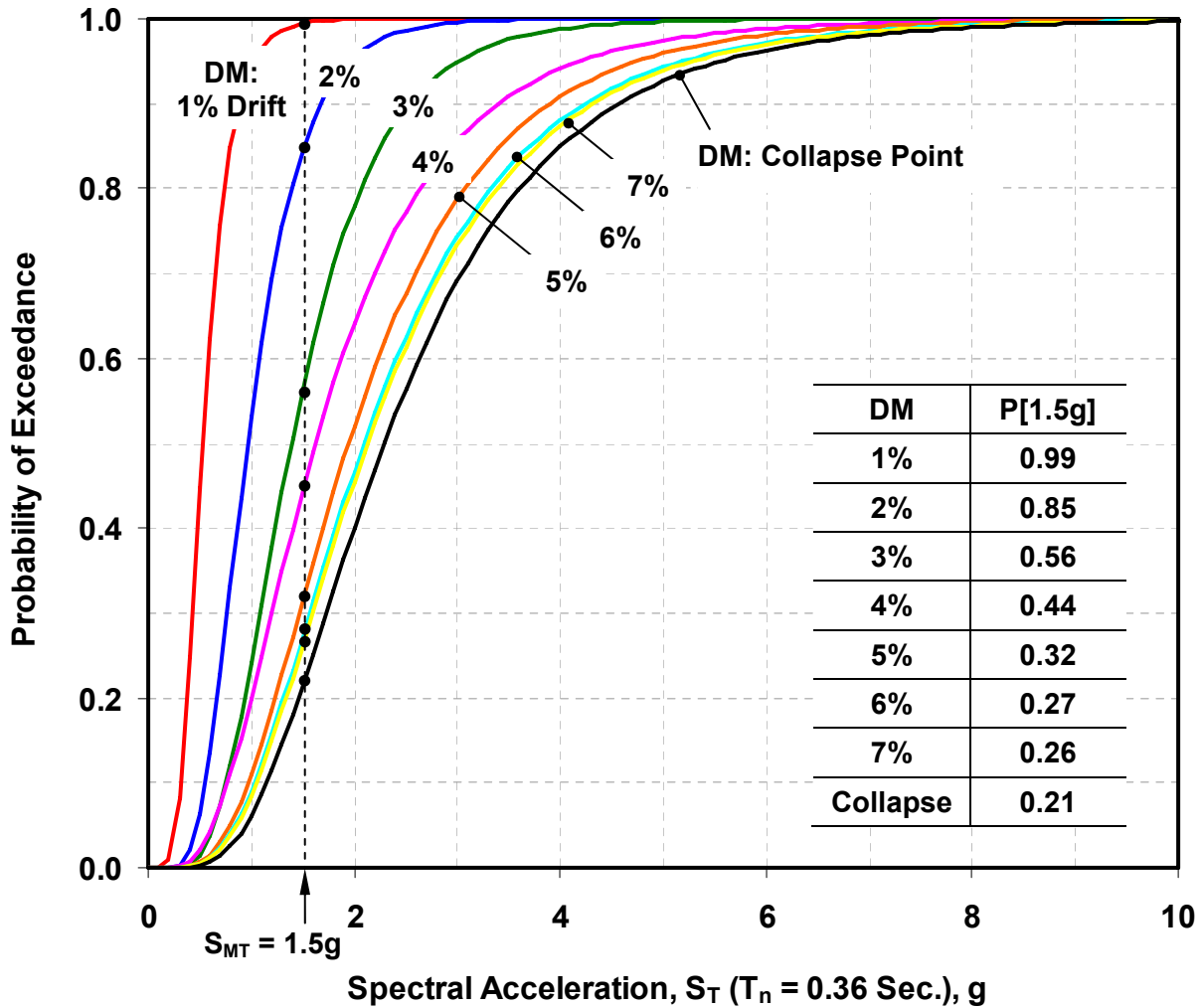
Figure 8-9 Exceedance Fragility Curves for SW320K using Various Levels of Inter-story Drift as Damage Measure

motions cause an archetype to reach a given DM ($S_{DM=x\%}$) (i.e., an interstory drift of x%) and spectral acceleration intensity at the MCE level (S_{MT}):

$$EMR = \frac{S_{DM=x\%}}{S_{MT}} \tag{8-1}$$

The EMR for each level of DM is compared in Figure 8-10 for SW320 and SW320K. The conventional archetype has higher EMR for each DM considered. For example, consider a DM of 3% interstory drift, the spectral acceleration intensity at which 22 ground motions caused 3% interstory drift for SW320 is approximately 1.5 times above the MCE level, while for SW320K, 1.0 times the MCE ground motions caused the same interstory drift (i.e., EMR ≈ 1.0). Note that

356
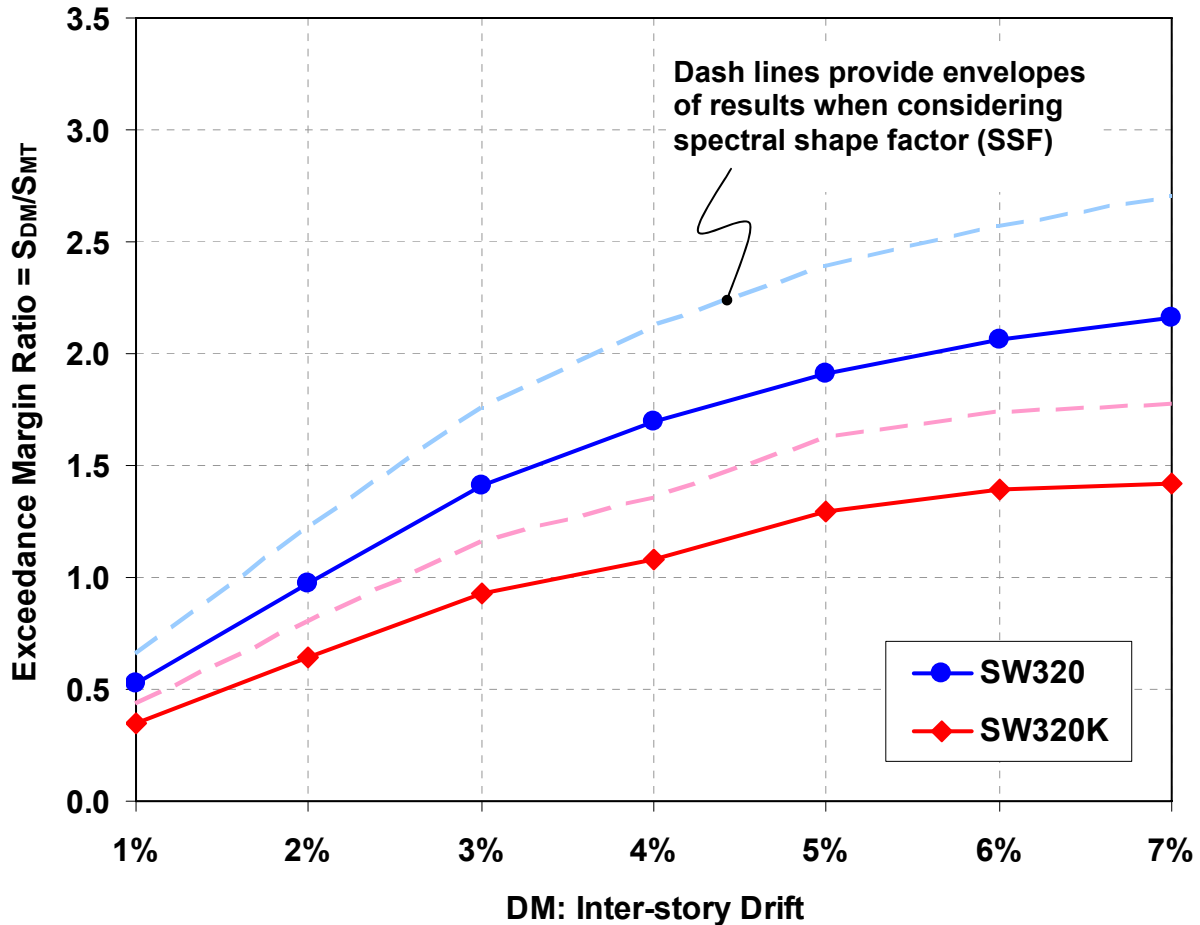
Figure 8-10 Margin Ratio versus Interstory Damage Measure for 3-story Archetypes

EMR less than 1.0 should be understood as a condition of which ground motions with median intensity level lower than the MCE level caused the corresponding damage measure. For example, ground motions with median intensity of approximately $0.64S_{MT}$ (i.e., approximately equals to the DBE ground motions) caused a 2% interstory drift in SW320K. Also note that the dashed lines in the figure represent the adjusted values when considering spectral shape factor (SSF).

8.4.3 Non-Deteriorated Material Model

It was reported in Section 6 that the degradation models selected for boundary elements and infill plates were developed based on the most severe degradation that occurred in the four considered specimens against which the models were calibrated. As a result, there may be a concern that the strength degradation rate selected could be overly conservative and resulted in smaller margins to collapse for the SPSW archetypes considered. To investigate this concern, another set of IDA on

357

SW320 archetype was conducted but in this case, the elasto-perfectly plastic (EPP) material model was assigned to boundary elements and infill plates. Note that gravity leaning columns remained in the analytical model to account for P-Δ effects. The resulting fragility curve from this analysis would serve as an 'upper bound' envelope against which conservativeness of the current fragility curve (Figure 8-7) can be assessed. IDA results for the non-deteriorating bi-linear inelastic material model are plotted in Figure 8-11.

The figure contains the following annotations:

$$CMR = \frac{\hat{S}_{CT-NSC}}{S_{MT}} = 4.91$$

$$\hat{S}_{CT-NSC} = 7.4g$$

$$\hat{S}_{CT-NSC} = 4.7g$$

$$CMR = \frac{\hat{S}_{CT-NSC}}{S_{MT}} = 3.13$$

$$S_{MT} = 1.5g$$

Axis labels: Sa (g) (vertical); Max Inter-Story Drift (horizontal).
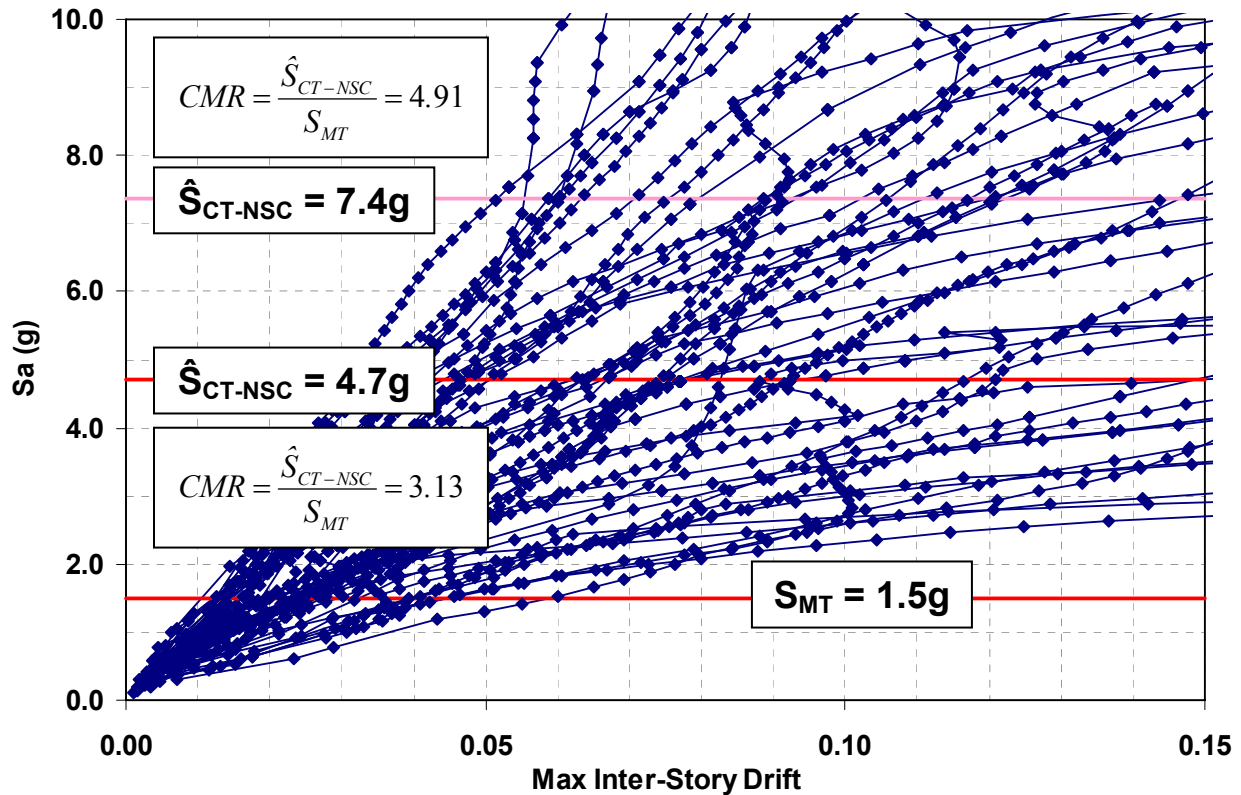
Figure 8-11 Incremental Dynamic Analysis (IDA) Results for SW320 with Non-Deteriorated Material Model

As expected, no flat-lines were observed in the IDA curves up to 15% inter-story drift. For this case where the collapse point is not evident, different limits must be selected for the purpose of estimating the median 'collapse' intensity. Here though, the term 'collapse' does not refer to an actual archetype collapse but rather to a condition where a given parameter limit is reached (this is called a non-simulated collapse limit state in the FEMA P695 methodology). Several DMs can be selected as the relevant limit states and judgment must be exercised to select the appropriate one. For example, if a damage measure corresponding to a relatively large interstory drift

358

condition (i.e., 15% drift) was selected as the limit state, the corresponding median collapse limit intensity, $\hat{S}_{CT\text{-}NSC}$, would be 7.4g and the CMR would be 4.2. Obviously, this resulting CMR is significantly higher than the previous CMR of 2.4 obtained for SW320 with degradation material model. Alternatively, considering that the SW320 median collapse interstory drift occurred at 7.6% drift (Figure 8-7), and arbitrarily selecting this level as the limit for the damage measure, the values of $\hat{S}_{CT\text{-}NSC}$ and CMR would drop down to 4.7g and 3.1, respectively.

Using the latter results to assess the objective mentioned in the first paragraph of this sub-section, the collapse fragility curve for SW320 with EPP material is compared in Figure 8-12 to the previous results for SW320 with deteriorated material model (for completeness, the collapse fragility curve for SW320K is also included in that figure). The fragility curve for the former case shifts to the right of that for the latter case. In other words, CMR increases from 2.4 for the SW320 with severe deteriorated material model, to 3.1 for the SW320 with non-deteriorated (EPP) material model. Hence, if using a material model having a less severe degradation than what was defined in Figure 6-31 for SW320, the resulting CMR would be between these lower- and upper-bound values. The fragility curves shown in Figure 8-12 illustrate how results of this study could be possibly affected if future research was to be conducted with models having less severe strength degradation. At this time, however, the more severe degradation model was retained for reasons presented above.

8.5   Comparison of IDA Results between 3- and 10-Story SPSW Archetypes

To investigate how the observations made on the seismic performance of the 3-story SPSW archetypes would vary as a function of number of stories, it was decided to consider archetypes with a greater number of stories. As a starting point, it was decided to investigate 10-story archetypes. For design, it was assumed that uniform infill plate yielding could develop over the entire wall 10-story SPSW (per the sway plastic collapse mechanism). Consequently, the same capacity design principle used to design the 3-story archetypes were applied to design the 10-story archetypes, with the expectation that comparable observations on the seismic behaviors between the two groups of archetypes could be established.
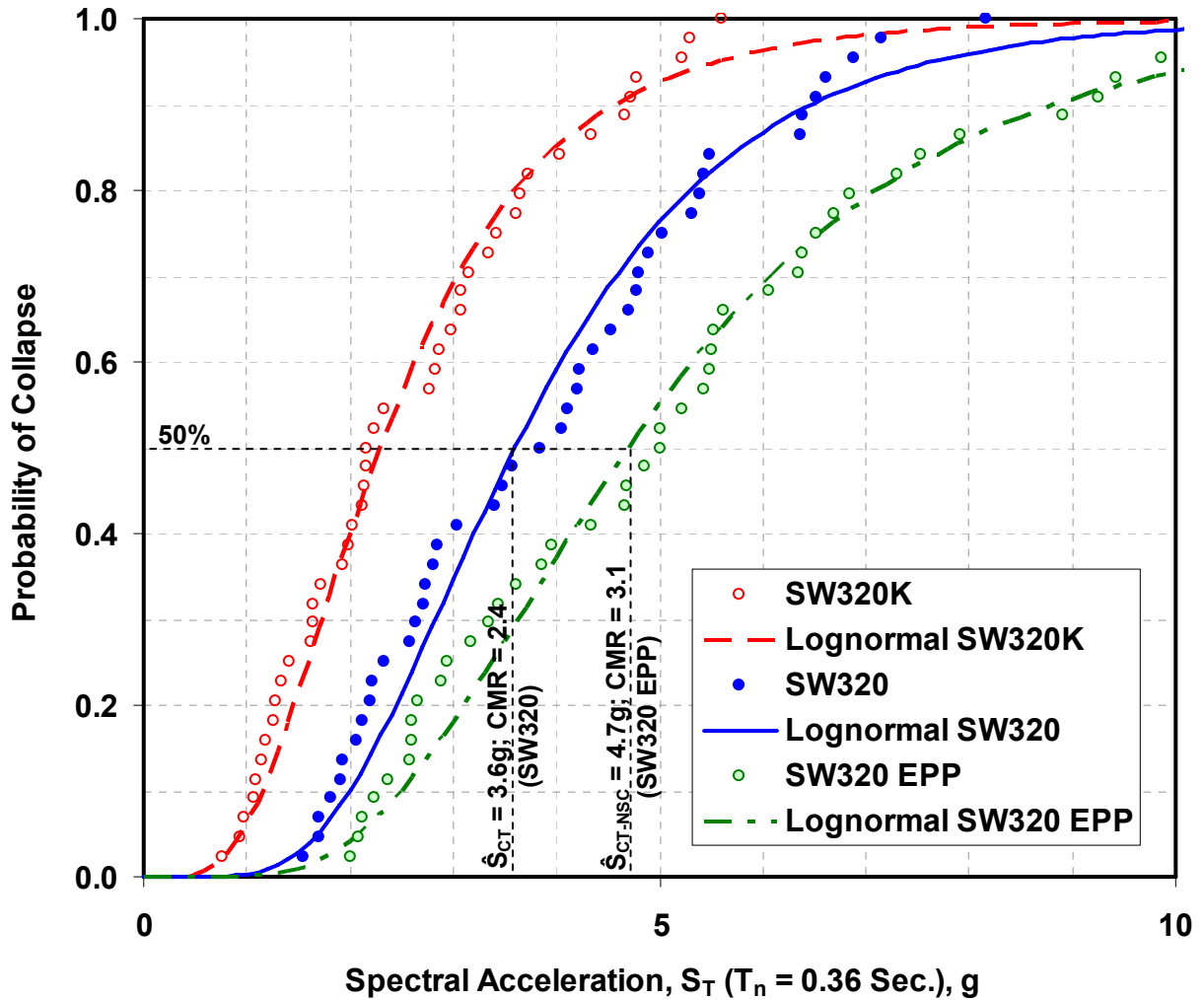
Figure 8-12 Comparison of Collapse Fragility Curves between Archetypes with Deteriorated and Non-Deteriorated Material Model

As was done for the 3-story archetypes, two 10-story SPSW archetypes were designed considering 100% of the design force resisted by the web alone (SW1020) and a corresponding balanced design (SW1020K) case. The resulting member sizes were presented in Table 7-8. This section presents IDA results for these 10-story archetypes; the resulting CMR values are compared to those reported for the 3-story archetypes (i.e., SW320 and SW320K).

Collapse fragility curves for SW1020 and SW1020K are presented in Figure 8-13: Spectral acceleration intensities at which 22 ground motions caused the two archetypes to collapse (median collapse capacities) are 3.40g and 1.92g, respectively. In this case, on the basis of the response spectra plotted in Figure 7-9, spectral acceleration at the MCE level (S_{MT}) for the

$$CMR_{SW1020} = \frac{\hat{S}_{CT}}{S_{MT}} = \frac{3.40}{0.83} = 4.08$$

$$CMR_{SW1020K} = \frac{\hat{S}_{CT}}{S_{MT}} = \frac{1.92}{0.83} = 2.30$$
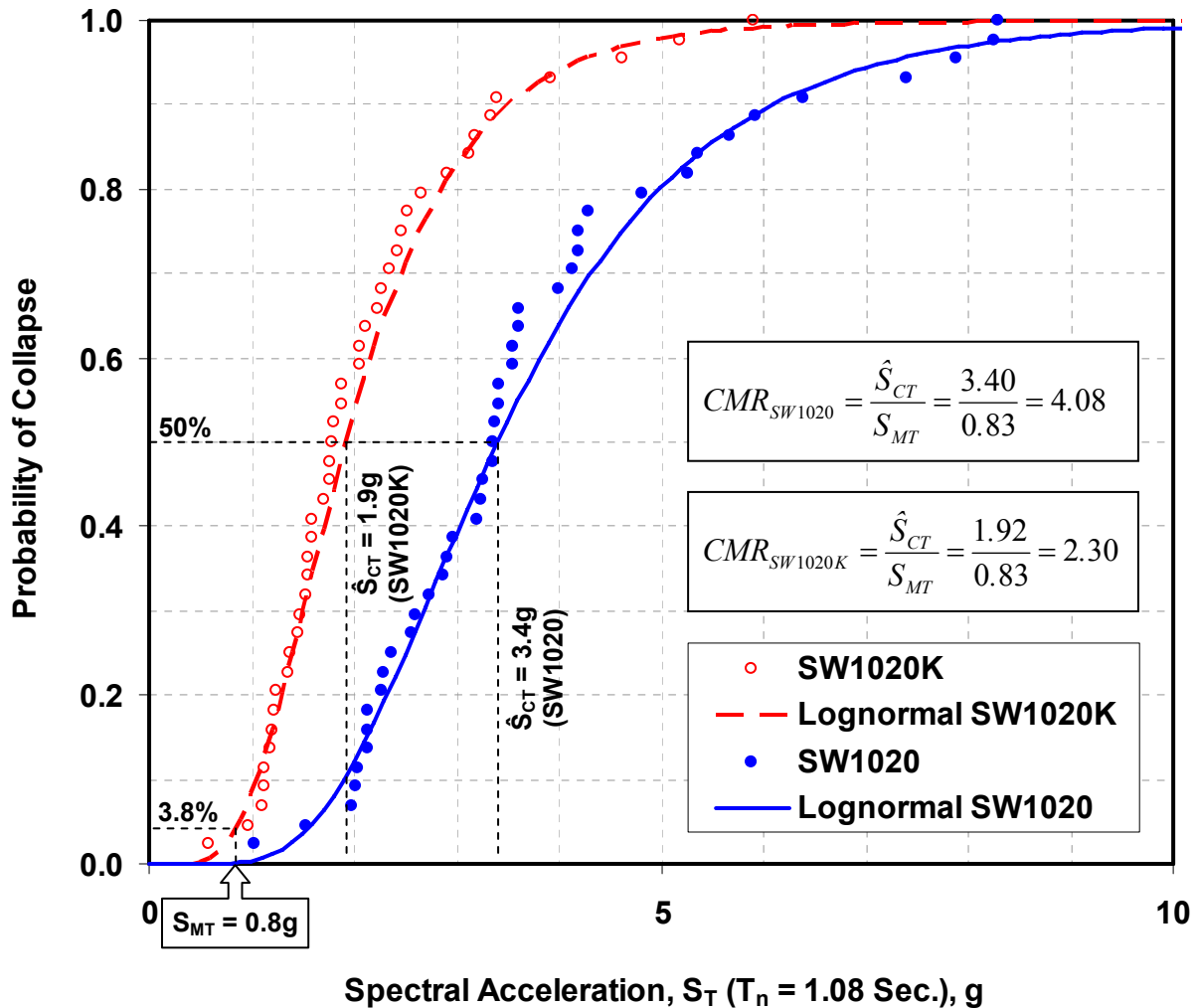
Figure 8-13 Collapse Fragility Curves for SW1020 and SW1020K

archetype fundamental period of 1.08 seconds is 0.83g. Hence, the CMR values for SW1020 and SW1020K are 4.08 and 2.30, respectively. The same trend previously observed in the 3-story archetypes is also observed here for the 10-story archetypes, in that the balanced design case has a CMR lower than the 100% design case. Under MCE level ground motions, SW1020 has a less than 0.1% probability of collapse, while SW1020K has 3.8% probability of collapse. As previously mentioned, the theoretical fundamental period was used for the purpose of evaluating the CMR. While both SW1020 and SW1020K have the same theoretical fundamental period of 1.08 sec., their fundamental periods obtained from eigenvalue analysis in OpenSees framework were respectively 1.0 and 1.47 seconds. For the same reason explained in Section 8.3.3, this slight discrepancy would have a marginal impact on the SSF values of both archetypes. As such,

the resulting ACMR (= SSF × CMR) would only change by less than 5% if analytical fundamental periods were used instead.

Figure 8-14 compares collapse fragility curves of the 3- and 10-story archetypes. The fragility curves were developed using spectral acceleration and PGA as the intensity measures, shown respectively in Figures 8-14a and 8-14b. Since both sets of archetypes have different fundamental periods and spectral accelerations at the MCE level, the horizontal axis of Figure 8-14a is presented in terms of CMR (i.e., by normalizing $\hat{S}_{CT}$ with S_{MT}). Though the IM used for Figure 8-14b is independent of the fundamental period, for consistency, the horizontal axis is also presented in terms of CMR by normalizing PGA_{CT} with PGA_{MT}. As shown in the figure for the two basic configurations considered (i.e., 100% and balanced design cases), the 10-story archetypes have larger margin to collapse compared to the 3-story archetypes. Using spectral acceleration as the IM, CMR for the 10-story archetypes are at least 1.5 times larger than that in the 3-story archetypes. The difference is even larger (i.e., approximately twice) when using PGA as the IM. Moreover, probability of collapse at the MCE level (i.e., when CMR = 1.0) is lower for the 10-story archetypes, especially for the balanced design case. From Figure 8-14a, the collapse probability reduces from approximately 20% for SW320K to 4% for SW1020K. The difference is marginal for the 100% design case, as both SW320 and SW1020 already have relatively low probabilities of collapse at the MCE level.

The fact that the 10-story archetypes exhibited significantly higher CMR compared to the 3-story archetypes was initially suspected to maybe indicate that a uniform sway plastic collapse mechanism had not fully developed over the full height of the 10-story archetypes at the MCE level. Specifically, it was suspected that the infill plates at several stories in the 10-story archetypes (possibly at the lower stories) had not yielded and that several boundary elements had not reached a complete plastification at the MCE level. If this hypothesis was true, these archetypes would then have significant strength to sustain ground motion intensities larger than that at the MCE level. In order for these archetypes to reach the uniform sway plastic mechanism, to start experiencing strength deterioration, and to eventually collapse, the ground motion intensity would have to be further increased. By comparison, the 3-story archetypes were suspected have reached their uniform sway plastic mechanism at the MCE level, with collapse
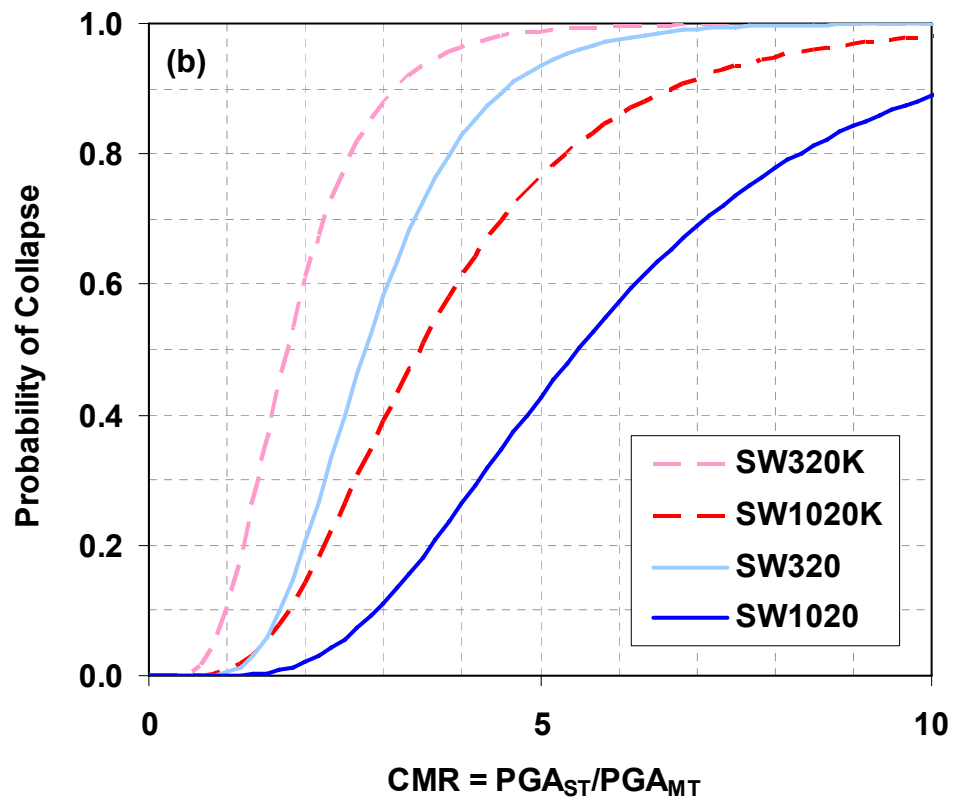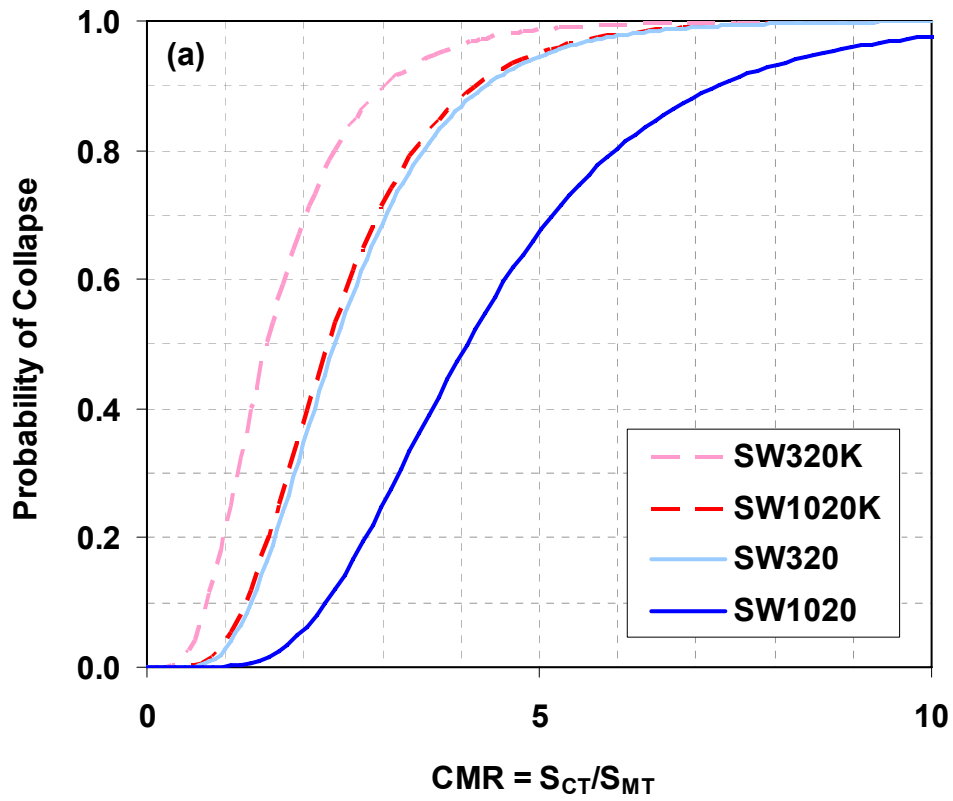
Figure 8-14 Collapse Fragility Curves for 3- and 10-Story Archetypes: (a) Spectral Acceleration as IM; (b) PGA as IM

occurring soon after. As such, the resulting CMR for the 10-story archetypes would be higher compared to that for the 3-story archetypes.

To investigate whether the above hypothesis indeed explained the aforementioned phenomenon, the local behavior of both sets of archetypes were examined. Specifically, infill plate yielding and plastic hinge distributions, cross-section rotations, and inter-story drifts of both groups were compared at the MCE level, the last stable point, and the collapse point. For this investigation, results from 3 arbitrarily selected ground motions were examined, namely, ground motion HDLT262, HE11230, and YER270. Their spectral accelerations and acceleration time histories are shown in Figure 8-15. Spectral acceleration intensities when these ground motions caused the 3- and 10-story archetypes to collapse (S_{CT}) are shown in Figure 8-16, plotted relative to that of the MCE response spectra. The following two sub-sections present the observation of these local behaviors of both groups of archetypes.

8.5.1 Conventional Design Case ($\kappa = 1$): SW320 versus SW1020

A first comparison was conducted on the infill plate yielding and plastic hinge distributions, as shown in Figures 8-17 and 8-18, respectively, for SW320 and SW1020. In each figure, the distributions present the results at the end of time history analyses for three considered ground motions at 3 different ground motion intensity levels, namely: (a) at the MCE level, when spectral intensities of the ground motions reached that of the MCE spectra; (b) at the last stable point, before the ground motions caused the archetypes to reach a near collapse stage (Figure 8-1); and (c) at the collapse point, when the ground motions caused the archetypes to collapse. Note that the results for the collapse point were actually taken when interstory drift reached a 15% drift (i.e. on their way toward infinity, due to dynamic instability), in order to keep reasonable comparisons of observed behaviors with those of the other two conditions. Note that the yielding distribution results in the positive and negative directions are generally different (partly because ground motion time histories are typically un-symmetric), and that the worse state of damage between the two directions was selected to represent the condition at one particular intensity level. As shown in those figures for the MCE level, the 3- and 10-story archetypes exhibited somewhat similar infill plate yielding patterns. The results under HDLT262 ground motion are used to explain observed behaviors (Figures 8-17a and 8-18a). The 3-story archetype (SW320) exhibited
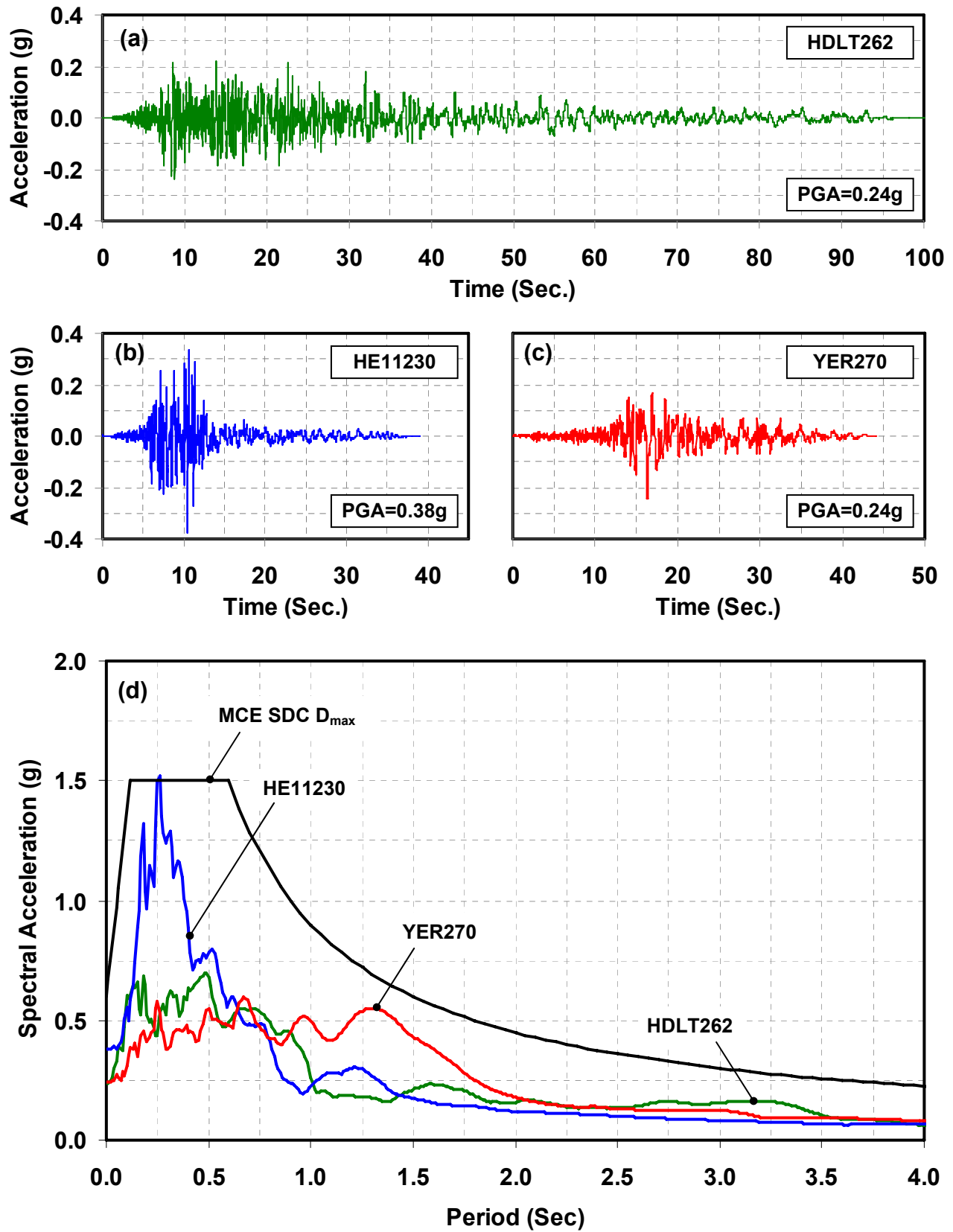
Figure 8-15 Acceleration Time Histories and Spectral Accelerations for 3 Ground Motions
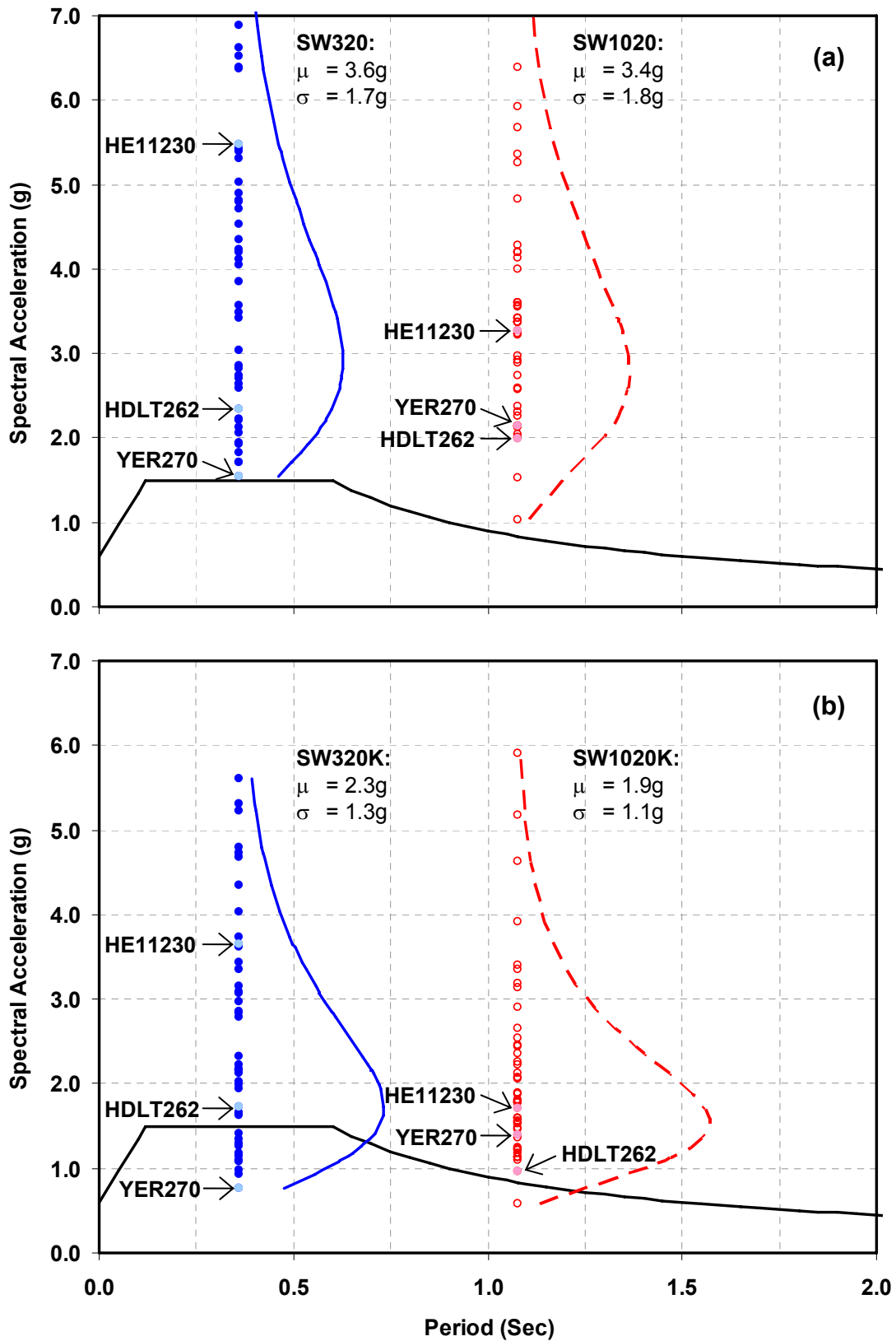
Figure 8-16 MCE Response Spectra and Logarithmic Distribution of S$_{CT}$:
(a) SW320 versus SW1020; (b) SW320K versus SW1020K
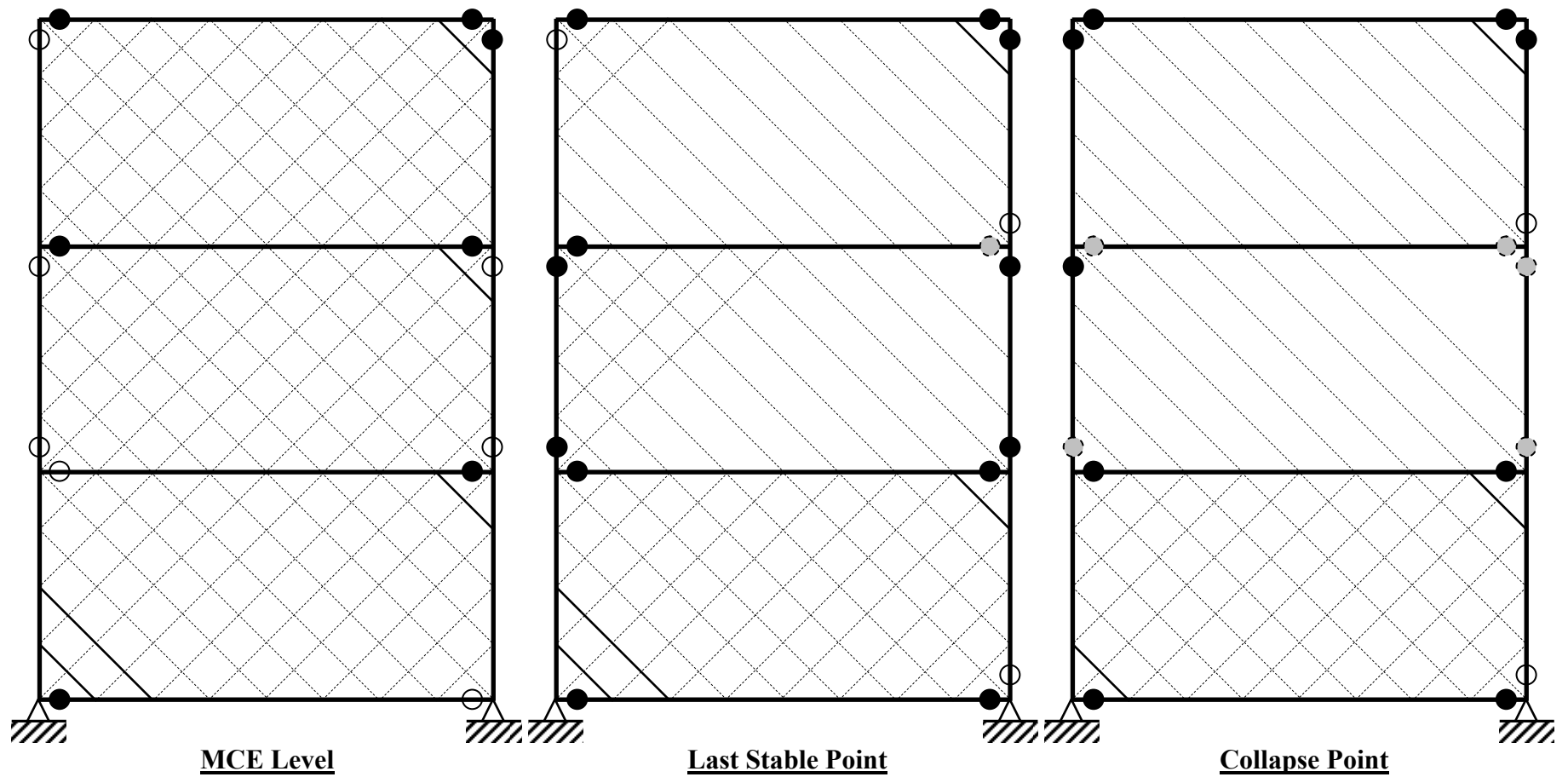
366

Legend:

○ = yielding condition (yielding remains within HBE flanges)

● = full plastic condition of fiber hinge

◍ = strength degradation of fiber hinge

········· = strip yielding ($P = P_y$)

Figure 8-17 Plastic Hinge and Strip Yielding Distributions for SW320 under Three Selected Ground Motions: (a) HDLT262

MCE Level   **Last Stable Point**   **Collapse Point**
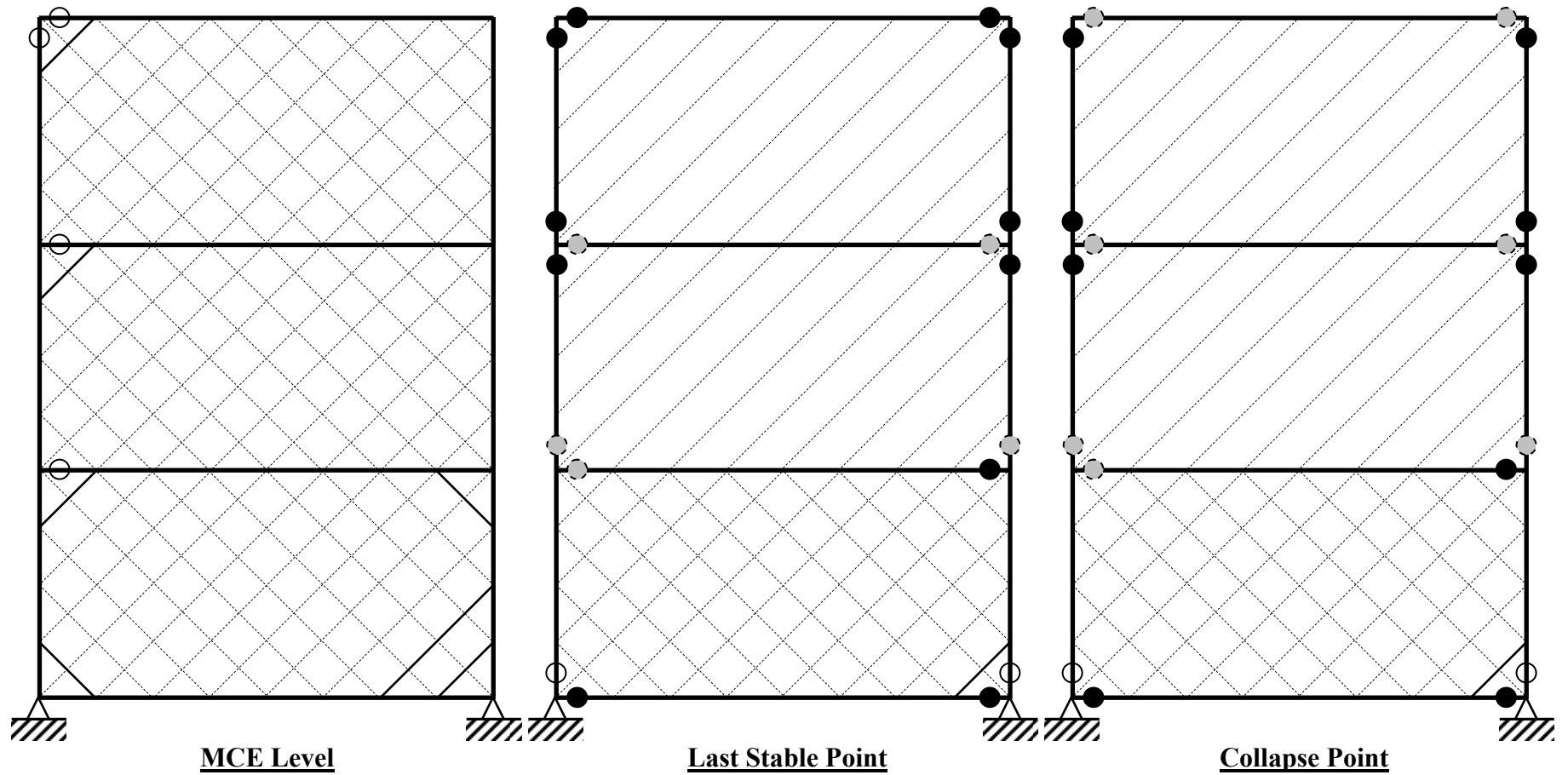
Legend:

○ = yielding condition (yielding remains within HBE flanges)

● = full plastic condition of fiber hinge

◐ = strength degradation of fiber hinge

----------- = strip yielding ($P = P_y$)

Figure 8-17 Plastic Hinge and Strip Yielding Distributions for SW320 under Three Selected GMs – Cont'd: (b) HE11230

Subjected to YER270 GM,
SW320 collapse point was
below the MCE Level

Collapse Point

Legend:

○ = yielding condition (yielding remains within HBE flanges)

● = full plastic condition of fiber hinge

◔ = strength degradation of fiber hinge

············ = strip yielding $(P = P_y)$

Figure 8-17 Plastic Hinge and Strip Yielding Distributions for SW320 under Three Selected GMs – Cont'd: (c) YER270

Strength degradation on strips

MCE Level   Last Stable Point   Collapse Point

Legend: [See Figure 8-17]

Figure 8-18 Plastic Hinge and Strip Yielding Distributions for SW1020 under Three Selected Ground Motions: (a) HDLT262

MCE Level   **Last Stable Point**   **Collapse Point**

Legend: [See Figure 8-17]

Figure 8-18 Plastic Hinge and Strip Yielding Distributions for SW1020 under Three Selected Ground Motions – Cont'd: (b) HE11230

371

MCE Level　　　　**Last Stable Point**　　　　**Collapse Point**

Legend: [See Figure 8-17]

**Figure 8-18 Plastic Hinge and Strip Yielding Distributions for SW1020 under Three
Selected Ground Motions – Cont'd: (c) YER270**

a fully yielded condition and the 10-story archetype (SW1020) had a few corner strips remaining elastic at the lower stories while the remaining strips yielded. In addition, several strips of SW1020 at the top story started to deteriorate at that MCE level. With respect to the plastic hinge distribution on boundary elements in SW320, except for those two joints at the right and left joints of the bottom two HBEs that started to yield, all other HBE ends have reached a full plastification stage; signs of yielding also occurred at its second story VBEs. As for SW1020, except for the HBEs at the first two floors, all other HBEs have reached their full plastic condition. As a consequence of strength deterioration in several of strips at the tenth floor of SW1020, the VBEs at this floor experienced yielding and full plastification of hinges.

As the intensity of ground motion increased, plastification in HBEs progressed and infill plates progressively lost their strength; as a result of this loss of strength, story shears caused plastification of the VBEs. Specifically for SW320 at the collapse point (Figure 8-17a), the top two infill plates have completely lost their strength (i.e., see the infill plate distribution in the positive direction) and a soft-story mechanism occurred at the second story as indicated by deteriorating plastic hinge at the bottom of the second story VBEs. The same condition also occurred for SW1020 (Figure 8-18a), where infill plates at the top six stories have no strength left and a soft-story mechanism occurred at the fifth floor.

The collapse mechanisms for both archetypes can also be observed by plotting lateral displacements along the height of the building, as shown in Figure 8-19. The figure plots absolute lateral displacements recorded at each considered intensity level and ground motions. Here, story drift at one particular floor is defined as the floor displacement divided by its height measured from the base (also known as the total drift). In combination with the previous two figures, the results in Figure 8-19 allow observations of the consequences of soft story-mechanism which caused steel walls at levels below the location of the soft-story mechanism to experience smaller deformations compared to those above. Hence, infill plates at the lower levels remained in the plastic condition and no strength loss was observed.

Furthermore, Figure 8-20 compares maximum cross-section rotation recorded at boundary elements (i.e., HBEs and VBEs) and interstory story drift along the height of the archetypes.
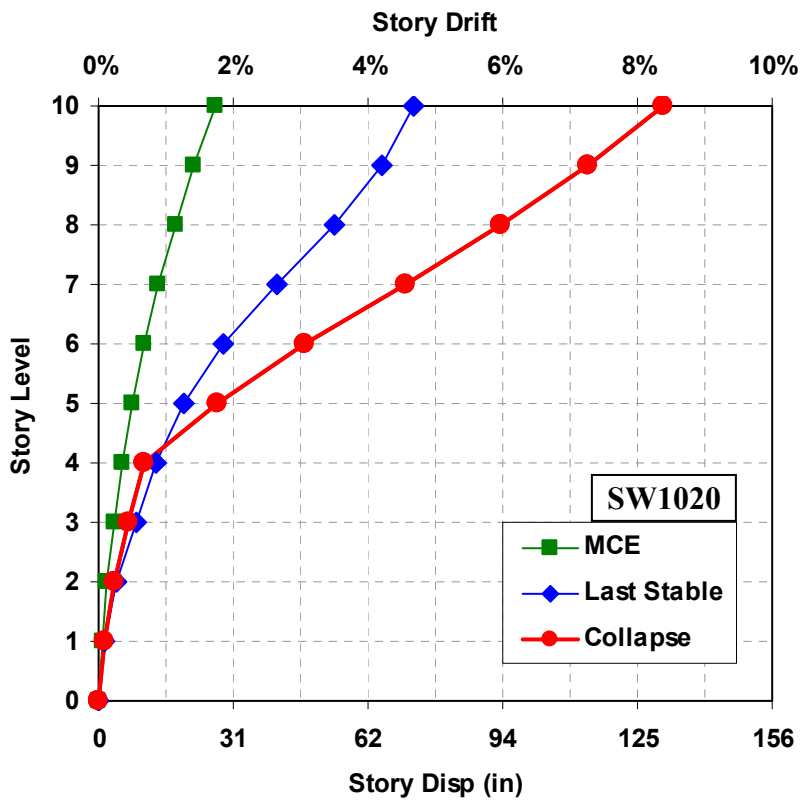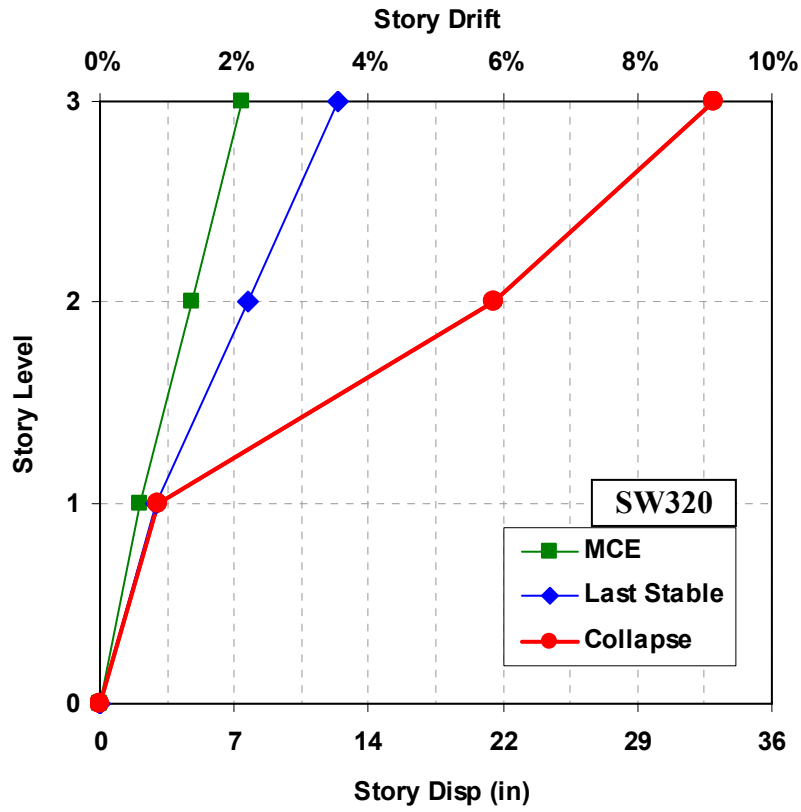
**Figure 8-19 Deformed Shapes under Three Selected Ground Motions ($\kappa = 1$):
(a) HDLT262**
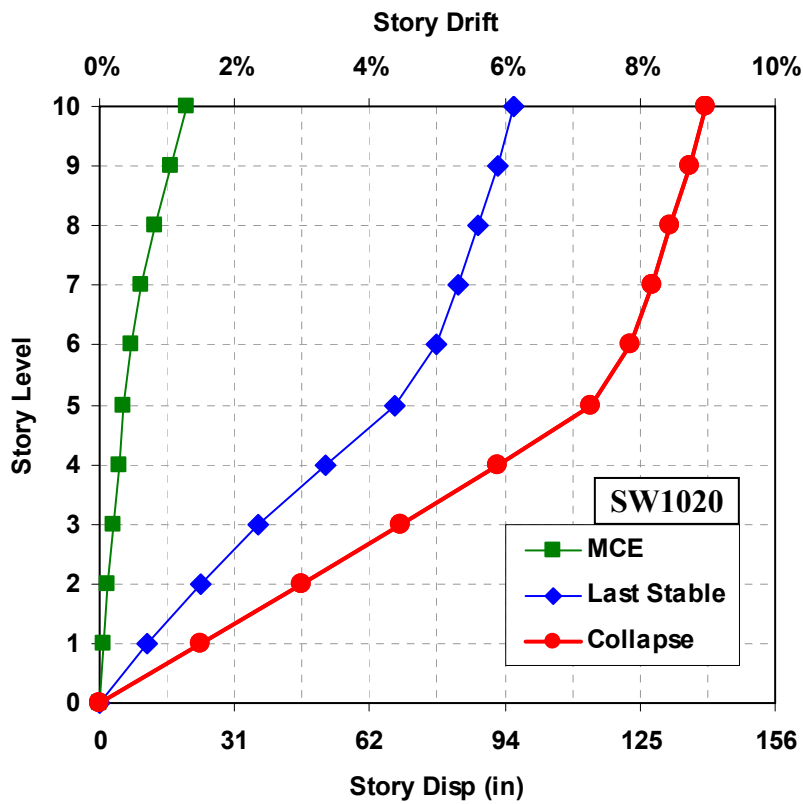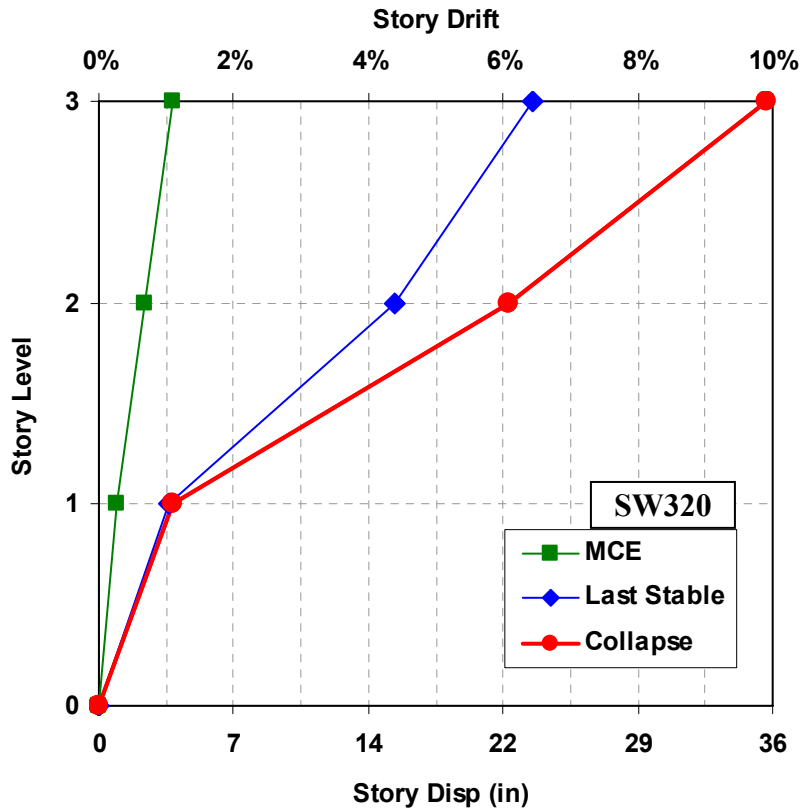
**Figure 8-19 Deformed Shapes under Three Selected Ground Motions (κ = 1) – Cont'd:
(b) HE11230**
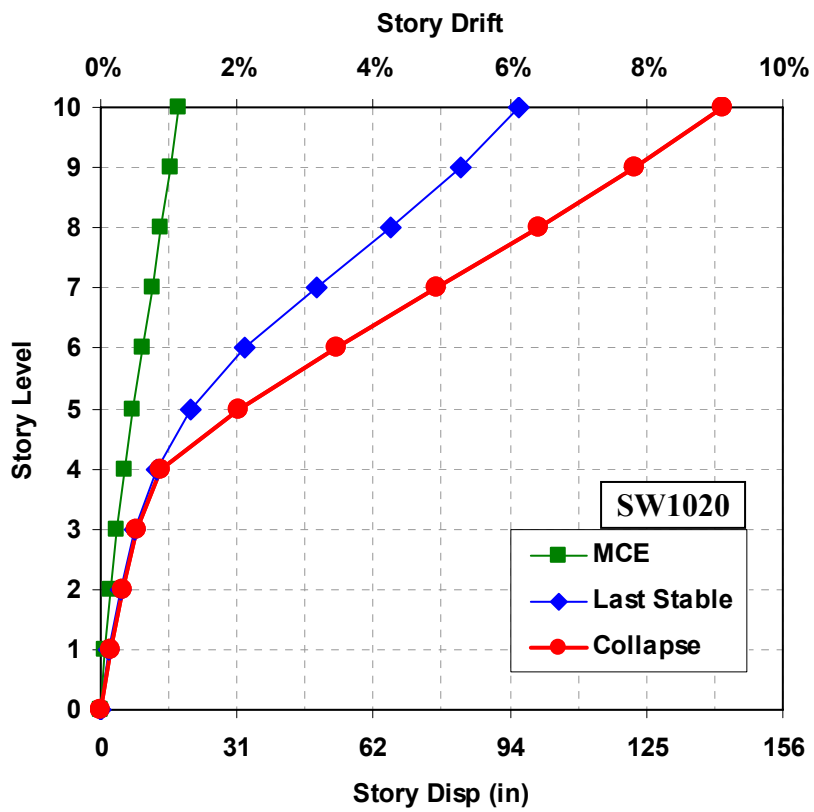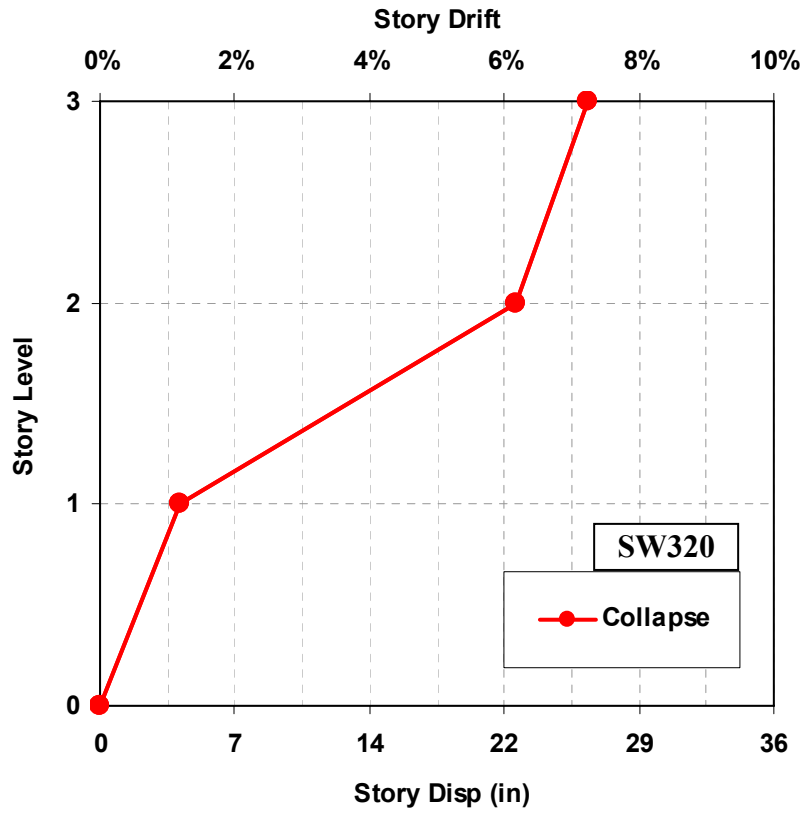
Figure 8-19 Deformed Shapes under Three Selected Ground Motions (κ = 1) – Cont'd: (c) YER270
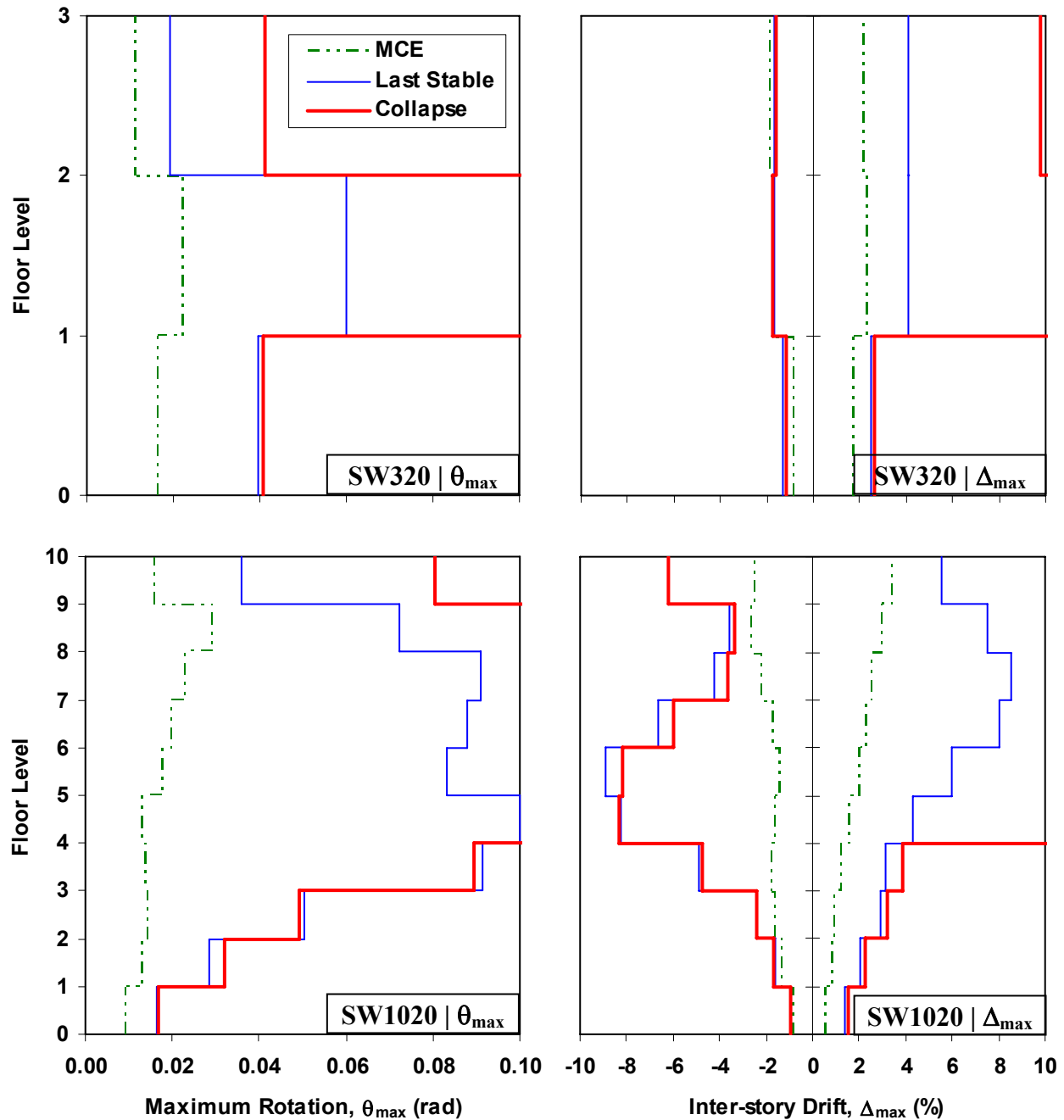
Figure 8-20 Maximum Cross-Section Rotation and Interstory Drift under Three Considered Ground Motion (κ = 1): (a) HDLT262

Plotted on the top row are curves for SW320, whereas on the bottom row are curves for SW1020. Again, the results are presented for the three aforementioned intensity levels. In terms of cross-section rotations, both archetypes have comparable maximum cross-section rotations, θ_{max}, at the MCE level; the largest θ_{max} among stories were 0.02 and 0.03 radians for SW320 and SW1020,
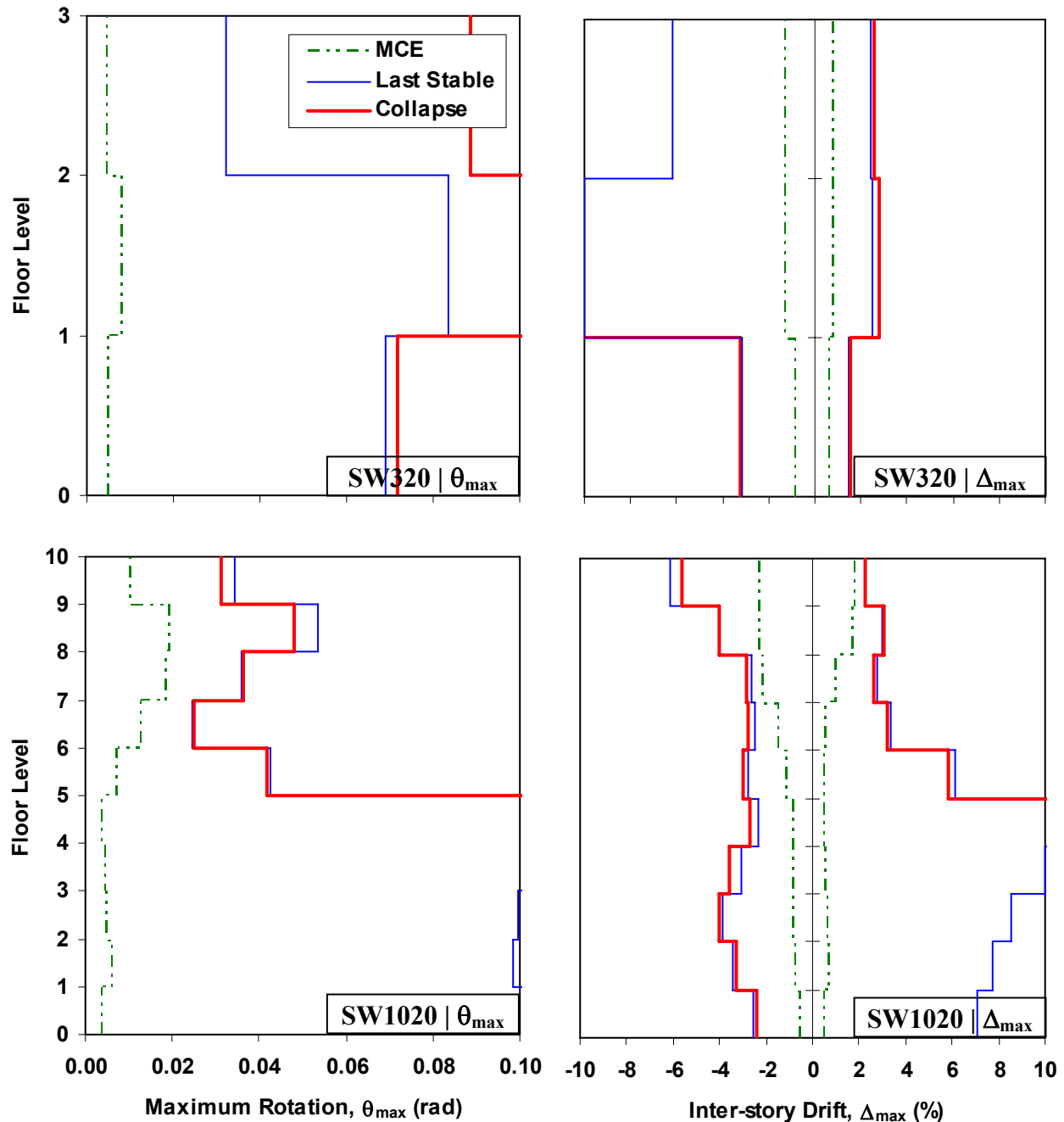
Figure 8-20 Maximum Cross-Section Rotation and Interstory Drift under Three Considered Ground Motion (κ = 1) – Cont'd: (b) HE11230

respectively. At the last stable condition however, both archetypes reached considerably different values of θ_{max}. Maximum rotations varied from 0.02 to 0.04 radians for SW320, while those for SW1020 varied from 0.02 to 0.10 radians. When collapse occurred, both archetypes experienced cross-section rotations larger than 0.10 radians. This is consistent with the material model
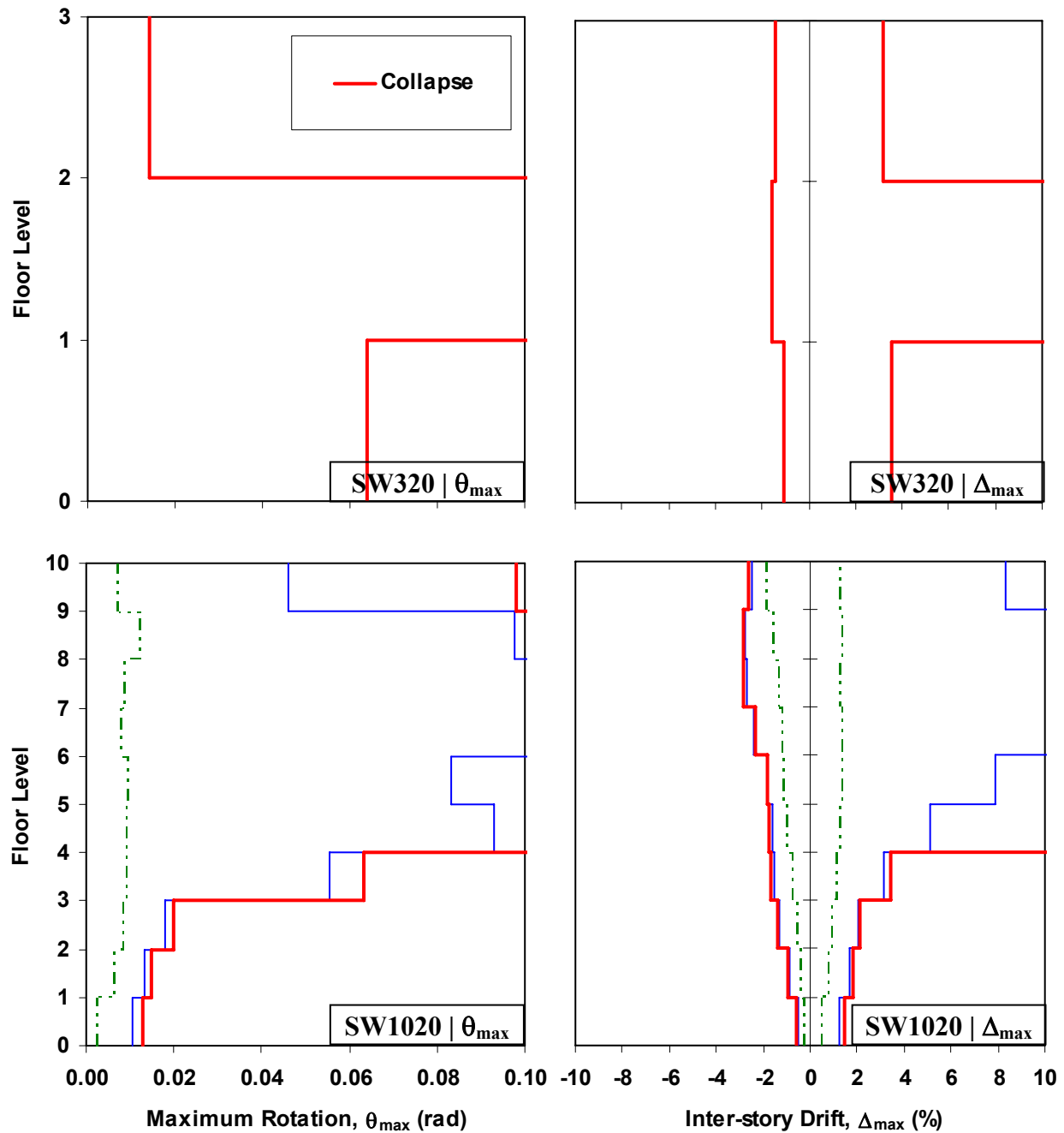
Figure 8-20 Maximum Cross-Section Rotation and Interstory Drift under Three Considered Ground Motion (κ = 1) – Cont'd: (c) YER270

presented in Figure 7-10. The same trend was also observed in terms of interstory drift. At the MCE level, the largest interstory drifts were 2.3% and 3.4% for SW320 and SW1020, respectively. Prior to collapse (the last stable point), the interstory drift varied from 2.5 to 4.1% for the former and from 1.4 to 8.9% for the latter archetype.

8.5.2 Balanced Design Case ($\kappa = \kappa_{balanced}$): SW320K versus SW1020K

The same comparison of local behaviors as in the conventional design case ($\kappa = 1$) archetypes was conducted for the balanced design case ($\kappa = \kappa_{balanced}$) archetypes. Overall, the same trend as reported in the previous section was observed for the balanced design case but with greater infill plate yielding and boundary element plastification. Infill plate yielding and plastic hinge distributions for SW320K and SW1020K are presented in Figures 8-21 and 8-22, respectively. Again, the results under the HDLT262 ground motion are used to explain observed behaviors (Figures 8-21a and 8-22a). In contrast with their counterpart archetypes (i.e., SW320 and SW1020), these archetypes have lost several of strips at the MCE level. Infill plates of SW320K at the top two stories have partial shear capacity to sustain lateral loads beyond the MCE level, while the same condition occurred at the top four stories of SW1020K. Plastification occurred at each end of every HBE and at the second story VBEs for SW320K. As for SW1020K, except for the bottom anchor beam, all other HBEs have reached their fully plastic condition and several plastic hinges (i.e., at the 6th to 9th stories) even have started to deteriorate, which led to a soft-story mechanism. The mechanism occurred at the second floor for SW320K while that for SW1020K occurred at the fifth floor, which can be confirmed by observing lateral displacements along the height of the building in Figure 8-23.

Furthermore, the maximum cross-section rotation recorded at boundary elements and interstory drift along the height of the archetypes are compared in Figure 8-24 for SW320K and SW1020K under all considered ground motions. In terms of these two local behaviors, both archetypes exhibited comparable outcomes. Consider the last stable point prior to collapse for HDLT262 as an example. The largest θ_{max} were 0.06 and 0.07 radians for SW320K and SW1020K, respectively, while the largest interstory drifts were 4.4% and 5.9% for the same respective archetypes. As in the case of conventional archetypes, collapse of these balanced archetypes occurred at larger than 0.10 radians cross-section rotations and 10% interstory drifts.

At this point, no conclusive evidence from investigating these local behaviors that can explain why the 10-story archetypes have higher CMRs compared to the 3-story archetypes. In contrast with the original hypothesis, both archetype groups actually have comparable local damages at the MCE level (i.e., approaching uniform infill plate yielding and plastic hinge distribution); yet
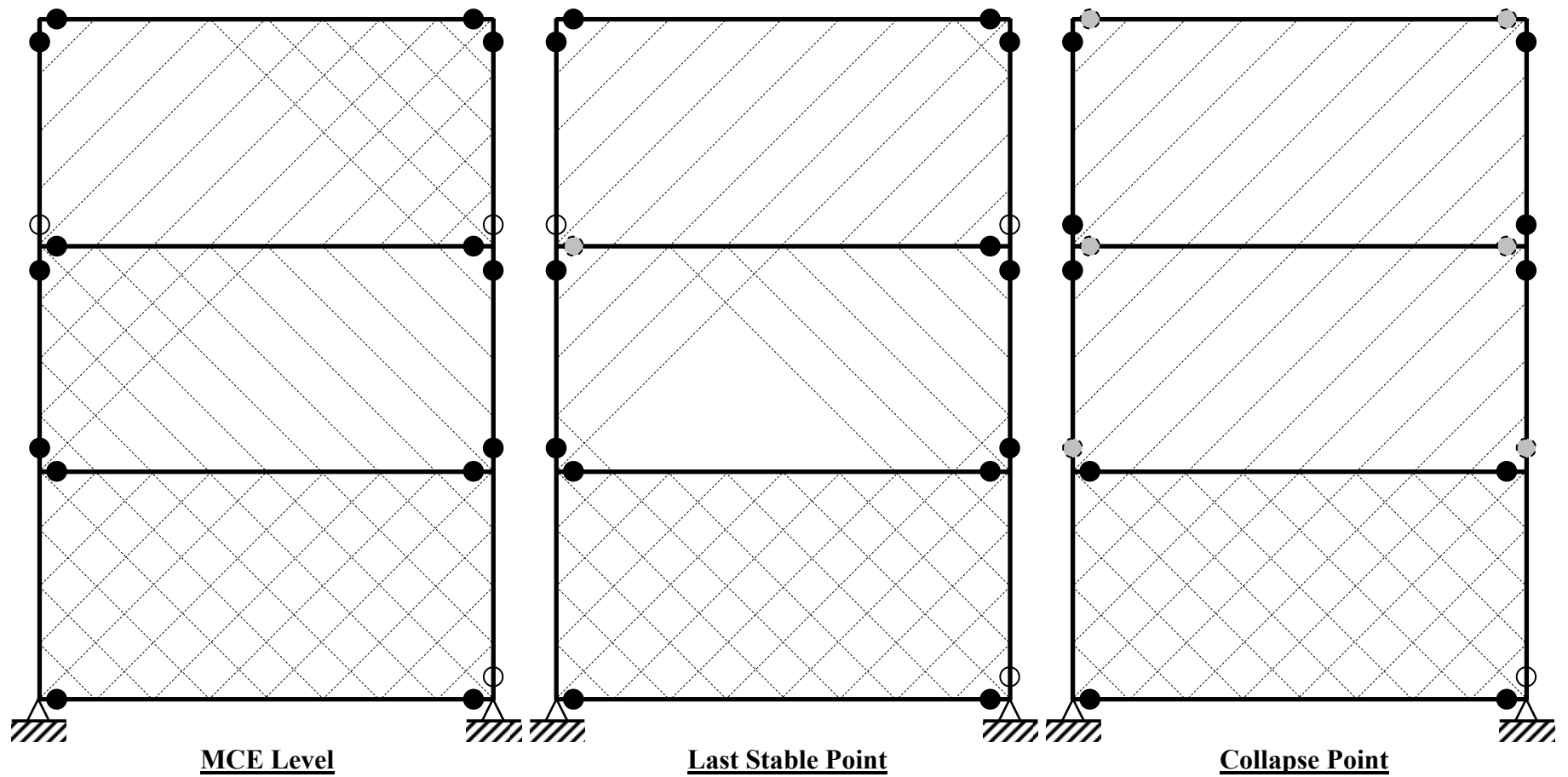
MCE Level **Last Stable Point** **Collapse Point**

Legend:

○ = yielding condition (yielding remains within HBE flanges)

● = full plastic condition of fiber hinge

◐ = strength degradation of fiber hinge

--------- = strip yielding ($P = P_y$)

Figure 8-21 Plastic Hinge and Strip Yielding Distributions for SW320K under Three Selected Ground Motions: (a) HDLT262

| MCE Level | Last Stable Point | Collapse Point |
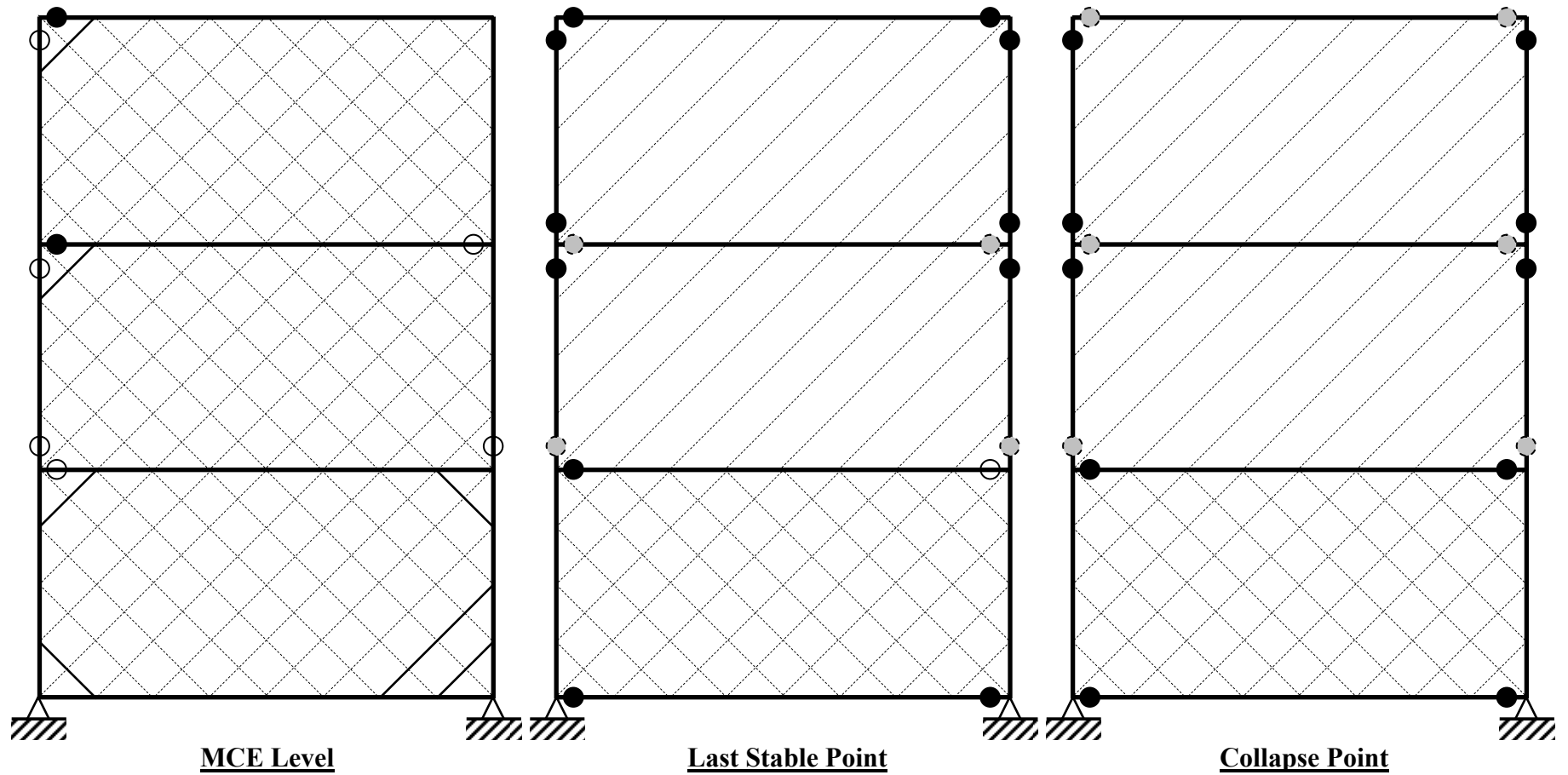
Legend:

   ○ = yielding condition (yielding remains within HBE flanges)

   ● = full plastic condition of fiber hinge

   ◐ = strength degradation of fiber hinge

   ···· = strip yielding ($P = P_y$)

Figure 8-21 Plastic Hinge and Strip Yielding Distributions for SW320K under Three Selected GMs – Cont'd: (b) HE11230

Subjected to YER270 GM,
SW320K collapse point was
below the MCE Level

Collapse Point

○ = yielding condition (yielding remains within HBE flanges)
● = full plastic condition of fiber hinge
◐ = strength degradation of fiber hinge
.... = strip yielding ($P = P_y$)

Figure 8-21 Plastic Hinge and Strip Yielding Distributions for SW320K under Three Selected GMs – Cont'd: (c) YER270

383

Strength degradation on strips

MCE Level   Last Stable Point   Collapse Point

Legend: [See Figure 8-21]

Figure 8-22 Plastic Hinge and Strip Yielding Distributions for SW1020K under Three Selected Ground Motions: (a) HDLT262

| MCE Level | Last Stable Point | Collapse Point |

Legend: [See Figure 8-21]

Figure 8-22 Plastic Hinge and Strip Yielding Distributions for SW1020K under Three Selected Ground Motions – Cont'd: (b) HE11230

MCE Level   **Last Stable Point**   **Collapse Point**

Legend: [See Figure 8-21]

Figure 8-22 Plastic Hinge and Strip Yielding Distributions for SW1020K under Three Selected Ground Motions – Cont'd: (c) YER270

386

Figure 8-23 Deformed Shapes under Three Selected Ground Motions ($\kappa = \kappa_{balanced}$): (a) HDLT262
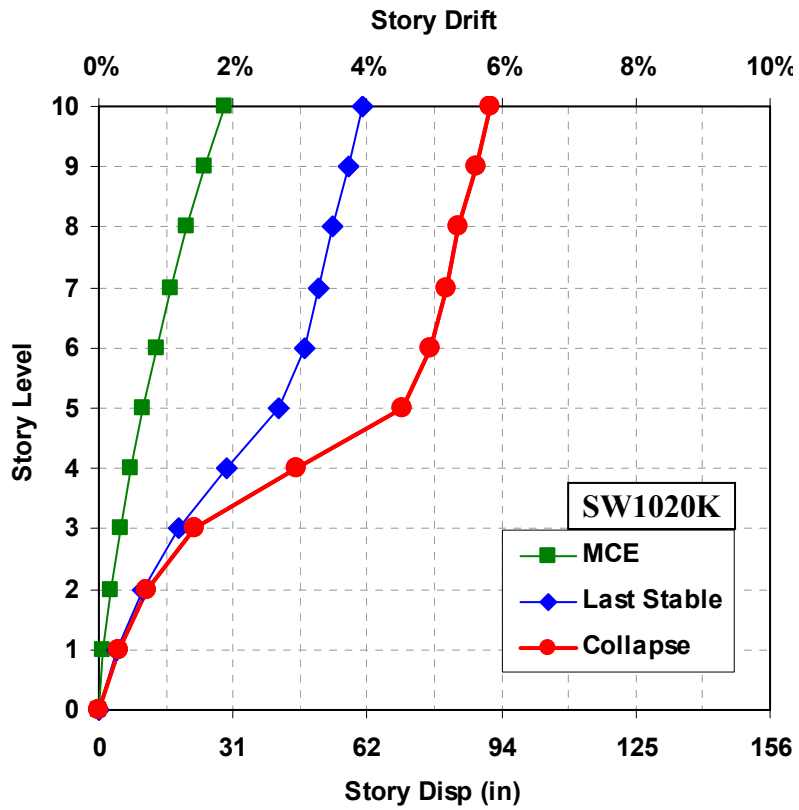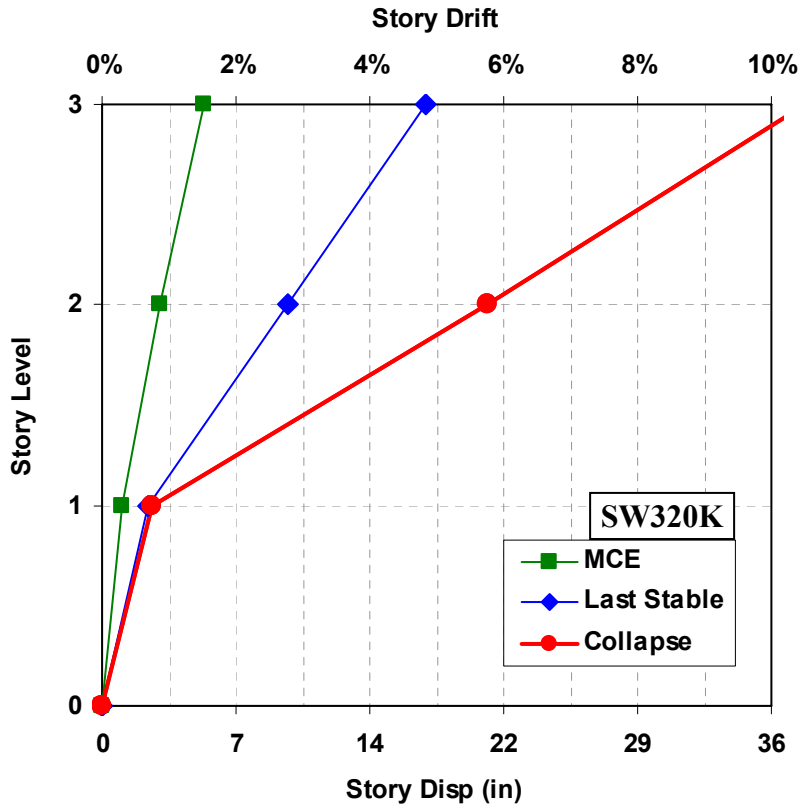
387

Figure 8-23 Deformed Shapes under Three Selected GMs (κ = κ_{balanced}) − Cont'd: (b) HE11230

388
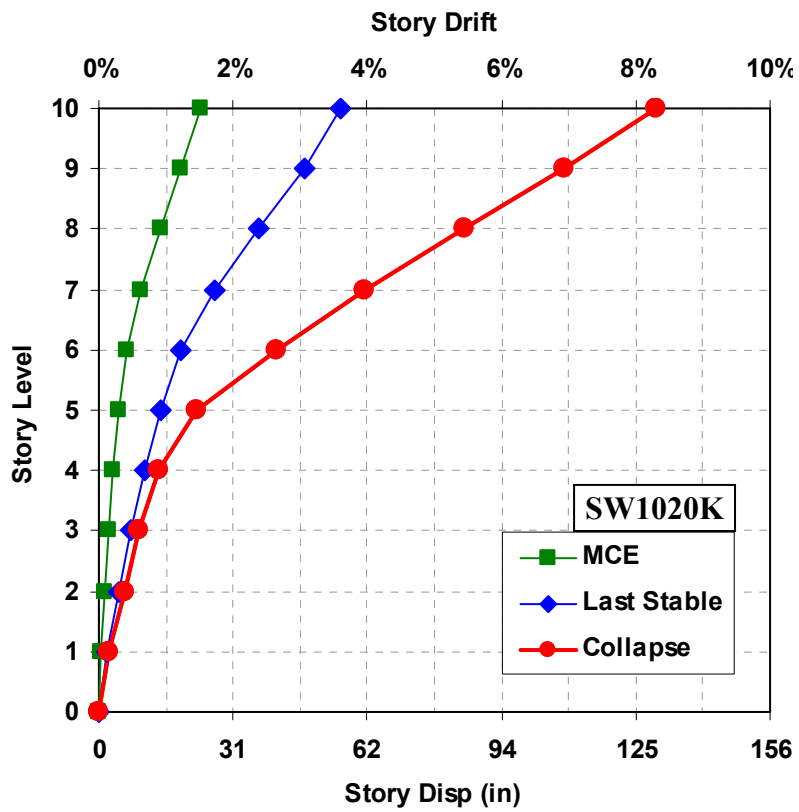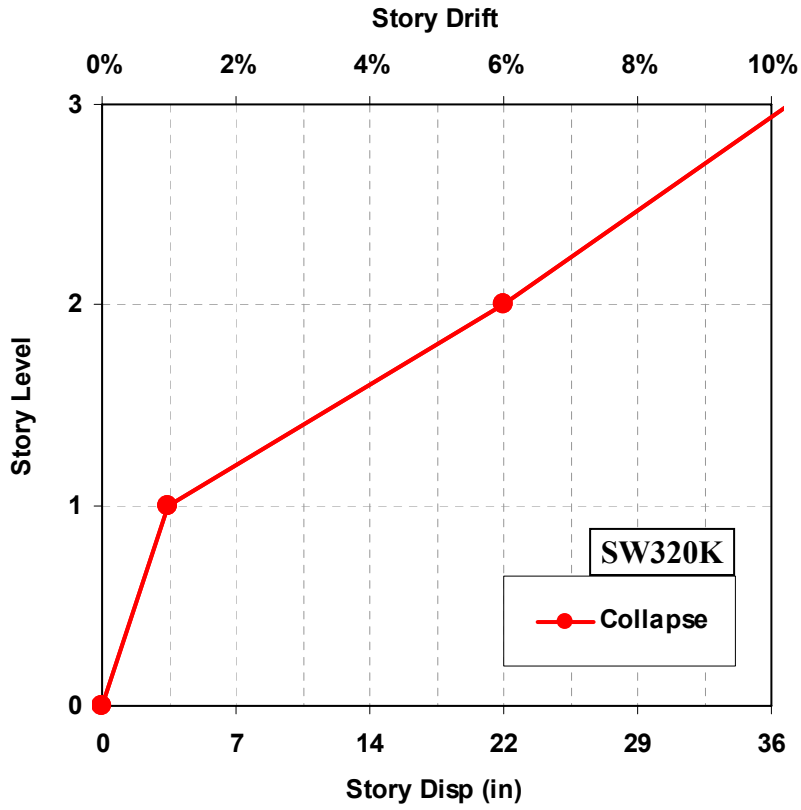
Figure 8-23 Deformed Shapes under Three Selected GM ($\kappa = \kappa_{balanced}$) – Cont'd:
(c) YER270
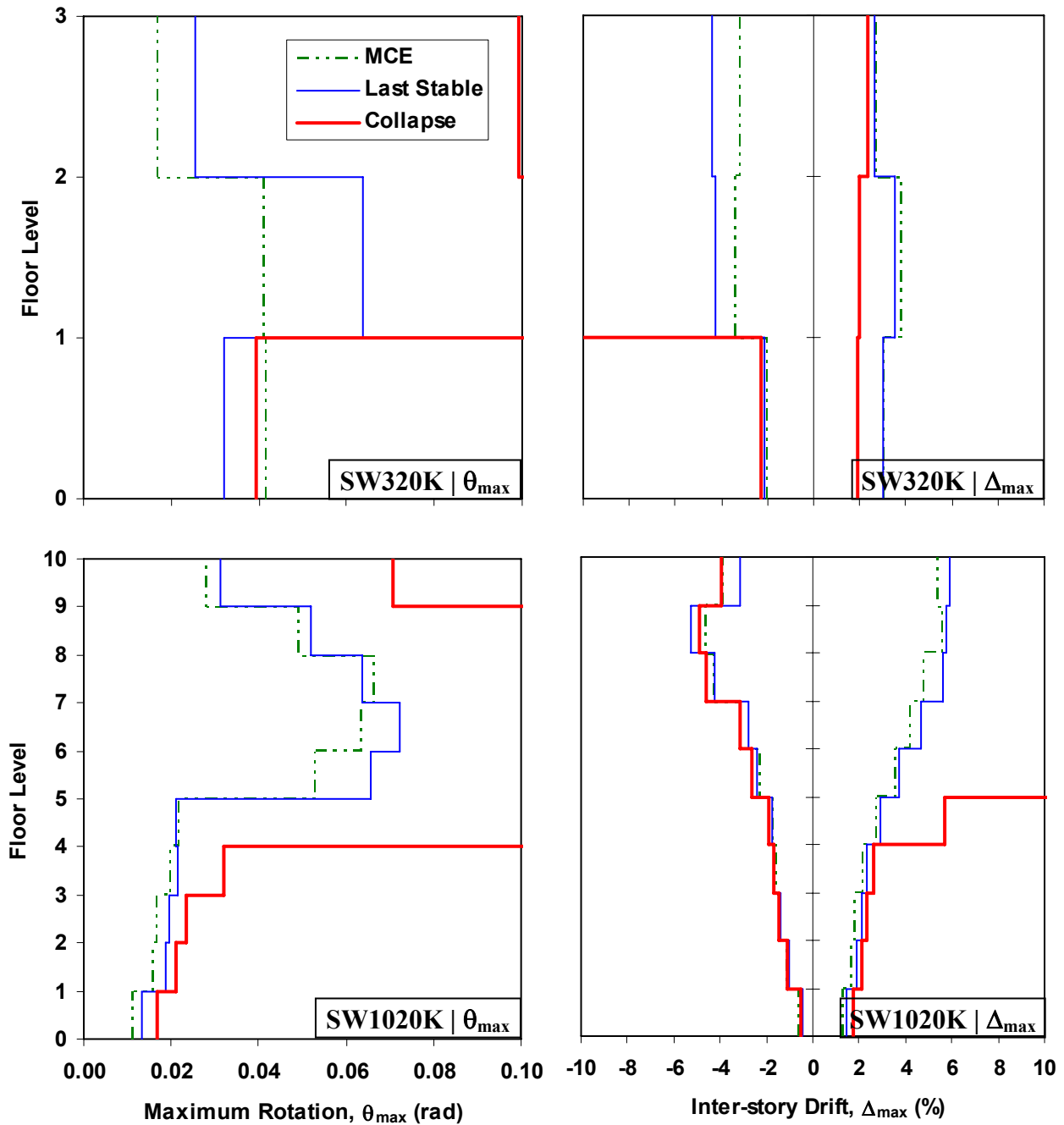
Figure 8-24 Maximum Cross-Section Rotation and Interstory Drift under Three Considered Ground Motion ($\kappa = \kappa_{balanced}$): (a) HDLT262

the 3-story archetypes reached the collapse point sooner than the 10-story archetypes for the conventional archetypes. At the collapse point, spectral acceleration intensities, S_{CT}, for SW320 and SW1020 were 1.56 and 2.38 times higher than their respective spectral acceleration at the MCE level (S_{MT}), respectively. For the balanced archetypes however, the margin between the

390

collapse point and MCE level was smaller. The margins for SW320K and SW1020K were 1.15 and 1.16, respectively.
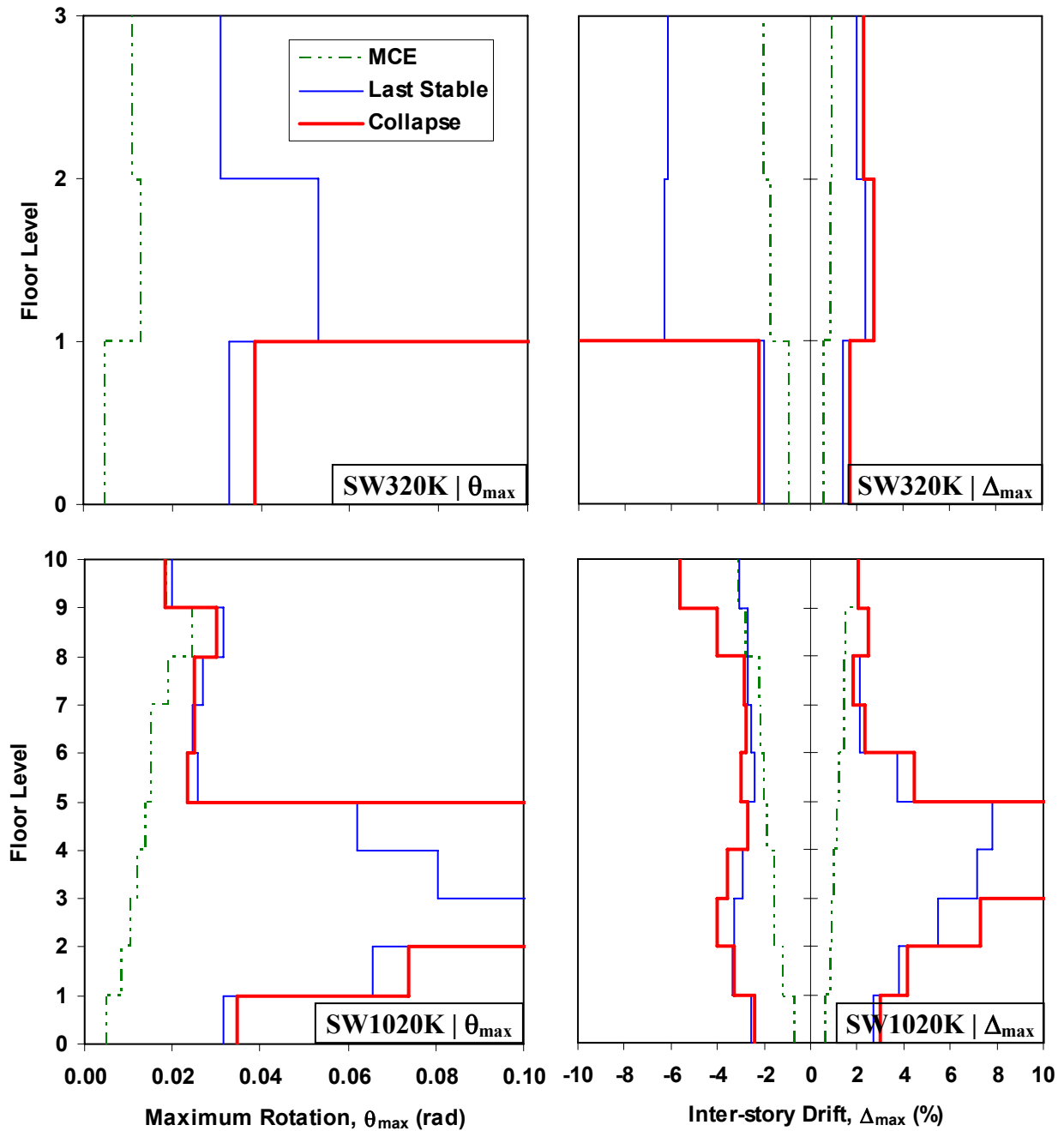
Figure 8-24 Maximum Cross-Section Rotation and Interstory Drift under Three Considered Ground Motion ($\kappa = \kappa_{balanced}$) – Cont'd: (b) HE11230
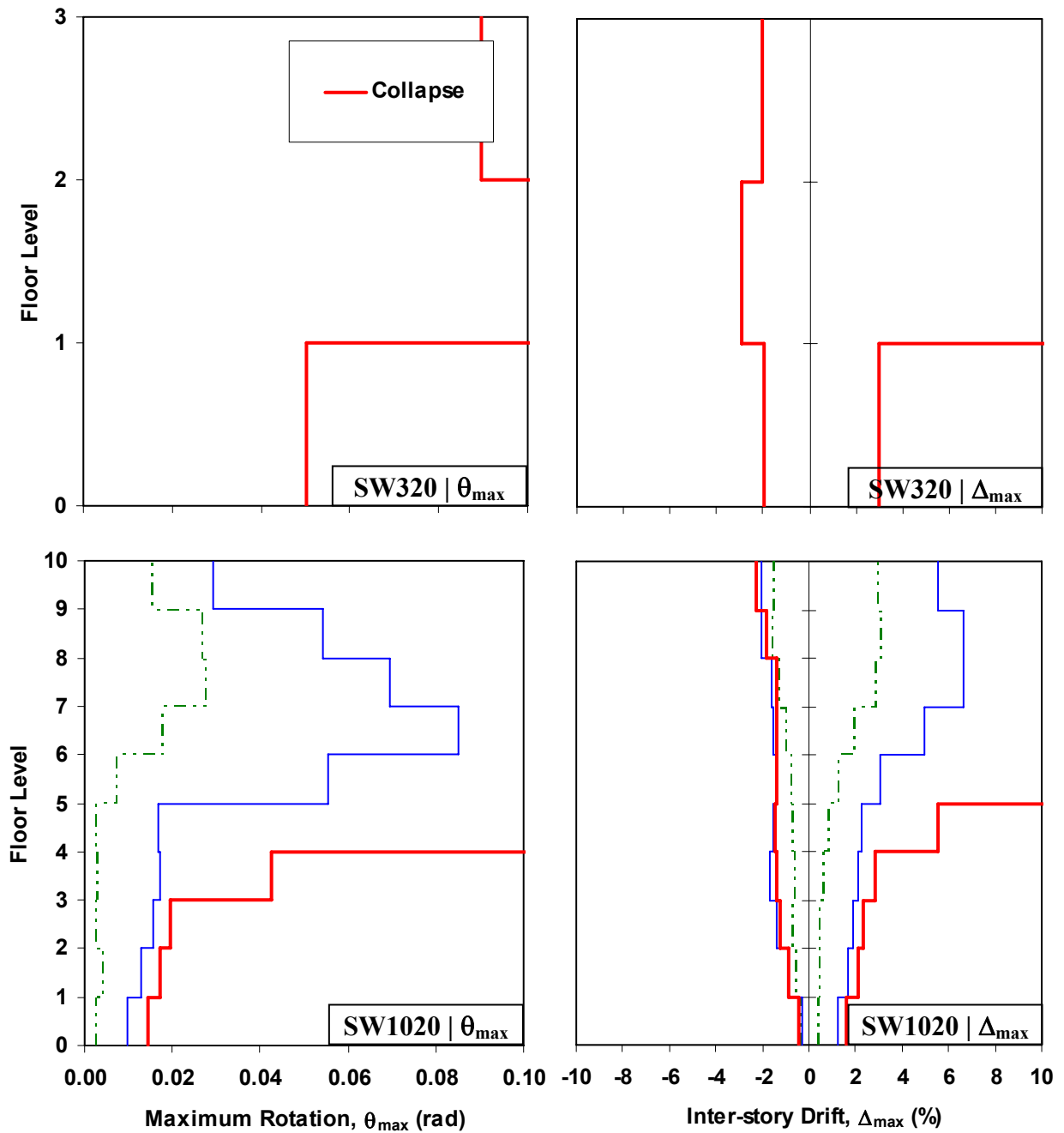
Figure 8-24 Maximum Cross-Section Rotation and Interstory Drift under Three Considered Ground Motion ($\kappa = \kappa_{balanced}$) – Cont'd: (c) YER270

Incidentally, while the main focus of the two preceding comparisons was to examine seismic performance of 3- and 10-story archetypes, they also provide additional information on the performance of the conventional and balanced archetypes. In both 3- and 10-story cases, the balanced archetypes suffered larger cross-section rotation and interstory drift compared to the

conventional archetypes at the same level of ground motion intensity (i.e., at the MCE level). This explains why the balanced archetypes have a lower margin to collapse compared to the conventional archetypes.

8.5.3 Impact of Ground Motion Record Sets on Collapse Margin Ratio

In the two preceding sub-sections, investigation on local behaviors of archetype components (i.e., infill plate yielding, boundary frame plastification, interstory drift, cross-section rotation) was conducted in an attempt to understand why the 10-story archetypes have higher CMR values compared to the 3-story archetypes. This sub-section addresses the same concern by investigating the impact of selected ground motion record sets on CMR values between short- and long-period archetypes. As described in Section 2, the ground motion records used in the nonlinear dynamic analyses for collapse assessment consist of 44 individual far-field ground motions.

For the purpose of the current investigation, a new archetype was prepared which has similar geometric properties and distribution of gravity loads to that of SW320, but with a different story seismic mass. The story seismic mass was tuned such that this hypothetical archetype had the same fundamental period as that of SW1020 ($T_1 = 1.08$ sec). IDA was performed and the resulting collapse fragility curve is plotted in Figure 8-25 (i.e., denoted as SW320PeriodSW1020). Though not comparable to that of SW1020, as initially expected, the resulting CMR value is higher than that of SW320. Here, the resulting CMR value for this hypothetical archetype is 3.5, which is between the CMR values for SW320 and SW1020 of 2.4 and 4.1, respectively.

The above result indicates a possible trend for long-period archetypes to have larger CMR values compared to short-period archetypes under the ground motion record sets selected. Therefore, for the same intensity of ground motions (e.g., at MCE level), long-period archetypes have a lower probability to collapse compared to short-period archetypes. This finding is similarly observed when looking at examples in the FEMA P695 document for both reinforced concrete special moment frame and wood light-frame archetype systems, where short-period archetypes (i.e., $T_1 <$ 0.6 sec for SDC D_{max}) had lower value of CMR. In other words, to achieve the same level of collapse margin as long-period archetypes, short-period archetypes for these systems required additional strength or other form of modifications to improve their collapse performance. The

393
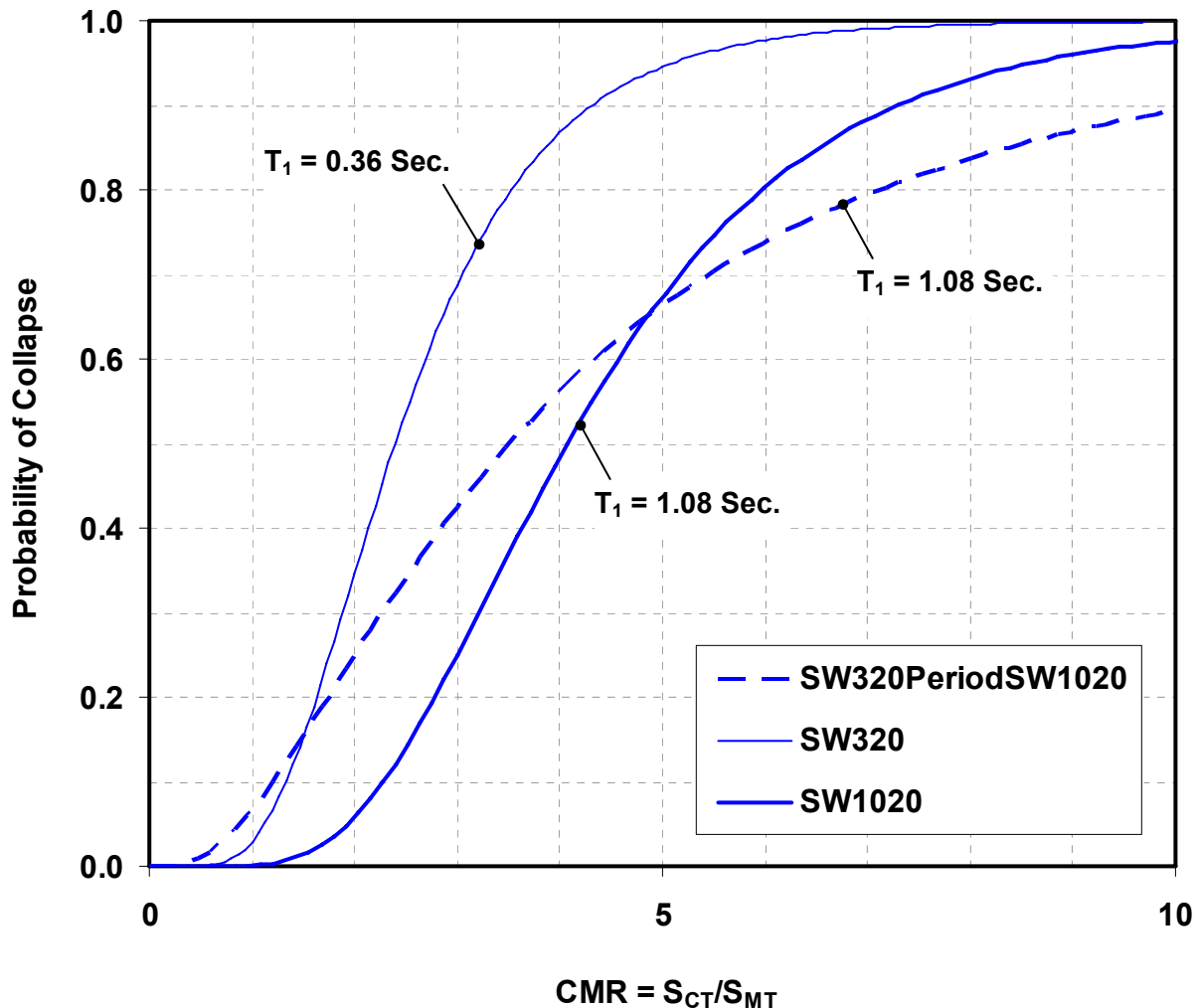
Figure 8-25 Comparison of Collapse Fragility Curves between Archetypes with Different Fundamental Periods

FEMA P695 document referenced several previous research on single and multiple degree of freedom structural systems that reported similar findings (e.g., Newmark and Hall 1973; Lai and Biggs 1980; Elghadamsi and Mohraz 1987; Riddell *et al*. 1989; Nassar and Krawinkler 1991; Vidic *et al*. 1992; Miranda and Bertero 1994; Takeda *et al*. 1988; Krawinkler and Zareian 2007).

8.5.4 Comparison of IDA Results using Interstory Drift as Damage Measure

Another comparison on seismic performance of 3- and 10-story archetypes was conducted using interstory drift as the damage measure. Exceedance fragility curves for the 3-story archetypes at different level of interstory drifts were plotted in Figures 8-8 and 8-9. The same analysis was conducted on SW1020 and SW1020K for DM varying from 1 to 7% interstory drift and the

resulting exceedance fragility curves for these archetypes are respectively plotted in Figures 8-26 and 8-27. The results under MCE ground motions are considered for comparison purpose (i.e., at S_{MT} equals to 1.5g and 0.8g for 3- and 10 story archetypes, respectively). For the conventional archetypes, half of the ground motions resulted in approximately 2% interstory drift for both SW320 and SW1020. However, SW1020 has a lower probability of exceeding larger interstory drift selected as the DM. For example, only 5 ground motions (i.e., 10% probability of exceedance) caused 3% interstory drift on SW1020, while 10 ground motions (i.e., 22% probability of exceedance) caused the same drift magnitude on SW320. As for the balanced archetypes, 22 ground motions resulted in approximately 3.5% and 3% interstory drift for SW320K and SW1020K, respectively. In both design cases, the 10-story archetypes exhibited superior seismic performance with respect to the 3-story archetypes.

DM	P[0.8g]
1%	0.98
2%	0.53
3%	0.10
4%	0.04
5%	0.01
6%	0.01
7%	< 0.01
Collapse	< 0.01
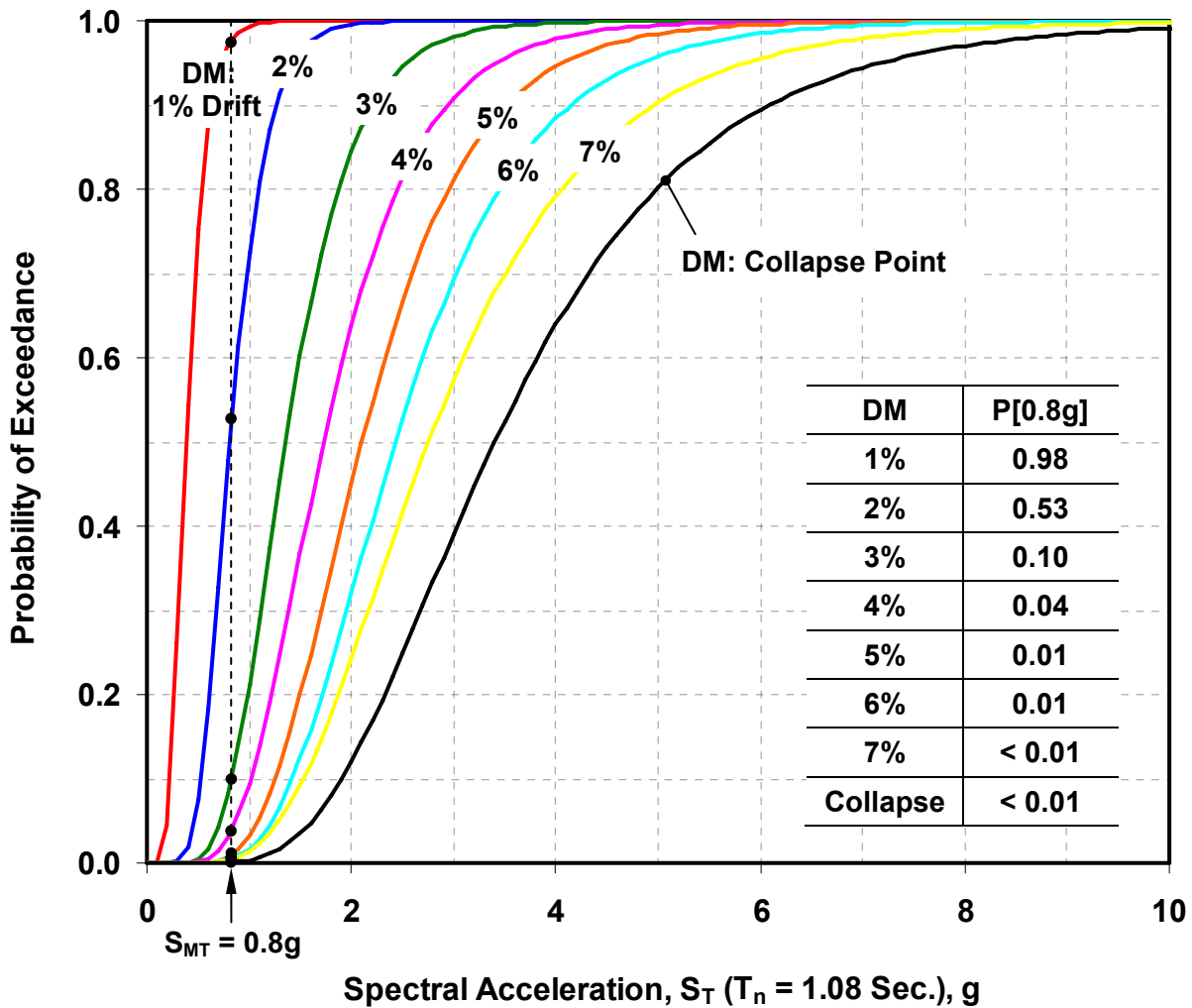
Figure 8-26 Exceedance Fragility Curves for SW1020 using Various Levels of Inter-story Drift as Damage Measure
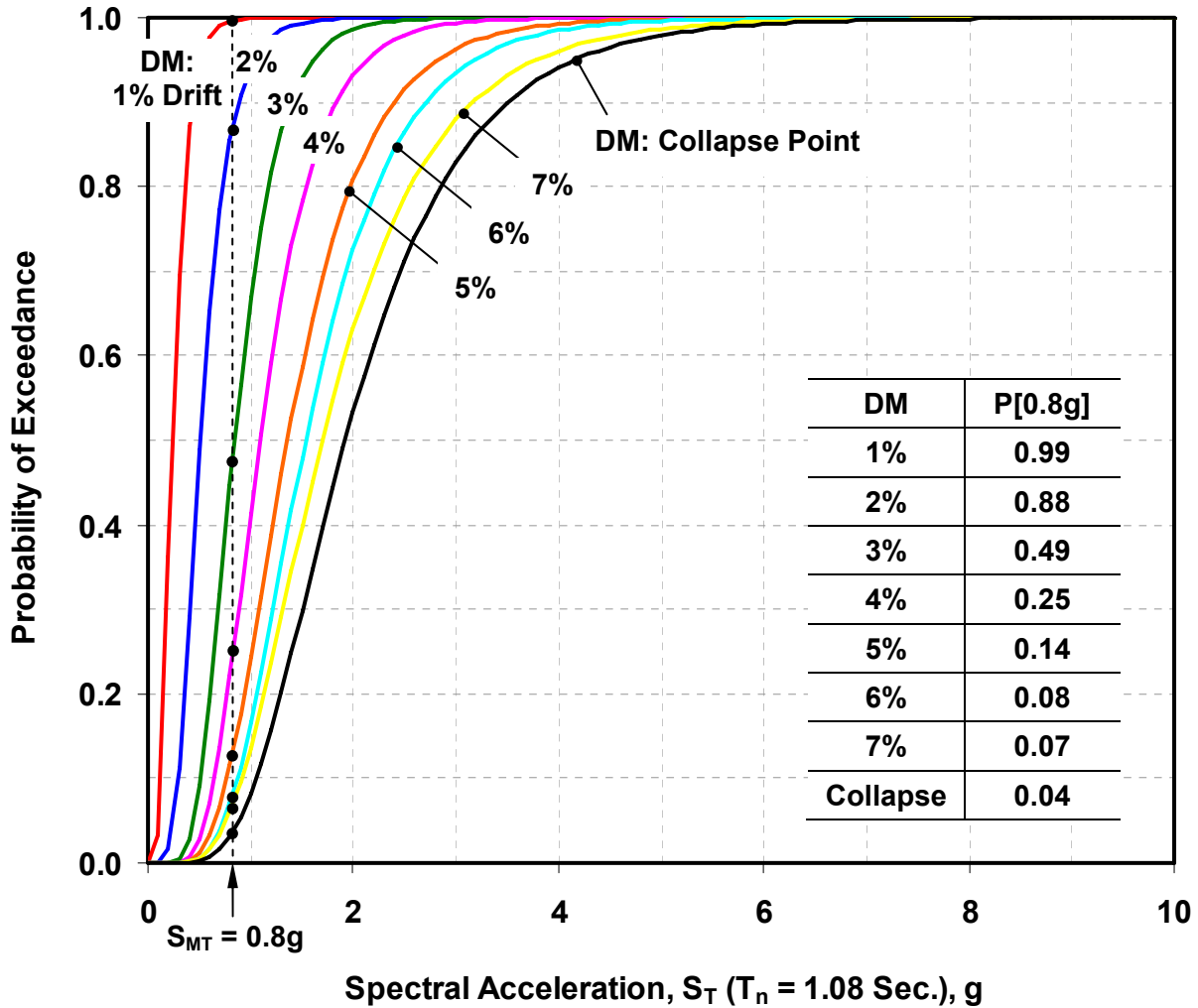
Figure 8-27 Exceedance Fragility Curves for SW1020K using Various Levels of Inter-story Drift as Damage Measure

In terms of exceedance margin ratio (compared in Figure 8-28), the 10-story archetypes consistently have higher exceedance margins for DM of 3% or larger interstory drifts compared to that of the 3-story archetypes. For DM of smaller than 3% interstory drift however, both archetypes have comparable exceedance margin ratios.

8.6 Collapse Fragility Curves for Archetypes with Various Configurations

Twelve SPSW archetypes with various structural configurations (Section 7) were designed for the purpose of quantifying SPSW seismic performance factors by investigating their collapse performances. This section presents collapse fragility curves for these 12 archetypes and
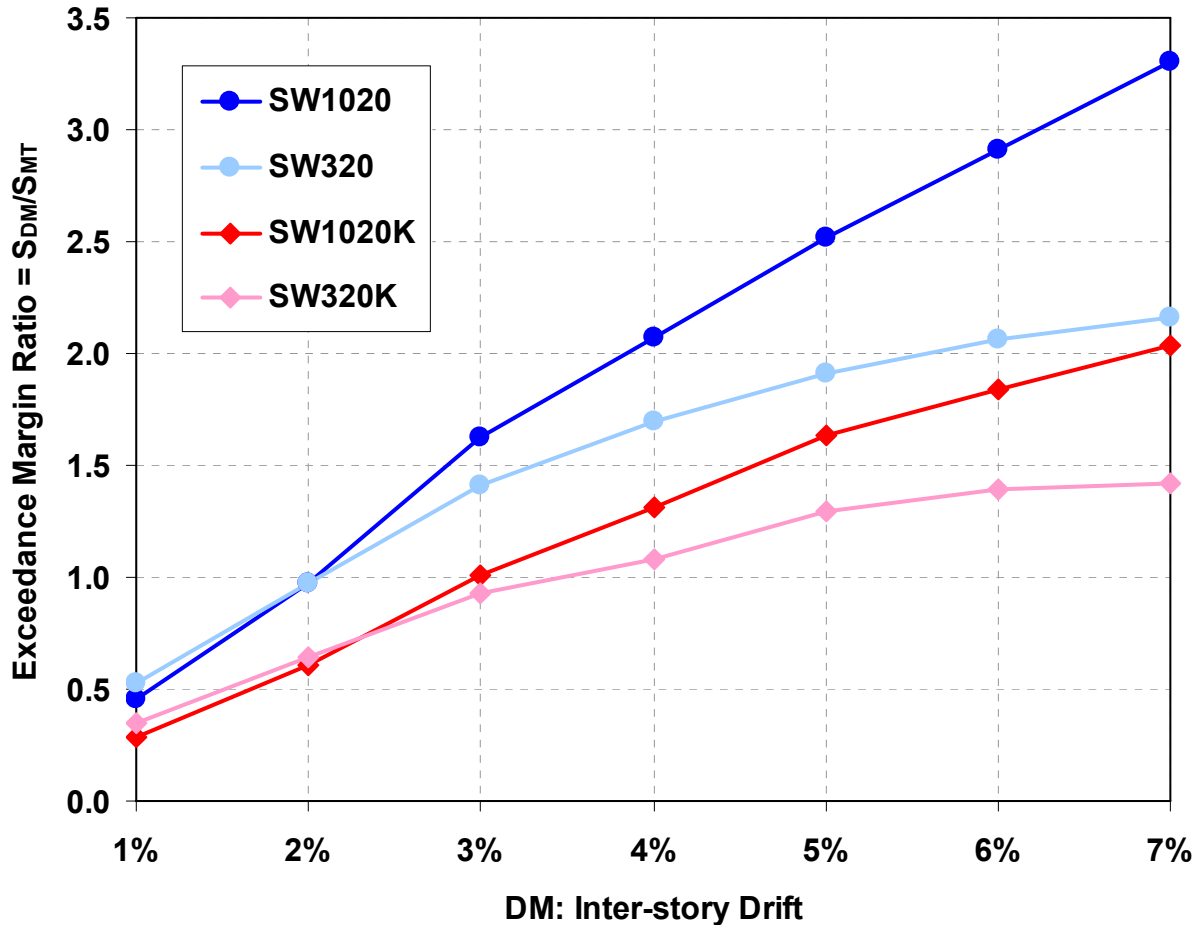
Figure 8-28 Margin Ratio versus Interstory Damage Measure for 10-story Archetypes

compares collapse margin ratios for archetypes with different panel aspect ratios, intensities of active seismic weight, and number of stories. The resulting collapse fragility curves and the corresponding collapse margin ratios are presented in Figure 8-29.

8.6.1 Impact of Panel Aspect Ratio on Collapse Margin Ratio

To observe the impact of panel aspect ratio on collapse margin ratios, collapse fragility curves for SW310 and SW310K were compared to those of benchmark archetypes (i.e., SW320 and SW320K, respectively). As shown in Figure 8-29a for the conventional design case ($\kappa = 1$), CMR for SW310 (i.e., 3-story archetype with panel aspect ratio of 1.0) is 2.10, which is 12.5% smaller than that of SW320 (i.e., 3-story archetype with panel aspect ratio of 2.0). This CMR for archetypes with smaller panel aspect ratio is reasonable in light of the information presented in Figure 7-2, which shows that overstrength decreases as panel aspect ratio decreases. In other
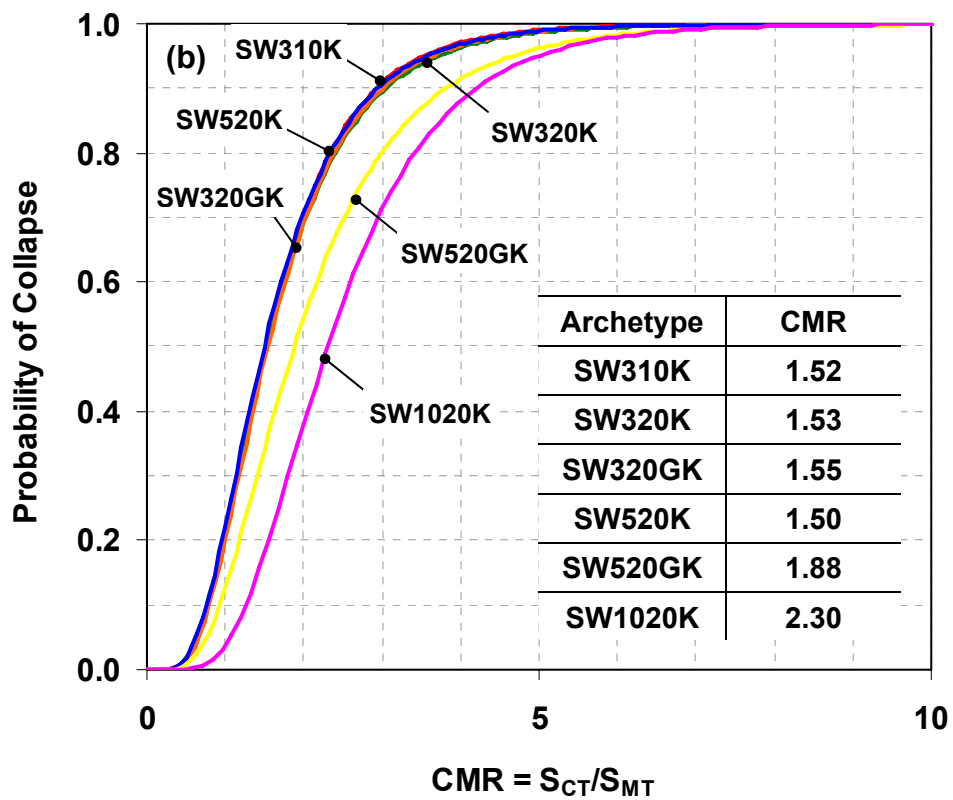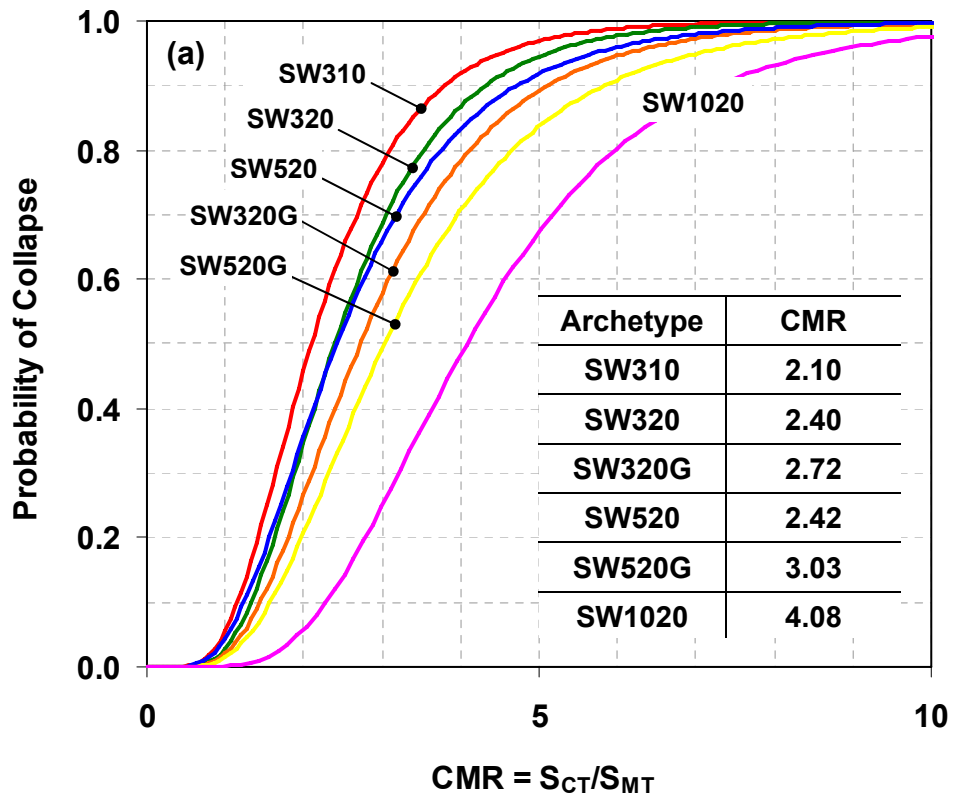
Figure 8-29 Collapse Fragility Curves for Archetypes with Various Configurations: (a) 100% Design Case; (b) Balanced Design Case

398

words, as a consequence of less overstrength present in SW310 compared to that of SW320, its probability of collapse under MCE ground motions is higher (i.e., its margin to collapse is smaller). However, the 12.5% CMR difference between SW310 and SW320 is somewhat small considering the large difference in overstrength between the two archetypes shown in Figure 7-2. Here, for the case when the κ factor equals 1.0, a 25% overstrength difference theoretically exists between these archetypes. This indicates that, while Figure 7-2 provides insights as to the relative magnitude of CMRs between archetypes having different aspect ratios, the relationship between overstrength and CMR values is not necessary linearly correlated.

By contrast, the balanced archetypes (i.e., SW310K versus SW320K) have practically similar margins to collapse. As shown in Figure 8-29b, their collapse fragility curves are on top of each other and their respective CMR values are 1.52 and 1.53. One might expect this result considering that both archetypes have the same amount of overstrength (i.e., an inherent overstrength of 1.33 as a consequence of compliance with the AISC 2010 design procedure for SPSW, for reasons described in Section 7.2.3).

8.6.2 Impact of Seismic Weight on Collapse Margin Ratio

All SPSW archetypes presented up to this point were designed to sustain tributary seismic weight equal to one-sixth of the total story seismic weight in the prototype buildings selected (i.e., the SAC model buildings). Here, this seismic weight intensity is denoted as "Low" seismic weight. To investigate the impact of "High" seismic weight on archetype collapse performance, four archetypes (i.e., SW320G, SW320GK, SW520G, and SW520GK) were designed to sustain half of the total story seismic weight. When comparing IDA results for these archetypes to the results for their corresponding archetypes designed with low seismic weight (i.e., SW320, SW320K, SW520, and SW520K), observations can be conducted on the impact of high seismic weight as a function of number of stories (i.e., for 3- and 5-story archetypes) and basic configurations (i.e., conventional versus balanced design cases). It should be emphasized that the terms "Low" and "High" seismic weight used here can be interpreted to correspond to the cases termed low and high gravity loads in FEMA P-695, respectively, assigned to the gravity leaning column system (P-Δ column). For example, gravity loads assigned to the VBEs of both SW320 and SW320G are the same but the latter has higher gravity loads assigned to its P-Δ columns. Distribution of

gravity loads assigned to VBEs and gravity leaning columns was presented in Table 7-5 for all archetypes considered.

Initially, it was suspected that archetypes designed with high seismic weight would have lower (or, at worst, similar) margins to collapse compared to those with low seismic weight. This hypothesis was founded on the idea that the fundamental period of both archetypes would be comparable, because the ratio between their structural masses and stiffness would be similar (i.e., archetypes with low seismic weight would have smaller component sizes and therefore lower stiffness, while those with high seismic weight would have bigger component sizes and therefore higher stiffness). Indeed, calculations confirmed that the fundamental periods of archetypes designed with high and low seismic weights, for the same number of stories, were similar, as shown later in Table 8-2. Accordingly, their responses under one particular ground motion were expected to be comparable at lower levels of earthquake excitations. However, in the case for which gravity loads on the leaning columns are considerably larger, P-Δ effects could cause archetypes designed with high seismic weight to reach collapse sooner than those with low seismic weight. On that basis, 5-story archetypes were expected to possibly have smaller CMR compared to 3-story archetypes, since P-Δ effects would be more pronounced in higher buildings.

Interestingly, contrary to the initial expectation, the archetypes designed with higher seismic weight were found to actually have higher CMR values. This result can be observed in all cases considered (Figure 8-29). Specifically, the conventional 3-story archetypes, SW320G (designed with high seismic weight) has a 13% higher CMR than SW320 (designed with low seismic weight). The difference is even higher for the conventional 5-story archetypes, where the CMR of SW520G (equal to 3.03) is 25% higher than that of SW520. For the balanced 3-story archetypes, however, the difference between CMR values of archetypes designed with high and low seismic weight was insignificant, with CMR values for SW320GK and SW320K of 1.55 and 1.53, respectively. Differing from these results, the CMR of SW520GK (i.e., balanced 5-story archetype designed with high seismic weight) was 25% higher than the CMR of its counterpart archetype SW520K designed with low seismic weight (a difference similar to that observed for the conventional 5-story archetypes).

As a first attempt to comprehend the cause for the above trends, the intensity of each ground motion that caused the archetype designed with high seismic weight to collapse (S_{CT}) was compared to the ground motion intensity that caused the same on the archetype designed with low seismic weight. Figure 8-30 shows such comparison for the 3-story archetypes. In part (a), the figure plots collapse intensity ratio for the conventional archetypes (i.e., between SW320G and SW320), while part (b) shows the same for the balanced archetypes (i.e., between SW320GK and SW320K). For the conventional archetypes, most of the ratios are larger than 1.0 (i.e., for 41 GMs), which means the majority of ground motions have to be scaled up to a higher intensity to cause collapse of SW320G as opposed to that of SW320. By contrast, for the balanced archetypes, the numbers of intensity ratio larger and smaller than 1.0 are comparable (i.e., 26 ground motions caused collapse of SW320GK at a higher intensity than for SW320K, and 18 at a lower intensity). Note that results were sensibly the same for the 5-story archetypes, although only the results for the 3-story archetypes are presented here.
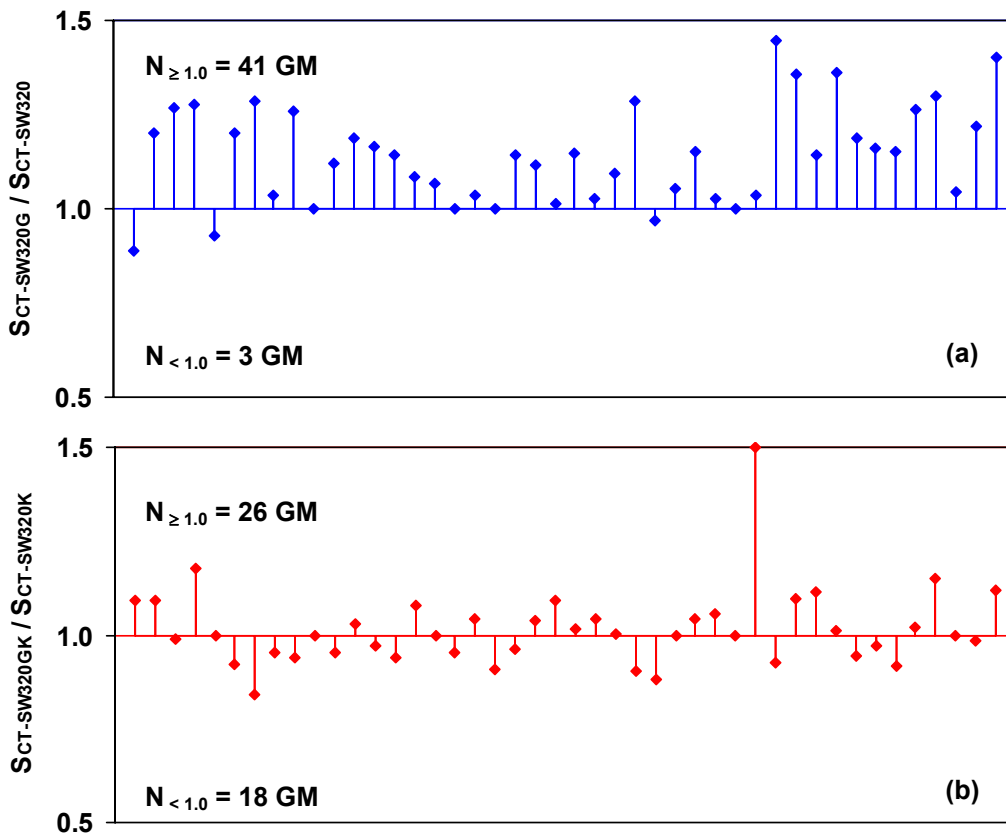
Figure 8-30 Comparison of Collapse Intensity (S_{CT}) under Individual Ground Motion between Archetypes Designed with High and Low Seismic Weights: (a) 100% Design Case; (b) Balanced Design Case

While the above provides some statistical quantification supporting the observation of higher CMR for archetypes designed with high seismic weight (because CMR is linearly correlated to the median collapse intensity of the 44 ground motions), further investigation is required to understand the actual reason for the aforementioned trends. For this purpose, a series of monotonic pushover analyses were conducted to investigate the impact of P-Δ columns and deteriorated material models on archetypes designed with high and low seismic weights. The analyses were conducted on the 3- and 5-story archetypes as well as on the conventional and balanced design archetypes (i.e., total of 8 archetypes).

In a first set of analyses, non-deteriorated material models were used for the 3-story conventional and balanced archetypes, and followed by a second set of analyses on the same archetypes with deteriorated material models. For simplicity, material strain hardening was excluded in both sets of analyses. The resulting pushover curves are compared in Figure 8-31. Plotted on the left side are curves for the conventional archetypes, whereas on the right are curves for the balanced archetypes. Pushover curves on top and bottom rows are the results for non-deteriorated and deteriorated material models, respectively. When no strength degradation was considered in the nonlinear model, P-Δ practically has the same effects on both conventional and balanced archetypes irrespective of seismic weight intensity considered (Figure 8-31a and Figure 8-31c). After reaching their ultimate strength, normalized base shears for archetypes with high and low seismic weight decreased at the same rate either in the conventional or balanced design cases.

By contrast, when strength degradation was considered, pushover curves of archetypes designed with high and low seismic weights were significantly different for the conventional design case (Figure 8-31b), while that was not the case for the balanced design case (Figure 8-31d). For the conventional archetypes, strength degradation occurred in SW320 at 2.2% top story drift, which is sooner than that in SW320G at 2.5%. Incidentally, the 13% difference between these two starting points of strength degradation is similar to the difference between their CMR values. As for the balanced archetypes, both SW320K and SW320GK experienced strength degradation approximately at the same 2.1% top story drift.
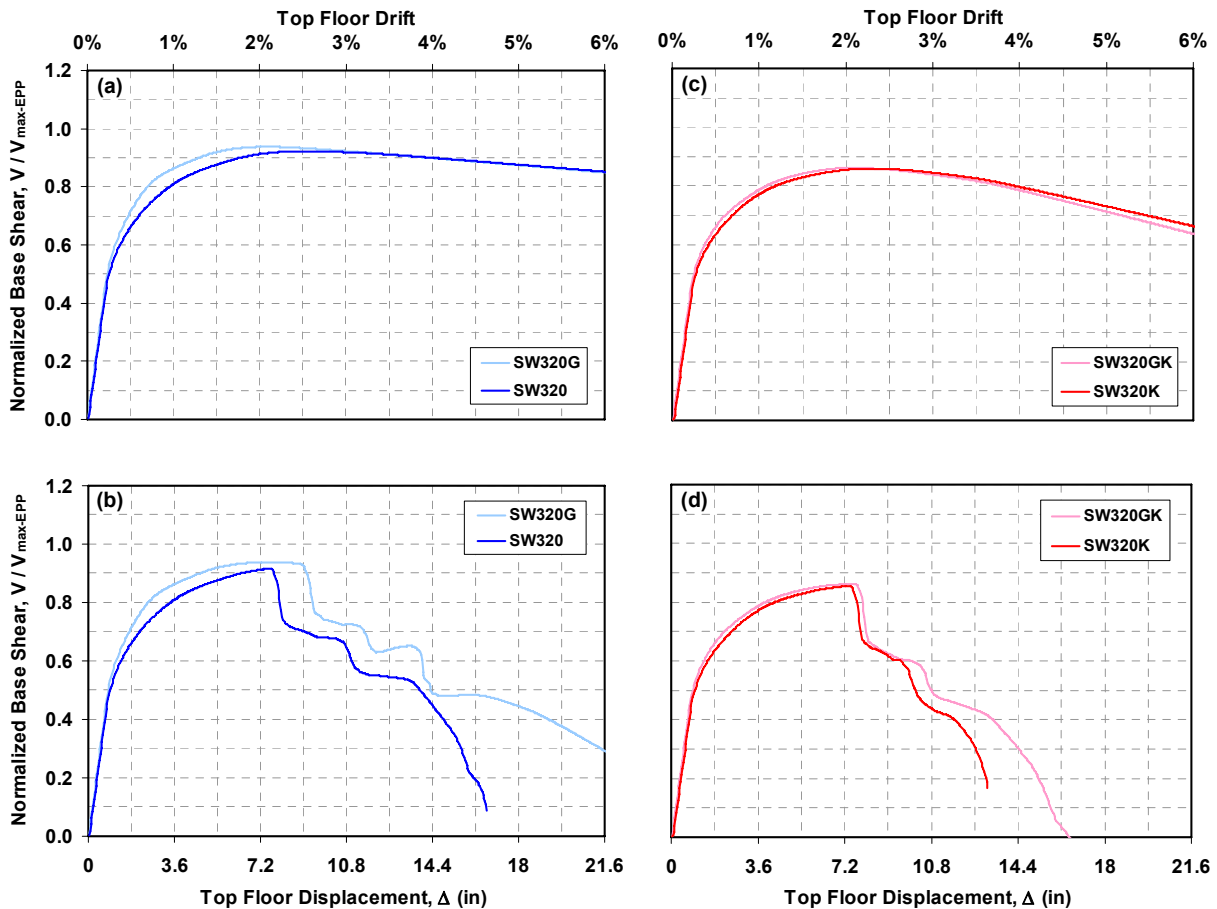
Figure 8-31 Seismic Weight Influence as seen through Monotonic Pushover Analysis on 3-story Archetypes: (a) and (b) 100% Design Case with and without Deteriorated Material Model; (c) and (d) Balanced Design Case with and without Deteriorated Material Model

Additionally, monotonic pushover analyses were conducted on the 5-story conventional and balanced archetypes designed with high and low seismic weights. Again, in the first set of analyses, non-deteriorated material models were used and followed by a second set of analyses on the same archetypes with deteriorated material models. The resulting pushover curves are compared in Figure 8-32. The same observations reported for the 3-story archetypes are also evident for the 5-story archetypes when no strength degradation was considered in the nonlinear model. Here, P-Δ has practically the same effects on both conventional and balanced archetypes irrespective of seismic weight intensity. When strength degradation was considered, high seismic weight had a more pronounced impact on the conventional archetypes compared to the balanced archetypes. As plotted in Figure 8-32b, strength degradation occurred in SW520 at 1.9% top story drift while that in SW520G occurred at 2.4% top story drift. As for the balanced archetypes

shown in Figure 8-32d, SW320K and SW320GK experienced strength degradation at approximately 1.8 and 2.2% top story drift, respectively.
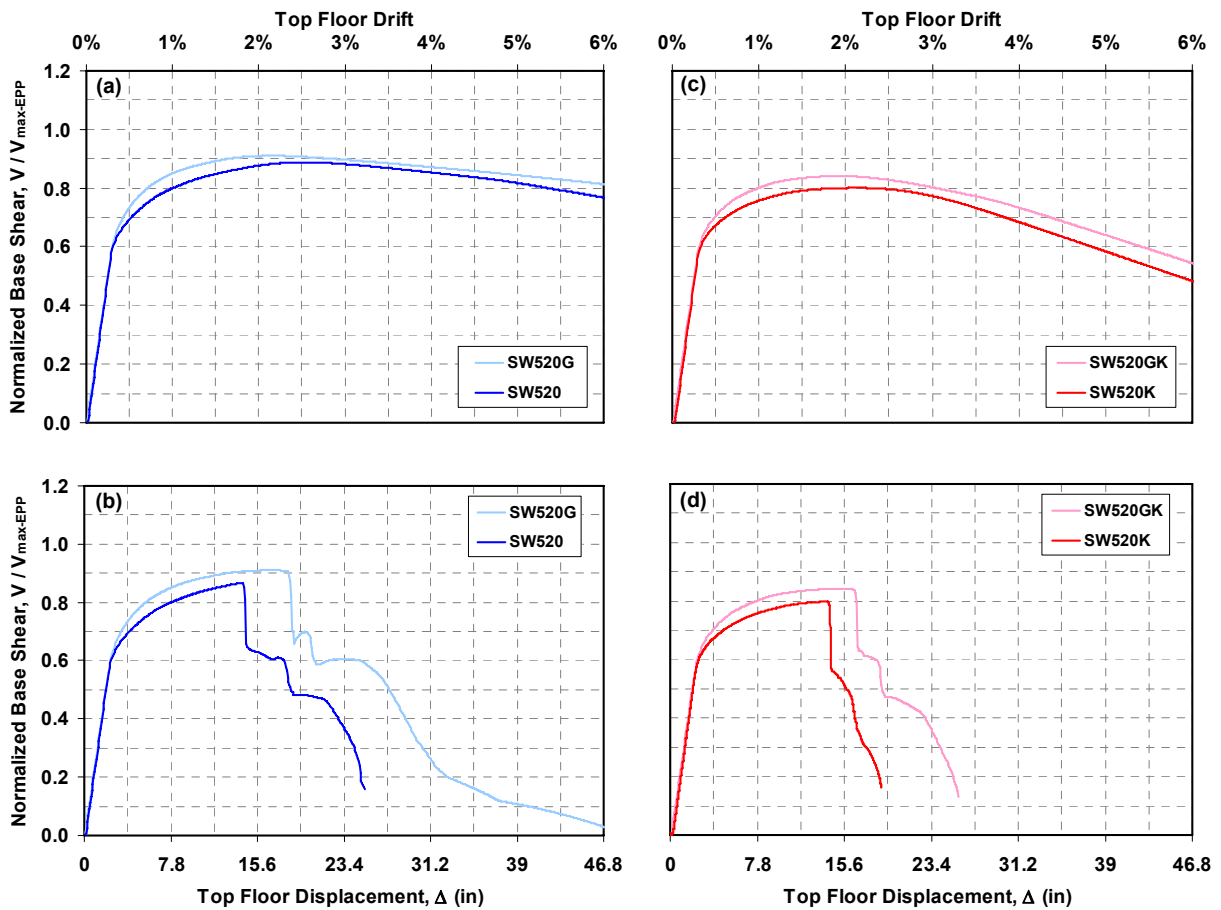
Figure 8-32 Seismic Weight Influence as seen through Monotonic Pushover Analysis on 5-story Archetypes: (a) and (b) 100% Design Case with and without Deteriorated Material Model; (c) and (d) Balanced Design Case with and without Deteriorated Material Model

Having observed that both the 3- and 5-story conventional archetypes designed with low seismic weight exhibited strength degradation sooner compared to that with high seismic weight, a subsequent investigation was directed to compare cross-section moment capacities of W-sections used for boundary elements of each archetype. As explained in Section 6, during modeling, the moment-rotation relationship at the cross section level was converted into a stress-strain relationship for fibers in OpenSees model using the following equation.

$$\varepsilon = \frac{0.5d \times \theta}{L_p} \tag{8-2}$$

where ε is the fiber strain at the top and bottom of the cross-section for pure bending; d is the cross-section total depth; θ is cross-section rotation; and L_p is plastic hinge length (= 0.9d). In the absence of axial forces, given that the plastic hinge length is a function of d, the above equation simplifies such that the furthest fiber from the neutral axis of any cross section reaches the same strain for a given cross-section rotation, irrespective of section depth. For example, to reach the onset of strength degradation at 0.039 radians (as shown in Figure 7-10c), the furthest fiber from the neutral axis has to reach a strain level of 0.022. However, when axial force is present in a cross-section (which typically the case for boundary elements), the degradation behavior of deep and shallow cross sections will vary because the axial load causes the neutral axis to move away from the center of gravity of the cross section. The larger the axial load, the further the neutral axis shifts away from the center. For shallow cross-sections, the strain corresponding to the onset of degradation would be reached at a smaller rotation than those in deeper cross-sections, and strength degradation would take place faster.

As presented in Table 7-6, cross-section depths for the 3-story conventional archetypes designed with low and high seismic masses are significantly different. The latter case has relatively larger cross-sections. By contrast, that was not the case for the 3-story balanced archetypes. Both archetypes designed with low and high seismic masses have comparable sizes of HBEs and VBEs. This explains the results plotted in Figure 8-31, where strength of the conventional archetype with relatively shallower cross-section (i.e., SW320) deteriorated faster than for the case with deeper cross sections (i.e., SW320G). For the balanced case, (i.e., SW320K and SW320GK) the strength of both archetypes deteriorated at the same time as a consequence of having comparable depth of boundary elements. Hence, the higher CMR values for archetypes designed with high seismic weight are an artifact of the selected boundary element sizes, and are not so much impacted by the P-Δ effect as initially predicted.

8.6.3 Impact of Number of Stories on Collapse Margin Ratio

Another variation of structural configuration considered in this research is the archetype number of story (or total building height). As a result of different fundamental period and spectral acceleration at the MCE level, collapse margin ratio more likely would vary from one low-rise archetype to another mid-rise archetype. To examine variation of CMR between several

archetypes with different numbers of stories, IDA results of the following archetype groups are compared, namely: (1) SW320, SW520, and SW1020; (2) SW320K, SW520K, and SW1020K; (3) SW320G and SW520G; and (4) SW320GK and SW520GK. Their fragility curves and corresponding CMR values are presented in Figure 8-29.

In general, CMR increases as the number of stories increases, irrespective of design approaches followed (i.e., conventional versus balanced design cases) and level of seismic weight intensity considered (i.e., low versus high seismic weight). The CMR increment, however, is not linearly corresponding to the increment of number of story. Consider the results of the first group above as an example. CMR values were 2.40, 2.42, and 4.08 for SW320, SW520, and SW1020, respectively. The less than 1% CMR increase from the 3- to 5-story was not as significant as the approximately 70% increase from the 5- to 10-story archetypes. The same trend was also evident for the second group (i.e., balanced archetypes). In addition, while CMR discrepancies between the 3- and 5-story archetypes in the first and second groups were less than 1%, the CMR discrepancies in their counterpart archetypes (i.e., archetypes in the third and fourth group, which were designed with high seismic weight) were more than 11%.

8.6.4 Additional Observations on IDA Results

The preceding discussion on collapse fragility curve and CMR for various archetypes focused on the results using spectral acceleration as the intensity measure. Table 8-2 presents summary of IDA results with different IM and DM for all considered archetypes. Specifically, the table presents information of CMR values using PGA as the intensity measure (i.e., CMR_{PGA}), probability of collapse at MCE level (i.e., $P[S_{MT}]$), probability of interstory drift exceeding 2% drift under MCE ground motions (i.e., $P[DM_{2\%}]$), and maximum interstory drift corresponding to 50% probability of exceedance under MCE ground motions (i.e., $P[DM_{x\%}] = 0.5$). Several additional observations on these IDA results are presented in the following paragraphs.

First, the same trends as what was presented in the previous sub-sections can generally be obtained using PGA as the intensity measure. Specifically, conventional archetypes with larger panel aspect ratios have higher CMRs, while balanced archetypes have practically the same CMR values for different aspect ratios considered. As shown in Table 8-2, CMR_{PGA} for SW310 and

Table 8-2 Summary of Incremental Dynamic Analysis (IDA) on SPSW Archetypes with Various Structural Configurations

Archetype ID	$T_{\text{Theoretical}}$ (Sec.)	T_{Analysis} (Sec.)	IM: Spectral Acc.		IM: PGA		$P[S_{MT}]$	$P[DM_{2\%}]$	$P[DM_{x\%}]$ = 50%
			$\hat{S}_{CT}$ (g)	CMR_{Sa}	PGA_{CT} (g)	CMR_{PGA}			
SW310	0.36	0.47	3.14	2.10	1.45	2.42	5.5%	64.7%	2.5%
SW320	0.36	0.35	3.60	2.40	1.66	2.76	2.8%	52.2%	2.0%
SW320G	0.36	0.37	4.08	2.72	1.87	3.12	2.1%	48.7%	2.0%
SW520	0.64	0.60	3.40	2.42	2.03	3.38	4.5%	57.8%	2.5%
SW520G	0.64	0.61	4.26	3.03	2.53	4.23	1.5%	53.2%	2.0%
SW1020	1.08	1.00	3.40	4.08	3.29	5.48	< 1.0%	52.7%	2.0%
SW310K	0.36	0.58	2.28	1.52	1.05	1.75	20.6%	82.9%	3.0%
SW320K	0.36	0.50	2.29	1.53	1.06	1.76	21.5%	84.6%	3.5%
SW320GK	0.36	0.53	2.32	1.55	1.07	1.78	20.1%	85.1%	3.5%
SW520K	0.64	0.85	2.10	1.50	1.25	2.09	26.2%	83.4%	3.0%
SW520GK	0.64	0.87	2.64	1.88	1.57	2.62	15.3%	87.1%	3.0%
SW1020K	1.08	1.47	1.92	2.30	2.08	3.46	3.8%	87.6%	3.0%

Note:

CMR_{Sa} = $\hat{S}_{CT}/S_{MT}$, where S_{MT} = 1.5g, 1.4g, and 0.83g for 3-, 5-, and 10-story archetypes, respectively.

CMR_{PGA} = PGA_{CT}/PGA_{MT}, where PGA_{MT} = 0.6g for all archetypes.

$P[S_{MT}]$ = Probability of collapse at S_{MT} level.

$P[DM_{2\%}]$ = Probability of exceedance when maximum interstory drift reaches 2% interstory drift under MCE ground motions.

$P[DM_{x\%}]$ = Maximum interstory drift corresponding to 50% probability of exceedance under MCE ground motions.

SW320 are 2.42 and 2.76, respectively, while that for SW310K and SW320K are 1.75 and 1.76, respectively. Impact of higher seismic weight, which resulted in higher CMR values for conventional archetypes but resulted insignificant difference of CMR values for balanced archetypes, was once again confirmed here. For example, CMR_{PGA} for 5-story conventional archetypes with high and low seismic weights (i.e., SW520G and SW520) were 4.23 and 3.38, respectively; while the balanced archetypes, SW320GK and SW320K have comparable margin to collapse when using PGA as the IM (i.e., 1.78 and 1.76, respectively). As for the influence of number of stories, CMR_{PGA} increases as number of stories increase irrespective of design approaches selected and level of seismic weight intensities considered. For example, CMR_{PGA} values for the conventional 3-, 5-, and 10-story archetypes (i.e., SW320, SW520, and SW1020) were 2.76, 3.38, and 5.48, respectively. When using PGA as the IM, increase of CMR_{PGA} values from 3- to 5-story and from 5- to 10-story archetypes were approximately 22 and 62%, respectively. In comparison to the previous results using spectral acceleration as the IM, the increase of margin to collapse in the former case was significantly higher while that in the latter case was somewhat comparable (i.e., respectively compared to less than 1% and 70% as reported Section 8.6.3)

Second, the probability of collapse at MCE level (i.e., using spectral acceleration as the IM), $P[S_{MT}]$, was less than 6% for the conventional archetypes, regardless of the basic structural configurations considered. Except for the 10-story archetypes, the balanced archetypes however have significantly higher probability of collapse at MCE level compared to those of the conventional archetypes. In this case, $P[S_{MT}]$ of the balanced archetypes was larger than 15%.

Third, another indicator reported in Table 8-2 that can be used to assess seismic performance of considered archetypes is probability of exceedance for a given interstory drift. In terms of interstory drift as a damage measure, probability of conventional archetypes exceeding a 2% interstory drift under MCE ground motions was between 52 and 65%, while that for balanced archetypes was between 83 and 88%. These results can also be interpreted as follows: at MCE level, half of the specified ground motions caused an approximately 2.0 to 2.5% and 3.0 to 3.5% maximum interstory drifts on the conventional and balanced archetypes, respectively. More significantly, this fragility curve shows that there is a 20% chance that, at the MCE level, average

interstory drifts of 3% and 7% will be reached for the conventional and balanced archetypes, respectively. This indicates that excessive drift demands are likely when balanced design is used, which may be the most significant drawback of the balanced design approach.

In summary, for all performance indicators considered (i.e., CMR using spectral acceleration and PGA as the IM, probability of collapse at MCE level, probability of maximum interstory drift exceeds a certain drift), the balanced archetypes consistently exhibited inferior seismic performance compared to the conventional archetypes.

8.7   Seismic Performance Factors for Steel Plate Shear Walls

Table 8-3 presents a summary of performance evaluation of all archetypes considered. The table provides key results from monotonic pushover and incremental dynamic analyses, computed adjusted collapse margin ratio (ACMR) to account for the effects of spectral shape, and whether the computed ACMR values pass the acceptable value according to the FEMA P695 requirements. Since only a limited numbers of SPSW archetypes were designed in this research and they were not grouped into several performance groups, instead, each archetype was evaluated individually using the procedure explained in Section 8.3.4. In other words, performance evaluation for SPSW archetypes was conducted by comparing the computed ACMR with the acceptable ACMR associated with a 10% probability of collapse ($ACMR_{10\%}$). Note that the use of $ACMR_{10\%}$ for the performance evaluation is consistent with the recommendations specified in Appendix F of the FEMA P695 document for individual buildings.

All conventional archetypes passed the performance criteria. The computed ACMR for each archetype was larger than $ACMR_{10\%}$ of 2.16. These results indicate that each archetype has a reasonable safety margin against collapse (i.e., a lower probability of collapse) as a result of the overstrength reserve provided by the boundary frame. For this type of SPSW, results indicate that the seismic modification coefficient (R factor) of 7 used in design is adequate (i.e. the resulting design satisfied the ACMR requirement). The system overstrength factors (Ω_o) for the archetypes considered (based on the pushover analysis results and computed per the procedure described in Section 2.3) varied from 2.3 to 3.1. Considering the limited numbers of SPSW archetypes

Table 8-3 Summary of Performance Evaluation

Archetype ID	Pushover Results						IDA Results		Performance Evaluation		
	V_d (kips)	V_{max} (kips)	$\delta_{y,eff}$ (in)	δ_u (in)	$\Omega_0 =$ V_d/V_{max}	$\mu_T =$ $\delta_u/\delta_{y,eff}$	$\hat{S}_{CT}$ (g)	CMR = $\hat{S}_{CT}/S_{MT}$	SSF[1]	ACMR[2]	Pass/ Fail[3]
SW310	155	401	2.1	11.7	2.6	5.5	3.14	2.10	1.26	2.64	**Pass**
SW320	176	495	1.8	8.9	2.8	4.9	3.60	2.40	1.25	3.00	**Pass**
SW320G	465	1440	1.8	9.9	3.1	5.5	4.08	2.72	1.26	3.43	**Pass**
SW520	255	578	3.9	16.3	2.3	4.2	3.40	2.42	1.25	3.03	**Pass**
SW520G	766	1924	4.1	19.5	2.5	4.8	4.26	3.03	1.27	3.85	**Pass**
SW1020	681	1975	7.8	40.6	2.9	5.2	3.40	4.08	1.36	5.58	**Pass**
SW310K	155	236	2.1	10.5	1.5	5.0	2.28	1.52	1.25	1.90	**Fail**
SW320K	176	226	1.8	8.6	1.3	4.8	2.29	1.53	1.24	1.90	**Fail**
SW320GK	465	618	1.7	8.9	1.3	5.1	2.32	1.55	1.25	1.93	**Fail**
SW520K	255	254	3.8	16.1	1.0	4.3	2.10	1.50	1.25	1.80	**Fail**
SW520GK	766	837	3.8	17.9	1.1	4.7	2.64	1.88	1.27	2.39	**Pass**
SW1020K	681	953	7.9	41.1	1.4	5.2	1.92	2.30	1.36	3.16	**Pass**

Note:

[1] SSF obtained from Table 2.1 for a given T and μ_T

[2] ACMR = SSF $(T, \mu_T) \times$ CMR

S_{MT} = 1.5g, 1.4g, and 0.83g for 3-, 5-, and 10-story archetypes, respectively.

[3] Acceptance criteria: $ACMR_{10\%}$ (Table 2.5 for β_{TOT} of 0.6) = **2.16**

Pass if ACMR $\geq ACMR_{10\%}$, otherwise Fail

designed in this research, the Ω_o factor of 2.0 can be considered adequate for conventional SPSW. Assuming the inherent damping available in SPSW to be 5% of critical damping, a deflection amplification factor (C_d factor) of 7 (equal to R factor per the procedure described in Section 2.3) can be considered for conventional SPSWs. In other words, the resulting seismic performance factors for conventional SPSW obtained in this case are somewhat similar to those specified in the ASCE 7-10 (i.e., R, Ω_o, and C_d factors are 7, 2, and 6, respectively).

For the balanced archetypes, except for the 10-story archetype and 5-story archetype design with high seismic weight (i.e., SW1020K and SW520GK), all other archetypes did not meet the performance criteria because their computed ACMR was smaller than $ACMR_{10\%}$. These results indicate that the R factor of 7 used in the initial step to design the balanced SPSW would not lead to an adequate design (i.e., the results did not satisfy the ACMR requirement). Design iterations would be required to determine acceptable seismic performance factors for SPSW designed with $\kappa_{balanced}$. Several possible adjustments could be applied to improve collapse performance of the balanced archetypes and they are addressed in the subsequent section.

It should be emphasized that even though the 10-story balanced archetype (i.e., SW1020K) had a calculated ACMR that met the acceptable ACMR limit, its probability to undergo significantly large interstory drift (i.e., $\geq 3\%$) can be as high as 50% under MCE ground motions (Figure 8-27). While this SPSW designed with balanced case and R factor of 7 have sufficient margin to collapse, its ability to prevent damages especially to drift-sensitive non-structural components is significantly less than for its counterpart archetype (i.e., SW1020). Hence, the need to design balanced archetypes with smaller R factor is deemed necessary.

8.8   Adjustments to Satisfy Collapse Performance of Balanced Archetypes

The preceding section reported that the balanced archetypes designed with an initial R factor of 7 did not meet the performance criteria. There are three possible adjustments that can be applied to these balanced archetypes, namely: (1) reducing the total system collapse uncertainty factor (β_{TOT}); (2) accepting a higher probability of collapse; and (3) designing the balanced archetypes with a lower value of R factor. In the first two adjustments, basically, the demand for the

balanced archetypes to satisfy the collapse performance criteria is lowered, while that in the last adjustment, the capacity of the balanced archetypes is increased. Details on how each adjustment could alleviate the concern at hand is explained in the following paragraphs.

8.8.1   First Adjustment: Reducing System Collapse Uncertainty Factor (β_{TOT})

The performance chart shown in Figure 8-33, which was developed based on information in Table 2-5, is used to illustrate the first adjustment. This performance chart shows acceptable ACMR for different levels of collapse probabilities and total system collapse uncertainties, β_{TOT}. The value shown in the middle of each cell is the acceptable ACMR for a given collapse probability and total system collapse uncertainty. A linear interpolation could be applied to obtain acceptable ACMR for a condition in between two levels of β_{TOT}. Consider the current β_{TOT} of 0.6, which is between Good (B) and Fair (C), as an example. For β_{TOT} of 0.6 and collapse probability of 10%, the previous $ACMR_{10\%}$ of 2.16 can be obtained from a linear interpolation between 2.53 and 1.96. For a given performance evaluation, a star-shaped marker is located above the thick gray line if a calculated ACMR is higher than an acceptable ACMR; otherwise, the marker is located below the thick gray line. The thick gray line constitutes a less than 5% difference between the calculated and acceptable ACMRs. As shown in this performance chart, a lower total system collapse uncertainty with higher collapse probability allowed results in a lower acceptable ACMR.

The calculated ACMR for balanced archetypes (e.g., SW320K) was 1.90, which was lower than the $ACMR_{10\%}$ of 2.16. This condition is indicated in the performance chart by the star-marker #1. To reiterate information in Section 8.3.3, the current acceptable ACMR used to assess the seismic performance of SW320K was based on β_{TOT} equals 0.6, which was an aggregate of several uncertainty factors related to SPSW design requirements (β_{DR}), SPSW test data (β_{TD}), and the nonlinear model developed (β_{MDL}). Here, they were rated as B (Good, $\beta_{DR} = 0.2$), C (Fair, $\beta_{TD} = 0.35$), and B (Good, $\beta_{MDL} = 0.2$), respectively. To reduce total system collapse uncertainty factor (β_{TOT}), hypothetically, one could optimistically rate the current SPSW design requirements, SPSW experimental data available at the time of this writing (Section 7), and the nonlinear model developed to model SPSW as A (Superior, $\beta_{DR} = 0.1$), B (Good, $\beta_{TD} = 0.2$), and B (Good, $\beta_{MDL} = 0.2$), respectively, to give a resulting β_{TOT} of 0.5 (2-5). As a result of the smaller collapse
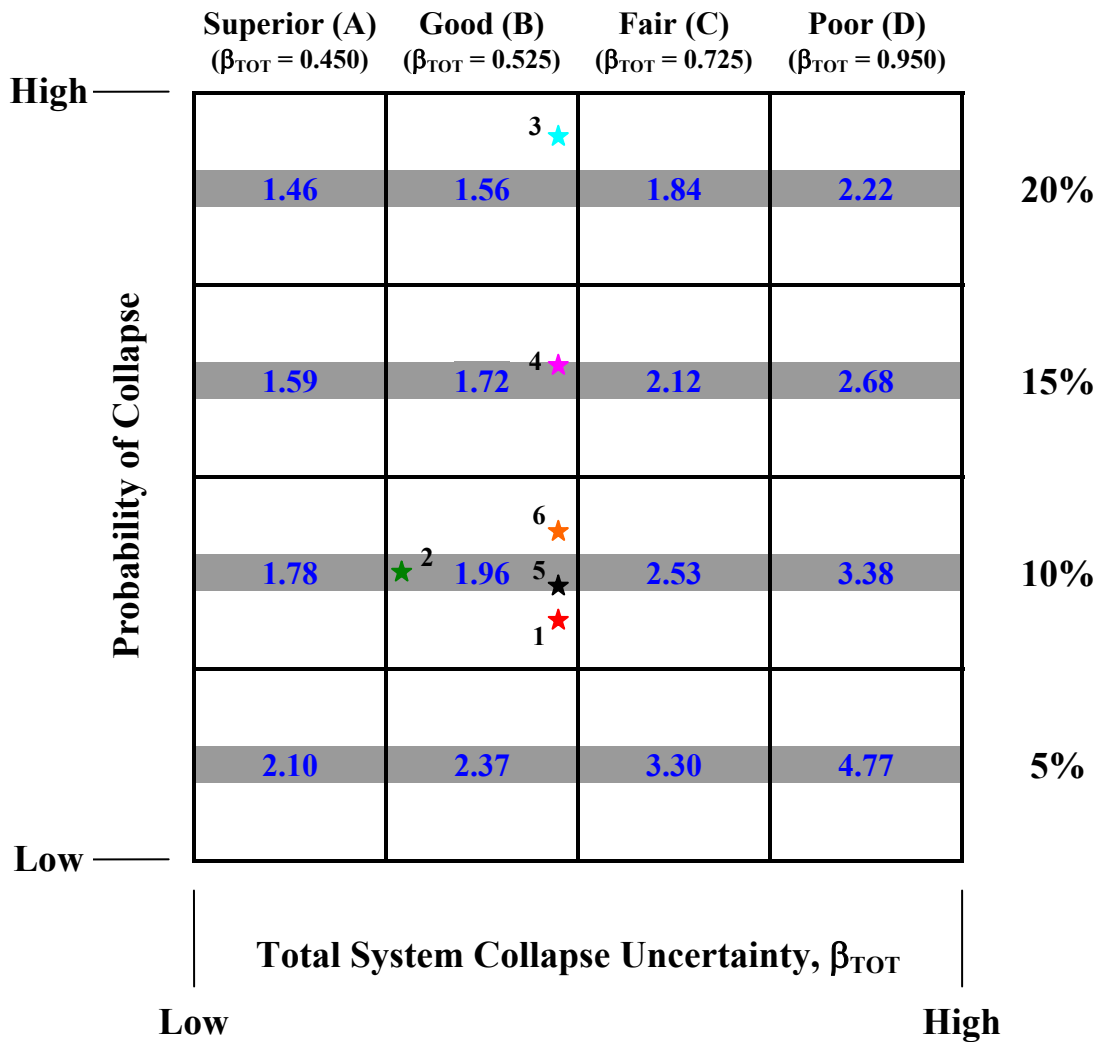
Figure 8-33 Performance Chart (SW320K): Acceptable ACMR for Specific Probability of Collapse and Total System Uncertainty

uncertainty, for the same collapse probability of 10%, the resulting $ACMR_{10\%}$ would become 1.90, obtained from a linear interpolation of the values in the performance chart in Figure 8-33 between 1.78 (Superior, A) and 1.96 (Good, B) for β_{TOT} of 0.5. Hence, the performance point moves from star-marker #1 to #2, which now satisfies the performance criterion.

It should be emphasized, however, that adjusting uncertainty factors by selecting lower values is somewhat subjective. The current uncertainty factors selected for this research were deemed appropriate considering the current understanding of SPSW behavior. As more research on SPSWs becomes available, expert opinions could determine whether lower uncertainty factors for

SPSWs are acceptable. Hence, the above theoretical adjustment is only presented here for illustration purposes, to show the potential benefits in improving knowledge on the collapse performance of balanced archetypes.

8.8.2 Second Adjustment: Accepting Higher Probability of Collapse

The second possible adjustment is to accept a higher probability of collapse. If a collapse probability of 20% is considered acceptable and the same level of total system collapse uncertainty of 0.6 is selected, the threshold value for the balanced archetypes (i.e. $ACMR_{20\%}$) reduces to 1.66. In this case, the performance point in the performance chart (Figure 8-33) moves from star-marker #1 to #3, which satisfies the performance criterion. According to the FEMA P695 methodology however, doing so would be acceptable only if many more archetypes were designed such they can be grouped into several performance groups with at least 3 archetypes in each performance group. Alternatively, one could also select different acceptable collapse probability (for example 15%, which would give $ACMR_{15\%} = 1.86$ for $\beta_{TOT} = 0.6$) to satisfy the performance criterion (i.e., indicated by star-marker #4). Again, expert opinions would be required to decide an appropriate level of collapse probability for SPSWs other than what is currently specified in the FEMA P695 methodology.

8.8.3 Third Adjustment: Designing Balanced Archetypes with Lower *R*-Factor

The third possible adjustment to improve the balanced archetypes collapse performance is to design them with a lower value of the *R* factor and repeat the performance evaluation with the same collapse probability of 10% and total system collapse uncertainty (β_{TOT}) of 0.6. Here, this was done by designing another 3-story balanced archetype with *R* factor of 6. The archetype was denoted as SW320KR6 and geometric properties of its boundary elements and infill plates were presented in Table 7-9.

The resulting collapse fragility curve for SW320KR6 obtained from IDA using spectral acceleration as the intensity measure is plotted in Figure 8-34a, superimposed with the fragility curves for SW320 and SW320K. Interestingly, contrary to initial expectations, reducing the *R* factor from 7 to 6 did not result in a significant improvement of the collapse margin ratio. The CMR for SW320KR6 is 1.65, which is approximately an 8% increase from that of SW320K. In addition, the same result was obtained when using PGA as the intensity measure (Table 8-4). In
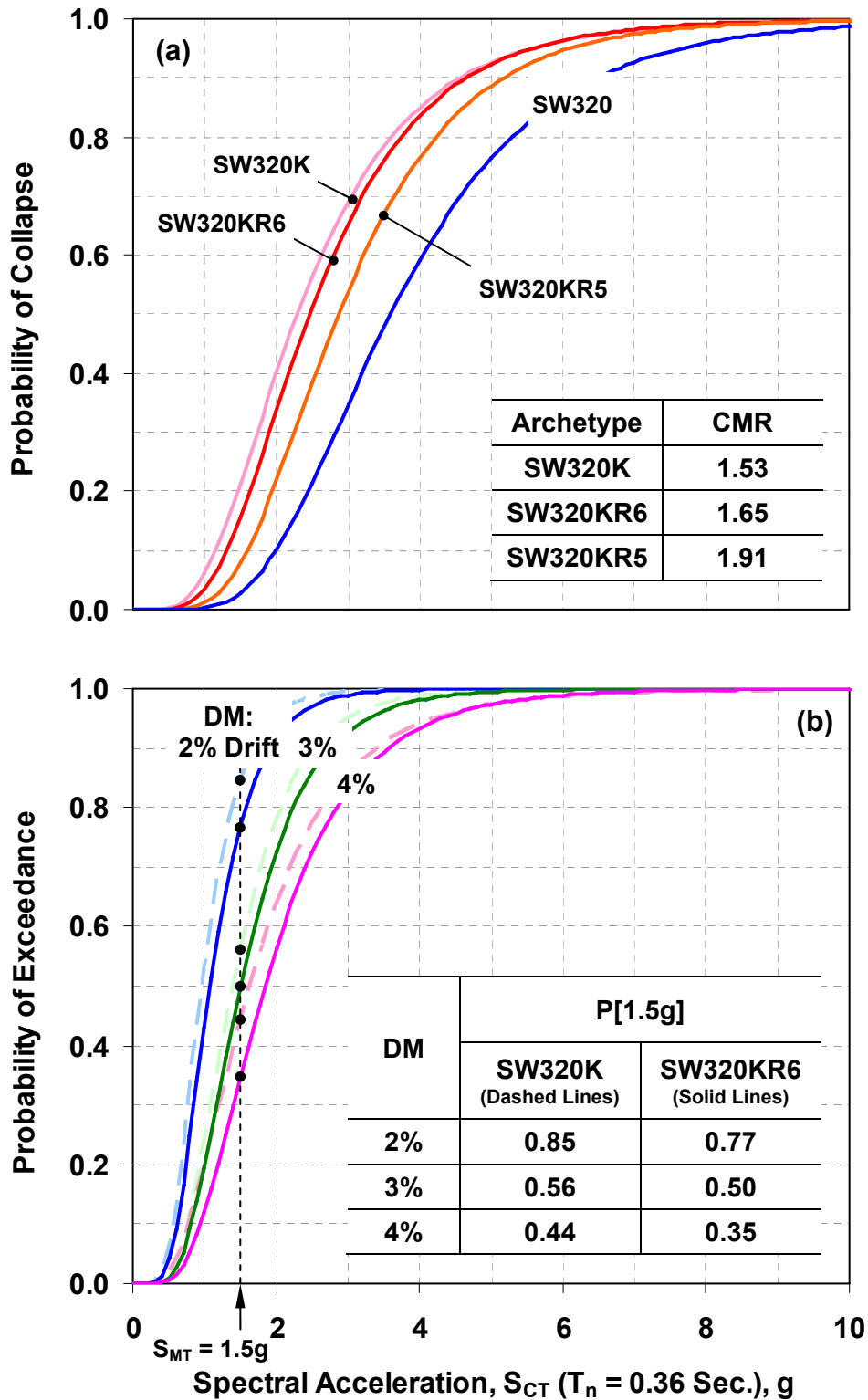
**Figure 8-34 Fragility Curves for Archetypes with Different *R* Factors:
(a) Spectral Acceleration as IM; (b) Interstory Drift as DM**

415

terms of the probability of exceeding the damage measures of 2, 3, and 4% interstory drift, results shown in Figure 8-34b indicate that reducing the R factor from 7 to 6 resulted in an improvement of exceedance probability of no more than 10% for SW320KR6 compared to SW320K. More specifically, whereas half of the considered ground motions at the MCE level resulted in approximately 3.5% interstory drifts for SW320K, this slightly improved to 3.0% interstory drifts for SW320KR6 (Table 8-4).

Table 8-5 summarizes the performance evaluation for SW320KR6. Comparison with the results for SW320K, SW320KR6 shows a slight improvement in period-based ductility, a similar system overstrength, and a slight increase in the calculated ACMR. The calculated ACMR of 2.06 is approximately 5% below the acceptable $ACMR_{10\%}$ of 2.16 (i.e., indicated by star-marker #5 in Fig. 8.33). Although some could consider that difference acceptable, to be rigorous, another design iteration was performed using an R factor of 5; the resulting balanced archetype is denoted as SW320KR5. The IDA results and performance evaluation for this archetype are also presented in Figure 8-34, Table 8-4, and Table 8-5. As hoped, SW320KR5 satisfied the performance criteria. Here, the calculated ACMR of 2.39 is 11% higher than the threshold $ACMR_{10\%}$ (i.e., indicated by star-marker #6) Half of the considered ground motions at the MCE level caused approximately 2.5% maximum interstory drifts for SW320KR5, which is tolerable and closer to what is expected for the conventional SPSWs.

For completeness, the same iteration process with R factor lower than 7 should be conducted on the other balanced archetypes that did not satisfy the performance criteria (i.e., SW310K, SW320GK, and SW520K). Considering that these archetypes have practically the same ACMR as SW320K with R factor of 7, it was assumed that comparable results to that of SW320KR5 would be obtained if these archetypes were to be designed with an R factor of 5. Hence, such redesigns were not attempted, and the R factor of 5 was deemed adequate for all balanced case.

Based on the above results, seismic performance factors for SPSWs designed with $\kappa_{balanced}$ are recommended to be smaller compared to that for conventional SPSWs (i.e., the 100% design case, $\kappa = 1.0$). Results above indicate that an R factor of 5 should be used for the design of balanced SPSWs. No system overstrength factor is available in balanced SPSWs (i.e., $\Omega_o = 1$). Like for conventional SPSWs, the deflection amplification factor (C_d factor) for balanced SPSWs should be taken as similar to the assigned R factor (i.e., $C_d = 5.0$).

Table 8-4 Summary of Incremental Dynamic Analysis (IDA) on SPSW Archetypes with Different *R* Factors

Archetype ID	$T_{\text{Theoretical}}$ (Sec.)	T_{Analysis} (Sec.)	IM: Spectral Acc.		IM: PGA		$P[S_{MT}]$	$P[DM_{2\%}]$	$P[DM_{x\%}]$ = 50%
			$\hat{S}_{CT}$ (g)	CMR_{Sa}	PGA_{CT} (g)	CMR_{PGA}			
SW320K	0.36	0.50	2.29	1.53	1.06	1.76	21.5%	84.6%	3.5%
SW320KR6	0.36	0.46	2.47	1.65	1.14	1.90	15.7%	76.9%	3.0%
SW320KR5	0.36	0.42	2.87	1.91	1.32	2.20	8.0%	62.3%	2.5%

Note: CMR_{Sa} = $\hat{S}_{CT}/S_{MT}$, where S_{MT} = 1.5g for 3-story archetypes.
CMR_{PGA} = PGA_{CT}/PGA_{MT}, where PGA_{MT} = 0.6g for 3-story archetypes.
$P[S_{MT}]$ = Probability of collapse at S_{MT} level.
$P[DM_{2\%}]$ = Probability of exceedance when maximum interstory drift reaches 2% interstory drift.
$P[DM_{x\%}]$ = Maximum interstory drift corresponding to 50% probability of exceedance.

Table 8-5 Summary of Performance Evaluation for Archetypes with Different *R* Factors

Archetype ID	Pushover Results						IDA Results		Performance Evaluation		
	V_d (kips)	V_{max} (kips)	$\delta_{y,eff}$ (in)	δ_u (in)	$\Omega_0 =$ V_d/V_{max}	$\mu_T =$ $\delta_u/\delta_{y,eff}$	$\hat{S}_{CT}$ (g)	$CMR =$ $\hat{S}_{CT}/S_{MT}$	SSF^{1}	$ACMR^{2}$	Pass/ Fail[3]
SW320K	176	226	1.8	8.6	1.3	4.8	2.29	1.53	1.24	1.90	**Fail**
SW320KR6	205	270	1.7	8.6	1.3	5.0	2.47	1.65	1.25	2.06	**Fail**
SW320KR5	246	334	1.8	9.1	1.4	5.1	2.87	1.91	1.25	2.39	**Pass**

Note: [1] SSF obtained from Table 2.1 for a given T and μ_T [3] Acceptance criteria: $ACMR_{10\%}$ (Table 2.5 for β_{TOT} of 0.6) = **2.16**
[2] ACMR = SSF (T, μ_T) × CMR   Pass if ACMR ≥ $ACMR_{10\%}$, otherwise Fail
S_{MT} = 1.5g for 3-story archetypes.

Table 8-6 compares the total steel weight for archetypes designed with different R factors. For example, comparing results for the three story archetypes, the "reference" conventional SPSW (designed per AISC 2010 with an R factor of 7) requires a total of 10,459 pounds of steel. The case designed with $\kappa_{balanced}$ with R factor of 7, SW320K, requires a total of 5737 pounds of steel, which is approximately 55% less than what is required for the conventional design, but, as indicated above, SW320K did not meet the collapse performance criteria according to the FEMA P695 methodology and a lower R factor must be used. Designed with R factor of 6 and 5, SW320KR6 and SW320KR5 require 17 and 31% more steel than SW320K, but SW320KR5 still provides a 28% reduction in the total weight of steel from that is required for the conventional SPSW. However, that savings in steel comes at the cost the SPSW designed for $\kappa_{balanced}$ developing larger interstory drifts compared to the conventional SPSWs (i.e., 2.5% versus 2.0% interstory drift) under MCE ground motions.

Table 8-6 Comparison of Steel Weight for Archetypes Designed with Different R Factors

SPSW Components	SW320[a] (R = 7.0)	SW320KR5[a] (R = 5.0)	SW320KR6[b] (R = 6.0)	SW320K[b] (R = 7.0)
HBE	5980	4500	4000	3380
VBE	3110	2090	1910	1690
Infill Plate	1369	951	784	667
Total	**10459**	**7541**	**6694**	**5737**

Note: Unit: weight in pounds.
 [a] Complies with the FEMA P695 collapse performance criterion
 [b] Does not comply with the FEMA P695 collapse performance criterion

8.9 Summary

Collapse assessment of steel plate shear walls under 44 specified ground motions was presented. The main objective of this assessment was to quantify the seismic performance factors (SPF), namely: response modification coefficient (R factor), system overstrength factor (Ω_o factor), and deflection amplification factor (C_d factor) for SPSWs designed per different approaches. Two different basic configurations of SPSWs were considered in this assessment: conventional design (κ = 1.0) and balanced design (κ = $\kappa_{balanced}$) cases. The FEMA P695 methodology was used for

the above purpose. Detailed application of this methodology was illustrated for two 3-story SPSW archetypes, including descriptions of the structural system archetypes, nonlinear analytical model used, nonlinear static and dynamic analyses conducted, collapse performance evaluation, and evaluation of SPF. It was identified that collapse margin ratio (CMR) played a significant role in determining whether the proposed SPFs satisfy the FEMA P695 performance criteria. Factors that affect CMR were investigated such as intensity measure, damage measure, and non-deteriorated material model.

Following the example of collapse performance evaluation on the 3-story archetypes, comparison of IDA results between 3- and 10-story SPS archetypes was presented. The 10-story archetypes have significant larger margin to collapse compared to the 3-story archetypes. The CMRs for the 10-story archetypes were at least 1.5 times larger than that in the 3-story archetypes. Investigation on local behaviors of both groups of archetypes was conducted in an attempt to explain this observation by comparing infill plate yielding and plastic hinge distributions, cross-section rotations, and inter-story drifts of both groups at the MCE level, the last stable point, and the collapse point. No conclusive evidence was found through this investigation. When using interstory drift as the damage measure (DM), both archetypes have comparable exceedance margin ratio (EMR) for DM of smaller than 3% interstory drift. However, the 10-story archetypes consistently have higher exceedance margins for DM of 3% or larger interstory drifts compared to those of the 3-story archetypes.

Collapse fragility curves for archetypes with various structural configurations (i.e., panel aspect ratio, seismic weight intensity, and number of story) were presented. Archetypes with smaller panel aspect ratios have smaller CMR as a consequence of less overstrength available in these archetypes, though the amount of CMR reduction between two different aspect ratios was not as high as indicated by the theoretical overstrength differences. Interestingly, the conventional archetypes designed with higher seismic weight actually have higher CMR values. This phenomenon was found to be a consequence of the use of deeper cross-sections for archetypes with higher seismic weight, as deeper cross-sections were less affected by axial forces compared to those selected for archetypes with lower seismic weight. Moreover, CMR increased as number of stories increased irrespective of design approaches selected (i.e., conventional versus balanced

419

design cases) and seismic weight intensity level considered (i.e., low versus high seismic weight). The CMR increment however was not linearly proportional to the increment in number of story.

All conventional archetypes met the FEMA P695 performance criteria for the R factor of 7 used in their design. System overstrength Ω_o of 2 can be considered for conventional SPSW. Assuming the inherent damping available in SPSW to be 5% of critical damping, a deflection amplification factor (C_d factor) of 7 (equals to R factor) was considered for conventional SPSWs. The resulting seismic performance factors for conventional SPSW obtained in this case are somewhat similar to those specified in the ASCE 7-10 (i.e., R, Ω_o, and C_d factors are 7, 2, and 6, respectively).

By contrast, the balanced archetypes designed with an R factor of 7 did not meet the FEMA P695 performance criteria. Adjusted seismic performance factors for the balanced archetypes were obtained by design iterations with a lower value of R factor. It was found that an R factor of 5 was required for the balanced SPSWs to rigorously meet the FEMA P695 performance criteria. No system overstrength factor was available for balanced SPSWs (i.e., $\Omega_o = 1$). It should be noted, however, that an inherent design overstrength factor exists in balanced SPSWs as a consequence of complying with the current AISC design procedure for SPSW (i.e., using $\Omega_s = 1.2$ and $\phi = 0.9$, Section 7.2.3). Like for conventional SPSWs, deflection amplification factor (C_d factor) for balanced SPSWs should be taken as similar to the assigned R factor (i.e., $C_d = 5.0$).

Most importantly, the balanced archetypes were found to have a higher probability to suffer significantly larger interstory drift than the conventional archetypes. For example at the MCE level (i.e., $S_{MT} = 1.5g$), there was approximately a 50% probability that drifts will exceed 2% and 3.5% interstory drifts for SW320 and SW320K, respectively. More significantly at a 20% probability of exceedance, the respective archetypes will exceed 3% and 7% interstory drifts. The same results were also obtained when comparing SW1020 and SW1020K. For the conventional archetype, half of the ground motions resulted in approximately 2% interstory drift, while that for the balance archetype resulted in 3% interstory drift. At a 20% probability of exceedance, the respective 10 story archetypes will exceed 2.5% and 4.5% interstory drifts. The results indicate that the ability of balanced archetypes to prevent damage to the structure and to drift-sensitive

non-structural components was significantly less than that of conventional archetypes. Savings in steel when designing balanced SPSWs with a lower *R* factor came at the cost of the SPSWs developing larger interstory drifts compared to the conventional SPSWs under MCE ground motions. These findings suggest that the infill plates of SPSWs should be designed to resist the total specified story shears, rather than designed by sharing those forces between the boundary frame and infill.

SECTION 9

SUMMARY, CONCLUSIONS, AND RECOMMENDATIONS

9.1   Summary

Research was conducted to investigate the seismic performance of steel plate shear walls (SPSWs) considering different design philosophies of horizontal boundary elements (HBEs) and infill plates (webs). First, a three-story SPSW specimen was developed to experimentally investigate the impact of HBE in-span hinges on the seismic behavior of steel plate shear walls (to complement a previously published analytical study that demonstrated the undesirable behavior of such in-span hinging). Second, the collapse assessment of SPSWs having infill plates designed to sustain different percentages of the applied lateral loads was investigated.

In the first study, the experimental program was conducted at the Structural Engineering and Earthquake Simulation Laboratory (SEESL) of the University at Buffalo. The specimen roughly corresponded to a 1/3-scale model of a SPSW that could be implemented in the three-story SAC model building (FEMA 355-C). The specimen was chosen to reflect a case when in-span plastic hinging was predicted to develop. Fabrication process, experimental setting (i.e., how the specimen, gravity column and lateral support systems, actuators, and instrumentation were assembled), and loading protocol development (i.e., how force was distributed among three dynamic actuators) were presented. Observation and results from this experimental investigation (e.g., hysteretic behavior of story shear versus specimen lateral displacement, plastic hinge and infill plate yielding distributions, HBE vertical deformations, and moment-rotation hysteresis) were used to substantiate the experimental objectives.

A finite element investigation of the tested SPSW specimen was conducted using the finite element software ABAQUS/Standard (Dassault Systèmes 2009b). Specific finite element features to capture the SPSW specimen behavior were described. Finite element monotonic pushover analyses with a fixed support at the base of columns and with floor plate included were conducted. The interaction between the floor plate and the rigid concrete floor was not considered

423

in the latter model. Though the analytical model still overestimated the experimental strength at the onset of yielding, an improved result was observed in the latter model compared to that in the former. Afterward, a finite element cyclic pushover analysis was conducted. Results were presented in terms of the hysteresis of base shear versus lateral displacement at the top floor, plastification in the FE model, HBE vertical deformations, and moment-rotation hysteresis at HBE connections to VBEs.

For the second study, deterioration models for infill plates and boundary elements were developed in a format compatible with the FEMA P695 methodology, for use in the collapse assessment of SPSWs having infill plates designed to sustain different percentages of the applied lateral loads. Based on a review of 36 conventional unstiffened slender-web SPSW specimens, the possible causes of deterioration of structural components that lead to failures of SPSWs were identified, namely: deteriorations associated with web tearing (WT), shear or flexural failures of boundary elements (FBE), and instability of boundary elements (IBE). In well-designed SPSWs, shear failure and instability of boundary elements can be prevented by designing boundary elements according to capacity design principles and selecting seismically compact sections. Hence, of these failure modes, only web tearing and flexural failure of boundary elements were considered to quantify the deterioration parameters of SPSWs. The parameters for the chosen deteriorated material models for infill plates and boundary elements were statistically quantified and calibrated to four selected SPSW specimens varying from one- to four-story.

The calibration process was performed using the OpenSees framework. Unstiffened infill plates were modeled as series of the *Truss Element* oriented in the direction of the tension field. Boundary elements were modeled using the *Beam with Concentrated Hinge Element* (BCH) elements with fiber sections. The *Hysteretic Uniaxial Material* model was selected to define the inelastic behavior of these truss and BCH elements. Various case studies were conducted to obtain satisfactory degradation models. The case studies included investigation of different deterioration behaviors for corner and middle strips based on sequence of infill plate fractures observed in past experiments (i.e., severe and moderate strength degradations for corner and middle strips, respectively), and with strength degradation only occurring in a few SPSW

components (i.e., elasto-plastic material for infill plates and degradation material model for boundary elements, and vice versa).

Development and design of archetypes for the collapse assessment of SPSWs was presented. Archetypes were categorized into two basic configurations. In the first group of archetypes, infill plates were designed to resist the entire lateral load, without considering the possible contribution from the surrounding boundary moment-resisting frames. In the second group of archetypes, infill plates were designed to resist a portion of the lateral loads and the boundary frame resisted the remaining portion of the lateral loads. Review of previous research conducted by Qu and Bruneau (2009) was performed and a limited case study was conducted to develop an understanding of the behavior of archetypes in the second group, and to decide what percentage of lateral loads distributed between infill plates and boundary frame should be used in the design of these archetypes. The "balanced" distribution of lateral loads ($\kappa = \kappa_{balanced}$) was selected for the design of the second group of archetypes because SPSWs designed per this approach exhibited similar behavior under monotonic and cyclic pushover analyses to that of the first group of archetypes designed per the AISC 2010 Seismic Provisions.

Archetypes developed were limited to low- and mid-rise SPSWs having low to high aspect ratio (i.e., 1.0 to 2.0.). In-span hinges were explicitly prevented in HBEs of the archetypes. Low and high tributary seismic mass intensity were considered and all archetypes were designed to resist forces obtained from a design response spectra for a high seismicity zone (i.e., SDC D_{max} of FEMA P695: $S_{DS} = 1.0g$ and $S_{D1} = 0.6g$). Archetype elevation and plan configuration were similar to the SAC model building. A total of 14 archetypes were considered.

Nonlinear models developed for collapse simulation featured a dual strip model with gravity leaning columns. The model incorporated an axial hinge at every strip, concentrated fiber plastic hinges at both ends of boundary elements, and material models that accommodated strength degradation. Added to capture the P-Δ effects of gravity loads that were not located on the SPSWs, the gravity leaning column was modeled in OpenSees using the *Elastic Beam-Column Element* with cross section area increased by 100 times the regular column cross section area, but with moment of inertia reduced to be 100 times smaller than the actual regular column moment

of inertia. Rigid links modeled with the *Truss Element* (with cross section arbitrarily increased to 100 times the HBE cross section at the corresponding floor) were used to connect the leaning column and SPSW. No seismic mass was applied on the leaning column; all seismic masses were applied to the SPSW and distributed equally on the left and right of HBE-to-VBE joints at every story.

Collapse assessment of SPSWs under 44 specified ground motions was presented. The main objective of this assessment was to quantify the seismic performance factors (SPF), namely: response modification coefficient (R factor), system overstrength factor (Ω_o factor), and deflection amplification factor (C_d factor) for SPSWs designed per different approaches. Two different basic configurations of SPSWs were considered in this assessment: conventional design ($\kappa = 1.0$) and balanced design ($\kappa = \kappa_{balanced}$) cases. The FEMA P695 methodology was used for the above purpose. Detailed application of this methodology was illustrated for two 3-story SPSW archetypes, including descriptions of the structural system archetypes, nonlinear analytical model used, nonlinear static and dynamic analyses conducted, collapse performance evaluation, and evaluation of SPF. It was identified that collapse margin ratio (CMR) played a significant role in determining whether the proposed SPFs satisfy the FEMA P695 performance criteria. Factors that affect CMR, such as intensity measure, damage measure, and non-deteriorated material model were investigated.

Following the example of collapse performance evaluation on the 3-story archetypes, comparison of IDA results between 3- and 10-story SPS archetypes was presented. The 10-story archetypes have significant larger margin to collapse compared to the 3-story archetypes. The CMRs for the 10-story archetypes were at least 1.5 times larger than those in the 3-story archetypes. Investigation of local behaviors of both groups of archetypes was conducted in an attempt to explain this observation by comparing infill plate yielding and plastic hinge distributions, cross-section rotations, and inter-story drifts of both groups at the maximum considered earthquake (MCE) level, the last stable point, and the collapse point. No conclusive evidence was found through this investigation. When using interstory drift as the damage measure (DM), both archetypes have comparable exceedance margin ratio (EMR) for DM of smaller than 3%

interstory drift. However, the 10-story archetypes consistently have higher exceedance margin for DM of 3% or larger interstory drifts compared to that of the 3-story archetypes.

9.2   Conclusions

9.2.1   Impact of In-Span Plastic Hinges

Experimental investigation of the three-story SPSW specimen, for which in-span plastic hinging was predicted to develop, demonstrated the development of in-span plastification and accumulation of plastic incremental deformations. Note that in-span plastification was not localized within a finite length but rather distributed within a longer span. The initially predicted un-symmetric hysteresis was indeed confirmed during this experimental investigation. Several special moment connections that exhibited this behavior were found to remain intact up to the conclusion of the experimental program in spite of its higher maximum rotations. In contrast, other special moment connections that experienced lower maximum rotations suffered connection fractures. Higher rotation range in the latter connections compared to that in the former ones in large contributed to the fracture of these connections. A finite element investigation of the tested specimen showed similar overall behavior to that observed during the experiment.

9.2.2   Deterioration Models for SPSW Components

The deterioration model for boundary elements was characterized with strain hardening of 2%, up to a capping point at 0.04 radians, and gradually losing its entire strength at 0.10 radians. This deterioration material model however was only applied to fibers at the bottom and top flanges of W-sections, while those on the webs were modeled with no degradation to maintain numerical stability during the analysis by allowing boundary elements to resist axial forces. As for the infill plates, strips were modeled to start to deteriorate at 1.5% axial strain (i.e., $9.0\delta_y$) and lost their capacity to sustain loads due to plate tearing rather quick at 1.8% axial strain (i.e., $10.7\delta_y$). All strips were set to have the same deterioration model irrespective of the location of strips (i.e., corner or middle strips, or floor level). This model exhibited stable behavior and was found to provide an acceptable match with experimental results in the perspective of investigating seismic performance of SPSW having infill plates designed considering two different design philosophies.

Note that, beyond the current purpose, the resulting calibrated models can also be valuable for use by engineers in progressive collapse assessments or performance based design of individual buildings.

9.2.3   Collapse Assessment of Steel Plate Shear Walls

Collapse fragility curves for archetypes with various structural configurations (i.e., panel aspect ratio, seismic weight intensity, and number of story) indicated that archetypes with smaller panel aspect ratios have smaller CMR as a consequence of less overstrength available in these archetypes, though the amount of CMR reduction between two different aspect ratios was not as high as indicated by the theoretical overstrength differences. Interestingly, the conventional archetypes designed with higher seismic weight actually have higher CMR values. This phenomenon was found to be a consequence of the use of deeper cross-sections for archetypes with higher seismic weight, as deeper cross-sections were less affected by axial forces compared to those selected for archetypes with lower seismic weight. Moreover, CMR increased as number of stories increased irrespective of design approaches selected (i.e., conventional versus balanced design cases) and seismic weight intensity level considered (i.e., low versus high seismic weight). The CMR increment, however, was not linearly proportional to the increment in number of story.

All conventional archetypes met the FEMA P695 performance criteria for the R factor of 7 used in their design. The Ω_o factor of 2 and C_d factor of 7 can be considered for conventional SPSW. The resulting seismic performance factors for conventional SPSW obtained in this case are somewhat similar to those specified in the ASCE 7-10 (i.e., R, Ω_o, and C_d factors are 7, 2, and 6, respectively). By contrast, the balanced archetypes designed with an R factor of 7 did not meet the FEMA P695 performance criteria. Adjusted seismic performance factors for the balanced archetypes were obtained by design iterations with a lower value of R factor. It was found that an R factor of 5 was required for the balanced SPSWs to rigorously meet the FEMA P695 performance criteria. No system overstrength factor was available for balanced SPSWs (i.e., $\Omega_o = 1$) and the C_d factor for balanced SPSWs should be taken similar to the assigned R factor.

Most importantly, the balanced archetypes were found to have a higher probability to suffer significantly larger interstory drift than the conventional archetypes. For example at the MCE

level (i.e., $S_{MT} = 1.5g$), there was approximately a 50% probability that drifts will exceed 2% and 3.5% interstory drifts for SW320 and SW320K, respectively. More significantly at a 20% probability of exceedance, the respective archetypes will exceed 3% and 7% interstory drifts. The same results were also obtained when comparing SW1020 and SW1020K. For the conventional archetype, half of the ground motions resulted in approximately 2% interstory drift, while that for the balance archetype resulted in 3% interstory drift. At a 20% probability of exceedance, the respective 10 story archetypes will exceed 2.5% and 4.5% interstory drifts. The results indicate that the ability of balanced archetypes to prevent damage to the structure and to drift-sensitive non-structural components was significantly less than that of conventional archetypes. Savings in steel when designing balanced SPSWs with a lower R factor came at the cost of the SPSWs developing larger interstory drifts compared to the conventional SPSWs under MCE ground motions. These findings suggest that the infill plates of SPSWs should be designed to resist the total specified story shears, rather than designed by sharing those forces between the boundary frame and infill.

9.3   Recommendations for Future Research

Seismic performance factors (SPF) for balanced SPSWs have been proposed, and the values currently specified for conventional SPSW have been verified to be adequate. These factors were obtained from collapse performance evaluation of several SPSW archetypes designed to consider key structural configurations such as panel aspect ratio, seismic weight intensity level, and number of stories (building height). To further substantiate the proposed SPF for balanced design, considering a larger number of SPSW archetypes might be desirable. In particular, SPSW archetypes designed in different seismic design categories could be examined in this more comprehensive investigation.

In Section 8, collapse performances for archetypes with different panel aspect ratios, seismic weight intensity level, and building height were compared. Among these considered structural configurations, building height significantly affected values of the collapse margin ratio. Taller archetypes tend to have higher CMR compared to shorter archetypes, and variations of CMR values between the two were considerably large, especially for the conventional archetypes. For

example, CMR values for the shorter and taller conventional archetypes varied from 2.1 to 4.08 while those for the balanced archetypes varied from 1.52 to 2.30. This is consistent with trends reported in FEMA P695 for other types of structural systems. As such, further investigation of the FEMA P695 procedure might be desirable to elucidate the causes of this trend, and to investigate whether SPF (in particular R factor) should vary for SPSWs in the short and long period range.

In this research, SPFs were investigated for conventional SPSW (designed with $\kappa = 1.0$) and balanced SPSWs (designed with $\kappa = \kappa_{balanced}$). Although one might be able to interpolate SPFs for other SPSWs designed with $\kappa_{balanced} < \kappa < 1.0$, further investigation would be required to quantify SPFs for other κ factors different from those investigated in this research.

Note that an unintended source of overstrength might be also be introduced during the design of SPSWs. For example, selecting uniform columns and beams sizes over several stories is common in engineering practice for construction simplicity. In SPSW design, structural engineers might select similar VBEs, HBEs, and infill plates over several adjacent stories, and some of those might have additional strength beyond what is required to sustain loads. In addition, the minimum hot-rolled plate thickness available may also be thicker than what is required by design, thus providing another source of overstrength to the system (assuming Special Perforated SPSW design provisions are not used). The resulting additional overstrength could increase the margin to collapse, which would most benefit the balanced archetypes in this case. Further research could investigate the conditions when such overstrength can be systematically relied upon as a way to possibly increase the R factor. Lastly, as more research on SPSWs becomes available, impact of total system collapse uncertainty and rate of deteriorated material models on SPSW collapse performance can be re-assessed.

SECTION 10

REFERENCES

AISC. (2005a). "Specification for Structural Steel Buildings." ANSI/AISC 360-05, American Institute of Steel Construction, Inc., Chicago, Illinois.

AISC. (2005b). "Seismic Provisions for Structural Steel Buildings." ANSI/AISC 341-05, American Institute of Steel Construction, Inc., Chicago, Illinois.

AISC. (2008). "L.A. Live Hotel & Residences - An Innovative Steel-Plate Shear Wall Solution." <http://www.aisc.org/content.aspx?id=16012> (October 2008).

AISC. (2010a). "Specification for Structural Steel Buildings." ANSI/AISC 360-10, American Institute of Steel Construction, Inc., Chicago, Illinois.

AISC. (2010b). "Seismic Provisions for Structural Steel Buildings." ANSI/AISC 341-10, American Institute of Steel Construction, Inc., Chicago, Illinois.

Alinia, M.M., and Dastfan, M. (2006). "Behavior of Thin Steel Plate Shear Walls Regarding Frame Members" *Journal of Constructional Steel Research*, Vol. 62, pp. 730-738.

Ang, A. H-S., and Tang, W. H. (2007). "Probability Concepts in Engineering: Emphasis on Applications to Civil and Environmental Engineering", 2nd Edition, John Wiley and Sons, New Jersey.

ASCE. (2010). "Minimum Design Loads for Buildings and Other Structures." ASCE Standard ASCE/SEI 7-10, American Society of Civil Engineers, Reston, Virginia.

ASCE. (2013). "Seismic Evaluation and Retrofit of Existing Buildings." ASCE Standard ASCE/SEI 41-13, American Society of Civil Engineers, Reston, Virginia.

Astaneh-Asl, A. (2001). "Seismic Behavior of Steel Plate Shear Walls." *Steel Tips Report*, Structural Steel Education Council, Moraga, California.

Astaneh-Asl, A. and Zhao, Q. (2002). "Cyclic Behavior of Steel Shear Wall Systems." *Proceedings, Annual Stability Conference, Structural Stability Research Council*, April, Seattle.

ATC-24 (1992). "Guidelines for Cyclic Seismic Testing of Components of Steel Structures." Applied Technology Council, Redwood City, CA.

AWS. (2008). "AWS D1.1 Structural Welding Code Steel." Reference Manual, American Welding Society, Miami, Florida"

Behbahanifard, M. R., Grondin, G. Y., and Elwi, A. E. (2003). "Experimental and Numerical Investigation of Steel Plate Shear Wall." *Structural Engineering Report 254,* Department of Civil Engineering, University of Alberta, Edmonton, Alberta, Canada.

Baldvins, N. M., Berman, J. W., Lowes, L. N., Janes, T. M., and Lowa, N. A. (2012). "Fragility Functions for Steel Plate Shear Walls." *Earthquake Spectra*, EERI, Vol. 28, No. 2, pp 405-426.

Berman, J. W., and Bruneau, M. (2003). "Plastic Analysis and Design of Steel Plate Shear Walls." *Journal of Structural Engineering*, ASCE, Vol. 129, No. 11, pp. 1448-1456.

Berman, J. W. and Bruneau, M. (2004). "Steel Plate Shear Walls Are Not Plate Girders." *AISC Engineering Journal*, Third Quarter, pp. 95-106.

Berman, J. W. and Bruneau, M. (2005). "Experimental Investigation of Light-Gauge Steel Plate Shear Walls." *Journal of Structural Engineering*, ASCE, Vol. 131, No. 2, pp. 259-267.

Berman, J. W., and Bruneau, M. (2008). "Capacity Design of Vertical Boundary Elements in Steel Plate Shear Walls." *AISC Engineering Journal*, First Quarter, pp. 57-71.

Bhowmick, A. K., Grondin, G. Y., and Driver, R. G. (2010). "Performance of Type D and Type LD Steel Plate Walls." *Canadian Journal of Civil Engineering*, Vol. 37, pp. 88-98.

Bruneau, M., Uang, C. M., and Sabelli R. (2011). "Ductile Design of Steel Structures", 2nd Edition, McGraw-Hill, New York.

Caccese, V., Elgaaly, M., and Chen, R. (1993). "Experimental Study of Thin Steel Plate Shear Walls under Cyclic Load." *Journal of Structural Engineering*, ASCE, Vol. 119, No. 2, pp. 573-587.

Canadian Standards Association (CSA). (2009). "Design of Steel Structures." CAN/CSA S16-09, Willowdale, Ontario, Canada.

Chen, S-J., and Jhang, C. (2006). "Cyclic Behavior of Low Yield Point Steel Shear Walls." *Thin-Walled Structures*, Vol. 44, pp. 730-738.

Choi, I-R., and Park, H-G. (2008). "Ductility and Energy Dissipation Capacity of Shear-Dominated Steel Plate Walls." *Journal of Structural Engineering*, ASCE, Vol. 134, No. 9, pp. 1495-1507.

Choi, I-R., and Park, H-G. (2009). "Steel Plate Shear Walls with Various Infill Plate Designs." *Journal of Structural Engineering*, ASCE, Vol. 135, No. 7, pp. 785-796.

Choi, I-R., and Park, H-G. (2010). "Hysteresis Model of Thin Infill Plate for Cyclic Nonlinear Analysis of Steel Plate Shear Walls." *Journal of Structural Engineering*, ASCE, Vol. 136, No. 11, pp. 1423-1434.

Choi, I-R., and Park, H-G. (2011). "Cyclic Loading Test for Reinforced Concrete Frame with Thin Steel Infill Plate." *Journal of Structural Engineering*, ASCE, Vol. 137, No. 6, pp. 654-664.

Clayton, P. M., Berman, J. W., and Lowes, L. N. (2012). "Seismic Design and Performance of Self-Centering Steel Plate Shear Walls." *Journal of Structural Engineering*, ASCE, Vol. 138, No. 1, pp. 22-30.

Clough, R.W., and Johnston, S.B. (1966). "Effects of Stiffness Degradation on Earthquake Ductility Requirements." *Proceeding 2nd Japan Earthquake Eng. Symposium*, pp. 227-232.

Coleman, J., and Spacone, E. (2001). "Localization Issue in Force-Based Frame Elements." *Journal of Structural Engineering*, ASCE, Vol. 127, No. 11, pp. 1257-1265.

Computer and Structures, Inc. (CSI) (2007) "CSI Analysis Reference Manual for SAP2000." Version 11.0.8, Computer and Structures, Inc., Berkeley, California.

Dassault Systèmes (2009a). "ABAQUS/CAE User's Manual." Version 6.9-1, Dassault Systèmes Simulia Corporation, Providence, Rhode Island.

Dassault Systèmes (2009b). "ABAQUS/Standard User's Manual." Version 6.9-1, Dassault Systèmes Simulia Corporation, Providence, Rhode Island.

Dastfan, M. and Driver, R.G. (2008), "Flexural Stiffness Limits for Frame Members of Steel Plate Shear Wall Systems," *Proceedings of Annual Stability Conference*, Nashville, Structural Stability Research Council, Rolla, MO.

Dastfan, M. (2011), "Ductile Steel Plate Shear Walls with PEC Columns," Ph.D. Dissertation, University of Alberta, Edmonton, Alberta, Canada.

Deng, X. (2012). "Behaviour of Steel Plate Shear Walls Fabricated with Partially Encased Composite Columns." Ph.D. Dissertation, University of Alberta, Edmonton, Alberta, Canada.

Dowden, D., Purba, R., and Bruneau, M., (2012). "Behavior of Self-Centering Steel Plate Shear Walls and Design Considerations" *Journal of Structural Engineering*, American Society of Civil Engineers (ASCE), Vol. 138, No. 1, pp. 11 - 21.

Dowden, D., and Bruneau, M. (2014). "Analytical and Experimental Investigation of Self-Centering Steel Plate Shear Walls." *Tech. Rep. MCEER-14-0010*, Multidisciplinary Center for Earthquake Engineering Research, State University of New York at Buffalo, Buffalo, New York.

Driver, R. G., Kulak, G. L., Kennedy, D. J. L., and Elwi, A. E. (1997). "Seismic Behavior of Steel Plate Shear Walls." *Structural Engineering Report 215,* Department of Civil Engineering, University of Alberta, Edmonton, Alberta, Canada.

Driver, R. G., Kulak, G. L., Kennedy, D. J. L., and Elwi, A. E. (1998). "FE and Simplified Models of Steel Plate Shear Walls." *Journal of Structural Engineering,* ASCE, Vol. 124, No. 2, pp. 121-130.

Eads, L. (2012). "Pushover Analysis of 2-Story Moment Frame." OpenSees Structural Examples, <http://opensees.berkeley.edu/wiki/index.php/Pushover_Analysis_of_2-Story_Moment_Frame>. (November 2012).

Elgaaly, M., Caccese, V., and Du, C. (1993). "Postbuckling Behavior of Steel-Plate Shear Walls Under Cyclic Loads," *Journal of Structural Engineering*, ASCE, Vol. 119, No. 2, pp. 588-605.

Elgaaly, M. and Lui, Y. (1997), "Analysis of Thin-Steel-Plate Shear Walls," *Journal of Structural Engineering*, ASCE, Vol. 123, No. 11, pp. 1487-1496.

Elgaaly, M. (1998). "Thin Steel Plate Shear Walls Behavior and Analysis." *Thin Walled Structures*, Vol. 32, pp. 151-180.

Elghadamsi, F.E., and Mohraz, B. (1987). "Inelastic Earthquake Spectra," *Earthquake Engineering and Structural Dynamics*, Vol. 15, pp. 91-104.

Ericksen, J., and Sabelli, R. (2008). "A Closer Look at Steel Plate Shear Walls." *Modern Steel Construction* Magazine, American Institute of Steel Construction, Inc., Chicago, Illinois.

FEMA. (2000a). "State of the Art Report on Systems Performance of Steel Moment Frames Subject to Earthquake Ground Shaking." *FEMA Report No. 355C*, Prepared by the SAC Joint Venture Partnership for the Federal Emergency Management Agency, Washington, D.C.

FEMA. (2000b). "Prestandard and Commentary for Seismic Rehabilitation of Buildings." *FEMA Report No. 356,* Prepared by the American Society of Civil Engineers for the Federal Emergency Management Agency, Washington, D.C.

FEMA. (2003). "NEHRP Recommended Provisions for Seismic Regulations for New Buildings and Other Structures." *FEMA Report No. 450*, Building Seismic Safety Council for FEMA, Washington, D.C.

FEMA. (2009a). "Effects of Strength and Stiffness Degradation on Seismic Response." *FEMA Report No. P440A*, Prepared by the Applied Technology Council for the Federal Emergency Management Agency, Washington, D.C.

FEMA. (2009b). "Quantification of Building Seismic Performance Factors." *FEMA Report No. P695*, Prepared by the Applied Technology Council for the Federal Emergency Management Agency, Washington, D.C.

Hitaka, T. and Matsui, C. (2003). "Experimental Study on Steel Shear Wall with Slits." *Journal of Structural Engineering*, ASCE, Vol. 129, No. 5, pp. 586-595.

Haselton, C. B., and Deierlein, G. G. (2007). "Assessing Seismic Collapse Safety of Modern Reinforced Concrete Frame Buildings." *John A. Blume Earthquake Engineering Center, Technical Report No. 156*, Stanford University, Stanford, California.

Hatami, F., Ghamari, A., and Rahai, A. (2012. "Investigating the Properties of Steel Shear Walls Reinforced with Carbon Fiber Polymers (CFRP)." *Journal of Constructional Steel Research*, Vol. 70, pp. 36-42.

Ibarra, L. F., and Krawinkler, H. (2005). "Global Collapse of Frame Structures Under Seismic Excitations." *John A. Blume Earthquake Engineering Center*, *Technical Report No. 152*, Department of Civil Engineering, Stanford University, Stanford, California.

Jahanpour, A., Jönsson., J., and Moharrami, H. (2012). "Seismic Behavior of Semi-Supported Steel Shear Walls." *Journal of Constructional Steel Research*, Vol. 74, pp. 118-133.

Jalali, A., and Sazgari, A., (2006). "Experimental and Theoretical Post-Buckling Study of Steel Shear Walls." *Proceeding, 4th International Conference on Earthquake Engineering*, Taipei, Taiwan.

Kharrazi, M. H. K., Prion, H. G. L., and Ventura, C. E. (2008). "Implementation of M-PFI Method in Design of Steel Plate Walls." *Journal of Constructional Steel Research*, Vol. 64, pp. 465-479.

Krawinkler, H., and Zareian, F. (2007). "Prediction of Collapse – How Realistic and Practical Is It, and What Can We Learn from It?" *The Structural Design of Tall and Special Buildings*, Vol. 16, No. 5, pp. 633-653.

Krypton Manual (2003). "Krypton Help Pages on K400/K600 - Hardware and Software Guide." Krypton Electric Engineering, Belgium.

Kurata, M., Leon, R.T., DesRoches, R., Nakashima, M. (2012). "Steel Plate Shear Wall with Tension-Bracing for Seismic Rehabilitation of Steel Frames." *Journal of Constructional Steel Research*, Vol. 71, pp. 92-103.

Kusumastuti, D., Reinhorn, A.M., and Rutenberg, A (2005). "A Versatile Experimentation Model for Study of Structures Near Collapse Applied to Seismic Evaluation of Irregular Structures" *Technical Rep. No. MCEER-05-0002*, Multidisciplinary Center for Earthquake Engineering Research, Buffalo, New York.

Lai, S.P., and Biggs, J.M. (1980), "Inelastic Response Spectra for Aseismic Buildings," *Journal of the Structural Division*, ASCE, Vol. 106, No. ST6, pp. 1295-1310.

Li, C-H., Tsai, K-C, Lin, C-H, and Chen, P-C. (2010). "Cyclic Tests of Four Two-Story Narrow Steel Plate Shear Walls. Part 2: Experimental Results and Design Implications." *Earthquake Engineering & Structural Dynamics*, Vol. 39, No. 7, pp. 801-826.

Liel, A. B., and Deierlein, G.G. (2008). "Assessing the Collapse Risk of California's Existing Reinforced Concrete Frame Structures: Metrics for Seismic Safety Decisions." *John A. Blume Earthquake Engineering Center, Technical Report No. 166,* Department of Civil Engineering, Stanford University, Stanford, California.

Lignos, D. G., and Krawinkler, H. (2009). "Sidesway Collapse of Deteriorating Structural Systems under Seismic Excitations." *John A. Blume Earthquake Engineering Center, Technical Report No. 172*, Department of Civil Engineering, Stanford University, Stanford, California.

Lin, Y.C. and Tsai, K.C. (2004). "Seismic Responses of Steel Shear Wall Constructed with Restrainers" (in Chinese) *Technical Report NCREE-04-015*, National Center for Research on Earthquake Engineering, Taipei, Taiwan, R.O.C., September 2004.

Lubell, A. S., Prion, H. G. L., Ventura, C. E., and Rezai, M. (2000). "Unstiffened Steel Plate Shear Wall Performance under Cyclic Loading." *Journal of Structural Engineering*, ASCE, Vol. 126, No. 4, pp. 453-460.

Mazzoni, S., McKenna, F., Scott, M. H., and Fenves, G. L. (2009). "Open System for Earthquake Engineering Simulation (OpenSees) User Command-Language Manual Version 2.0." Pacific Earthquake Engineering Research Center, University of California, Berkeley, Berkeley, CA.

Miranda, E. and Bertero, V.V. (1994). "Evaluation of Strength Reduction Factors for Earthquake-Resistant Design." *Earthquake Spectra*, Vol. 10, No. 2, pp. 357-379.

Montgomery, C.J. and Medhekar, M. (2001), "Discussion on Unstiffened Steel Plate Shear Wall Performance under Cyclic Loading." *Journal of Structural Engineering*, ASCE, Vol. 127, No. 8, p. 973.

Nassar, A.A. and Krawinkler, H. (1991). "Seismic Demands for SDOF and MDOF Systems.", *The John A. Blume Earthquake Engineering Center*, Technical Report No. 95, Stanford University, Stanford, California.

Neagu, C., Dinu, F., and Dubina, D. (2011). "Seismic Performance of Steel Plate Shear Walls Structures." *Pollack Periodica - An International Journal for Engineering and Information Sciences*, Vol.6, No. 1, pp. 47-58.

Newmark, N.M. and Hall, W.J. (1973). "Seismic Design Criteria for Nuclear Reactor Facilities," Building Practices for Disaster Mitigation, Report No. 46, National Bureau of Standards, U.S. Department of Commerce, pp. 209-236.

Nie, J., Fan, J., Liu, X, and Huang, Y. (2013). "Comparative Study on Steel Plate Shear Walls Used in a High-Rise Building." *Journal of Structural Engineering*, ASCE, Vol. 139, No. 1, p. 85-97.

Park, Y.J., and Ang, A. (1985). "Mechanistic Seismic Damage Model for Reinforced Concrete." *Journal of Structural Engineering*, ASCE, Vol. 111, No. 4, pp. 722-739.

Park, Y. J., Reinhorn, A.M., and Kunnath, S.K. (1987) "IDARC: Inelastic Damage Analysis of Reinforced Concrete Frame, Shear-wall, Structures." *Tech. Rep. NCEER-87-0008*, State University of New York at Buffalo, Buffalo, New York.

Park, H.G., Kwack, J.H., Jeon, S.W., Kim, W.K. and Choi, I.R. (2007), "Framed Steel Plate Wall Behavior under Cyclic Lateral Loading." *Journal of Structural Engineering*, ASCE, Vol. 133, No. 3, pp. 378-388.

PEER. (2005). "PEER NGA Database." Pacific Earthquake Engineering Research Center (PEER), University of California, Berkeley, California. <http://peer.berkeley.edu/nga/>.

Purba, R., and Bruneau, M. (2007). "Design Recommendations for Perforated Steel Plate Shear Walls." *Technical Rep. No. MCEER-07-0011*, Multidisciplinary Center for Earthquake Engineering Research, Buffalo, New York.

Purba, R., and Bruneau, M. (2009), "Finite Element Investigation and Design Recommendations for Perforated Steel Plate Shear Walls," *Journal of Structural Engineering*, ASCE, Vol.135, No. 11, pp.1367–1376.

Purba, R., and Bruneau, M. (2010). "Impact of Horizontal Boundary Elements Design on Seismic Behavior of Steel Plate Shear Walls." *Technical Rep. No. MCEER-10-0007*, Multidisciplinary Center for Earthquake Engineering Research, Buffalo, NY.

Qu, B., and Bruneau. M. (2008). "Seismic Behavior and Design of Boundary Frame Members of Steel Plate Shear Walls." *Technical Report MCEER-08-0012*, Multidisciplinary Center for Earthquake Engineering Research, Buffalo, New York.

Qu, B., Bruneau, M., Lin, C.H., and Tsai, K.C. (2008). "Testing of Full Scale Two-story Steel Plate Shear Walls with Reduced Beam Section Connections and Composite Floors." *Journal of Structural Engineering*, ASCE, Vol. 134, No. 3, pp. 364-373.

Qu, B., and Bruneau, M. (2009). "Design of Steel Plate Shear Walls Considering Boundary Frame Moment Resisting Action." *Journal of Structural Engineering*, ASCE, Vol. 135, No. 12, pp. 1511-1521.

Qu, B., and Bruneau, M. (2010). "Behavior of Vertical Boundary Elements in Steel Plate Shear Walls." *AISC Engineering Journal*, 2nd Quarter, pp. 109-122.

Rahnama, M., and Krawinkler, H. (1993). "Effects of Soft Soil and Hysteretic Models on Seismic Demands." *Report No. 108*, John A. Blume Earthquake Engineering Center, Department of Civil and Environmental Engineering, Stanford University, Stanford, California.

Rezai, M. (1999). "Seismic Behavior of Steel Plate Shear Walls by Shake Table Testing." Ph.D. Dissertation, University of British Columbia, Vancouver, BC, Canada.

Rezai, M., and Ventura, C. E. (2008). "Seismic Loading Behavior of Thin Steel Plate Walls." *Proceeding, Structural Congress: Crossing Borders*. Vancouver, BC, Canada.

Riddell, R., Hidalgo, P., and Cruz, E. (1989). "Response Modification Factors for Earthquake-Resistant Design of Short-Period Structures," *Earthquake Spectra*, Vol. 5, No. 3, pp. 571-590.

Roberts, T. and Sabouri-Ghomi, S. (1991). "Hysteretic Characteristics of Unstiffened Plate Shear Panels." *Thin Walled Structures*, Vol. 12, No. 2, pp. 145-162.

Roberts, T. and Sabouri-Ghomi, S. (1992). "Hysteretic characteristics of unstiffened perforated steel plate shear panels." *Thin Walled Structures*, Vol. 14, pp. 139-151.

Sabelli, R., and Bruneau, M. (2007). "Steel Plate Shear Walls (AISC Design Guide)." American Institute of Steel Construction, Inc., Chicago, Illinois, 144 p.

Sabouri-Ghomi, S., Ventura, C. E., and Kharrazi, M. H. K. (2005). "Shear Analysis and Design of Ductile Steel Plate Walls" *Journal of Structural Engineering*, ASCE, Vol. 131, No. 6, pp. 878-889.

Sabouri-Ghomi, S., and Gholhaki, M. (2008). "Tests of Two Three-Story Ductile Steel Plate Shear Walls." *Proceeding, Structural Congress: Crossing Borders*. Vancouver, BC, Canada.

Sabouri-Ghomi, S., and Sajjadi, S. R. A. (2012). "Experimental and Theoretical Studies of Steel Shear Walls with and without Stiffeners." *Journal of Constructional Steel Research*, Vol. 75, pp. 152-159.

Schumacher, A., Grodin, G.Y., and Kulak, G.L. (1997). "Connection of Infill Panels in Steel Plate Shear Walls." *Structural Engineering Report No. 217,* Department of Civil Engineering, University of Alberta, Edmonton, Alberta, Canada.

Scott, M. H., and Fenves, G. L. (2006). "Plastic Hinge Integration Methods for Force-Based Beam-Column Elements." *Journal of Structural Engineering*, ASCE, Vol. 132, No. 2, pp. 244-252.

Shishkin, J.J., Driver, R.G., and Grondin, G.Y. (2009), "Analysis of Steel Plate Shear Walls Using the Modified Strip Model," *Journal of Structural Engineering*, ASCE, Vol. 135, No. 11, pp. 1357–1366.

Sivaselvan, M., and Reinhorn, A. (2000). "Hysteretic Models for Deteriorating Inelastic Structures," *Journal of Engineering Mechanics*, Vol. 126. No. 6., pp. 633-640.

Song J.-K., and Pincheira, J.A. (2000). "Seismic Analysis of Older Reinforced Concrete Columns." *Earthquake Spectra*, Vol. 16, No. 4, pp. 817–851.

Sucuoglu, H., and Erberik, A. (2004). "Energy-Based Hysteresis and Damage Models for Deteriorating Systems." *Earthquake Engineering & Structural Dynamics*, Vol. 33, pp. 69-88.

Takeda, T., Hwang, H.H.M., and Shinozuka, M. (1988). "Response Modification Factors for Multiple-Degree-of-Freedom Systems." Proceedings, 9th World Conference on Earthquake Engineering, Tokyo-Kyoto, Japan, Vol. V, pp. 129-134.

Takeda, T., Sozen, M.A., and Nielsen, N.N. (1970). "Reinforced Concrete Response to Simulated Earthquakes," *Journal of the Structure Division*, ASCE, ST12, pp. 2557-2573.

Thorburn, L. J., Kulak, G. L., and Montgomery, C. J. (1983). "Analysis of Steel Plate Shear Walls." *Structural Engineering Report No. 107,* Department of Civil Engineering, University of Alberta, Edmonton, Alberta, Canada.

Timler, P. A., and Kulak, G. L. (1983). "Experimental Study of Steel Plate Shear Walls." *Structural Engineering Report No. 114,* Department of Civil Engineering, University of Alberta, Edmonton, Alberta, Canada.

Timler, P.A., Ventura, C.E., Prion, H., and Anjam, R. (1998). "Experimental and Analytical Studies of Steel Plate Shear Walls as Applied to the Design of Tall Buildings.", *Structural Design of Tall Buildings*, Vol. 7, pp. 233-249.

Timoshenko, S. P., Gere, J. M. (1961). "Theory of Elastic Stability." 2nd Ed, McGraw-Hill, New York, NY.

Tromposch, E.W., and Kulak, G.L. (1987). "Cyclic and Static Behavior of Thin Panel Steel Plate Shear Walls.", *Structural Engineering Report No. 145*, Department of Civil Engineering, University of Alberta, Edmonton, Alberta, Canada.

Tsai, K. C., Lin, C. H., Lin, Y. C., Hsieh, W. D., and Qu, B. (2006). "Sub-structural Hybrid Tests of a Full Scale Two-Story Steel Plate Shear Wall." *Technical Rep. No. NCREE-06-017*, National Center for Research on Earthquake Engineering, Taipei, Taiwan (in Chinese).

Tsai, K-C, Li, C-H., Lin, C-H, Tsai, C-Y, and Yu, Y-J. (2010). "Cyclic Tests of Four Two-Story Narrow Steel Plate Shear Walls. Part 2: Part 1: Analytical Studies and Specimen Design." *Earthquake Engineering & Structural Dynamics*, Vol. 39, No. 7, pp. 801-826.

Vamvatsikos, D., and Cornell, C. A. (2002). "Incremental Dynamic Analysis." *Earthquake Engineering and Structural Dynamics*, Vol. 31, No. 3, pp. 491-514.

Valizadeh, H., Sheidaii, M., and Showkati, H. (2012). "Experimental Investigation on Cyclic Behavior of Perforated Steel Plate Shear Walls." *Journal of Constructional Steel Research*, Vol. 70, pp. 308-316.

Vian, D., and Bruneau, M. (2005). "Steel Plate Shear Walls for Seismic Design And Retrofit of Building Structures." *Tech. Rep. MCEER-05-0010*, Multidisciplinary Center for Earthquake Engineering Research, State University of New York at Buffalo, Buffalo, New York.

Vidic, T., Fajfar, P., and Fischinger, M. (1992). "A procedure for Determining Consistent Inelastic Design Spectra," Proceedings, Workshop on Nonlinear Seismic Analysis of RC Structures, Bled, Slovenia.

Warn, G. P., and Bruneau, M. (2009). "Blast Resistance of Steel Plate Shear Walls Designed for Seismic Loading." *Journal of Structural Engineering*, ASCE, Vol. 135, No. 10, pp. 1222-1230.

Zhao, Q. and Astaneh-Asl, A. (2004), "Cyclic Behavior of Traditional and Innovative Composite Shear Walls," *Journal of Structural Engineering*, ASCE, Vol. 130, No. 2, pp. 271-284.

APPENDIX A

SUPPORTING INFORMATION ON THE DESIGN OF EXPERIMENTAL PROGRAM: CYCLIC PUSHOVER TESTING OF THREE-STORY SPSW

A.1 Design of 3-Story SPSW Specimen

Geometry and Loads

Number of stories

	NF :	3 stories

Height of stories

h_1 :	1270		50.00	
h_2 :	1289	mm	50.75	in.
h_3 :	1276		50.25	

Bay width

b_w :	2296	mm	90.38	in.

Story weight

W_1 :	1564		351.60	
W_2 :	1564	kN	351.60	kips
W_3 :	1694		380.83	

Total Weight

W_s :	4822	kN	1084.03	kips

Earthquake loads

Location : Sherman Oaks, California

Type of Soil : B

Design Base Earthquake (DBE), plotted in Fig. 1

S_{DS} :	1.3 g	S_{D1} :	0.58 g
T_S :	0.446 sec	T_0 :	0.089 sec

Approximate Natural Period

H :	3835.4 mm		12.583 ft
T_n :	0.134 sec		

Importance Factor

I :	1.0

Seismic coeficient

C_s :	0.186 (Assuming Viscous Damping

ξ = 5 %)　　　FEMA 356

Response Modification Factor

R :	7.0

Total Base Shear

V_{base} :   99.502 kN   22.369 kips

Fig. 1 Design Spectrum 5% Damping San Fransisco, CA
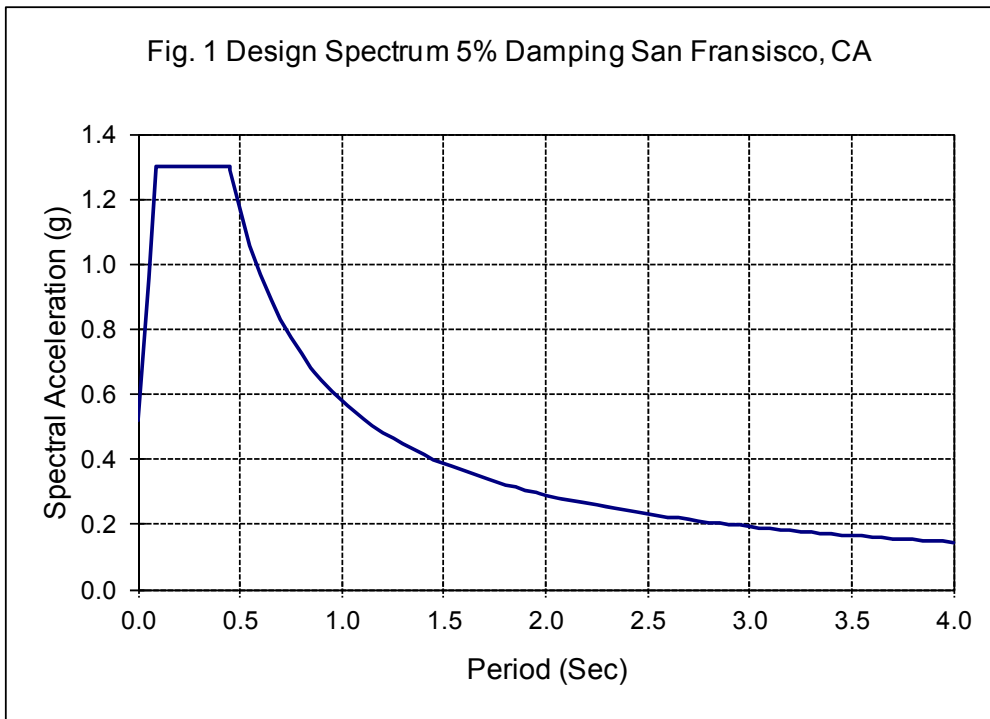
Calculation of earthquake load on every floor

W_1 :	173.78		Therefore:	
W_2 :	173.78	kN	Earthquake load on every floor	
W_3 :	188.22		F_1 :	3.56

Floor Height from base

h_{10} :	1270	
h_{20} :	2559	mm
h_{30} :	3835	

Earthquake load on every floor

F_1 :	3.56
F_2 :	7.17 kips
F_3 :	11.64

Applied Eq. load both on left and right side

F_{1-half} :	1.78
F_{2-half} :	3.59 kips
F_{3-half} :	5.82

Story Shear

V_1 :	22.37
V_2 :	18.81 kip
V_3 :	11.64

Primary Design: Plate

Material Properties

     E :   29000 ksi

A572 Gr. 50 Steel will be used for HBEs and VBEs

     F_y :   50 ksi R_y :   1.0   FEMA 350

442

Light Gauge Steel will be used for the web plates

F_{yp} :   30 ksi R_{yp} :   1.0   FEMA 350

For preliminary design assume a tension field angle for sizing the web plates

α_{assume} :   42.448 degree   0.740863 radians

Resistance factor for SPSW strength

ϕ :   0.9

Assume the clear distance between panels to be the bay width minus depth of VBE

b_w :	7.53 ft	2.296 m
h_w :	3.58 ft	1.092 m
L_{cf1} :	7.00	
L_{cf2} :	7.00 ft	
L_{cf3} :	7.00	

Plate thickness required   Gage Thickness

t_{req} :	0.024		t_{prov} :	0.0897		G13	0.0897
	0.020 in			0.0747 in		G15	0.0673
	0.012			0.0418		G19	0.0418

Primary Design: Boundary Elements

Vertical Boundary Elements (VBE)

Floor	1	2	3
Section	W6X25	W6X25	W6X25
A (in^2)	7.36	7.36	7.36
d (in)	6.38	6.38	6.38
$b/2tf$	6.68	6.68	6.68
h/tw	15.2	15.2	15.2
I_{xx} (in^4)	53.6	53.6	53.6
Z_{xx} (in^3)	19	19	19
r_y (in)	1.52	1.52	1.52
r_x (in)	2.7	2.7	2.7
KL/rx			
KL/ry			

Column Minimum Inertia criteria

I_{min1} :   10.41675 OK

I_{min2} :   8.67482 OK

I_{min3} :   4.854183 OK

Horizontal Boundary Elements (HBE)

Floor	0	1	2	3
Section	W8X13	S5X10	S5X10	W6X12
A (in^2)	3.84	2.93	2.93	3.55
d (in)	7.99	5	5	6.03
b/2tf	7.84	4.61	4.61	7.14
h/tw	29.9	16.8	16.8	21.6
I_{xx} (in^4)	39.6	12.3	12.3	22.1
Z_{xx} (in^3)	11.4	5.66	5.66	8.3
r_y (in)	0.843	0.638	0.638	0.918
r_x (in)	3.21	2.01	2.01	2.49
KL/rx	1.53	2.44	2.43	1.97
KL/ry	4.47	5.90	5.90	4.10

Strip Model Development

Calculation of α for selected Preliminary Shapes

α_1 :	0.735		42.134	
α_2 :	0.732	radians	41.925	degrees
α_3 :	0.752		43.109	
α_{ave} :	0.740	radians	42.3894	degrees
$\alpha_{SAP2000}$:			47.6106	degrees

Strip model set-up and strip dimensions

L_α :	95.742	in		
n :	14	pcs	Spasing for corner if needed	
S :	6.3828	in	3.1914	in
Sx :	8.6420	in	4.321	in
Sz :	9.468	in	4.734	in
As :	0.57			
	0.48	in^2		
	0.27			

B-values for strip model   Then

V_{e1} :	112.553		B_1 :	5.03
V_{e2} :	93.731	kip	B_2 :	4.98
V_{e3} :	52.449		B_3 :	4.51

Strip Model Analysis Results (using SAP2000 v.11)

Interstory drift calculation

Δ_1 :	0.06687		δ_1 :	0.067
Δ_2 :	0.10117 in		δ_2 :	0.034 in
Δ_3 :	0.14822		δ_3 :	0.047

Displacement amplification factor

C_d :   6 SPSW

Story drift limit

δ_a :   0.02 H

Δ_{a1} :	1.0000		δ_{a1} :	1.000
Δ_{a2} :	2.0150 in		δ_{a2} :	1.015 in
Δ_{a3} :	3.0200		δ_{a3} :	1.005

I :   1.0

Amplified Interstory drift calculation

Δ_{1A} :	0.4012		δ_{1A} :	0.4012	**Satisfied**
Δ_{2A} :	0.6070 in		δ_{2A} :	0.2058 in	**Satisfied**
Δ_{3A} :	0.8893		δ_{3A} :	0.2823	**Satisfied**

Compactness Check on VBEs and HBEs

Vertical Boundary Elements (VBE)

Floor	1	2	3
Section	W6X25	W6X25	W6X25
A (in^2)	7.36	7.36	7.36
b/2tf	6.68	6.68	6.68
h/tw	15.2	15.2	15.2
Web Criterion for Compactness			
P_u			
$\phi*P_y$	331.2	331.2	331.2
C_a	0.0000	0.0000	0.0000
λ_w	75.62	75.62	75.62
Status	OK	OK	OK
Flange Criterion for Compactness			
λ_f	7.225	7.225	7.225
Status	OK	OK	OK

Horizontal Boundary Elements (HBE)

Floor	0	1	2	3
Section	W8X13	S5X10	S5X10	W6X12
A (in^2)	3.84	2.93	2.93	3.55
b/2tf	7.84	4.61	4.61	7.14
h/tw	29.9	16.8	16.8	21.6
Web Criterion for Compactness				
P_u				
$\phi*P_y$	172.8	131.85	131.85	159.75
C_a	0	0	0	0
λ_w	75.62	75.62	75.62	75.62
Status	OK	OK	OK	OK
Flange Criterion for Compactness				
λ_f	7.224957	7.224957	7.224957	7.224957
Status	NOT OK	OK	OK	OK

Connection of HBE0 to VBE1

Section Properties and Loads

W-section properties for VBE and HBE

Item	VBE	HBE
Section	W6X25	W8X13
A (in^2)	7.36	3.84
Z (in^3)	19.00	11.40
d (in)	6.38	7.99
tw (in)	0.320	0.230
b (in)	6.08	4.00
tf (in)	0.455	0.255
k (in)	0.754	0.555

Material Properties

E :   29000 ksi

A572 Gr. 50 Steel will be used for HBEs and VBEs

F_y :   50 ksi R_y :   1.1   FEMA 350

A572 Gr. 50 Steel will be used for stiffeners

F_y :	50 ksi	R_y :	1.1	FEMA 350

Moment applied to the connection $\quad C_{pr}$: $\quad$ 1.2 $\qquad$ FEMA 350

$\quad M_p$: $\quad$ 752.40 kips-in

Story shear applied to the connection $\qquad$ Shear forces applied to the shear tab

$\quad V_u$: $\quad$ 0 (not considered) $\qquad V_u$: $\quad$ 79.927 kips

Concentrated forces applied on flange: $\qquad$ Axial Force on HBE:

$\quad P_u$: $\quad$ 99.124 kips $\qquad P_{HBE}$: $\quad$ 43.105 kips

Design of Transverse Stiffeners (Continuity Plates)

Limit states for tensile and compresive flange force

Limit States	ϕ	R_n (kips)	AISC Eq.	Status
Flange Local Bending	0.9	58.226	K1-1	**NOT OK**
Web Local Yielding	1.0	64.400	K1-2	**NOT OK**
Web Crippling	0.75	94.459	K1-4	**NOT OK**
Web Compression Buckling	0.90	215.116	K1-8	**OK**

Overall Status :

Transverse stiffeners are required

The required strength for the transverse stiffners is

$\quad R_{u\text{-st}}$: $\quad$ 84.003 kips

The minimum required cross sectional area of the transverse stiffeners

$\quad A_{min}$: $\quad$ 1.867 in^2

The following criteria should be used to size the transverse stiffener dimension

Stiffner width (AISC K1-9.1) $\qquad$ Stiffner Dimension provided:

$\quad b_{stiffner} \geq \quad$ 1.173 in $\qquad b_{stiffner\text{-prov'd}}$: $\quad$ 2.210 in $\quad$ **OK**

Stiffner thickness (AISC K1-9.2) $\qquad t_{stiffner\text{-prov'd}}$: $\quad$ 1/2 in $\quad$ **OK**

$\quad t_{stiffner} \geq \quad$ 0.128 in $\qquad A_{stiffner\text{-prov'd}}$: $\quad$ 2.210 in^2 $\quad$ **OK**

Minimum stiffener thickness (AISC DG 4.3-5)

$\quad t_{s\text{-min}}$: $\quad$ 0.313 in

Web Panel-Zone Shear (Design of Doubler Plate)

Plastic panel-zone deformation is considered in the calculation.

$\quad \Sigma F_u$: $\quad$ 99.124 kips

$\quad P_y$: $\quad$ 368 kips

$\quad$ Zone: Pu < 0.75Py

$\quad \phi v$: $\quad$ 0.90

$\quad R_v$: $\quad$ 67.884 kips $\qquad\qquad\qquad\qquad$ AISC K1-11/12

Status : **Panel-zone is not strong, doubler plate is required**

The required strength for the doubler plate is

$V_{u\text{-}dp}$:   42.002 kips

Doubler plate will resist the remaining applied forces (AISC K1-10.1). The minimum required thickness of doubler plate

t_{min} :   0.244 in

Code requirement for minimum thickness of panel zone

$t_{min\text{-}seismic}$:   0.145 in (Seismic 9-2)

$t_{min\text{-}LRFD}$:   0.083 in (AISC F2-1)

Doubler plate thickness provided   Both web and doubler plate thickness **satisfied**

$t_{doubler\text{-}prov'd}$:   1/4   in   **OK**   the code minimum thickness requirement

Shear Tab Design

Shear tab dimension provided: Force per inch on the fillet weld:

$d_{shear\text{-}prov'd}$:   6 in R_n :   6.661 kips/in

$b_{shear\text{-}prov'd}$:   4 in   Design Strength of fillet weld

$t_{shear\text{-}prov'd}$:   1/2   in $\phi R_{nw\text{-}fillet}$:   22.271 t_e

                                $t_{e\text{-}min}$:   0.299 in

                                $t_{e\text{-}prov'd}$:   5/16 in   **OK**

Fillet weld strength

$\phi R_{nw\text{-}fillet}$:   13.919 kips/in ϕV_{nw} :   83.514 kips

Base metal strength V_u :   79.927 kips

$\phi R_{nw\text{-}metal}$:   14.625 kips/in   Status :   **OK**

Welding Information

Welding Electrode: 70 ksi

Doubler Plate to Column Flange: $^1/_4$ in CJP welds

Doubler Plate to Column Web: $^3/_{16}$ in fillet welds   AISC Table J2.4

$t_{doubler\text{-}prov'd}$:   0.250 in

t_w :   0.320 in

Transverse Stiffeners to Column Flange: $^3/_8$ in fillet welds double side   AISC Table J2.4

w_{min} :   0.337 in   AISC DG 4.3-6

$t_{stiffner\text{-}prov'd}$:   0.500 in

t_f :   0.455 in

Transverse Stiffeners to Doubler Plate: $^3/_{16}$ in fillet welds double side AISC Table J2.4

$t_{doubler-prov'd}$:   0.250 in

$t_{stiffner-prov'd}$:   0.500 in

Shear Tab to Column Flange: $^5/_{16}$ in fillet welds double side

Shear Tab to Beam Web: $^5/_{16}$ in fillet welds around

Design of Base Plate

Reaction forces at 5% drift (with actual material properties)

Item	Left Column	Right Column
P (kips)	-153.63	153.63
V (kips)	79.22	52.58
M (kip-in)	738.92	752.28

Slip-Critical Connection

Bolts :   A490

d_{bolt} :   3/4   in ϕF_t :   84.75 ksi

Design shear strength subject to shear alone

T_u :   35 kips   AISC -Table J3.1

ϕ :   0.9 ~~for standard holes~~ for oversized holes (05/02/2011)

N_s :   1

μ :   0.33

ϕR_{str} :   11.09 kips n_v =   8 bolts, required for shear alone

Design tension strength subject to tension alone

ϕ :   0.75 for standard holes

ϕR_t :   37.40 kips   AISC -Table 7-14

n_t =   5 bolts, required for tension alone

Estimation number of bolts due to moment alone

d :   9.4 in (moment arm)

T :   78.61 kips

n_m =   3 bolts, required for tension due to moment

Try bolt configuration as shown on the figure below :

# of bolts :   12

Effect of tension forces on slip critical bolts

# of bolts in tension :   12 (all bolts)

Reduction Factor :   0.68 (AISC - J3.9a)

$\phi R_{str-reduced}$:   7.50 kips/bolt

For 12 bolts :   90.03 kips

Status :   **OK**
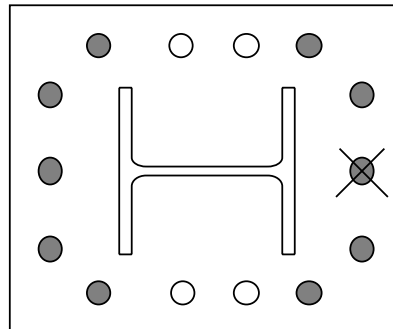
Tension/compression forces due to moments

$\qquad$ # of bolts affected : $\qquad$ 5 (shaded bolts, one side only)

$\qquad$ T_{ave} : $\qquad$ 15.72 kips/bolt

$\qquad$ T_{in} : $\qquad$ 12.54 kips for inner side bolts $\qquad$ 7.5 $\qquad$ in. moment arm

$\qquad$ T_{out} : $\qquad$ 18.90 kips for outter side bolts $\qquad$ 11.3 $\qquad$ in. moment arm

Check for tension capacity

$\qquad$ T_{pure} : $\qquad$ 12.80 kips

$\qquad$ T_{in} : $\qquad$ 25.35 kips $\qquad$ $< \phi R_t$: 37.40 kips $\qquad$ **OK**

$\qquad$ T_{out} : $\qquad$ 31.70 kips $\qquad$ $\approx \phi R_t$: 37.40 kips $\qquad$ **OK**

Effect of moment --> adding/reducing tension forces on slip critical bolts

Group	# of Bolts	Reduction Factor	$\phi R_{str-reduced}$	$\Sigma \phi R_{str-reduced}$
1	4	0.28	3.09	12.37
2	4	0.68	7.50	30.01
3	4	1.00	11.09	44.38

<u>Note :</u> $\qquad$ Total = $\qquad$ 86.76 $\qquad$ **OK**

$\qquad$ Group 1 = bolts that are in tension due to moments

$\qquad$ Group 2 = bolts that are close to moment neutral axis

$\qquad$ Group 3 = bolts that are in compression, no reduction occurred

Plate Thickness

A572 Gr. 50 Steel

$\qquad$ F_y : $\qquad$ 50 ksi $\qquad$ F_u : $\qquad$ 65 ksi

Bolt spacing $\qquad$ Edge Distance $\qquad$ Dimension of Base Plate

$\qquad$ S_{min} : $\qquad$ 2.25 in $\qquad$ L_{min} : $\qquad$ 1.125 in $\qquad$ B : $\qquad$ 12 in

$\qquad$ $S_{prov'd}$: $\qquad$ 2.50 in $\qquad$ $L_{prov'd}$: $\qquad$ 1.50 in $\qquad$ D : $\qquad$ 14.25 in

Calculation of plate thickness according to Cantilever Method (Base Plate in Compression)

References: $\qquad$ Chapter 13 - Salmon & Johnson (1990); AISC - DG 1

Critical Section for Bending $\qquad$ Cantilever length

$\qquad$ 0.8b : $\qquad$ 4.864 in $\qquad$ m : $\qquad$ 4.095 in. (controls)

$\qquad$ 0.95d : $\qquad$ 6.061 in $\qquad$ n : $\qquad$ 3.568 in.

$\qquad$ ϕ_b : $\qquad$ 0.9

$\qquad$ t_{min} : $\qquad$ 0.818 in.

Calculation of plate thickness to avoid Prying Action (Base Plate in Tension)

References: $\qquad$ Chapter 13 - Salmon & Johnson (1990)

d :   5.9   in (moment arm: flange-to-flange distance)

T :   124.71   kips

b' :   2.125   in

w :   12   in

ϕ_b :   0.9

t_{min} :   0.991   in. (controls) $\therefore$ **Use 14 - $^3/_4$" diam A490 bolts**

$t_{prov'd}$:   1.0   in   **OK**   **Base Plate t = 1"**

Design as End-Plate Moment Connection   AISC - DG 4

Connection design moment

M_{pe} :   950   kip-in

Connection configuration   Estimation of bolt diameter

b_p :   7.08   in $d_{b-req'd}$:   0.56   in

g :   5.56   in d_{bolt} :   3/4   in   **OK**

p_{f1} :   2.4   in

p_{f0} :   2.05   in

d_e :   1.5   in

h_0 :   8.20   in

h_1 :   3.30   in

Calculation of bolt moment and end plate thickness

ϕM_{np} :   1105.31   kip-in   **OK**

s :   3.14   in

Y_p :   27.544   in

$t_{req'd}$:   0.990   in   **OK**

Check shear yielding and shear rupture of extended portion of end plate

F_{pu} :   160.34   kips $F_{pu}/2$:   80.17   kips

A_n :   5.33 in^2

ϕR_{ny} :   191.2   kips   **OK**

ϕR_{nf} :   155.90   kips   **OK**

Welding Information for Base Plate

Welding Electrode: 70   ksi

Column to Base Plate: $^5/_{16}$ in fillet welds around   AISC Table J2.4

t_w :   0.320   in   **--> only in the webs, CJP for the flanges**

t_f :   0.455   in   **(05/02/2011)**

t_p :   1.0   in

104$^{7/8}$"

3$^{1/8}$"

SOUTH

(E) Steel Base Plate. Other existing
holes are not shown for clarity

$\dfrac{11a}{S6}$

EAST

center line of plate

WEST

$\dfrac{11b}{S6}$

NORTH

5"

14$^{3/8}$"

93$^{5/8}$"

103"
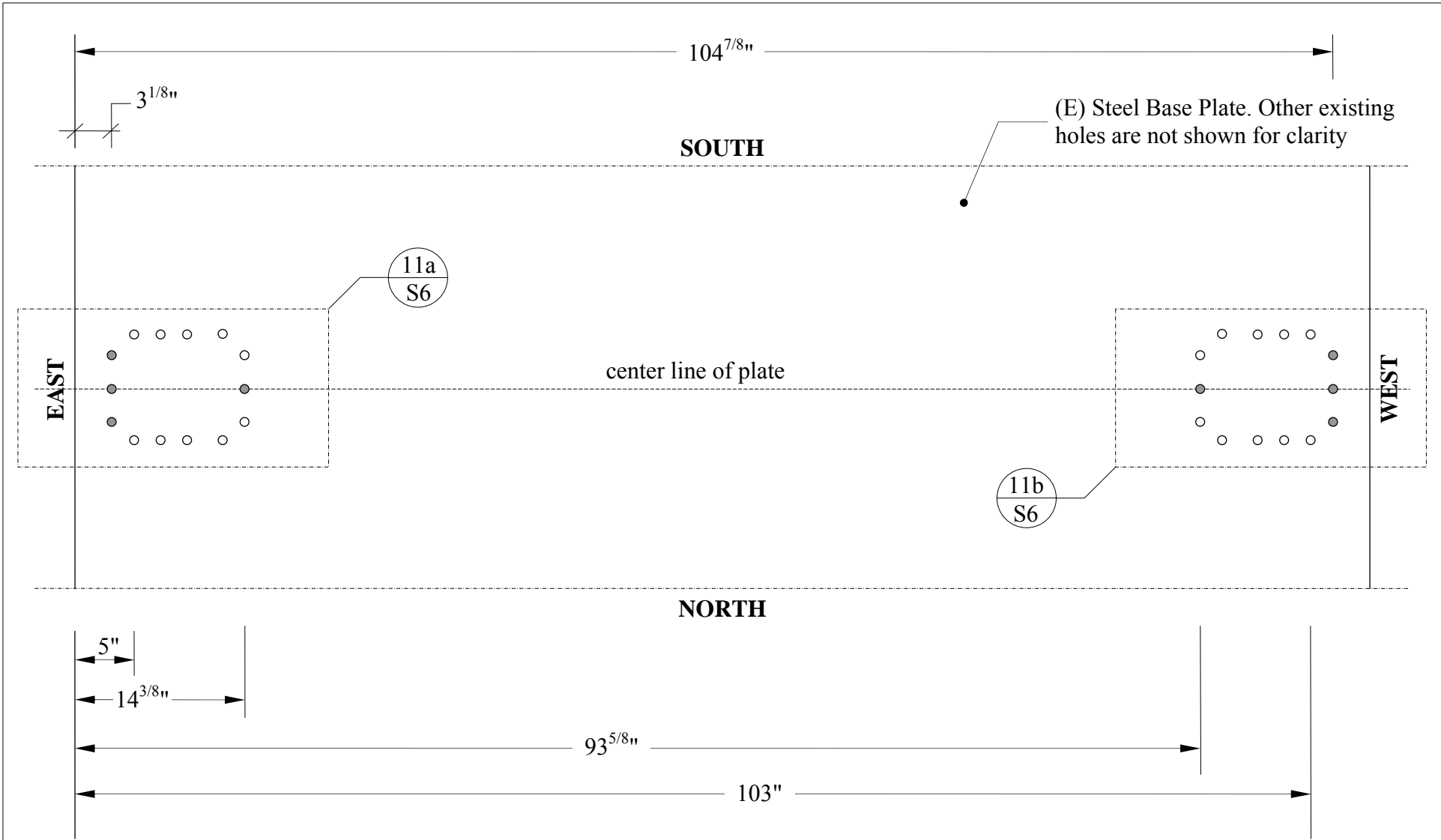
PLAN DETAIL

University at Buffalo		
Dept. of Civil, Structural, and Environmental Engineering		
Project:	**Content:**	**Drawing:**
In-Span Hinging SPSW	Existing Hole Layout	11/S6
Prepared by:	**Revision:**	**Date:**	**Scale:**
Ronny Purba	1	06/01/2011	1" = 12"

452

¾" Dia. Holes (Typ.)

New Holes

SOUTH

EAST

$2^{13/16"}$

$2^{13/16"}$

$4^{9/16"}$ $4^{9/16"}$ $4^{9/16"}$ $4^{5/8"}$

$2^{13/16"}$

center line
of plate

WEST

$4^{3/8"}$ $4^{3/8"}$ $4^{3/8"}$ $4^{3/8"}$

$2^{13/16"}$

NORTH

$3^{1/8"}$

5"

$7^{1/4"}$

$9^{1/2"}$

$12^{1/2"}$

$14^{3/8"}$

DETAIL 11a

453

¾" Dia. Holes (Typ.)

SOUTH

EAST

center line
of plate

$2^{3/4}$"

$2^{13/16}$"

$4^{9/16}$" $4^{1/2}$" $4^{3/8}$" $4^{7/16}$"

$4^{7/16}$" $4^{7/16}$" $4^{1/2}$" $4^{1/2}$"

WEST

$2^{3/4}$"

$2^{13/16}$"

NORTH

New Holes

Distance from East Side

$93^{5/8}$"

$95^{1/2}$"

$98^{1/2}$"

$100^{3/4}$"

103"

$104^{7/8}$"

DETAIL 11b

454

University at Buffalo		
Dept. of Civil, Structural, and Environmental Engineering		
Project:	**Content:**	**Drawing:**
In-Span Hinging SPSW	Right-Hole Layout	11b/S6
Prepared by:	**Revision:**	**Date:**	**Scale:**
Ronny Purba	1	06/01/2011	1" = 5"

A.2 Tensile Testing Program

A total of 27 tension coupons from 7 different sources are needed. A group of four coupons is cut from each source (i.e., 13GA, 14GA, 19GA steel plate, W6x25, W6x12, and W8x13 section), except from S5x10 which a group of three coupons are prepared. As listed in the following table, one coupon of steel plate is taken from both plate directions (i.e., parallel to and perpendicular to the rolling direction) while the other two coupons are cut at an angle of 45° to the rolling direction. Two coupons are taken both from web and flange (either top flange or bottom flange) of each W-section and three coupons from web of S5x10 section.

Table A-1. List of Tensile Testing Coupons (Steel Plate)

Coupon-ID	Source	Nominal Thickness (in)	Total per Component
GA13-1	13 GA Plate parallel to the rolling direction	0.0897	
GA13-2	13 GA Plate perpendicular to the rolling direction	0.0897	
GA13-3	13 GA Plate 45° angle from the rolling direction	0.0897	4
GA13-4	13 GA Plate 45° angle from the rolling direction	0.0897	
GA14-1	14 GA Plate parallel to the rolling direction	0.0747	
GA14-2	14 GA Plate perpendicular to the rolling direction	0.0747	
GA14-3	14 GA Plate 45° angle from the rolling direction	0.0747	4
GA14-4	14 GA Plate 45° angle from the rolling direction	0.0747	
GA19-1	19 GA Plate parallel to the rolling direction	0.0418	
GA19-2	19 GA Plate perpendicular to the rolling direction	0.0418	
GA19-3	19 GA Plate 45° angle from the rolling direction	0.0418	4
GA19-4	19 GA Plate 45° angle from the rolling direction	0.0418	

Updated
For all GA14 and GA19 coupons are taken from plate parallel to the rolling direction

Table A-2. List of Tensile Testing Coupons (W-Section)

Coupon-ID	Source	Nominal Thickness (in)	Total per Component
VBE-1	W6x25 Web	0.320	
VBE-2	W6x25 Web	0.320	
VBE-3	W6x25 Flange	0.455	4
VBE-4	W6x25 Flange	0.455	
HBE-T1	W6x12 Web	0.230	
HBE-T2	W6x12 Web	0.230	
HBE-T3	W6x12 Flange	0.280	4
HBE-T4	W6x12 Flange	0.280	
HBE-I1	S5x10 Web	0.214	
HBE-I2	S5x10 Web	0.214	3
HBE-I3	S5x10 Web	0.214	
HBE-B1	W8x13 Web	0.230	
HBE-B2	W8x13 Web	0.230	
HBE-B3	W8x13 Flange	0.255	4
HBE-B4	W8x13 Flange	0.255	

Table A-3. Test Results (Infill Plate)

Coupon-ID	Nominal Thickness (in)	Actual Thickness (in)	Modulus of Elasticity (ksi)	Yield Strength (ksi)	Ultimate Strength (ksi)	Rupture Strain (%)
GA13-1	0.0897	0.0855	23864	27.561	47.519	43.96
GA13-2	0.0897	0.0908	28913	24.869	42.906	40.67
GA13-3	0.0897	0.0903	29366	25.844	44.996	36.10
GA13-4	0.0897	0.0880	31537	28.399	48.310	36.50
	Average =	**0.0886**	**28420**	**26.668**	**45.933**	**39.31**
GA14-1	0.0747	0.0713	23554	24.756	43.154	41.99
GA14-2	0.0747	0.0697	34220	23.890	42.929	47.82
GA14-3	0.0747	0.0728	n.a.	n.a.	n.a.	n.a
GA14-4	0.0747	0.0713	25434	22.147	40.794	49.07
	Average =	**0.0713**	**27736**	**23.598**	**42.292**	**46.29**
GA19-1	0.0418	0.0390	33122	22.275	41.689	39.84
GA19-2	0.0418	0.0413	23515	18.264	36.386	44.04
GA19-3	0.0418	0.0410	n.a.	n.a.	n.a.	n.a
GA19-4	0.0418	0.0393	23679	19.564	39.735	43.85
	Average =	**0.0402**	**26772**	**20.034**	**39.270**	**42.58**

Table A-4 Test Results (Boundary Frame)

Coupon-ID	Nominal Thickness (in)	Actual Thickness (in)	Modulus of Elasticity (ksi)	Yield Strength (ksi)	Ultimate Strength (ksi)	Rupture Strain (%)
VBE-1	0.320	0.3472	29722	53.500	65.947	35.53
VBE-2	0.320	0.3443	37321	52.250	65.381	32.42
	Average =	**0.3458**	**33522**	**52.875**	**65.664**	**33.97**
VBE-3	0.455	0.4325	28472	51.250	64.926	35.36
VBE-4	0.455	0.4318	35800	53.700	68.609	33.18
	Average =	**0.4322**	**32136**	**52.475**	**66.768**	**34.27**
HBE-T1	0.230	0.2258	38857	54.400	65.332	34.98
HBE-T2	0.230	0.2277	30088	51.150	63.587	38.31
	Average =	**0.2268**	**34473**	**52.775**	**64.460**	**36.65**
HBE-T3	0.280	0.2903	26225	52.450	64.148	35.50
HBE-T4	0.280	0.2695	32656	52.250	63.403	31.78
	Average =	**0.2799**	**29441**	**52.350**	**63.776**	**33.64**
HBE-I1	0.214	0.2017	25075	50.150	70.699	28.12
HBE-I2	0.214	0.2053	n.a.	n.a.	n.a.	n.a
HBE-I3	0.214	0.2013	35571	49.800	70.343	27.58
	Average =	**0.2028**	**30323**	**49.975**	**70.521**	**27.85**
HBE-B1	0.230	0.2367	24500	56.350	69.089	34.02
HBE-B2	0.230	0.2353	23659	52.050	63.260	31.94
	Average =	**0.2360**	**24080**	**54.200**	**66.175**	**32.98**
HBE-B3	0.255	0.2473	32173	48.260	58.670	32.92
HBE-B4	0.255	0.2337	28079	53.350	65.773	29.53
	Average =	**0.2405**	**30126**	**50.805**	**62.222**	**31.22**

GA13

GA14

GA19

VBE

460

HBE-T

HBE-I

461

HBE-B
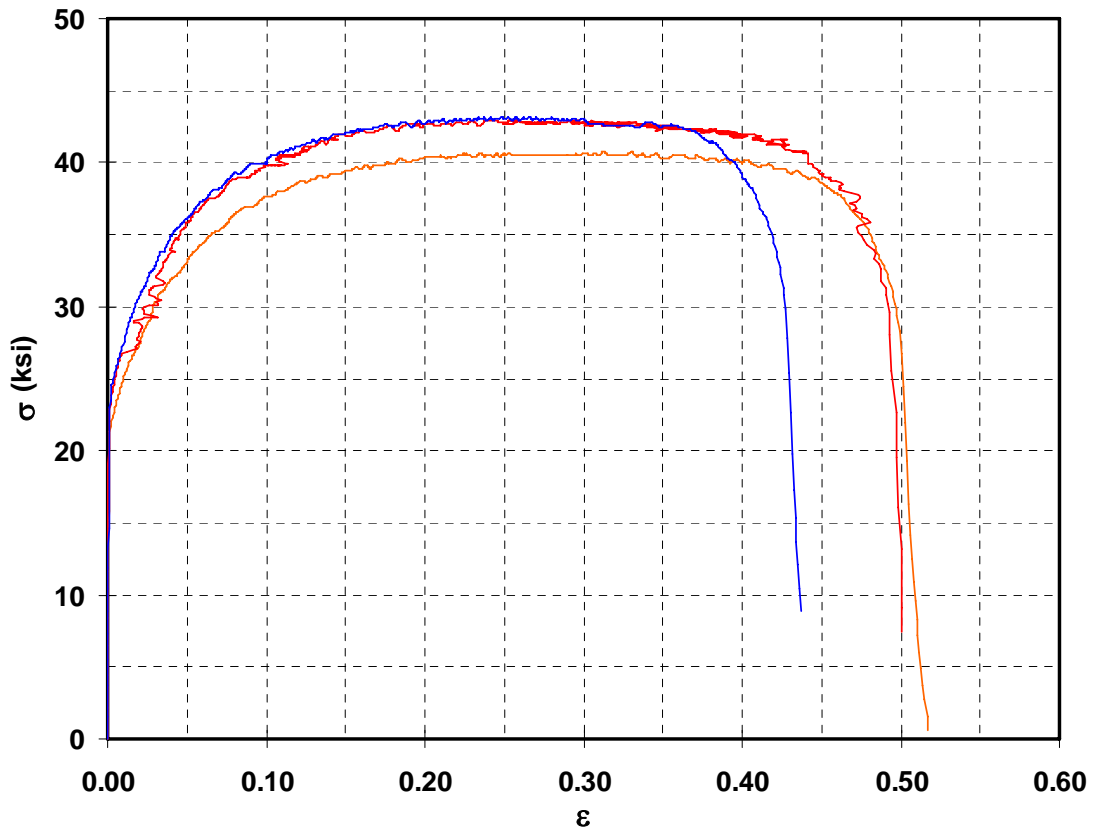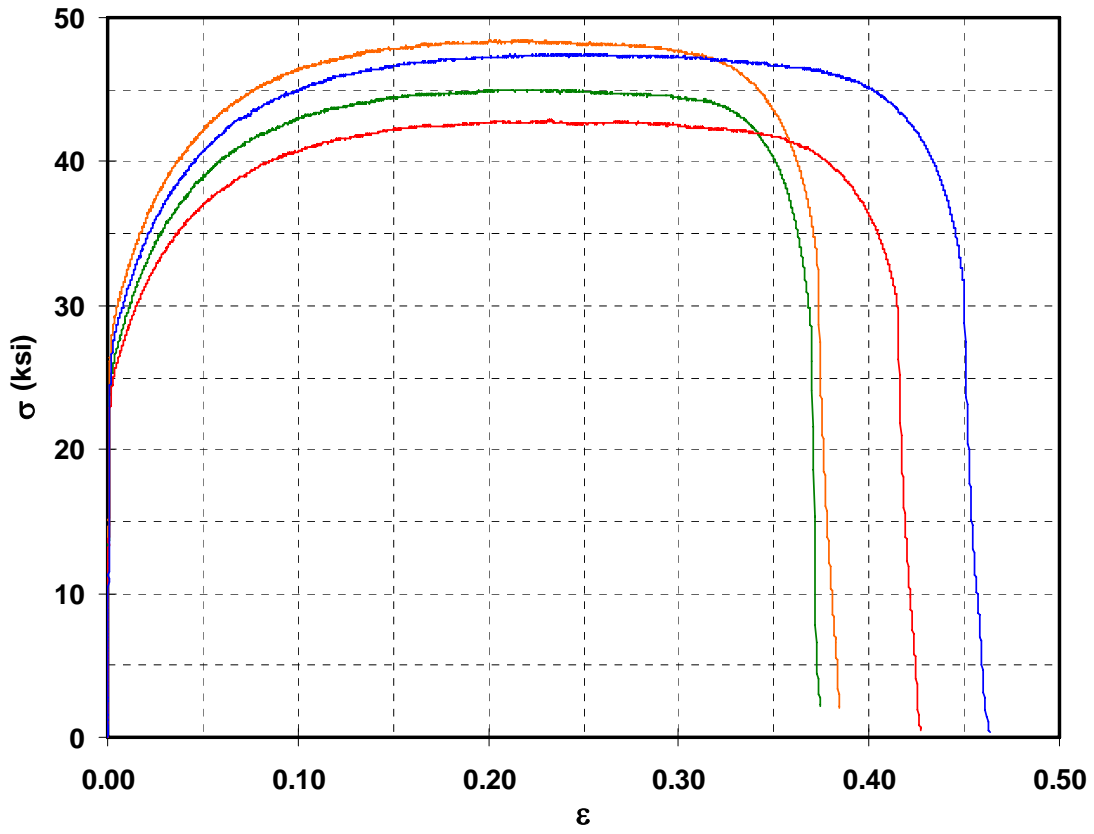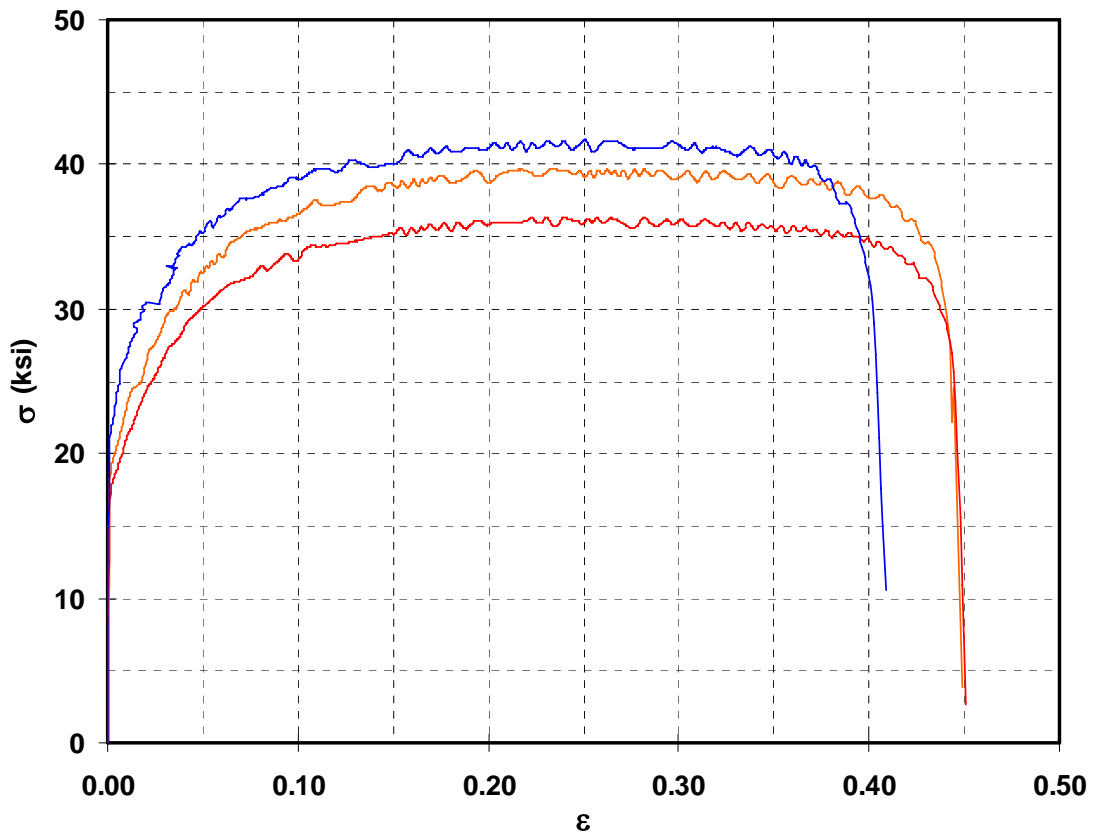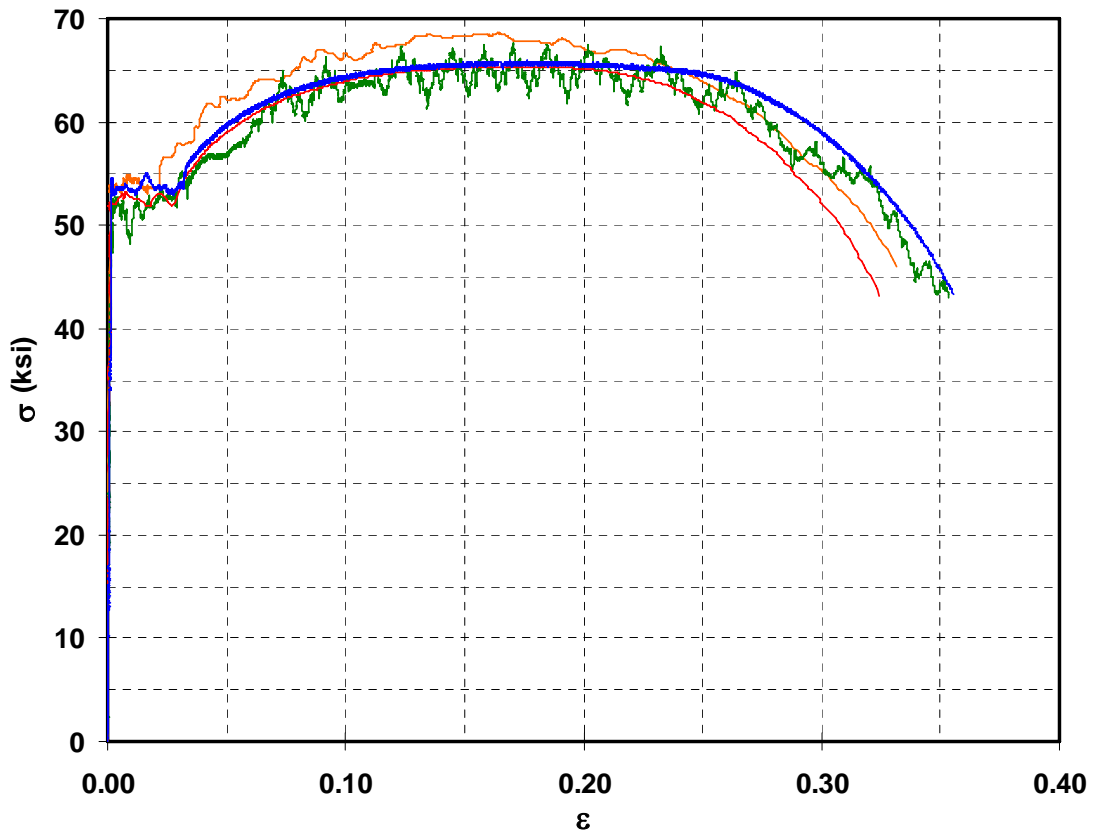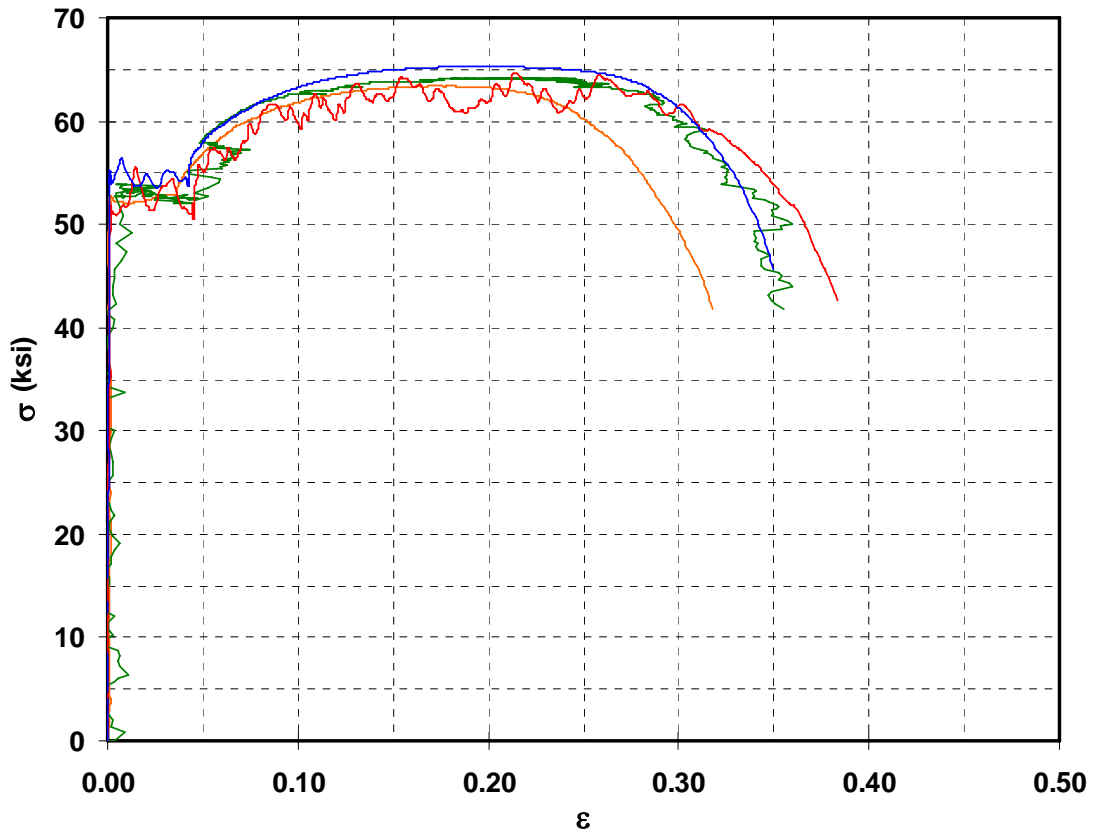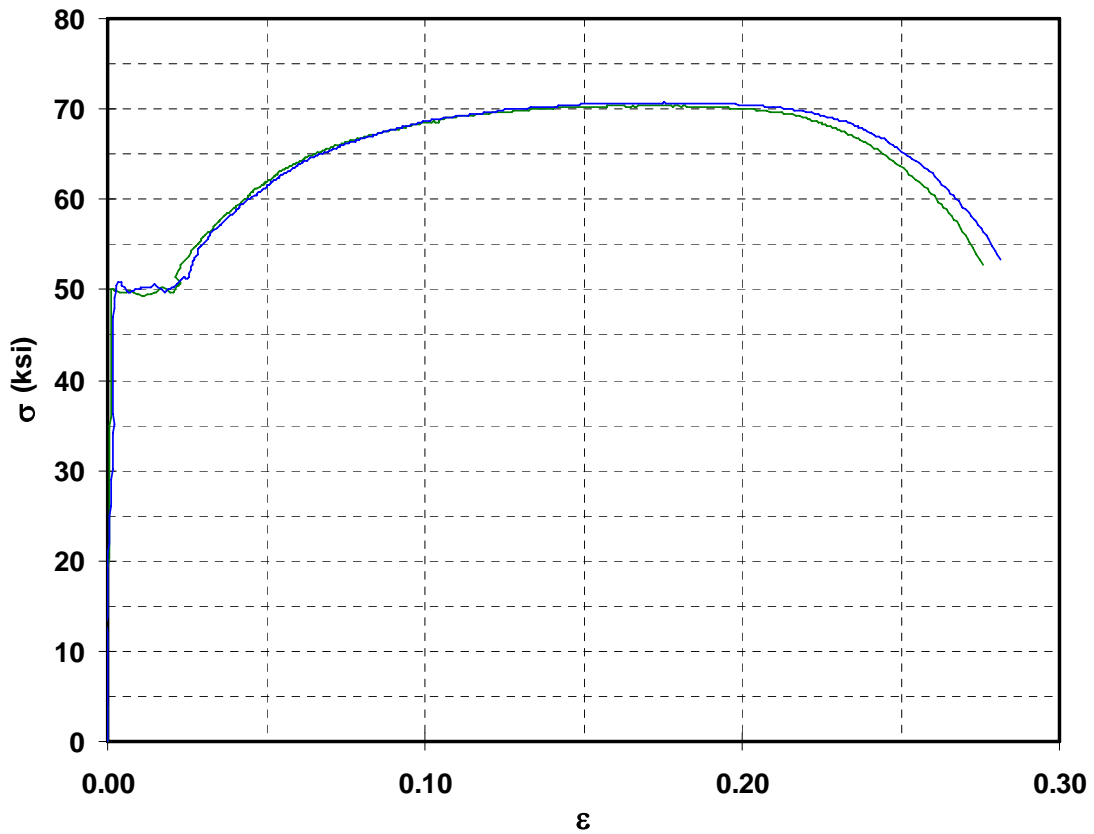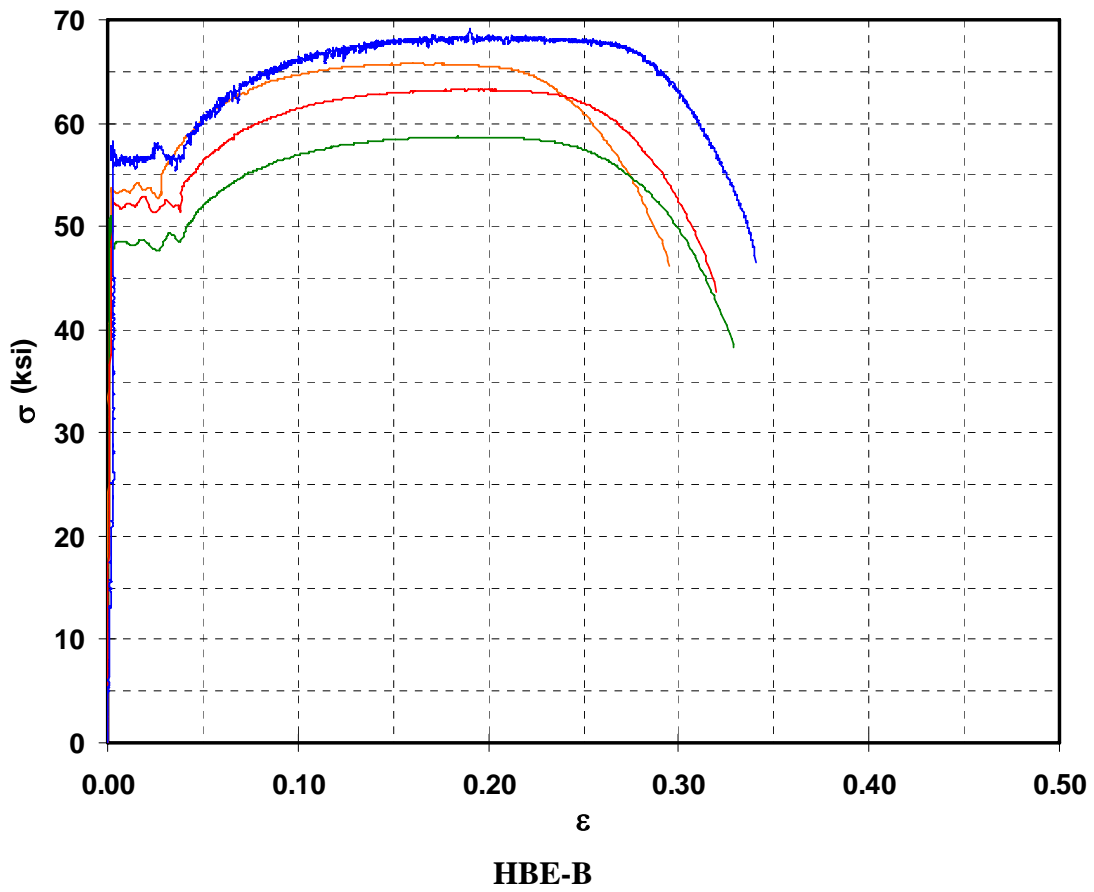
A.3 Instrumentation List

Table A-5. Instrumentation List: Strain Gauge (78 Channels)

Channel No.	Instrument ID	Strain Gauges Type	Attached to Element	Instrument Location			
				Level	Section	Plate	Side
1	**SGB0-11**	Uniaxial	Beam	Base	1	TF	South
2	**SGB0-12**	Uniaxial	Beam	Base	1	TF	North
3	**SGB0-13**	Uniaxial	Beam	Base	1	BF	South
4	**SGB0-14**	Uniaxial	Beam	Base	1	BF	North
5	**SGB0-21**	Uniaxial	Beam	Base	2	TF	South
6	**SGB0-22**	Uniaxial	Beam	Base	2	TF	North
7	**SGB0-23**	Uniaxial	Beam	Base	2	BF	South
8	**SGB0-24**	Uniaxial	Beam	Base	2	BF	North
9	**SGB0-31**	Uniaxial	Beam	Base	3	TF	South
10	**SGB0-32**	Uniaxial	Beam	Base	3	TF	North
11	**SGB0-33**	Uniaxial	Beam	Base	3	BF	South
12	**SGB0-34**	Uniaxial	Beam	Base	3	BF	North
13	**SGB0-41**	Uniaxial	Beam	Base	4	TF	South
14	**SGB0-42**	Uniaxial	Beam	Base	4	TF	North
15	**SGB0-43**	Uniaxial	Beam	Base	4	BF	South
16	**SGB0-44**	Uniaxial	Beam	Base	4	BF	North
17	**SGB1-11**	Uniaxial	Beam	1st Floor	1	TF	South
18	**SGB1-12**	Uniaxial	Beam	1st Floor	1	TF	North
19	**SGB1-13**	Uniaxial	Beam	1st Floor	1	BF	South
20	**SGB1-14**	Uniaxial	Beam	1st Floor	1	BF	North
21	**SGB1-21**	Uniaxial	Beam	1st Floor	2	TF	South
22	**SGB1-22**	Uniaxial	Beam	1st Floor	2	TF	North
23	**SGB1-23**	Uniaxial	Beam	1st Floor	2	BF	South
24	**SGB1-24**	Uniaxial	Beam	1st Floor	2	BF	North
25	**SGB1-31**	Uniaxial	Beam	1st Floor	3	TF	South
26	**SGB1-32**	Uniaxial	Beam	1st Floor	3	TF	North

Table A-5. Instrumentation List: Strain Gauge – Cont'd

Channel No.	Instrument ID	Strain Gauges Type	Attached to Element	Instrument Location			
				Level	Section	Plate	Side
27	**SGB1-33**	Uniaxial	Beam	1st Floor	3	BF	South
28	**SGB1-34**	Uniaxial	Beam	1st Floor	3	BF	North
29	**SGB1-41**	Uniaxial	Beam	1st Floor	4	TF	South
30	**SGB1-42**	Uniaxial	Beam	1st Floor	4	TF	North
31	**SGB1-43**	Uniaxial	Beam	1st Floor	4	BF	South
32	**SGB1-44**	Uniaxial	Beam	1st Floor	4	BF	North
33	**SGB2-11**	Uniaxial	Beam	2nd Floor	1	TF	South
34	**SGB2-12**	Uniaxial	Beam	2nd Floor	1	TF	North
35	**SGB2-13**	Uniaxial	Beam	2nd Floor	1	BF	South
36	**SGB2-14**	Uniaxial	Beam	2nd Floor	1	BF	North
37	**SGB2-21**	Uniaxial	Beam	2nd Floor	2	TF	South
38	**SGB2-22**	Uniaxial	Beam	2nd Floor	2	TF	North
39	**SGB2-23**	Uniaxial	Beam	2nd Floor	2	BF	South
40	**SGB2-24**	Uniaxial	Beam	2nd Floor	2	BF	North
41	**SGB2-31**	Uniaxial	Beam	2nd Floor	3	TF	South
42	**SGB2-32**	Uniaxial	Beam	2nd Floor	3	TF	North
43	**SGB2-33**	Uniaxial	Beam	2nd Floor	3	BF	South
44	**SGB2-34**	Uniaxial	Beam	2nd Floor	3	BF	North
45	**SGB2-41**	Uniaxial	Beam	2nd Floor	4	TF	South
46	**SGB2-42**	Uniaxial	Beam	2nd Floor	4	TF	North
47	**SGB2-43**	Uniaxial	Beam	2nd Floor	4	BF	South
48	**SGB2-44**	Uniaxial	Beam	2nd Floor	4	BF	North
49	**SGB3-11**	Uniaxial	Beam	3rd Floor	1	TF	South
50	**SGB3-12**	Uniaxial	Beam	3rd Floor	1	TF	North
51	**SGB3-13**	Uniaxial	Beam	3rd Floor	1	BF	South
52	**SGB3-14**	Uniaxial	Beam	3rd Floor	1	BF	North

Table A-5. Instrumentation List: Strain Gauge – Cont'd

Channel No.	Instrument ID	Strain Gauges Type	Attached to Element	Instrument Location			
				Level	Section	Plate	Side
53	**SGB3-21**	Uniaxial	Beam	3rd Floor	2	TF	South
54	**SGB3-22**	Uniaxial	Beam	3rd Floor	2	TF	North
55	**SGB3-23**	Uniaxial	Beam	3rd Floor	2	BF	South
56	**SGB3-24**	Uniaxial	Beam	3rd Floor	2	BF	North
57	**SGB3-31**	Uniaxial	Beam	3rd Floor	3	TF	South
58	**SGB3-32**	Uniaxial	Beam	3rd Floor	3	TF	North
59	**SGB3-33**	Uniaxial	Beam	3rd Floor	3	BF	South
60	**SGB3-34**	Uniaxial	Beam	3rd Floor	3	BF	North
61	**SGB3-41**	Uniaxial	Beam	3rd Floor	4	TF	South
62	**SGB3-42**	Uniaxial	Beam	3rd Floor	4	TF	North
63	**SGB3-43**	Uniaxial	Beam	3rd Floor	4	BF	South
64	**SGB3-44**	Uniaxial	Beam	3rd Floor	4	BF	North
65	**SGEC1-11**	Uniaxial	East Col.	1st Story	1	TF	South
66	**SGEC1-12**	Uniaxial	East Col.	1st Story	1	TF	North
67	**SGEC1-13**	Uniaxial	East Col.	1st Story	1	BF	South
68	**SGEC1-14**	Uniaxial	East Col.	1st Story	1	BF	North
69	**RGEC1-15**	Rosette	East Col.	1st Story	1	W	–
70	**RGEC2-15**	Rosette	East Col.	2nd Story	1	W	–
71	**RGEC3-15**	Rosette	East Col.	3rd Story	1	W	–
72	**SGWC1-11**	Uniaxial	West Col.	1st Story	1	TF	South
73	**SGWC1-12**	Uniaxial	West Col.	1st Story	1	TF	North
74	**SGWC1-13**	Uniaxial	West Col.	1st Story	1	BF	South
75	**SGWC1-14**	Uniaxial	West Col.	1st Story	1	BF	North
76	**RGWC1-15**	Rosette	West Col.	1st Story	1	W	–
77	**RGWC2-15**	Rosette	West Col.	2nd Story	1	W	–
78	**RGWC3-15**	Rosette	West Col.	3rd Story	1	W	–

Table A-6. Instrumentation List: Transducer (71 Channels)

Channel No.	Instrument ID	Transducer Type	Attached to Element	Reference Point	Instrument Location	
					Level	Position
79	**SPEC0**	String Pot	East Col.	Instr. Frame	Base	Center of BP
80	**SPWC0**	String Pot	West Col.	Instr. Frame	Base	Center of BP
81	**SPWC1**	String Pot	West Col.	Instr. Frame	1st Story	Center of TF
82	**SPWC2**	String Pot	West Col.	Instr. Frame	2nd Story	Center of TF
83	**SPWC3**	String Pot	West Col.	Instr. Frame	3rd Story	Center of TF
84	**SPB2-1**	String Pot	Beam	Gravity Mass	2nd Story	¼-Point
85	**SPB2-2**	String Pot	Beam	Gravity Mass	2nd Story	Mid-Point
86	**SPB2-3**	String Pot	Beam	Gravity Mass	2nd Story	¾-Point
87	**SPB3-1**	String Pot	Beam	Gravity Mass	3rd Story	¼-Point
88	**SPB3-2**	String Pot	Beam	Gravity Mass	3rd Story	Mid-Point
89	**SPB3-3**	String Pot	Beam	Gravity Mass	3rd Story	¾-Point
90	**SPG3**	String Pot	Gravity Mass	Gravity Mass	2nd Story	Possible Loc.
91	**SPG3**	String Pot	Gravity Mass	Gravity Mass	1st Story	Possible Loc.
92	**SPG1**	String Pot	Gravity Mass	Strong Floor	Base	Possible Loc.
93	**SPR2-1**	String Pot 45°	East Col.	2nd Fl. Beam	2nd Story	North Side
94	**SPR2-2**	String Pot 45°	East Col.	2nd Fl. Beam	2nd Story	North Side
95	**SPR2-3**	String Pot 45°	East Col.	2nd Fl. Beam	2nd Story	North Side
96	**SPR2-4**	String Pot 45°	1st Fl. Beam	2nd Fl. Beam	2nd Story	North Side
97	**SPR2-5**	String Pot 45°	1st Fl. Beam	West Col.	2nd Story	North Side
98	**SPR3-1**	String Pot 45°	East Col.	3rd Fl. Beam	3rd Story	North Side
99	**SPR3-2**	String Pot 45°	East Col.	3rd Fl. Beam	3rd Story	North Side
100	**SPR3-3**	String Pot 45°	East Col.	3rd Fl. Beam	3rd Story	North Side
101	**SPR3-4**	String Pot 45°	2nd Fl. Beam	3rd Fl. Beam	3rd Story	North Side
102	**SPR3-5**	String Pot 45°	2nd Fl. Beam	West Col.	3rd Story	North Side
103	**SPL2-1**	String Pot 45°	West Col.	2nd Fl. Beam	2nd Story	South Side
104	**SPL2-2**	String Pot 45°	West Col.	2nd Fl. Beam	2nd Story	South Side
105	**SPL2-3**	String Pot 45°	West Col.	2nd Fl. Beam	2nd Story	South Side

Channel No.	Instrument ID	Transducer Type	Attached to Element	Reference Point	Instrument Location	
					Level	Position
106	**SPL2-4**	String Pot 45°	1st Fl. Beam	2nd Fl. Beam	2nd Story	South Side
107	**SPL2-5**	String Pot 45°	1st Fl. Beam	East Col.	2nd Story	South Side
108	**SPL3-1**	String Pot 45°	West Col.	3rd Fl. Beam	3rd Story	South Side
109	**SPL3-2**	String Pot 45°	West Col.	3rd Fl. Beam	3rd Story	South Side
110	**SPL3-3**	String Pot 45°	West Col.	3rd Fl. Beam	3rd Story	South Side
111	**SPL3-4**	String Pot 45°	2nd Fl. Beam	3rd Fl. Beam	3rd Story	South Side
112	**SPL3-5**	String Pot 45°	2nd Fl. Beam	East Col.	3rd Story	South Side
113	**KRB1-1**	Krypton	1st Fl. Beam	Device	1st Story	45° of #128
114	**KRB1-2**	Krypton	1st Fl. Beam	Device	1st Story	45° of #127
115	**KRB1-3**	Krypton	1st Fl. Beam	Device	1st Story	45° of #126
116	**KRB1-4**	Krypton	1st Fl. Beam	Device	1st Story	135° of #124
117	**KRB1-5**	Krypton	1st Fl. Beam	Device	1st Story	45° of #121
118	**KRB1-6**	Krypton	1st Fl. Beam	Device	1st Story	135° of #129
119	**KRB1-7**	Krypton	1st Fl. Beam	Device	1st Story	135° of #130
120	**KRB1-8**	Krypton	1st Fl. Beam	Device	1st Story	135° of #131
121	**KRB0-1**	Krypton	Base Beam	Device	1st Story	-45° of #126
122	**KRB0-2**	Krypton	Base Beam	Device	1st Story	-45° of #127
123	**KRB0-3**	Krypton	Base Beam	Device	1st Story	-45° of #128
124	**KRB0-4**	Krypton	Base Beam	Device	1st Story	-135° of #131
125	**KRB0-5**	Krypton	Base Beam	Device	1st Story	-135° of #130
126	**KRB0-6**	Krypton	Base Beam	Device	1st Story	-135° of #129
127	**KRB0-7**	Krypton	Base Beam	Device	1st Story	Bot. Flange
128	**KRB0-8**	Krypton	Base Beam	Device	1st Story	Bot. Flange
129	**KREC1-1**	Krypton	East Col.	Device	1st Story	Panel Zone
130	**KREC1-2**	Krypton	East Col.	Device	1st Story	¼-Point
131	**KREC1-3**	Krypton	East Col.	Device	1st Story	Mid-Point
132	**KREC1-4**	Krypton	East Col.	Device	1st Story	¾-Point

Table A-6. Instrumentation List: Transducers – Cont'd

Channel No.	Instrument ID	Strain Gauges Type	Attached to Element	Instrument Location		
				Level	Position	Plate
133	**KRWC1-1**	Krypton	West Col.	Device	1st Story	Panel Zone
134	**KRWC1-2**	Krypton	West Col.	Device	1st Story	¼-Point
135	**KRWC1-3**	Krypton	West Col.	Device	1st Story	Mid-Point
136	**KRWC1-4**	Krypton	West Col.	Device	1st Story	¾-Point
137	**SPθB1-1**	Potentiometer	Beam	1st Story	East-end	TF
138	**SPθB1-2**	Potentiometer	Beam	1st Story	West-end	TF
139	**SPθB2-1**	Potentiometer	Beam	2nd Floor	East-end	TF
140	**SPθB2-2**	Potentiometer	Beam	2nd Floor	East-end	BF
141	**SPθB2-3**	Potentiometer	Beam	2nd Floor	West-end	TF
142	**SPθB2-4**	Potentiometer	Beam	2nd Floor	West-end	BF
143	**SPθB3-1**	Potentiometer	Beam	3rd Floor	East-end	TF
144	**SPθB3-2**	Potentiometer	Beam	3rd Floor	East-end	BF
145	**SPθB3-3**	Potentiometer	Beam	3rd Floor	West-end	TF
146	**SPθB3-4**	Potentiometer	Beam	3rd Floor	West-end	BF
147	**KRGB**	Krypton	Gravity Mass	Device	Base	Pos. Loc.
148	**KRGM1**	Krypton	Gravity Mass	Device	1st Story	Pos. Loc.
149	**KRGM2**	Krypton	Gravity Mass	Device	1st Story	Pos. Loc.

APPENDIX B

SUPPORTING STUDIES ON THE COLLAPSE ASSESSMENT OF STEEL PLATE SHEAR WALLS

B.1 Review of SAP2000 Analysis Capability with Degradation Models

(a)

(b)

P = 0

P = 0.1 Py = 300 kN

V/2   W18x65   **V/2**

2.0 m

W18x71

PL 0.5" × 10"

4.0 m

(a)

σ

ASTM A572 Gr. 50   σ_y
σ_y = 50 ksi

E_s

(b)

ε_y ε

472

V/2   W18x65   **V/2**

2.0 m

W18x71

PL 0.5" × 10"

4.0 m

(a)

σ

ASTM A572 Gr. 50 σ_y
$\sigma_y = 50$ ksi

E_s

(b)

ε_y ε

472
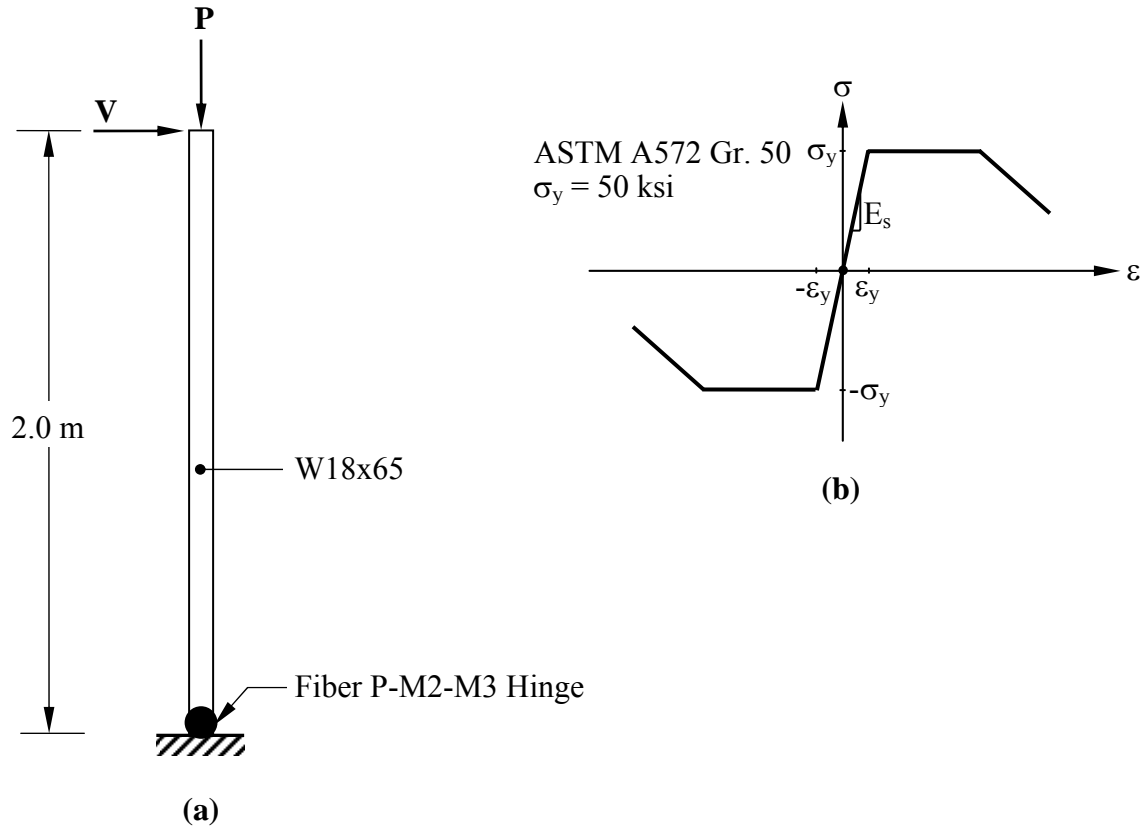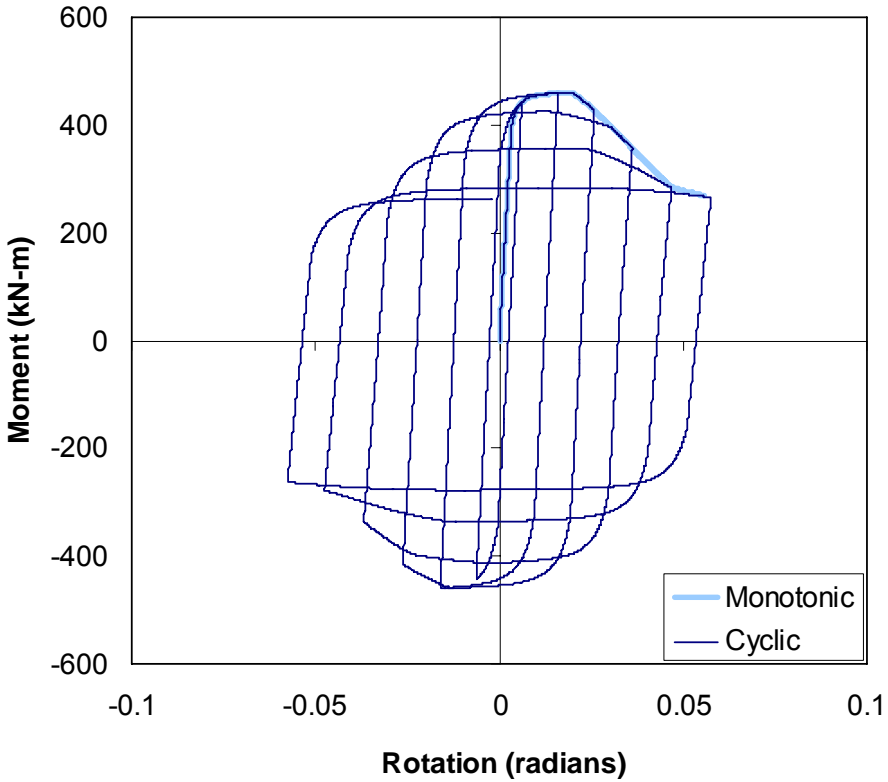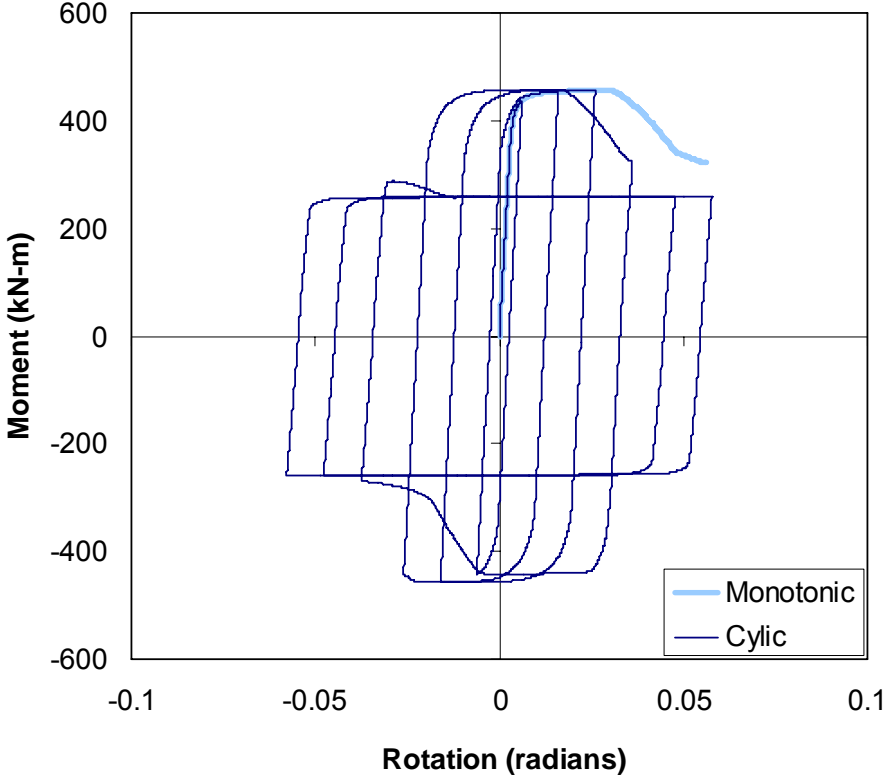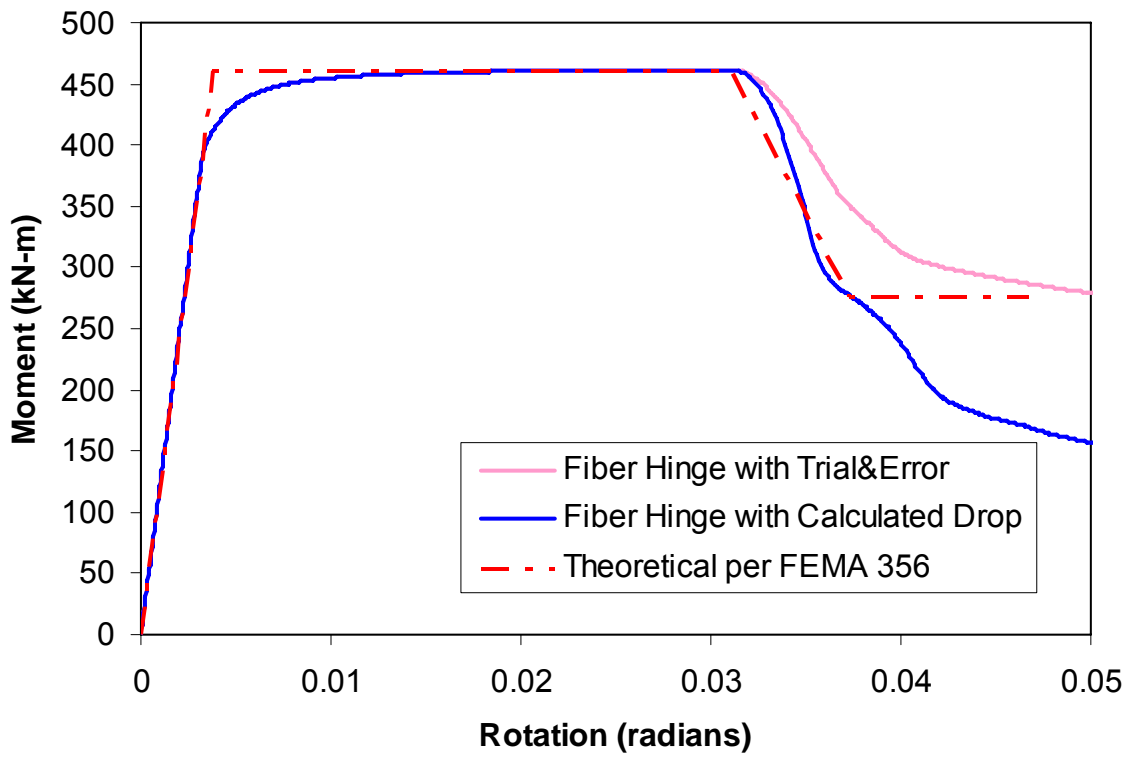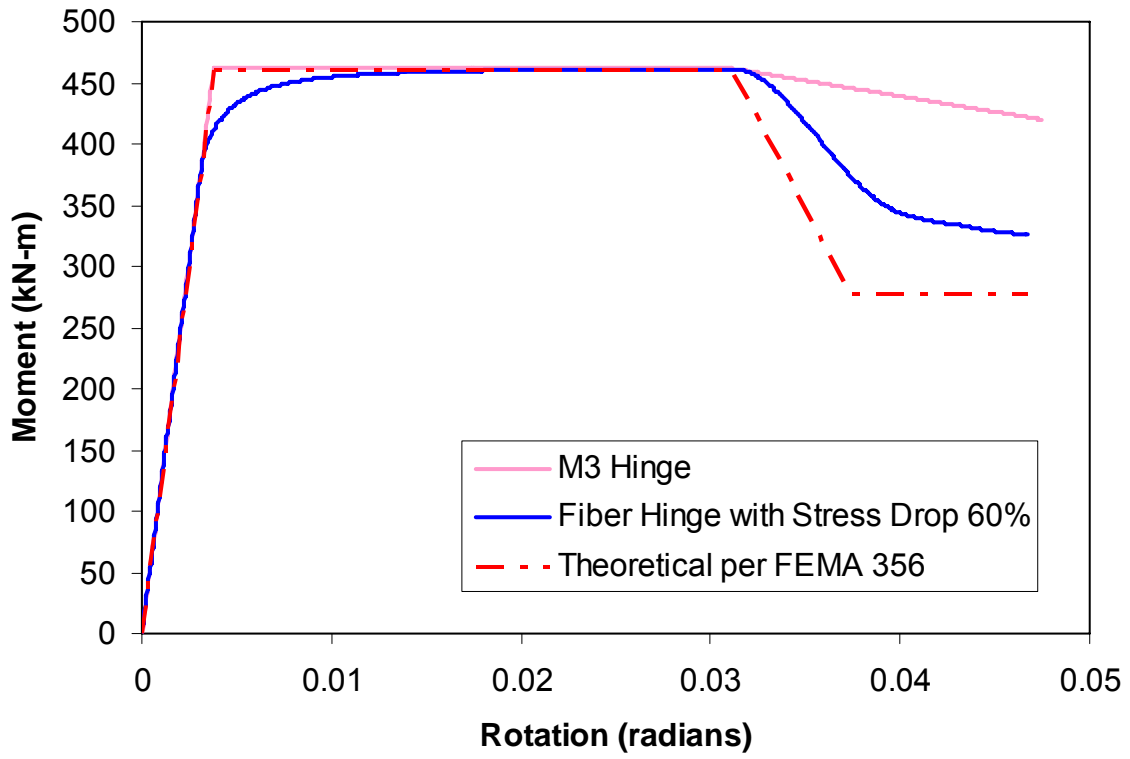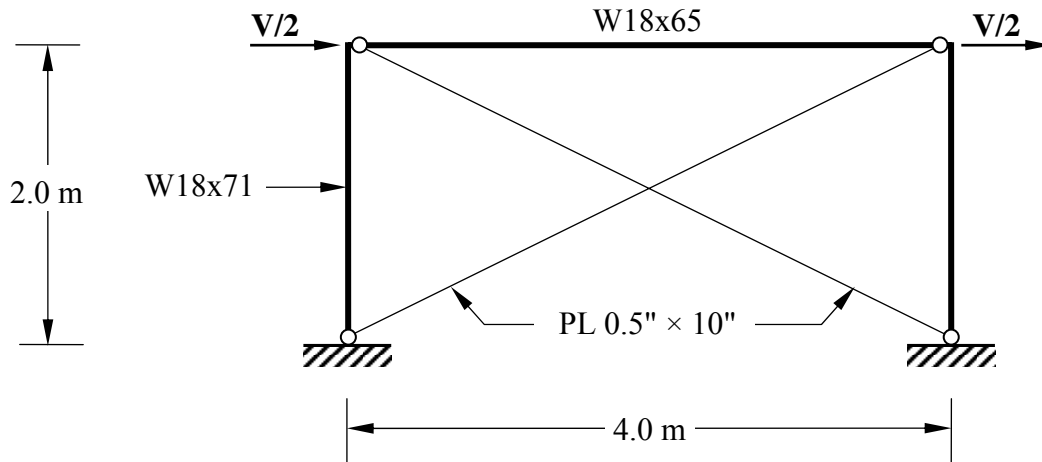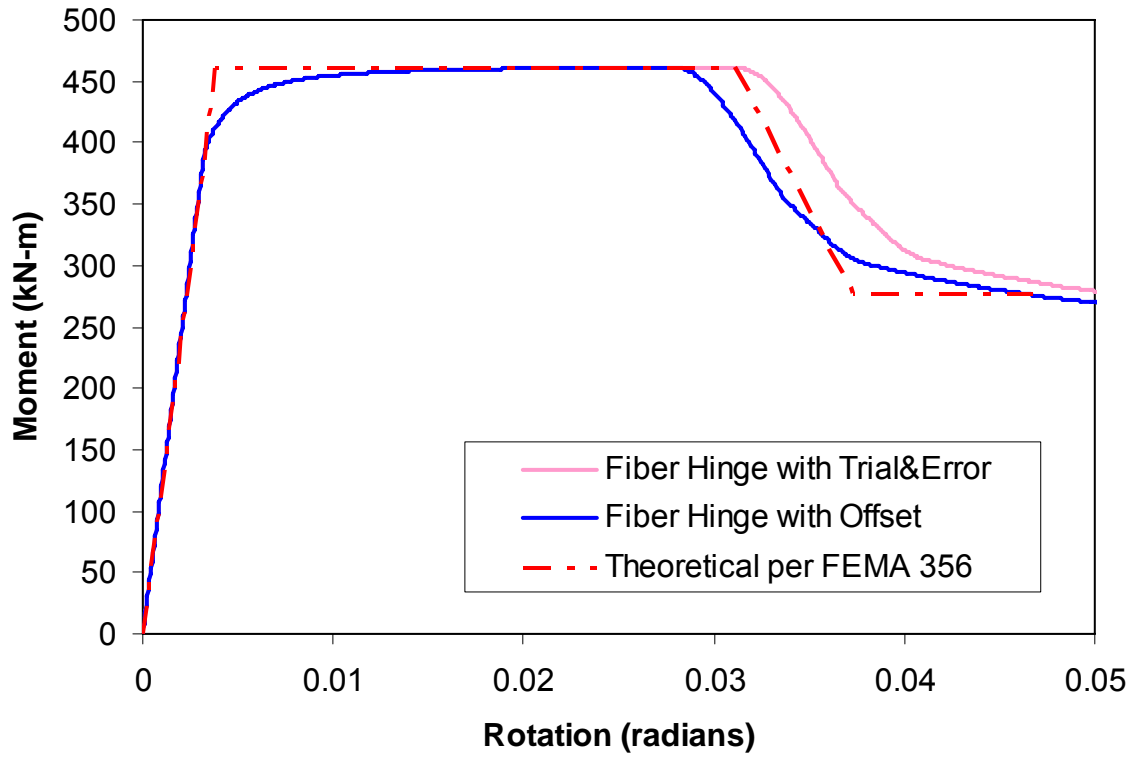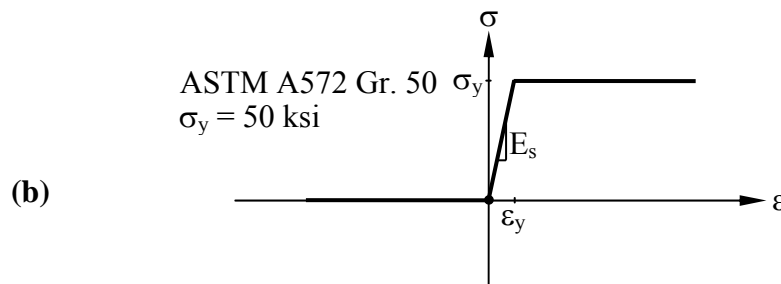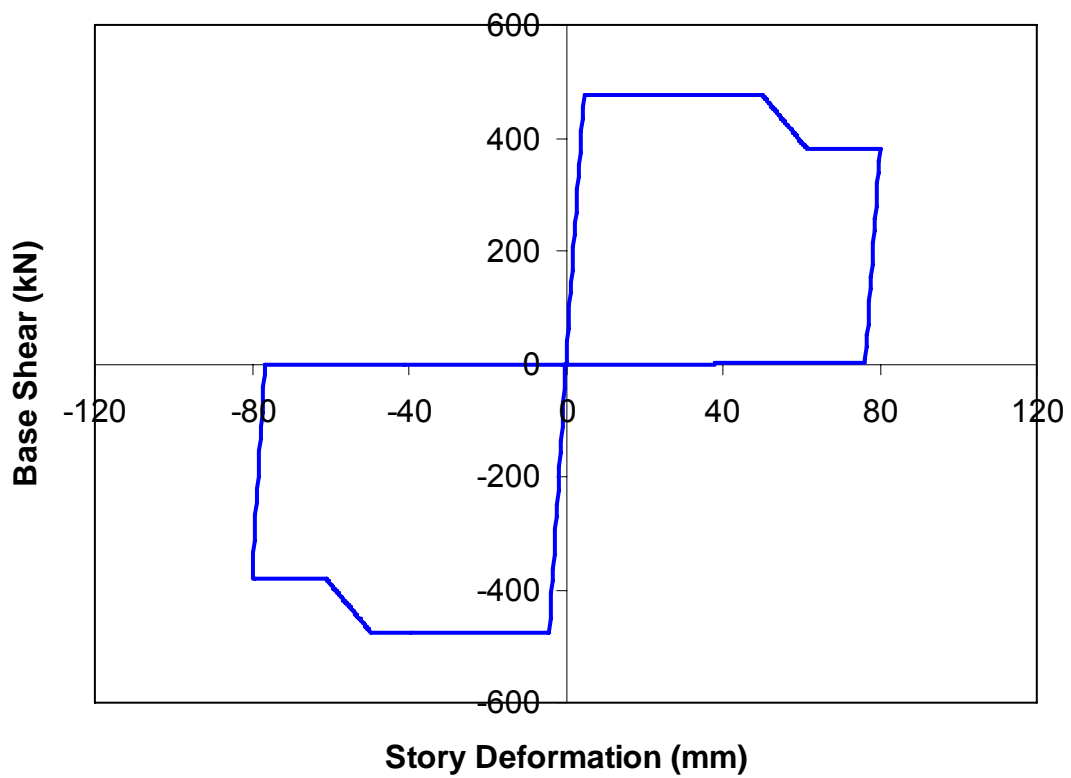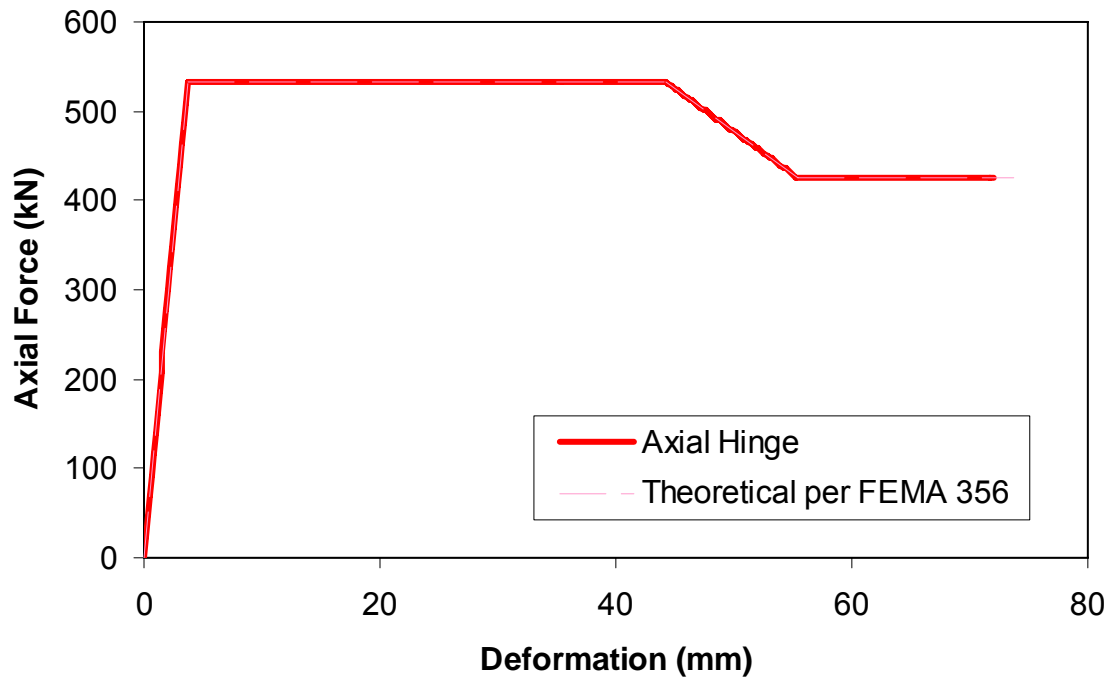
Problem:
Error results when unloading on path CD

B.2 Review of OpenSees Analysis Capability with Degradation Models

(a)

(b)

ASTM A572 Gr. 50 σ_y
$\sigma_y = 50$ ksi

W18x65

Fiber P-M2-M3 Hinge

2.0 m
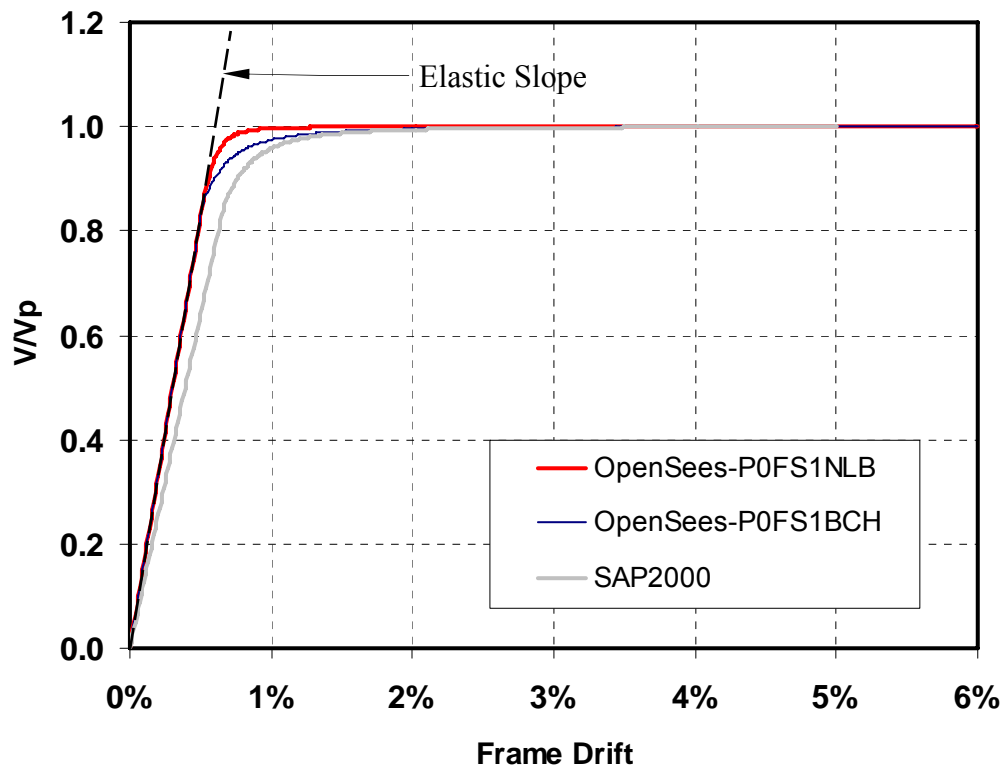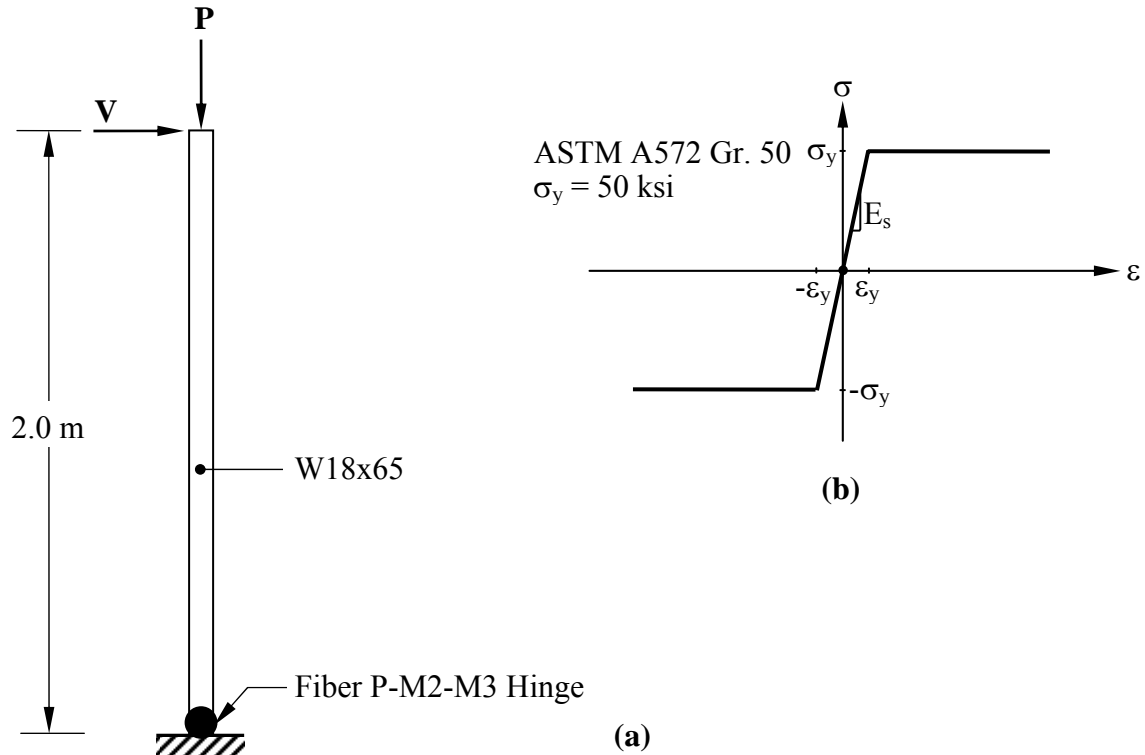
Monotonic Pushover Curve: Elasto-Plastic Material Model
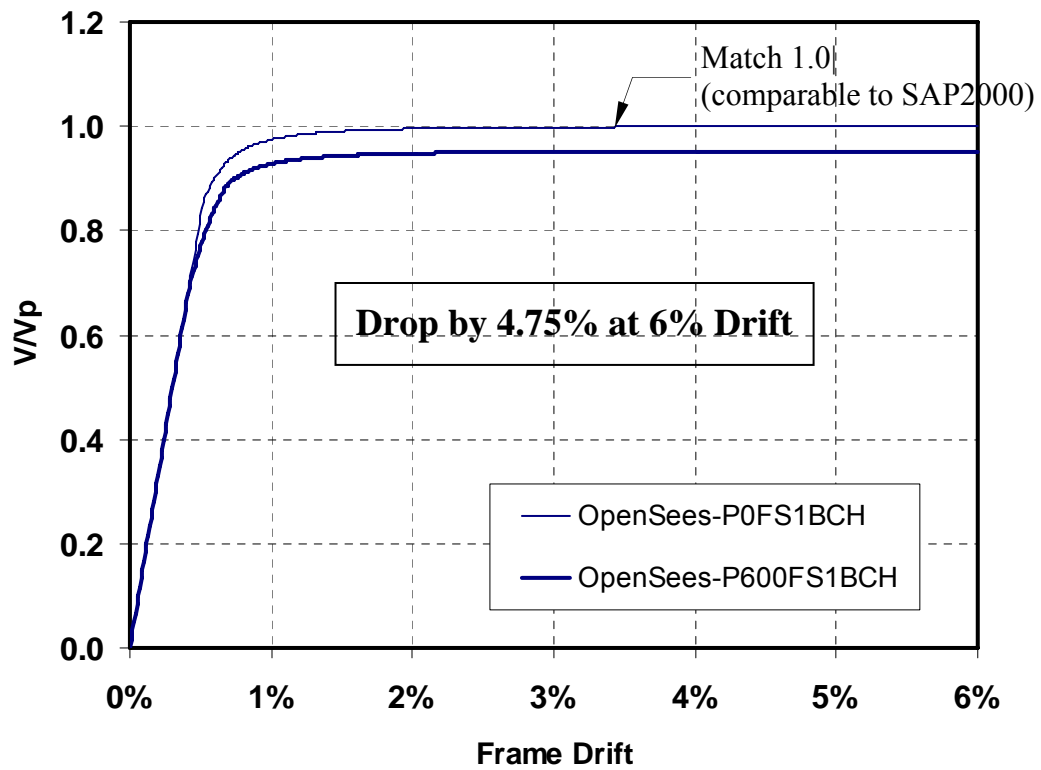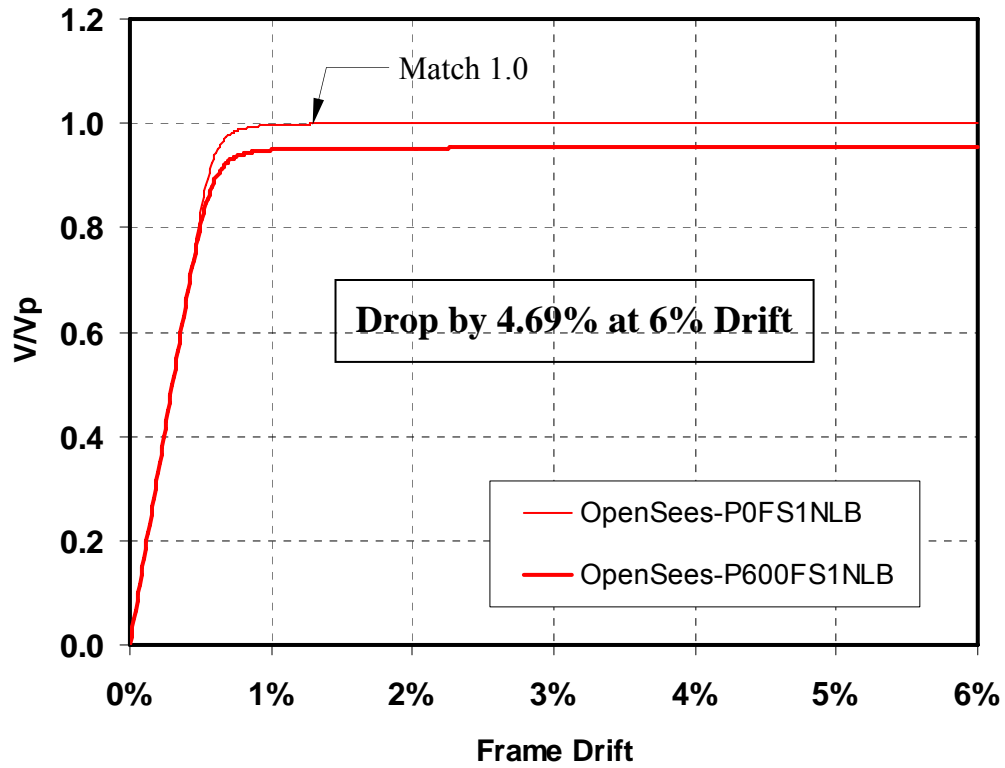
Monotonic Pushover Curve: Effect of Axial Forces P = 600 kN = 0.2P$_y$

Both have the same amount of drops at 4% drift: 4.69%. Theoretical value: drop **4.68%**.
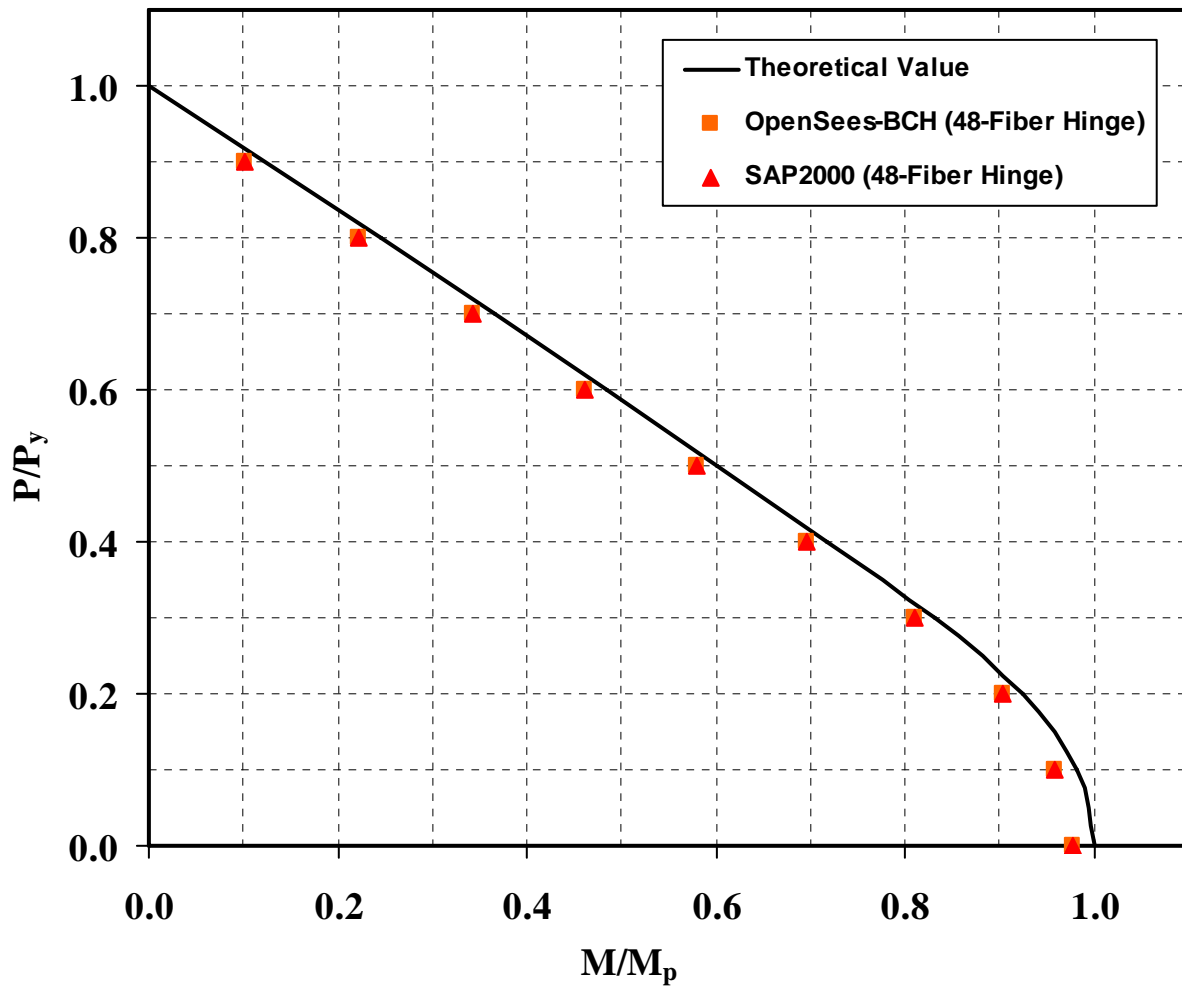
P-M Interaction Comparison OPENSEES vs. SAP2000
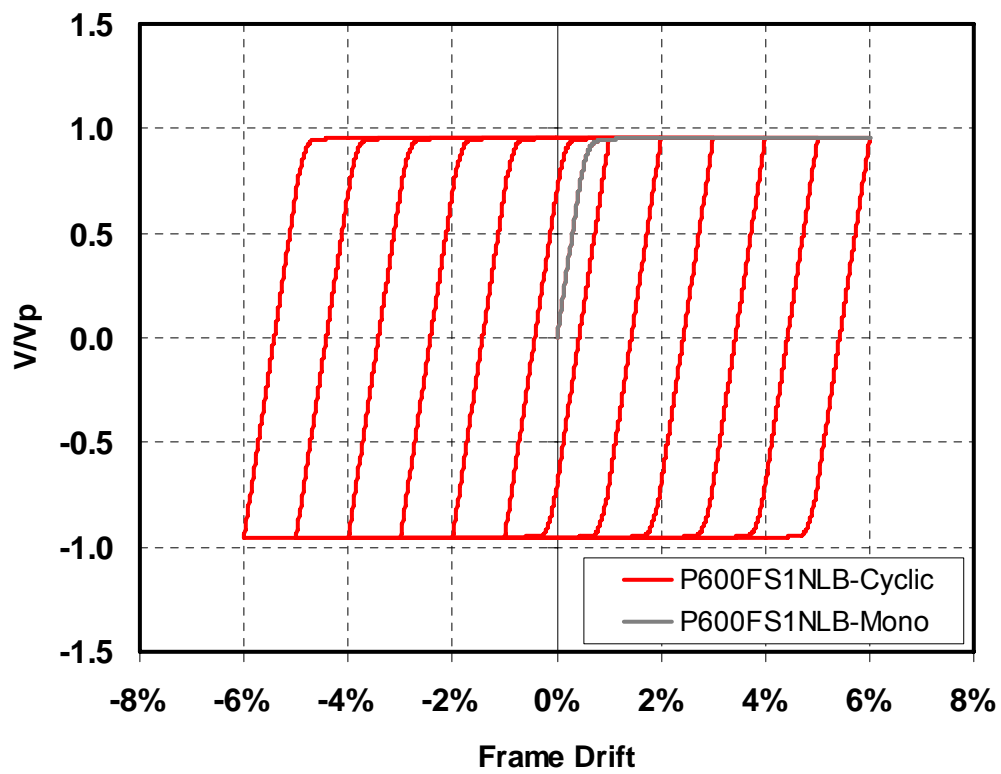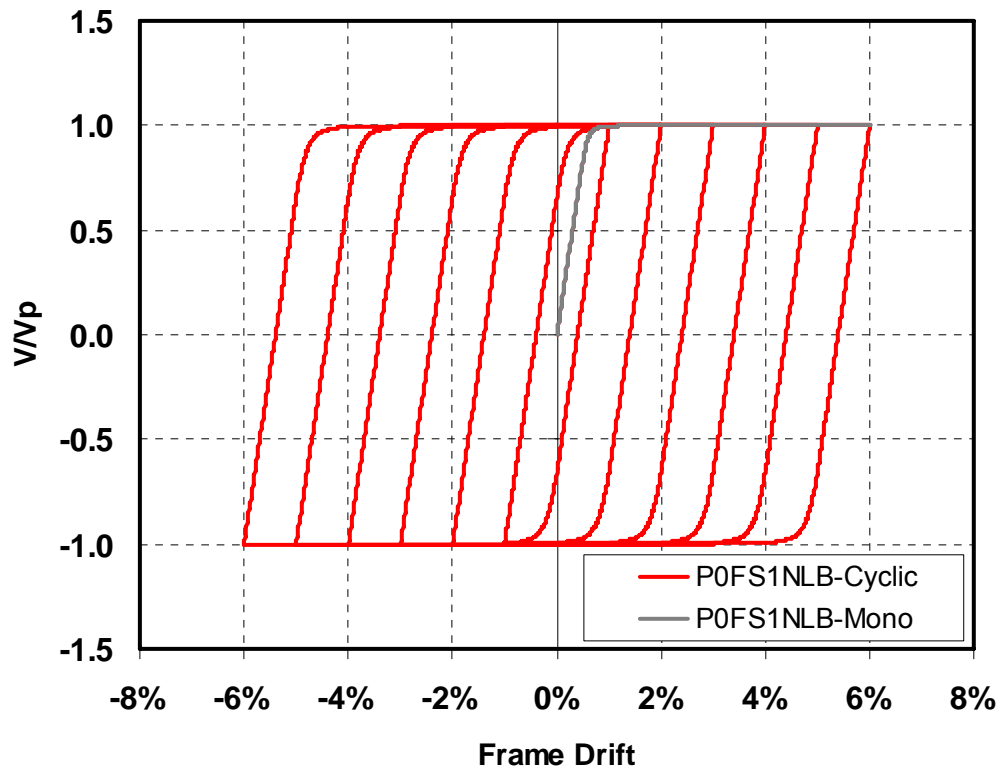
Cyclic Pushover Curve with and without Axial Forces

Monotonic with Degradation Model

(a)

(b)

ASTM A572 Gr. 50
$\sigma_y = 50$ ksi

W18x65

Fiber P-M2-M3 Hinge

2.0 m
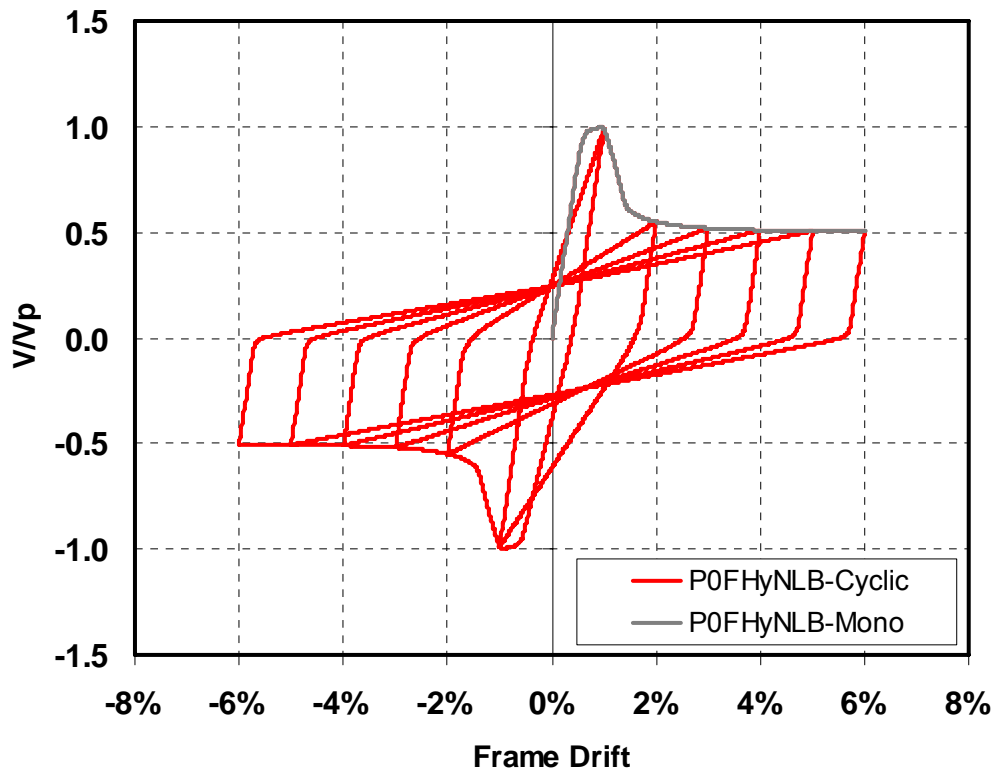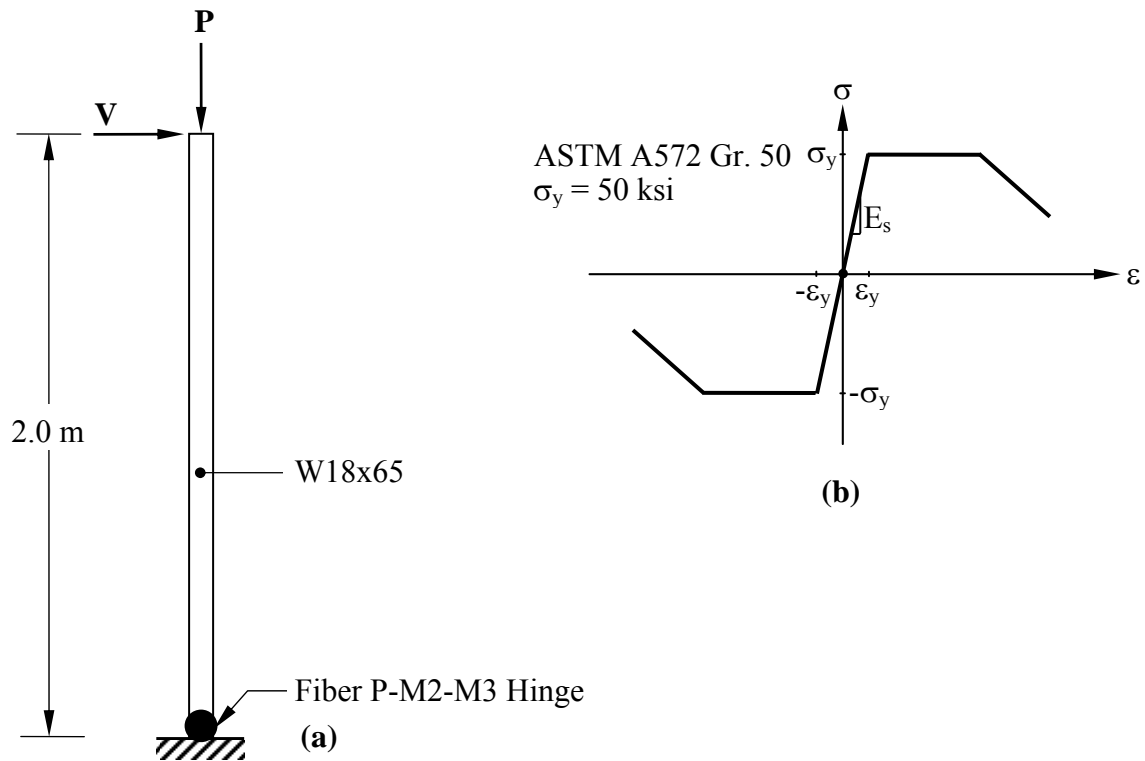
Pushover Analysis with Hysteretic Material Model Pinch {1.0, 1.0} → {0.5, 0.5}
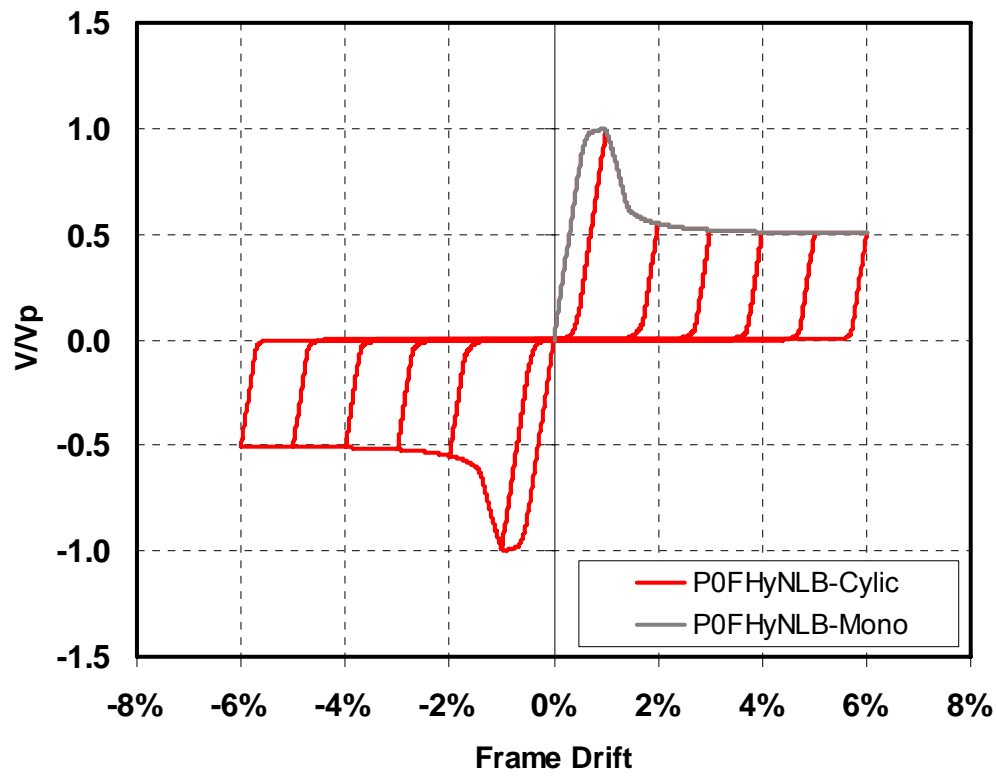
Hysteretic Material Model Pinch {1.0, 0.00001} as in Tension-only Element
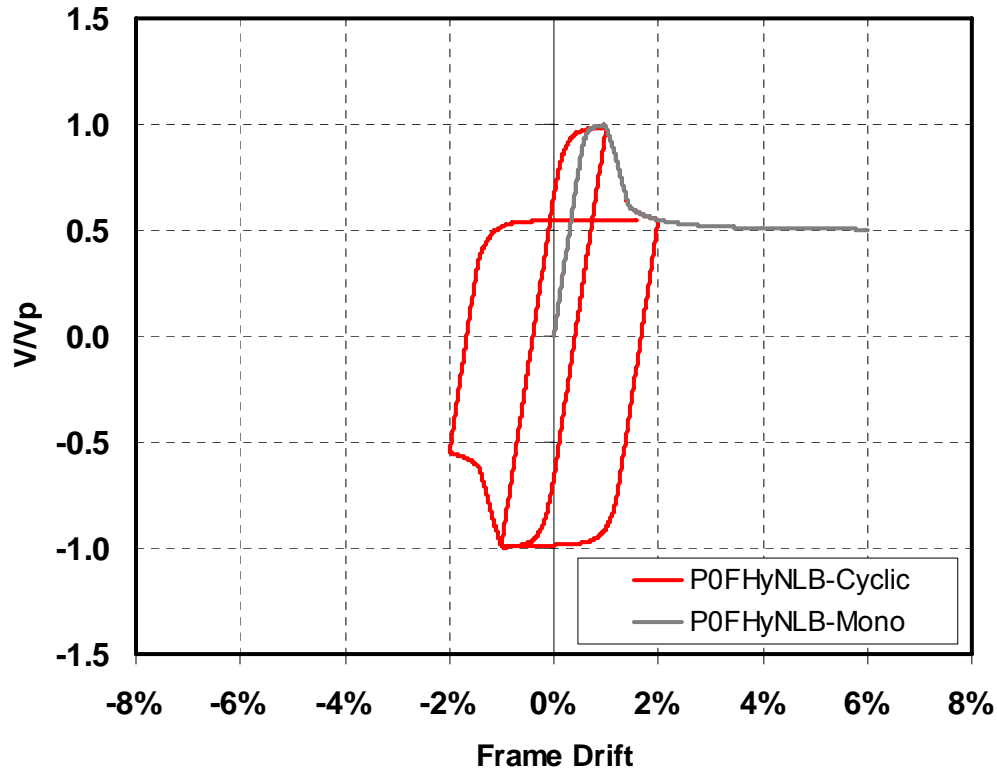
Hysteretic Material Model Pinch {0.00001, 1.0} → Convergence Issue
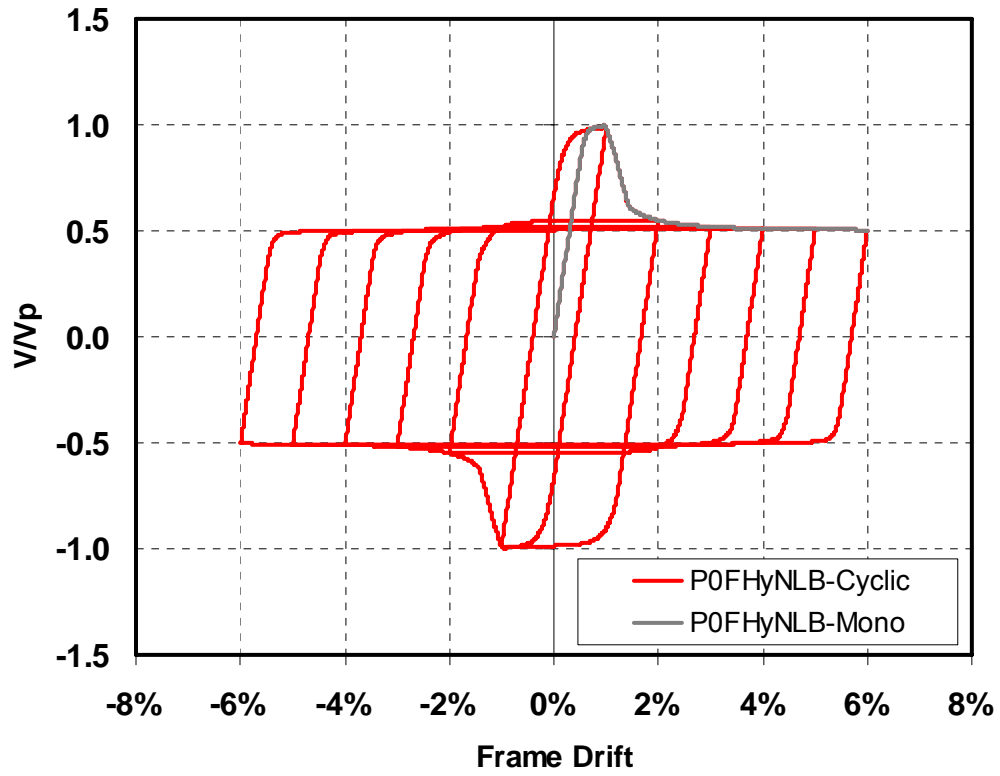
Hysteretic Material Model Pinch {0.00001, 0.99999} → Convergence Issue Solved
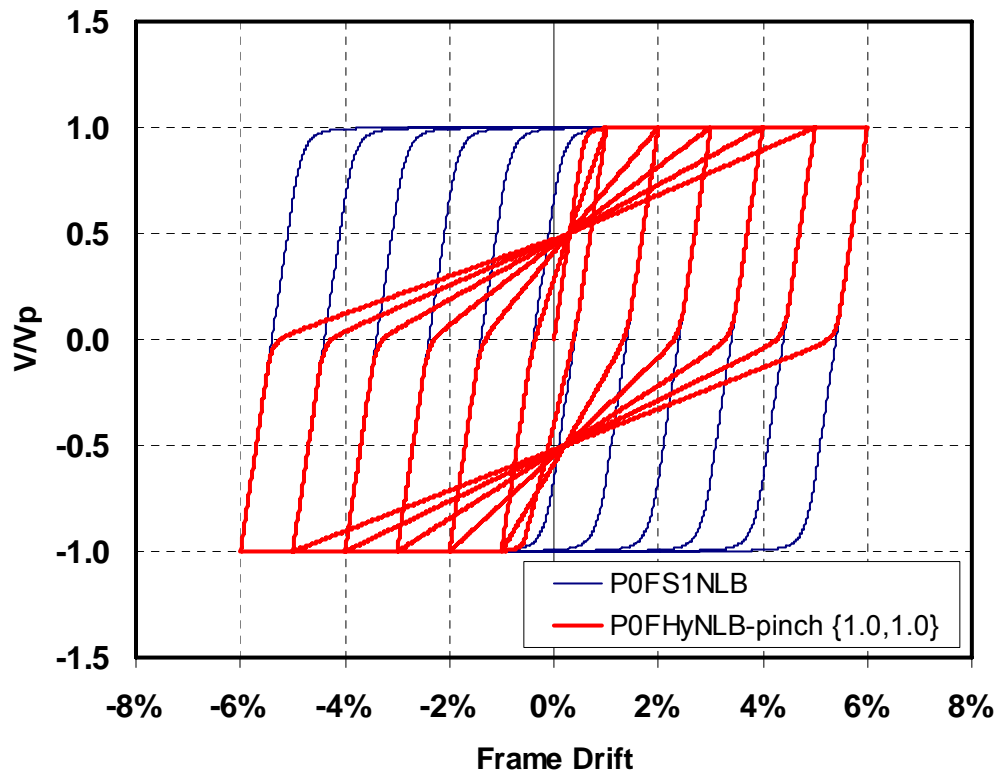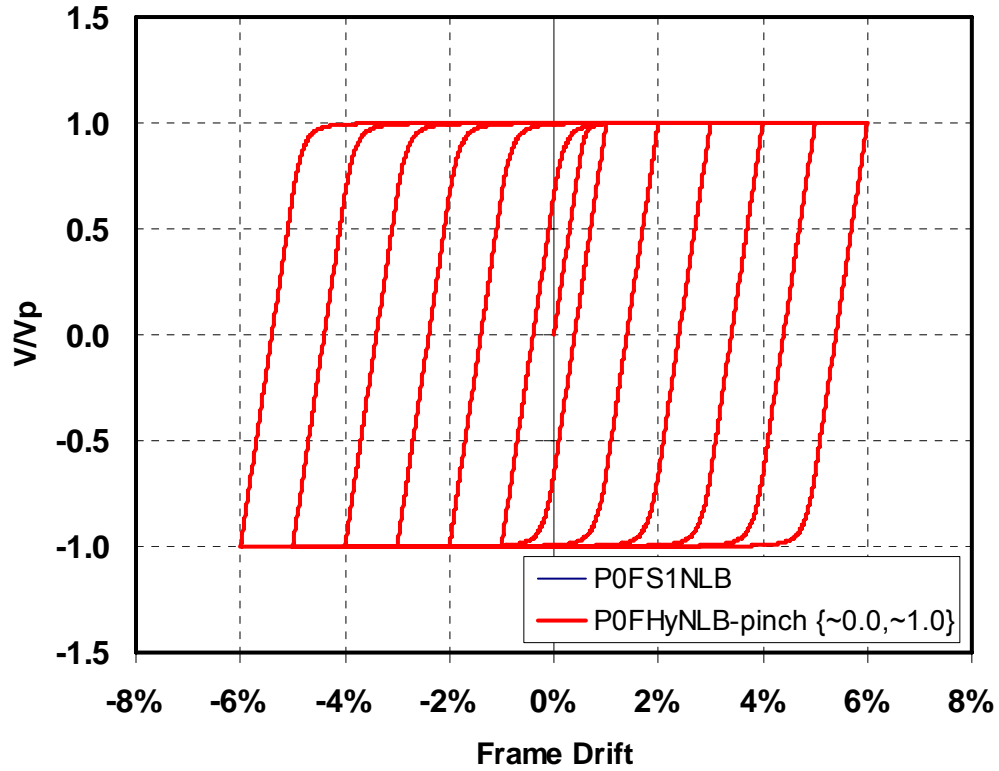
Cyclic Pushover Analysis with Hysteretic Material Model Vs. Steel01
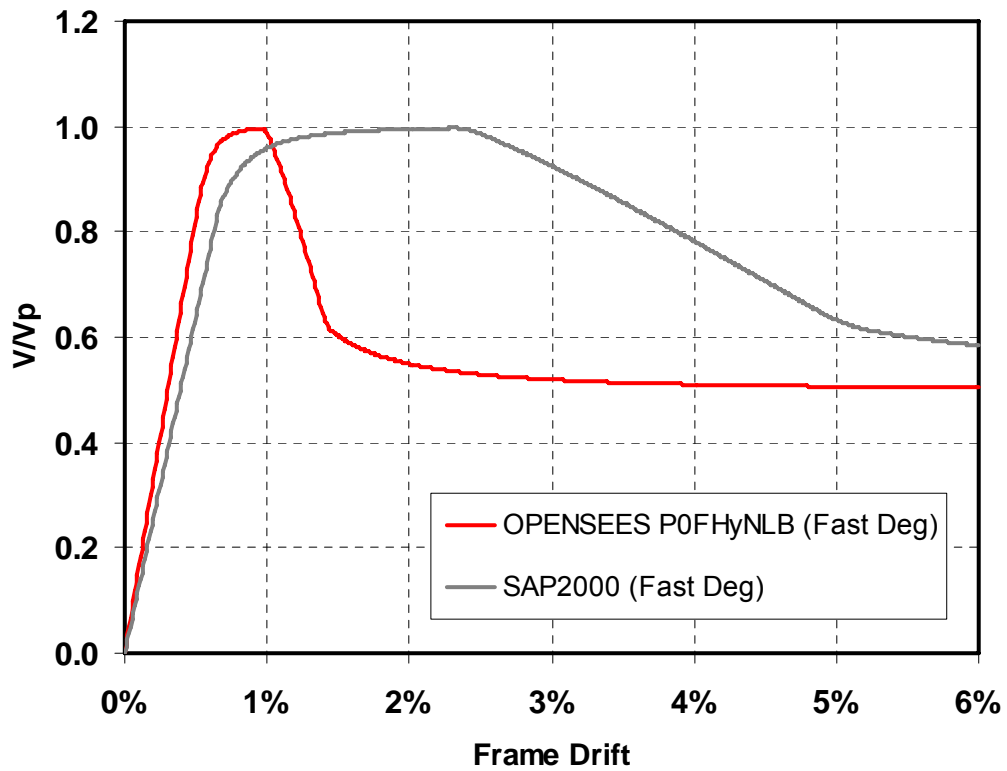
Monotonic Pushover Analysis: Hysteretic Material (NLB) Vs. SAP2000
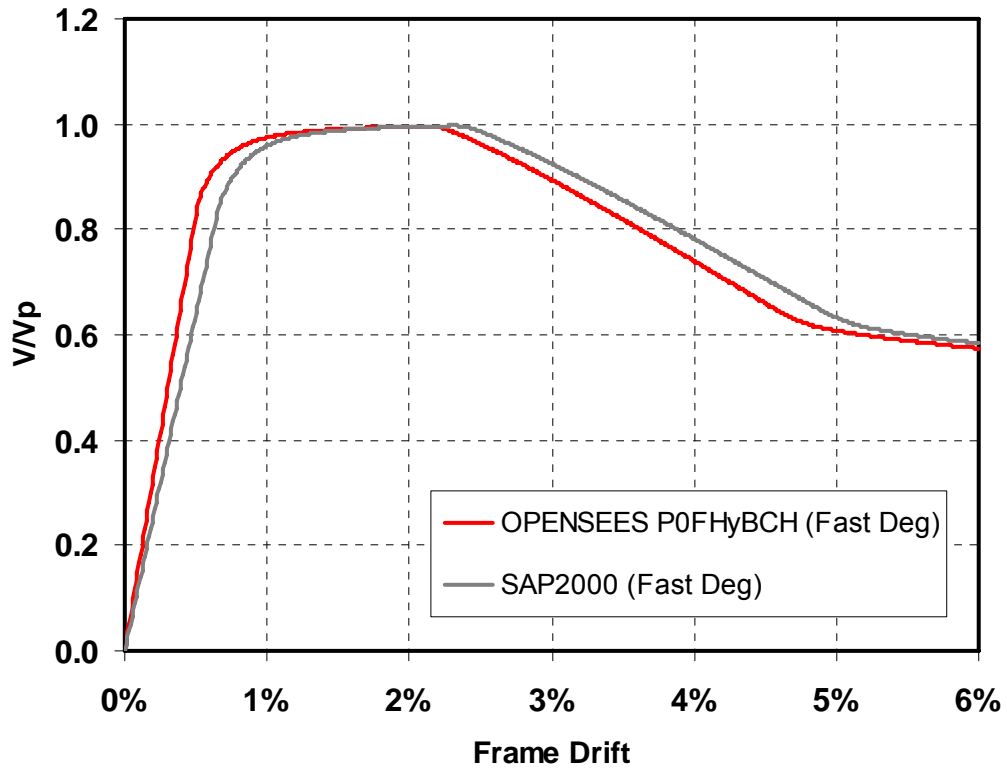
Monotonic Pushover Analysis: Hysteretic Material (BCH) Vs. SAP2000
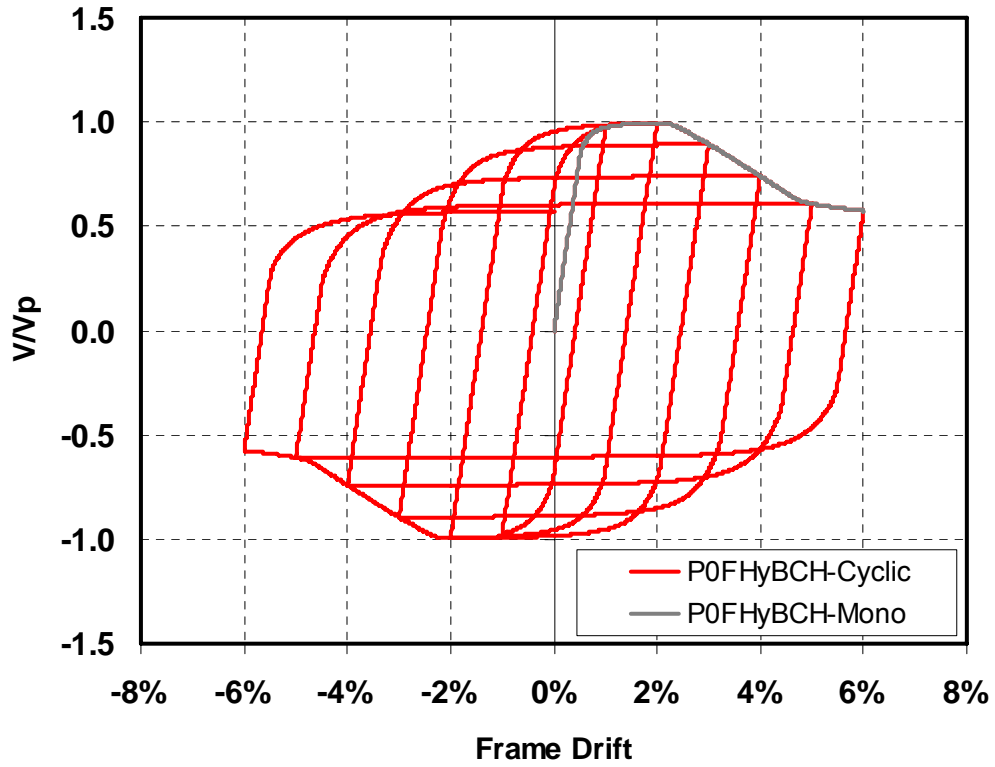
Pushover Analysis with Hysteretic Material (BCH)
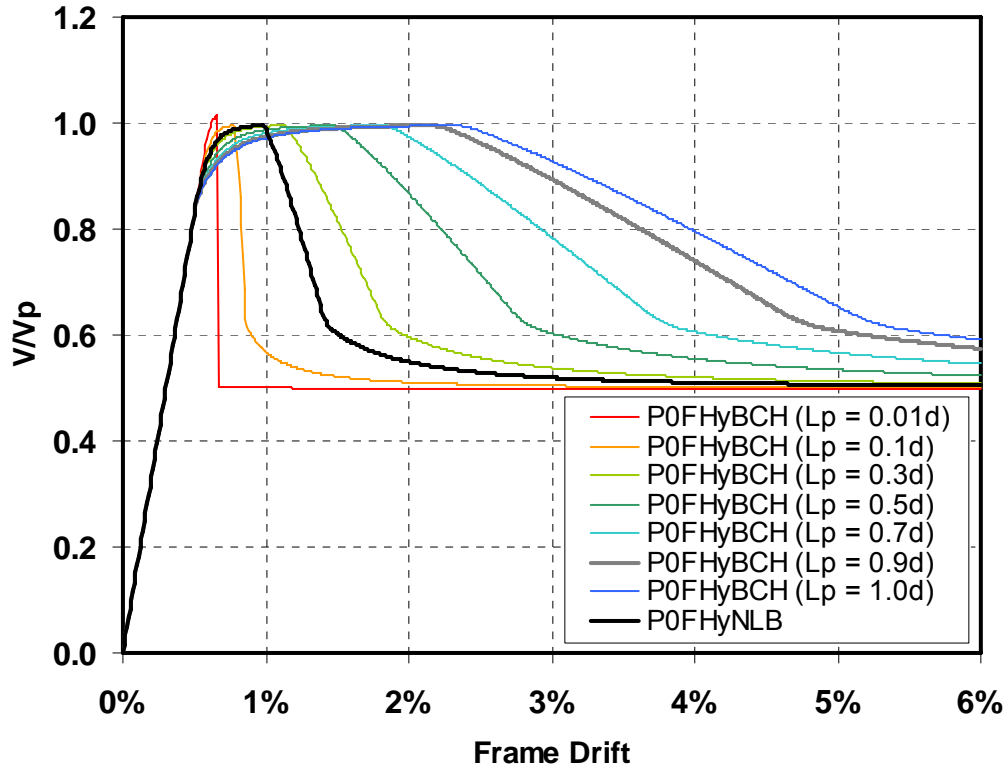
Pushover Analysis NLB vs. BCH with Various Lp
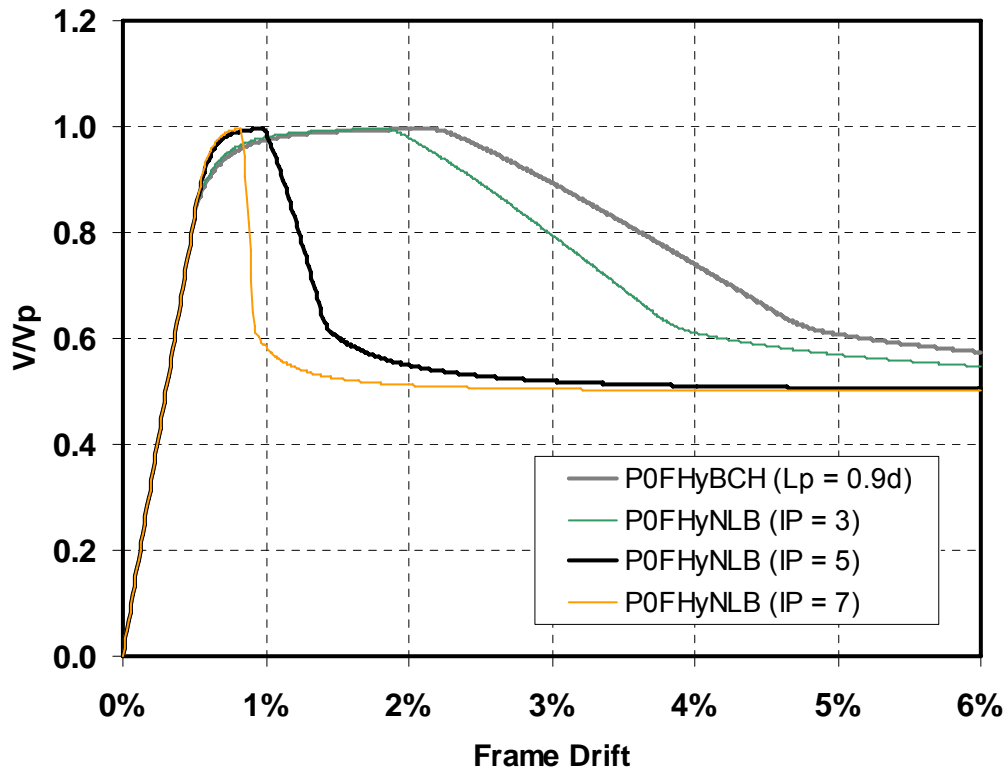
Pushover Analysis BCH vs. NLB with Various Integration Points
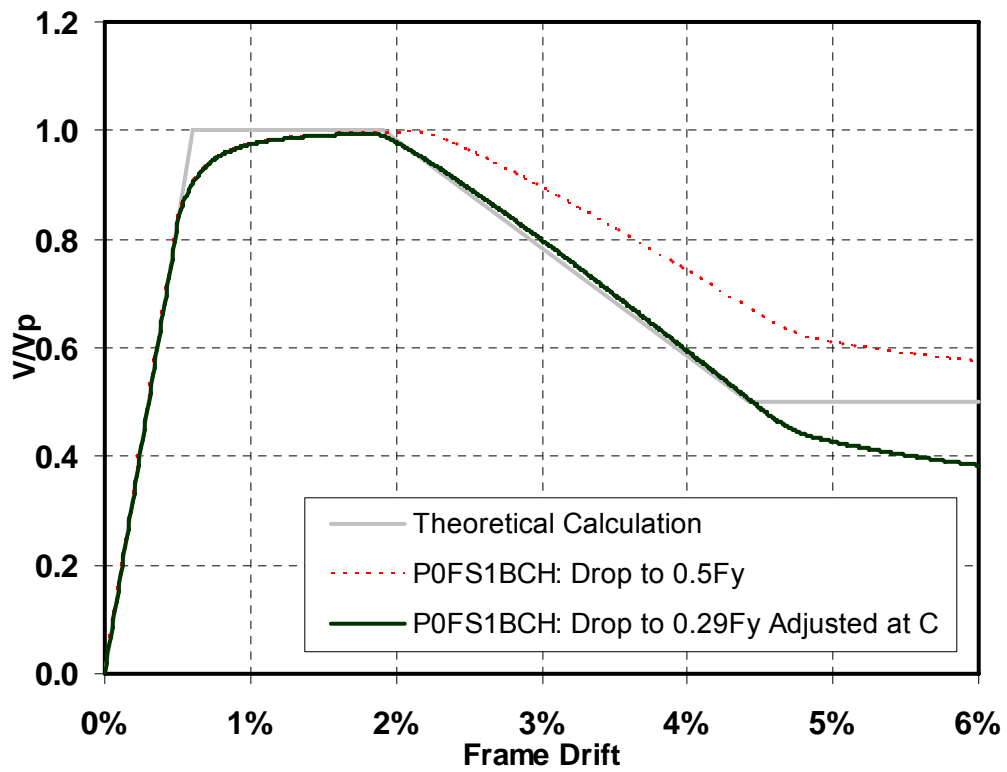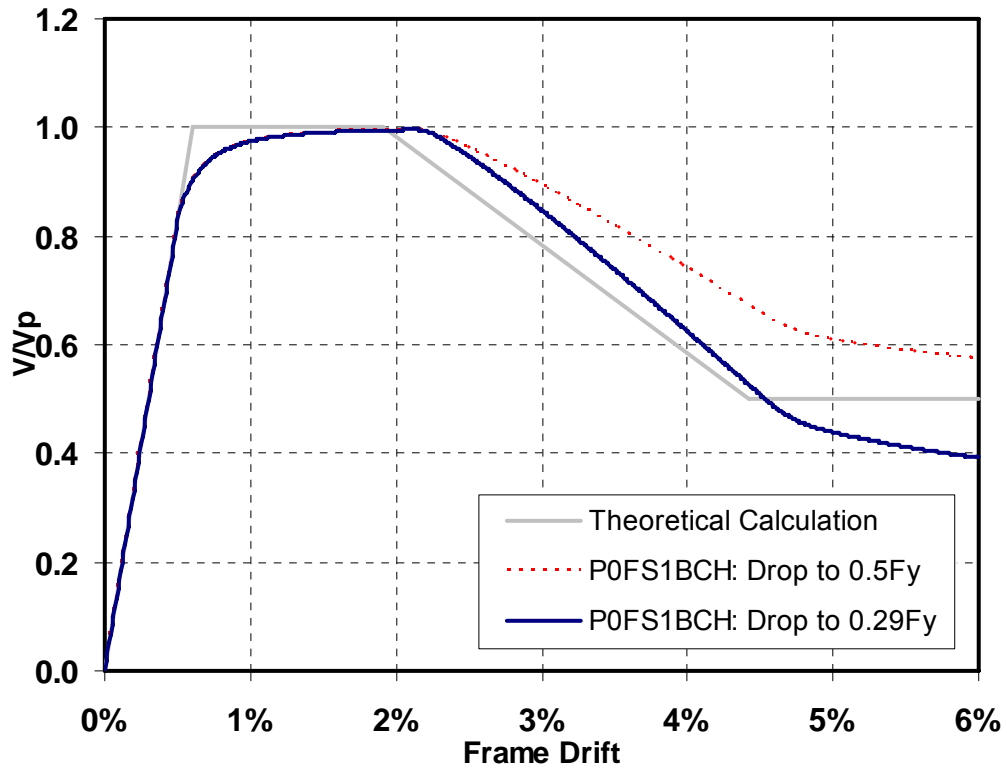
Monotonic Pushover Curve: Original vs. Adjusted Stress Diagram

Tension-only Element

a. Truss Element with Hysteretic Material Model (No Degradation)
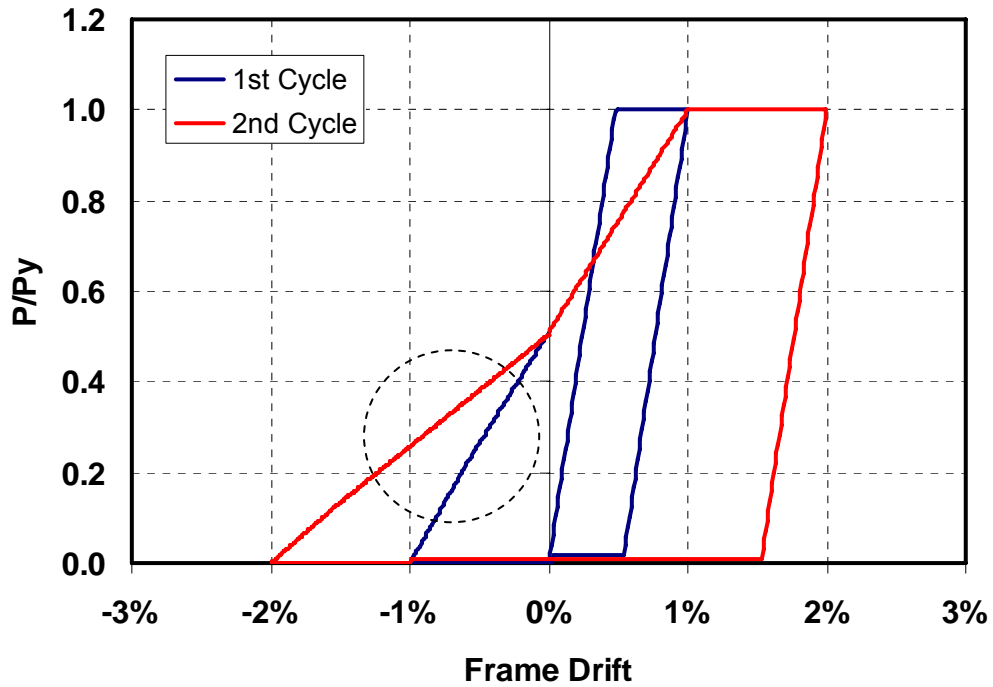
Right-Leaning Brace Hysteretic Curve
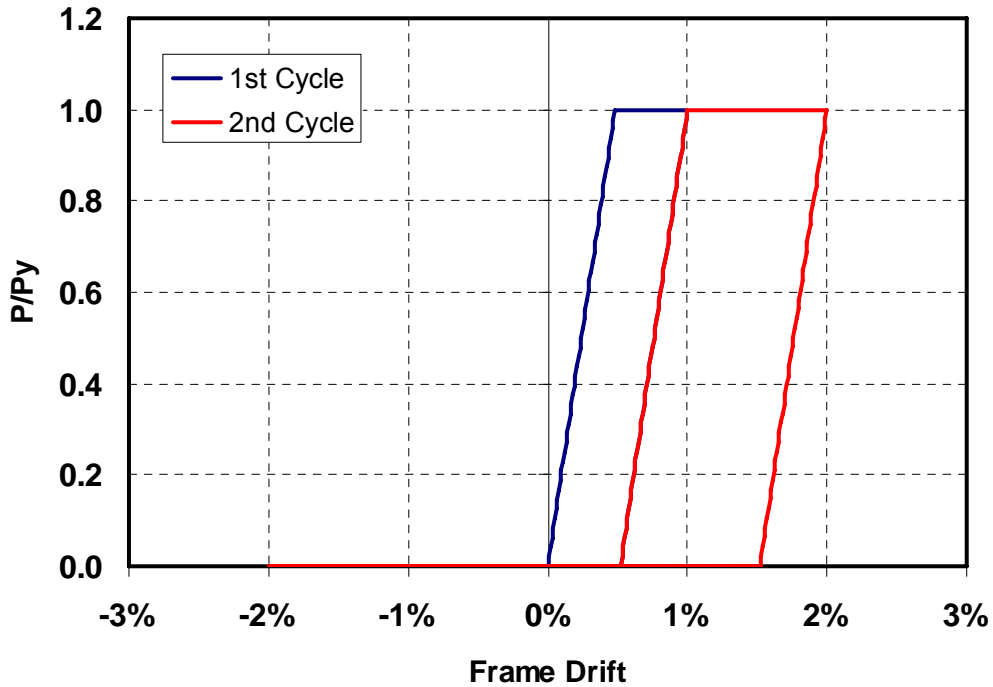
Right-Leaning Brace Hysteretic Curve - Modified
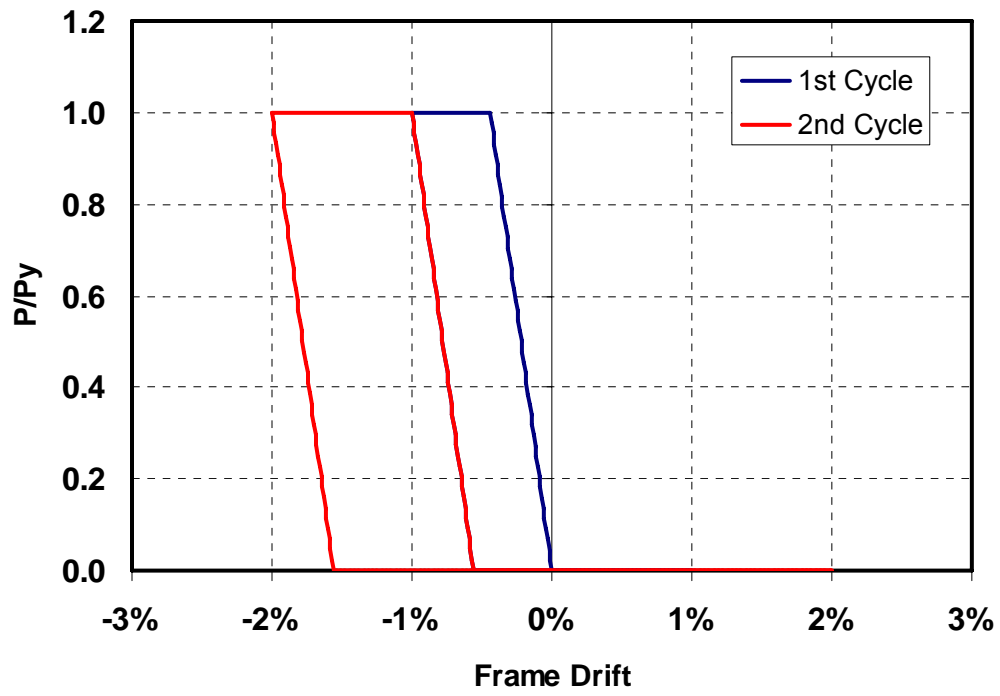
Left-Leaning Brace Hysteretic Curve - Modified
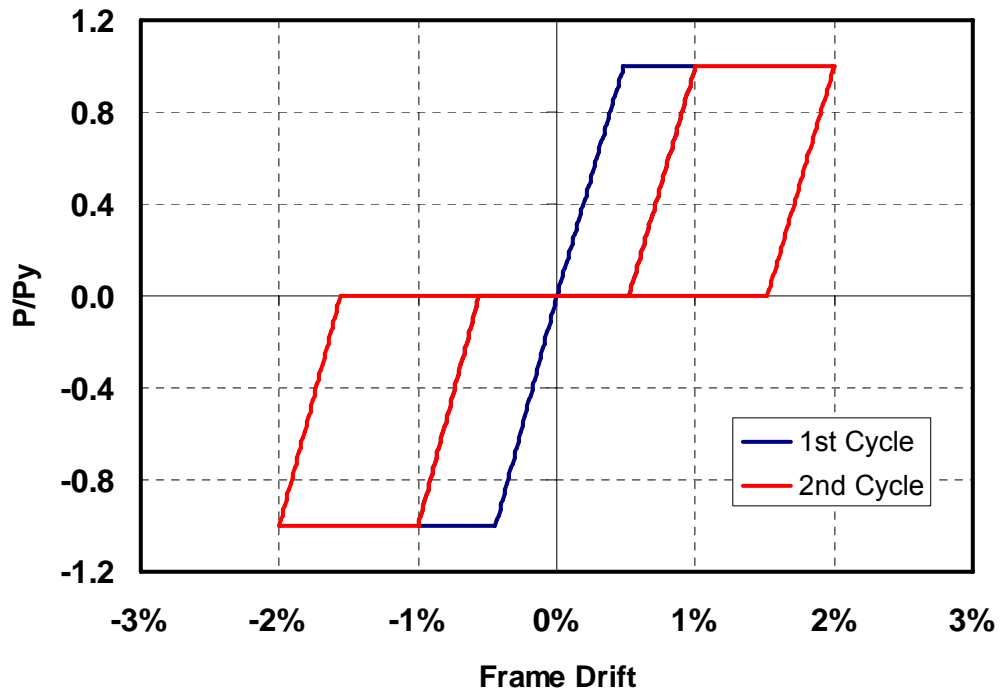
Complete Brace Hysteretic Curve

The same behavior is also observed up to 4% cyclic drifts.

b. Truss Element with Hysteretic Material Degradation Model
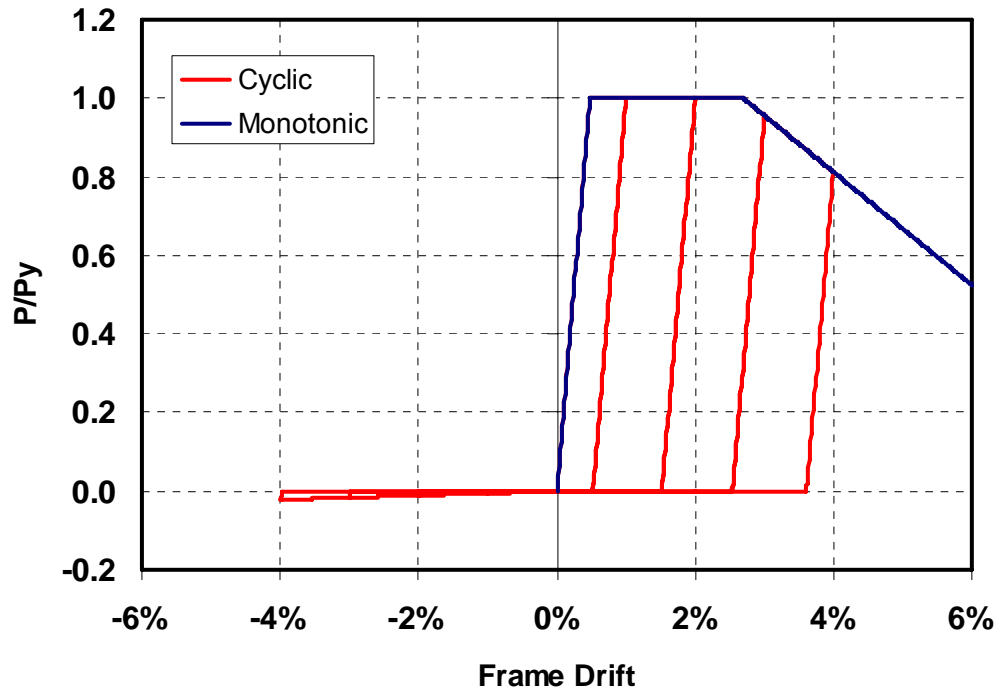
Right-Leaning Brace Hysteretic Curve – Option 1
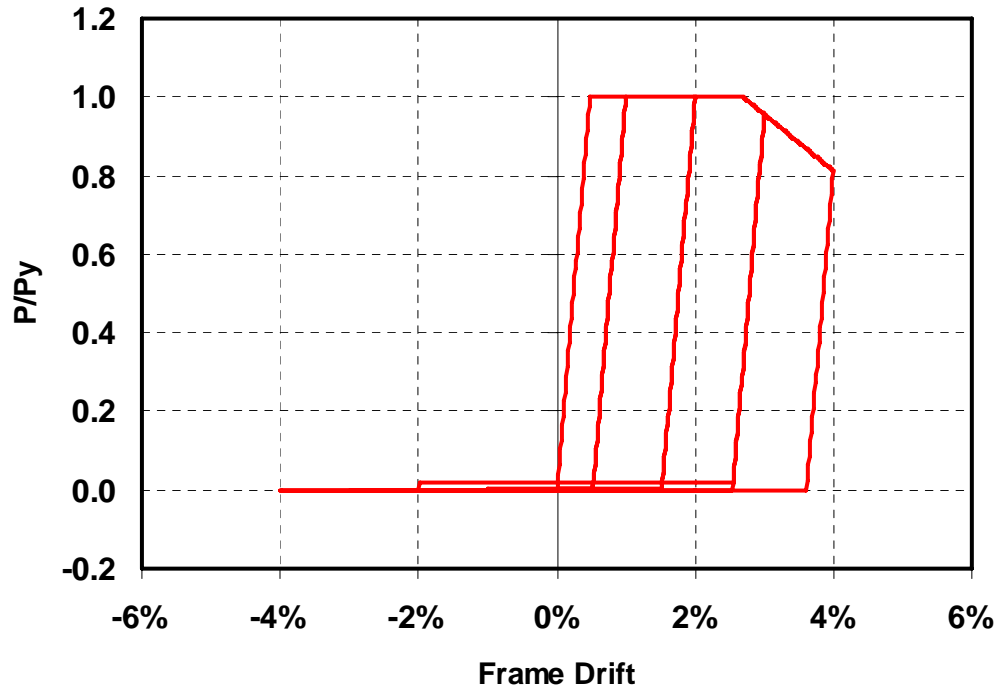
Right-Leaning Brace Hysteretic Curve – Option 2

Option 1: cut the negative part close to origin → best for cyclic pushover analysis
Option 2: extend the strain with close to zero stress
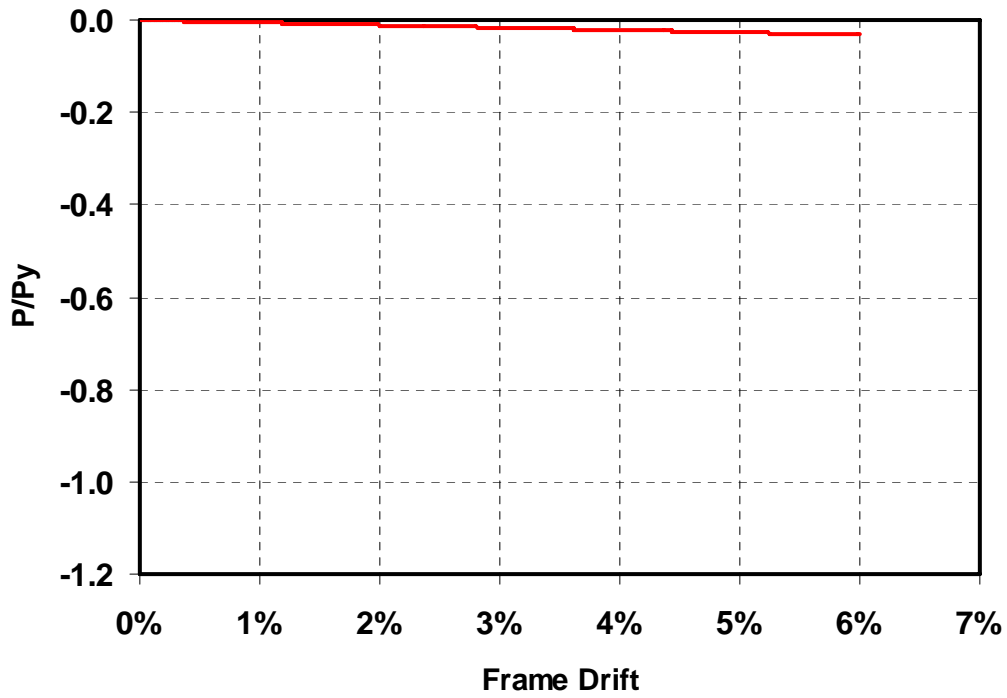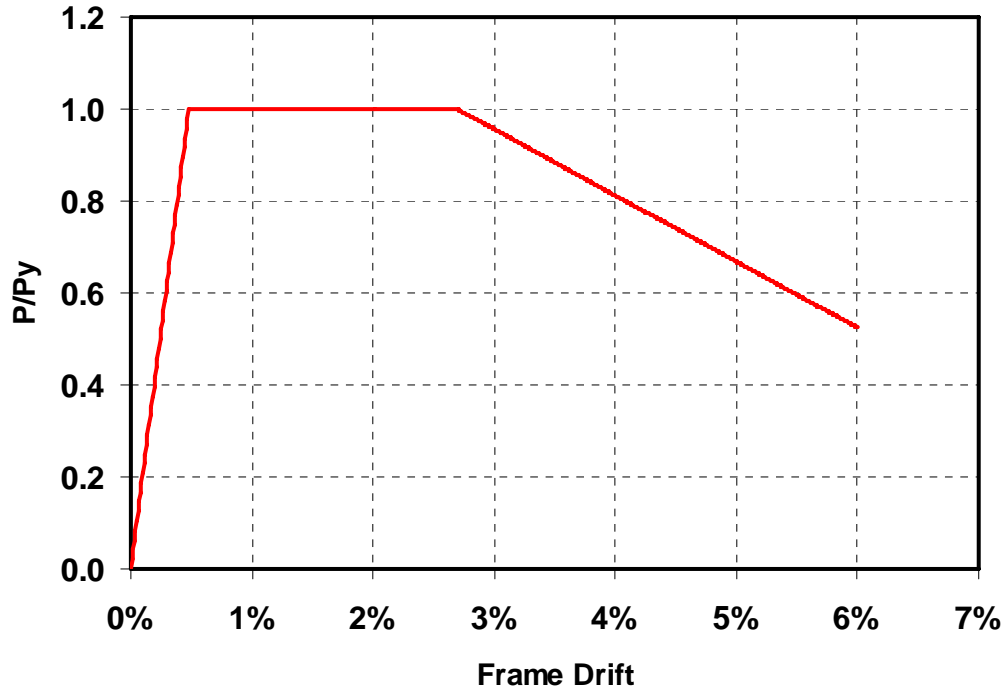
Monotonic Curve – Option 1: Right and Left-Leaning Braces
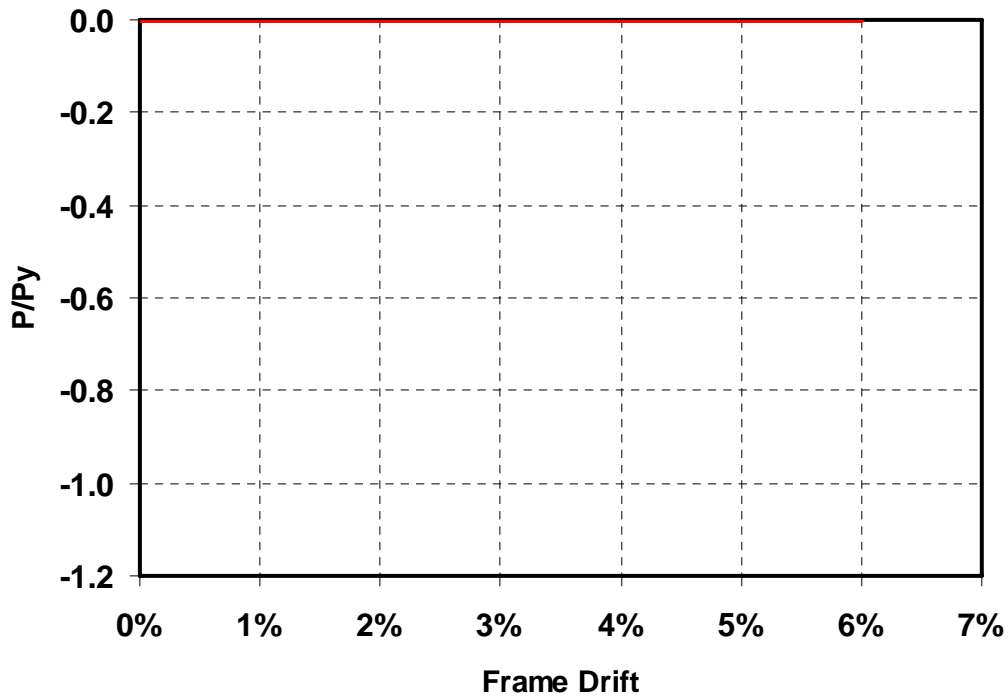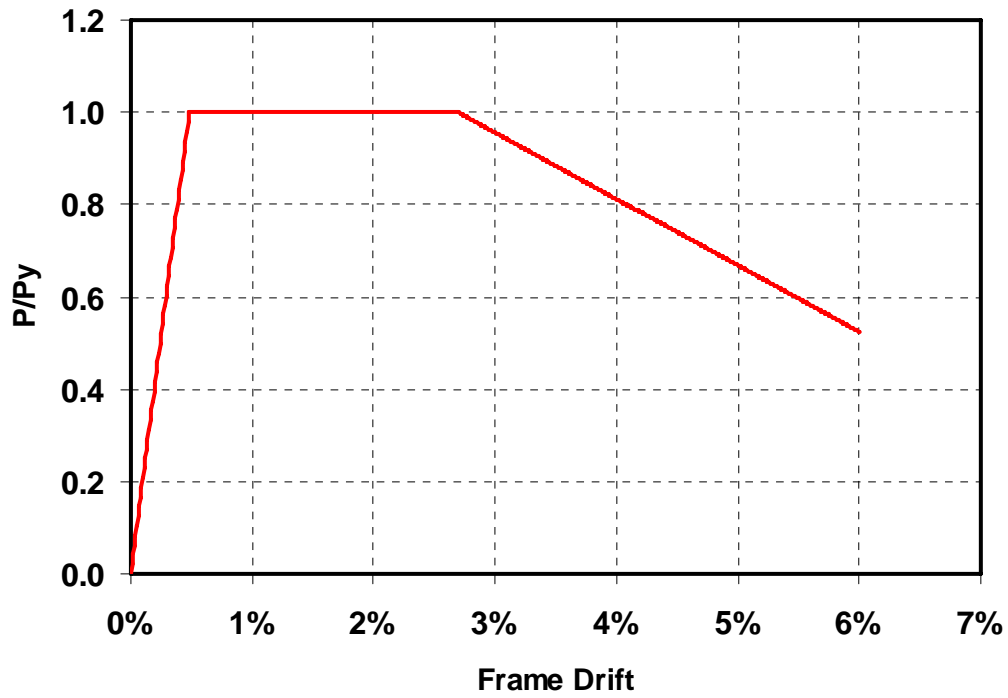
Monotonic Curve – Option 2: Right and Left-Leaning Braces

B.3 Case Study on Deterioration Models

a. Plastic Hinge Location in VBEs

(0.98M_p)
7934

-7960
(0.99M_p)

(1.0P_{y3})
126.0

(0.25)
59.0

(0.49)
112.7

(0.26)
59.1

(0.93M_p)
4675

-4676
(0.93M_p)

(1.0P_{y2})
206.5

(0.28)
84.5

(0.49)
184.7

(0.23)
103.6

(0.83M_p)
2641

-2638
(0.83M_p)

(1.0P_{y1})
252.0

(0.27)
118.8

(0.51)
225.4

(0.22)
99.6

(1.00M_p)
16227

-16208
(1.00M_p)
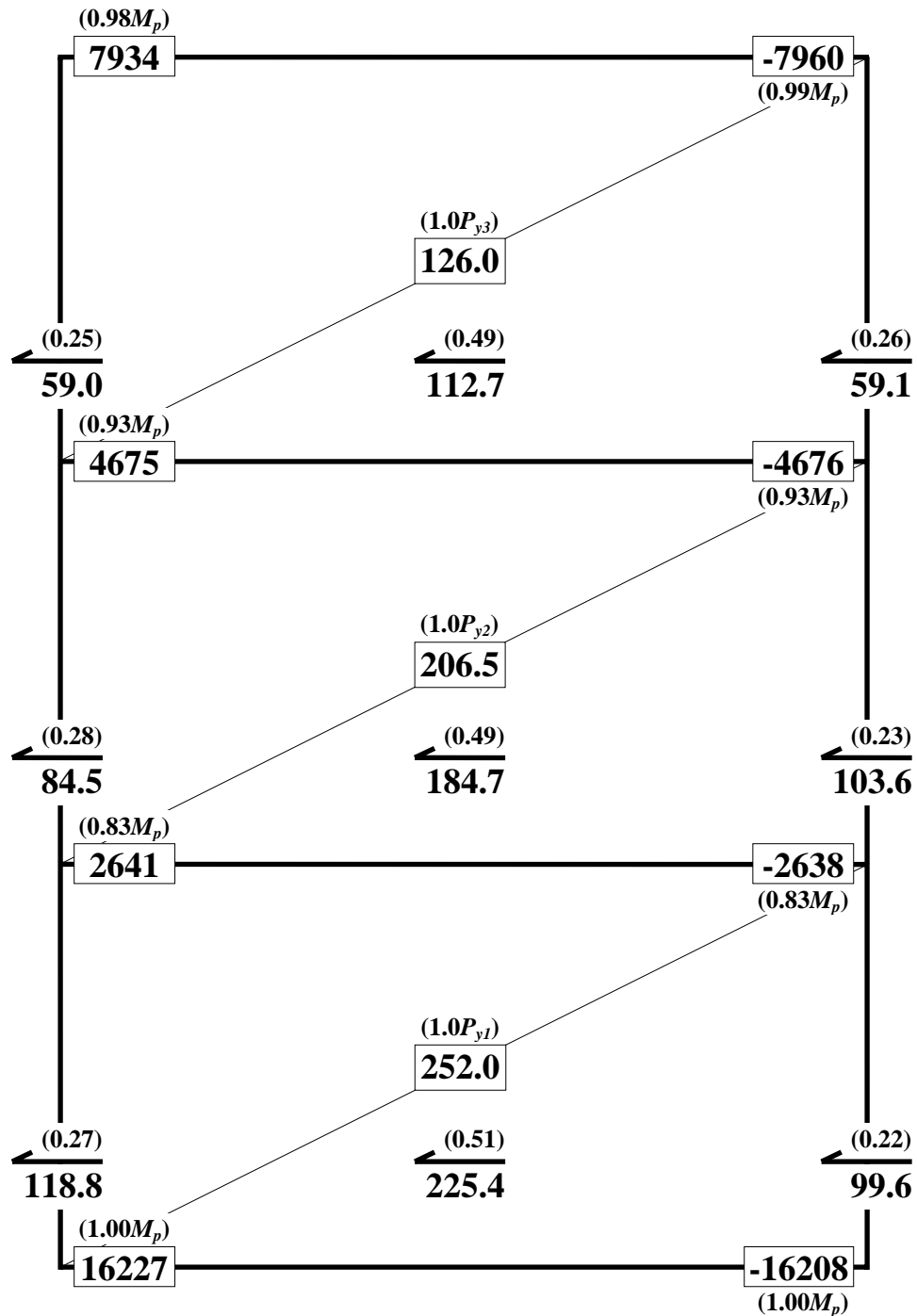
OPENSEES: Step 264 (2.64% Drift)

(0.89M_p)
7199

-7093
(0.88M_p)

(0.89P_y3)
112.4

(0.21)
35.3

(0.59)
100.6

(0.20)
33.3

(0.93M_p)
4682

-4637
(0.92M_p)

0

(0.47)
128.9

0

(0.53)
144.4

(0.80M_p)
2540

-2576
(0.81M_p)

(0.83P_y1)
209.3

(0.23)
74.5

(0.57)
187.2

(0.20)
63.6

(0.87M_p)
14222

-14650
(0.90M_p)
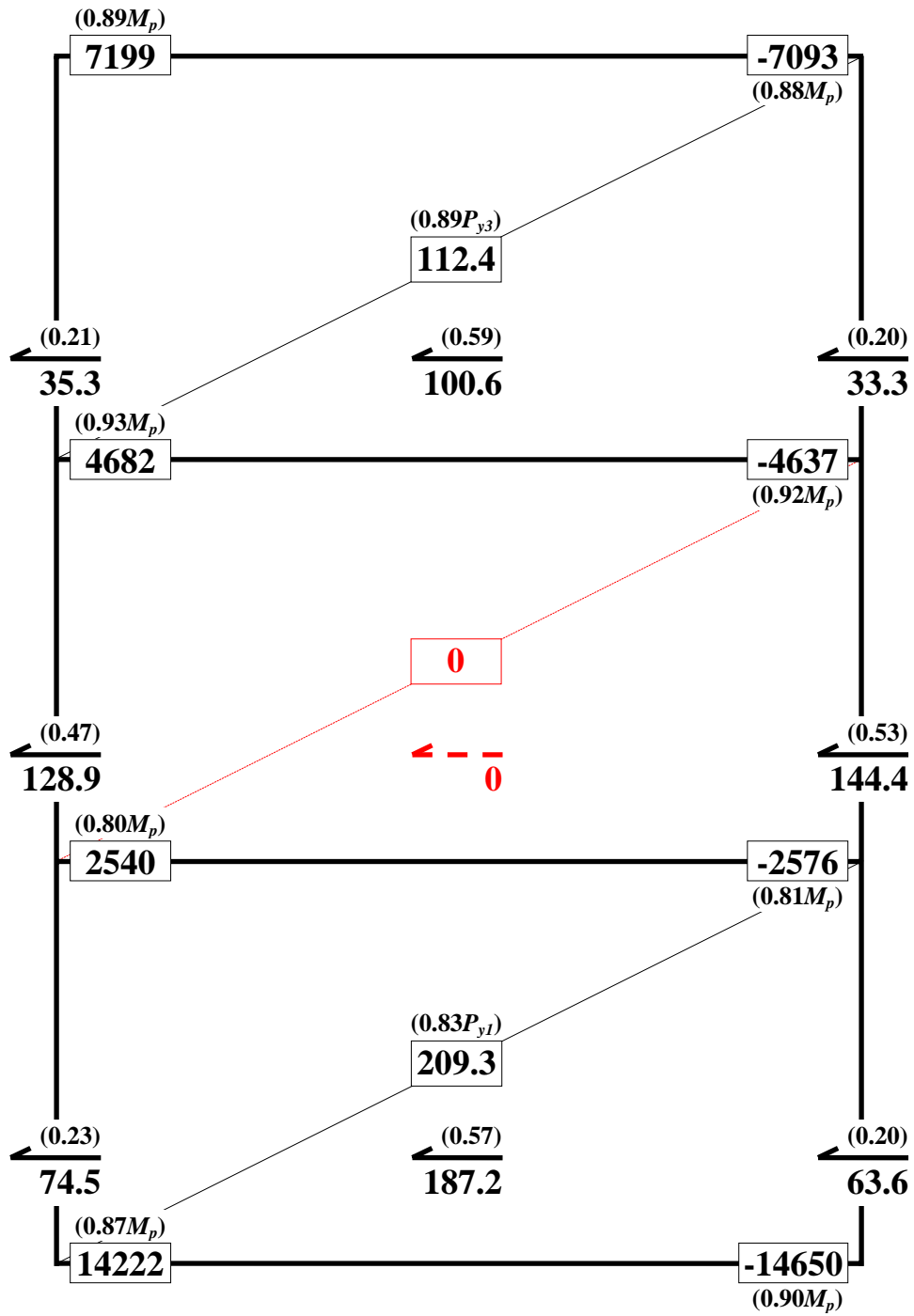
OPENSEES: Step 265 (2.65% Drift)
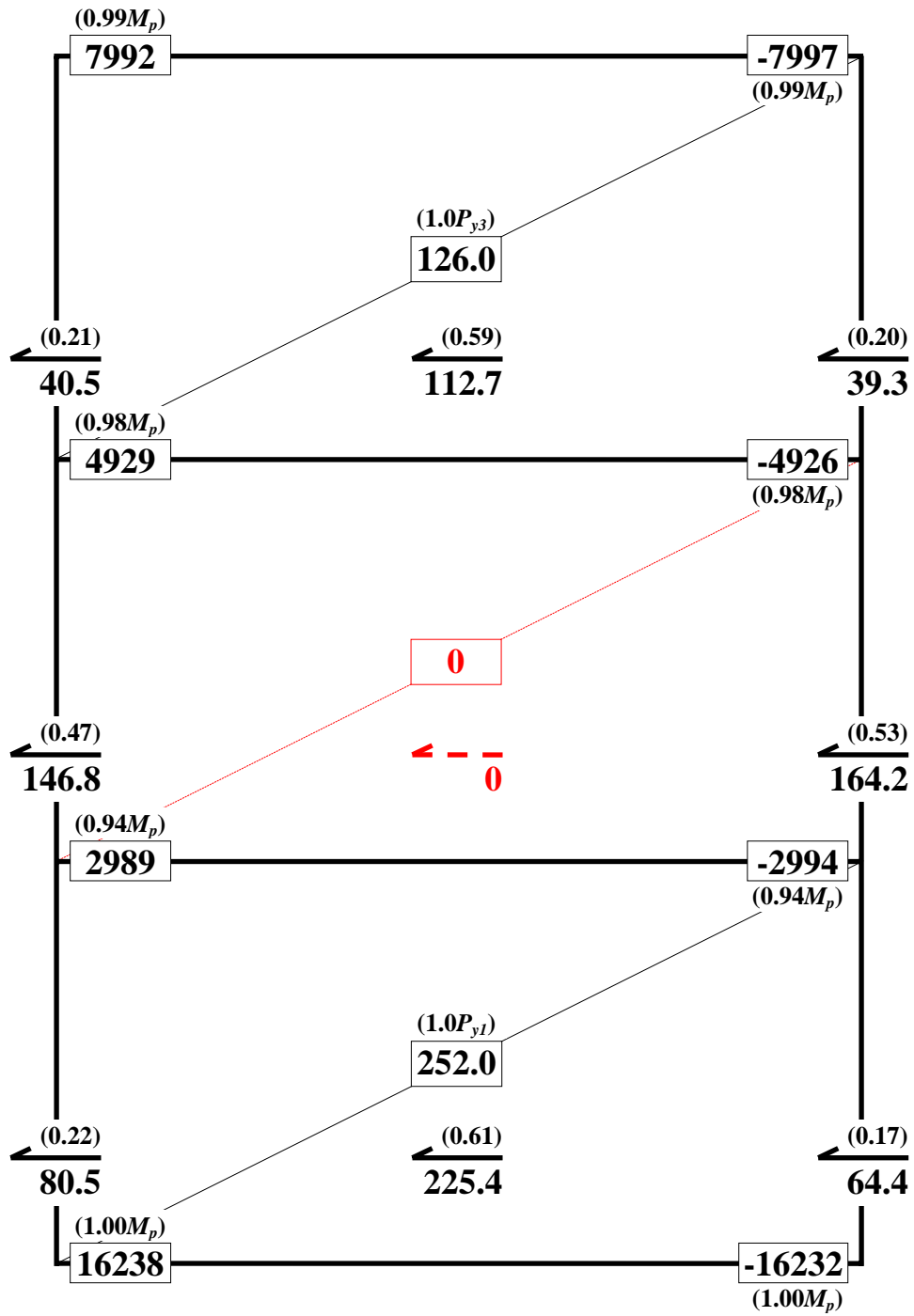
OPENSEES: Step 333 (3.33% Drift)

b. Different Material Models Explanation:

1. Initial 1st Results: Controller Factors = 1, 1, 1, 1; drop to 50% theoretical (β=0.5); drop to 50% strips at $15\varepsilon_y$; tolerance = 10^{-4} with 4000 max iterations
→ [1111; 50%@0.0332; 50%@$15\varepsilon_y$; 10^{-4}; 4000]
Variation: practically the same curve for [1111; **50%β@0.0332**; 50%@$15\varepsilon_y$; 10^{-4}; 4000]. Obvious effect, less base shear. Meaning better "approaching" (Fig. 1S).

2. [1111; **50%@0.0332**; 50%@11to15ε_y for middle strip; 50%@5to11ε_y for corner strip; 10^{-4}; 4000]
Variation: [1111; **50%β@0.0332**; 50%@11to15ε_y for middle strip; 50%@5to11ε_y for corner strip; 10^{-4}; 4000]. See Fig. 2S.

3. [1111; 50%@0.0332; 50%@**21ε_y**; **10^{-6}**; 4000]. The correct drop at 50% on strip actually at $21\varepsilon_y$. Change in tolerance is actually not significant here. 10^{-4} and 10^{-6} gave practically identical results. The latter might need more iterations to achieve convergence. The first gave some 'noise' in the results (e.g., effects on ratio of pushover load distribution).
Variation: [1111; 50%@0.0332; **50%@11to21ε_y for middle strip; 50%@5to11ε_y for corner strip;** 10^{-4}; 4000]. See Fig. 3S.

4. [1111; **90%@0.0359; 90%@29ε_y**; 10^{-4}; 4000].
Variation: Finest step up to 100,000 steps to reach 1% didn't change the results. Beside Modified Newton-Raphson, other algorithms have been tried. Some of them fail to converge and some of them gave the same results (consult hand notes). Practically the same results were observed, if 0.0359 (extrapolation from revised by β) is changed to 0.0444 (extrapolation from un-revised). See Fig. 4S.

5. [1111; **90%@0.0559 start from 0.092; 90%@49ε_y start from 11ε_y**; 10^{-4}; 4000] → sort of arbitrary case with less stiff of the negative stiffness when degradation occurred both on BE and Strips. Another variation that is not completely true shown in Fig. 5S for [1111; **50%@0.0332; 90%@29ε_y**; 10^{-4}; 4000]. More variation: Fig 6S → [1110; 90%@29ε_y; 10^{-4}; 4000]
Fig 7S → [1101; 90%@0.0444; 10^{-4}; 4000]
Fig 8S → [1101; 90%@0.0359; 10^{-4}; 4000]
Fig 9S → [1101; 50%@0.0332; 10^{-4}; 4000]

6. [1120; 10^{-4}; 4000].
Variation: Fig 10S → [1121; 50%@0.0332; 10^{-4}; 4000]. The same trend with [1121; 50%@0.0444; 10^{-4}; 4000]. Not printed the curve.
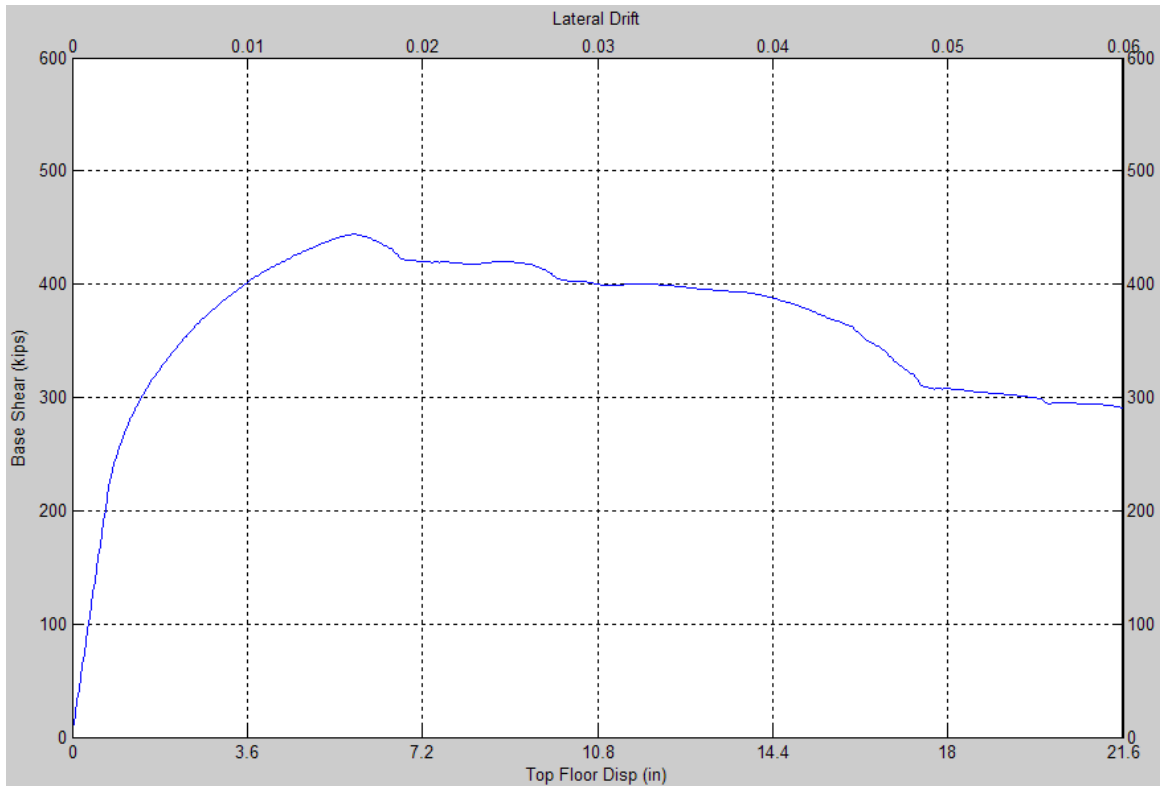
[1111; 50%@0.0332; 50%@15ε$_v$; 10^{-4}; 4000]
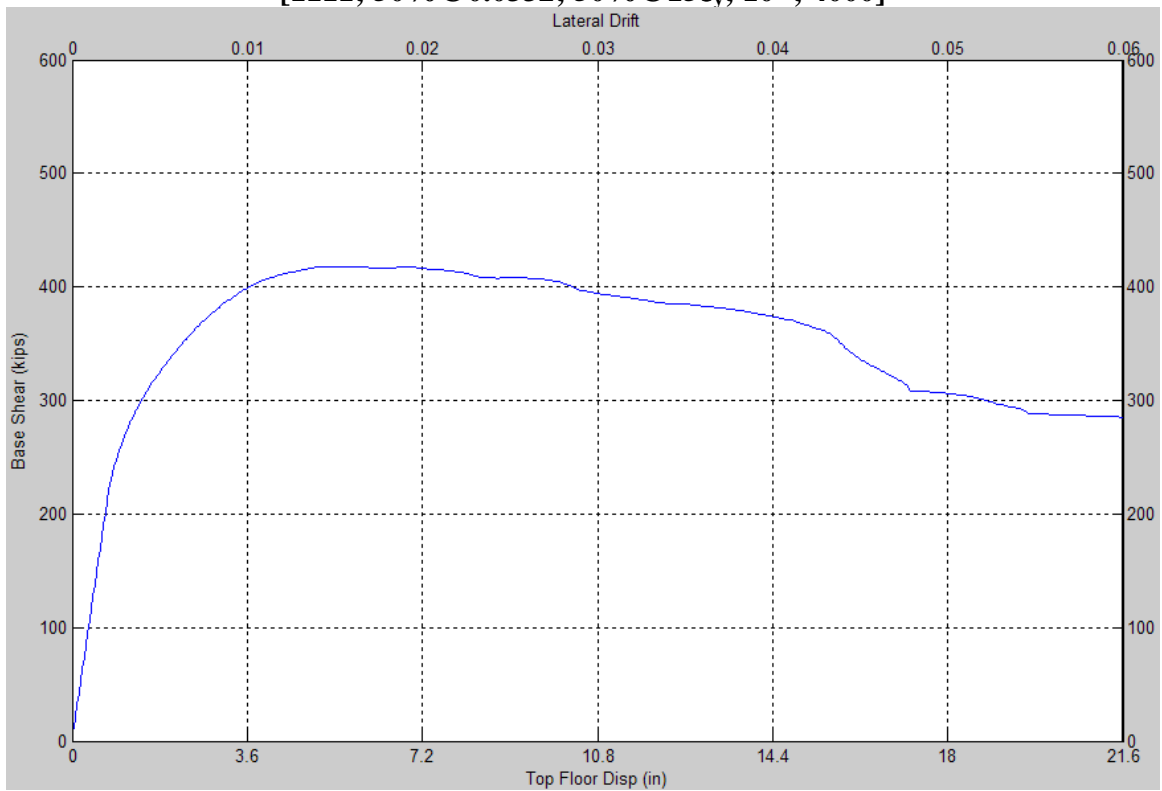
[1111; 50%@0.0332; <u>50%@11to15ε$_v$ for middle strip; 50%@5to11ε$_v$ for corner strip;</u> 10^{-4}; 4000]
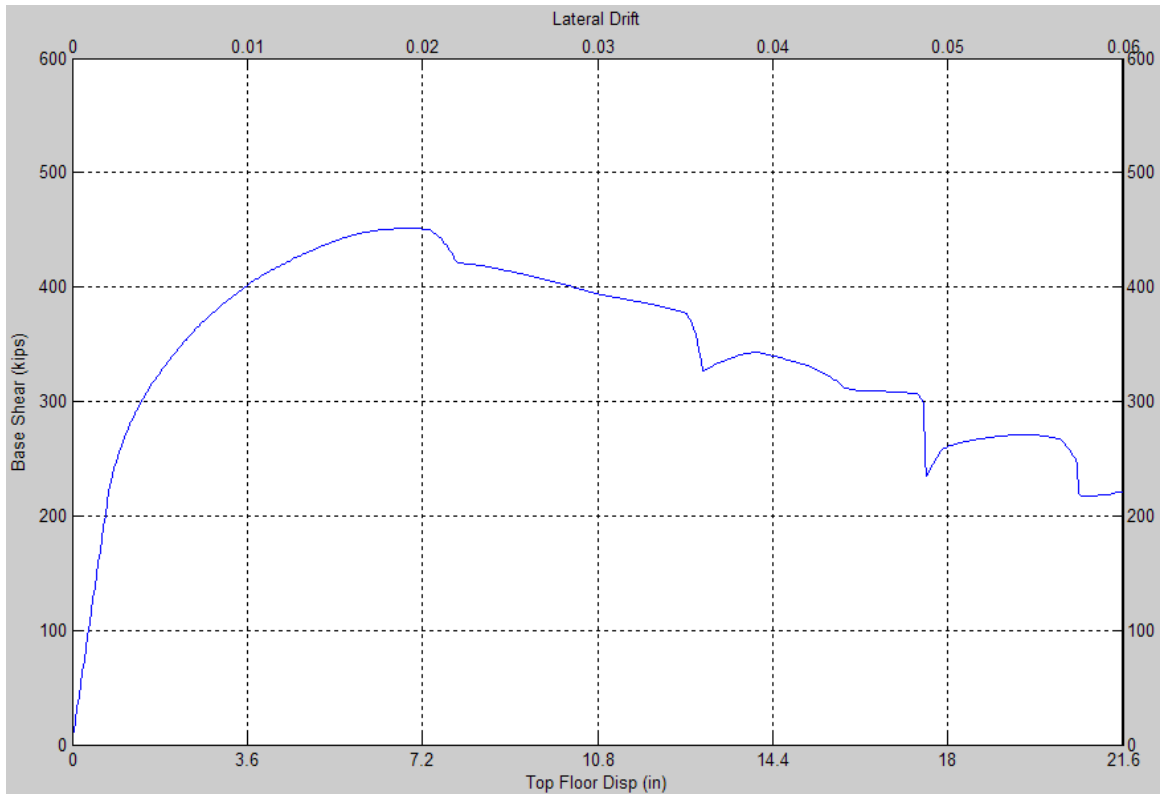
[1111; <u>90%@0.0359</u>; 90%@29ε_y; 10^{-4}; 4000]
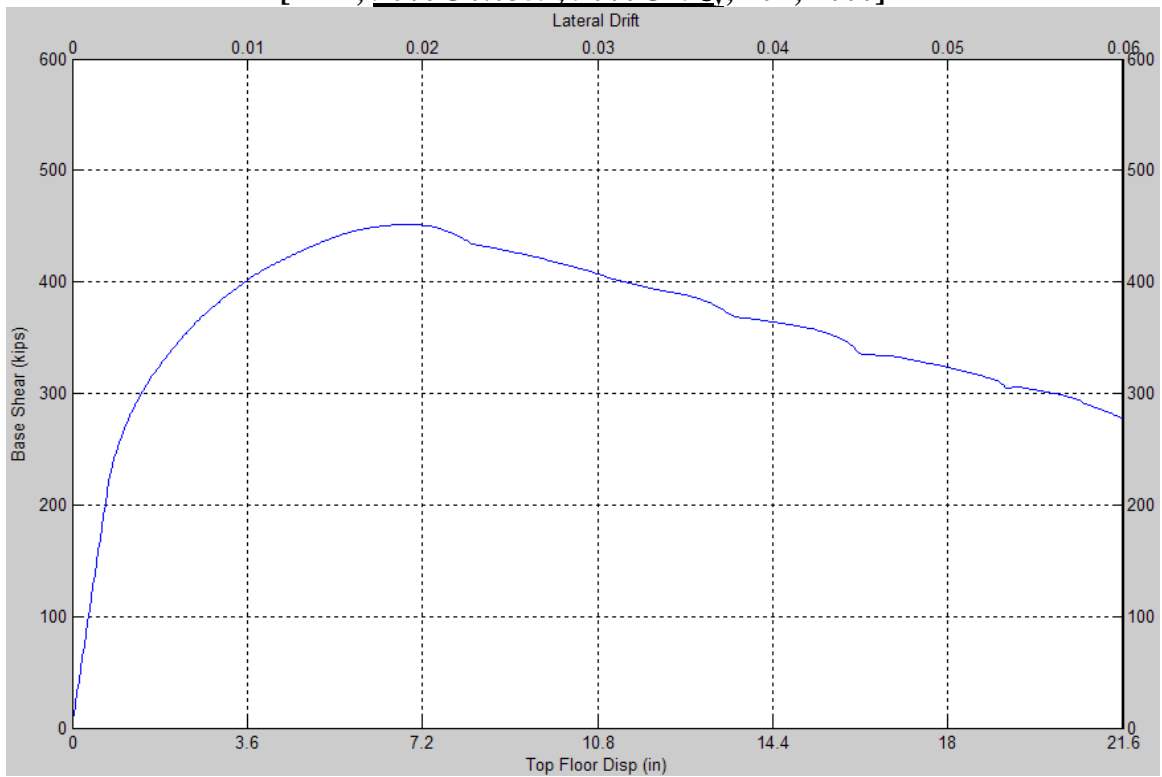
[1111; <u>50%@0.0332</u>; 90%@29ε_y; 10^{-4}; 4000]
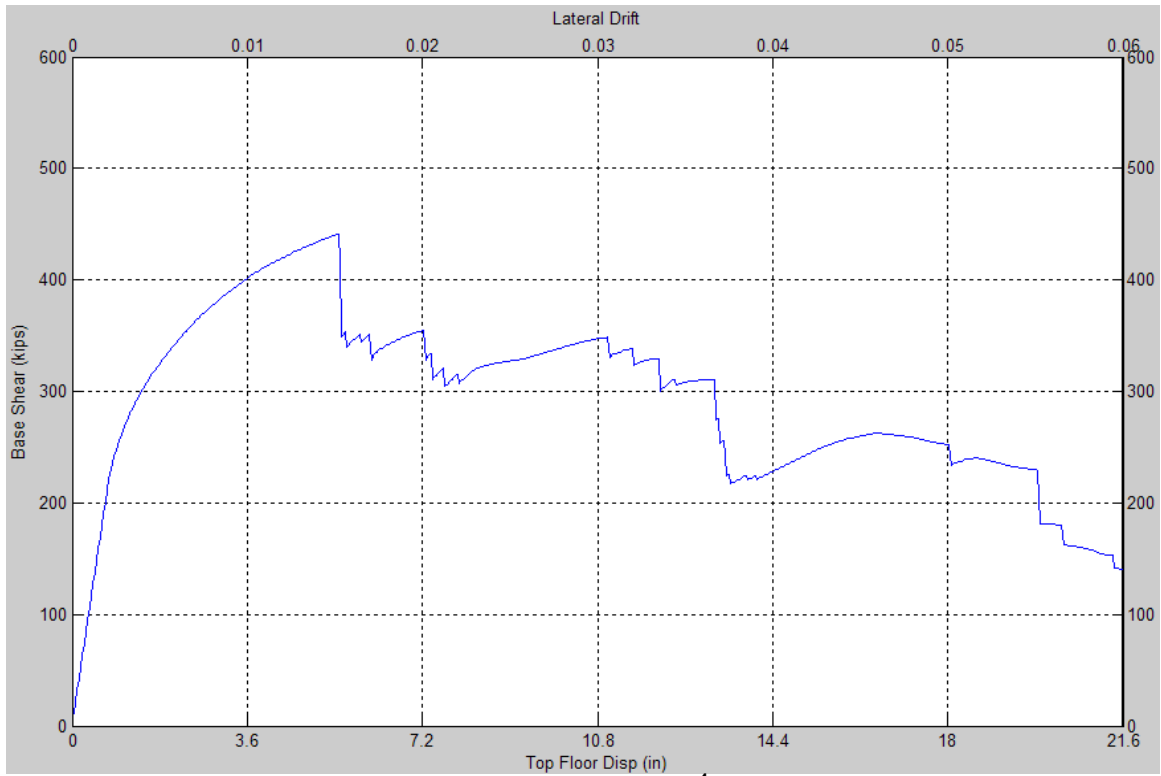
[**1121**; 50%@0.0332; 10^{-4}; 4000]
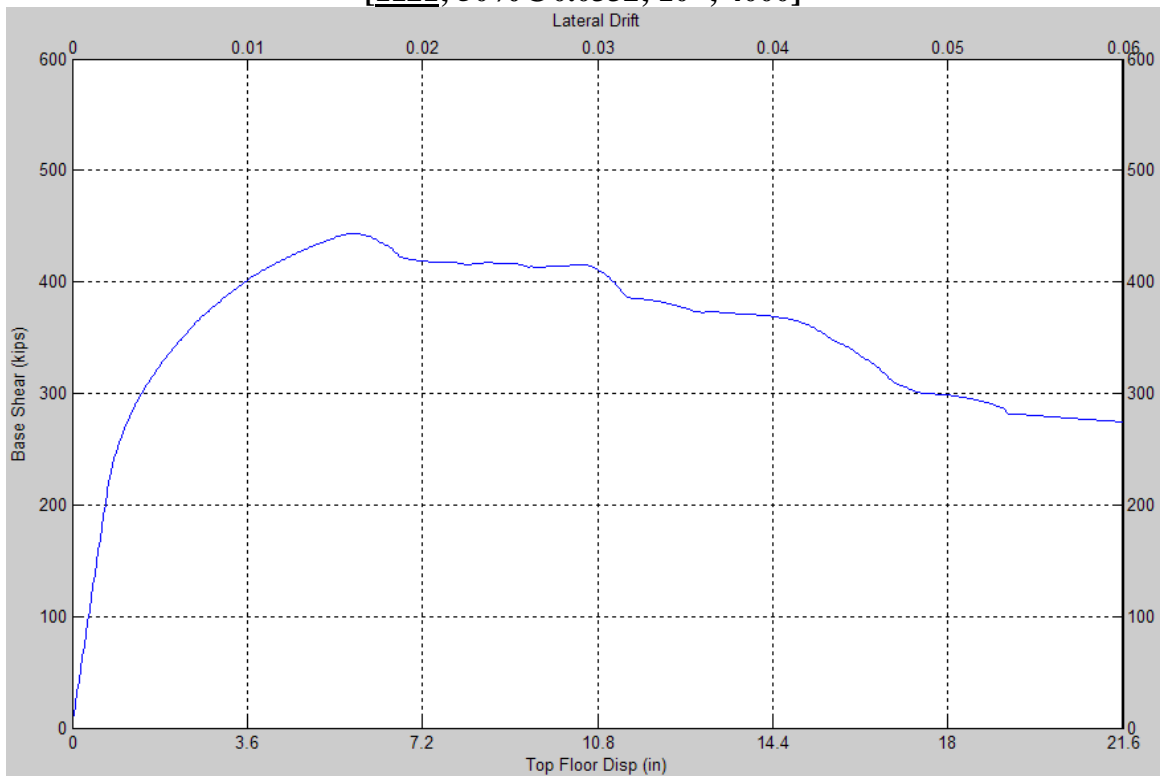
[**2111**; 50%@0.0332; 50%@15ε_y; 10^{-4}; 4000]
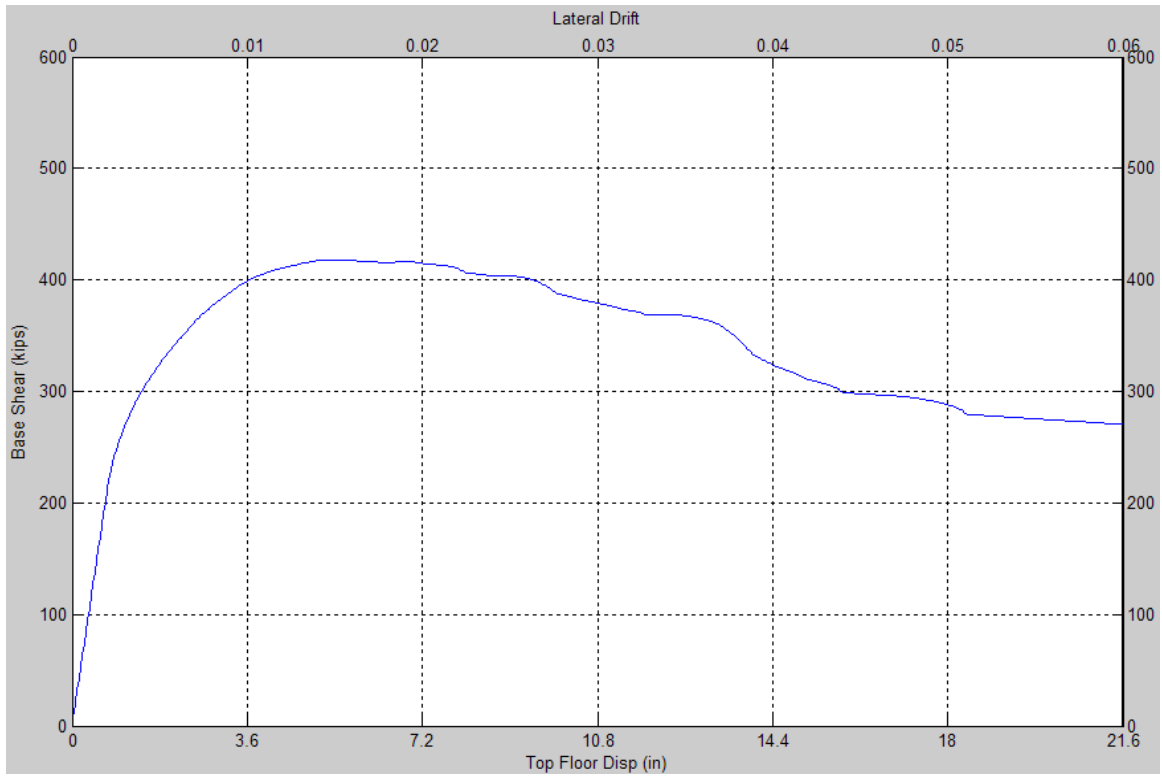
[<u>2111</u>; 50%@0.0332; 50%@11to15ε_y for middle strip; 50%@5to11ε_y for corner strip; 10^{-4}; 4000]
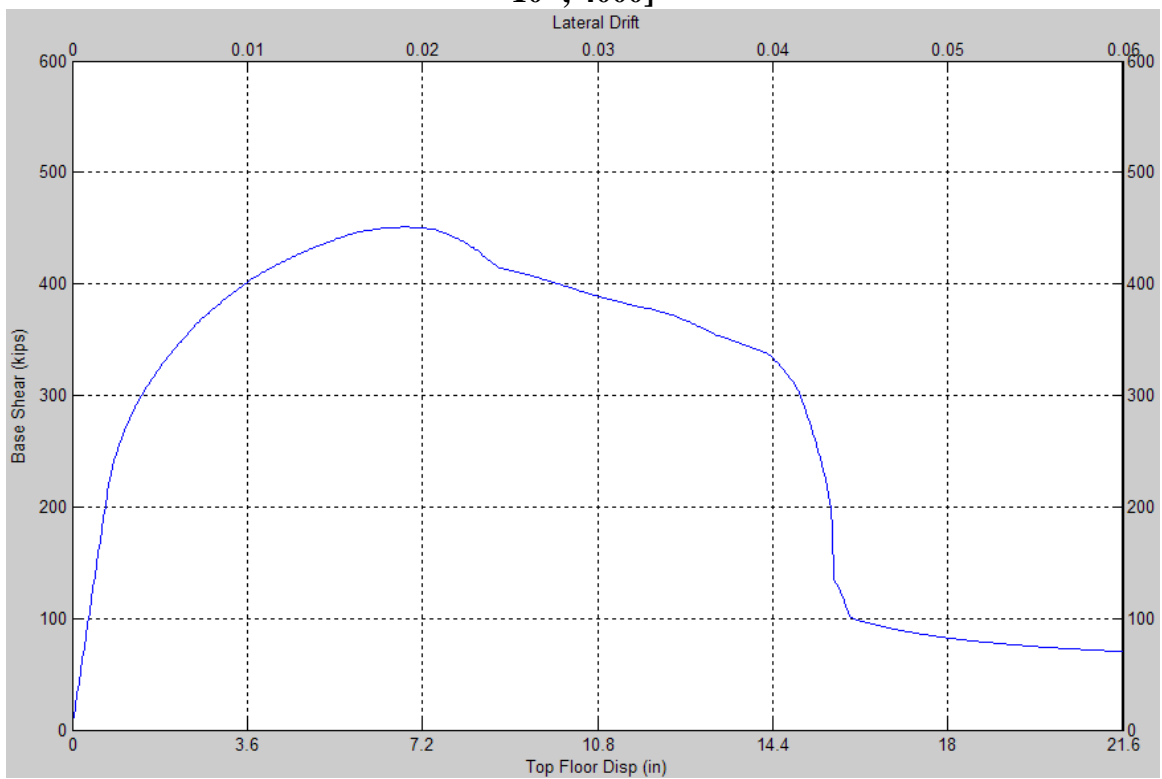
[<u>2111</u>; 90%@<u>0.0444</u>; 90%@29ε_y; 10^{-4}; 4000]
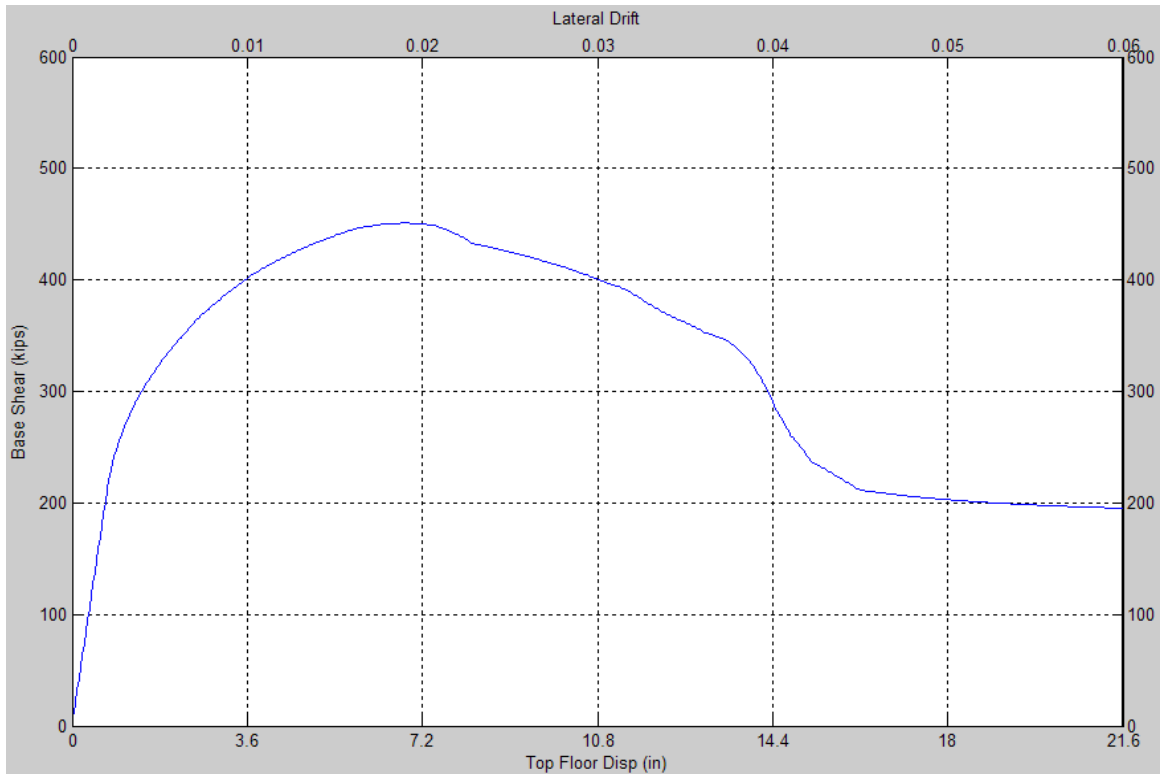
[<u>2111</u>; 50%@0.0332; 90%@29ε$_y$; 10^{-4}; 4000]
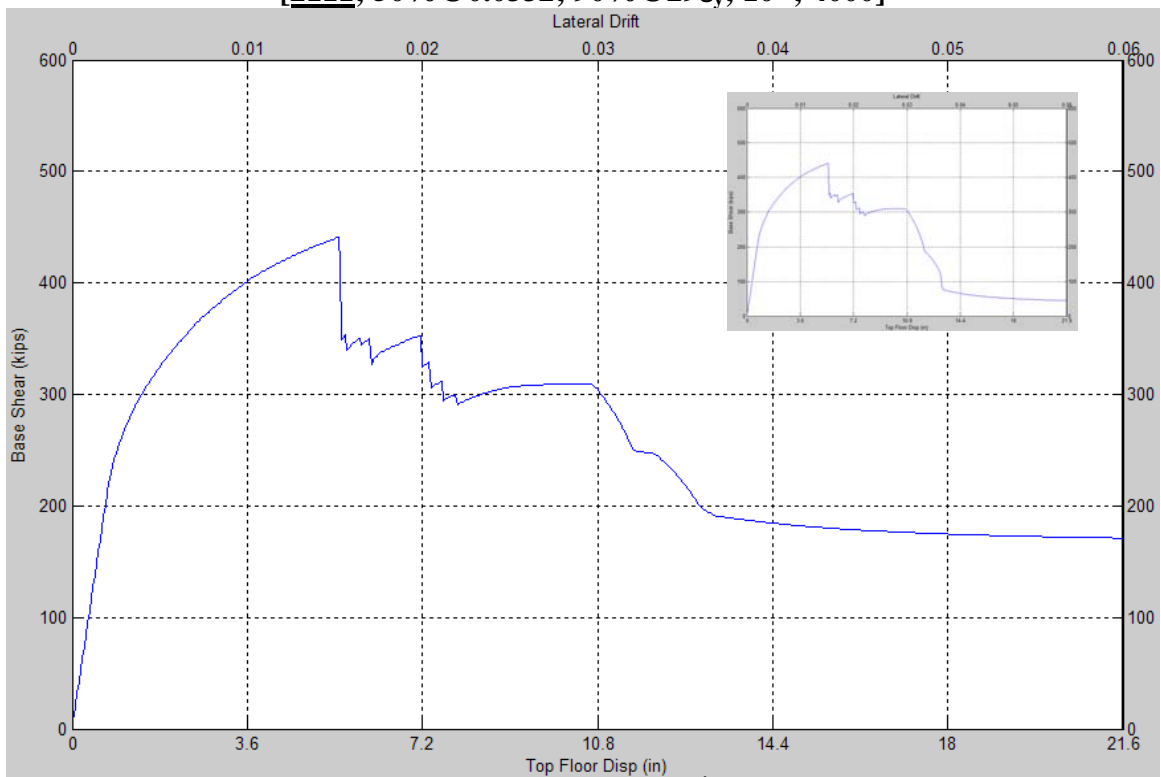
[<u>2121</u>; 50%@0.0332; 10^{-4}; 4000]

498

B.4 Summary of PEER NGA Database Information for Far-Field Record Set

Ground motion records used in the nonlinear dynamic analyses for collapse assessment consist of 22 ground motion record pairs (44 individual components) of large magnitude (M > 6.5) from sites located at distances greater than or equal to 10 km from fault rupture (i.e., "Far-Field" record set), made available in the Pacific Earthquake Engineering Research Center (PEER) Next Generation Attenuation (NGA) database (PEER 2005). A summary of the far-field record sets specified in the FEMA P695 procedure is presented in the following Table B-1.

Table B-1. Summary of Far-Field Ground Motion Records (FEMA P695)

ID No.	PEER-NGA Record Information				Recorded Motions	
	Record Seq. No.	Lowest Freq (Hz.)	File Names - Horizontal Records		PGA_{max} (g)	PGV_{max} (cm/s.)
			Component 1	Component 2		
1	953	0.25	NORTHR/MUL009	NORTHR/MUL279	0.52	63
2	960	0.13	NORTHR/LOS000	NORTHR/LOS270	0.48	45
3	1602	0.06	DUZCE/BOL000	DUZCE/BOL090	0.82	62
4	1787	0.04	HECTOR/HEC000	HECTOR/HEC090	0.34	42
5	169	0.06	IMPVALL/H-DLT262	IMPVALL/H-DLT352	0.35	33
6	174	0.25	IMPVALL/H-E11140	IMPVALL/H-E11230	0.38	42
7	1111	0.13	KOBE/NIS000	KOBE/NIS090	0.51	37
8	1116	0.13	KOBE/SHI000	KOBE/SHI090	0.24	38
9	1158	0.24	KOCAELI/DZC180	KOCAELI/DZC270	0.36	59
10	1148	0.09	KOCAELI/ARC000	KOCAELI/ARC090	0.22	40
11	900	0.07	LANDERS/YER270	LANDERS/YER360	0.24	52
12	848	0.13	LANDERS/CLW-LN	LANDERS/CLW-TR	0.42	42
13	752	0.13	LOMAP/CAP000	LOMAP/CAP090	0.53	35
14	767	0.13	LOMAP/G03000	LOMAP/G03090	0.56	45
15	1633	0.13	MANJIL/ABBAR--L	MANJIL/ABBAR--T	0.51	54
16	721	0.13	SUPERST/B-ICC000	SUPERST/B-ICC090	0.36	46
17	725	0.25	SUPERST/B-POE270	SUPERST/B-POE360	0.45	36
18	829	0.07	CAPEMEND/RIO270	CAPEMEND/RIO360	0.55	44
19	1244	0.05	CHICHI/CHY101-E	CHICHI/CHY101-N	0.44	115
20	1485	0.05	CHICHI/TCU045-E	CHICHI/TCU045-N	0.51	39
21	68	0.25	SFERN/PEL090	SFERN/PEL180	0.21	19
22	125	0.13	FRIULI/A-TMZ000	FRIULI/A-TMZ270	0.35	31

Table B-1. Summary of Far-Field Ground Motion Records, Cont'd

ID No.	Site Data		Source (Fault Type)	Site-Source Distance (km)			
	NEHRP Class	Vs_30 (m/sec)		Epicentral	Closest to Plane	Campbell	Joyner-Boore
1	D	356	Thrust	13.3	17.2	17.2	9.4
2	D	309	Thrust	26.5	12.4	12.4	11.4
3	D	326	Strike-slip	41.3	12	12.4	12
4	C	685	Strike-slip	26.5	11.7	12	10.4
5	D	275	Strike-slip	33.7	22	22.5	22
6	D	196	Strike-slip	29.4	12.5	13.5	12.5
7	C	609	Strike-slip	8.7	7.1	25.2	7.1
8	D	256	Strike-slip	46	19.2	28.5	19.1
9	D	276	Strike-slip	98.2	15.4	15.4	13.6
10	C	523	Strike-slip	53.7	13.5	13.5	10.6
11	D	354	Strike-slip	86	23.6	23.8	23.6
12	D	271	Strike-slip	82.1	19.7	20	19.7
13	D	289	Strike-slip	9.8	15.2	35.5	8.7
14	D	350	Strike-slip	31.4	12.8	12.8	12.2
15	C	724	Strike-slip	40.4	12.6	13	12.6
16	D	192	Strike-slip	35.8	18.2	18.5	18.2
17	D	208	Strike-slip	11.2	11.2	11.7	11.2
18	D	312	Thrust	22.7	14.3	14.3	7.9
19	D	259	Thrust	32	10	15.5	10
20	C	705	Thrust	77.5	26	26.8	26
21	D	316	Thrust	39.5	22.8	25.9	22.8
22	C	425	Thrust	20.2	15.8	15.8	15

MCEER Technical Reports

MCEER publishes technical reports on a variety of subjects written by authors funded through MCEER. These reports are available from both MCEER Publications and the National Technical Information Service (NTIS). Requests for reports should be directed to MCEER Publications, MCEER, University at Buffalo, State University of New York, 133A Ketter Hall, Buffalo, New York 14260. Reports can also be requested through NTIS, P.O. Box 1425, Springfield, Virginia 22151. NTIS accession numbers are shown in parenthesis, if available.

NCEER-87-0001   "First-Year Program in Research, Education and Technology Transfer," 3/5/87, (PB88-134275, A04, MF-A01).

NCEER-87-0002   "Experimental Evaluation of Instantaneous Optimal Algorithms for Structural Control," by R.C. Lin, T.T. Soong and A.M. Reinhorn, 4/20/87, (PB88-134341, A04, MF-A01).

NCEER-87-0003   "Experimentation Using the Earthquake Simulation Facilities at University at Buffalo," by A.M. Reinhorn and R.L. Ketter, not available.

NCEER-87-0004   "The System Characteristics and Performance of a Shaking Table," by J.S. Hwang, K.C. Chang and G.C. Lee, 6/1/87, (PB88-134259, A03, MF-A01). This report is available only through NTIS (see address given above).

NCEER-87-0005   "A Finite Element Formulation for Nonlinear Viscoplastic Material Using a Q Model," by O. Gyebi and G. Dasgupta, 11/2/87, (PB88-213764, A08, MF-A01).

NCEER-87-0006   "Symbolic Manipulation Program (SMP) - Algebraic Codes for Two and Three Dimensional Finite Element Formulations," by X. Lee and G. Dasgupta, 11/9/87, (PB88-218522, A05, MF-A01).

NCEER-87-0007   "Instantaneous Optimal Control Laws for Tall Buildings Under Seismic Excitations," by J.N. Yang, A. Akbarpour and P. Ghaemmaghami, 6/10/87, (PB88-134333, A06, MF-A01). This report is only available through NTIS (see address given above).

NCEER-87-0008   "IDARC: Inelastic Damage Analysis of Reinforced Concrete Frame - Shear-Wall Structures," by Y.J. Park, A.M. Reinhorn and S.K. Kunnath, 7/20/87, (PB88-134325, A09, MF-A01). This report is only available through NTIS (see address given above).

NCEER-87-0009   "Liquefaction Potential for New York State: A Preliminary Report on Sites in Manhattan and Buffalo," by M. Budhu, V. Vijayakumar, R.F. Giese and L. Baumgras, 8/31/87, (PB88-163704, A03, MF-A01). This report is available only through NTIS (see address given above).

NCEER-87-0010   "Vertical and Torsional Vibration of Foundations in Inhomogeneous Media," by A.S. Veletsos and K.W. Dotson, 6/1/87, (PB88-134291, A03, MF-A01). This report is only available through NTIS (see address given above).

NCEER-87-0011   "Seismic Probabilistic Risk Assessment and Seismic Margins Studies for Nuclear Power Plants," by Howard H.M. Hwang, 6/15/87, (PB88-134267, A03, MF-A01). This report is only available through NTIS (see address given above).

NCEER-87-0012   "Parametric Studies of Frequency Response of Secondary Systems Under Ground-Acceleration Excitations," by Y. Yong and Y.K. Lin, 6/10/87, (PB88-134309, A03, MF-A01). This report is only available through NTIS (see address given above).

NCEER-87-0013   "Frequency Response of Secondary Systems Under Seismic Excitation," by J.A. HoLung, J. Cai and Y.K. Lin, 7/31/87, (PB88-134317, A05, MF-A01). This report is only available through NTIS (see address given above).

NCEER-87-0014   "Modelling Earthquake Ground Motions in Seismically Active Regions Using Parametric Time Series Methods," by G.W. Ellis and A.S. Cakmak, 8/25/87, (PB88-134283, A08, MF-A01). This report is only available through NTIS (see address given above).

NCEER-87-0015   "Detection and Assessment of Seismic Structural Damage," by E. DiPasquale and A.S. Cakmak, 8/25/87, (PB88-163712, A05, MF-A01). This report is only available through NTIS (see address given above).

NCEER-87-0016   "Pipeline Experiment at Parkfield, California," by J. Isenberg and E. Richardson, 9/15/87, (PB88-163720, A03, MF-A01). This report is available only through NTIS (see address given above).

NCEER-87-0017   "Digital Simulation of Seismic Ground Motion," by M. Shinozuka, G. Deodatis and T. Harada, 8/31/87, (PB88-155197, A04, MF-A01). This report is available only through NTIS (see address given above).

NCEER-87-0018   "Practical Considerations for Structural Control: System Uncertainty, System Time Delay and Truncation of Small Control Forces," J.N. Yang and A. Akbarpour, 8/10/87, (PB88-163738, A08, MF-A01). This report is only available through NTIS (see address given above).

NCEER-87-0019   "Modal Analysis of Nonclassically Damped Structural Systems Using Canonical Transformation," by J.N. Yang, S. Sarkani and F.X. Long, 9/27/87, (PB88-187851, A04, MF-A01).

NCEER-87-0020   "A Nonstationary Solution in Random Vibration Theory," by J.R. Red-Horse and P.D. Spanos, 11/3/87, (PB88-163746, A03, MF-A01).

NCEER-87-0021   "Horizontal Impedances for Radially Inhomogeneous Viscoelastic Soil Layers," by A.S. Veletsos and K.W. Dotson, 10/15/87, (PB88-150859, A04, MF-A01).

NCEER-87-0022   "Seismic Damage Assessment of Reinforced Concrete Members," by Y.S. Chung, C. Meyer and M. Shinozuka, 10/9/87, (PB88-150867, A05, MF-A01). This report is available only through NTIS (see address given above).

NCEER-87-0023   "Active Structural Control in Civil Engineering," by T.T. Soong, 11/11/87, (PB88-187778, A03, MF-A01).

NCEER-87-0024   "Vertical and Torsional Impedances for Radially Inhomogeneous Viscoelastic Soil Layers," by K.W. Dotson and A.S. Veletsos, 12/87, (PB88-187786, A03, MF-A01).

NCEER-87-0025   "Proceedings from the Symposium on Seismic Hazards, Ground Motions, Soil-Liquefaction and Engineering Practice in Eastern North America," October 20-22, 1987, edited by K.H. Jacob, 12/87, (PB88-188115, A23, MF-A01). This report is available only through NTIS (see address given above).

NCEER-87-0026   "Report on the Whittier-Narrows, California, Earthquake of October 1, 1987," by J. Pantelic and A. Reinhorn, 11/87, (PB88-187752, A03, MF-A01). This report is available only through NTIS (see address given above).

NCEER-87-0027   "Design of a Modular Program for Transient Nonlinear Analysis of Large 3-D Building Structures," by S. Srivastav and J.F. Abel, 12/30/87, (PB88-187950, A05, MF-A01). This report is only available through NTIS (see address given above).

NCEER-87-0028   "Second-Year Program in Research, Education and Technology Transfer," 3/8/88, (PB88-219480, A04, MF-A01).

NCEER-88-0001   "Workshop on Seismic Computer Analysis and Design of Buildings With Interactive Graphics," by W. McGuire, J.F. Abel and C.H. Conley, 1/18/88, (PB88-187760, A03, MF-A01). This report is only available through NTIS (see address given above).

NCEER-88-0002   "Optimal Control of Nonlinear Flexible Structures," by J.N. Yang, F.X. Long and D. Wong, 1/22/88, (PB88-213772, A06, MF-A01).

NCEER-88-0003   "Substructuring Techniques in the Time Domain for Primary-Secondary Structural Systems," by G.D. Manolis and G. Juhn, 2/10/88, (PB88-213780, A04, MF-A01).

NCEER-88-0004   "Iterative Seismic Analysis of Primary-Secondary Systems," by A. Singhal, L.D. Lutes and P.D. Spanos, 2/23/88, (PB88-213798, A04, MF-A01).

NCEER-88-0005   "Stochastic Finite Element Expansion for Random Media," by P.D. Spanos and R. Ghanem, 3/14/88, (PB88-213806, A03, MF-A01).

NCEER-88-0006   "Combining Structural Optimization and Structural Control," by F.Y. Cheng and C.P. Pantelides, 1/10/88, (PB88-213814, A05, MF-A01).

NCEER-88-0007   "Seismic Performance Assessment of Code-Designed Structures," by H.H-M. Hwang, J-W. Jaw and H-J. Shau, 3/20/88, (PB88-219423, A04, MF-A01). This report is only available through NTIS (see address given above).

NCEER-88-0008   "Reliability Analysis of Code-Designed Structures Under Natural Hazards," by H.H-M. Hwang, H. Ushiba and M. Shinozuka, 2/29/88, (PB88-229471, A07, MF-A01). This report is only available through NTIS (see address given above).

NCEER-88-0009   "Seismic Fragility Analysis of Shear Wall Structures," by J-W Jaw and H.H-M. Hwang, 4/30/88, (PB89-102867, A04, MF-A01).

NCEER-88-0010   "Base Isolation of a Multi-Story Building Under a Harmonic Ground Motion - A Comparison of Performances of Various Systems," by F-G Fan, G. Ahmadi and I.G. Tadjbakhsh, 5/18/88, (PB89-122238, A06, MF-A01). This report is only available through NTIS (see address given above).

NCEER-88-0011   "Seismic Floor Response Spectra for a Combined System by Green's Functions," by F.M. Lavelle, L.A. Bergman and P.D. Spanos, 5/1/88, (PB89-102875, A03, MF-A01).

NCEER-88-0012   "A New Solution Technique for Randomly Excited Hysteretic Structures," by G.Q. Cai and Y.K. Lin, 5/16/88, (PB89-102883, A03, MF-A01).

NCEER-88-0013   "A Study of Radiation Damping and Soil-Structure Interaction Effects in the Centrifuge," by K. Weissman, supervised by J.H. Prevost, 5/24/88, (PB89-144703, A06, MF-A01).

NCEER-88-0014   "Parameter Identification and Implementation of a Kinematic Plasticity Model for Frictional Soils," by J.H. Prevost and D.V. Griffiths, not available.

NCEER-88-0015   "Two- and Three- Dimensional Dynamic Finite Element Analyses of the Long Valley Dam," by D.V. Griffiths and J.H. Prevost, 6/17/88, (PB89-144711, A04, MF-A01).

NCEER-88-0016   "Damage Assessment of Reinforced Concrete Structures in Eastern United States," by A.M. Reinhorn, M.J. Seidel, S.K. Kunnath and Y.J. Park, 6/15/88, (PB89-122220, A04, MF-A01). This report is only available through NTIS (see address given above).

NCEER-88-0017   "Dynamic Compliance of Vertically Loaded Strip Foundations in Multilayered Viscoelastic Soils," by S. Ahmad and A.S.M. Israil, 6/17/88, (PB89-102891, A04, MF-A01).

NCEER-88-0018   "An Experimental Study of Seismic Structural Response With Added Viscoelastic Dampers," by R.C. Lin, Z. Liang, T.T. Soong and R.H. Zhang, 6/30/88, (PB89-122212, A05, MF-A01). This report is available only through NTIS (see address given above).

NCEER-88-0019   "Experimental Investigation of Primary - Secondary System Interaction," by G.D. Manolis, G. Juhn and A.M. Reinhorn, 5/27/88, (PB89-122204, A04, MF-A01).

NCEER-88-0020   "A Response Spectrum Approach For Analysis of Nonclassically Damped Structures," by J.N. Yang, S. Sarkani and F.X. Long, 4/22/88, (PB89-102909, A04, MF-A01).

NCEER-88-0021   "Seismic Interaction of Structures and Soils: Stochastic Approach," by A.S. Veletsos and A.M. Prasad, 7/21/88, (PB89-122196, A04, MF-A01). This report is only available through NTIS (see address given above).

NCEER-88-0022   "Identification of the Serviceability Limit State and Detection of Seismic Structural Damage," by E. DiPasquale and A.S. Cakmak, 6/15/88, (PB89-122188, A05, MF-A01). This report is available only through NTIS (see address given above).

NCEER-88-0023   "Multi-Hazard Risk Analysis: Case of a Simple Offshore Structure," by B.K. Bhartia and E.H. Vanmarcke, 7/21/88, (PB89-145213, A05, MF-A01).

NCEER-88-0024   "Automated Seismic Design of Reinforced Concrete Buildings," by Y.S. Chung, C. Meyer and M. Shinozuka, 7/5/88, (PB89-122170, A06, MF-A01). This report is available only through NTIS (see address given above).

NCEER-88-0025   "Experimental Study of Active Control of MDOF Structures Under Seismic Excitations," by L.L. Chung, R.C. Lin, T.T. Soong and A.M. Reinhorn, 7/10/88, (PB89-122600, A04, MF-A01).

NCEER-88-0026   "Earthquake Simulation Tests of a Low-Rise Metal Structure," by J.S. Hwang, K.C. Chang, G.C. Lee and R.L. Ketter, 8/1/88, (PB89-102917, A04, MF-A01).

NCEER-88-0027   "Systems Study of Urban Response and Reconstruction Due to Catastrophic Earthquakes," by F. Kozin and H.K. Zhou, 9/22/88, (PB90-162348, A04, MF-A01).

NCEER-88-0028   "Seismic Fragility Analysis of Plane Frame Structures," by H.H-M. Hwang and Y.K. Low, 7/31/88, (PB89-131445, A06, MF-A01).

NCEER-88-0029   "Response Analysis of Stochastic Structures," by A. Kardara, C. Bucher and M. Shinozuka, 9/22/88, (PB89-174429, A04, MF-A01).

NCEER-88-0030   "Nonnormal Accelerations Due to Yielding in a Primary Structure," by D.C.K. Chen and L.D. Lutes, 9/19/88, (PB89-131437, A04, MF-A01).

NCEER-88-0031   "Design Approaches for Soil-Structure Interaction," by A.S. Veletsos, A.M. Prasad and Y. Tang, 12/30/88, (PB89-174437, A03, MF-A01). This report is available only through NTIS (see address given above).

NCEER-88-0032   "A Re-evaluation of Design Spectra for Seismic Damage Control," by C.J. Turkstra and A.G. Tallin, 11/7/88, (PB89-145221, A05, MF-A01).

NCEER-88-0033   "The Behavior and Design of Noncontact Lap Splices Subjected to Repeated Inelastic Tensile Loading," by V.E. Sagan, P. Gergely and R.N. White, 12/8/88, (PB89-163737, A08, MF-A01).

NCEER-88-0034   "Seismic Response of Pile Foundations," by S.M. Mamoon, P.K. Banerjee and S. Ahmad, 11/1/88, (PB89-145239, A04, MF-A01).

NCEER-88-0035   "Modeling of R/C Building Structures With Flexible Floor Diaphragms (IDARC2)," by A.M. Reinhorn, S.K. Kunnath and N. Panahshahi, 9/7/88, (PB89-207153, A07, MF-A01).

NCEER-88-0036   "Solution of the Dam-Reservoir Interaction Problem Using a Combination of FEM, BEM with Particular Integrals, Modal Analysis, and Substructuring," by C-S. Tsai, G.C. Lee and R.L. Ketter, 12/31/88, (PB89-207146, A04, MF-A01).

NCEER-88-0037   "Optimal Placement of Actuators for Structural Control," by F.Y. Cheng and C.P. Pantelides, 8/15/88, (PB89-162846, A05, MF-A01).

NCEER-88-0038   "Teflon Bearings in Aseismic Base Isolation: Experimental Studies and Mathematical Modeling," by A. Mokha, M.C. Constantinou and A.M. Reinhorn, 12/5/88, (PB89-218457, A10, MF-A01). This report is available only through NTIS (see address given above).

NCEER-88-0039   "Seismic Behavior of Flat Slab High-Rise Buildings in the New York City Area," by P. Weidlinger and M. Ettouney, 10/15/88, (PB90-145681, A04, MF-A01).

NCEER-88-0040   "Evaluation of the Earthquake Resistance of Existing Buildings in New York City," by P. Weidlinger and M. Ettouney, 10/15/88, not available.

NCEER-88-0041   "Small-Scale Modeling Techniques for Reinforced Concrete Structures Subjected to Seismic Loads," by W. Kim, A. El-Attar and R.N. White, 11/22/88, (PB89-189625, A05, MF-A01).

NCEER-88-0042   "Modeling Strong Ground Motion from Multiple Event Earthquakes," by G.W. Ellis and A.S. Cakmak, 10/15/88, (PB89-174445, A03, MF-A01).

NCEER-88-0043   "Nonstationary Models of Seismic Ground Acceleration," by M. Grigoriu, S.E. Ruiz and E. Rosenblueth, 7/15/88, (PB89-189617, A04, MF-A01).

NCEER-88-0044   "SARCF User's Guide: Seismic Analysis of Reinforced Concrete Frames," by Y.S. Chung, C. Meyer and M. Shinozuka, 11/9/88, (PB89-174452, A08, MF-A01).

NCEER-88-0045   "First Expert Panel Meeting on Disaster Research and Planning," edited by J. Pantelic and J. Stoyle, 9/15/88, (PB89-174460, A05, MF-A01).

NCEER-88-0046   "Preliminary Studies of the Effect of Degrading Infill Walls on the Nonlinear Seismic Response of Steel Frames," by C.Z. Chrysostomou, P. Gergely and J.F. Abel, 12/19/88, (PB89-208383, A05, MF-A01).

NCEER-88-0047   "Reinforced Concrete Frame Component Testing Facility - Design, Construction, Instrumentation and Operation," by S.P. Pessiki, C. Conley, T. Bond, P. Gergely and R.N. White, 12/16/88, (PB89-174478, A04, MF-A01).

NCEER-89-0001   "Effects of Protective Cushion and Soil Compliancy on the Response of Equipment Within a Seismically Excited Building," by J.A. HoLung, 2/16/89, (PB89-207179, A04, MF-A01).

NCEER-89-0002   "Statistical Evaluation of Response Modification Factors for Reinforced Concrete Structures," by H.H-M. Hwang and J-W. Jaw, 2/17/89, (PB89-207187, A05, MF-A01).

NCEER-89-0003   "Hysteretic Columns Under Random Excitation," by G-Q. Cai and Y.K. Lin, 1/9/89, (PB89-196513, A03, MF-A01).

NCEER-89-0004   "Experimental Study of `Elephant Foot Bulge' Instability of Thin-Walled Metal Tanks," by Z-H. Jia and R.L. Ketter, 2/22/89, (PB89-207195, A03, MF-A01).

NCEER-89-0005   "Experiment on Performance of Buried Pipelines Across San Andreas Fault," by J. Isenberg, E. Richardson and T.D. O'Rourke, 3/10/89, (PB89-218440, A04, MF-A01). This report is available only through NTIS (see address given above).

NCEER-89-0006   "A Knowledge-Based Approach to Structural Design of Earthquake-Resistant Buildings," by M. Subramani, P. Gergely, C.H. Conley, J.F. Abel and A.H. Zaghw, 1/15/89, (PB89-218465, A06, MF-A01).

NCEER-89-0007   "Liquefaction Hazards and Their Effects on Buried Pipelines," by T.D. O'Rourke and P.A. Lane, 2/1/89, (PB89-218481, A09, MF-A01).

NCEER-89-0008   "Fundamentals of System Identification in Structural Dynamics," by H. Imai, C-B. Yun, O. Maruyama and M. Shinozuka, 1/26/89, (PB89-207211, A04, MF-A01).

NCEER-89-0009   "Effects of the 1985 Michoacan Earthquake on Water Systems and Other Buried Lifelines in Mexico," by A.G. Ayala and M.J. O'Rourke, 3/8/89, (PB89-207229, A06, MF-A01).

NCEER-89-R010   "NCEER Bibliography of Earthquake Education Materials," by K.E.K. Ross, Second Revision, 9/1/89, (PB90-125352, A05, MF-A01). This report is replaced by NCEER-92-0018.

NCEER-89-0011   "Inelastic Three-Dimensional Response Analysis of Reinforced Concrete Building Structures (IDARC-3D), Part I - Modeling," by S.K. Kunnath and A.M. Reinhorn, 4/17/89, (PB90-114612, A07, MF-A01). This report is available only through NTIS (see address given above).

NCEER-89-0012   "Recommended Modifications to ATC-14," by C.D. Poland and J.O. Malley, 4/12/89, (PB90-108648, A15, MF-A01).

NCEER-89-0013   "Repair and Strengthening of Beam-to-Column Connections Subjected to Earthquake Loading," by M. Corazao and A.J. Durrani, 2/28/89, (PB90-109885, A06, MF-A01).

NCEER-89-0014   "Program EXKAL2 for Identification of Structural Dynamic Systems," by O. Maruyama, C-B. Yun, M. Hoshiya and M. Shinozuka, 5/19/89, (PB90-109877, A09, MF-A01).

NCEER-89-0015   "Response of Frames With Bolted Semi-Rigid Connections, Part I - Experimental Study and Analytical Predictions," by P.J. DiCorso, A.M. Reinhorn, J.R. Dickerson, J.B. Radziminski and W.L. Harper, 6/1/89, not available.

NCEER-89-0016   "ARMA Monte Carlo Simulation in Probabilistic Structural Analysis," by P.D. Spanos and M.P. Mignolet, 7/10/89, (PB90-109893, A03, MF-A01).

NCEER-89-P017   "Preliminary Proceedings from the Conference on Disaster Preparedness - The Place of Earthquake Education in Our Schools," Edited by K.E.K. Ross, 6/23/89, (PB90-108606, A03, MF-A01).

NCEER-89-0017   "Proceedings from the Conference on Disaster Preparedness - The Place of Earthquake Education in Our Schools," Edited by K.E.K. Ross, 12/31/89, (PB90-207895, A012, MF-A02). This report is available only through NTIS (see address given above).

NCEER-89-0018   "Multidimensional Models of Hysteretic Material Behavior for Vibration Analysis of Shape Memory Energy Absorbing Devices, by E.J. Graesser and F.A. Cozzarelli, 6/7/89, (PB90-164146, A04, MF-A01).

NCEER-89-0019   "Nonlinear Dynamic Analysis of Three-Dimensional Base Isolated Structures (3D-BASIS)," by S. Nagarajaiah, A.M. Reinhorn and M.C. Constantinou, 8/3/89, (PB90-161936, A06, MF-A01). This report has been replaced by NCEER-93-0011.

NCEER-89-0020   "Structural Control Considering Time-Rate of Control Forces and Control Rate Constraints," by F.Y. Cheng and C.P. Pantelides, 8/3/89, (PB90-120445, A04, MF-A01).

NCEER-89-0021   "Subsurface Conditions of Memphis and Shelby County," by K.W. Ng, T-S. Chang and H-H.M. Hwang, 7/26/89, (PB90-120437, A03, MF-A01).

NCEER-89-0022   "Seismic Wave Propagation Effects on Straight Jointed Buried Pipelines," by K. Elhmadi and M.J. O'Rourke, 8/24/89, (PB90-162322, A10, MF-A02).

NCEER-89-0023   "Workshop on Serviceability Analysis of Water Delivery Systems," edited by M. Grigoriu, 3/6/89, (PB90-127424, A03, MF-A01).

NCEER-89-0024   "Shaking Table Study of a 1/5 Scale Steel Frame Composed of Tapered Members," by K.C. Chang, J.S. Hwang and G.C. Lee, 9/18/89, (PB90-160169, A04, MF-A01).

NCEER-89-0025   "DYNA1D: A Computer Program for Nonlinear Seismic Site Response Analysis - Technical Documentation," by Jean H. Prevost, 9/14/89, (PB90-161944, A07, MF-A01). This report is available only through NTIS (see address given above).

NCEER-89-0026   "1:4 Scale Model Studies of Active Tendon Systems and Active Mass Dampers for Aseismic Protection," by A.M. Reinhorn, T.T. Soong, R.C. Lin, Y.P. Yang, Y. Fukao, H. Abe and M. Nakai, 9/15/89, (PB90-173246, A10, MF-A02). This report is available only through NTIS (see address given above).

NCEER-89-0027   "Scattering of Waves by Inclusions in a Nonhomogeneous Elastic Half Space Solved by Boundary Element Methods," by P.K. Hadley, A. Askar and A.S. Cakmak, 6/15/89, (PB90-145699, A07, MF-A01).

NCEER-89-0028   "Statistical Evaluation of Deflection Amplification Factors for Reinforced Concrete Structures," by H.H.M. Hwang, J-W. Jaw and A.L. Ch'ng, 8/31/89, (PB90-164633, A05, MF-A01).

NCEER-89-0029   "Bedrock Accelerations in Memphis Area Due to Large New Madrid Earthquakes," by H.H.M. Hwang, C.H.S. Chen and G. Yu, 11/7/89, (PB90-162330, A04, MF-A01).

NCEER-89-0030   "Seismic Behavior and Response Sensitivity of Secondary Structural Systems," by Y.Q. Chen and T.T. Soong, 10/23/89, (PB90-164658, A08, MF-A01).

NCEER-89-0031   "Random Vibration and Reliability Analysis of Primary-Secondary Structural Systems," by Y. Ibrahim, M. Grigoriu and T.T. Soong, 11/10/89, (PB90-161951, A04, MF-A01).

NCEER-89-0032   "Proceedings from the Second U.S. - Japan Workshop on Liquefaction, Large Ground Deformation and Their Effects on Lifelines, September 26-29, 1989," Edited by T.D. O'Rourke and M. Hamada, 12/1/89, (PB90-209388, A22, MF-A03).

NCEER-89-0033   "Deterministic Model for Seismic Damage Evaluation of Reinforced Concrete Structures," by J.M. Bracci, A.M. Reinhorn, J.B. Mander and S.K. Kunnath, 9/27/89, (PB91-108803, A06, MF-A01).

NCEER-89-0034   "On the Relation Between Local and Global Damage Indices," by E. DiPasquale and A.S. Cakmak, 8/15/89, (PB90-173865, A05, MF-A01).

NCEER-89-0035   "Cyclic Undrained Behavior of Nonplastic and Low Plasticity Silts," by A.J. Walker and H.E. Stewart, 7/26/89, (PB90-183518, A10, MF-A01).

NCEER-89-0036   "Liquefaction Potential of Surficial Deposits in the City of Buffalo, New York," by M. Budhu, R. Giese and L. Baumgrass, 1/17/89, (PB90-208455, A04, MF-A01).

NCEER-89-0037   "A Deterministic Assessment of Effects of Ground Motion Incoherence," by A.S. Veletsos and Y. Tang, 7/15/89, (PB90-164294, A03, MF-A01).

NCEER-89-0038   "Workshop on Ground Motion Parameters for Seismic Hazard Mapping," July 17-18, 1989, edited by R.V. Whitman, 12/1/89, (PB90-173923, A04, MF-A01).

NCEER-89-0039   "Seismic Effects on Elevated Transit Lines of the New York City Transit Authority," by C.J. Costantino, C.A. Miller and E. Heymsfield, 12/26/89, (PB90-207887, A06, MF-A01).

NCEER-89-0040   "Centrifugal Modeling of Dynamic Soil-Structure Interaction," by K. Weissman, Supervised by J.H. Prevost, 5/10/89, (PB90-207879, A07, MF-A01).

NCEER-89-0041   "Linearized Identification of Buildings With Cores for Seismic Vulnerability Assessment," by I-K. Ho and A.E. Aktan, 11/1/89, (PB90-251943, A07, MF-A01).

NCEER-90-0001   "Geotechnical and Lifeline Aspects of the October 17, 1989 Loma Prieta Earthquake in San Francisco," by T.D. O'Rourke, H.E. Stewart, F.T. Blackburn and T.S. Dickerman, 1/90, (PB90-208596, A05, MF-A01).

NCEER-90-0002   "Nonnormal Secondary Response Due to Yielding in a Primary Structure," by D.C.K. Chen and L.D. Lutes, 2/28/90, (PB90-251976, A07, MF-A01).

NCEER-90-0003   "Earthquake Education Materials for Grades K-12," by K.E.K. Ross, 4/16/90, (PB91-251984, A05, MF-A05). This report has been replaced by NCEER-92-0018.

NCEER-90-0004   "Catalog of Strong Motion Stations in Eastern North America," by R.W. Busby, 4/3/90, (PB90-251984, A05, MF-A01).

NCEER-90-0005   "NCEER Strong-Motion Data Base: A User Manual for the GeoBase Release (Version 1.0 for the Sun3)," by P. Friberg and K. Jacob, 3/31/90 (PB90-258062, A04, MF-A01).

NCEER-90-0006   "Seismic Hazard Along a Crude Oil Pipeline in the Event of an 1811-1812 Type New Madrid Earthquake," by H.H.M. Hwang and C-H.S. Chen, 4/16/90, (PB90-258054, A04, MF-A01).

NCEER-90-0007   "Site-Specific Response Spectra for Memphis Sheahan Pumping Station," by H.H.M. Hwang and C.S. Lee, 5/15/90, (PB91-108811, A05, MF-A01).

NCEER-90-0008   "Pilot Study on Seismic Vulnerability of Crude Oil Transmission Systems," by T. Ariman, R. Dobry, M. Grigoriu, F. Kozin, M. O'Rourke, T. O'Rourke and M. Shinozuka, 5/25/90, (PB91-108837, A06, MF-A01).

NCEER-90-0009   "A Program to Generate Site Dependent Time Histories: EQGEN," by G.W. Ellis, M. Srinivasan and A.S. Cakmak, 1/30/90, (PB91-108829, A04, MF-A01).

NCEER-90-0010   "Active Isolation for Seismic Protection of Operating Rooms," by M.E. Talbott, Supervised by M. Shinozuka, 6/8/9, (PB91-110205, A05, MF-A01).

NCEER-90-0011   "Program LINEARID for Identification of Linear Structural Dynamic Systems," by C-B. Yun and M. Shinozuka, 6/25/90, (PB91-110312, A08, MF-A01).

NCEER-90-0012   "Two-Dimensional Two-Phase Elasto-Plastic Seismic Response of Earth Dams," by A.N. Yiagos, Supervised by J.H. Prevost, 6/20/90, (PB91-110197, A13, MF-A02).

NCEER-90-0013   "Secondary Systems in Base-Isolated Structures: Experimental Investigation, Stochastic Response and Stochastic Sensitivity," by G.D. Manolis, G. Juhn, M.C. Constantinou and A.M. Reinhorn, 7/1/90, (PB91-110320, A08, MF-A01).

NCEER-90-0014   "Seismic Behavior of Lightly-Reinforced Concrete Column and Beam-Column Joint Details," by S.P. Pessiki, C.H. Conley, P. Gergely and R.N. White, 8/22/90, (PB91-108795, A11, MF-A02).

NCEER-90-0015   "Two Hybrid Control Systems for Building Structures Under Strong Earthquakes," by J.N. Yang and A. Danielians, 6/29/90, (PB91-125393, A04, MF-A01).

NCEER-90-0016   "Instantaneous Optimal Control with Acceleration and Velocity Feedback," by J.N. Yang and Z. Li, 6/29/90, (PB91-125401, A03, MF-A01).

NCEER-90-0017   "Reconnaissance Report on the Northern Iran Earthquake of June 21, 1990," by M. Mehrain, 10/4/90, (PB91-125377, A03, MF-A01).

NCEER-90-0018   "Evaluation of Liquefaction Potential in Memphis and Shelby County," by T.S. Chang, P.S. Tang, C.S. Lee and H. Hwang, 8/10/90, (PB91-125427, A09, MF-A01).

NCEER-90-0019   "Experimental and Analytical Study of a Combined Sliding Disc Bearing and Helical Steel Spring Isolation System," by M.C. Constantinou, A.S. Mokha and A.M. Reinhorn, 10/4/90, (PB91-125385, A06, MF-A01). This report is available only through NTIS (see address given above).

NCEER-90-0020   "Experimental Study and Analytical Prediction of Earthquake Response of a Sliding Isolation System with a Spherical Surface," by A.S. Mokha, M.C. Constantinou and A.M. Reinhorn, 10/11/90, (PB91-125419, A05, MF-A01).

NCEER-90-0021   "Dynamic Interaction Factors for Floating Pile Groups," by G. Gazetas, K. Fan, A. Kaynia and E. Kausel, 9/10/90, (PB91-170381, A05, MF-A01).

NCEER-90-0022   "Evaluation of Seismic Damage Indices for Reinforced Concrete Structures," by S. Rodriguez-Gomez and A.S. Cakmak, 9/30/90, PB91-171322, A06, MF-A01).

NCEER-90-0023   "Study of Site Response at a Selected Memphis Site," by H. Desai, S. Ahmad, E.S. Gazetas and M.R. Oh, 10/11/90, (PB91-196857, A03, MF-A01).

NCEER-90-0024   "A User's Guide to Strongmo: Version 1.0 of NCEER's Strong-Motion Data Access Tool for PCs and Terminals," by P.A. Friberg and C.A.T. Susch, 11/15/90, (PB91-171272, A03, MF-A01).

NCEER-90-0025   "A Three-Dimensional Analytical Study of Spatial Variability of Seismic Ground Motions," by L-L. Hong and A.H.-S. Ang, 10/30/90, (PB91-170399, A09, MF-A01).

NCEER-90-0026   "MUMOID User's Guide - A Program for the Identification of Modal Parameters," by S. Rodriguez-Gomez and E. DiPasquale, 9/30/90, (PB91-171298, A04, MF-A01).

NCEER-90-0027   "SARCF-II User's Guide - Seismic Analysis of Reinforced Concrete Frames," by S. Rodriguez-Gomez, Y.S. Chung and C. Meyer, 9/30/90, (PB91-171280, A05, MF-A01).

NCEER-90-0028   "Viscous Dampers: Testing, Modeling and Application in Vibration and Seismic Isolation," by N. Makris and M.C. Constantinou, 12/20/90 (PB91-190561, A06, MF-A01).

NCEER-90-0029   "Soil Effects on Earthquake Ground Motions in the Memphis Area," by H. Hwang, C.S. Lee, K.W. Ng and T.S. Chang, 8/2/90, (PB91-190751, A05, MF-A01).

NCEER-91-0001   "Proceedings from the Third Japan-U.S. Workshop on Earthquake Resistant Design of Lifeline Facilities and Countermeasures for Soil Liquefaction, December 17-19, 1990," edited by T.D. O'Rourke and M. Hamada, 2/1/91, (PB91-179259, A99, MF-A04).

NCEER-91-0002   "Physical Space Solutions of Non-Proportionally Damped Systems," by M. Tong, Z. Liang and G.C. Lee, 1/15/91, (PB91-179242, A04, MF-A01).

NCEER-91-0003   "Seismic Response of Single Piles and Pile Groups," by K. Fan and G. Gazetas, 1/10/91, (PB92-174994, A04, MF-A01).

NCEER-91-0004   "Damping of Structures: Part 1 - Theory of Complex Damping," by Z. Liang and G. Lee, 10/10/91, (PB92-197235, A12, MF-A03).

NCEER-91-0005   "3D-BASIS - Nonlinear Dynamic Analysis of Three Dimensional Base Isolated Structures: Part II," by S. Nagarajaiah, A.M. Reinhorn and M.C. Constantinou, 2/28/91, (PB91-190553, A07, MF-A01). This report has been replaced by NCEER-93-0011.

NCEER-91-0006   "A Multidimensional Hysteretic Model for Plasticity Deforming Metals in Energy Absorbing Devices," by E.J. Graesser and F.A. Cozzarelli, 4/9/91, (PB92-108364, A04, MF-A01).

NCEER-91-0007   "A Framework for Customizable Knowledge-Based Expert Systems with an Application to a KBES for Evaluating the Seismic Resistance of Existing Buildings," by E.G. Ibarra-Anaya and S.J. Fenves, 4/9/91, (PB91-210930, A08, MF-A01).

NCEER-91-0008   "Nonlinear Analysis of Steel Frames with Semi-Rigid Connections Using the Capacity Spectrum Method," by G.G. Deierlein, S-H. Hsieh, Y-J. Shen and J.F. Abel, 7/2/91, (PB92-113828, A05, MF-A01).

NCEER-91-0009   "Earthquake Education Materials for Grades K-12," by K.E.K. Ross, 4/30/91, (PB91-212142, A06, MF-A01). This report has been replaced by NCEER-92-0018.

NCEER-91-0010   "Phase Wave Velocities and Displacement Phase Differences in a Harmonically Oscillating Pile," by N. Makris and G. Gazetas, 7/8/91, (PB92-108356, A04, MF-A01).

NCEER-91-0011   "Dynamic Characteristics of a Full-Size Five-Story Steel Structure and a 2/5 Scale Model," by K.C. Chang, G.C. Yao, G.C. Lee, D.S. Hao and Y.C. Yeh," 7/2/91, (PB93-116648, A06, MF-A02).

NCEER-91-0012   "Seismic Response of a 2/5 Scale Steel Structure with Added Viscoelastic Dampers," by K.C. Chang, T.T. Soong, S-T. Oh and M.L. Lai, 5/17/91, (PB92-110816, A05, MF-A01).

NCEER-91-0013   "Earthquake Response of Retaining Walls; Full-Scale Testing and Computational Modeling," by S. Alampalli and A-W.M. Elgamal, 6/20/91, not available.

NCEER-91-0014   "3D-BASIS-M: Nonlinear Dynamic Analysis of Multiple Building Base Isolated Structures," by P.C. Tsopelas, S. Nagarajaiah, M.C. Constantinou and A.M. Reinhorn, 5/28/91, (PB92-113885, A09, MF-A02).

NCEER-91-0015   "Evaluation of SEAOC Design Requirements for Sliding Isolated Structures," by D. Theodossiou and M.C. Constantinou, 6/10/91, (PB92-114602, A11, MF-A03).

NCEER-91-0016   "Closed-Loop Modal Testing of a 27-Story Reinforced Concrete Flat Plate-Core Building," by H.R. Somaprasad, T. Toksoy, H. Yoshiyuki and A.E. Aktan, 7/15/91, (PB92-129980, A07, MF-A02).

NCEER-91-0017   "Shake Table Test of a 1/6 Scale Two-Story Lightly Reinforced Concrete Building," by A.G. El-Attar, R.N. White and P. Gergely, 2/28/91, (PB92-222447, A06, MF-A02).

NCEER-91-0018   "Shake Table Test of a 1/8 Scale Three-Story Lightly Reinforced Concrete Building," by A.G. El-Attar, R.N. White and P. Gergely, 2/28/91, (PB93-116630, A08, MF-A02).

NCEER-91-0019   "Transfer Functions for Rigid Rectangular Foundations," by A.S. Veletsos, A.M. Prasad and W.H. Wu, 7/31/91, not available.

NCEER-91-0020   "Hybrid Control of Seismic-Excited Nonlinear and Inelastic Structural Systems," by J.N. Yang, Z. Li and A. Danielians, 8/1/91, (PB92-143171, A06, MF-A02).

NCEER-91-0021   "The NCEER-91 Earthquake Catalog: Improved Intensity-Based Magnitudes and Recurrence Relations for U.S. Earthquakes East of New Madrid," by L. Seeber and J.G. Armbruster, 8/28/91, (PB92-176742, A06, MF-A02).

NCEER-91-0022   "Proceedings from the Implementation of Earthquake Planning and Education in Schools: The Need for Change - The Roles of the Changemakers," by K.E.K. Ross and F. Winslow, 7/23/91, (PB92-129998, A12, MF-A03).

NCEER-91-0023   "A Study of Reliability-Based Criteria for Seismic Design of Reinforced Concrete Frame Buildings," by H.H.M. Hwang and H-M. Hsu, 8/10/91, (PB92-140235, A09, MF-A02).

NCEER-91-0024   "Experimental Verification of a Number of Structural System Identification Algorithms," by R.G. Ghanem, H. Gavin and M. Shinozuka, 9/18/91, (PB92-176577, A18, MF-A04).

NCEER-91-0025   "Probabilistic Evaluation of Liquefaction Potential," by H.H.M. Hwang and C.S. Lee," 11/25/91, (PB92-143429, A05, MF-A01).

NCEER-91-0026   "Instantaneous Optimal Control for Linear, Nonlinear and Hysteretic Structures - Stable Controllers," by J.N. Yang and Z. Li, 11/15/91, (PB92-163807, A04, MF-A01).

NCEER-91-0027   "Experimental and Theoretical Study of a Sliding Isolation System for Bridges," by M.C. Constantinou, A. Kartoum, A.M. Reinhorn and P. Bradford, 11/15/91, (PB92-176973, A10, MF-A03).

NCEER-92-0001   "Case Studies of Liquefaction and Lifeline Performance During Past Earthquakes, Volume 1: Japanese Case Studies," Edited by M. Hamada and T. O'Rourke, 2/17/92, (PB92-197243, A18, MF-A04).

NCEER-92-0002   "Case Studies of Liquefaction and Lifeline Performance During Past Earthquakes, Volume 2: United States Case Studies," Edited by T. O'Rourke and M. Hamada, 2/17/92, (PB92-197250, A20, MF-A04).

NCEER-92-0003   "Issues in Earthquake Education," Edited by K. Ross, 2/3/92, (PB92-222389, A07, MF-A02).

NCEER-92-0004   "Proceedings from the First U.S. - Japan Workshop on Earthquake Protective Systems for Bridges," Edited by I.G. Buckle, 2/4/92, (PB94-142239, A99, MF-A06).

NCEER-92-0005   "Seismic Ground Motion from a Haskell-Type Source in a Multiple-Layered Half-Space," A.P. Theoharis, G. Deodatis and M. Shinozuka, 1/2/92, not available.

NCEER-92-0006   "Proceedings from the Site Effects Workshop," Edited by R. Whitman, 2/29/92, (PB92-197201, A04, MF-A01).

NCEER-92-0007   "Engineering Evaluation of Permanent Ground Deformations Due to Seismically-Induced Liquefaction," by M.H. Baziar, R. Dobry and A-W.M. Elgamal, 3/24/92, (PB92-222421, A13, MF-A03).

NCEER-92-0008   "A Procedure for the Seismic Evaluation of Buildings in the Central and Eastern United States," by C.D. Poland and J.O. Malley, 4/2/92, (PB92-222439, A20, MF-A04).

NCEER-92-0009   "Experimental and Analytical Study of a Hybrid Isolation System Using Friction Controllable Sliding Bearings," by M.Q. Feng, S. Fujii and M. Shinozuka, 5/15/92, (PB93-150282, A06, MF-A02).

NCEER-92-0010   "Seismic Resistance of Slab-Column Connections in Existing Non-Ductile Flat-Plate Buildings," by A.J. Durrani and Y. Du, 5/18/92, (PB93-116812, A06, MF-A02).

NCEER-92-0011   "The Hysteretic and Dynamic Behavior of Brick Masonry Walls Upgraded by Ferrocement Coatings Under Cyclic Loading and Strong Simulated Ground Motion," by H. Lee and S.P. Prawel, 5/11/92, not available.

NCEER-92-0012   "Study of Wire Rope Systems for Seismic Protection of Equipment in Buildings," by G.F. Demetriades, M.C. Constantinou and A.M. Reinhorn, 5/20/92, (PB93-116655, A08, MF-A02).

NCEER-92-0013   "Shape Memory Structural Dampers: Material Properties, Design and Seismic Testing," by P.R. Witting and F.A. Cozzarelli, 5/26/92, (PB93-116663, A05, MF-A01).

NCEER-92-0014   "Longitudinal Permanent Ground Deformation Effects on Buried Continuous Pipelines," by M.J. O'Rourke, and C. Nordberg, 6/15/92, (PB93-116671, A08, MF-A02).

NCEER-92-0015   "A Simulation Method for Stationary Gaussian Random Functions Based on the Sampling Theorem," by M. Grigoriu and S. Balopoulou, 6/11/92, (PB93-127496, A05, MF-A01).

NCEER-92-0016   "Gravity-Load-Designed Reinforced Concrete Buildings: Seismic Evaluation of Existing Construction and Detailing Strategies for Improved Seismic Resistance," by G.W. Hoffmann, S.K. Kunnath, A.M. Reinhorn and J.B. Mander, 7/15/92, (PB94-142007, A08, MF-A02).

NCEER-92-0017   "Observations on Water System and Pipeline Performance in the Limón Area of Costa Rica Due to the April 22, 1991 Earthquake," by M. O'Rourke and D. Ballantyne, 6/30/92, (PB93-126811, A06, MF-A02).

NCEER-92-0018   "Fourth Edition of Earthquake Education Materials for Grades K-12," Edited by K.E.K. Ross, 8/10/92, (PB93-114023, A07, MF-A02).

NCEER-92-0019   "Proceedings from the Fourth Japan-U.S. Workshop on Earthquake Resistant Design of Lifeline Facilities and Countermeasures for Soil Liquefaction," Edited by M. Hamada and T.D. O'Rourke, 8/12/92, (PB93-163939, A99, MF-E11).

NCEER-92-0020   "Active Bracing System: A Full Scale Implementation of Active Control," by A.M. Reinhorn, T.T. Soong, R.C. Lin, M.A. Riley, Y.P. Wang, S. Aizawa and M. Higashino, 8/14/92, (PB93-127512, A06, MF-A02).

NCEER-92-0021   "Empirical Analysis of Horizontal Ground Displacement Generated by Liquefaction-Induced Lateral Spreads," by S.F. Bartlett and T.L. Youd, 8/17/92, (PB93-188241, A06, MF-A02).

NCEER-92-0022   "IDARC Version 3.0: Inelastic Damage Analysis of Reinforced Concrete Structures," by S.K. Kunnath, A.M. Reinhorn and R.F. Lobo, 8/31/92, (PB93-227502, A07, MF-A02).

NCEER-92-0023   "A Semi-Empirical Analysis of Strong-Motion Peaks in Terms of Seismic Source, Propagation Path and Local Site Conditions, by M. Kamiyama, M.J. O'Rourke and R. Flores-Berrones, 9/9/92, (PB93-150266, A08, MF-A02).

NCEER-92-0024   "Seismic Behavior of Reinforced Concrete Frame Structures with Nonductile Details, Part I: Summary of Experimental Findings of Full Scale Beam-Column Joint Tests," by A. Beres, R.N. White and P. Gergely, 9/30/92, (PB93-227783, A05, MF-A01).

NCEER-92-0025   "Experimental Results of Repaired and Retrofitted Beam-Column Joint Tests in Lightly Reinforced Concrete Frame Buildings," by A. Beres, S. El-Borgi, R.N. White and P. Gergely, 10/29/92, (PB93-227791, A05, MF-A01).

NCEER-92-0026   "A Generalization of Optimal Control Theory: Linear and Nonlinear Structures," by J.N. Yang, Z. Li and S. Vongchavalitkul, 11/2/92, (PB93-188621, A05, MF-A01).

NCEER-92-0027   "Seismic Resistance of Reinforced Concrete Frame Structures Designed Only for Gravity Loads: Part I - Design and Properties of a One-Third Scale Model Structure," by J.M. Bracci, A.M. Reinhorn and J.B. Mander, 12/1/92, (PB94-104502, A08, MF-A02).

NCEER-92-0028   "Seismic Resistance of Reinforced Concrete Frame Structures Designed Only for Gravity Loads: Part II - Experimental Performance of Subassemblages," by L.E. Aycardi, J.B. Mander and A.M. Reinhorn, 12/1/92, (PB94-104510, A08, MF-A02).

NCEER-92-0029   "Seismic Resistance of Reinforced Concrete Frame Structures Designed Only for Gravity Loads: Part III - Experimental Performance and Analytical Study of a Structural Model," by J.M. Bracci, A.M. Reinhorn and J.B. Mander, 12/1/92, (PB93-227528, A09, MF-A01).

NCEER-92-0030   "Evaluation of Seismic Retrofit of Reinforced Concrete Frame Structures: Part I - Experimental Performance of Retrofitted Subassemblages," by D. Choudhuri, J.B. Mander and A.M. Reinhorn, 12/8/92, (PB93-198307, A07, MF-A02).

NCEER-92-0031   "Evaluation of Seismic Retrofit of Reinforced Concrete Frame Structures: Part II - Experimental Performance and Analytical Study of a Retrofitted Structural Model," by J.M. Bracci, A.M. Reinhorn and J.B. Mander, 12/8/92, (PB93-198315, A09, MF-A03).

NCEER-92-0032   "Experimental and Analytical Investigation of Seismic Response of Structures with Supplemental Fluid Viscous Dampers," by M.C. Constantinou and M.D. Symans, 12/21/92, (PB93-191435, A10, MF-A03). This report is available only through NTIS (see address given above).

NCEER-92-0033   "Reconnaissance Report on the Cairo, Egypt Earthquake of October 12, 1992," by M. Khater, 12/23/92, (PB93-188621, A03, MF-A01).

NCEER-92-0034   "Low-Level Dynamic Characteristics of Four Tall Flat-Plate Buildings in New York City," by H. Gavin, S. Yuan, J. Grossman, E. Pekelis and K. Jacob, 12/28/92, (PB93-188217, A07, MF-A02).

NCEER-93-0001   "An Experimental Study on the Seismic Performance of Brick-Infilled Steel Frames With and Without Retrofit," by J.B. Mander, B. Nair, K. Wojtkowski and J. Ma, 1/29/93, (PB93-227510, A07, MF-A02).

NCEER-93-0002   "Social Accounting for Disaster Preparedness and Recovery Planning," by S. Cole, E. Pantoja and V. Razak, 2/22/93, (PB94-142114, A12, MF-A03).

NCEER-93-0003   "Assessment of 1991 NEHRP Provisions for Nonstructural Components and Recommended Revisions," by T.T. Soong, G. Chen, Z. Wu, R-H. Zhang and M. Grigoriu, 3/1/93, (PB93-188639, A06, MF-A02).

NCEER-93-0004   "Evaluation of Static and Response Spectrum Analysis Procedures of SEAOC/UBC for Seismic Isolated Structures," by C.W. Winters and M.C. Constantinou, 3/23/93, (PB93-198299, A10, MF-A03).

NCEER-93-0005   "Earthquakes in the Northeast - Are We Ignoring the Hazard? A Workshop on Earthquake Science and Safety for Educators," edited by K.E.K. Ross, 4/2/93, (PB94-103066, A09, MF-A02).

NCEER-93-0006   "Inelastic Response of Reinforced Concrete Structures with Viscoelastic Braces," by R.F. Lobo, J.M. Bracci, K.L. Shen, A.M. Reinhorn and T.T. Soong, 4/5/93, (PB93-227486, A05, MF-A02).

NCEER-93-0007   "Seismic Testing of Installation Methods for Computers and Data Processing Equipment," by K. Kosar, T.T. Soong, K.L. Shen, J.A. HoLung and Y.K. Lin, 4/12/93, (PB93-198299, A07, MF-A02).

NCEER-93-0008   "Retrofit of Reinforced Concrete Frames Using Added Dampers," by A. Reinhorn, M. Constantinou and C. Li, not available.

NCEER-93-0009   "Seismic Behavior and Design Guidelines for Steel Frame Structures with Added Viscoelastic Dampers," by K.C. Chang, M.L. Lai, T.T. Soong, D.S. Hao and Y.C. Yeh, 5/1/93, (PB94-141959, A07, MF-A02).

NCEER-93-0010   "Seismic Performance of Shear-Critical Reinforced Concrete Bridge Piers," by J.B. Mander, S.M. Waheed, M.T.A. Chaudhary and S.S. Chen, 5/12/93, (PB93-227494, A08, MF-A02).

NCEER-93-0011   "3D-BASIS-TABS: Computer Program for Nonlinear Dynamic Analysis of Three Dimensional Base Isolated Structures," by S. Nagarajaiah, C. Li, A.M. Reinhorn and M.C. Constantinou, 8/2/93, (PB94-141819, A09, MF-A02).

NCEER-93-0012   "Effects of Hydrocarbon Spills from an Oil Pipeline Break on Ground Water," by O.J. Helweg and H.H.M. Hwang, 8/3/93, (PB94-141942, A06, MF-A02).

NCEER-93-0013   "Simplified Procedures for Seismic Design of Nonstructural Components and Assessment of Current Code Provisions," by M.P. Singh, L.E. Suarez, E.E. Matheu and G.O. Maldonado, 8/4/93, (PB94-141827, A09, MF-A02).

NCEER-93-0014   "An Energy Approach to Seismic Analysis and Design of Secondary Systems," by G. Chen and T.T. Soong, 8/6/93, (PB94-142767, A11, MF-A03).

NCEER-93-0015   "Proceedings from School Sites: Becoming Prepared for Earthquakes - Commemorating the Third Anniversary of the Loma Prieta Earthquake," Edited by F.E. Winslow and K.E.K. Ross, 8/16/93, (PB94-154275, A16, MF-A02).

NCEER-93-0016   "Reconnaissance Report of Damage to Historic Monuments in Cairo, Egypt Following the October 12, 1992 Dahshur Earthquake," by D. Sykora, D. Look, G. Croci, E. Karaesmen and E. Karaesmen, 8/19/93, (PB94-142221, A08, MF-A02).

NCEER-93-0017   "The Island of Guam Earthquake of August 8, 1993," by S.W. Swan and S.K. Harris, 9/30/93, (PB94-141843, A04, MF-A01).

NCEER-93-0018   "Engineering Aspects of the October 12, 1992 Egyptian Earthquake," by A.W. Elgamal, M. Amer, K. Adalier and A. Abul-Fadl, 10/7/93, (PB94-141983, A05, MF-A01).

NCEER-93-0019   "Development of an Earthquake Motion Simulator and its Application in Dynamic Centrifuge Testing," by I. Krstelj, Supervised by J.H. Prevost, 10/23/93, (PB94-181773, A-10, MF-A03).

NCEER-93-0020   "NCEER-Taisei Corporation Research Program on Sliding Seismic Isolation Systems for Bridges: Experimental and Analytical Study of a Friction Pendulum System (FPS)," by M.C. Constantinou, P. Tsopelas, Y-S. Kim and S. Okamoto, 11/1/93, (PB94-142775, A08, MF-A02).

NCEER-93-0021   "Finite Element Modeling of Elastomeric Seismic Isolation Bearings," by L.J. Billings, Supervised by R. Shepherd, 11/8/93, not available.

NCEER-93-0022   "Seismic Vulnerability of Equipment in Critical Facilities: Life-Safety and Operational Consequences," by K. Porter, G.S. Johnson, M.M. Zadeh, C. Scawthorn and S. Eder, 11/24/93, (PB94-181765, A16, MF-A03).

NCEER-93-0023   "Hokkaido Nansei-oki, Japan Earthquake of July 12, 1993, by P.I. Yanev and C.R. Scawthorn, 12/23/93, (PB94-181500, A07, MF-A01).

NCEER-94-0001   "An Evaluation of Seismic Serviceability of Water Supply Networks with Application to the San Francisco Auxiliary Water Supply System," by I. Markov, Supervised by M. Grigoriu and T. O'Rourke, 1/21/94, (PB94-204013, A07, MF-A02).

NCEER-94-0002   "NCEER-Taisei Corporation Research Program on Sliding Seismic Isolation Systems for Bridges: Experimental and Analytical Study of Systems Consisting of Sliding Bearings, Rubber Restoring Force Devices and Fluid Dampers," Volumes I and II, by P. Tsopelas, S. Okamoto, M.C. Constantinou, D. Ozaki and S. Fujii, 2/4/94, (PB94-181740, A09, MF-A02 and PB94-181757, A12, MF-A03).

NCEER-94-0003   "A Markov Model for Local and Global Damage Indices in Seismic Analysis," by S. Rahman and M. Grigoriu, 2/18/94, (PB94-206000, A12, MF-A03).

NCEER-94-0004   "Proceedings from the NCEER Workshop on Seismic Response of Masonry Infills," edited by D.P. Abrams, 3/1/94, (PB94-180783, A07, MF-A02).

NCEER-94-0005   "The Northridge, California Earthquake of January 17, 1994: General Reconnaissance Report," edited by J.D. Goltz, 3/11/94, (PB94-193943, A10, MF-A03).

NCEER-94-0006   "Seismic Energy Based Fatigue Damage Analysis of Bridge Columns: Part I - Evaluation of Seismic Capacity," by G.A. Chang and J.B. Mander, 3/14/94, (PB94-219185, A11, MF-A03).

NCEER-94-0007   "Seismic Isolation of Multi-Story Frame Structures Using Spherical Sliding Isolation Systems," by T.M. Al-Hussaini, V.A. Zayas and M.C. Constantinou, 3/17/94, (PB94-193745, A09, MF-A02).

NCEER-94-0008   "The Northridge, California Earthquake of January 17, 1994: Performance of Highway Bridges," edited by I.G. Buckle, 3/24/94, (PB94-193851, A06, MF-A02).

NCEER-94-0009   "Proceedings of the Third U.S.-Japan Workshop on Earthquake Protective Systems for Bridges," edited by I.G. Buckle and I. Friedland, 3/31/94, (PB94-195815, A99, MF-A06).

NCEER-94-0010   "3D-BASIS-ME: Computer Program for Nonlinear Dynamic Analysis of Seismically Isolated Single and Multiple Structures and Liquid Storage Tanks," by P.C. Tsopelas, M.C. Constantinou and A.M. Reinhorn, 4/12/94, (PB94-204922, A09, MF-A02).

NCEER-94-0011   "The Northridge, California Earthquake of January 17, 1994: Performance of Gas Transmission Pipelines," by T.D. O'Rourke and M.C. Palmer, 5/16/94, (PB94-204989, A05, MF-A01).

NCEER-94-0012   "Feasibility Study of Replacement Procedures and Earthquake Performance Related to Gas Transmission Pipelines," by T.D. O'Rourke and M.C. Palmer, 5/25/94, (PB94-206638, A09, MF-A02).

NCEER-94-0013   "Seismic Energy Based Fatigue Damage Analysis of Bridge Columns: Part II - Evaluation of Seismic Demand," by G.A. Chang and J.B. Mander, 6/1/94, (PB95-18106, A08, MF-A02).

NCEER-94-0014   "NCEER-Taisei Corporation Research Program on Sliding Seismic Isolation Systems for Bridges: Experimental and Analytical Study of a System Consisting of Sliding Bearings and Fluid Restoring Force/Damping Devices," by P. Tsopelas and M.C. Constantinou, 6/13/94, (PB94-219144, A10, MF-A03).

NCEER-94-0015   "Generation of Hazard-Consistent Fragility Curves for Seismic Loss Estimation Studies," by H. Hwang and J-R. Huo, 6/14/94, (PB95-181996, A09, MF-A02).

NCEER-94-0016   "Seismic Study of Building Frames with Added Energy-Absorbing Devices," by W.S. Pong, C.S. Tsai and G.C. Lee, 6/20/94, (PB94-219136, A10, A03).

NCEER-94-0017   "Sliding Mode Control for Seismic-Excited Linear and Nonlinear Civil Engineering Structures," by J. Yang, J. Wu, A. Agrawal and Z. Li, 6/21/94, (PB95-138483, A06, MF-A02).

NCEER-94-0018   "3D-BASIS-TABS Version 2.0: Computer Program for Nonlinear Dynamic Analysis of Three Dimensional Base Isolated Structures," by A.M. Reinhorn, S. Nagarajaiah, M.C. Constantinou, P. Tsopelas and R. Li, 6/22/94, (PB95-182176, A08, MF-A02).

NCEER-94-0019   "Proceedings of the International Workshop on Civil Infrastructure Systems: Application of Intelligent Systems and Advanced Materials on Bridge Systems," Edited by G.C. Lee and K.C. Chang, 7/18/94, (PB95-252474, A20, MF-A04).

NCEER-94-0020   "Study of Seismic Isolation Systems for Computer Floors," by V. Lambrou and M.C. Constantinou, 7/19/94, (PB95-138533, A10, MF-A03).

NCEER-94-0021   "Proceedings of the U.S.-Italian Workshop on Guidelines for Seismic Evaluation and Rehabilitation of Unreinforced Masonry Buildings," Edited by D.P. Abrams and G.M. Calvi, 7/20/94, (PB95-138749, A13, MF-A03).

NCEER-94-0022   "NCEER-Taisei Corporation Research Program on Sliding Seismic Isolation Systems for Bridges: Experimental and Analytical Study of a System Consisting of Lubricated PTFE Sliding Bearings and Mild Steel Dampers," by P. Tsopelas and M.C. Constantinou, 7/22/94, (PB95-182184, A08, MF-A02).

NCEER-94-0023   "Development of Reliability-Based Design Criteria for Buildings Under Seismic Load," by Y.K. Wen, H. Hwang and M. Shinozuka, 8/1/94, (PB95-211934, A08, MF-A02).

NCEER-94-0024   "Experimental Verification of Acceleration Feedback Control Strategies for an Active Tendon System," by S.J. Dyke, B.F. Spencer, Jr., P. Quast, M.K. Sain, D.C. Kaspari, Jr. and T.T. Soong, 8/29/94, (PB95-212320, A05, MF-A01).

NCEER-94-0025   "Seismic Retrofitting Manual for Highway Bridges," Edited by I.G. Buckle and I.F. Friedland, published by the Federal Highway Administration (PB95-212676, A15, MF-A03).

NCEER-94-0026   "Proceedings from the Fifth U.S.-Japan Workshop on Earthquake Resistant Design of Lifeline Facilities and Countermeasures Against Soil Liquefaction," Edited by T.D. O'Rourke and M. Hamada, 11/7/94, (PB95-220802, A99, MF-E08).

NCEER-95-0001 "Experimental and Analytical Investigation of Seismic Retrofit of Structures with Supplemental Damping: Part 1 - Fluid Viscous Damping Devices," by A.M. Reinhorn, C. Li and M.C. Constantinou, 1/3/95, (PB95-266599, A09, MF-A02).

NCEER-95-0002 "Experimental and Analytical Study of Low-Cycle Fatigue Behavior of Semi-Rigid Top-And-Seat Angle Connections," by G. Pekcan, J.B. Mander and S.S. Chen, 1/5/95, (PB95-220042, A07, MF-A02).

NCEER-95-0003 "NCEER-ATC Joint Study on Fragility of Buildings," by T. Anagnos, C. Rojahn and A.S. Kiremidjian, 1/20/95, (PB95-220026, A06, MF-A02).

NCEER-95-0004 "Nonlinear Control Algorithms for Peak Response Reduction," by Z. Wu, T.T. Soong, V. Gattulli and R.C. Lin, 2/16/95, (PB95-220349, A05, MF-A01).

NCEER-95-0005 "Pipeline Replacement Feasibility Study: A Methodology for Minimizing Seismic and Corrosion Risks to Underground Natural Gas Pipelines," by R.T. Eguchi, H.A. Seligson and D.G. Honegger, 3/2/95, (PB95-252326, A06, MF-A02).

NCEER-95-0006 "Evaluation of Seismic Performance of an 11-Story Frame Building During the 1994 Northridge Earthquake," by F. Naeim, R. DiSulio, K. Benuska, A. Reinhorn and C. Li, not available.

NCEER-95-0007 "Prioritization of Bridges for Seismic Retrofitting," by N. Basöz and A.S. Kiremidjian, 4/24/95, (PB95-252300, A08, MF-A02).

NCEER-95-0008 "Method for Developing Motion Damage Relationships for Reinforced Concrete Frames," by A. Singhal and A.S. Kiremidjian, 5/11/95, (PB95-266607, A06, MF-A02).

NCEER-95-0009 "Experimental and Analytical Investigation of Seismic Retrofit of Structures with Supplemental Damping: Part II - Friction Devices," by C. Li and A.M. Reinhorn, 7/6/95, (PB96-128087, A11, MF-A03).

NCEER-95-0010 "Experimental Performance and Analytical Study of a Non-Ductile Reinforced Concrete Frame Structure Retrofitted with Elastomeric Spring Dampers," by G. Pekcan, J.B. Mander and S.S. Chen, 7/14/95, (PB96-137161, A08, MF-A02).

NCEER-95-0011 "Development and Experimental Study of Semi-Active Fluid Damping Devices for Seismic Protection of Structures," by M.D. Symans and M.C. Constantinou, 8/3/95, (PB96-136940, A23, MF-A04).

NCEER-95-0012 "Real-Time Structural Parameter Modification (RSPM): Development of Innervated Structures," by Z. Liang, M. Tong and G.C. Lee, 4/11/95, (PB96-137153, A06, MF-A01).

NCEER-95-0013 "Experimental and Analytical Investigation of Seismic Retrofit of Structures with Supplemental Damping: Part III - Viscous Damping Walls," by A.M. Reinhorn and C. Li, 10/1/95, (PB96-176409, A11, MF-A03).

NCEER-95-0014 "Seismic Fragility Analysis of Equipment and Structures in a Memphis Electric Substation," by J-R. Huo and H.H.M. Hwang, 8/10/95, (PB96-128087, A09, MF-A02).

NCEER-95-0015 "The Hanshin-Awaji Earthquake of January 17, 1995: Performance of Lifelines," Edited by M. Shinozuka, 11/3/95, (PB96-176383, A15, MF-A03).

NCEER-95-0016 "Highway Culvert Performance During Earthquakes," by T.L. Youd and C.J. Beckman, available as NCEER-96-0015.

NCEER-95-0017 "The Hanshin-Awaji Earthquake of January 17, 1995: Performance of Highway Bridges," Edited by I.G. Buckle, 12/1/95, not available.

NCEER-95-0018 "Modeling of Masonry Infill Panels for Structural Analysis," by A.M. Reinhorn, A. Madan, R.E. Valles, Y. Reichmann and J.B. Mander, 12/8/95, (PB97-110886, MF-A01, A06).

NCEER-95-0019 "Optimal Polynomial Control for Linear and Nonlinear Structures," by A.K. Agrawal and J.N. Yang, 12/11/95, (PB96-168737, A07, MF-A02).

NCEER-95-0020 "Retrofit of Non-Ductile Reinforced Concrete Frames Using Friction Dampers," by R.S. Rao, P. Gergely and R.N. White, 12/22/95, (PB97-133508, A10, MF-A02).

NCEER-95-0021 "Parametric Results for Seismic Response of Pile-Supported Bridge Bents," by G. Mylonakis, A. Nikolaou and G. Gazetas, 12/22/95, (PB97-100242, A12, MF-A03).

NCEER-95-0022 "Kinematic Bending Moments in Seismically Stressed Piles," by A. Nikolaou, G. Mylonakis and G. Gazetas, 12/23/95, (PB97-113914, MF-A03, A13).

NCEER-96-0001 "Dynamic Response of Unreinforced Masonry Buildings with Flexible Diaphragms," by A.C. Costley and D.P. Abrams," 10/10/96, (PB97-133573, MF-A03, A15).

NCEER-96-0002 "State of the Art Review: Foundations and Retaining Structures," by I. Po Lam, not available.

NCEER-96-0003 "Ductility of Rectangular Reinforced Concrete Bridge Columns with Moderate Confinement," by N. Wehbe, M. Saiidi, D. Sanders and B. Douglas, 11/7/96, (PB97-133557, A06, MF-A02).

NCEER-96-0004 "Proceedings of the Long-Span Bridge Seismic Research Workshop," edited by I.G. Buckle and I.M. Friedland, not available.

NCEER-96-0005 "Establish Representative Pier Types for Comprehensive Study: Eastern United States," by J. Kulicki and Z. Prucz, 5/28/96, (PB98-119217, A07, MF-A02).

NCEER-96-0006 "Establish Representative Pier Types for Comprehensive Study: Western United States," by R. Imbsen, R.A. Schamber and T.A. Osterkamp, 5/28/96, (PB98-118607, A07, MF-A02).

NCEER-96-0007 "Nonlinear Control Techniques for Dynamical Systems with Uncertain Parameters," by R.G. Ghanem and M.I. Bujakov, 5/27/96, (PB97-100259, A17, MF-A03).

NCEER-96-0008 "Seismic Evaluation of a 30-Year Old Non-Ductile Highway Bridge Pier and Its Retrofit," by J.B. Mander, B. Mahmoodzadegan, S. Bhadra and S.S. Chen, 5/31/96, (PB97-110902, MF-A03, A10).

NCEER-96-0009 "Seismic Performance of a Model Reinforced Concrete Bridge Pier Before and After Retrofit," by J.B. Mander, J.H. Kim and C.A. Ligozio, 5/31/96, (PB97-110910, MF-A02, A10).

NCEER-96-0010 "IDARC2D Version 4.0: A Computer Program for the Inelastic Damage Analysis of Buildings," by R.E. Valles, A.M. Reinhorn, S.K. Kunnath, C. Li and A. Madan, 6/3/96, (PB97-100234, A17, MF-A03).

NCEER-96-0011 "Estimation of the Economic Impact of Multiple Lifeline Disruption: Memphis Light, Gas and Water Division Case Study," by S.E. Chang, H.A. Seligson and R.T. Eguchi, 8/16/96, (PB97-133490, A11, MF-A03).

NCEER-96-0012 "Proceedings from the Sixth Japan-U.S. Workshop on Earthquake Resistant Design of Lifeline Facilities and Countermeasures Against Soil Liquefaction, Edited by M. Hamada and T. O'Rourke, 9/11/96, (PB97-133581, A99, MF-A06).

NCEER-96-0013 "Chemical Hazards, Mitigation and Preparedness in Areas of High Seismic Risk: A Methodology for Estimating the Risk of Post-Earthquake Hazardous Materials Release," by H.A. Seligson, R.T. Eguchi, K.J. Tierney and K. Richmond, 11/7/96, (PB97-133565, MF-A02, A08).

NCEER-96-0014 "Response of Steel Bridge Bearings to Reversed Cyclic Loading," by J.B. Mander, D-K. Kim, S.S. Chen and G.J. Premus, 11/13/96, (PB97-140735, A12, MF-A03).

NCEER-96-0015 "Highway Culvert Performance During Past Earthquakes," by T.L. Youd and C.J. Beckman, 11/25/96, (PB97-133532, A06, MF-A01).

NCEER-97-0001 "Evaluation, Prevention and Mitigation of Pounding Effects in Building Structures," by R.E. Valles and A.M. Reinhorn, 2/20/97, (PB97-159552, A14, MF-A03).

NCEER-97-0002 "Seismic Design Criteria for Bridges and Other Highway Structures," by C. Rojahn, R. Mayes, D.G. Anderson, J. Clark, J.H. Hom, R.V. Nutt and M.J. O'Rourke, 4/30/97, (PB97-194658, A06, MF-A03).

NCEER-97-0003   "Proceedings of the U.S.-Italian Workshop on Seismic Evaluation and Retrofit," Edited by D.P. Abrams and G.M. Calvi, 3/19/97, (PB97-194666, A13, MF-A03).

NCEER-97-0004   "Investigation of Seismic Response of Buildings with Linear and Nonlinear Fluid Viscous Dampers," by A.A. Seleemah and M.C. Constantinou, 5/21/97, (PB98-109002, A15, MF-A03).

NCEER-97-0005   "Proceedings of the Workshop on Earthquake Engineering Frontiers in Transportation Facilities," edited by G.C. Lee and I.M. Friedland, 8/29/97, (PB98-128911, A25, MR-A04).

NCEER-97-0006   "Cumulative Seismic Damage of Reinforced Concrete Bridge Piers," by S.K. Kunnath, A. El-Bahy, A. Taylor and W. Stone, 9/2/97, (PB98-108814, A11, MF-A03).

NCEER-97-0007   "Structural Details to Accommodate Seismic Movements of Highway Bridges and Retaining Walls," by R.A. Imbsen, R.A. Schamber, E. Thorkildsen, A. Kartoum, B.T. Martin, T.N. Rosser and J.M. Kulicki, 9/3/97, (PB98-108996, A09, MF-A02).

NCEER-97-0008   "A Method for Earthquake Motion-Damage Relationships with Application to Reinforced Concrete Frames," by A. Singhal and A.S. Kiremidjian, 9/10/97, (PB98-108988, A13, MF-A03).

NCEER-97-0009   "Seismic Analysis and Design of Bridge Abutments Considering Sliding and Rotation," by K. Fishman and R. Richards, Jr., 9/15/97, (PB98-108897, A06, MF-A02).

NCEER-97-0010   "Proceedings of the FHWA/NCEER Workshop on the National Representation of Seismic Ground Motion for New and Existing Highway Facilities," edited by I.M. Friedland, M.S. Power and R.L. Mayes, 9/22/97, (PB98-128903, A21, MF-A04).

NCEER-97-0011   "Seismic Analysis for Design or Retrofit of Gravity Bridge Abutments," by K.L. Fishman, R. Richards, Jr. and R.C. Divito, 10/2/97, (PB98-128937, A08, MF-A02).

NCEER-97-0012   "Evaluation of Simplified Methods of Analysis for Yielding Structures," by P. Tsopelas, M.C. Constantinou, C.A. Kircher and A.S. Whittaker, 10/31/97, (PB98-128929, A10, MF-A03).

NCEER-97-0013   "Seismic Design of Bridge Columns Based on Control and Repairability of Damage," by C-T. Cheng and J.B. Mander, 12/8/97, (PB98-144249, A11, MF-A03).

NCEER-97-0014   "Seismic Resistance of Bridge Piers Based on Damage Avoidance Design," by J.B. Mander and C-T. Cheng, 12/10/97, (PB98-144223, A09, MF-A02).

NCEER-97-0015   "Seismic Response of Nominally Symmetric Systems with Strength Uncertainty," by S. Balopoulou and M. Grigoriu, 12/23/97, (PB98-153422, A11, MF-A03).

NCEER-97-0016   "Evaluation of Seismic Retrofit Methods for Reinforced Concrete Bridge Columns," by T.J. Wipf, F.W. Klaiber and F.M. Russo, 12/28/97, (PB98-144215, A12, MF-A03).

NCEER-97-0017   "Seismic Fragility of Existing Conventional Reinforced Concrete Highway Bridges," by C.L. Mullen and A.S. Cakmak, 12/30/97, (PB98-153406, A08, MF-A02).

NCEER-97-0018   "Loss Asssessment of Memphis Buildings," edited by D.P. Abrams and M. Shinozuka, 12/31/97, (PB98-144231, A13, MF-A03).

NCEER-97-0019   "Seismic Evaluation of Frames with Infill Walls Using Quasi-static Experiments," by K.M. Mosalam, R.N. White and P. Gergely, 12/31/97, (PB98-153455, A07, MF-A02).

NCEER-97-0020   "Seismic Evaluation of Frames with Infill Walls Using Pseudo-dynamic Experiments," by K.M. Mosalam, R.N. White and P. Gergely, 12/31/97, (PB98-153430, A07, MF-A02).

NCEER-97-0021   "Computational Strategies for Frames with Infill Walls: Discrete and Smeared Crack Analyses and Seismic Fragility," by K.M. Mosalam, R.N. White and P. Gergely, 12/31/97, (PB98-153414, A10, MF-A02).

NCEER-97-0022   "Proceedings of the NCEER Workshop on Evaluation of Liquefaction Resistance of Soils," edited by T.L. Youd and I.M. Idriss, 12/31/97, (PB98-155617, A15, MF-A03).

MCEER-98-0001   "Extraction of Nonlinear Hysteretic Properties of Seismically Isolated Bridges from Quick-Release Field Tests," by Q. Chen, B.M. Douglas, E.M. Maragakis and I.G. Buckle, 5/26/98, (PB99-118838, A06, MF-A01).

MCEER-98-0002   "Methodologies for Evaluating the Importance of Highway Bridges," by A. Thomas, S. Eshenaur and J. Kulicki, 5/29/98, (PB99-118846, A10, MF-A02).

MCEER-98-0003   "Capacity Design of Bridge Piers and the Analysis of Overstrength," by J.B. Mander, A. Dutta and P. Goel, 6/1/98, (PB99-118853, A09, MF-A02).

MCEER-98-0004   "Evaluation of Bridge Damage Data from the Loma Prieta and Northridge, California Earthquakes," by N. Basoz and A. Kiremidjian, 6/2/98, (PB99-118861, A15, MF-A03).

MCEER-98-0005   "Screening Guide for Rapid Assessment of Liquefaction Hazard at Highway Bridge Sites," by T. L. Youd, 6/16/98, (PB99-118879, A06, not available on microfiche).

MCEER-98-0006   "Structural Steel and Steel/Concrete Interface Details for Bridges," by P. Ritchie, N. Kauhl and J. Kulicki, 7/13/98, (PB99-118945, A06, MF-A01).

MCEER-98-0007   "Capacity Design and Fatigue Analysis of Confined Concrete Columns," by A. Dutta and J.B. Mander, 7/14/98, (PB99-118960, A14, MF-A03).

MCEER-98-0008   "Proceedings of the Workshop on Performance Criteria for Telecommunication Services Under Earthquake Conditions," edited by A.J. Schiff, 7/15/98, (PB99-118952, A08, MF-A02).

MCEER-98-0009   "Fatigue Analysis of Unconfined Concrete Columns," by J.B. Mander, A. Dutta and J.H. Kim, 9/12/98, (PB99-123655, A10, MF-A02).

MCEER-98-0010   "Centrifuge Modeling of Cyclic Lateral Response of Pile-Cap Systems and Seat-Type Abutments in Dry Sands," by A.D. Gadre and R. Dobry, 10/2/98, (PB99-123606, A13, MF-A03).

MCEER-98-0011   "IDARC-BRIDGE: A Computational Platform for Seismic Damage Assessment of Bridge Structures," by A.M. Reinhorn, V. Simeonov, G. Mylonakis and Y. Reichman, 10/2/98, (PB99-162919, A15, MF-A03).

MCEER-98-0012   "Experimental Investigation of the Dynamic Response of Two Bridges Before and After Retrofitting with Elastomeric Bearings," by D.A. Wendichansky, S.S. Chen and J.B. Mander, 10/2/98, (PB99-162927, A15, MF-A03).

MCEER-98-0013   "Design Procedures for Hinge Restrainers and Hinge Sear Width for Multiple-Frame Bridges," by R. Des Roches and G.L. Fenves, 11/3/98, (PB99-140477, A13, MF-A03).

MCEER-98-0014   "Response Modification Factors for Seismically Isolated Bridges," by M.C. Constantinou and J.K. Quarshie, 11/3/98, (PB99-140485, A14, MF-A03).

MCEER-98-0015   "Proceedings of the U.S.-Italy Workshop on Seismic Protective Systems for Bridges," edited by I.M. Friedland and M.C. Constantinou, 11/3/98, (PB2000-101711, A22, MF-A04).

MCEER-98-0016   "Appropriate Seismic Reliability for Critical Equipment Systems: Recommendations Based on Regional Analysis of Financial and Life Loss," by K. Porter, C. Scawthorn, C. Taylor and N. Blais, 11/10/98, (PB99-157265, A08, MF-A02).

MCEER-98-0017   "Proceedings of the U.S. Japan Joint Seminar on Civil Infrastructure Systems Research," edited by M. Shinozuka and A. Rose, 11/12/98, (PB99-156713, A16, MF-A03).

MCEER-98-0018   "Modeling of Pile Footings and Drilled Shafts for Seismic Design," by I. PoLam, M. Kapuskar and D. Chaudhuri, 12/21/98, (PB99-157257, A09, MF-A02).

MCEER-99-0001 "Seismic Evaluation of a Masonry Infilled Reinforced Concrete Frame by Pseudodynamic Testing," by S.G. Buonopane and R.N. White, 2/16/99, (PB99-162851, A09, MF-A02).

MCEER-99-0002 "Response History Analysis of Structures with Seismic Isolation and Energy Dissipation Systems: Verification Examples for Program SAP2000," by J. Scheller and M.C. Constantinou, 2/22/99, (PB99-162869, A08, MF-A02).

MCEER-99-0003 "Experimental Study on the Seismic Design and Retrofit of Bridge Columns Including Axial Load Effects," by A. Dutta, T. Kokorina and J.B. Mander, 2/22/99, (PB99-162877, A09, MF-A02).

MCEER-99-0004 "Experimental Study of Bridge Elastomeric and Other Isolation and Energy Dissipation Systems with Emphasis on Uplift Prevention and High Velocity Near-source Seismic Excitation," by A. Kasalanati and M. C. Constantinou, 2/26/99, (PB99-162885, A12, MF-A03).

MCEER-99-0005 "Truss Modeling of Reinforced Concrete Shear-flexure Behavior," by J.H. Kim and J.B. Mander, 3/8/99, (PB99-163693, A12, MF-A03).

MCEER-99-0006 "Experimental Investigation and Computational Modeling of Seismic Response of a 1:4 Scale Model Steel Structure with a Load Balancing Supplemental Damping System," by G. Pekcan, J.B. Mander and S.S. Chen, 4/2/99, (PB99-162893, A11, MF-A03).

MCEER-99-0007 "Effect of Vertical Ground Motions on the Structural Response of Highway Bridges," by M.R. Button, C.J. Cronin and R.L. Mayes, 4/10/99, (PB2000-101411, A10, MF-A03).

MCEER-99-0008 "Seismic Reliability Assessment of Critical Facilities: A Handbook, Supporting Documentation, and Model Code Provisions," by G.S. Johnson, R.E. Sheppard, M.D. Quilici, S.J. Eder and C.R. Scawthorn, 4/12/99, (PB2000-101701, A18, MF-A04).

MCEER-99-0009 "Impact Assessment of Selected MCEER Highway Project Research on the Seismic Design of Highway Structures," by C. Rojahn, R. Mayes, D.G. Anderson, J.H. Clark, D'Appolonia Engineering, S. Gloyd and R.V. Nutt, 4/14/99, (PB99-162901, A10, MF-A02).

MCEER-99-0010 "Site Factors and Site Categories in Seismic Codes," by R. Dobry, R. Ramos and M.S. Power, 7/19/99, (PB2000-101705, A08, MF-A02).

MCEER-99-0011 "Restrainer Design Procedures for Multi-Span Simply-Supported Bridges," by M.J. Randall, M. Saiidi, E. Maragakis and T. Isakovic, 7/20/99, (PB2000-101702, A10, MF-A02).

MCEER-99-0012 "Property Modification Factors for Seismic Isolation Bearings," by M.C. Constantinou, P. Tsopelas, A. Kasalanati and E. Wolff, 7/20/99, (PB2000-103387, A11, MF-A03).

MCEER-99-0013 "Critical Seismic Issues for Existing Steel Bridges," by P. Ritchie, N. Kauhl and J. Kulicki, 7/20/99, (PB2000-101697, A09, MF-A02).

MCEER-99-0014 "Nonstructural Damage Database," by A. Kao, T.T. Soong and A. Vender, 7/24/99, (PB2000-101407, A06, MF-A01).

MCEER-99-0015 "Guide to Remedial Measures for Liquefaction Mitigation at Existing Highway Bridge Sites," by H.G. Cooke and J. K. Mitchell, 7/26/99, (PB2000-101703, A11, MF-A03).

MCEER-99-0016 "Proceedings of the MCEER Workshop on Ground Motion Methodologies for the Eastern United States," edited by N. Abrahamson and A. Becker, 8/11/99, (PB2000-103385, A07, MF-A02).

MCEER-99-0017 "Quindío, Colombia Earthquake of January 25, 1999: Reconnaissance Report," by A.P. Asfura and P.J. Flores, 10/4/99, (PB2000-106893, A06, MF-A01).

MCEER-99-0018 "Hysteretic Models for Cyclic Behavior of Deteriorating Inelastic Structures," by M.V. Sivaselvan and A.M. Reinhorn, 11/5/99, (PB2000-103386, A08, MF-A02).

MCEER-99-0019   "Proceedings of the 7th U.S.- Japan Workshop on Earthquake Resistant Design of Lifeline Facilities and Countermeasures Against Soil Liquefaction," edited by T.D. O'Rourke, J.P. Bardet and M. Hamada, 11/19/99, (PB2000-103354, A99, MF-A06).

MCEER-99-0020   "Development of Measurement Capability for Micro-Vibration Evaluations with Application to Chip Fabrication Facilities," by G.C. Lee, Z. Liang, J.W. Song, J.D. Shen and W.C. Liu, 12/1/99, (PB2000-105993, A08, MF-A02).

MCEER-99-0021   "Design and Retrofit Methodology for Building Structures with Supplemental Energy Dissipating Systems," by G. Pekcan, J.B. Mander and S.S. Chen, 12/31/99, (PB2000-105994, A11, MF-A03).

MCEER-00-0001   "The Marmara, Turkey Earthquake of August 17, 1999: Reconnaissance Report," edited by C. Scawthorn; with major contributions by M. Bruneau, R. Eguchi, T. Holzer, G. Johnson, J. Mander, J. Mitchell, W. Mitchell, A. Papageorgiou, C. Scaethorn, and G. Webb, 3/23/00, (PB2000-106200, A11, MF-A03).

MCEER-00-0002   "Proceedings of the MCEER Workshop for Seismic Hazard Mitigation of Health Care Facilities," edited by G.C. Lee, M. Ettouney, M. Grigoriu, J. Hauer and J. Nigg, 3/29/00, (PB2000-106892, A08, MF-A02).

MCEER-00-0003   "The Chi-Chi, Taiwan Earthquake of September 21, 1999: Reconnaissance Report," edited by G.C. Lee and C.H. Loh, with major contributions by G.C. Lee, M. Bruneau, I.G. Buckle, S.E. Chang, P.J. Flores, T.D. O'Rourke, M. Shinozuka, T.T. Soong, C-H. Loh, K-C. Chang, Z-J. Chen, J-S. Hwang, M-L. Lin, G-Y. Liu, K-C. Tsai, G.C. Yao and C-L. Yen, 4/30/00, (PB2001-100980, A10, MF-A02).

MCEER-00-0004   "Seismic Retrofit of End-Sway Frames of Steel Deck-Truss Bridges with a Supplemental Tendon System: Experimental and Analytical Investigation," by G. Pekcan, J.B. Mander and S.S. Chen, 7/1/00, (PB2001-100982, A10, MF-A02).

MCEER-00-0005   "Sliding Fragility of Unrestrained Equipment in Critical Facilities," by W.H. Chong and T.T. Soong, 7/5/00, (PB2001-100983, A08, MF-A02).

MCEER-00-0006   "Seismic Response of Reinforced Concrete Bridge Pier Walls in the Weak Direction," by N. Abo-Shadi, M. Saiidi and D. Sanders, 7/17/00, (PB2001-100981, A17, MF-A03).

MCEER-00-0007   "Low-Cycle Fatigue Behavior of Longitudinal Reinforcement in Reinforced Concrete Bridge Columns," by J. Brown and S.K. Kunnath, 7/23/00, (PB2001-104392, A08, MF-A02).

MCEER-00-0008   "Soil Structure Interaction of Bridges for Seismic Analysis," I. PoLam and H. Law, 9/25/00, (PB2001-105397, A08, MF-A02).

MCEER-00-0009   "Proceedings of the First MCEER Workshop on Mitigation of Earthquake Disaster by Advanced Technologies (MEDAT-1), edited by M. Shinozuka, D.J. Inman and T.D. O'Rourke, 11/10/00, (PB2001-105399, A14, MF-A03).

MCEER-00-0010   "Development and Evaluation of Simplified Procedures for Analysis and Design of Buildings with Passive Energy Dissipation Systems, Revision 01," by O.M. Ramirez, M.C. Constantinou, C.A. Kircher, A.S. Whittaker, M.W. Johnson, J.D. Gomez and C. Chrysostomou, 11/16/01, (PB2001-105523, A23, MF-A04).

MCEER-00-0011   "Dynamic Soil-Foundation-Structure Interaction Analyses of Large Caissons," by C-Y. Chang, C-M. Mok, Z-L. Wang, R. Settgast, F. Waggoner, M.A. Ketchum, H.M. Gonnermann and C-C. Chin, 12/30/00, (PB2001-104373, A07, MF-A02).

MCEER-00-0012   "Experimental Evaluation of Seismic Performance of Bridge Restrainers," by A.G. Vlassis, E.M. Maragakis and M. Saiid Saiidi, 12/30/00, (PB2001-104354, A09, MF-A02).

MCEER-00-0013   "Effect of Spatial Variation of Ground Motion on Highway Structures," by M. Shinozuka, V. Saxena and G. Deodatis, 12/31/00, (PB2001-108755, A13, MF-A03).

MCEER-00-0014   "A Risk-Based Methodology for Assessing the Seismic Performance of Highway Systems," by S.D. Werner, C.E. Taylor, J.E. Moore, II, J.S. Walton and S. Cho, 12/31/00, (PB2001-108756, A14, MF-A03).

MCEER-01-0001 "Experimental Investigation of P-Delta Effects to Collapse During Earthquakes," by D. Vian and M. Bruneau, 6/25/01, (PB2002-100534, A17, MF-A03).

MCEER-01-0002 "Proceedings of the Second MCEER Workshop on Mitigation of Earthquake Disaster by Advanced Technologies (MEDAT-2)," edited by M. Bruneau and D.J. Inman, 7/23/01, (PB2002-100434, A16, MF-A03).

MCEER-01-0003 "Sensitivity Analysis of Dynamic Systems Subjected to Seismic Loads," by C. Roth and M. Grigoriu, 9/18/01, (PB2003-100884, A12, MF-A03).

MCEER-01-0004 "Overcoming Obstacles to Implementing Earthquake Hazard Mitigation Policies: Stage 1 Report," by D.J. Alesch and W.J. Petak, 12/17/01, (PB2002-107949, A07, MF-A02).

MCEER-01-0005 "Updating Real-Time Earthquake Loss Estimates: Methods, Problems and Insights," by C.E. Taylor, S.E. Chang and R.T. Eguchi, 12/17/01, (PB2002-107948, A05, MF-A01).

MCEER-01-0006 "Experimental Investigation and Retrofit of Steel Pile Foundations and Pile Bents Under Cyclic Lateral Loadings," by A. Shama, J. Mander, B. Blabac and S. Chen, 12/31/01, (PB2002-107950, A13, MF-A03).

MCEER-02-0001 "Assessment of Performance of Bolu Viaduct in the 1999 Duzce Earthquake in Turkey" by P.C. Roussis, M.C. Constantinou, M. Erdik, E. Durukal and M. Dicleli, 5/8/02, (PB2003-100883, A08, MF-A02).

MCEER-02-0002 "Seismic Behavior of Rail Counterweight Systems of Elevators in Buildings," by M.P. Singh, Rildova and L.E. Suarez, 5/27/02. (PB2003-100882, A11, MF-A03).

MCEER-02-0003 "Development of Analysis and Design Procedures for Spread Footings," by G. Mylonakis, G. Gazetas, S. Nikolaou and A. Chauncey, 10/02/02, (PB2004-101636, A13, MF-A03, CD-A13).

MCEER-02-0004 "Bare-Earth Algorithms for Use with SAR and LIDAR Digital Elevation Models," by C.K. Huyck, R.T. Eguchi and B. Houshmand, 10/16/02, (PB2004-101637, A07, CD-A07).

MCEER-02-0005 "Review of Energy Dissipation of Compression Members in Concentrically Braced Frames," by K.Lee and M. Bruneau, 10/18/02, (PB2004-101638, A10, CD-A10).

MCEER-03-0001 "Experimental Investigation of Light-Gauge Steel Plate Shear Walls for the Seismic Retrofit of Buildings" by J. Berman and M. Bruneau, 5/2/03, (PB2004-101622, A10, MF-A03, CD-A10).

MCEER-03-0002 "Statistical Analysis of Fragility Curves," by M. Shinozuka, M.Q. Feng, H. Kim, T. Uzawa and T. Ueda, 6/16/03, (PB2004-101849, A09, CD-A09).

MCEER-03-0003 "Proceedings of the Eighth U.S.-Japan Workshop on Earthquake Resistant Design f Lifeline Facilities and Countermeasures Against Liquefaction," edited by M. Hamada, J.P. Bardet and T.D. O'Rourke, 6/30/03, (PB2004-104386, A99, CD-A99).

MCEER-03-0004 "Proceedings of the PRC-US Workshop on Seismic Analysis and Design of Special Bridges," edited by L.C. Fan and G.C. Lee, 7/15/03, (PB2004-104387, A14, CD-A14).

MCEER-03-0005 "Urban Disaster Recovery: A Framework and Simulation Model," by S.B. Miles and S.E. Chang, 7/25/03, (PB2004-104388, A07, CD-A07).

MCEER-03-0006 "Behavior of Underground Piping Joints Due to Static and Dynamic Loading," by R.D. Meis, M. Maragakis and R. Siddharthan, 11/17/03, (PB2005-102194, A13, MF-A03, CD-A00).

MCEER-04-0001 "Experimental Study of Seismic Isolation Systems with Emphasis on Secondary System Response and Verification of Accuracy of Dynamic Response History Analysis Methods," by E. Wolff and M. Constantinou, 1/16/04 (PB2005-102195, A99, MF-E08, CD-A00).

MCEER-04-0002 "Tension, Compression and Cyclic Testing of Engineered Cementitious Composite Materials," by K. Kesner and S.L. Billington, 3/1/04, (PB2005-102196, A08, CD-A08).

MCEER-04-0003   "Cyclic Testing of Braces Laterally Restrained by Steel Studs to Enhance Performance During Earthquakes," by O.C. Celik, J.W. Berman and M. Bruneau, 3/16/04, (PB2005-102197, A13, MF-A03, CD-A00).

MCEER-04-0004   "Methodologies for Post Earthquake Building Damage Detection Using SAR and Optical Remote Sensing: Application to the August 17, 1999 Marmara, Turkey Earthquake," by C.K. Huyck, B.J. Adams, S. Cho, R.T. Eguchi, B. Mansouri and B. Houshmand, 6/15/04, (PB2005-104888, A10, CD-A00).

MCEER-04-0005   "Nonlinear Structural Analysis Towards Collapse Simulation: A Dynamical Systems Approach," by M.V. Sivaselvan and A.M. Reinhorn, 6/16/04, (PB2005-104889, A11, MF-A03, CD-A00).

MCEER-04-0006   "Proceedings of the Second PRC-US Workshop on Seismic Analysis and Design of Special Bridges," edited by G.C. Lee and L.C. Fan, 6/25/04, (PB2005-104890, A16, CD-A00).

MCEER-04-0007   "Seismic Vulnerability Evaluation of Axially Loaded Steel Built-up Laced Members," by K. Lee and M. Bruneau, 6/30/04, (PB2005-104891, A16, CD-A00).

MCEER-04-0008   "Evaluation of Accuracy of Simplified Methods of Analysis and Design of Buildings with Damping Systems for Near-Fault and for Soft-Soil Seismic Motions," by E.A. Pavlou and M.C. Constantinou, 8/16/04, (PB2005-104892, A08, MF-A02, CD-A00).

MCEER-04-0009   "Assessment of Geotechnical Issues in Acute Care Facilities in California," by M. Lew, T.D. O'Rourke, R. Dobry and M. Koch, 9/15/04, (PB2005-104893, A08, CD-A00).

MCEER-04-0010   "Scissor-Jack-Damper Energy Dissipation System," by A.N. Sigaher-Boyle and M.C. Constantinou, 12/1/04 (PB2005-108221).

MCEER-04-0011   "Seismic Retrofit of Bridge Steel Truss Piers Using a Controlled Rocking Approach," by M. Pollino and M. Bruneau, 12/20/04 (PB2006-105795).

MCEER-05-0001   "Experimental and Analytical Studies of Structures Seismically Isolated with an Uplift-Restraint Isolation System," by P.C. Roussis and M.C. Constantinou, 1/10/05 (PB2005-108222).

MCEER-05-0002   "A Versatile Experimentation Model for Study of Structures Near Collapse Applied to Seismic Evaluation of Irregular Structures," by D. Kusumastuti, A.M. Reinhorn and A. Rutenberg, 3/31/05 (PB2006-101523).

MCEER-05-0003   "Proceedings of the Third PRC-US Workshop on Seismic Analysis and Design of Special Bridges," edited by L.C. Fan and G.C. Lee, 4/20/05, (PB2006-105796).

MCEER-05-0004   "Approaches for the Seismic Retrofit of Braced Steel Bridge Piers and Proof-of-Concept Testing of an Eccentrically Braced Frame with Tubular Link," by J.W. Berman and M. Bruneau, 4/21/05 (PB2006-101524).

MCEER-05-0005   "Simulation of Strong Ground Motions for Seismic Fragility Evaluation of Nonstructural Components in Hospitals," by A. Wanitkorkul and A. Filiatrault, 5/26/05 (PB2006-500027).

MCEER-05-0006   "Seismic Safety in California Hospitals: Assessing an Attempt to Accelerate the Replacement or Seismic Retrofit of Older Hospital Facilities," by D.J. Alesch, L.A. Arendt and W.J. Petak, 6/6/05 (PB2006-105794).

MCEER-05-0007   "Development of Seismic Strengthening and Retrofit Strategies for Critical Facilities Using Engineered Cementitious Composite Materials," by K. Kesner and S.L. Billington, 8/29/05 (PB2006-111701).

MCEER-05-0008   "Experimental and Analytical Studies of Base Isolation Systems for Seismic Protection of Power Transformers," by N. Murota, M.Q. Feng and G-Y. Liu, 9/30/05 (PB2006-111702).

MCEER-05-0009   "3D-BASIS-ME-MB: Computer Program for Nonlinear Dynamic Analysis of Seismically Isolated Structures," by P.C. Tsopelas, P.C. Roussis, M.C. Constantinou, R. Buchanan and A.M. Reinhorn, 10/3/05 (PB2006-111703).

MCEER-05-0010   "Steel Plate Shear Walls for Seismic Design and Retrofit of Building Structures," by D. Vian and M. Bruneau, 12/15/05 (PB2006-111704).

MCEER-05-0011   "The Performance-Based Design Paradigm," by M.J. Astrella and A. Whittaker, 12/15/05 (PB2006-111705).

MCEER-06-0001   "Seismic Fragility of Suspended Ceiling Systems," H. Badillo-Almaraz, A.S. Whittaker, A.M. Reinhorn and G.P. Cimellaro, 2/4/06 (PB2006-111706).

MCEER-06-0002   "Multi-Dimensional Fragility of Structures," by G.P. Cimellaro, A.M. Reinhorn and M. Bruneau, 3/1/06 (PB2007-106974, A09, MF-A02, CD A00).

MCEER-06-0003   "Built-Up Shear Links as Energy Dissipators for Seismic Protection of Bridges," by P. Dusicka, A.M. Itani and I.G. Buckle, 3/15/06 (PB2006-111708).

MCEER-06-0004   "Analytical Investigation of the Structural Fuse Concept," by R.E. Vargas and M. Bruneau, 3/16/06 (PB2006-111709).

MCEER-06-0005   "Experimental Investigation of the Structural Fuse Concept," by R.E. Vargas and M. Bruneau, 3/17/06 (PB2006-111710).

MCEER-06-0006   "Further Development of Tubular Eccentrically Braced Frame Links for the Seismic Retrofit of Braced Steel Truss Bridge Piers," by J.W. Berman and M. Bruneau, 3/27/06 (PB2007-105147).

MCEER-06-0007   "REDARS Validation Report," by S. Cho, C.K. Huyck, S. Ghosh and R.T. Eguchi, 8/8/06 (PB2007-106983).

MCEER-06-0008   "Review of Current NDE Technologies for Post-Earthquake Assessment of Retrofitted Bridge Columns," by J.W. Song, Z. Liang and G.C. Lee, 8/21/06 (PB2007-106984).

MCEER-06-0009   "Liquefaction Remediation in Silty Soils Using Dynamic Compaction and Stone Columns," by S. Thevanayagam, G.R. Martin, R. Nashed, T. Shenthan, T. Kanagalingam and N. Ecemis, 8/28/06 (PB2007-106985).

MCEER-06-0010   "Conceptual Design and Experimental Investigation of Polymer Matrix Composite Infill Panels for Seismic Retrofitting," by W. Jung, M. Chiewanichakorn and A.J. Aref, 9/21/06 (PB2007-106986).

MCEER-06-0011   "A Study of the Coupled Horizontal-Vertical Behavior of Elastomeric and Lead-Rubber Seismic Isolation Bearings," by G.P. Warn and A.S. Whittaker, 9/22/06 (PB2007-108679).

MCEER-06-0012   "Proceedings of the Fourth PRC-US Workshop on Seismic Analysis and Design of Special Bridges: Advancing Bridge Technologies in Research, Design, Construction and Preservation," Edited by L.C. Fan, G.C. Lee and L. Ziang, 10/12/06 (PB2007-109042).

MCEER-06-0013   "Cyclic Response and Low Cycle Fatigue Characteristics of Plate Steels," by P. Dusicka, A.M. Itani and I.G. Buckle, 11/1/06 06 (PB2007-106987).

MCEER-06-0014   "Proceedings of the Second US-Taiwan Bridge Engineering Workshop," edited by W.P. Yen, J. Shen, J-Y. Chen and M. Wang, 11/15/06 (PB2008-500041).

MCEER-06-0015   "User Manual and Technical Documentation for the REDARS™ Import Wizard," by S. Cho, S. Ghosh, C.K. Huyck and S.D. Werner, 11/30/06 (PB2007-114766).

MCEER-06-0016   "Hazard Mitigation Strategy and Monitoring Technologies for Urban and Infrastructure Public Buildings: Proceedings of the China-US Workshops," edited by X.Y. Zhou, A.L. Zhang, G.C. Lee and M. Tong, 12/12/06 (PB2008-500018).

MCEER-07-0001   "Static and Kinetic Coefficients of Friction for Rigid Blocks," by C. Kafali, S. Fathali, M. Grigoriu and A.S. Whittaker, 3/20/07 (PB2007-114767).

MCEER-07-0002   "Hazard Mitigation Investment Decision Making: Organizational Response to Legislative Mandate," by L.A. Arendt, D.J. Alesch and W.J. Petak, 4/9/07 (PB2007-114768).

MCEER-07-0003   "Seismic Behavior of Bidirectional-Resistant Ductile End Diaphragms with Unbonded Braces in Straight or Skewed Steel Bridges," by O. Celik and M. Bruneau, 4/11/07 (PB2008-105141).

MCEER-07-0004   "Modeling Pile Behavior in Large Pile Groups Under Lateral Loading," by A.M. Dodds and G.R. Martin, 4/16/07(PB2008-105142).

MCEER-07-0005   "Experimental Investigation of Blast Performance of Seismically Resistant Concrete-Filled Steel Tube Bridge Piers," by S. Fujikura, M. Bruneau and D. Lopez-Garcia, 4/20/07 (PB2008-105143).

MCEER-07-0006   "Seismic Analysis of Conventional and Isolated Liquefied Natural Gas Tanks Using Mechanical Analogs," by I.P. Christovasilis and A.S. Whittaker, 5/1/07, not available.

MCEER-07-0007   "Experimental Seismic Performance Evaluation of Isolation/Restraint Systems for Mechanical Equipment – Part 1: Heavy Equipment Study," by S. Fathali and A. Filiatrault, 6/6/07 (PB2008-105144).

MCEER-07-0008   "Seismic Vulnerability of Timber Bridges and Timber Substructures," by A.A. Sharma, J.B. Mander, I.M. Friedland and D.R. Allicock, 6/7/07 (PB2008-105145).

MCEER-07-0009   "Experimental and Analytical Study of the XY-Friction Pendulum (XY-FP) Bearing for Bridge Applications," by C.C. Marin-Artieda, A.S. Whittaker and M.C. Constantinou, 6/7/07 (PB2008-105191).

MCEER-07-0010   "Proceedings of the PRC-US Earthquake Engineering Forum for Young Researchers," Edited by G.C. Lee and X.Z. Qi, 6/8/07 (PB2008-500058).

MCEER-07-0011   "Design Recommendations for Perforated Steel Plate Shear Walls," by R. Purba and M. Bruneau, 6/18/07, (PB2008-105192).

MCEER-07-0012   "Performance of Seismic Isolation Hardware Under Service and Seismic Loading," by M.C. Constantinou, A.S. Whittaker, Y. Kalpakidis, D.M. Fenz and G.P. Warn, 8/27/07, (PB2008-105193).

MCEER-07-0013   "Experimental Evaluation of the Seismic Performance of Hospital Piping Subassemblies," by E.R. Goodwin, E. Maragakis and A.M. Itani, 9/4/07, (PB2008-105194).

MCEER-07-0014   "A Simulation Model of Urban Disaster Recovery and Resilience: Implementation for the 1994 Northridge Earthquake," by S. Miles and S.E. Chang, 9/7/07, (PB2008-106426).

MCEER-07-0015   "Statistical and Mechanistic Fragility Analysis of Concrete Bridges," by M. Shinozuka, S. Banerjee and S-H. Kim, 9/10/07, (PB2008-106427).

MCEER-07-0016   "Three-Dimensional Modeling of Inelastic Buckling in Frame Structures," by M. Schachter and AM. Reinhorn, 9/13/07, (PB2008-108125).

MCEER-07-0017   "Modeling of Seismic Wave Scattering on Pile Groups and Caissons," by I. Po Lam, H. Law and C.T. Yang, 9/17/07 (PB2008-108150).

MCEER-07-0018   "Bridge Foundations: Modeling Large Pile Groups and Caissons for Seismic Design," by I. Po Lam, H. Law and G.R. Martin (Coordinating Author), 12/1/07 (PB2008-111190).

MCEER-07-0019   "Principles and Performance of Roller Seismic Isolation Bearings for Highway Bridges," by G.C. Lee, Y.C. Ou, Z. Liang, T.C. Niu and J. Song, 12/10/07 (PB2009-110466).

MCEER-07-0020   "Centrifuge Modeling of Permeability and Pinning Reinforcement Effects on Pile Response to Lateral Spreading," by L.L Gonzalez-Lagos, T. Abdoun and R. Dobry, 12/10/07 (PB2008-111191).

MCEER-07-0021   "Damage to the Highway System from the Pisco, Perú Earthquake of August 15, 2007," by J.S. O'Connor, L. Mesa and M. Nykamp, 12/10/07, (PB2008-108126).

MCEER-07-0022   "Experimental Seismic Performance Evaluation of Isolation/Restraint Systems for Mechanical Equipment – Part 2: Light Equipment Study," by S. Fathali and A. Filiatrault, 12/13/07 (PB2008-111192).

MCEER-07-0023   "Fragility Considerations in Highway Bridge Design," by M. Shinozuka, S. Banerjee and S.H. Kim, 12/14/07 (PB2008-111193).

MCEER-07-0024   "Performance Estimates for Seismically Isolated Bridges," by G.P. Warn and A.S. Whittaker, 12/30/07 (PB2008-112230).

MCEER-08-0001   "Seismic Performance of Steel Girder Bridge Superstructures with Conventional Cross Frames," by L.P. Carden, A.M. Itani and I.G. Buckle, 1/7/08, (PB2008-112231).

MCEER-08-0002   "Seismic Performance of Steel Girder Bridge Superstructures with Ductile End Cross Frames with Seismic Isolators," by L.P. Carden, A.M. Itani and I.G. Buckle, 1/7/08 (PB2008-112232).

MCEER-08-0003   "Analytical and Experimental Investigation of a Controlled Rocking Approach for Seismic Protection of Bridge Steel Truss Piers," by M. Pollino and M. Bruneau, 1/21/08 (PB2008-112233).

MCEER-08-0004   "Linking Lifeline Infrastructure Performance and Community Disaster Resilience: Models and Multi-Stakeholder Processes," by S.E. Chang, C. Pasion, K. Tatebe and R. Ahmad, 3/3/08 (PB2008-112234).

MCEER-08-0005   "Modal Analysis of Generally Damped Linear Structures Subjected to Seismic Excitations," by J. Song, Y-L. Chu, Z. Liang and G.C. Lee, 3/4/08 (PB2009-102311).

MCEER-08-0006   "System Performance Under Multi-Hazard Environments," by C. Kafali and M. Grigoriu, 3/4/08 (PB2008-112235).

MCEER-08-0007   "Mechanical Behavior of Multi-Spherical Sliding Bearings," by D.M. Fenz and M.C. Constantinou, 3/6/08 (PB2008-112236).

MCEER-08-0008   "Post-Earthquake Restoration of the Los Angeles Water Supply System," by T.H.P. Tabucchi and R.A. Davidson, 3/7/08 (PB2008-112237).

MCEER-08-0009   "Fragility Analysis of Water Supply Systems," by A. Jacobson and M. Grigoriu, 3/10/08 (PB2009-105545).

MCEER-08-0010   "Experimental Investigation of Full-Scale Two-Story Steel Plate Shear Walls with Reduced Beam Section Connections," by B. Qu, M. Bruneau, C-H. Lin and K-C. Tsai, 3/17/08 (PB2009-106368).

MCEER-08-0011   "Seismic Evaluation and Rehabilitation of Critical Components of Electrical Power Systems," S. Ersoy, B. Feizi, A. Ashrafi and M. Ala Saadeghvaziri, 3/17/08 (PB2009-105546).

MCEER-08-0012   "Seismic Behavior and Design of Boundary Frame Members of Steel Plate Shear Walls," by B. Qu and M. Bruneau, 4/26/08 . (PB2009-106744).

MCEER-08-0013   "Development and Appraisal of a Numerical Cyclic Loading Protocol for Quantifying Building System Performance," by A. Filiatrault, A. Wanitkorkul and M. Constantinou, 4/27/08 (PB2009-107906).

MCEER-08-0014   "Structural and Nonstructural Earthquake Design: The Challenge of Integrating Specialty Areas in Designing Complex, Critical Facilities," by W.J. Petak and D.J. Alesch, 4/30/08 (PB2009-107907).

MCEER-08-0015   "Seismic Performance Evaluation of Water Systems," by Y. Wang and T.D. O'Rourke, 5/5/08 (PB2009-107908).

MCEER-08-0016   "Seismic Response Modeling of Water Supply Systems," by P. Shi and T.D. O'Rourke, 5/5/08 (PB2009-107910).

MCEER-08-0017   "Numerical and Experimental Studies of Self-Centering Post-Tensioned Steel Frames," by D. Wang and A. Filiatrault, 5/12/08 (PB2009-110479).

MCEER-08-0018   "Development, Implementation and Verification of Dynamic Analysis Models for Multi-Spherical Sliding Bearings," by D.M. Fenz and M.C. Constantinou, 8/15/08 (PB2009-107911).

MCEER-08-0019   "Performance Assessment of Conventional and Base Isolated Nuclear Power Plants for Earthquake Blast Loadings," by Y.N. Huang, A.S. Whittaker and N. Luco, 10/28/08 (PB2009-107912).

MCEER-08-0020   "Remote Sensing for Resilient Multi-Hazard Disaster Response – Volume I: Introduction to Damage Assessment Methodologies," by B.J. Adams and R.T. Eguchi, 11/17/08 (PB2010-102695).

MCEER-08-0021   "Remote Sensing for Resilient Multi-Hazard Disaster Response – Volume II: Counting the Number of Collapsed Buildings Using an Object-Oriented Analysis: Case Study of the 2003 Bam Earthquake," by L. Gusella, C.K. Huyck and B.J. Adams, 11/17/08 (PB2010-100925).

MCEER-08-0022   "Remote Sensing for Resilient Multi-Hazard Disaster Response – Volume III: Multi-Sensor Image Fusion Techniques for Robust Neighborhood-Scale Urban Damage Assessment," by B.J. Adams and A. McMillan, 11/17/08 (PB2010-100926).

MCEER-08-0023   "Remote Sensing for Resilient Multi-Hazard Disaster Response – Volume IV: A Study of Multi-Temporal and Multi-Resolution SAR Imagery for Post-Katrina Flood Monitoring in New Orleans," by A. McMillan, J.G. Morley, B.J. Adams and S. Chesworth, 11/17/08 (PB2010-100927).

MCEER-08-0024   "Remote Sensing for Resilient Multi-Hazard Disaster Response – Volume V: Integration of Remote Sensing Imagery and VIEWS^{TM} Field Data for Post-Hurricane Charley Building Damage Assessment," by J.A. Womble, K. Mehta and B.J. Adams, 11/17/08 (PB2009-115532).

MCEER-08-0025   "Building Inventory Compilation for Disaster Management: Application of Remote Sensing and Statistical Modeling," by P. Sarabandi, A.S. Kiremidjian, R.T. Eguchi and B. J. Adams, 11/20/08 (PB2009-110484).

MCEER-08-0026   "New Experimental Capabilities and Loading Protocols for Seismic Qualification and Fragility Assessment of Nonstructural Systems," by R. Retamales, G. Mosqueda, A. Filiatrault and A. Reinhorn, 11/24/08 (PB2009-110485).

MCEER-08-0027   "Effects of Heating and Load History on the Behavior of Lead-Rubber Bearings," by I.V. Kalpakidis and M.C. Constantinou, 12/1/08 (PB2009-115533).

MCEER-08-0028   "Experimental and Analytical Investigation of Blast Performance of Seismically Resistant Bridge Piers," by S.Fujikura and M. Bruneau, 12/8/08 (PB2009-115534).

MCEER-08-0029   "Evolutionary Methodology for Aseismic Decision Support," by Y. Hu and G. Dargush, 12/15/08.

MCEER-08-0030   "Development of a Steel Plate Shear Wall Bridge Pier System Conceived from a Multi-Hazard Perspective," by D. Keller and M. Bruneau, 12/19/08 (PB2010-102696).

MCEER-09-0001   "Modal Analysis of Arbitrarily Damped Three-Dimensional Linear Structures Subjected to Seismic Excitations," by Y.L. Chu, J. Song and G.C. Lee, 1/31/09 (PB2010-100922).

MCEER-09-0002   "Air-Blast Effects on Structural Shapes," by G. Ballantyne, A.S. Whittaker, A.J. Aref and G.F. Dargush, 2/2/09 (PB2010-102697).

MCEER-09-0003   "Water Supply Performance During Earthquakes and Extreme Events," by A.L. Bonneau and T.D. O'Rourke, 2/16/09 (PB2010-100923).

MCEER-09-0004   "Generalized Linear (Mixed) Models of Post-Earthquake Ignitions," by R.A. Davidson, 7/20/09 (PB2010-102698).

MCEER-09-0005   "Seismic Testing of a Full-Scale Two-Story Light-Frame Wood Building: NEESWood Benchmark Test," by I.P. Christovasilis, A. Filiatrault and A. Wanitkorkul, 7/22/09 (PB2012-102401).

MCEER-09-0006   "IDARC2D Version 7.0: A Program for the Inelastic Damage Analysis of Structures," by A.M. Reinhorn, H. Roh, M. Sivaselvan, S.K. Kunnath, R.E. Valles, A. Madan, C. Li, R. Lobo and Y.J. Park, 7/28/09 (PB2010-103199).

MCEER-09-0007   "Enhancements to Hospital Resiliency: Improving Emergency Planning for and Response to Hurricanes," by D.B. Hess and L.A. Arendt, 7/30/09 (PB2010-100924).

MCEER-09-0008 "Assessment of Base-Isolated Nuclear Structures for Design and Beyond-Design Basis Earthquake Shaking," by Y.N. Huang, A.S. Whittaker, R.P. Kennedy and R.L. Mayes, 8/20/09 (PB2010-102699).

MCEER-09-0009 "Quantification of Disaster Resilience of Health Care Facilities," by G.P. Cimellaro, C. Fumo, A.M Reinhorn and M. Bruneau, 9/14/09 (PB2010-105384).

MCEER-09-0010 "Performance-Based Assessment and Design of Squat Reinforced Concrete Shear Walls," by C.K. Gulec and A.S. Whittaker, 9/15/09 (PB2010-102700).

MCEER-09-0011 "Proceedings of the Fourth US-Taiwan Bridge Engineering Workshop," edited by W.P. Yen, J.J. Shen, T.M. Lee and R.B. Zheng, 10/27/09 (PB2010-500009).

MCEER-09-0012 "Proceedings of the Special International Workshop on Seismic Connection Details for Segmental Bridge Construction," edited by W. Phillip Yen and George C. Lee, 12/21/09 (PB2012-102402).

MCEER-10-0001 "Direct Displacement Procedure for Performance-Based Seismic Design of Multistory Woodframe Structures," by W. Pang and D. Rosowsky, 4/26/10 (PB2012-102403).

MCEER-10-0002 "Simplified Direct Displacement Design of Six-Story NEESWood Capstone Building and Pre-Test Seismic Performance Assessment," by W. Pang, D. Rosowsky, J. van de Lindt and S. Pei, 5/28/10 (PB2012-102404).

MCEER-10-0003 "Integration of Seismic Protection Systems in Performance-Based Seismic Design of Woodframed Structures," by J.K. Shinde and M.D. Symans, 6/18/10 (PB2012-102405).

MCEER-10-0004 "Modeling and Seismic Evaluation of Nonstructural Components: Testing Frame for Experimental Evaluation of Suspended Ceiling Systems," by A.M. Reinhorn, K.P. Ryu and G. Maddaloni, 6/30/10 (PB2012-102406).

MCEER-10-0005 "Analytical Development and Experimental Validation of a Structural-Fuse Bridge Pier Concept," by S. El-Bahey and M. Bruneau, 10/1/10 (PB2012-102407).

MCEER-10-0006 "A Framework for Defining and Measuring Resilience at the Community Scale: The PEOPLES Resilience Framework," by C.S. Renschler, A.E. Frazier, L.A. Arendt, G.P. Cimellaro, A.M. Reinhorn and M. Bruneau, 10/8/10 (PB2012-102408).

MCEER-10-0007 "Impact of Horizontal Boundary Elements Design on Seismic Behavior of Steel Plate Shear Walls," by R. Purba and M. Bruneau, 11/14/10 (PB2012-102409).

MCEER-10-0008 "Seismic Testing of a Full-Scale Mid-Rise Building: The NEESWood Capstone Test," by S. Pei, J.W. van de Lindt, S.E. Pryor, H. Shimizu, H. Isoda and D.R. Rammer, 12/1/10 (PB2012-102410).

MCEER-10-0009 "Modeling the Effects of Detonations of High Explosives to Inform Blast-Resistant Design," by P. Sherkar, A.S. Whittaker and A.J. Aref, 12/1/10 (PB2012-102411).

MCEER-10-0010 "L'Aquila Earthquake of April 6, 2009 in Italy: Rebuilding a Resilient City to Withstand Multiple Hazards," by G.P. Cimellaro, I.P. Christovasilis, A.M. Reinhorn, A. De Stefano and T. Kirova, 12/29/10.

MCEER-11-0001 "Numerical and Experimental Investigation of the Seismic Response of Light-Frame Wood Structures," by I.P. Christovasilis and A. Filiatrault, 8/8/11 (PB2012-102412).

MCEER-11-0002 "Seismic Design and Analysis of a Precast Segmental Concrete Bridge Model," by M. Anagnostopoulou, A. Filiatrault and A. Aref, 9/15/11.

MCEER-11-0003 'Proceedings of the Workshop on Improving Earthquake Response of Substation Equipment," Edited by A.M. Reinhorn, 9/19/11 (PB2012-102413).

MCEER-11-0004 "LRFD-Based Analysis and Design Procedures for Bridge Bearings and Seismic Isolators," by M.C. Constantinou, I. Kalpakidis, A. Filiatrault and R.A. Ecker Lay, 9/26/11.

MCEER-11-0005 "Experimental Seismic Evaluation, Model Parameterization, and Effects of Cold-Formed Steel-Framed Gypsum Partition Walls on the Seismic Performance of an Essential Facility," by R. Davies, R. Retamales, G. Mosqueda and A. Filiatrault, 10/12/11.

MCEER-11-0006 "Modeling and Seismic Performance Evaluation of High Voltage Transformers and Bushings," by A.M. Reinhorn, K. Oikonomou, H. Roh, A. Schiff and L. Kempner, Jr., 10/3/11.

MCEER-11-0007 "Extreme Load Combinations: A Survey of State Bridge Engineers," by G.C. Lee, Z. Liang, J.J. Shen and J.S. O'Connor, 10/14/11.

MCEER-12-0001 "Simplified Analysis Procedures in Support of Performance Based Seismic Design," by Y.N. Huang and A.S. Whittaker.

MCEER-12-0002 "Seismic Protection of Electrical Transformer Bushing Systems by Stiffening Techniques," by M. Koliou, A. Filiatrault, A.M. Reinhorn and N. Oliveto, 6/1/12.

MCEER-12-0003 "Post-Earthquake Bridge Inspection Guidelines," by J.S. O'Connor and S. Alampalli, 6/8/12.

MCEER-12-0004 "Integrated Design Methodology for Isolated Floor Systems in Single-Degree-of-Freedom Structural Fuse Systems," by S. Cui, M. Bruneau and M.C. Constantinou, 6/13/12.

MCEER-12-0005 "Characterizing the Rotational Components of Earthquake Ground Motion," by D. Basu, A.S. Whittaker and M.C. Constantinou, 6/15/12.

MCEER-12-0006 "Bayesian Fragility for Nonstructural Systems," by C.H. Lee and M.D. Grigoriu, 9/12/12.

MCEER-12-0007 "A Numerical Model for Capturing the In-Plane Seismic Response of Interior Metal Stud Partition Walls," by R.L. Wood and T.C. Hutchinson, 9/12/12.

MCEER-12-0008 "Assessment of Floor Accelerations in Yielding Buildings," by J.D. Wieser, G. Pekcan, A.E. Zaghi, A.M. Itani and E. Maragakis, 10/5/12.

MCEER-13-0001 "Experimental Seismic Study of Pressurized Fire Sprinkler Piping Systems," by Y. Tian, A. Filiatrault and G. Mosqueda, 4/8/13.

MCEER-13-0002 "Enhancing Resource Coordination for Multi-Modal Evacuation Planning," by D.B. Hess, B.W. Conley and C.M. Farrell, 2/8/13.

MCEER-13-0003 "Seismic Response of Base Isolated Buildings Considering Pounding to Moat Walls," by A. Masroor and G. Mosqueda, 2/26/13.

MCEER-13-0004 "Seismic Response Control of Structures Using a Novel Adaptive Passive Negative Stiffness Device," by D.T.R. Pasala, A.A. Sarlis, S. Nagarajaiah, A.M. Reinhorn, M.C. Constantinou and D.P. Taylor, 6/10/13.

MCEER-13-0005 "Negative Stiffness Device for Seismic Protection of Structures," by A.A. Sarlis, D.T.R. Pasala, M.C. Constantinou, A.M. Reinhorn, S. Nagarajaiah and D.P. Taylor, 6/12/13.

MCEER-13-0006 "Emilia Earthquake of May 20, 2012 in Northern Italy: Rebuilding a Resilient Community to Withstand Multiple Hazards," by G.P. Cimellaro, M. Chiriatti, A.M. Reinhorn and L. Tirca, June 30, 2013.

MCEER-13-0007 "Precast Concrete Segmental Components and Systems for Accelerated Bridge Construction in Seismic Regions," by A.J. Aref, G.C. Lee, Y.C. Ou and P. Sideris, with contributions from K.C. Chang, S. Chen, A. Filiatrault and Y. Zhou, June 13, 2013.

MCEER-13-0008 "A Study of U.S. Bridge Failures (1980-2012)," by G.C. Lee, S.B. Mohan, C. Huang and B.N. Fard, June 15, 2013.

MCEER-13-0009 "Development of a Database Framework for Modeling Damaged Bridges," by G.C. Lee, J.C. Qi and C. Huang, June 16, 2013.

MCEER-13-0010   "Model of Triple Friction Pendulum Bearing for General Geometric and Frictional Parameters and for Uplift Conditions," by A.A. Sarlis and M.C. Constantinou, July 1, 2013.

MCEER-13-0011   "Shake Table Testing of Triple Friction Pendulum Isolators under Extreme Conditions," by A.A. Sarlis, M.C. Constantinou and A.M. Reinhorn, July 2, 2013.

MCEER-13-0012   "Theoretical Framework for the Development of MH-LRFD," by G.C. Lee (coordinating author), H.A Capers, Jr., C. Huang, J.M. Kulicki, Z. Liang, T. Murphy, J.J.D. Shen, M. Shinozuka and P.W.H. Yen, July 31, 2013.

MCEER-13-0013   "Seismic Protection of Highway Bridges with Negative Stiffness Devices," by N.K.A. Attary, M.D. Symans, S. Nagarajaiah, A.M. Reinhorn, M.C. Constantinou, A.A. Sarlis, D.T.R. Pasala, and D.P. Taylor, September 3, 2014.

MCEER-14-0001   "Simplified Seismic Collapse Capacity-Based Evaluation and Design of Frame Buildings with and without Supplemental Damping Systems," by M. Hamidia, A. Filiatrault, and A. Aref, May 19, 2014.

MCEER-14-0002   "Comprehensive Analytical Seismic Fragility of Fire Sprinkler Piping Systems," by Siavash Soroushian, Emmanuel "Manos" Maragakis, Arash E. Zaghi, Alicia Echevarria, Yuan Tian and Andre Filiatrault, August 26, 2014.

MCEER-14-0003   "Hybrid Simulation of the Seismic Response of a Steel Moment Frame Building Structure through Collapse," by M. Del Carpio Ramos, G. Mosqueda and D.G. Lignos, October 20, 2014.

MCEER-14-0005   "Seismic Performance of Steel Plate Shear Walls Considering Various Design Approaches," by R. Purba and M. Bruneau, October 31, 2014.